COLLECTED PAPERS on

Dressed Photon Science and Technology

Vol. 28

August 2012 – July 2013

Prof. Motoichi OHTSU

MEMBERS

(From April 1, 2014)

[I] The University of Tokyo*

Professor

Motoichi OHTSU[(a-c)] (Dr. Eng.)

Associate Professor

Takashi YATSUI (Dr. Eng.)

Researcher

Makoto NARUSE (Dr. Eng.)
Senior Researcher, National Institute of Information and Communications Technology (NICT)

Graduate Students (Doctor Candidate)

Hajime TANAKA
KIM JunHyoung

Graduate Students (Master Course)

YU Byungho
Naoki WADA
Nabila TANJEEM
Maiku YAMAGUCHI

Undergraduate Students

Ko CHIEDA
Vo Quoc HUY
Kentaro SUZUKI

Assistants

Sachiyo KOJIMA
Noriko KUROKI
Kumiko NOZAWA

a) Also a director “Nanophotonics Research Center, The Institute of Engineering Innovation, School of Engineering The University of Tokyo”
b) Also a director, “Development of Next-generation High-performance Technology for Photovoltaic Power Generation System and NEDO (New Energy and Industrial Technology Development Organization)
c) Also a director, NPO-Research Institute of Nanophotonics

(*)
Department of Electronics Engineering and Information Systems,
Graduate School of Engineering,
The University of Tokyo
(Room 215, Bldg. Eng. 9)
2-11-16 Yayoi, Bunkyo-ku, Tokyo 113-8656, Japan
Phone: +81-3-5841-1189
FAX: +81-3-5841-1140
E-mail: ohtsu@ee.t.u-tokyo.ac.jp
URL:http://uuu.t.u-tokyo.ac.jp/

東京大学大学院 工学系研究科 電気系工学専攻
〒113-8656　東京都文京区弥生 2-11-16　工学部 9 号館 215 号室
電話: 03-5841-1189, ファックス: 03-5841-1140
E-mail: ohtsu@ee.t.u-tokyo.ac.jp
URL: http://uuu.t.u-tokyo.ac.jp/

[Ⅱ] Development of Next-generation High-performance Technology for Photovoltaic Power Generation System, NEDO project*

Professor

Motoichi OHTSU (Dr. Eng.)

Associate Professor

Takashi YATSUI (Dr. Eng.)

Researcher

Tadashi KAWAZOE (Dr. Sci.)
Wataru NOMURA (Dr. Eng.)
Naoya TATE (Dr. Info. Sci.)

Research Assistant

Teruo MURAKAMI
Shinko MAKIYAMA
Ayako MIZUSHIMA
Chiaki AMAGAI

Assistants

Sachiyo KOJIMA
Noriko KUROKI
Kumiko NOZAWA

(*)
Department of Electronics Engineering and Information Systems,
Graduate School of Engineering,
The University of Tokyo
(Room 219, Bldg. Eng. 9)
2-11-16 Yayoi, Bunkyo-ku, Tokyo 113-8656, Japan
Phone: +81-3-5841-1670
FAX: +81-3-5841-1140
E-mail: info@ nanophotonics.t.u-tokyo.ac.jp
URL: http://uuu.t.u-tokyo.ac.jp/

東京大学大学院 工学系研究科 電気系工学専攻
〒113-8656 東京都文京区弥生 2-11-16 工学部 9 号館 219 号室
電話：+81-3-5841-1670, ファックス: +81-3-5841-1140
E-mail: info@ nanophotonics.t.u-tokyo.ac.jp
URL: http://uuu.t.u-tokyo.ac.jp/

[Ⅲ]Nanophotonics Research Center*

Director

Motoichi OHTSU, Professor (core member)

Members

Kazuo HOTATE, Professor (core member)
Hitoshi TABATA, Professor (core member)
Masaaki TANAKA, Professor (core member)
Takao SOMEYA, Professor
Shinji YAMASHITA, Professor
Yuichiro KATO, Associate Professor
Shinobu OHYA, Associate Professor
Masakazu SUGIYAMA, Associate Professor
Takashi YATSUI, Associate Professor
Munetoshi SEKI, Assistant Professor
Masanori KUBOTA, Assistant Professor
Tadashi KAWAZOE, Researcher
Wataru NOMURA, Researcher
Naoya TATE, Researcher

(*)
Institute of Engineering Innovation,
School of Engineering, The University of Tokyo
(Room 219, Bldg. Eng. 9)
2-11-16 Yayoi, Bunkyo-ku, Tokyo 113-8656, Japan
Phone: +81-3-5841-1670
FAX: +81-3-5841-1140
E-mail: info@ nanophotonics.t.u-tokyo.ac.jp
URL: http://www.npc.t.u-tokyo.ac.jp/

東京大学大学院 工学系研究科　総合研究機構
〒113-8656 東京都文京区弥生 2-11-16 工学部 9 号館 219 号室
電話：+81-3-5841-1670, ファックス: +81-3-5841-1140
E-mail: info@ nanophotonics.t.u-tokyo.ac.jp
URL: http://www.npc.t.u-tokyo.ac.jp/

[Ⅳ] Research Institute of Nanophotonics*

Director

Motoichi OHTSU

(*)
Research Institute of Nanophotonics,
Nonprofit Organization
1-20-10 Sekiguchi, Bunkyo-ku, Tokyo 112-0014, Japan
Phone: +81-3-3267-6790. Fax: +81-3-5261-9788
E-mail: ohtsu-rinps@nanophotonics.t.u-tokyo.ac.jp
URL: http://www.nanophotonics.info/

特定非営利法人 ナノフォトニクス工学推進機構
〒112-0014 東京都文京区関口 1-20-10
電話: 03-3267-6790, ファックス: 03-5261-9788
E-mail: ohtsu-rinps@nanophotonics.t.u-tokyo.ac.jp
URL: http://www.nanophotonics.info/

[Ⅴ] Other Members*

Researcher

Wataru YAMAGISHI (NPO) [(a)]

Research Assistant

Etsuko OTA (JST ALCA Project) [(b)]
Chie IMAI (NPO) [(a)]
Aya KANATANI (NPO) [(a)]
Michiko ONO (NPO) [(a)]

(*)

a) (Room 301, Bldg. Eng. 9)
b) (Room 225, Bldg. Eng. 9)
Department of Electronics Engineering and Information Systems,
Graduate School of Engineering,
The University of Tokyo
2-11-16 Yayoi, Bunkyo-ku, Tokyo 113-8656, Japan
Phone: +81-3-5841-1189
FAX: +81-3-5841-1140
URL:http://uuu.t.u-tokyo.ac.jp/

a)工学部 9 号館 301 号室
b)工学部 9 号館 225 号室
東京大学大学院 工学系研究科 電気系工学専攻
〒113-8656 東京都文京区弥生 2-11-16
電話: 03-5841-1189, ファックス: 03-5841-1140
URL: http://uuu.t.u-tokyo.ac.jp/

LIST OF PAPERS

[(pp. XX-XX); pages in this issue of the COLLECTED PAPERS**]**

[ⅰ] ORIGINAL PAPERS

[6] N. Tate, Y. Liu, T. Kawazoe, M. Naruse, T. Yatsui, and M. Ohtsu, “Fixed-distance coupling and encapsulation of heterogeneous quantum dots using phonon-assisted photo-curing,” Appl. Phys. B- Lasers and Optics, Vol. 110, Issue 1, January 2013, pp. 39-45.

(pp. 77-83).

[7] P. N. Hai, W. Nomura, T. Yatsui, M. Ohtsu, and M. Tanaka, “Effects of laser irradiation on the self-assembly of MnAs nanoparticles in a GaAs matrix,” Appl. Phys. Lett., Vol. 101, Issue 19, November 2012, pp. 193102-1-4.

(pp. 85-88)

[8] T. Yatsui, W. Nomura, M. Naruse, and M. Ohtsu, “Realization of an atomically flat surface of diamond using dressed photon-phonon etching,” J. Phys. D, Vol. 45, No. 47, November 2012, pp. 475302-1-4.

(pp. 89-92)

[9] Y. Liu, T. Yatsui, and M. Ohtsu, “Controlling the sizes of ZnO quantum dots using the dressed photon-phonon assisted sol-gel method,” Appl. Phys. B- Lasers and Optics, Vol. 108, Issue 4, September 2012, pp. 707-711.

(pp. 93-97)

[10] M. Naruse, M. Aono, S-J. Kim, T. Kawazoe, W. Nomura, H. Hori, M. Hara, and M. Ohtsu, “Spatiotemporal dynamics in optical energy transfer on the nanoscale and its application to constraint satisfaction problems,” Physical Review B, Vol. 86, Issue 12, September 2012, pp. 125407-1-10.

(pp. 99-108)

[Ⅲ] PRESENTATIONS IN INTERNATIONAL CONFERENCES

[1] M. Naruse, M. Aono, S.-J. Kim, N. Tate, M. Ohtsu, "Information Systems based on Optical Near-Field Processes at the Nanoscale," The 12th Workshop on Information Optics (WIO), July 15-19, 2013, Tenerife, Spain.
[Invited presentation]

(pp. 109-110)

[2] M. Ohtsu, "Dressed photon science and technology for novel devices, fabrications, and energy conversion systems", Book of Abstracts, The 9th Asia-Pacific Conference on Near-field Optics, July 3-6, 2013, Singapore, Singapore, pp. 21-22.
[Plenary presentation]

(pp. 111-112)

[3] W. Nomura, T. Yatsui, T. Kawazoe, M. Naruse, and M. Ohtsu, "Spatiotemporal optical energy transfer in randomly distributed quantum dots system," Book of Abstracts, The 9th Asia-Pacific Conference on Near-field Optics, July 3-6, 2013, Singapore, Singapore, p.33.

(p. 113)

[4] N. Tate, Y. Liu, T. Kawazoe, M. Naruse, T. Yatsui, and M. Ohtsu, "Phonon-assisted photo-curing method for autonomous formation of Nanophotonic Droplets," Book of Abstracts, The 9th Asia-Pacific Conference on Near-field Optics, July 3-6, 2013, Singapore, Singapore, pp. 47-48.

(pp. 115-116)

[5] N. Wada, M.-A. Tran, T. Kawazoe, and M. Ohtsu, "THz coherent phonon generation using dressed-photon-phonons in a Si homojunction-structured LED," Book of Abstracts, The 9th Asia-Pacific Conference on Near-field Optics, July 3-6, 2013, Singapore, Singapore, pp. 75-76.

(pp. 117-118)

[6] H. Tanaka, T. Kawazoe, and M. Ohtsu, "Si photodetectors with optical gain using dressed-photon-phonons," Book of Abstracts, The 9th Asia-Pacific Conference on Near-field Optics, July 3-6, 2013, Singapore, Singapore, pp. 77-78.

(pp. 119-120)

[7] M. Yamaguchi, M.-A. Tran, T. Kawazoe, and M. Ohtsu, "EL emission with the higher photon energy than the bandgap energy from a Silicon homojunction LED based on dressed photon-phonons," Book of Abstracts, The 9th Asia-Pacific Conference on Near-field Optics, July 3-6, 2013, Singapore, Singapore, pp. 79-80.

(pp. 121-122)

[8] T. Kawazoe, A. Mizushima, K. Matsue, and M. Ohtsu, "Highly efficient SiC homojunction structured white- and UV- LEDs based on the dressed photon-assisted process," Book of Abstracts, The 9th Asia-Pacific Conference on Near-field Optics, July 3-6, 2013, Singapore, Singapore, p. 104.

(p. 123)

[9] T. Yatsui, W. Nomura, T. Mano, H. Miyazaki, K. Sakoda, T. Kawazoe, and M. Ohtsu, "Emission from a dipole-forbidden energy state in a GaAs quantum ring induced by near-field interaction with a fiber probe," Book of Abstracts, The 9th Asia-Pacific Conference on Near-field Optics, July 3-6, 2013, Singapore, Singapore, p. 109.

(p. 125)

[10] M.-A. Tran, M. Yamaguchi, T. Kawazoe, and M. Ohtsu, "Dressed photon phonon assisted electroluminescence mechanism in Si homojunction visible LED," Book of Abstracts, The 9th Asia-Pacific Conference on Near-field Optics, July 3-6, 2013, Singapore, Singapore, p. 130.

(p. 127)

[11] T. Yatsui, M. Ohtsu, and G.-C. Yi, "ZnO quantum structure based nanophotonic device," Book of Abstracts, 16th International Symposium on the Physics of Semiconductors and Applications (ISPSA-2013), July 2-5, 2013, Jeju, Korea, paper number D2-I-01.
[Invited presentation]

(p. 129)

[12] M. Naruse, N. Tate, M. Aono, S.-J. Kim, and M. Ohtsu, "Intelligence by Nanophotonics," Book of Abstracts, Solution Searching and Information Security Applications, 2013 Asia-Pacific Workshop on Fundamentals and Applications of Advanced Semiconductor Devices (AWAD), June 26-28, 2013, Seoul, Korea, pp. 185-188.
[Invited presentation]

(pp. 131-134)

[13] M. Ohtsu, "Dressed photon science and applications," Book of Abstracts of Sweden-Japan Collaboration Symposium: Exploring the Future of Light, Matter, and Information on the Nanoscale, June 3-4, 2013, Lund, Sweden, pp. 34-35.
[Invited presentation]

(pp. 135-136)

[14] T. Yatsui, W. Nomura, T. Mano, H. Miyazaki, K. Sakoda, T. Kawazoe, and M. Ohtsu, "Emission from a dipole-forbidden energy state in a GaAs quantum-ring induced by dressed photon," Technical digest of Conference on Lasers and Electro-Optics 2013 (CLEO2013), June 10-14, 2013, San Jose, CL., USA., paper number JW2A.055.

(pp. 137-138)

[15] M. Ohtsu, "Dressed photon for energy conversion," Technical Digest of The France -Japan Workshop on Atom Optics 2013, April 25, 2013, Villetaneuse, France, pp. 3-4.
[Invited presentation]

(pp. 139-140)

[16] M. Ohtsu, "Concepts of dressed photon science and technology," Book of abstracts of The First Italy-Japan Workshop on Nanophotonics, April 22-23, 2013, Pisa, Italy, pp. 1-2.
[Invited presentation]

(pp. 141-142)

[17] R. Teki, A. J. Kadaksham, F. Goodwin, T. Yatsui, M. Ohtsu, "Dressed-photon nanopolishing for EUV mask substrate defect mitigation, " Proceedings of SPIE, The Society of Photo-optical Instrumentation Engineers (SPIE) Advanced Lithography, February 24 – 28, 2013, San Jose, CL., USA., Paper 8679-14.

(pp. 143-150)

[18] M. Naruse, N. Tate, M. Aono, and M. Ohtsu, "Information Systems based on Optical Near-Field Processes at the Nanoscale," Department of Engineering Seminar Series, Princeton University, January 16, 2013, Princeton, NJ., USA.

(p. 151)

[19] M. Naruse, N. Tate, and M. Ohtsu, "Optical security based on optical near-field processes," Seminar Talk, Electrical and Computer Engineering Department, University of Connecticut, January 15, 2013, Mansfield, CT.,USA.

(pp. 153-154)

[20] M. Naruse, M. Aono, H. Hori, M. Hara, and M. Ohtsu, "Network of Energy Transfer on the Nanoscale and its Application to Solving Constraint Satisfaction Problems," Proceedings of The 2012 International Symposium on Nonlinear Theory and its Applications (NOLTA), October 22-26, 2012, Majorca, Spain, pp. 578-581.

(pp. 155-158)

[21] M. Aono, S.-J. Kim, L. Zhu, M. Naruse, M. Ohtsu, H. Hori, M. Hara, "Amoeba-inspired SAT solver", Proceedings of The 2012 International Symposium on Nonlinear Theory and its Applications (NOLTA), October 22-26, 2012, Majorca, Spain, pp. 586-589.

(pp. 159-162)

[22] T. Kawazoe, T. Fujita, H. Fujiwara, M. Niigaki, and M. Ohtsu, "Infrared-visible light conversion using dcm dye micrograins embedded in a resin sheet and application to an ir sensor card," Congress Proceedings of 31st International Congress on Application of Lasers & Electro-Optics (ICALEO), September 23-27, 2012, Anaheim, CL., USA, Paper M1001.

(pp. 163-164)

[23] H. Tanaka, T. Kawazoe, and M. Ohtsu, "1.3 μm-Band Si Photodetectors with Optical Gains Fabricated by Dressed Photon Assisted Annealing," Congress Proceedings of 31st International Congress on Application of Lasers & Electro-Optics (ICALEO), September 23-27, 2012, Anaheim, CL., USA, Paper M1105.

(pp. 165-172)

[24] T. Yatsui and M. Ohtsu, "A dressed-photon phonon etching of substrate," Abstracts of IUMRS-International Conference on Electronic Materials, September, 23-28, 2012, Kanagawa, Japan, D-9-O24-002.
[Invited presentation]

(p. 173)

[25] M. Naruse, N. Tate, M. Aono, and M. Ohtsu, "Information Physics in Nanophotonics," Technical Digest of The First International Workshop on Information Physics and Computing in Nano-scale Photonics and Materials (IPCN), September 7, 2012, Orleans, France, Paper Number IPCN1-1.

(pp. 175-177)

[26] N. Tate, M. Naruse, M. Ohtsu, "Engineering of nanometric optical system based on optical near-field interactions for macro-scale applications," Technical Digest of The First International Workshop on Information Physics and Computing in Nano-scale Photonics and Materials (IPCN), September 7, 2012, Orleans, France, Paper Number IPCN1-12.

(pp. 179-181)

[27] M. Aono, M. Naruse, S.-J. Kim, M. Ohtsu, H. Hori, and M. Hara, " Amoeba-inspired Model of Quantum Dot-based SAT Solver," Technical Digest of The First International Workshop on Information Physics and Computing in Nano-scale Photonics and Materials (IPCN), September 7, 2012, Orleans, France, Paper Number IPCN1-13.

(pp. 183-185)

[28] S.-J. Kim, M. Naruse, M. Aono, M. Ohtsu, M. Hara, “A Model of Quantum Dot-based Decision Maker,” Technical Digest of The First International Workshop on Information Physics and Computing in Nano-scale Photonics and Materials (IPCN), September 7, 2012, Orleans, France, Paper Number IPCN 1-14.

(pp. 187-189)

[29] T. Yatsui, W. Nomura, and M. Ohtsu, “Realization of an ultra-flat diamond substrate using a dressed-photon phonon etching,” Programme Book of International Conference on Diamond and Carbon Materials, September 2-7, 2012, Granada, Spain, Paper Number O97.

(p. 191)

[Ⅲ] REVIEW PAPERS

[1] M. Ohtsu, T. Saiki, and M. Naruse, “JSPS Sweden-Japan Collaboration Symposium - June 3-4 2013 :Exploring the Future of Light, Matter, and Information on the Nanoscale,” JSPS Stockholm News Letter, Vol. 38, June, 2013, p 3.
【大津元一、斎木敏治、成瀬誠、「JSPS Sweden-Japan Collaboration Symposium - June 3-4 2013 :Exploring the Future of Light, Matter, and Information on the Nanoscale」、日本学術振興会ストックホルムニュースレター、Vol. 38、2013 年 6 月、 p. 3,p. 8】
(pp. 193-194)

[2] T. Yatsui and M. Ohtsu, “Recent Progress of a Dressed Photon Technology,” The Review of Laser Engineering, Vol. 41, No.3, March 2013, pp.166-170.
【八井崇、大津元一、「ドレストフォトンを用いた新産業応用の開拓」、レーザ研究, Vol. 41、No. 3、2013 年 3 月、pp. 166-170】
(pp. 195-199)

[3] M. Ohtsu, “Generation of dressed photons and its application to generic technology,” OPTICAL AND ELECTRO-OPTICAL ENGINEERING CONTACT, Vol. 51, No.1, January 2013, pp. 29-34.
【大津元一、「ドレスト光子の発生と基盤技術としての展開」、光技術コンタクト、1 月号、第 51 巻、第 1 号、2013 年 1 月、pp. 29-34】
(pp. 201-206)

[4] T. Yatsui and M. Ohtsu, “Future Prospects of the World When the Material Without Optical Loss Comes True,” MATERIAL STAGE, Vol. 12, No.5, August 2012, pp. 1-4.
【八井 崇、大津元一、「もし「光ロスが発生しない光学材料」が実用化されたら世の中はどう変わるのか？」、MATERIAL STAGE、第 12 巻、第 5 号、2012 年 8 月、pp. 1-4】
(pp. 207-210)

[5] N. Tate, M. Naruse, and M. Ohtsu, “Nano-photonic information system based on dressed photon technology”, CHEMICAL INDUSTRY Vol. 63, No.8, August 2012, pp. 49-54.
【竪直也、成瀬誠、大津元一、「近接場光を用いたナノ光情報システム」、化学工業、第 63 巻、第 8 号、pp. 49-54】
(pp. 211-216)

[Ⅳ] PUBLISHED BOOKS

[1] M. Ohtsu (ed.), *Handbook of Nano-Optucs and Nanophotonics*, Springer-Verlag, Berlin, June 2013, (1071 pages)

(pp. 227-220)

[2] 大津元一、「ドレスト光子-光・物質融合工学の原理-」、”朝倉書店、 東京、日本、March 2013、 (320 pages)

(pp. 221-225)

[3] M. Ohtsu (ed.), *Progress in Nanophotonics Ⅱ*, Springer-Verlag, Berlin, February 2013. (182 pages)

(pp. 227-230)

[Ⅴ] AWARDS

[1] N. Wada, Best Young Researcher Award, “THz coherent phonon generation using dressed-photon－phonons in a Si homojunction-structured LED” The 9th Asia-Pacific Conference on Near-field Optics (APNFO2013), July 06, 2013
【和田直樹, Best Young Researcher Award, “THz coherent phonon generation using dressed-photon－phonons in a Si homojunction-structured LED” The 9th Asia-Pacific Conference on Near-field Optics (APNFO2013), 2013 年 7 月 6 日】

[2] M. Yamaguchi, International Advisory Committe Award, “EL emission with the higher photon energy than the bandgap energy from a Silicon homojunction LED based on dressed photon-phonons,” The 9th Asia-Pacific Conference on Near-field Optics (APNFO2013), July 06, 2013
【山口真生, International Advisory Committe Award, “EL emission with the higher photon energy than the bandgap energy from a Silicon homojunction LED based on dressed photon-phonons,” The 9th Asia-Pacific Conference on Near-field Optics (APNFO2013), 2013 年 7 月 6 日】

[3] Tran Anh Minh, International Advisory Committe Award, “Dressed photon phonon assisted electroluminescence mechanism in Si homojunction visible LED,” The 9th Asia-Pacific Conference on Near-field Optics (APNFO2013), July 06, 2013
【チャン アン ミン, International Advisory Committe Award, “Dressed photon phonon assisted electroluminescence mechanism in Si homojunction visible LED,” The 9th Asia-Pacific Conference on Near-field Optics (APNFO2013), 2013 年 7 月 6 日】

[4] H. Tanaka, Award for excellent poster presentation, “1.3 μm-band Silicon photodetectors using dressed photons,” Scientific study on Tokyo branch, The laser society of Japan, March, 2013
【田中肇, ポスター講演　優秀賞, 「ドレスト光子による 1.3μm帯シリコン光検出器」、２０１３年第１３回レーザー学会東京支部研究会、 2013 年 3 月】

[5] N. Wada, The Best Presentation Award , “Measurement of coherent phonon in a bulk Si pn-junction diode and its application to the control of the EL spectrum of Si-LED,” The 3rd Student Research Meeting on Nanophotonics, November 2012.

【和田直樹、優秀発表賞、「バルク Si pn 接合素子におけるコヒーレントフォノンと Si EL 発光波長制御への応用」、第３回ナノフォトニクス学生研究講演会、2012 年 11 月】

[Ⅵ] PRESENTED PH.D THESIS

[1] Y. Liu, “Study on controlling size distribution of ZnO quantum dot by using light-assisted process”, March, 2013.
【劉洋、「光援用過程による酸化亜鉛量子ドットの寸法分布制御に関する研究」、2013 年 3 月】

[I] ORIGINAL PAPERS

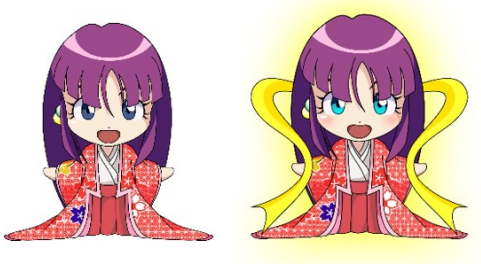

nature photonics

LETTERS

PUBLISHED ONLINE: 7 JULY 2013 | DOI: 10.1038/NPHOTON.2013.179

Brightening of excitons in carbon nanotubes on dimensionality modification

Yuhei Miyauchi[1,2]*, Munechiyo Iwamura[1], Shinichiro Mouri[1], Tadashi Kawazoe[3], Motoichi Ohtsu[3] and Kazunari Matsuda[1]

Despite the attractive one-dimensional characteristics of carbon nanotubes[1], their typically low luminescence quantum yield, restricted because of their one-dimensional nature[2–9], has limited the performance of nanotube-based light-emitting devices[10,11]. Here, we report the striking brightening of excitons (bound electron–hole pairs)[12,13] in carbon nanotubes through an artificial modification of their effective dimensionality from one dimension to zero dimensions. Exciton dynamics in carbon nanotubes with luminescent, local zero-dimension-like states generated by oxygen doping[14] were studied as model systems. We found that the luminescence quantum yield of the excitons confined in the zero-dimension-like states can be more than at least one order larger (∼18%) than that of the intrinsic one-dimensional excitons (typically ∼1%), not only because of the reduced non-radiative decay pathways but also due to an enhanced radiative recombination probability beyond that of intrinsic one-dimensional excitons. Our findings are extendable to the realization of future nanoscale photonic devices including a near-infrared single-photon emitter operable at room temperature.

The low luminescence quantum yield of semiconducting carbon nanotubes (hereafter, termed (carbon) nanotubes), which is typically, at most, only a few percent for dispersed nanotubes[7,8,15–17], is deeply related to their one-dimensional nature. The balance between radiative and non-radiative relaxation rates (that is, the probability) of electron–hole bound states, termed excitons[12,13], determines the nanotube luminescence quantum yield. Fast non-radiative decay, which dominates exciton recombination in nanotubes and results in their low luminescence quantum yield, is mainly caused by the quenching of one-dimensional mobile excitons due to the rapid collision between these excitons and local quencher states, which include nanotube defects and end sites[4–6,8,9]. Moreover, the temperature-limited radiative relaxation rate ($\propto T^{-1/2}$), characteristic of one-dimensional excitons, substantially reduces the quantum yield at room temperature[2,3,7]. Efforts to improve the luminescence quantum yield by reducing the defect quenching of excitons[18,19] have been reported. Conversely, if a local defect is not an exciton quencher[18–20] but is luminescent by virtue of appropriate local electronic structures[14,21–25], the local state may function as a zero-dimension-like quantum state that captures mobile excitons and converts them to photons (as shown in Fig. 1) with a radiative relaxation rate possibly lying beyond that of intrinsic one-dimensional excitons. Therefore, one-dimensional nanotubes with luminescent, local zero-dimension-like states offer a unique opportunity for photophysical investigation of nearly ideal zero-dimensional–one-dimensional hybrid systems. Moreover, understanding the excitonic properties of these states can lead to the development of novel strategies for brightening nanotube excitons beyond the intrinsic limit for future photonics applications.

We examined the excitonic characteristics of luminescent, local zero-dimension-like states embedded in one-dimensional carbon nanotubes. Figure 2a shows photoluminescence excitation maps of carbon nanotubes with and without the doping of oxygen atoms that generate these local states[14]. The distinct luminescence peak at E_{11}^* (∼1.07 eV) appears after oxygen-doping treatment[14] (see Methods and Supplementary Section S1), while the change in the intrinsic luminescence feature at E_{11} (∼1.25 eV) is small. The luminescence peak at E_{11}^* has been attributed to light emission from the zero-dimension-like local states generated by oxygen doping in carbon nanotubes[14]. The excitation maxima at E_{11} and E_{11}^* are coincident with the second sub-band exciton energy E_{22} of (6,5) nanotubes, indicating that the photogenerated intrinsic excitons are converted into local excitons with energy E_{11}^*.

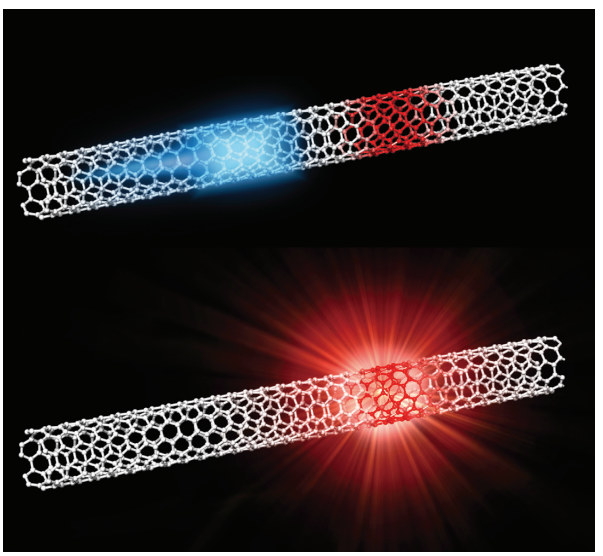

Figure 1 | Schematic of a carbon nanotube with a luminescent local state. A photoexcited intrinsic exciton is mobile along the nanotube axis (blue spot). When the mobile exciton collides with a local state (red spot), where the exciton energy becomes lower than that of the intrinsic state, the mobile exciton can be trapped by the local state. If the local state has no efficient non-radiative decay paths, it should work as a luminescence centre, and the exciton can decay radiatively by emitting a photon.

[1]Institute of Advanced Energy, Kyoto University, Uji, Kyoto 611-0011, Japan, [2]PRESTO, Japan Science and Technology Agency, 4-1-8 Honcho Kawaguchi, Saitama 332-0012, Japan, [3]Department of Electrical Engineering and Information Systems, Graduate School of Engineering, The University of Tokyo, Hongo 7-3-1, Bunkyo-ku, Tokyo 113-8656, Japan. *e-mail: miyauchi@iae.kyoto-u.ac.jp

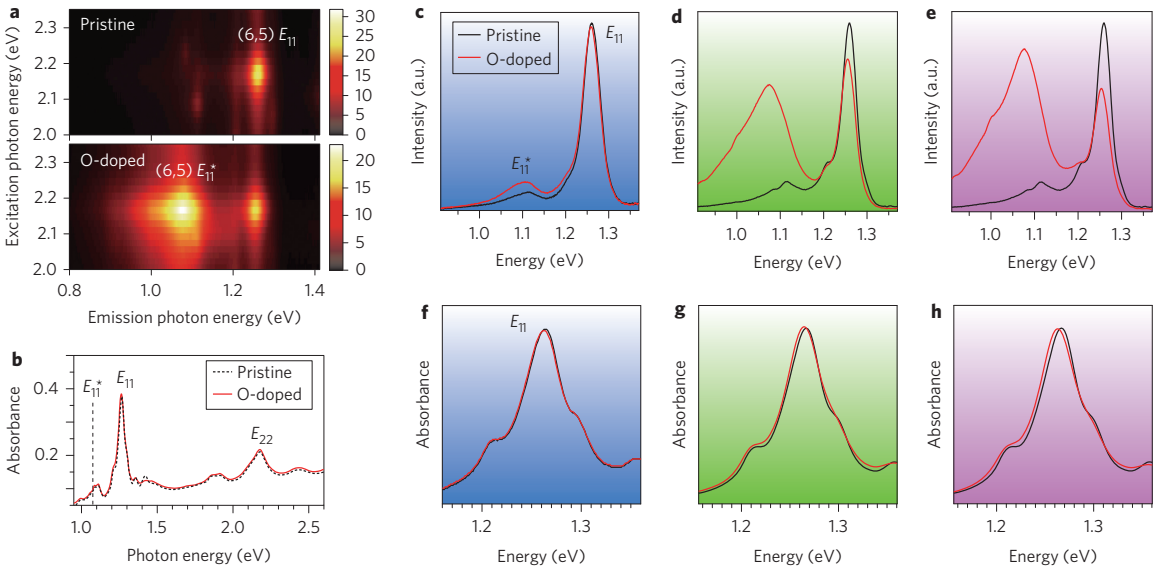

Figure 2 | Optical spectra of carbon nanotubes with luminescent local states. a, Photoluminescence excitation maps of nanotubes before (pristine) and after (O-doped) oxygen-doping treatment. Vertical and horizontal axes correspond to the excitation and emission photon energies, respectively. Colours in the map correspond to the photoluminescence intensity (white being the highest and black the lowest). **b**, Optical absorption spectra of the pristine (black dotted curve) and oxygen-doped (red solid curve) nanotubes. The vertical dotted line indicates energy E_{11}^* (~1.07 eV). **c**–**e**, Photoluminescence spectra of the various nanotubes with variable oxygen-doping measured under E_{22} energy excitation (2.175 eV). The slight differences observed for the pristine spectra are due to the use of different batches of starting material. **f**–**h**, Optical absorption spectra of various nanotubes around the E_{11} energy. The photoluminescence and absorption spectra with the same background colours [(**c**,**f**), (**d**,**g**), (**e**,**h**)] were taken from the same nanotubes. In **c**–**h**, the black and red solid curves correspond to optical spectra of pristine and oxygen-doped carbon nanotubes, respectively.

Hereafter, we denote the intrinsic exciton state with energy E_{ii} as X_{ii}, and the oxygen-derived local states with energy E_{11}^* as X_{11}^*. Figure 2b compares the absorption spectra of pristine (non-doped) and oxygen-doped nanotubes. The distinct absorption peaks of intrinsic X_{11} and X_{22} excitons of (6,5) nanotubes are almost unchanged, and there are no prominent absorption features originating from the X_{11}^* excitons around E_{11}^*. The small changes in the absorption spectra indicate that the number density of the X_{11}^* sites is very small (deduced to be on the order of one X_{11}^* site per micrometre; Supplementary Section S4), and most parts of the nanotubes, except for the oxygen-doped sites, remain unchanged.

Figure 2c–h compares the photoluminescence and absorption spectra of various oxygen-doped nanotubes with different X_{11}^* peak intensities, which reflect the variable density of the local X_{11}^* states. We see a considerable change in the photoluminescence spectra of the pristine nanotubes, as shown in Fig. 2c–e. As the integrated photoluminescence intensity of the X_{11} peak at E_{11} (I_{11}) decreases slightly, that of the X_{11}^* peak at E_{11}^* (I_{11}^*) appears and increases drastically.

In Fig. 3a we plot the integrated photoluminescence intensity of the X_{11}^* state, I_{11}^*, as a function of the decreasing X_{11} photoluminescence intensity ΔI_{11}. Here, ΔI_{11} is defined as $\Delta I_{11} = |I_{11} - I_0|$, where I_0 is the X_{11} photoluminescence intensity of the pristine nanotubes. A linear relationship was found to exist between the change in I_{11} (ΔI_{11}) and the value of I_{11}^*, as indicated by the dotted, straight line in Fig. 3a, where the slope of the line, $I_{11}^*/\Delta I_{11}$, is 7.5 ± 0.6. This linear relation contains rich information on the photophysical parameters of the zero-dimension-like X_{11}^* states.

In this study, as shown in Fig. 3b, we consider the migration (diffusion) of the intrinsic one-dimensional excitons along the nanotube and the successive trapping at extrinsic local quenching sites (defect sites), with a density of n_q, or at local luminescent sites (X_{11}^* sites), with a density of n_x. Based on a one-dimensional diffusion-limited exciton contact-quenching mechanism[8,9] that predicts the luminescence quantum yield η of one-dimensional excitons, where $\eta \propto (n_q + n_x)^{-2}$, the ratio of I_{11}^* to ΔI_{11} (for $\Delta I_{11} \ll I_0$) is evaluated as (Supplementary Section S2)

$$\frac{I_{11}^*}{\Delta I_{11}} \leq \frac{1}{2}\left(\frac{\eta^*}{\eta_0}\right)\left(\frac{E_{11}^*}{E_{11}}\right) \quad (1)$$

where η_0 and η^* are the luminescence quantum yields of an exciton in the X_{11} (non-doped) and X_{11}^* states, respectively. Hence, a linear relationship between I_{11}^* and ΔI_{11} is expected for small ΔI_{11}. From equation (1), a value of $\eta^*/\eta_0 \geq 18 \pm 1$ is derived from the experimental results in Fig. 3a. That is, the quantum yield of a single X_{11}^* site is at least ~18 times larger than that obtained from a X_{11} state. Thus, at room temperature, the luminescence quantum yield of the X_{11}^* state, η^*, is estimated to be $\eta^* \geq 18 \pm 6\%$, given that the quantum yield of the X_{11} excitons is $\eta_0 = 1.0 \pm 0.3\%$, as calculated from the reported radiative lifetime of 1.6 ± 0.3 ns (ref. 8) and the observed photoluminescence decay of X_{11} excitons, described in the following (Supplementary Section S3).

To clarify the mechanism of the large quantum yield enhancement of the X_{11}^* states discussed above, we examined photoluminescence decay in pristine and oxygen-doped nanotubes (Fig. 4a,b). Clearly, the photoluminescence decay of the X_{11}^* excitons at E_{11}^* (red filled circles in Fig. 4b) is much slower than that of the X_{11} excitons at E_{11}. We conducted a numerical fitting procedure of the intensity decay $I_{11}^{(*)}(t)$ using the stretched exponential function $\exp[-(t/\tau_0)^{1/2}]$ with a characteristic timescale τ_0 for the E_{11} photoluminescence decay based on a kinetic model of the diffusion-limited one-dimensional exciton contact quenching[8], and using the double exponential functions for the decay of the one-dimension-like X_{11}^* excitons at E_{11}^* (Supplementary Section S3).

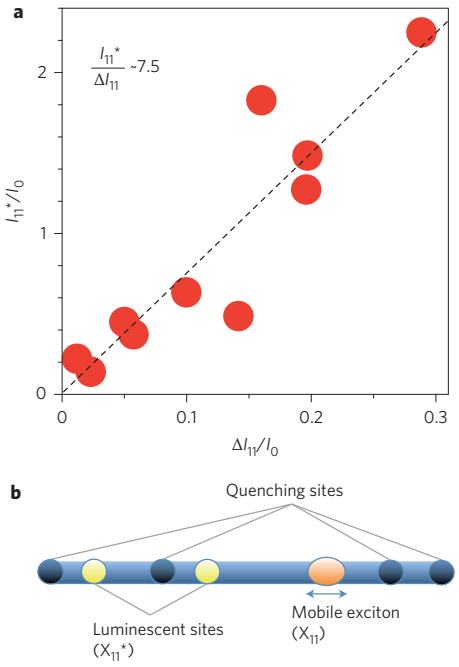

Figure 3 | Relationship of luminescence intensities from mobile and local excitons. a, Integrated photoluminescence intensity of the X_{11}^* peak (I_{11}^*) as a function of the absolute value of the change in photoluminescence intensity of the X_{11} peak ΔI_{11}. I_{11}^* and ΔI_{11} are normalized by the photoluminescence intensity of the X_{11} peak (I_0) of pristine (non-doped) nanotubes. The integrated photoluminescence intensities are evaluated by peak decomposition procedures, where the X_{11}^* peak is fit by a Voigt function, and where the weak and broad intensity tail of the lower energy side is not included as I_{11}^*. **b**, Schematic of exciton migration and successive trapping by local quenching sites (including the end sites of nanotubes) with density n_q or by local luminescent (X_{11}^*) sites with density n_x.

Here, we define a quantity $\langle\tau^{(*)}\rangle = \int_0^\infty I_{11}^{(*)}(t)/I_{11}^{(*)}(0)\mathrm{d}t$, which corresponds to the time-integrated exciton number normalized by the initial exciton number and related to η_0 and η^* as $\eta_0 = \tau_R^{-1}\langle\tau\rangle$ and $\eta^* = \tau_R^{*-1}\langle\tau^*\rangle$, respectively, where τ_R and τ_R^* are the radiative lifetimes of the X_{11} and X_{11}^* states, respectively. From the fitting procedure (Supplementary Section S3), the values $\langle\tau\rangle = 16 \pm 4$ ps and $\langle\tau^*\rangle = 95 \pm 7$ ps are obtained. This contributes to an enhancement of the quantum yield of the X_{11}^* excitons equivalent to approximately six times that of the intrinsic X_{11} excitons.

The further quantum yield enhancement necessary to account for the net 18× quantum yield enhancement is attributed to the shortened radiative lifetime. Considering the experimentally estimated values of $\eta^*/\eta_0 \geq 18 \pm 1$ and $\langle\tau\rangle/\langle\tau^*\rangle = 0.17 \pm 0.04 \approx 1/6$, the ratio of the radiative lifetimes can be evaluated through the relation $\tau_R/\tau_R^* = (\eta^*/\eta_0)(\langle\tau\rangle/\langle\tau^*\rangle)$ as $\tau_R/\tau_R^* \geq 3.0 \pm 0.8$, which indicates that the radiative decay rate of the X_{11}^* exciton ($1/\tau_R^*$) is more than approximately three times that of the intrinsic X_{11} excitons ($1/\tau_R$).

Let us now discuss the mechanisms of the reduced non-radiative decay rate, given as a factor of 1/6× (the extended exciton lifetime), and the enhanced radiative decay rate, given as a factor of ≥3× (the shortened radiative lifetime), of the X_{11}^* excitons relative to the X_{11} excitons. First, the reduced non-radiative exciton decay is mainly attributed to exciton immobilization by the localization effect. Once the mobile exciton is stopped at a local X_{11}^* state, the exciton can avoid collision with quenching sites and live longer, which contributes to the ~6× quantum yield enhancement. If only this 6× enhancement is considered, the quantum yield is evaluated to be 6 ± 2%, which is close to the quantum yield of ~7% estimated for a clean air suspended nanotube[26].

The dimensionality modification of the excitons is more critical for understanding the further quantum yield enhancement than recovering the original quantum yield of intrinsic one-dimensional excitons. Because of the one-dimensional nature of the intrinsic X_{11} excitons, their effective radiative decay rates are limited by the momentum mismatch between photons and thermally excited excitons in the one-dimensional band dispersion[2,3,7]. This restriction is responsible for the characteristic one-dimensional radiative decay rate that is proportional to $T^{-1/2}$. In contrast, the spatially localized zero-dimension-like states should be free from this momentum restriction, which could lead to enhancement of the radiative decay rate. Considering the possible E_{11} homogeneous line width of at least 10 meV at room temperature[7], however, the enhancement factor due to this effect is at most 1.6. Hence, to fully explain the enhancement of the radiative decay rate by a factor of 3 ± 0.8, an additional enhancement mechanism of a factor of at least 1.9 ± 0.5 is required.

The remaining issue that should be addressed before we further discuss the enhancement mechanism is whether there is a lower-lying dark (optically forbidden) X_{11}^* exciton state. If a lower-lying dark state exists, the effective radiative decay rate of excitons can be reduced due to the accumulation of excitons in this dark state, as is actually the case for the intrinsic X_{11} excitons[2,3]. In contrast, if there is no X_{11}^* dark state, excitons in the X_{11}^* sites can be free from the restriction caused by the dark state and may achieve a larger effective radiative decay rate. To examine this issue, we conducted temperature-dependent photoluminescence studies (Fig. 4c–e). The major findings are summarized as follows. The temperature-dependent variations of both I_{11} and I_{11}^* in the low-temperature range shown in Fig. 4d,e are reproduced well by considering exciton diffusional transport and reduction of the bright exciton population due to the existence of lower-lying dark states, not only in the X_{11} states, but also in the X_{11}^* states, which is consistent with a theoretical prediction of an impurity-bound exciton in carbon nanotubes[27] (Supplementary Sections S5, S6). From the numerical fitting results, we infer the existence of the X_{11}^* dark state, eventually leading to no significant change in the X_{11}^* effective radiative decay rate compared to that of the X_{11} excitons at room temperature (Supplementary Section S6).

Given the negligible change related to the existence of the dark state, we attribute the remaining enhancement of the radiative decay rate by a factor of ~2 to the increased oscillator strength due to the squeezing of an exciton in the zero-dimension-like X_{11}^* state, which is known as the 'giant-oscillator-strength effect' of a localized exciton[28]. The radiative decay rate τ_R^{-1} and the oscillator strength f of an exciton follow the relation $\tau_R^{-1} \propto E^2 f$, where E is the exciton energy and f is approximately inversely proportional to the average electron–hole separation, that is, the exciton size in a one-dimensional nanotube. Hence, the radiative decay rate can be enhanced by a factor of ~2 for an exciton squeezed to be ~40% of its original size, considering the different exciton energies E_{11} and E_{11}^*. From the size of the X_{11} exciton[29] (~2 nm in (6,5) nanotubes), the size of the X_{11}^* exciton is deduced to be ~0.8 nm.

Our findings regarding the strongly enhanced luminescence properties of sparsely distributed, zero-dimension-like excitonic states beyond the intrinsic properties in one-dimensional carbon nanotubes will stimulate research on the physics of zero-dimensional–one-dimensional hybrid systems. Furthermore, the findings presented here will allow the development of nanotube-based novel optoelectronic devices while utilizing the advantages of both zero-dimensional and one-dimensional electronic systems, such as a near-infrared single-photon emitter[21] driven by direct carrier-injection[30] that can be operated even at room temperature.

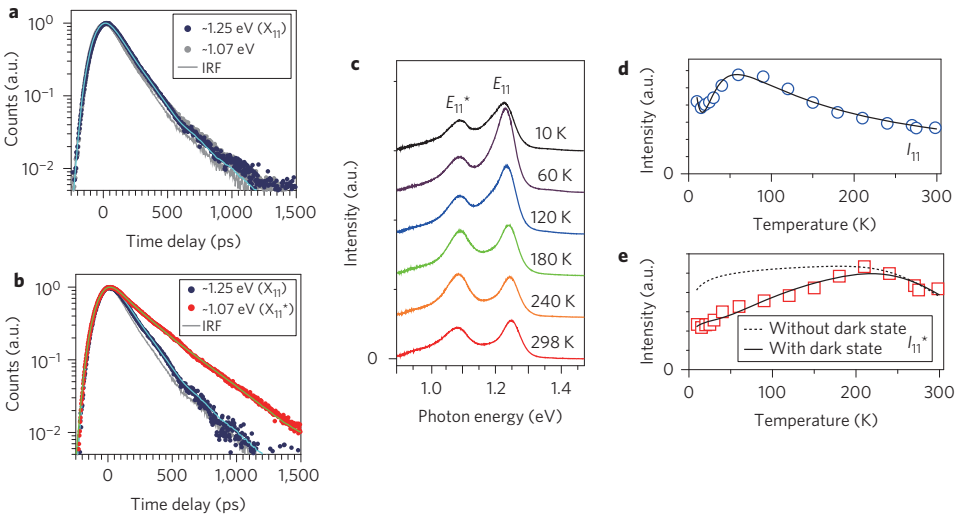

Figure 4 | Time-resolved and temperature-dependent luminescence studies. a,**b**, Time-resolved photoluminescence decay profiles of pristine (non-doped) (**a**) and oxygen-doped (**b**) nanotubes. Blue circles in **a** and **b** indicate the photoluminescence decay of X_{11} excitons taken at E_{11} (~1.25 eV), and the red circles in **b** indicate the photoluminescence decay at E_{11}^* that corresponds to the decay of local X_{11}^* states. The grey solid curve is the IRF. **c**, Photoluminescence spectra of moderately oxygen-doped nanotubes measured at various temperatures. **d**,**e**, Temperature-dependent variation of I_{11} (blue circles, **d**) and I_{11}^* (red squares, **e**). The solid curves in **d** and **e** are reproduced by numerical fitting considering the diffusional transport of X_{11} excitons, exciton trapping at the X_{11}^* sites, and the probability that the X_{11} (**d**) and X_{11}^* (**e**) excitons are in their bright states (calculated by taking into account the lower-lying dark states that reside 6.6 meV (**d**) and 15 meV (**e**) below the bright states). The dotted curve in **e** is calculated without taking the existence of the lower-lying dark state into account (Supplementary Sections S5 and S6).

Methods

Sample preparation. The oxygen-doped (6,5) carbon nanotubes dispersed in a D_2O solution used in this work were prepared with ozone using the procedure reported by Ghosh *et al.*[14], but the experimental conditions and parameters were considerably modified so that the broadening of the absorption peak[14], indicating the degradation of the intrinsic part of the nanotubes, could be minimized. Details of the sample preparation procedure are described in Supplementary Section S1. In short, (6,5)-rich CoMoCAT nanotubes were isolated by dispersion in D_2O with 0.2% (wt/vol) sodium dodecyl benzene sulphonate (SDBS), 60 min of moderate bath sonication, 40 min of vigorous sonication with a tip-type sonicator, and centrifugation at 130,000*g* for 4 h. A 0.75 ml volume of D_2O, containing dissolved ozone with variable density, was added to the resulting 2 ml of isolated nanotube dispersion. For the control samples that were denoted as 'pristine' (non-doped) nanotubes, 0.75 ml of D_2O was added without dissolved ozone. The samples were left under a lighted desk lamp (~5 mW cm^{-2}), typically overnight, before conducting the optical measurements. In our protocol, the relative oxygen-doping level (number density of the X_{11}^* site) was mainly controlled by the density of ozone dissolved in the D_2O solution. The relation between I_{11}^* and the estimated absorbance of ozone at 260 nm in the added D_2O solution is presented in Supplementary Fig. S2. The moderately oxygen-doped nanotubes utilized for the temperature-dependent photoluminescence measurements were deposited on a membrane filter and dried in vacuum before the measurements. Further details of the sample preparation protocols and parameters are presented in Supplementary Section S1.

Optical measurements and data analysis. Continuous-wave absorption and photoluminescence spectra of dispersed nanotubes in D_2O were measured at room temperature using a near-infrared spectrometer with monochromated incident light. All the optical measurements at room temperature were conducted on the liquid samples in optical quartz cells. The time-resolved photoluminescence decay profiles of the dispersed nanotubes in D_2O were recorded at room temperature using a time-correlated, single-photon counting technique under pulsed laser excitation (80 MHz, ~6 ps pulse duration with a photon energy of 1.378 eV) with a liquid-nitrogen-cooled near-infrared photomultiplier attached with a microchannel plate. The photoluminescence from each peak feature (E_{11} or E_{11}^*) was separated using optical filters with a bandpass of ~0.1 eV. The time-resolved measurements were conducted on the same nanotubes for which the photoluminescence excitation maps shown in Fig. 2a were taken. We fitted the data using the convolution of the instrumental response function (IRF) with model functions to obtain the original photoluminescence decay profiles (Supplementary Section S3). Temperature-dependent photoluminescence measurements were performed on the as-deposited samples attached to the cold finger of a liquid-helium-cooled microscopy cryostat, with monochromated light from a broadband light source (Fianium, SC450) used for photoexcitation. The measurements were conducted with an excitation energy of 2.175 eV (570 nm), corresponding to the second sub-band exciton energy E_{22} of (6,5) nanotubes. The photoluminescence peaks of the nanotubes cast on a membrane filter were broadened, suggesting a more inhomogeneous environment for the cast nanotubes than that of the micelle-suspended nanotubes. We confirmed that the temperature-dependent variation of the E_{22} exciton energy is sufficiently small by observing the photoluminescence excitation spectra at 5 K and 298 K.

Received 1 October 2012; accepted 7 June 2013;
published online 7 July 2013

References

1. Saito, R., Dresselhaus, G. & Dresselhaus, M. S. *Physical Properties of Carbon Nanotubes* (Imperial College Press, 1998).
2. Perebeinos, V., Tersoff, J. & Avouris, P. Radiative lifetime of excitons in carbon nanotubes. *Nano Lett.* **5,** 2495–2499 (2005).
3. Spataru, C. D., Ismail-Beigi, S., Capaz, R. B. & Louie, S. G. Theory and *ab initio* calculation of radiative lifetime of excitons in semiconducting carbon nanotubes. *Phys. Rev. Lett.* **95,** 247402 (2005).
4. Cognet, L. *et al.* Stepwise quenching of exciton fluorescence in carbon nanotubes by single-molecule reactions. *Science* **316,** 1465–1468 (2007).
5. Rajan, A., Strano, M. S., Heller, D. A., Hertel, T. & Schulten, K. Length-dependent optical effects in single walled carbon nanotubes. *J. Phys. Chem. B* **112,** 6211–6213 (2008).
6. Miyauchi, Y., Matsuda, K., Yamamoto, Y., Nakashima, N. & Kanemitsu, Y. Length-dependent photoluminescence lifetimes in single-walled carbon nanotubes. *J. Phys. Chem. C* **114,** 12905–12908 (2010).
7. Miyauchi, Y., Hirori, H., Matsuda, K. & Kanemitsu, Y. Radiative lifetimes and coherence lengths of one-dimensional excitons in single-walled carbon nanotubes. *Phys. Rev. B* **80,** 081410(R) (2009).
8. Hertel, T., Himmelein, S., Ackermann, T., Stich, D. & Crochet, J. Diffusion limited photoluminescence quantum yields in 1-D semiconductors: single-wall carbon nanotubes. *ACS Nano* **4,** 7161–7168 (2010).
9. Harrah, D. M. & Swan, A. K. The role of length and defects on optical quantum efficiency and exciton decay dynamics in single-walled carbon nanotubes. *ACS Nano* **5,** 647–655 (2011).
10. Mueller, T. *et al.* Efficient narrow-band light emission from a single carbon nanotube p–n diode. *Nature Nanotech.* **5,** 27–31 (2010).
11. Hertel, T. Carbon nanotubes: a brighter future. *Nature Photon.* **4,** 77–78 (2010).
12. Ando, T. Excitons in carbon nanotubes. *J. Phys. Soc. Jpn* **66,** 1066–1073 (1997).
13. Wang, F., Dukovic, G., Brus, L. E. & Heinz, T. F. The optical resonances in carbon nanotubes arise from excitons. *Science* **308,** 838–841 (2005).
14. Ghosh, S., Bachilo, S. M., Simonette, R. A., Beckingham, K. M. & Weisman, R. B. Oxygen doping modifies near-infrared band gaps in fluorescent single-walled carbon nanotubes. *Science* **330,** 1656–1659 (2010).

15. O'Connell, M. J. *et al.* Band gap fluorescence from individual single-walled carbon nanotubes. *Science* **297,** 593–596 (2002).
16. Lebedkin, S. *et al.* FTIR-luminescence mapping of dispersed single-walled carbon nanotubes. *New J. Phys.* **5,** 140 (2003).
17. Crochet, J., Clemens, M. & Hertel, T. Quantum yield heterogeneities of aqueous single-wall carbon nanotube suspensions. *J. Am. Chem. Soc.* **129,** 8058–8059 (2007).
18. Ju, S.-Y., Kopcha, W. P. & Papadimitrakopoulos, F. Brightly fluorescent single-walled carbon nanotubes via an oxygen-excluding surfactant organization. *Science* **323,** 1319–1323 (2009).
19. Lee, A. J. *et al.* Bright fluorescence from individual single-walled carbon nanotubes. *Nano Lett.* **11,** 1636–1640 (2011).
20. Crochet, J. J., Duque, J. G., Werner, J. H. & Doorn, S. K. Photoluminescence imaging of electronic-impurity-induced exciton quenching in single-walled carbon nanotubes. *Nature Nanotech.* **7,** 126–132 (2012).
21. Högele, A., Galland, C., Winger, M. & Imamoğlu, A. Photon antibunching in the photoluminescence spectra of a single carbon nanotube. *Phys. Rev. Lett.* **100,** 217401 (2008).
22. Hirori, H., Matsuda, K., Miyauchi, Y., Maruyama, S. & Kanemitsu, Y. Exciton localization of single-walled carbon nanotubes revealed by femtosecond excitation correlation spectroscopy. *Phys. Rev. Lett.* **97,** 257401 (2006).
23. Kilina, S., Ramirez, J. & Tretiak, S. Brightening of the lowest exciton in carbon nanotubes via chemical functionalization. *Nano Lett.* **12,** 2306–2312 (2012).
24. Nagatsu, K., Chiashi, S., Konabe, S. & Homma, Y. Brightening of triplet dark excitons by atomic hydrogen adsorption in single-walled carbon nanotubes observed by photoluminescence spectroscopy. *Phys. Rev. Lett.* **105,** 157403 (2010).
25. Iakoubovskii, K. *et al.* Midgap luminescence centers in single-wall carbon nanotubes created by ultraviolet illumination. *Appl. Phys. Lett.* **89,** 173108 (2006).
26. Lefebvre, J., Austing, D. G., Bond, J. & Finnie, P. Photoluminescence imaging of suspended single-walled carbon nanotubes. *Nano Lett.* **6,** 1603–1608 (2006).
27. Tomio, Y. & Suzuura, H. Aharonov–Bohm effect on impurity-bound excitons in semiconducting carbon nanotubes. *J. Phys. Conf. Ser.* **302,** 012005 (2011).
28. Takagahara, T. & Hanamura, E. Giant-oscillator-strength effect on excitonic optical nonlinearities due to localization. *Phys. Rev. Lett.* **56,** 2533–2536 (1986).
29. Lüer, L. *et al.* Size and mobility of excitons in (6, 5) carbon nanotubes. *Nature Phys.* **5,** 54–58 (2009).
30. Mizuochi, N. *et al.* Electrically driven single-photon source at room temperature in diamond. *Nature Photon.* **6,** 299–303 (2012).

Acknowledgements

This research was supported by Precursory Research for Embryonic Science and Technology (PRESTO) programme (no. 3538 from the Japan Science and Technology Agency (JST)), by Grants-in-Aid for Scientific Research (nos 24681031, 22740195 and 23340085 from the Japan Society for the Promotion of Science (JSPS); no. 22016007 from the Ministry of Education, Culture, Sports, Science and Technology, Japan (MEXT)), and by Asahi Glass Foundation. The authors thank Y. Kawazoe, M. Uesugi, N. Tokitoh, T. Murakami, T. Umeyama and H. Imahori for experimental equipment and T. F. Heinz for discussions.

Author contributions

Y.M. developed the concept, designed the experiment and prepared the manuscript. Y.M. and M.I. performed the optical measurements. T.K. and M.O. contributed to the time-resolved photoluminescence measurements. M.I. prepared the samples. Y.M., M.I., S.M. and K.M. contributed to interpreting the results and writing the manuscript. All authors discussed the results and commented on the manuscript.

Additional information

Supplementary information is available in the online version of the paper. Reprints and permissions information is available online at www.nature.com/reprints. Correspondence and requests for materials should be addressed to Y.M.

Competing financial interests

The authors declare no competing financial interests.

Langmuir

Article

pubs.acs.org/Langmuir

Amoeba-Inspired Nanoarchitectonic Computing: Solving Intractable Computational Problems Using Nanoscale Photoexcitation Transfer Dynamics

Masashi Aono,*[,†] Makoto Naruse,[‡,§] Song-Ju Kim,[†] Masamitsu Wakabayashi,[⊥] Hirokazu Hori,[#] Motoichi Ohtsu,[§,∥] and Masahiko Hara[†]

[†]Flucto-Order Functions Research Team, RIKEN-HYU Collaboration Research Center, RIKEN Advanced Science Institute, 2-1 Hirosawa, Wako, Saitama 351-0198, Japan

[‡]Photonic Network Research Institute, National Institute of Information and Communications Technology, 4-2-1 Nukui-kita, Koganei, Tokyo 184-8795, Japan

[§]Nanophotonics Research Center and [∥]Department of Electrical Engineering and Information Systems, Graduate School of Engineering, The University of Tokyo, Japan

[⊥]Department of Biomolecular Engineering, Tokyo Institute of Technology, 4259 Nagatsuta, Midori-ku, Yokohama 226-8501, Japan

[#]Interdisciplinary Graduate School of Medicine and Engineering, University of Yamanashi, Takeda 4-3-11, Kofu, Yamanashi 400-8511, Japan

ABSTRACT: Biologically inspired computing devices and architectures are expected to overcome the limitations of conventional technologies in terms of solving computationally demanding problems, adapting to complex environments, reducing energy consumption, and so on. We previously demonstrated that a primitive single-celled amoeba (a plasmodial slime mold), which exhibits complex spatiotemporal oscillatory dynamics and sophisticated computing capabilities, can be used to search for a solution to a very hard combinatorial optimization problem. We successfully extracted the essential spatiotemporal dynamics by which the amoeba solves the problem. This amoeba-inspired computing paradigm can be implemented by various physical systems that exhibit suitable spatiotemporal dynamics resembling the amoeba's problem-solving process. In this Article, we demonstrate that photoexcitation transfer phenomena in certain quantum nanostructures mediated by optical near-field interactions generate the amoebalike spatiotemporal dynamics and can be used to solve the satisfiability problem (SAT), which is the problem of judging whether a given logical proposition (a Boolean formula) is self-consistent. SAT is related to diverse application problems in artificial intelligence, information security, and bioinformatics and is a crucially important nondeterministic polynomial time (NP)-complete problem, which is believed to become intractable for conventional digital computers when the problem size increases. We show that our amoeba-inspired computing paradigm dramatically outperforms a conventional stochastic search method. These results indicate the potential for developing highly versatile nanoarchitectonic computers that realize powerful solution searching with low energy consumption.

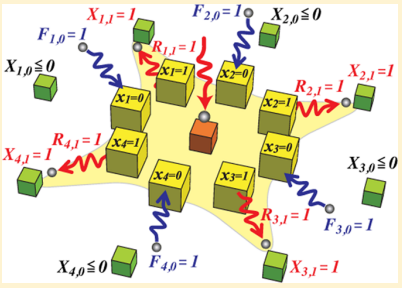

INTRODUCTION

Biological systems can be regarded as powerful computers in which massive numbers of elements such as biopolymers, proteins, and cells interact with each other and process vast amounts of environmental information in a self-organized manner.[1] For example, chains of amino acids promptly solve the protein folding problem, which is believed to be impossible for conventional digital computers to solve in a practical polynomial time.[2] For such an intractable problem, the number of all solution candidates, which should be examined thoroughly, grows exponentially as a function of the problem size and reaches an astronomical number, causing a combinatorial explosion.[3] What could be the source of the tremendous computational powers of biological systems? We believe that a key would be interactions among the elements.[1] More specifically, the interactions, which involve dynamic instabilities such as oscillations and fluctuations and physical constraints such as conservation laws of several resources, would generate complex spatiotemporal dynamics that could explore a state space broadly and efficiently. Learning how interacting biological elements perform powerful computations will provide insightful role models for promoting nanoarchitectonics, which aims to exploit novel functionalities using interacting nanoscale elements.

Natural computing is an emerging research field that uses the knowledge obtained from various natural phenomena, includ-

Special Issue: Interfacial Nanoarchitectonics

Received: January 22, 2013
Revised: March 22, 2013
Published: April 8, 2013

ing biological processes, to complement and overcome the limitations of conventional digital computers in solving computationally demanding problems in a decentralized manner, making optimal decisions adaptively in uncertain environments, reducing energy consumption, and so on.[4,5] Several algorithms for solving computationally demanding problems have been abstracted from biological processes such as information processing in neural networks,[6] evolutionary processes in genetic systems,[7] optimal path finding by ants,[8] and optimal solution search by swarms of insects.[9] In this context, a single-celled amoeboid organism, a plasmodium of the true slime mold *Physarum polycephalum* (Figure 1a), has been actively investigated owing to its intriguing computational capabilities. For example, this amoeba, despite the absence of a central nervous system, connects the optimal routes among food sources by changing its amorphous shape.[10,11] These computational capabilities were expected to emerge from its complex spatiotemporal behavior in which the volume of each part oscillates with a period of approximately 1 to 2 min in a fluctuating manner.[12,13]

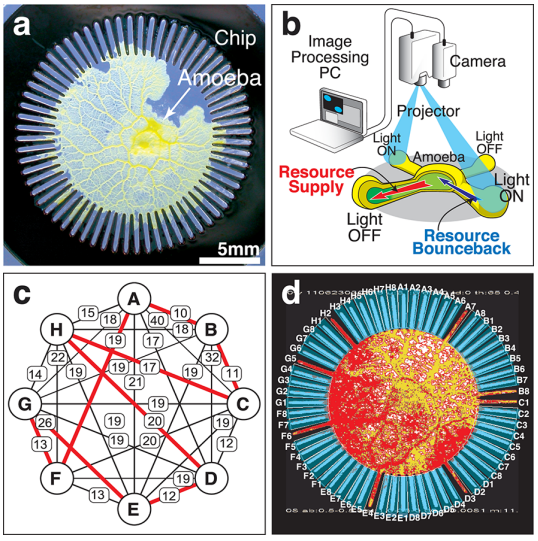

Figure 1. Amoeba-based computing. (a) Amoeboid organism *P. polycephalum* and Au-coated 64-lane chip resting on a nutrient-rich agar plate. The amoeba remains inside the chip because of its attraction to nutrients in the plate and its aversion to metal. (b) Experimental setup. The image of the amoeba recorded by a video camera was processed using a PC to update the image pattern for illumination with a projector. (c) Example of the eight-city map in the traveling salesman problem. The distance between each pair of cities is indicated on the corresponding edge. There uniquely exist shortest and longest routes having lengths of 100 and 200, respectively, where the average route length for all possible 2520 solutions was 149.1. (d) High-quality solution found by the amoeba-based computer. The amoeba's shape represents the route CHDEGFABC with a length of 128 (the red unicursal line in c), which is evaluated as being in the top 10% of solutions with regard to quality (shortness). Each lane of the chip is labeled *Vk*, which indicates the city name *V* and its visiting order *k*. Red and yellow pixels indicate increasing and decreasing thicknesses, respectively. Blue trapezoids indicate illuminated regions.

Aono et al. devised an amoeba-based computer (ABC)[14,15] that incorporates an amoeba to solve various optimization problems. In the ABC, we harnessed complex spatiotemporal oscillatory dynamics of the amoeba in a multilane chip (Figure 1a) by introducing unique optical feedback control (Figure 1b), which we call bounceback control. Under normal conditions, the amoeba supplies its intracellular resource (protoplasm) to its pseudopod-like branches so that they elongate by repeating several cycles of oscillations while conserving the total volume of the entire body. However, the branches retreat when stimulated by visible light as the resource bounces back from the illuminated region owing to the photoavoidance response. Sharing the constant volume of the resource, these branches interact with each other by transmitting information on their stimulated experiences through exchanging the resource to make an optimal decision on resource allocation. In the ABC, we updated the light stimulation of all of the lanes at 6 s intervals, depending on the change in the amoeba's shape. Under this dynamic environment, the organism tried to deform into an optimal shape, maximizing the body area for maximal nutrient absorption while minimizing the risk of being exposed to light stimuli.

We designed a rule for updating the light stimulation based on certain recurrent neural network dynamics so that the amoeba could search for a solution to the traveling salesman problem (TSP).[16] The TSP, one of the best-studied intractable problems, is stated as follows: given a map of n cities that defines the travel distance from any city to any other city (Figure 1c), find the shortest route for visiting each city exactly once and returning to the starting city. In the ABC, the challenge for the amoeba to find the shortest route is that its branches should not enter frequently illuminated lanes and should elongate into the optimal combination of the least frequently illuminated lanes. Note that the optimal combination cannot be found if this organism always obeys the optical feedback control rule. To compare the route lengths of solution candidates, it is necessary for the amoeba to make "errors" at appropriate frequencies. That is, to explore the state space broadly, sometimes the organism needs to misallocate the resource to its branches, contrary to their normal photoavoidance response, so that the branches expand even when illuminated and shrink even when unilluminated. In reality, owing to the intrinsic spatiotemporal oscillatory dynamics, each branch could vary its responses to light stimuli suitably depending on its oscillation phase, so the amoeba could find a high-quality solution through trial and error, as shown in Figure 1d.[17]

We evaluated the computational performance of the ABC by increasing the problem size n from 4 to 8 to explore how the explosive growth in the number of solutions $[(n-1)!/2 = 3, 12, 60, 360,$ and $2520]$ affects the performance.[18] Interestingly, the ABC found a high-quality solution (a shorter route) with a high probability and robustly maintained the high quality independently of n. Moreover, the search time required to find the solution grew almost linearly as a function of n, despite the explosive expansion of the state space. These results suggested that the ABC has an economical search ability to find a satisfactory high-quality solution at a low exploration cost, including a short search time. This might be a strategy of this organism to survive adaptively in uncertain environments.

Extracting the essential factors from the amoeba's economical search process, Aono et al. formulated an amoeba-inspired computing paradigm as a hybrid process of two spatiotemporal dynamics that are counterparts of the shape-changing behavior of the amoeba and the illumination-updating rule of the optical feedback control.[19] The former dynamics, which allocate the resource so that it is supplied to nonstimulated units and is

dx.doi.org/10.1021/la400301p | *Langmuir* 2013, 29, 7557−7564

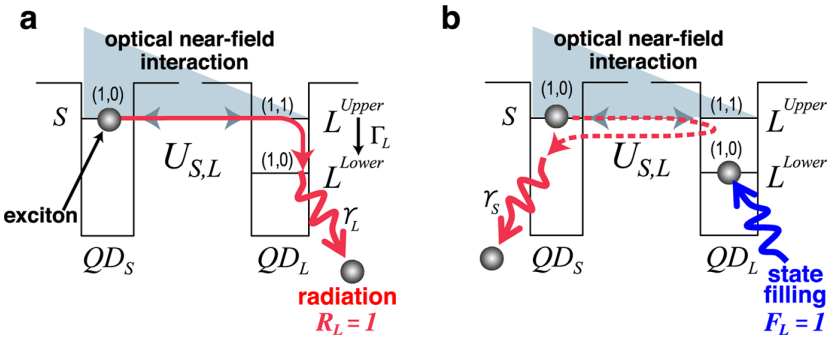

Figure 2. Photoexcitation transfer between QDs. (a) Exciton in QD_S is transferred to QD_L, from which it subsequently radiates. (b) Exciton population bounced back from QD_L when the lower energy level, L^{lower}, is filled with another exciton.

bounced back from stimulated units, must generate appropriate fluctuations in the stimulus response to make errors at optimal frequencies. In addition, the latter dynamics, which we call the bounceback control dynamics, should update the stimulations depending on the former states and should adequately apply repulsive stimulation to unfavorable units from which the resource should be bounced back.

These observations imply that, to develop novel computing devices that operate much faster than the amoeba, it would be possible to use the stimulus-responsive spatiotemporal dynamics of various physical systems in which some resource of the system is transferred to its subsystems in a fluctuating manner.

In fact, Naruse et al. showed that the spatiotemporal dynamics of photoexcitation transfer between quantum mechanical electronic states (excitonic states), which are implemented in semiconductor nanostructures and are mediated by optical near-field interactions, could be used to solve constraint satisfaction problems.[20,21] Optical near-field interactions occur at scales far below the wavelength of light and enable photoexcitation transfer to dipole-forbidden energy levels, which cannot be realized by conventional optical far fields. A useful theoretical treatment of the near-field optical excitation transfer process has been established on the basis of the dressed-photon model,[22] and the process has been experimentally demonstrated in quantum dot (QD) systems based on various semiconductors such as InGaAs,[23] ZnO,[24] and CdSe.[25] Kawazoe et al. demonstrated room-temperature photoexcitation transfer using two layers of 2D-ordered InGaAs QDs.[26] Akahane et al. fabricated 60 highly stacked layers of InAs QDs and produced a system with a total QD density of $4.73 \times 10^{12}/\mathrm{cm}^2$.[27] Moreover, Naruse et al. showed that the minimum energy dissipation in photoexcitation transfer has been shown to be 10^4 less than that required for a bit flip in a CMOS logic gate in conventional electrically wired devices.[28] These facts suggest that, by exploiting these photoexcitation transfer dynamics, our amoeba-inspired computing paradigm can be implemented on highly integrated low-energy-use quantum nanostructures.

Our paradigm is applied to solving the satisfiability problem (SAT), which is one of the most important intractable problems in computer science. In computational complexity theory, the complexity class NP (nondeterministic polynomial time) includes many difficult problems in which no polynomial time algorithm has been found so far. That is, these difficult problems often require an exponential time for conventionally known algorithms to solve. SAT was the first problem shown to be NP-complete, that is, the most difficult problem among those that belong to the class NP.[3] The NP completeness implies that all NP problems, including thousands of practical real-world problems, can be reduced to SAT. A powerful SAT solver, therefore, has enormous versatility. In fact, it is applied to a wide range of application problems such as software and hardware design, planning, constraint optimization, automatic inference, cryptography, and protein structure prediction.

In this Article, we first introduce the photoexcitation transfer dynamics, review the satisfiability problem, and describe our newly developed computing paradigm. Then, we compare the performance of our paradigm with that of a well-known algorithm. Finally, we discuss the origin of our paradigm's high performance and conclude the Article.

EXPERIMENTAL SECTION

Photoexcitation Transfer between Quantum Dots. We assume two spherical QDs whose radii are r_S and r_L ($>r_S$), which we call a small QD (QD_S) and a large QD (QD_L), respectively, as shown in Figure 2a. Under irradiation by input light, an exciton (electron−hole pair) is generated in QD_S. We consider photoexcitation transfer phenomena between QD_S and QD_L (i.e., transitions of exciton to states specified by (q_1, q_2), where q_1 and q_2 are the orbital angular momentum quantum number and magnetic quantum number, respectively). The energy eigenvalues of the states are given by

$$E_{(q_1,q_2)} = E_g + E_{ex} + \frac{\hbar^2 \alpha_{(q_1,q_2)}^2}{2mr^2} (q_1 = 1, 2, 3, \ldots) \quad (1)$$

where E_g is the band gap energy of the bulk semiconductor, E_{ex} is the exciton binding energy in the bulk system, m is the effective mass of the exciton, and $\alpha_{(q_1,q_2)}$ are determined from the boundary conditions, for example, $\alpha_{(q_1,0)} = q_1\pi$, $\alpha_{(1,1)} = 4.49$.

According to eq 1, there exists a resonance between the level with quantum number (1, 0) in QD_S, denoted by S in Figure 2a, and that with quantum number (1, 1) in QD_L, denoted by L^{upper}, if $r_L/r_S = 4.49/\pi \approx 1.43$. These energy levels S and L^{upper} are in resonance with each other and are connected by an interdot optical near-field interaction, $U_{S,L}$, which is given by a Yukawa-type potential

$$U_{S,L} = \frac{\nu \exp(-\mu \mathrm{dst}(S, L))}{\mathrm{dst}(S, L)} \quad (2)$$

where dst(S, L) denotes the distance between QD_S and QD_L and ν and μ are constants.[22,29] Note that, in typical light−matter interactions via optical far fields, transitions to states specified by (q_1, q_2) = (1, 1) are not allowed because this is a dipole-forbidden energy level. However, in optical near-field interactions, because of the large spatial inhomogeneity of the localized optical near fields at the surface of nanoscale materials, L^{upper} is allowed to be populated by excitons,

dx.doi.org/10.1021/la400301p | Langmuir 2013, 29, 7557−7564

violating the conventional optical selection rules.[29] Therefore, the exciton at level S in QD_S could be transferred to level L^{upper} in QD_L.

In QD_L, because of the sublevel energy relaxation with a relaxation constant Γ_L, which is faster than the optical near-field interaction, the exciton relaxes to the (1, 0) level, denoted by L^{lower}, from where it radiatively dissipates (Figure 2a). In addition, because the radiation lifetime of QDs is inversely proportional to their volume,[30] finally we find "unidirectional" exciton transfer from QD_S to QD_L. We consider that the exciton is transferred from QD_S to QD_L when we observe light emission from QD_L due to the radiation of optical energy. The radiation from L^{lower} is represented by the relaxation constant γ_L.

The unidirectionality of exciton transfer originates from the energy dissipation occurring in QD_L. Therefore, by disturbing the sublevel energy relaxation in QD_L, we can block exciton transfer to QD_L. In fact, when the lower energy level L^{lower} of QD_L is filled with another exciton, the exciton in QD_S cannot move to QD_L. The blocked exciton will bounce back and forth between QD_L and QD_S (optical nutation) and will finally dissipate from QD_S according to the relaxation constant γ_S, as shown schematically in Figure 2b. We can fill the state L^{lower} of QD_L by light stimulation, which is referred to as state filling. Like the branch of the amoeba that shrinks when illuminated, the probability of exciton transfer to QD_L is reduced when it is state-filled, as described in the next section.

Spatiotemporal Dynamics of Photoexcitation Transfer. To implement the amoeba-inspired computing paradigm, we design a system where a QD_S is surrounded by a number of QD_L's, as shown in Figure 3a. For simplicity, we consider four QD_L's (QD_A, QD_B, QD_C, and QD_D), each of which has the same upper level, lower level, sublevel relaxation constant, and radiation constant L^{upper}, L^{lower}, Γ_L, and γ_L, respectively.

We describe the basic properties of the spatiotemporal dynamics of exciton transfer in this system. We assume that the system initially has one exciton in S. For each QD_L, through the interdot interaction $U_{S,L}$, the exciton in S could be transferred to L^{upper}. Accordingly, we can derive quantum master equations in the density matrix formalism.[29,31] The interaction Hamiltonian is given by

$$H_{int} = \begin{pmatrix} 0 & U_{S,A} & U_{S,B} & U_{S,C} & U_{S,D} \\ U_{S,A} & 0 & 0 & 0 & 0 \\ U_{S,B} & 0 & 0 & 0 & 0 \\ U_{S,C} & 0 & 0 & 0 & 0 \\ U_{S,D} & 0 & 0 & 0 & 0 \end{pmatrix} \quad (3)$$

Although interactions between the QD_L's occur, for simplicity they are not considered here. The relaxation regarding the above-mentioned states is described by $N_\Gamma = \mathrm{diag}(\gamma_S, \Gamma_A, \Gamma_B, \Gamma_C, \Gamma_D)$. Then the Liouville equation for the system is

$$\frac{d\rho(t)}{dt} = -\frac{i}{\hbar}[H_{int}, \rho(t)] - N_\Gamma \rho(t) - \rho(t) N_\Gamma \quad (4)$$

where $\rho(t)$ is the density matrix with respect to the five energy levels and $\hbar$ is Planck's constant divided by 2π. Similarly, we can derive ordinary differential equations with respect to L^{lower}, which is populated by the relaxations from L^{upper} with constants Γ_L, which decay radiatively with relaxation constants γ_L.

In the numerical calculation, we assume $U_{S,L}^{-1}$ = 100 ps, Γ_L^{-1} = 1 ps, γ_L^{-1} = 1 ns, and $\gamma_L^{-1} = (r_L/r_S)^3 \times \gamma_L^{-1} \approx 2.92$ ns as a typical parameter set. For instance, in experimental demonstrations based on a CdSe/ZnS core−shell QD,[32] the measured radiation lifetime of a CdSe/ZnS QD with a diameter of 2.8 nm (QD_L) was 2.1 ns, which is close to the radiation lifetimes γ_L^{-1} and γ_S^{-1}. In addition, the interaction time between QD_S and QD_L was estimated to be 135 ps,[32] which is also close to the above interdot interaction time $U_{S,L}^{-1}$.

When the above Liouville equation is solved numerically (eq 4), the time evolution of the populations of the lower energy levels of the QD_L's, which are relevant to occurrences of radiation, can be calculated. Figure 3b indicates that the system uniformly grows the

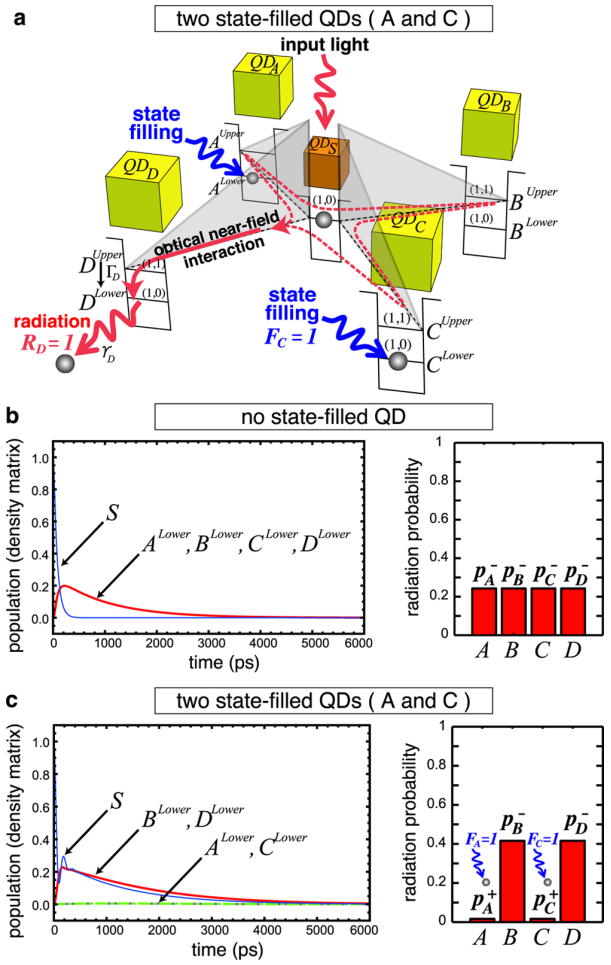

Figure 3. Spatiotemporal dynamics of photoexcitation transfer in the system with QD_S surrounded by four large QDs (QD_A, QD_B, QD_C, and QD_D). (a, c) When QD_A and QD_C are state-filled, the exciton is likely to be transferred to either QD_B or QD_D, from which it radiates. Each of radiation probabilities (right panel) is calculated as a time integration of each corresponding time evolution of populations (left panel) divided by a gain constant g. (b) In the absence of state-filling stimulation, radiation occurs in the four large dots with equal probability.

populations of A^{lower}, B^{lower}, C^{lower}, and D^{lower} while reducing the population of S and finally reaches equilibrium. Figure 3c shows the case where QD_A and QD_C are subjected to state filling by light stimulation. A way of describing such a state-filling effect in eq 4 is to induce a significant increase in the sublevel relaxation lifetime of the state-filled QD_A and QD_C; we assume that the lifetime increased to $\Gamma_A^{-1} = \Gamma_C^{-1} = 10^5$ ps. Such a formation has been validated in the literature.[21] Because of these changes in the parameters, the exciton is more likely be transferred to QD_B or QD_D than to QD_A or QD_C, as shown in Figure 3c.

Radiation Probability. We can obtain the probability p_L that the exciton in QD_S is transferred to QD_L, from which it subsequently radiates by numerically integrating the time evolution of the population of L_{lower} over 6000 ps and dividing it by a certain gain constant g, as shown in Figure 3b,c. In our numerical calculation, we assume that radiation occurs in QD_L if a uniformly generated random number in [0.0, 1.0] is less than the value of p_L. Therefore, p_L represents the probability that radiation from QD_L is observed within 6000 ps. Thus, more than one radiation event can occur in a number of QD_L's. This verifies that $p_A + p_B + p_C + p_D \neq 1$. The radiation

dx.doi.org/10.1021/la400301p | Langmuir 2013, 29, 7557−7564

probabilities when QD_L is state-filled and non-state-filled are denoted by p_L^+ and p_L^-, respectively.

We briefly discuss the similarities between the photoexcitation transfer dynamics and the shape-changing behavior of the amoeba. We consider that the amoeba's intracellular resource supply to its branch can be compared to exciton transfer to QD_L (i.e., radiation in QD_L). As the amoeba's intracellular resource is bounced back from illuminated branches, the exciton population is bounced back from state-filled QD_L's. However, as mentioned previously, to explore the state space broadly, the amoeba had to make errors at appropriate frequencies; the branch varied its normal photoavoidance response depending on its intrinsic oscillation phase so that it could expand even when illuminated and shrink even when unilluminated. In the photoexcitation transfer dynamics, these error mechanisms are implemented by the occurrence and nonoccurrence of radiation in state-filled and non-state-filled QD_L's with probabilities of p_L^+ and $1 - p_L^-$, respectively.

As shown in the right panels of Figure 3b,c, p_A and p_C decreased owing to state-filling stimulation, whereas p_B^- and p_D^- increased as if they tried to compensate for the decrements in p_A and p_C. That is, the radiation probability of each QD_L varies in response to the current state-filling stimulation applied to other distant QD_L's. In other words, the stimulus response of each QD_L is not determined locally. This nonlocal property is shown more clearly in Figure 4a,b. The radiation

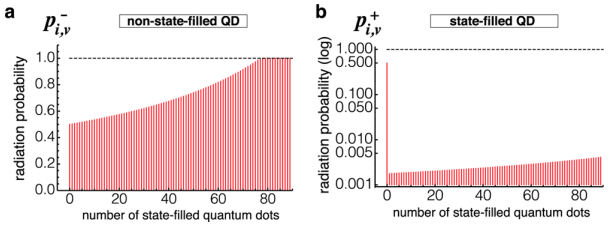

Figure 4. Dependence of the radiation probability on the number of all state-filled $QD_{j,u}$'s, $f = \Sigma_{j,u}F_{j,u}(t)$, in the system consisting of 150 $QD_{j,u}$'s for solving a 75-variable SAT. (a) Radiation probability $p_{i,v}^-$ in non-state-filled $QD_{i,v}$. (b) Radiation probability $p_{i,v}^+$ in state-filled $QD_{i,v}$. Each probability, which is obtained as a time integration of population evolution divided by g, grows nonlinearly as a function of f. We set g such that it gives $p_{i,v}^- = p_{i,v}^+ = 0.5$ when $f = 0$.

probabilities of non-state-filled and state-filled QD_L's, p_L^- and p_L^+, increased nonlinearly as a function of the number of all state-filled QD_L's. In case of the amoeba, the previously mentioned conservation law in the total resource volume entailed a nonlocal correlation among the amoeba's branches (i.e., a volume increment in one branch is immediately compensated for by a volume decrement(s) in the other branch(es)). This nonlocal correlation was shown to be useful for efficient and adaptive decision making.[33]

Satisfiability Problem. SAT is the problem of determining if a given Boolean formula ϕ of N variables $x_i \in \{0 \text{ (false)}, 1 \text{ (true)}\}$ $(i \in I = \{1, 2,..., N\})$ is satisfiable (i.e., there exists at least one assignment of truth values (0 or 1) to the variables that makes the formula true ($\phi = 1$)). Roughly speaking, ϕ represents a logical proposition, and the existence of a satisfying assignment verifies that the proposition is self-consistent. For example, a formula $\phi_{ex} = (x_1 \vee \neg x_2) \wedge (\neg x_2 \vee x_3 \vee \neg x_4) \wedge (x_1 \vee x_3) \wedge (x_2 \vee \neg x_3) \wedge (x_3 \vee \neg x_4) \vee (\neg x_1 \vee x_4)$ has a satisfying assignment $(x_1, x_2, x_3, x_4) = (1, 1, 1, 1)$, which is a uniquely existing solution. Even if ϕ has more than one solution, this instance can be solved when at least one solution is found. However, to prove unsatisfiability, the only sure method known to be applicable to arbitrary formulas is to check the inconsistency of all possible assignments, the number of which grows exponentially as 2^N.

SAT is called 3-SAT when ϕ consists of M clauses that are connected by $\wedge$ (and), and each clause connects at most three literals by $\vee$ (or) as $(x_j^* \vee x_k^* \vee x_l^*)$, where each literal x_i^* can be either x_i or $\neg x_i$. Any SAT instance can be transformed to a 3-SAT instance, and 3-SAT is also NP-complete. In this study, we design our computing paradigm for application to solving 3-SAT.

Amoeba-Inspired Nanoarchitectonic Computer. As shown in Figure 5, to solve an N-variable 3-SAT, we use $2N$ large QDs ($QD_{i,v}$'s)

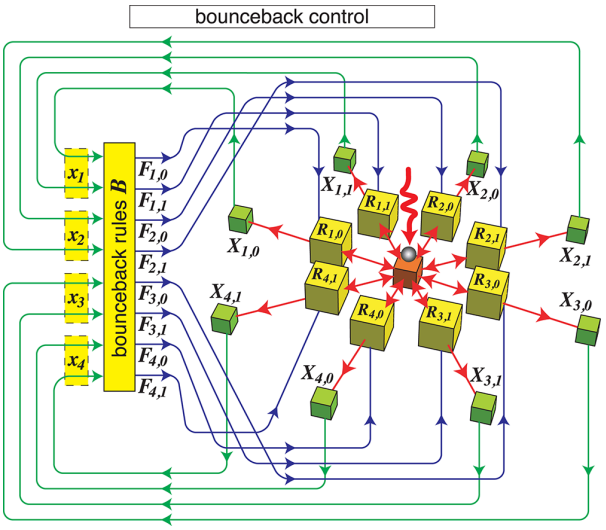

Figure 5. Data-flow diagram of the amoeba-inspired nanoarchitectonic computer.

that receive optical energy from QD_S, where the label (i,v) indicates that value $v \in \{0, 1\}$ is assigned to variable x_i $(i \in I = \{1, 2,..., N\})$ (i.e., $x_i = v$). When the exciton in QD_S is transferred to $QD_{i,v}$ and subsequently radiation is observed at a discrete time step t, we write this status as $R_{i,v}(t) = 1$, whereas $R_{i,v}(t) = 0$ indicates that no radiation occurs. When state-filling stimulation is applied to $QD_{i,v}$, we denote this status as $F_{i,v}(t) = 1$, whereas $F_{i,v}(t) = 0$ denotes no state filling. Thus, radiation $R_{i,v}(t) = 1$ occurs with a probability that depends on the state-filling stimulation $F_{i,v}(t)$ as follows:

$$R_{i,v}(t) = \begin{cases} 1 & (\text{with probability } p_{i,v}^+(t) \text{ if } F_{i,v}(t) = 1) \\ 1 & (\text{with probability } p_{i,v}^-(t) \text{ if } F_{i,v}(t) = 0) \\ 0 & (\text{otherwise}) \end{cases} \quad (5)$$

Figure 4 shows the dependence of the radiation probabilities of non-state-filled and state-filled $QD_{i,v}$'s, $p_{i,v}^-(t)$, and $p_{i,v}^+(t)$ on the number of all state-filled $QD_{j,u}$'s (i.e., $\Sigma_{j,u}F_{j,u}(t)$).

Each radiation event $R_{i,v}$ is accumulated by a newly introduced variable $X_{i,v} \in \{-1, 0, 1\}$ as follows:

$$X_{i,v}(t+1) = \begin{cases} X_{i,v}(t) + 1 & (\text{if } R_{i,v}(t) = 1 \text{ and } X_{i,v}(t) < 1) \\ X_{i,v}(t) - 1 & (\text{if } R_{i,v}(t) = 0 \text{ and } X_{i,v}(t) > -1) \\ X_{i,v}(t) & (\text{otherwise}) \end{cases} \quad (6)$$

Equation 6 can be implemented either physically or digitally; the values of $X_{i,v}$ can be stored either by some additional QDs or by some external control unit, as illustrated in Figures 5 and 1b, respectively. At each step t, the system transforms a configuration $X = (X_{1,0}, X_{1,1}, X_{2,0}, X_{2,1},..., X_{N,0}, X_{N,1})$ into an assignment $x = (x_1, x_2,..., x_N)$ as follows

$$x_i(t) = \begin{cases} 0 & (\text{if } X_{i,0}(t) = 1 \text{ and } X_{i,1}(t) \le 0) \\ 1 & (\text{if } X_{i,0}(t) \le 0 \text{ and } X_{i,1}(t) = 1) \\ x_i(t-1) & (\text{otherwise}) \end{cases} \quad (7)$$

where $x_i(0)$ = undefined for all i.

dx.doi.org/10.1021/la400301p | Langmuir 2013, 29, 7557−7564

Bounceback Control Dynamics. The state-filling stimulations $F_{i,v}$ are updated synchronously according to the following dynamics

$$F_{i,v}(t+1) = \begin{cases} 1 & (\text{if } \exists\ (P, Q) \in B(\ \forall\ (j, u) \in P(X_{j,u}(t) = 1) \\ & \quad \text{and } (i, v) \in Q)) \\ 0 & (\text{otherwise}) \end{cases} \tag{8}$$

where B is a set of bounceback rules to be explained in this section. Each element (P, Q) in B implies the following statement: if all of the $X_{j,u}$'s specified by P are positive at t, then stimulate all $QD_{i,v}$'s specified by Q to inhibit their radiation at $t + 1$. Stated simply, if $x_j = u$, then x_i should not be v.

To see the meaning of the bounceback rules, let us consider the example formula ϕ_{ex}, which is shown in Figure 6a. To satisfy this

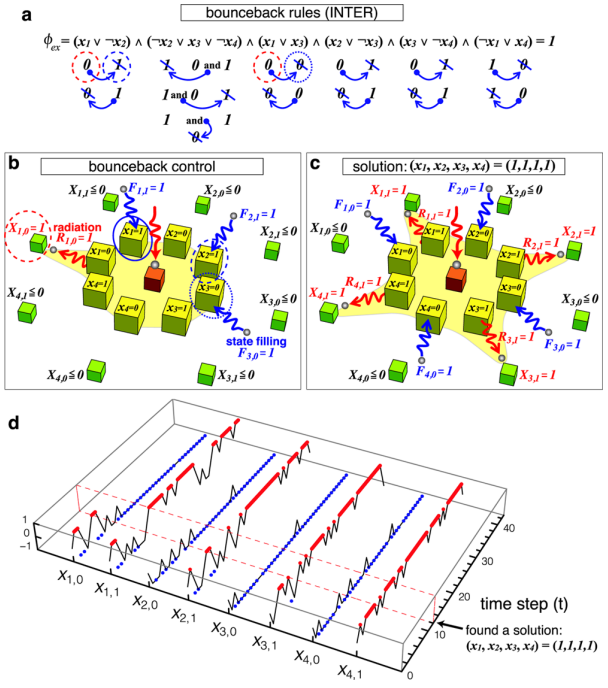

Figure 6. Bounceback control dynamics. (a) All bounceback rules in INTER for ϕ_{ex}. (b) Bounceback control applies state-filling stimulations $F_{1,1}(t + 1) = F_{2,1}(t + 1) = F_{3,0}(t + 1) = 1$ if $X_{1,0}(t) = 1$. (c) Configuration $X = (0, 1, 0, 1, 0, 1, 0, 1)$, which represents a solution $(x_1, x_2, x_3, x_4) = (1, 1, 1, 1)$. (d) Simulated time evolution. Red and blue dots indicate $X_{i,v}(t) = 1$ and $F_{i,v}(t) = 1$, respectively.

formula for $\phi_{ex} = 1$, we should make every clause true because all clauses are connected by $\wedge$. Suppose, for example, that the system tried to assign $x_1 = 0$ (i.e., $X_{1,0}(t) = 1$), as indicated by the red broken circle in Figure 6b. Now let us focus on the first clause $(x_1 \vee \neg x_2)$ in ϕ_{ex}. To make this clause true, if $x_1 = 0$ then x_2 should not be 1. Therefore, we apply state-filling stimulation $F_{2,1}(t + 1) = 1$ to inhibit the radiation $R_{2,1}(t + 1)$ of $QD_{2,1}$, as indicated by the blue broken circle. However, because x_3 in the third clause $(x_1 \vee x_3)$ should not be 0, we apply $F_{3,0}(t + 1) = 1$ (the blue dotted circle). In addition, we apply $F_{1,1}(t + 1) = 1$ (the blue solid circle) because if $x_1 = 0$ then obviously x_1 should not be 1. Likewise, the set of all bounceback rules B is determined by scanning all clauses in ϕ_{ex}, as shown in Table 1.

We formally define the set B = INTRA∪INTER∪CONTRA in what follows. INTRA forbids each variable i to take two values 0 and 1 simultaneously:

Table 1. All Bounceback Rules for ϕ_{ex}

B	P	Q
INTRA	{(1, 0)}	{(1, 1)}
	{(1, 1)}	{(1, 0)}
	{(2, 0)}	{(2, 1)}
	{(2, 1)}	{(2, 0)}
	{(3, 0)}	{(3, 1)}
	{(3, 1)}	{(3, 0)}
	{(4, 0)}	{(4, 1)}
	{(4, 1)}	{(4, 0)}
INTER	{(2, 1)}	{(1, 0)}
	{(1, 0)}	{(2, 1)}
	{(3, 0), (4, 1)}	{(2, 1)}
	{(2, 1), (4, 1)}	{(3, 0)}
	{(2, 1), (3, 0)}	{(4, 1)}
	{(3, 0)}	{(1, 0)}
	{(1, 0)}	{(3, 0)}
	{(3, 1)}	{(2, 0)}
	{(2, 0)}	{(3, 1)}
	{(4, 1)}	{(3, 0)}
	{(3, 0)}	{(4, 1)}
	{(4, 0)}	{(1, 1)}
	{(1, 1)}	{(4, 0)}
CONTRA	{(1, 1), (3, 0)}	{(1, 1), (3, 0)}
	{(1, 0), (2, 0)}	{(1, 0), (2, 0)}
	{(1, 0), (3, 1)}	{(1, 0), (3, 1)}
	{(2, 1), (4, 0)}	{(2, 1), (4, 0)}
	{(2, 0), (4, 1)}	{(2, 0), (4, 1)}
	{(3, 0), (4, 0)}	{(3, 0), (4, 0)}
	{(1, 1), (2, 1), (3, 0)}	{(1, 1), (2, 1), (3, 0)}
	{(2, 0), (2, 1), (4, 1)}	{(2, 0), (2, 1), (4, 1)}
	{(3, 0), (3, 1), (4, 1)}	{(3, 0), (3, 1), (4, 1)}

$$\text{INTRA} = \{(\{(i, v)\}, \{(i, 1 - v)\}) \mid i \in I \wedge v \in \{0, 1\}\} \tag{9}$$

Each clause $c = x_j^* \vee x_k^* \vee x_l^*$ in ϕ is represented as a set $C = \{j^*, k^*, l^*\}$ with its literals x_i^* mapped to $i^* = i$ if $x_i^* = x_i$ and to $-i$ otherwise, and the formula ϕ is expressed equivalently by a set Φ, which includes all of the clauses as their elements. The example formula ϕ_{ex} is transformed to $\Phi_{ex} = \{\{1, -2\}, \{-2, 3, -4\}, \{1, 3\}, \{2, -3\}, \{3, -4\}, \{-1, 4\}\}$. For each C in Φ and each variable i in C, INTER blocks the radiation [either $R_{i,0}(t + 1)$ or $R_{i,1}(t + 1)$] that makes c false

$$\text{INTER} = \{(P, \{(i, 0)\}) \mid i \in C \wedge C \in \Phi\} \cup \{(P, \{(i, 1)\}) \mid -i \in C \wedge C \in \Phi\} \tag{10}$$

where $P = \{(j, 0) \mid j \in C \wedge j \neq i\} \cup \{(j, 1) \mid -j \in C \wedge j \neq i\}$. Some rules in INTER may imply that neither 0 nor 1 can be assigned to a variable. To avoid this contradiction, for each variable i, we build CONTRA by checking all of the relevant rules in INTER:

$$\text{CONTRA} = \{(P \cup P', P \cup P') \mid i \in I \wedge (P, \{(i, 0)\}) \in \text{INTER} \wedge (P', \{(i, 1)\}) \in \text{INTER}\} \tag{11}$$

Before the computation, B is obtained in a polynomial time of $O(NM)$ by generating all of the bounceback rules in INTRA, INTER, and CONTRA according to the above procedures.

Note that the system can be stabilized if the following condition holds for all (i, v): if $X_{i,v}(t) = 1$ then $F_{i,v}(t) = 0$ or if $X_{i,v}(t) \leq 0$ then $F_{i,v}(t) = 1$. When this condition is not met, the system cannot be stabilized. Indeed, if $X_{i,v}(t) = 1$ and $F_{i,v}(t) = 1$, then radiation in $QD_{i,v}$ is likely to be inhibited as $R_{i,v}(t + 1) = 0$; consequently, $X_{i,v}(t + 2) = 0$. However, if $X_{i,v}(t) \leq 0$ and $F_{i,v}(t) = 0$, then radiation $R_{i,v}(t + 1) = 1$ is likely to be promoted to facilitate $X_{i,v}(t + 2) = 1$. These changes in the sign of $X_{i,v}$ make the system unstable. We designed the bounceback rules so that only satisfying assignments can be stabilized. This implies

dx.doi.org/10.1021/la400301p | Langmuir 2013, 29, 7557−7564

that if a configuration X represents a solution then X can be maintained for the longest duration and thus occurs with the highest frequency when the system evolves for a sufficiently large number of iteration steps.

AmoebaSATnano and WalkSAT. Our numerical calculation method for simulating the amoeba-inspired computing paradigm can be used as an algorithm for solving SAT. We call this algorithm AmoebaSATnano. We evaluate the performance of AmoebaSATnano in comparison with that of the best-studied stochastic search algorithm called WalkSAT, which finds a solution with a reasonably large probability after a fairly small number of iterations.[34]

WalkSAT starts from a randomly chosen assignment $x = (x_1, x_2, ..., x_N)$. At each iteration, by checking whether each clause in ϕ is satisfied by the current assignment x, WalkSAT randomly chooses one of the unsatisfied clauses and satisfies it by flipping one of its variables chosen at random (i.e., $0 \rightarrow 1$ and $1 \rightarrow 0$). This routine is iterated until x satisfies ϕ or we run out of time. Schöning estimated the average number of iterations that WalkSAT required to find a solution to a 3-SAT as an exponential function of $(^4/_3)^N \mathrm{poly}(N)$.[34] WalkSAT is one of the fastest algorithms.[35]

RESULTS

The computation of AmoebaSATnano starts at $X_{i,v}(0) = R_{i,v}(0) = F_{i,v}(0) = 0$ for all (i, v), and the time evolution of the system is simulated by updating eqs 5, 6, and 8 iteratively. Figure 6d shows that the system successfully found the solution of the example formula ϕ_{ex} at $t = 12$, which is represented by the configuration shown in Figure 6c. We can confirm that $X = (0, 1, 0, 1, 0, 1, 0, 1)$, which represents the solution $(x_1, x_2, x_3, x_4) = (1, 1, 1, 1)$ that is observed most frequently after $t = 12$.

We compared the performance of AmoebaSATnano and WalkSAT for benchmark SAT instances, which are provided to the public by SATLIB online.[36,37] We used a family of 3-SAT instance distributions, Uniform Random-3-SAT, which was obtained by randomly generating three-literal conjunctive normal form formulas. The hardness of a 3-SAT has been shown to be maximal when the ratio between the number of variables N and the number of clauses M is set at the phase-transition region around $M/N = 4.26$.[38,39] We chose 100 instances each from each of the test sets uf75−325 and uf100−430, which took satisfiable $N = 75 - M = 325$ and $N = 100 - M = 430$ formulas from the most difficult regions, $M/N \approx 4.333$ and $M/N = 4.3$, respectively.

For each instance, we conducted 500 trials consisting of Monte Carlo simulations to obtain the average number of iterations (time steps t) required to find a solution. Figure 7 shows that in almost all instances AmoebaSATnano found a solution more quickly than WalkSAT. In particular, AmoebaSATnano outperformed WalkSAT more significantly as N increased.

DISCUSSION AND CONCLUSIONS

We demonstrate that photoexcitation transfer phenomena in a QDs system mediated by optical near-field interactions can be used to solve SAT. Our amoeba-inspired computing paradigm is fundamentally different from conventional optical computing or optical signal processing, which are limited by the properties of propagating light. Our paradigm also differs from the quantum computing paradigm, which exploits a superposition of all possible states to produce a correct solution. This is because our paradigm exploits both coherent and dissipative processes. In fact, optical-near-field-mediated photoexcitation transfer is a coherent process, suggesting that an exciton could be transferred to all possible destination QD_L's via a resonance

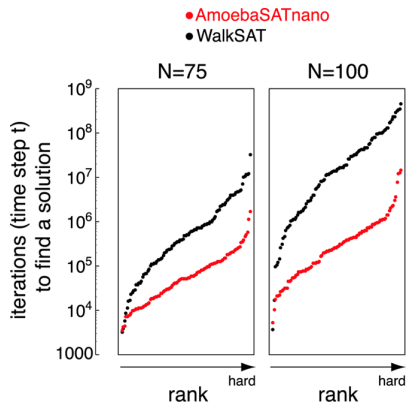

Figure 7. Performance comparison between our AmoebaSATnano (red) and the well-known WalkSAT (black) for benchmark 3-SAT instances of $N = 75$ and 100. Each point indicates the number of iterations required to find a solution for each instance, averaged over 500 trials. For each algorithm and each N, we evaluated 100 points (instances) and ranked (sorted) all of the points from easiest to most difficult (requiring the largest number of iterations). The results are compared on a logarithmic scale, which implies that AmoebaSATnano has a significant advantage over WalkSAT.

energy level, but such a coherent interaction produces a unidirectional transfer by an energy dissipation process occurring in QD_L. A strength of our paradigm is that photoexcitation transfer is 10^4 times more energy efficient than conventional electrically wired bit-flip circuits.[28]

An important issue that we should address to implement our paradigm experimentally is a means of introducing the bounceback control dynamics; at each iteration, the control dynamics should store the values of $X_{i,v}(t)$ by detecting the radiation values $R_{i,v}(t)$, determine the state-filling stimulations $F_{i,v}(t + 1)$ according to the set of bounceback rules B, and apply these stimulations to $QD_{i,v}$'s, as shown in Figure 5. An external approach would be to use an external control unit such as a combination of a PC with a projector, as we did for the amoeba-based computing (Figure 1b). However, the external control unit may impose additional energy costs and may limit the processing speed of our paradigm. However, an internal approach could implement the control dynamics using additional QDs without introducing the external control unit. It may be possible to embed the counterpart of the external control unit in the arrangement of QDs because the bounceback rules are expressed by combining elementary logical operations and these logical operations have already been implemented experimentally using several QD systems.[26]

Because SAT is NP-complete, a powerful SAT solver is useful for a broad spectrum of applications in artificial intelligence, information security, and bioinformatics. We demonstrated that, for benchmark 3-SAT instances chosen from the most difficult region, our paradigm found a solution much faster than did the conventionally known fastest algorithm. We believe that the origin of the high performance of our paradigm will be attributed to interactions among the QDs. At each iteration, the conventional algorithm flips a single state without implementing any interaction among the variables. In contrast, our paradigm updates at most $2N$ states through a large number of interactions among the QDs, which exchange information on stimulated experiences via the bounceback control dynamics. This difference in the number of interactions might produce a

dx.doi.org/10.1021/la400301p | Langmuir 2013, 29, 7557−7564

huge difference in the computing power.[1] This discussion would be supported by the fact that our paradigm became more advantageous as N increased.

Putting these facts together, this Article paves the way for applying nanometer-scale optical near-field interactions to develop novel low-energy-use highly versatile powerful computers. We believe that our amoeba-inspired computing paradigm presents a promising direction for nanoarchitectonics, which harnesses novel functionalities in the interactions among nanoscale elements.

AUTHOR INFORMATION

Corresponding Author

*E-mail: masashi.aono@elsi.jp.

Notes

The authors declare no competing financial interest.

REFERENCES

(1) Conrad, M. The Price of Programmability. In *The Universal Turing Machine: A Half-Century Survey*; Rolf, H., Ed.; Springer-Verlag: Wien, Austria, 1994; pp 261−281.

(2) Berger, B.; Leighton, T. Protein Folding in the Hydrophobic-Hydrophilic (HP) Model is NP-Complete. *J. Comput. Biol.* **1998**, *5*, 27−40.

(3) Garey, M. R.; Johnson, D. S. *Computers and Intractability: A Guide to the Theory of NP-Completeness*, W.H. Freeman and Co.: New York, 1979.

(4) Rozenberg, G., Bäck, T., Kok, J., Eds. *Handbook of Natural Computing*; Springer-Verlag: New York, 2012.

(5) *International Technology Roadmap for Semiconductors*. Emerging Research Devices, 2009.

(6) Hopfield, J. J.; Tank, D. W. Computing with Neural Circuits: A Model. *Science* **1986**, *233*, 625−633.

(7) Holland, J. H. *Adaptation in Natural and Artificial Systems*, 2nd ed.; MIT Press: Cambridge, MA, 1992.

(8) Dorigo, M.; Maniezzo, V.; Colorni, A. Ant System: Optimization by a Colony of Cooperating Agents. *IEEE Trans. Syst. Man Cybern. B* **1996**, *26*, 29−41.

(9) Poli, R.; Kennedy, J.; Blackwell, T. Particle Swarm Optimization. *Swarm Intell.* **2007**, *1*, 33−57.

(10) Nakagaki, T.; Yamada, H.; Toth, A. Intelligence: Maze-Solving by an Amoeboid Organism. *Nature* **2000**, *407*, 470.

(11) Tero, A.; Takagi, S.; Saigusa, T.; Ito, K.; Bebber, D. P.; Fricker, M. D.; Yumiki, K.; Kobayashi, R.; Nakagaki, T. Rules for Biologically Inspired Adaptive Network Design. *Science* **2010**, *327*, 439−442.

(12) Takamatsu, A.; Tanaka, R.; Yamada, H.; Nakagaki, T.; Fujii, T.; Endo, I. Spatiotemporal Symmetry in Rings of Coupled Biological Oscillators of Physarum Plasmodial Slime Mold. *Phys. Rev. Lett.* **2001**, *87*, 078102.

(13) Takagi, S.; Ueda, T. Emergence and Transitions of Spatiotemporal Patterns in Thickness Oscillation by the Plasmodium of the True Slime Mold Physarum Polycephalum. *Phys. D* **2008**, *237*, 420−427.

(14) Aono, M.; Gunji, Y.-P. Beyond Input-output Computings: Error-driven Emergence with Parallel Non-Distributed Slime Mold Computer. *BioSystems* **2003**, *71*, 257−287.

(15) Aono, M.; Hara, M.; Aihara, K. Amoeba-Based Neurocomputing with Chaotic Dynamics. *Commun. ACM* **2007**, *50*, 69−72.

(16) Aono, M.; Hirata, Y.; Hara, M.; Aihara, K. Amoeba-based Chaotic Neurocomputing: Combinatorial Optimization by Coupled Biological Oscillators. *New Gener. Comput.* **2009**, *27*, 129−157.

(17) Zhu, L.; Aono, M.; Kim, S.-J.; Hara, M. Amoeba-Based Computing for Traveling Salesman Problem: Long-Term Correlations between Spatially Separated Individual Cells of Physarum Polycephalum. *BioSystems* **2013**, *112*, 1−10.

(18) Zhu, L.; Aono, M.; Kim, S.-J.; Hara, M. Problem-Size Scalability of Amoeba-Based Neurocomputer for Traveling Salesman Problem. *Proc. NOLTA* **2011**, 108−111.

(19) Aono, M.; Kim, S.-J.; Zhu, L.; Naruse, M.; Ohtsu, M.; Hori, H.; Hara, M. Amoeba-Inspired SAT Solver. *Proc. NOLTA* **2012**, 586−589.

(20) Naruse, M.; Miyazaki, T.; Kawazoe, T.; Sangu, S.; Kobayashi, K.; Kubota, F.; Ohtsu, M. Nanophotonic Computing Based on Optical Near-Field Interactions Between Quantum Dots. *IEICE Trans. Electron. E88-C* **2005**, 1817−1823.

(21) Naruse, M.; Aono, M.; Kim, S.-J.; Kawazoe, T.; Nomura, W.; Hori, H.; Hara, M.; Ohtsu, M. Spatiotemporal Dynamics in Optical Energy Transfer on the Nanoscale and Its Application to Constraint Satisfaction Problems. *Phys. Rev. B* **2012**, *86*, 125407.

(22) Ohtsu, M.; Kawazoe, T.; Yatsui, T.; Naruse, M. Single-Photon Emitter Using Excitation Energy Transfer between Quantum Dots. *IEEE J. Sel. Top. Quantum Electron.* **2009**, *14*, 1404−1417.

(23) Kawazoe, T.; Kobayashi, K.; Akahane, K.; Naruse, M.; Yamamoto, N.; Ohtsu, M. Demonstration of Nanophotonic NOT Gate Using Near-Field Optically Coupled Quantum Dots. *Appl. Phys. B: Laser Opt.* **2006**, *84*, 243−246.

(24) Yatsui, T.; Sangu, S.; Kawazoe, T.; Ohtsu, M.; An, S. J.; Yoo, J.; Yi, G.-C. Nanophotonic Switch Using ZnO Nanorod Double-Quantum-Well Structures. *Appl. Phys. Lett.* **2007**, *90*, 223110.

(25) Nomura, W.; Yatsui, T.; Kawazoe, T.; Naruse, M.; Ohtsu, M. Structural Dependency of Optical Excitation Transfer via Optical Near-Field Interactions between Semiconductor Quantum Dots. *Appl. Phys. B: Laser Opt.* **2010**, *100*, 181−187.

(26) Kawazoe, T.; Ohtsu, M.; Aso, S.; Sawado, Y.; Hosoda, Y.; Yoshizawa, K.; Akahane, K.; Yamamoto, N.; Naruse, M. Two-Dimensional Array of Room-Temperature Nanophotonic Logic Gates Using InAs Quantum Dots in Mesa Structures. *Appl. Phys. B: Laser Opt.* **2011**, *103*, 537−546.

(27) Akahane, K.; Yamamoto, N.; Tsuchiya, M. Highly Stacked Quantum-Dot Laser Fabricated Using a Strain Compensation Technique. *Appl. Phys. Lett.* **2008**, *93*, 041121.

(28) Naruse, M.; Hori, H.; Kobayashi, K.; Holmström, P.; Thylén, L.; Ohtsu, M. Lower Bound of Energy Dissipation in Optical Excitation Transfer via Optical Near-Field Interactions. *Opt. Express* **2010**, *18*, A544−A553.

(29) Ohtsu, M.; Kobayashi, K.; Kawazoe, T.; Yatsui, T.; Naruse, M. *Principles of Nanophotonics*; Taylor and Francis: Boca Raton, FL, 2008.

(30) Itoh, T.; Furumiya, M.; Ikehara, T.; Gourdon, C. Size-dependent Radiative Decay Time of Confined Excitons in CuCl Microcrystals. *Solid State Commun.* **1990**, *73*, 271−274.

(31) Carmichael, H. J. *Statistical Methods in Quantum Optics 1*; Springer-Verlag: Berlin, 1999.

(32) Nomura, W.; Yatsui, T.; Kawazoe, T.; Ohtsu, M. The Observation of Dissipated Optical Energy Transfer between CdSe Quantum Dots. *J. Nanophotonics* **2007**, *011591*, 1−7.

(33) Kim, S.-J.; Aono, M.; Hara, M. Tug-of-War Model for the Two-Bandit Problem: Nonlocally-Correlated Parallel Exploration via Resource Conservation. *BioSystems* **2010**, *101*, 29−36.

(34) Schöning, U. A Probabilistic Algorithm for k-SAT and Constraint Satisfaction Problems. *Proceedings of the 40th Symposium on the Foundations of Computer Science*, 1999, pp 410−414.

(35) Iwama, K.; Tamaki, S. Improved Upper Bounds for 3-SAT.*Proceedings of the 15th Symposium on Discrete Algorithms*, 2004, pp 328−328

(36) http://www.cs.ubc.ca/~hoos/SATLIB/benchm.html.

(37) Hoos, H.; H., Stutzle, T. SATLIB: An Online Resource for Research on SAT. *Proc. SAT* **2000**, 283−292.

(38) Mitchell, D.; Selman, B.; Levesque, H. Hard and Easy Distributions of SAT Problems. *Proc. AAAI* **1992**, 459−465.

(39) Kirkpatrick, S.; Selman, B. Critical Behavior in the Satisfiability of Random Boolean Expressions. *Science* **1994**, *264*, 1297−1301.

Rep. Prog. Phys. **76** (2013) 056401 (50pp) doi:10.1088/0034-4885/76/5/056401

Information physics fundamentals of nanophotonics

Makoto Naruse[1], Naoya Tate[2], Masashi Aono[3] and Motoichi Ohtsu[2]

[1] Photonic Network Research Institute, National Institute of Information and Communications Technology, 4-2-1 Nukui-kita, Koganei, Tokyo 184-8795, Japan
[2] Department of Electrical Engineering and Information Systems and Nanophotonics Research Center, Graduate School of Engineering, The University of Tokyo, 2-11-16 Yayoi, Bunkyo-ku, Tokyo 113-8656, Japan
[3] RIKEN Advanced Science Institute, 2-1, Hirosawa, Wako, Saitama 351-0198, Japan

E-mail: naruse@nict.go.jp

Received 15 June 2011, in final form 15 February 2013
Published 11 April 2013
Online at stacks.iop.org/RoPP/76/056401

Abstract
Nanophotonics has been extensively studied with the aim of unveiling and exploiting light–matter interactions that occur at a scale below the diffraction limit of light, and recent progress made in experimental technologies—both in nanomaterial fabrication and characterization—is driving further advancements in the field. From the viewpoint of information, on the other hand, novel architectures, design and analysis principles, and even novel computing paradigms should be considered so that we can fully benefit from the potential of nanophotonics. This paper examines the information physics aspects of nanophotonics. More specifically, we present some fundamental and emergent information properties that stem from optical excitation transfer mediated by optical near-field interactions and the hierarchical properties inherent in optical near-fields. We theoretically and experimentally investigate aspects such as unidirectional signal transfer, energy efficiency and networking effects, among others, and we present their basic theoretical formalisms and describe demonstrations of practical applications. A stochastic analysis of light-assisted material formation is also presented, where an information-based approach provides a deeper understanding of the phenomena involved, such as self-organization. Furthermore, the spatio-temporal dynamics of optical excitation transfer and its inherent stochastic attributes are utilized for solution searching, paving the way to a novel computing paradigm that exploits coherent and dissipative processes in nanophotonics.

(Some figures may appear in colour only in the online journal)

This article was invited by Masud Mansuripur.

Contents

1. Introduction

1.1. Information physics approach to nanophotonics

Light plays a crucial role in a wide range of information devices and systems, covering fields such as communication, processing, imaging and displays [1]. There is no doubt that the superior physical attributes of light, such as its frequency, intensity, phase and polarization characteristics, constitute the foundations of the tremendous benefits for which we are indebted today. At the same time, however, ever-increasing quantitative demands, such as the massive amount of digital information transmitted on networks, necessitate further advancements in optics and photonics. In addition, there has been a surge in demand for qualitatively novel technologies, such as energy saving [2], mobile and ubiquitous devices [3], solid-state lighting and displays [4], healthcare and welfare, and safety and security [5, 6], to name a few. Conventional optics and photonics, however, suffer from difficulties in resolving these quantitative and qualitative challenges due to their fundamental limitations—principally, the diffraction limit of light [7].

Nanophotonics, which makes use of interactions between light and matter at a scale below the wavelength of light, has been at the forefront of optical science and technology, and remarkable progress has been made [8, 9]. An optical near-field is the optical field in the subwavelength vicinity of a light scattering object or optical source [10, 11]. Optical near-field interactions are optical interactions via optical near-fields localized in subwavelength space between the interacting objects. Since an optical near-field is free of the diffraction effects imposed on conventional propagating light, it allows breaking through the diffraction limit of light. For instance, technologies such as near-field spectroscopy [12], near-field-assisted information storage [13], bio-sensing and near-field lithography [14] have been developed. Furthermore, the nature of optical near-field interactions on the nanometer-scale, including higher-order atom–light interactions [15], has led to the discovery of unique phenomena observed only on the nanoscale, revealing a physical picture of 'dressed photons', or photons dressed by material excitations [16, 17]. Rigorously speaking, the dressed photon is a theoretical model or picture describing the optical near-field interactions of a short-range nature derived by renormalizing optical interactions with a specific material environment [16, 17]. It turns out that not only does nanophotonics possess the ability to break through the diffraction limit, but it also allows physical processes that are unachievable conventionally, such as dipole-forbidden transitions. The usage of dipole-forbidden transitions in optical excitation transfer is essential for clearly distinguishing between optical near-field excitation transfer confined in nanometer space, and radiation and excitation processes of excitonic states via interactions with incident and outgoing light waves. These novel optical near-field processes have led to various devices that have been experimentally demonstrated recently, including light concentration [18], infrared-to-visible light conversion [19], silicon light emission [20], solar cells [21], silicon lasers [22] and so forth. The rapid progress of experimental technologies, both in the fabrication and characterization of nanostructures, has been a key driving force behind the advances in nanophotonics; examples include, but are not limited to, ultrafast spectroscopy for nanostructured matter [23], and size- and/or position-controlled quantum nanostructures, such as InAs [24] and ZnO [25]. The technology of nanodiamonds with nitrogen vacancies has also been showing radical advances [12]. In addition, technology for producing shape-engineered nanostructures has matured thanks to advancements in lithography and nano-imprinting [26–29].

From the viewpoint of information or system design, on the other hand, there are many unresolved, important basic issues in nanophotonics. For example, system architectures, basic structures for achieving versatile functions, modeling, design, and analysis principles and methods that inherit the physical principles of nanophotonics, should be developed. The importance and benefits of these information-related, system-level concerns will be intuitively recognized by observing the history of electronics and photonics, as briefly mentioned below. This paper sheds new light on some system-level fundamentals and insights in nanophotonics, namely, its fundamental information properties, architectures, modeling and design issues.

Looking at very-large-scale integrated (VLSI) circuits, for example, we can observe a hierarchical structure: with electrons as the elemental carrier and silicon as the mother material, taking complementary metal-oxide semiconductor (CMOS) devices as the basic device structure, and digital information representation, all governed by a von Neumann architecture [30]. What should be noticed here is that, whereas quantum mechanics indeed plays a critical role in every single step of electron transfer, circuit- and system-level foundations are crucial in realizing VLSI devices as a whole. A related discussion can be found in nanocomputers [31] and emerging research devices and architectures [30], where the quest for overcoming the limitations of conventional principles that rely solely on electron transfer has been pursued. In the case of optical communication, while light propagation, for example, lies as the physical foundation, the performance in terms of information transmission is governed by information theory [32]. Information-related fundamentals regarding far-field light are well established, such as Fourier optics for optical signal processing [33], optical communications theory, etc. Thus, design guidelines are available, and these help in the systematic design of dedicated optical systems, as well as revealing their performance limitations [34]. These are just a portion of the vast literature suggesting the importance of system-oriented, information physics concerns for various physical processes.

At the same time, for nanophotonics, it should be emphasized that replacing or competing with conventional computing and information technologies is not necessarily the primary motivation. What should be pursued is to exploit and maximize the potential of the unique physical attributes inherent in nanophotonics. Nanophotonic security is one example application where accessibility via light is essential, and optical near-field processes provide unique solutions [5]. Furthermore, insights gained in the modeling and analysis of

nanophotonics are applicable to a wide range of applications besides computing or information processing. They can also contribute to design and analysis in solar energy applications [35] and nanofabrication [36]. Dwyer *et al* have been developing a nano-optical computer architecture for medical and healthcare applications based on resonant energy transfer made possible by DNA-based self-assembly [37, 38]. Catrysse *et al* have investigated nanostructures for imaging applications [39], where light–matter interactions are essentially and inevitably present, and the unique nanophotonic solutions offered are valuable.

Furthermore, system-oriented approaches are beneficial in investigating the basic mechanisms of material formation. Stochastic modeling and analysis in optical-near-field-assisted nanofabrication, which will be dealt with in section 4, are typical examples. In more general contexts, dealing with light and matter in an open system, which is indeed the concept of non-equilibrium physics [40], would provide new knowledge in nanophotonics too, as in other fields. Self-organized criticality [41], observed in some nanophotonic experiments [42, 43], is a natural emergent property thanks to the inclusion of energy flow in addition to elemental near-field interactions.

Summing up all of these related aspects, a system-oriented approach or, in other words, an *information physics approach* to nanophotonics will provide a solid foundation for achieving various functionalities and understanding the basic nature. This paper reviews nanophotonics from an information physics approach, in particular, by examining the three aspects described below.

1.2. Optical excitation transfer on the nanoscale and its information physics

First in section 2, we deal with localized optical excitation transfer and discuss its information-related aspects. Conventionally, propagating light is assumed to interact with nanostructured matter in a spatially uniform manner—a well-known principle referred to as the long-wavelength approximation—from which state transition rules for optical transitions are derived, including dipole-forbidden transitions. However, such an approximation is not valid in the case of optical near-field interactions in the subwavelength vicinity of an optical source; the inhomogeneity of optical near-fields of a rapidly decaying nature makes even conventionally dipole-forbidden transitions allowable [7]. The interaction Hamiltonian governing an optical near-field interaction is described by a Yukawa-type potential [44]. From a system-level viewpoint, we should emphasize that the principle of signal transfer in nanophotonics is very different from that in electrically wired circuits based on electron transfer—what we call an architectural shift from a wired architecture to an excitation-transfer-based architecture. Described intuitively, a wired architecture means that a device inevitably requires energy dissipation induced at the macroscale for signal transfer; energy transfer from the power supply to some reservoir guarantees signal processing [45]. On the other hand, signal transfer via excitation transfer is achieved by a tiny energy dissipation induced at the recipient of the information (section 2.1.3). We describe theoretical formulations of optical excitation transfer and the above-mentioned architectural shift, followed by a discussion of basic information attributes, such as minimum energy dissipation, interconnects, how to realize binary states, signal gathering and broadcast, multiplexing, and so forth (section 2.1).

Combinations of such localized optical excitation transfer, or in other words, networks of optical near-field interactions, provide versatile functionalities; the importance of modeling, design, and analysis also comes into play (section 2.2). After introducing extended theoretical formalisms, emerging attributes such as robustness, autonomy and reconfigurability will be discussed. Robustness, for instance, which is the ability to tolerate errors, is one of the most important characteristics of nanosystems [31], since certain kinds of errors on the nanoscale, such as material disorders, are inevitable. The time-domain behavior of optical excitation transfer, such as timing dependences and pulsation, is discussed in section 2.3. Nanophotonic circuits react differently depending on the arrival order of the incoming pulse inputs. It is known that information processing in the human brain, consisting of a vast number of neurons and connections among them, is based on pulse trains, and the so-called spike timing dependent plasticity (STDP) is important. The order of pulse arrival plays a critical role [46], which is also relevant to the characteristics inherent in nanophotonics.

1.3. Hierarchy in nanophotonics and its information physics

Another novel attribute found in nanophotonics is the hierarchical property of optical near-fields. An optical near-field is localized in the vicinity of nanostructured matter; however, it is not observable unless it is scattered by placing another piece of matter adjacent to it. We can see structure here: at scales larger than the light wavelength, information that can couple with the optical far-field is observed, whereas additional information is retrievable via optical near-fields [47]. Furthermore, at physical scales below the light wavelength, an optical near-field behaves differently depending on the physical scale involved. For example, a nanostructured material exhibits different responses depending on the scale of observation. This has led to the design and implementation of different functions depending on the physical scale involved, a concept that we call a *hierarchical architecture* [48]. It should also be noted that such a hierarchy in optical near-fields is in contrast to conventional electronics, where the correlation length of an electron is constant regardless of the scale of interest; electronic near-fields, utilized in scanning tunneling microscopy (STM) and related nanotechnologies, correspond simply to the evanescent tails of electronic waves in bulk crystal since no structures of electronic subwavelength size are available for the usual condensed matter.

Section 3 presents the concept of optical system design taking into account the hierarchy offered by nanophotonics, followed by three theoretical basics (section 3.1) and some design principles, particularly in the case of engineering metal nanostructures (section 3.2). Experimental demonstrations, including a hierarchical hologram and lock-and-key, will

also be shown (section 3.3). Finally, an information-theory approach to a hierarchical nanophotonic system is shown, with a discussion of the Shannon information capacity (section 3.4).

1.4. Statistical approach to nanophotonics

Statistical aspects of physical phenomena are important in physics in general [40], and statistical viewpoints provide fundamental insights and interesting novel applications for nanophotonics, too. Section 4 reviews two topics regarding a stochastic approach to nanophotonics: one concerns stochastic modeling of material formation involving optical near-field processes, such as enhanced material desorption (section 4.1), and the other concerns the possibility of building a novel computing paradigm by exploiting the unique stochastic nature inherent in nanophotonics (section 4.2).

First, light-assisted nanofabrication is described, such as the synthesis of quantum dots using photo-induced desorption that yields reduced size fluctuations [49], metal sputtering under light illumination resulting in self-organized, nanoparticle chains [50], and the interesting ability to achieve photosensitivity below the bandgap energy in a solar cell by engineering the surface morphology [21]. The physical mechanisms behind these processes have been attributed to material desorption and deposition induced by optical near-field processes. However, important stochastic phenomena are also present, necessitating further behaviors besides elemental optical near-field processes. We introduce stochastic models of the light-assisted processes that reproduce phenomenological characteristics consistent with the experimental observations.

Second, we outline the quest to develop novel computing paradigms based on the unique stochastic nature inherent in nanophotonics. Nature-inspired architectures are attracting a great deal of attention in various research areas, such as brain-like computing and computational neuroscience [51], stochastic-based computing and noise-based logic [52], and spatio-temporal computation dynamics [53]. Among these research topics, Nakagaki *et al* showed that a single-celled amoeba-like organism, a plasmodium of the true slime mold *Physarum polycephalum,* is capable of finding shortest-distance solutions between two food sources [54]. Also, Aono *et al* demonstrated 'amoeba-based computing' for solution searching, such as the traveling salesman problem (TSP) [55], by utilizing the spatio-temporal oscillatory dynamics of the photoresponsive amoeboid organism *Physarum*. In addition, Leibnitz *et al* showed a bio-inspired algorithm for controlling an information network by utilizing fluctuations stemming from biological observations, where the speed of fluorescence evolution of proteins in bacteria is observed to have a positive correlation with the phenotypic fluctuation of fluorescence over clone bacteria [56]. These demonstrations indicate that we can utilize the inherent fluctuations and spatial and temporal interaction dynamics. For instance, we describe the application of energy transfer dynamics mediated by optical near-fields to solution searching. Such an investigation is relevant to the quantum nature of optical excitation transfer in light-harvesting antenna [57, 58] and the quantum walk in energy transfer [59]. However, as discussed section 4, unlike quantum computing, which exploits coherent interactions, and unlike conventional electrical computing, which is based on dissipative processes at every single step, the physics of nanophotonics contains both coherent and dissipative processes.

Finally, section 5 summarizes the paper and discusses some future directions.

2. Optical excitation transfer on the nanoscale and its information physics

In this section, we discuss optical excitation transfer involving optical near-field interactions, together with various information-related aspects. In the literature, dipole–dipole interactions, such as Förster resonant energy transfer, are typically referred to in explaining energy transfer from smaller quantum dots (QDs) to larger ones [60, 61]. However, it should be noted that such modeling based on point dipoles does not allow dipole-forbidden transitions. Also, recent experimental observations in light-harvesting antenna indicate the inaccuracy of dipole-based modeling [62, 63]. On the other hand, as discussed below, the localized nature of optical near-fields frees us from conventional optical selection rules, meaning that optical excitation could excite QDs to energy levels that are conventionally electric dipole forbidden. Section 2.1 reviews the theoretical basis of optical excitation transfer, followed by some fundamental information-related properties, such as unidirectionality, energy efficiency, interconnects and binary states. Section 2.2 examines networking of optical excitation transfers. Section 2.3 focuses on time-domain-related foundations of optical excitation transfer.

2.1. Fundamentals

2.1.1. Modeling optical excitation transfers mediated by near-field interactions. We begin with the interaction Hamiltonian between an electron–hole pair and an electric field, which is given by

$$\hat{H}_{\rm int} = -\int {\rm d}^3 r \sum_{i,j={\rm e,h}} \hat{\psi}_i^{\dagger}(\boldsymbol{r}) e\boldsymbol{r} \bullet \boldsymbol{E}(\boldsymbol{r}) \hat{\psi}_j(\boldsymbol{r}), \qquad (1)$$

where e represents the electron charge, $\hat{\psi}_i^{\dagger}(\boldsymbol{r})$ and $\hat{\psi}_j(\boldsymbol{r})$ are, respectively, electronic wave operators corresponding to the creation and annihilation operators of either an electron ($i, j = {\rm e}$) or a hole ($i, j = {\rm h}$) at $\boldsymbol{r}$, and $\boldsymbol{E}(\boldsymbol{r})$ is the electric field [35].

We consider a quantum dot based on a semiconductor material with a bulk electric dipole moment for light-wave incidence at a specific resonance frequency. For the electronic system confined in a quantum dot, the electronic wave operator includes an envelope function of electronic waves in the quantum dot. In usual optical interactions of the quantum dot, the so-called long-wave approximation is employed, so that $\boldsymbol{E}(\boldsymbol{r})$ is considered to be a constant over the size of the quantum dot since the electric field of the propagating light wave is homogeneous on the nanometer scale. Depending on the symmetry of the electronic envelope function, numerical evaluation of the dipole transition matrix elements based on equation (1) results in selection rules for the optical transition

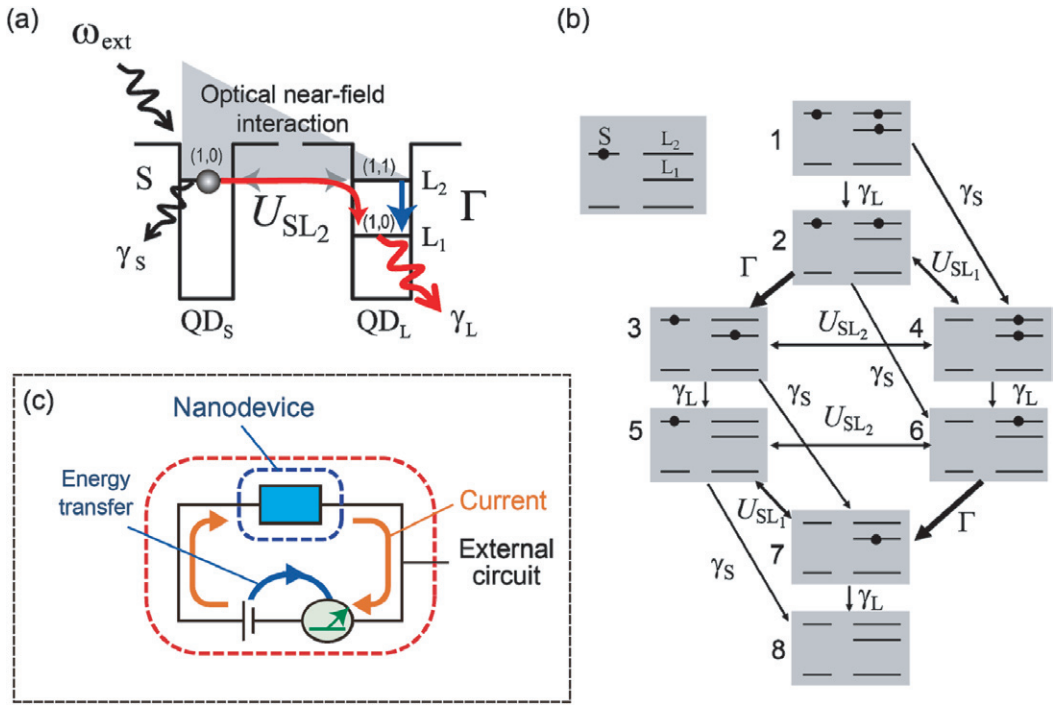

Figure 1. (*a*) Optical excitation transfer mediated by optical near-field interactions. Optical excitation in the smaller quantum dot (QD_S) can be transferred to the larger one (QD_L). Note that transition to the energy level L_2 in QD_L is conventionally dipole-forbidden. The optical near-field interaction, described by a Yukawa-type potential, allows such a transition on the nanoscale when QD_S and QD_L are located close to each other. The energy dissipation occurring at QD_L, or the relaxation from L_2 to L_1, guarantees unidirectionality. (*b*) State transition diagram for the purpose of modeling optical excitation transfer from QD_S to QD_L. (*c*) In contrast with nanoelectric devices that require wiring, such as those based on single electron tunneling, a high-impedance circuit is necessary for achieving unidirectional signal transfer.

for each excitonic state. For instance, in the case of spherical quantum dots, only optical transitions to the states specified by $l = m = 0$ are allowed, where l and m are the orbital angular momentum quantum number and magnetic quantum number for the envelope function, respectively. In the case of optical near-field interactions between a pair of resonant quantum dots separated by a subwavelength distance, on the other hand, due to the large spatial inhomogeneity of the optical near-fields of the source quantum dot, an optical transition that violates conventional optical selection rules becomes allowed, so that optical excitation transfer is possible between resonant states of quantum dots with different symmetries of the envelope functions via optical near-field interactions, regardless of the radiation capability of each state into the optical far-field. Detailed theory can be found in [17].

Here we assume two spherical quantum dots whose radii are R_S and R_L, which we call QD_S and QD_L, respectively, as shown in figure 1(*a*). The energy eigenvalues of states specified by quantum numbers (n, l) are given by

$$E_{nl} = E_g + E_{ex} + \frac{\hbar^2 \alpha_{nl}^2}{2MR^2} \qquad (n = 1, 2, 3, \ldots), \qquad (2)$$

where E_g is the bandgap energy of the bulk semiconductor, E_{ex} is the exciton binding energy in the bulk system, M is the effective mass of the exciton, and values of α_{nl} are determined from the boundary conditions, for example, as $\alpha_{n0} = n\pi, \alpha_{11} = 4.49$. According to equation (2), there exists a resonance between the level of quantum number (1,0) in QD_S and that of quantum number (1,1) in QD_L if $R_L/R_S = 4.49/\pi \approx 1.43$. Note that an optical excitation of the (1,1)-level in QD_L corresponds to an electric dipole-forbidden transition. However, an optical near-field, denoted by U_{SL_2} in figure 1(*a*), allows this level to be populated due to the steep electric field in the vicinity of QD_S. Therefore, an exciton in the (1,0)-level in QD_S could be transferred to the (1,1)-level in QD_L. In QD_L, the excitation undergoes intersublevel energy relaxation due to exciton–phonon coupling with a transition rate denoted by Γ, which is faster than the rate of the inter-quantum-dot optical near-field interaction [44, 64], and the excitation causes a transition to the (1,0)-level and radiation into the far-field. Also, since the radiation lifetime of quantum dots is inversely proportional to their volume [65], finally we find unidirectional optical excitation transfer from QD_S to QD_L. Here, we regard the optical excitation generated in QD_S as the *input* of the system and the radiation from QD_L as the *output*. Due to the energy dissipation (sublevel energy relaxation) in QD_L, the wavelength of the output light is red-shifted relative to the input light.

We first introduce quantum mechanical modeling of the total system based on a density matrix formalism. Let us denote the excitonic state of QD_S as S, and the lower and upper excitonic states in QD_L as L_1 and L_2, respectively. Since a fast intersublevel transition in QD_L is assumed, it is useful to establish theoretical treatments based on the exciton population in the system composed of QD_S and QD_L, where eight basis states are assumed, as schematically illustrated in figure 1(*b*). A master equation formalism is applied to evaluate the population dynamics with the transition matrix elements indicated in the figure. Here, the matrix elements for the

interactions between QD_S and QD_L are denoted by U_{SL_i} ($i = 1$, 2), and the radiative decay rates from S and L_1 are, respectively, given by γ_S and γ_L.

There are two ways to model the excitation dynamics, and we can choose an appropriate modeling strategy depending on the objective of the given design and the analysis constraints. The former way is suitable for calculating the evolution of the population without external inputs, and the latter gives solutions when the system is influenced by external inputs.

One way is to calculate populations evolving from an initial state that contains single or multiple excitations. Assuming optical near-field interaction U_{SL_2} between S and L_2, the model Hamiltonian of the coupled two-dot system is given by

$$H = \hbar \begin{pmatrix} \Omega_S & U_{SL_2} \\ U_{SL_2} & \Omega_{L_2} \end{pmatrix}, \tag{3}$$

where $\hbar U_{SL_2}$ is the optical near-field interaction, and $\hbar\Omega_S$ and $\hbar\Omega_{L_2}$, respectively, refer to the eigenenergies of QD_S and QD_L. The optical excitation transfer process is formulated according to the Lindblad form by introducing phenomenological relaxation terms into the equation of motion based on the Liouville equation, which is given by

$$\dot{\rho}(t) = -\frac{\mathrm{i}}{\hbar}[H, \rho(t)] - N_\Gamma \rho(t) - \rho(t) N_\Gamma, \tag{4}$$

where ρ is the density operator, and N_Γ is a diagonal matrix whose diagonal elements are $\gamma_{S_1}/2$ and $\Gamma/2$.

The other way is to explicitly introduce temporal evolution of the external excitation field, instead of assuming an initial state, as a time-dependent perturbation Hamiltonian, $H_{ext}(t)$. Letting the (i, i) element of the density matrix correspond to the state denoted by i in figure 1(b), the quantum master equation of the total system is [66]

$$\begin{aligned} \dot{\rho}(t) = &-\frac{\mathrm{i}}{\hbar}\left[H_{int} + H_{ext}(t), \rho(t)\right] \\ &+ \frac{\gamma_S}{2}\left(2S\rho(t)S^\dagger - S^\dagger S\rho(t) - \rho(t)S^\dagger S\right) \\ &+ \frac{\Gamma}{2}\left(2L_2\rho(t)L_2^\dagger - L_2^\dagger L_2\rho(t) - \rho(t)L_2^\dagger L_2\right) \\ &+ \frac{\gamma_L}{2}\left(2L_1\rho(t)L_1^\dagger - L_1^\dagger L_1\rho(t) - \rho(t)L_1^\dagger L_1\right), \end{aligned} \tag{5}$$

where the interaction Hamiltonian H_{int} is given by

$$H_{int} = \begin{pmatrix} 0 & 0 & 0 & 0 \\ 0 & 0 & 0 & U_{SL_1}e^{i(\Omega_S-\Omega_{L_1})} \\ 0 & 0 & 0 & U_{SL_2}e^{i(\Omega_S-\Omega_{L_2})} \\ 0 & U_{SL_1}e^{-i(\Omega_S-\Omega_{L_1})} & U_{SL_2}e^{-i(\Omega_S-\Omega_{L_2})} & 0 \\ 0 & 0 & 0 & 0 \\ 0 & 0 & 0 & 0 \\ 0 & 0 & 0 & 0 \\ 0 & 0 & 0 & 0 \end{pmatrix}$$

$$\begin{pmatrix} 0 & 0 & 0 & 0 \\ 0 & 0 & 0 & 0 \\ 0 & 0 & 0 & 0 \\ 0 & 0 & 0 & 0 \\ 0 & U_{SL_2}e^{i(\Omega_S-\Omega_{L_2})} & U_{SL_1}e^{i(\Omega_S-\Omega_{L_1})} & 0 \\ U_{SL_2}e^{-i(\Omega_S-\Omega_{L_2})} & 0 & 0 & 0 \\ U_{SL_1}e^{-i(\Omega_S-\Omega_{L_1})} & 0 & 0 & 0 \\ 0 & 0 & 0 & 0 \end{pmatrix}, \tag{6}$$

where Ω_{L_i} denotes the energy eigenvalue of the state L_i. The matrices $S^\dagger$, $L_1^\dagger$ and $L_2^\dagger$ are, respectively, creation operators that create excitations in S, L_1 and L_2, defined by

$$S^\dagger = \begin{pmatrix} 0 & 0 & 0 & 1 & 0 & 0 & 0 & 0 \\ 0 & 0 & 0 & 0 & 0 & 1 & 0 & 0 \\ 0 & 0 & 0 & 0 & 0 & 0 & 1 & 0 \\ 0 & 0 & 0 & 0 & 0 & 0 & 0 & 0 \\ 0 & 0 & 0 & 0 & 0 & 0 & 0 & 1 \\ 0 & 0 & 0 & 0 & 0 & 0 & 0 & 0 \\ 0 & 0 & 0 & 0 & 0 & 0 & 0 & 0 \\ 0 & 0 & 0 & 0 & 0 & 0 & 0 & 0 \end{pmatrix},$$

$$L_1^\dagger = \begin{pmatrix} 0 & 1 & 0 & 0 & 0 & 0 & 0 & 0 \\ 0 & 0 & 0 & 0 & 0 & 0 & 0 & 0 \\ 0 & 0 & 0 & 0 & 1 & 0 & 0 & 0 \\ 0 & 0 & 0 & 0 & 0 & 1 & 0 & 0 \\ 0 & 0 & 0 & 0 & 0 & 0 & 0 & 0 \\ 0 & 0 & 0 & 0 & 0 & 0 & 0 & 1 \\ 0 & 0 & 0 & 0 & 0 & 0 & 0 & 0 \end{pmatrix},$$

$$L_2^\dagger = \begin{pmatrix} 0 & 0 & 0 & 0 & 0 & 0 & 0 & 0 \\ 0 & 0 & 1 & 0 & 0 & 0 & 0 & 0 \\ 0 & 0 & 0 & 0 & 0 & 0 & 0 & 0 \\ 0 & 0 & 0 & 0 & 0 & 0 & 0 & 0 \\ 0 & 0 & 0 & 0 & 0 & 0 & 0 & 0 \\ 0 & 0 & 0 & 0 & 0 & 0 & 1 & 0 \\ 0 & 0 & 0 & 0 & 0 & 0 & 0 & 0 \\ 0 & 0 & 0 & 0 & 0 & 0 & 0 & 0 \end{pmatrix}, \tag{7}$$

and S, L_1 and L_2 in equation (5) are, respectively, annihilation operators given by the transposes of the matrices of equation (7). Here, H_{ext} indicates the Hamiltonian representing the interaction between the external input light at frequency ω_{ext} and the quantum dot system, and is given by

$$\begin{aligned} H_{ext}(t) = \mathrm{gate}(t) \times [&(\exp(\mathrm{i}(\Omega_S - \omega_{ext})S^\dagger \\ &+ \exp(-\mathrm{i}(\Omega_S - \omega_{ext})S) + (\exp(\mathrm{i}(\Omega_{L_1} - \omega_{ext}))L_1^\dagger \\ &+ \exp(-\mathrm{i}(\Omega_{L_1} - \omega_{ext}))L_1)], \end{aligned} \tag{8}$$

where gate(t) specifies the envelope function of the perturbation Hamiltonian. Also note that the input light could couple to the (1,0)-level in QD_S and to the (1,0)-level in QD_L, because those levels are electric dipole-allowed energy levels. Setting the initial condition as an empty state, and giving external input light in equation (8), the time evolution of the population is obtained by solving the master equation given by equation (5).

2.1.2. 'Excitation-transfer-based' architecture. Based on the theoretical elements described in section 2.1.1, we first discuss an important architectural difference when compared with electrically wired devices. The key is that the flow of information in nanoscale devices cannot be completed unless they are appropriately coupled with their environment [45]. For the sake of discussion, we introduce an electronic system based on single charge tunneling, in which a tunnel junction with capacitance C and tunneling resistance R_T is coupled to a voltage source V via an external impedance $Z(\omega)$. To accomplish tunneling of a single charge, besides

the condition that the electrostatic energy $E_C = e^2/2C$ of a single excess electron be greater than the thermal energy $k_B T$, the environment must have appropriate conditions [67]. For instance, with an inductance L in the external impedance, the fluctuation of the charge is given by $\langle \delta Q^2 \rangle = (e^2/4\eta) \coth(\beta \hbar \omega_s/2)$, where $\eta = E_C/\hbar\omega_S$, $\omega_S = (LC)^{-1/2}$, and $\beta = 1/k_B T$. Therefore, charge fluctuations cannot be small even at zero temperature unless $\eta \gg 1$, meaning that a high-impedance environment is necessary, leading to a significant amount of energy dissipation induced in external circuits. In other words, energy dissipation in external circuits guarantees the signal transfer event, as schematically shown in figure 1(*c*) [45].

In contrast, in the case of the optical excitation transfer (figure 1(*a*)), the transfer of an excitation from QD_S to QD_L is completed by means of the non-radiative relaxation process from L_2 to L_1 occurring at QD_L. Theoretically, the sublevel relaxation constant is given by $\Gamma = 2\pi |g(\omega)|^2 D(\omega)$, where $\hbar g(\omega)$ is the exciton–phonon coupling energy at frequency ω, $\hbar$ is Planck's constant divided by 2π, and $D(\omega)$ is the phonon density of states [66]. The energy dissipation occurring in the optical excitation transfer should be larger than the exciton–phonon coupling energy of $\hbar\Gamma$, which guarantees unidirectional signal flow. This is similar to the fact that the condition $\eta \gg 1$ is necessary in the electron tunneling example, which means that the mode energy $\hbar\omega_S$ is smaller than the required charging energy E_C. By regarding $\hbar\Gamma$ as a kind of mode energy in the optical excitation transfer, the difference between the optical excitation transfer and a conventional wired device is the physical scale at which this mode energy is realized: the nanoscale for optical excitation transfer ($\hbar\Gamma$) and the macroscale for electrical circuits ($\hbar\omega_S$). Additionally, it has been pointed out that about five stages of cascaded energy transfer involving sublevel relaxations can be supported in technologically feasible nanostructures; this is also in contrast to the architecture of electrically wired devices in which every single step of signal transfer requires charging and discharging.

Summing up, localized near-field interactions and energy dissipation occurring in the destination nanostructure provide unidirectional signal flow in the case of optical excitation transfer, whereas energy dissipation occurring on the macroscale determines the signal flow in the case of wired devices. This is manifested as a paradigm shift from a 'wire-based' architecture to an 'excitation-transfer-based' architecture.

One additional remark is that such an architectural shift has implications for security concerns in terms of tamper resistance against attacks [68]. A so-called side-channel attack, by which information is tampered with either invasively or non-invasively, is one of the most critical security issues. This may be achieved, for example, by monitoring the power consumption [69]. We consider that the physical reason behind this is the energy dissipation induced on the macroscale, discussed above, which could possibly be the weakest link in terms of being tampered with. Meanwhile, the amount of energy dissipation associated with optical excitation transfer is small, and it would be technologically difficult to tamper with non-invasively. Naruse *et al* also demonstrated that an invasive attack is easily recognized in the case of optical excitation transfer [68].

2.1.3. Energy efficiency. In this section we theoretically investigate the lower bound of energy dissipation required in signal transfer via optical near-field interactions. We will theoretically demonstrate that the energy dissipation could be as low as 25 μeV. Compared with the bit-flip energy of an electrically wired device, this is about 10^4 times more energy efficient. The achievable integration density of nanophotonic devices is also analyzed based on the energy dissipation and the error ratio while assuming a Yukawa-type potential for the optical near-field interactions [70].

We discuss the lower bound of energy dissipation by introducing two representative systems (system A and system B). The first one, system A in figure 2(*a*), consists of two closely located quantum dots, and thus, optical excitation transfer from QD_S to QD_L occurs. We assume an interaction time $U_{SL_2}^{-1}$ of 100 ps for system A, denoted by U_A^{-1} in figure 2(*a*). Such an interaction time is close to that of experimentally observed optical near-field interactions in CuCl QDs (130 ps) [71], ZnO quantum-well structures (130 ps) [25], ZnO QDs (144 ps) [72] and CdSe QDs (135 ps) [73]. The intersublevel relaxation time due to exciton–phonon coupling is in the 1–10 ps range [44, 64, 74], and here we assume $\Gamma^{-1} = 10$ ps. In system B on the other hand (figure 2(*a*)), the two quantum dots are intentionally located far away from each other. Therefore, the interactions between QD_S and QD_L should be negligible, and thus, optical excitation transfer from QD_S to QD_L should not occur; namely, the radiation from QD_L should normally be zero. We assume $U_{SL_2}^{-1} = 10\,000$ ps for system B, denoted by U_B^{-1} in figure 2(*a*), indicating effectively no interactions between the two.

One remark here is that the inter-dot interaction times of system A and system B are related to the distances between the two quantum dots. The optical near-field interaction between two nanoparticles is known to be expressed as a screened potential using a Yukawa function, given by

$$U = \frac{A \exp(-\mu r)}{r}, \tag{9}$$

where r is the distance between the two [75]. In this representation, the optical near-field is localized around nanoparticles, and its decay length is equivalent to the particle size. Here, it should be noted that the inter-dot distance of system B indicates how closely independent functional elements can be located. In other words, the interaction time of system B is correlated with the integration density of the total system. In order to analyze such spatial density dependences, we assume that the $U_{SL_2}^{-1}$ values of 100 ps and 10 000 ps, respectively, correspond to inter-dot distances of 50 nm and 500 nm. Here, the stronger interaction (100 ps) has been assumed, as already mentioned, based on a typical interaction time between closely spaced quantum dots. We also assume that the interaction with negligible magnitude (10 000 ps) corresponds to a situation where the inter-dot distance is close to the optical wavelength. Figure 2(*a*) shows

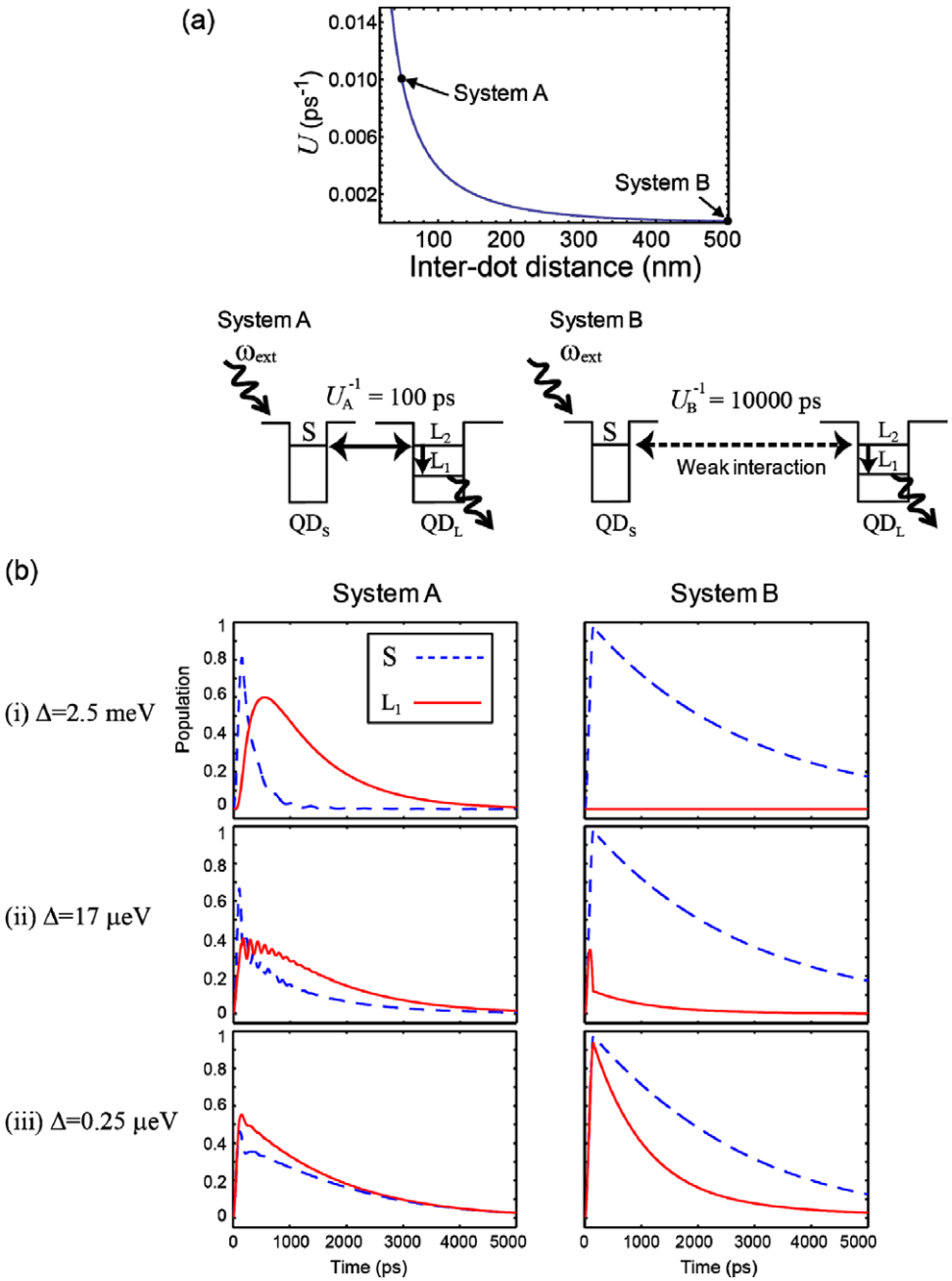

Figure 2. Analyzing the ultimate energy efficiency of optical excitation transfer for signal transport. (*a*) Yukawa-type screened potential of an optical near-field interaction between two QDs as a function of the inter-dot distance We assume two systems consisting of a small QD (QD_S) and a large QD (QD_L): system A has strong inter-dot near-field interactions (100 ps), whereas system B has negligible interaction (10 000 ps). The proper operation of these systems, when irradiated with propagating light of frequency ω_{ext}, is that system A should exhibit an output signal from QD_L (originating from the optical excitation transfer from QD_S to QD_L), whereas system B should exhibit no signal (because the inter-dot interaction is negligible). (*b*) When the energy dissipation induced at QD_L (Δ) is large (case (i)), the proper operation is observed; on the other hand, when the energy dissipation is too small, an output signal is produced even in system B (case (ii) and case (iii)) because the input light can directly couple to the L_1 level in QD_L.

the Yukawa-type potential curve given by equation (9). Further discussion on integration density will be given at the end of this subsection.

The energy dissipation in the optical excitation transfer from QD_S to QD_L is, as discussed in sections 2.1.1 and 2.1.2, the intersublevel relaxation in QD_L, given by $\Delta = E_{L_2} - E_{L_1}$, where E_{L_i} represents the energy of level L_i. Therefore, the issue is to derive the minimum energy difference Δ. When Δ is too small, the input light may directly couple to L_1, resulting in radiation from QD_L, even in system B. In other words, we would not be able to recognize the origin of the output radiation from QD_L if it involves optical excitation transfer from QD_S to QD_L in system A, or if it directly couples to L_1 in system B. Therefore, the *intended* system behavior is a higher population in L_2 in system A, and at the same time a lower population in L_2 in system B.

We first assume pulsed input light irradiation with a duration of 150 ps at 3.4 eV (wavelength 365 nm), and assume

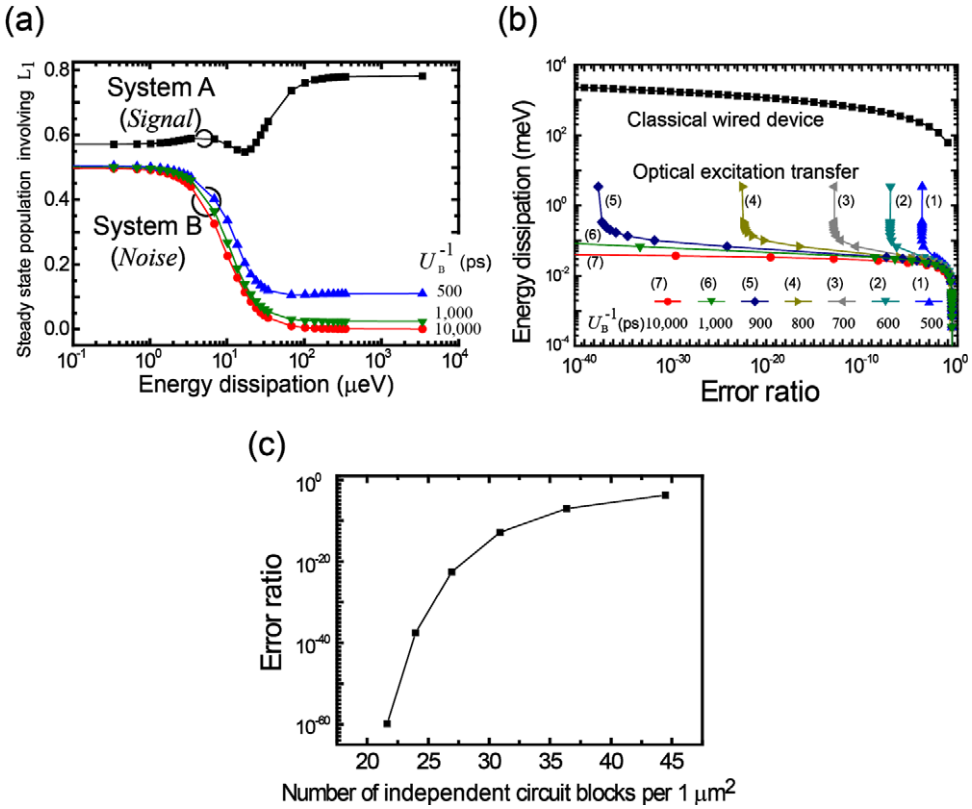

Figure 3. (*a*) Steady-state population involving energy level L_1 in system A (squares) and system B as a function of the energy dissipation. For system B, three different cases are shown, with U_B^{-1} of 500 ps, 1000 ps and 10 000 ps, respectively, indicated by ▲, ▼ and ● marks. (*b*) Energy dissipation as a function of error ratio regarding optical excitation transfer and the bit-flip energy required in a CMOS logic gate. The energy dissipation of optical excitation transfer is about 10^4-times lower than that in classical electrically wired devices. (*c*) As the optical near-field interaction in system B increases, the lower bound of the error ratio increases, indicating that the performance could be degraded with increasing integration density; namely, there is a tradeoff between the energy efficiency and the error rate. The error ratio is evaluated as a function of the number of independent functional blocks within an area of 1 μm^2.

that the energy level S is resonant with the input light. Also, we assume the radiation lifetime of QD_L to be $\gamma_L^{-1} = 1$ ns and that of QD_S to be $\gamma_S^{-1} = 2^{3/2} \times 1 \approx 2.83$ ns since it is inversely proportional to the volume of the QD. The solid and dashed curves in figure 2(*b*), respectively, represent the evolutions of populations related to the radiation from the energy levels L_1 and S for both system A and system B, assuming three different values of Δ: (i) $\Delta = 2.5$ meV, (ii) $\Delta = 17\,\mu$eV and (iii) $\Delta = 0.25\,\mu$eV.

In the case of (i), there is nearly zero population in L_1 in system B, which is the expected behavior. In system A, on the other hand, a population appears in L_1. In the case of (iii), due to the small energy difference, the input light directly couples with L_1; therefore, both system A and system B yield higher populations in L_1, which is an *unintended* system behavior. Finally, in case (ii), although the population in L_1 in system B is not as large as in case (iii), it exhibits a non-zero value compared with case (i), indicating that the energy difference $\Delta = 17\,\mu$eV may be around the middle of the intended and unintended system behaviors involving optical excitation transfer between QD_S and QD_L.

When we assume a longer duration of the input light, the population converges to a steady state. When radiating a pulse with a duration of 10 ns at the same wavelength (365 nm), figure 3(*a*) summarizes the steady-state output populations involving energy level L_1 evaluated at $t = 10$ ns as a function of the energy dissipation. The intended system behavior, that is, a higher output population in system A and a lower one in system B, is obtained in the region where the energy dissipation is larger than around 25 μeV. If we treat the population in system A as the amplitude of a '*signal*' and that in system B as '*noise*', the signal-to-noise ratio (SNR) can be evaluated based on the numerical values in figure 3(*a*). To put it another way, from the viewpoint of the destination QD (or QD_L), the signal should come from QD_S in its proximity (as in the case of system A), not from QD_S far from QD_L (as in the case of system B); such a picture will aid in understanding the physical meaning of the SNR defined here. Also, here we assume that the input data are coded in an external system, and that QD_S is irradiated with input light at frequency ω_{ext}. With the SNR, the error ratio (P_E), or equivalently the bit error rate (BER), is derived by the formula $P_E = (1/2)\mathrm{erfc}(\sqrt{\mathrm{SNR}}/2\sqrt{2})$ where $\mathrm{erfc}(x) = 2/\sqrt{\pi}\int_x^\infty \exp(-x^2)\,\mathrm{d}x$, called the complementary error function [76]. The circles in figure 3(*b*) represent the energy dissipation as a function of the error ratio assuming the photon energy used in the above study (3.4 eV). According to [77], the minimum energy dissipation (E_d) in classical electrically wired devices (specifically, the energy dissipation required for a single bit flip in a CMOS logic gate) is given by $E_d = k_B T \ln(\sqrt{3}P_E/2)$, which is indicated by the squares

in figure 3(*b*). For example, when the error ratio is 10^{-6}, the minimum Δ in the optical excitation transfer is about 0.024 meV, whereas that of the classical electrical device is about 303 meV; the former is about 10^4 times more energy efficient than the latter.

As mentioned earlier, the performance of system B depends on the distance between the QDs. When the interaction time of system B (U_B^{-1}) increases, such as 500 ps, the steady-state population involving L_1 is as indicated by the triangular marks in figure 3(*a*); the population stays higher even with increasing energy dissipation compared with the former case of $U_B^{-1} = 10\,000$ ps. This means that the lower bound of the SNR results in a poorer value. In fact, as demonstrated by the triangular marks (1) in figure 3(*b*), the BER cannot be smaller than around 10^{-4}, even with increasing energy dissipation. The lower bound of the BER decreases as the interaction time U_B^{-1} increases (namely, weaker inter-dot interaction), as demonstrated by the triangular and square marks (2) to (6) in figure 3(*b*).

Now, suppose that an independent nanophotonic circuit needs a spatial area specified by the square of the inter-dot distance corresponding to U_B so that no interference occurs between adjacent circuits; this gives the integration density of nanophotonic circuits in a unit area. When the energy cost paid is 3.4 meV, the BER of the system is evaluated, as shown by the square marks in figure 3(*c*), as a function of the number of independent functional blocks within an area of 1 μm^2; we can observe that the system likely produces more errors as the integration density increases.

Finally, here we make a few remarks regarding the discussion above. First, we assume arrays of identical independent circuits in the above discussion of density. Therefore, two circuits need spatial separations given by U_B so that unintended behavior does not occur. However, when two adjacent nanophotonic circuits are operated with different optical frequencies so that they can behave independently [78], those two circuits could be located more closely, which would greatly improve the integration density as a whole. Hierarchical properties of optical near-fields, discussed in section 3, would also significantly impact the integration density. Further analysis and design methodologies of complex nanophotonic systems, as well as comparison to electronic devices, are other topics to be pursued in future work. Second, because the energy separation in a single destination QD is limited by its size and lies in the range of meV, the results for energy separations in the μeV range correspond to cases where the destination dot QD_L represents a theoretical model of a coupled quantum dot system such as a pair of quantum dots. The coupled system exhibits optical near-field interactions with the smaller QD, followed by inter-dot electron transfer resulting in optical radiation. In fact, Matsumoto *et al* have demonstrated spin-dependent carrier transfer leading to optical radiation between a coupled double quantum-well system composed of magnetic and non-magnetic semiconductors [79], which can be applied to quantum dot systems [80]. Third, a discussion of input and output interfaces is necessary. The above discussion has focused on the lower bound of energy dissipation in the quantum dots. Practical operation of real devices requires input and output interfaces, and the minimum number of photons for a bit slot may be of concern when taking into account noise at the receivers. In [81], Naruse *et al* unified such considerations into an evaluation model and analyzed experimental results based on stacked QDs [24]. Optical excitation transfer still exhibits around 10^4-times better energy efficiency compared with electronic counterparts [81].

2.1.4. Interconnects. The energy transfer mechanism mediated by optical near-field interactions offers interesting attributes in interconnections, with significant differences to conventional propagating light. Here we discuss three examples of unique attributes.

Randomness and signal transfer. As long as near-field interactions exist and energy dissipation can be induced at the destination QD, multiple smaller-sized QDs can be present between the input QD and the output QD. Furthermore, the arrangements of QDs do not have to be ordered; that is, a *randomly arranged* QD formation is acceptable for signal transfer as long as near-field interactions are present between neighboring QDs [74]. Such structural flexibility in optical excitation transfer is another emergent attribute that is notably different from conventional propagating light. Nomura *et al* theoretically evaluated the superior tolerance to fluctuations in the positions of intermediate QDs [74] and also experimentally demonstrated successful long-range signal transmission in randomly distributed CdSe QDs over a transmission distance of more than 10 μm [74, 82].

Unidirectionality. Consider simple optical signal transport from a transmitter to a receiver through intermediate optical elements such as lenses and polarizers. Obviously, the presence of anti-reflection mechanisms associated with all of the intermediate optical elements is critically important, otherwise light would be reflected back to the transmitter, leading to serious errors in communication. In the case of optical excitation transfer mediated by optical near-field interactions, unidirectionality is provided by the energy dissipation mechanism induced at the destination quantum nanostructure, as discussed in section 2.1.2. Here we see a fundamental difference in the physical foundation of unidirectionality between propagating light and optical excitation transfer. The differences of unidirectionality compared with electron transfer have also been discussed in section 2.1.2.

Broadcast interconnects. The principle of merging, dividing and multiplexing signals are basic functions in optical communication and optical signal processing. For instance, planar lightwave circuits (PLCs) [83] provide a technological platform for various optical devices, such as broadcasting (1- to N-channel signal duplication), arrayed waveguide gratings (AWGs) [83], and so forth. Here, we pay attention to broadcast-type interconnects. 'Broadcast' is important in various applications, such as broadcast-and-select architectures [84], optical code generation [85], matrix-vector products [33, 86], etc. Optics is in fact well-suited

to such broadcast operations in the form of simple imaging optics [33, 86] or in optical waveguide couplers, thanks to the nature of wave propagation. However, the integration density of this approach is physically limited by the diffraction limit, which leads to bulky system configurations. Even with subwavelength technologies such as plasmon waveguides [87, 88] and nano-dot couplers [89], it is difficult to provide a high degree of interconnection.

In the case of optical excitation transfer, on the other hand, for a signal to be delivered to a designated quantum dot requires the presence of energy sublevels in nanostructures that can couple with far-field light. That is, through properly-sized quantum dots that couple to the frequency of the irradiated light, broadcast interconnects are realized merely by blanket photon irradiation without having to individually address each QD [78]. Suppose that arrays of nanophotonic circuit blocks are distributed within an area whose size is comparable to the wavelength. For broadcasting, multiple input QDs can be made to simultaneously accept identical input data carried by diffraction-limited far-field light by tuning their optical frequency so that the light is coupled to dipole-allowed energy sublevels. The far- and near-field coupling mentioned above is explained based on a model assuming cubic quantum dots. In this case, the energy eigenvalues for the quantum numbers (n_x, n_y, n_z) in a QD with side length L are given by

$$E_{(n_x,n_y,n_z)} = E_{\mathrm{B}} + \frac{\hbar^2\pi^2}{2ML^2}(n_x^2 + n_y^2 + n_z^2), \qquad (10)$$

where E_{B} is the energy of the bulk exciton, and M is the effective mass of the exciton. According to equation (10), there exists a resonance between the level of quantum number (1,1,1) in the QD with effective side length a and that of quantum number (2,1,1) in the QD with effective side length $\sqrt{2}a$. Energy transfer from the smaller QD to the larger one occurs via optical near-fields, which is forbidden for far-field light [71]. The input energy level for the QDs, that is, the (1,1,1)-level, can also couple to the far-field excitation. This fact can be utilized for data broadcasting.

One of the design restrictions is that energy sublevels for input channels should not overlap with those for output channels. Also, if there are QDs internally used for near-field coupling, dipole-allowed energy sublevels for those QDs cannot be used for input channels since the inputs are provided by far-field light, which may lead to misbehavior of internal near-field interactions if resonant levels exist. Therefore, frequency partitioning among the input, internal and output channels is important. The frequencies used for broadcasting, denoted by $\Omega_i = \{\omega_{i,1}, \omega_{i,2}, \ldots, \omega_{i,A}\}$, should be distinct values and should not overlap with the output channel frequencies $\Omega_o = \{\omega_{o,1}, \omega_{o,2}, \ldots, \omega_{o,B}\}$, where A and B indicate the number of frequencies used for input and output channels, respectively. Also, there will be frequencies needed for internal device operations, which are not used for either input or output, denoted by $\Omega_n = \{\omega_{n,1}, \omega_{n,2}, \ldots, \omega_{n,C}\}$, where C is the number of those frequencies. Therefore, the design criteria for global data broadcasting is to exclusively assign input, output and internal frequencies, Ω_i, Ω_o and Ω_n, respectively.

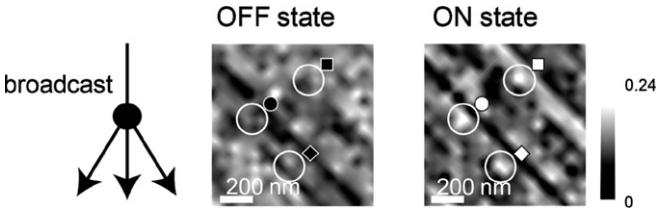

Figure 4. Broadcast interconnects based on optical excitation transfer. Three independent nanophotonic switches, indicated by ■, ● and ♦, are operated with common control light; that is, broadcast interconnects are realized.

To verify the broadcasting method, the following experiments were performed using CuCl QDs inhomogeneously distributed in an NaCl matrix at a temperature of 22 K [78]. To operate a three-dot nanophotonic switch (a two-input AND gate) in the device, at most two input light beams (IN1 and IN2) are radiated. When both inputs exist, an output signal is obtained from the positions where the switches exist. The operation of the AND gate is discussed in detail in section 2.1.5. In the experiment, IN1 and IN2 were assigned to 325 nm and 384.7 nm, respectively. They were radiated over the entire sample (global irradiation) via far-field light. The spatial intensity distribution of the output, at 382.6 nm, was measured by scanning a near-field fiber probe within an area of approximately 1 μm × 1 μm. When only IN1 was applied to the sample, the output of the AND gate was ZERO (OFF state). When both inputs were radiated, the output was ONE (ON state). Note the regions marked by ■, ● and ♦, and in figure 4. In those regions, the output signal levels were, respectively, low and high, which indicates that multiple AND gates were integrated at densities beyond the scale of the globally irradiated input beam area. That is to say, broadcast interconnects to nanophotonic switch arrays are accomplished by diffraction-limited far-field light.

2.1.5. Binary states and logical operations. Repeating what was mentioned above, localized near-field interactions and energy dissipation occurring in the destination quantum dot determine the unidirectionality of energy transfer. This means that when the lower energy level of the destination quantum dot is filled with another excitation (called 'state filling'), an optical excitation occurring in a smaller QD cannot move to a larger one. As a result, the optical excitation will go back and forth between these dots (optical nutation) and will finally decay from the smaller QD, as schematically shown in figure 5(*a*). Another mechanism for realizing two different states is to induce resonance or non-resonance between $\mathrm{QD_S}$ and $\mathrm{QD_{L_l}}$ due to many-body effects; details of this are discussed in [24].

This suggests that two different patterns of optical excitation transfer will appear depending on the occupation of the destination QD or the resonance between the QDs; in other words, the flow of optical excitation can be controlled. This is a critically important attribute for information processing. For example, Kawazoe *et al* proposed logical AND and NOT gates by using a combination of optical excitation transfer, as described briefly below [24, 64].

Take a two-input AND gate formed by three quantum dots as an example, as schematically shown in figure 5(*b*).

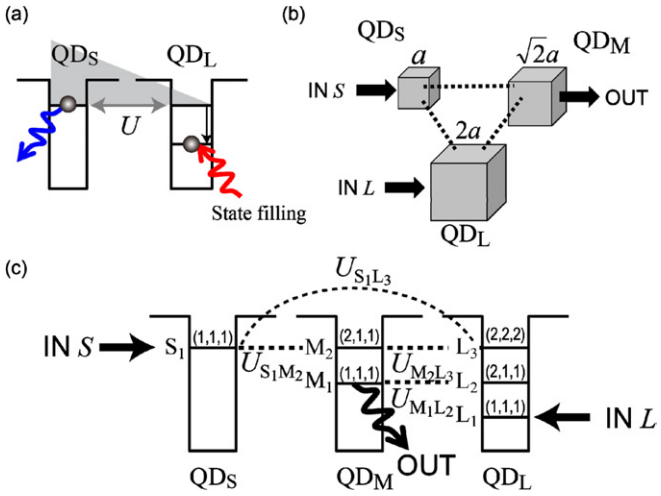

Figure 5. (*a*) If the destination energy level is occupied (state filling), an optical excitation located in the smaller QD (QD_S) will relax from QD_S; namely, the flow of optical excitation can be controlled. (*b*) A two-input AND-gate implemented by three quantum dots with inter-dot optical near-field interactions. Two inputs are indicated by IN *S* and IN *L*, which are applied to QD_S and QD_L, respectively. Output is associated with radiation from QD_M. (*c*) An energy diagram of the system shown in (*b*).

QD_S and QD_L, whose sizes are a and $2a$, work as the two input dots, accepting input signals denoted by 'IN *S*' and 'IN *L*', respectively, and QD_M, whose size is $\sqrt{2}a$, works as the output dot. The energy diagram is shown in figure 5(*c*), where the optical frequencies of the input signals IN *S* and IN *L* are resonant with the (1,1,1)-level of QD_S (S_1) and the (1,1,1)-level of QD_L (L_1), respectively. When both inputs are provided, it is not possible for the optical excitation occurring in S_1 induced by IN *S* to be transferred to L_1 in QD_L because L_1 is excited by IN *L*, and it should thus radiatively decay from the (1,1,1)-level of QD_M (M_1) (logically, IN $S = 1$, IN $L = 1 \rightarrow$ OUT $= 1$). On the other hand, when only IN *S* is given, the optical excitation induced in QD_S should be transferred to QD_L and radiatively decay from the (1,1,1)-level of QD_L, resulting in a lower radiation from QD_M (IN $S = 1$, IN $L = 0 \rightarrow$ OUT $= 0$). Finally, there is no output signal from QD_M when IN *S* is not given ([IN $S = 0$, IN $L = 1 \rightarrow$ OUT $= 0$] and [IN $S = 0$, IN $L = 0 \rightarrow$ OUT $= 0$]). Therefore, the above three-dot configuration, as the logical relation between input and output suggests, provides a logical AND gate operation. Such a mechanism was experimentally demonstrated first at low temperature by using CuCl QDs [71], and more recently at room temperature by using size- and position-controlled stacked InAs QDs [24].

In addition to the above-described architecture, the controllability of excitation flow also allows an architecture known as a binary decision diagram (BDD), where an arbitrary combinatorial logic operation is determined by the destination of a signal flowing from a root [90]. Also, Naruse *et al* demonstrated a content addressable memory by parallel arrangements of simple logic operations and the broadcast interconnects shown in section 2.1.4 [91]. Such a mechanism is possible in systems involving multiple quantum dots each of which could be subjected to state filling or external control. This indicates that versatile spatio-temporal dynamics are, in fact, inherent thanks to the near-field interactions. This can be exploited, for instance, in stochastic computing, as discussed in section 4.2.

2.2. *Networks of optical near-field interactions*

2.2.1. Basic model. Combinations of optical excitation transfer, or networks of optical excitation transfer, enable versatile functionalities, and their modeling, design and analysis are important. We first describe the basic strategy used in modeling. Assume a quantum dot system composed of multiple smaller dots and larger dots, as schematically shown in figure 6(*a*). The interaction between these dots is described by a Yukawa-type potential given by equation (9). We generalize the theoretical elements based on the density matrix formalism described in section 2.1.1 for characterizing the dynamics of optical excitations in such networked systems. We have to prepare multiple states involving zero, one or more excitations, depending on the system to be considered. Take a particular state denoted by $|\Psi_A\rangle$ in figure 6(*b*), where an optical excitation sits in an energy level denoted by $E_i^{(U)}$ in QD_i. This excitation can be transferred to QD_j through a near-field interaction denoted by U_{ij}, whose state is denoted by $|\Psi_{A'}\rangle$. Such an interaction should be manifested in the interaction Hamiltonian corresponding to equation (3) or equation (6). Also, if applicable, a radiative relaxation process transfers the state $|\Psi_A\rangle$ to other states; for example, radiation from the energy level $E_i^{(U)}$ in QD_i transfers the state from $|\Psi_A\rangle$ to the other state denoted by $|\Psi_B\rangle$ in figure 6(*b*). Also, if applicable, a non-radiative relaxation may transfer the state $|\Psi_A\rangle$ to the state $|\Psi_C\rangle$ in figure 6(*b*) where the excitation in QD_i relaxes to $E_i^{(L)}$ with a transition constant Γ_i.

As an example, we consider a quantum dot system where multiple smaller dots (denoted by S_i) surround one larger dot denoted by L, as shown in figure 6(*c*). We assume inter-dot interactions between adjacent smaller quantum dots; that is, (i) S_i interacts with S_{i+1} ($i = 1, \ldots, N-1$) and (ii) S_N interacts with S_1, where N is the number of smaller quantum dots. We call such a system an SN–L1 system. For instance, a system containing two smaller quantum dots and one larger dot is called an S2–L1 system. Similarly, S3–L1, S4–L1 and S5–L1 systems are, respectively, composed of three, four and five smaller quantum dots in addition to one larger quantum dot.

The dynamics of these networked systems is characterized through quantum master equations by following the procedure described above. In the case of the S2–L1 system, for example, which is composed of two smaller quantum dots and one larger quantum dot, the inter-dot interactions between the smaller dots and the larger one are denoted by U_{S_iL}, and the interaction between the smaller dots is denoted by $U_{S_1S_2}$. The radiations from S_1, S_2 and L are, respectively, represented by the relaxation constants γ_{S_1}, γ_{S_2} and γ_L. We derive quantum master equations with initial states in which all smaller quantum dots are excited based on the above procedure. Assuming $U_{S_iL}^{-1} = 200$ ps, $U_{S_1S_2}^{-1} = 100$ ps, $\gamma_L^{-1} = 1$ ns, $\gamma_{S_1}^{-1} = 2.92$ and $\Gamma^{-1} = 10$ ps as parameter values, we can calculate the population of the lower level of the larger quantum

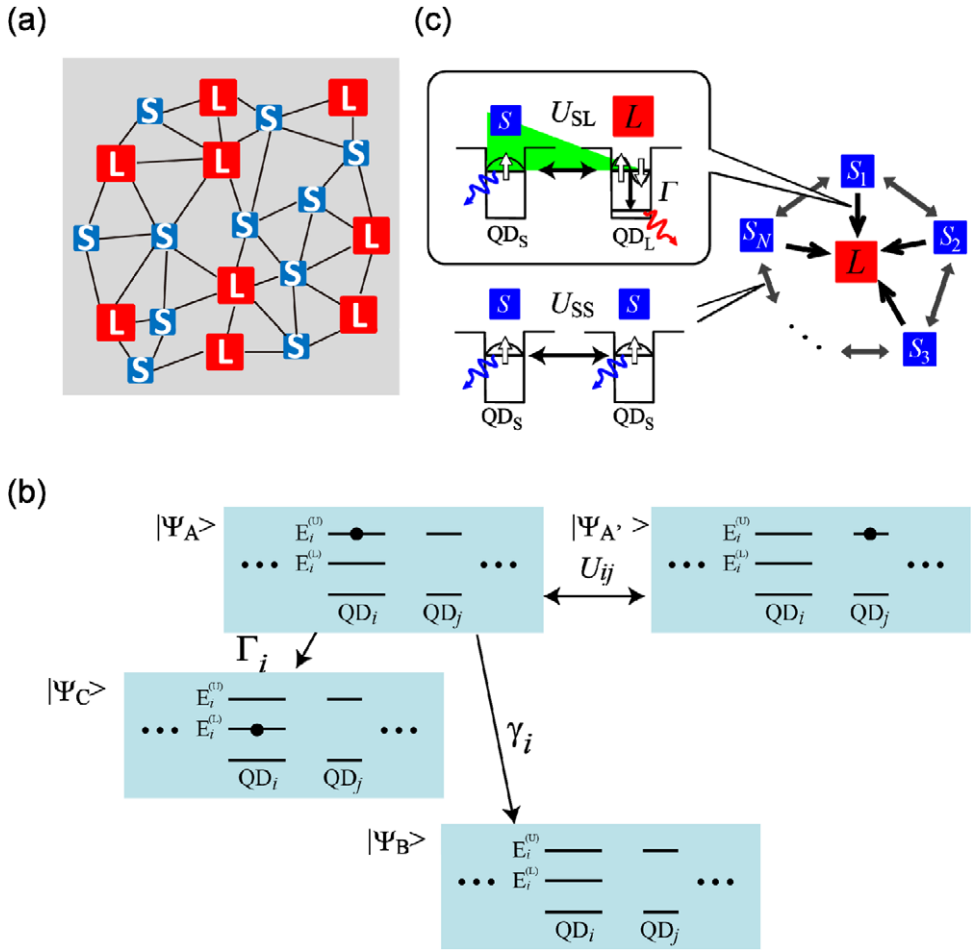

Figure 6. (*a*) An abstract representation of a network of optical near-field interactions. (*b*) A schematic diagram of state transitions mediated by inter-dot near-field interactions and radiative and non-radiative relaxations. (*c*) A quantum dot system in which a larger QD (L) is surrounded by N smaller QDs (S_i) (SN–L1 system).

dot, whose time integral we regard as the output signal. S3–L1, S4–L1 and S5–L1 systems can be analyzed in a similar manner.

Now, suppose that the total number of quantum dots in a given unit area is the same, regardless of their sizes (smaller or larger). The question is what configuration yields the maximum output signal, in other words, what configuration is superior in terms of excitation transfer. We compare the output signal as a function of the ratio of the number of smaller dots to the number of larger dots. As shown by the circles in figure 7(*a*), the most efficient transfer is obtained when the ratio of the number of smaller dots to the number of larger quantum dots is 4. In other words, increasing the number of smaller quantum dots beyond a certain level does not necessarily contribute to increased output signals. Because of the limited radiation lifetime of large quantum dots, not all of the initial excitations can be successfully transferred to the large quantum dots due to the states occupying the lower excitation levels of the large quantum dots. Therefore, part of the input populations of the smaller quantum dots must decay, which results in a loss in the transfer from the smaller quantum dots to a large quantum dot when there are too many excitations in the smaller quantum dots surrounding one large quantum dot.

Such an *optimal* mixture of smaller and larger QDs was experimentally demonstrated by using two kinds of CdSe/ZnS core/shell quantum dots whose diameters were 2.0 nm and 2.8 nm, respectively. The quantum dots were dispersed in a matrix composed of toluene and ultraviolet-curable resin, and the mixture was coated on the surface of a silicon photodiode (Hamamatsu Photonics K.K., Si Photodiode S2368). As schematically shown in figure 7(*b*), half of the surface of the photodiode was spin-coated with the ultraviolet-curable resin containing quantum dots and was cured by ultraviolet radiation, whereas the other half of the surface was coated with the same resin without the quantum dots. Input light was selectively radiated onto each area to evaluate the difference in the generated photocurrent. The increase of the induced photocurrent via the QD-coated area with input light wavelengths between 340 and 360 nm is shown by the squares in figure 7(*a*). We attribute such an increase to the optical excitation transfer through which the input light wavelength is red-shifted to wavelengths where the photodetector is more sensitive. The maximum increase was obtained when the ratio of the number of smaller QDs to larger QDs was 3 : 1. This agrees with the theoretical optimal ratio of the number of smaller quantum dots to larger ones discussed above. Also, [35] discusses in detail that the optimal mixture may

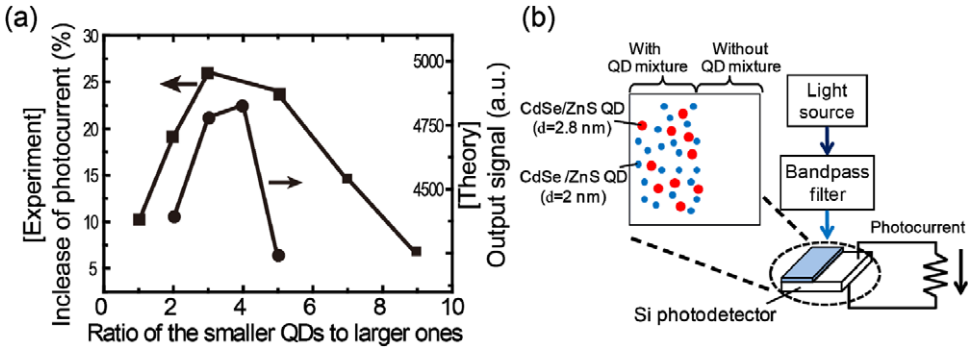

Figure 7. Designing an optimal mixture of smaller and larger QDs so that the optical excitation transfer from smaller to larger ones is maximized. (*a*) The optimal ratio of the smaller QDs to larger ones is around 3 or 4. Theory and experiment agree well. (*b*) Experimental setup for investigating mixture-dependent optical excitation transfer.

be a different one depending on the value of the relaxation parameters and the optical near-field interactions.

Efficient optical excitation transfer in layered quantum dot structures has also been experimentally demonstrated. The radiation from layered graded-size CdTe quantum dots exhibits a signal nearly four times larger that from structures composed of uniform-size quantum dots, a phenomenon which has been called exciton recycling [92] or super-efficient exciton funneling [93]. Adopting the theory of networks of optical excitation transfer mediated by optical near-field interactions allows systematic analysis of layered quantum dot systems, revealing dominant factors contributing to the efficient optical excitation transfer and demonstrating good agreement with previous experimental observations [94].

2.2.2. Autonomy and robustness. We highlight another function inherent in networks of optical near-field interactions. Figure 8(*a*) schematically represents systems where four smaller dots (QD S1,. . ., S4) surround one larger dot (QD L). Here, we assume that some of the interactions between the smaller dots and the larger one are degraded. Such a weak interaction could physically correspond to situations, for instance, where the distance between the smaller dots and the larger one is very large, or where the size or the shape of the quantum dots deviates from the required conditions for energy transfer. In system A, shown in the inset of figure 8(*a*), QD S2 and S4 have weak interactions with QD L. In system B, shown in figure 8(*a*), *all* of the interactions between smaller dots are assumed to be negligible, in addition to the weak interactions assumed in system A. What is of interest is to evaluate the impact of the interactions between smaller dots on the energy transfer from the smaller dots to the larger one as a total system. The curves A and B in figure 8(*a*) represent the evolutions of the population related to the radiation from QD L in system A and system B, respectively, where the former exhibits a higher population compared with the latter. In system A, thanks to the interactions between smaller dots, the excitations in S2 and S4 can be successfully transferred to L by way of the adjacent smaller dots. On the other hand, it is hard for the excitations in S2 and S4 in system B to be transferred to L due to the weak interactions with the surrounding dots. From a system perspective, the interactions among smaller dots provide *robustness* to degradation of the excitation transfer from the smaller dots to the larger one.

To quantitatively evaluate such robustness, we introduce the probability that an interaction between a smaller dot and a larger one suffers interaction degradation or loss; we denote it by $p (0 \leqslant p \leqslant 1)$. We can derive the expected output signal as a function of p. The curves A and B at the left-hand side of figure 8(*b*), respectively, represent the expected output signals corresponding to systems with and without interactions between smaller dots as a function of the interaction loss probability between a smaller dot and a larger one. The curves A′ and B′ at the right-hand side of figure 8(*c*) represent those when the number of smaller dots is five. As shown in curves A and A′, thanks to the existence of interactions between smaller dots, the expected output signal levels remain higher, even greater than the no-error situation ($p = 0$) especially in curve A′, although they suffer from a larger value of p. This is a manifestation of the improved robustness of the system provided by the interactions between smaller dots.

Behind such robustness, we emphasize the autonomous behavior of optical excitation transfer. As an example, take the S3–L1 system shown in figure 8(*c*) and assume that the interactions between S2 and L and between S3 and L are degraded. In such a situation, the excitations sitting at S2 and S3 should be transferred via S1. Figure 8(*c*) summarizes the evolutions of populations associated with S1, S2 and S3. Note that the populations associated with S2 and S3 remain at a higher level during the initial time (0–400 ps), indicating that the excitations in S2 and S3 are effectively 'waiting' in the smaller dots until they have the opportunity to be transferred to a large dot. The population associated with S1 decreases rapidly at around 400 ps, but then increases and becomes larger than the populations of S2 and S3 until 600 ps. There is no 'central controller' in the system, and yet efficient transport of the optical excitations is realized as if they are giving priority to each other in an interchangeable manner. Such an intrinsic, autonomous, seemingly intelligent behavior of optical excitation may also be the foundation of the interconnections in randomly distributed QDs discussed in section 2.1.4.

2.2.3. Reconfigurable near-field network. A network of optical near-field interactions obeys a Yukawa-type potential,

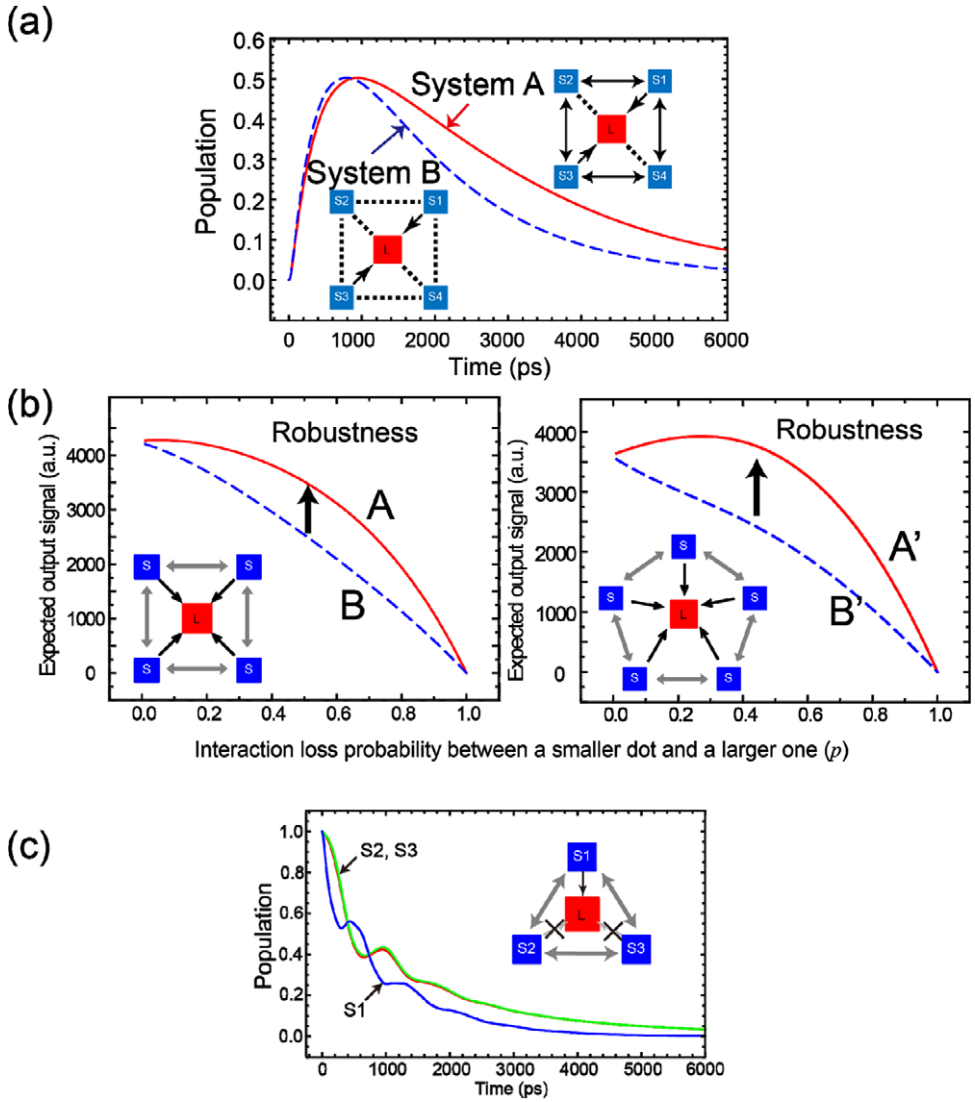

Figure 8. Robustness and autonomy. (*a*) When some of the interactions between the smaller and larger QDs are degraded, optical excitation can be transferred by way of adjacent dots. (*b*) Evaluation of robustness. (*c*) Autonomy in optical excitation transfer. The optical excitations located in S2 and S3, which have degraded interactions with the larger dot (L), are 'waiting' for some period until they have a chance to be transferred.

which is a function of the inter-dot distances, and thus the optical excitation flows differently if the positions of QDs are modified. We theoretically and experimentally demonstrated such dynamic reconfiguration of optical near-field interactions by fabricating different-sized QDs implemented in an elastic, flexible substrate which is mechanically stretchable and deformable [95].

To theoretically demonstrate the reconfiguration of optical near-fields, we assumed a model system consisting of four QDs arranged at the corners of a square grid. Smaller QDs (S1 and S2) are placed on the left, while larger QDs (L1 and L2) are arranged on the right (figure 9(*a*)). Near-field interactions are present among these QDs; in addition to the interactions along the horizontal direction (U_{S1L1} and U_{S2L2}) and the vertical direction (U_{S1S2} and U_{L1L2}), there are interactions along diagonal directions (U_{S1L2} and U_{S2L1}). Mechanical deformation, such as vertical and horizontal stretching and strain, respectively, change the relative positions of the QDs, which affects the inter-dot near-field interactions. We evaluated how the optical excitation transfer in the system differs depending on the deformations based on a theoretical model of networks of optical near-fields.

Here, we assume that the near-field interaction time, which follows a Yukawa potential, is given by $U^{-1} = 100$ ps when the inter-dot distance is 100 nm, and is given by $U^{-1} = 10\,000$ ps when the inter-dot distance is 10 000 nm. Also, as a typical parameter set, the relaxation constant Γ^{-1} is set at 10 ps, and the radiation lifetimes of $\mathrm{QD_S}$ and $\mathrm{QD_L}$, denoted as γ_{S}^{-1} and γ_{L}^{-1}, are, respectively, set at 2.83 ns and 1 ns. The time evolutions of populations, in terms of the radiation from the four QDs, were, respectively, evaluated with an initial condition that the two smaller QDs (S1 and S2) have their own excitations, and the integrated populations were calculated as the output signals from the four QDs.

Figure 9(*b*) summarizes the output signals from the four QDs as a function of vertical and horizontal stretching,

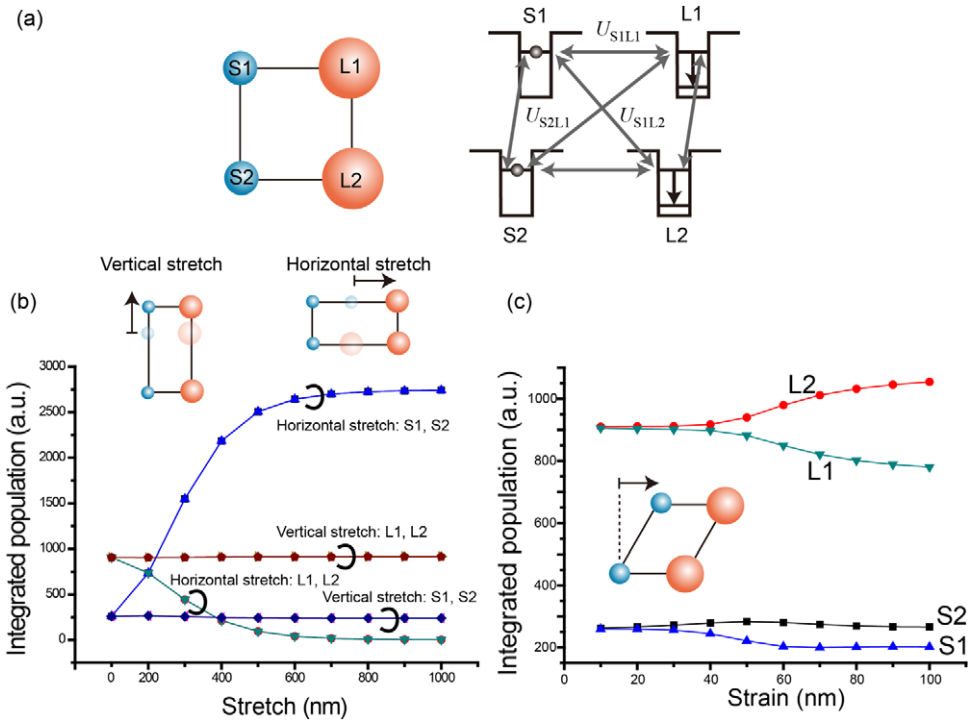

Figure 9. Reconfigurable near-field network. (*a*) A model system. Two smaller QDs (S1 and S2) and two larger QDs (L1 and L2) are arranged on the corners of a square. The optical near-field interactions in this model are shown on the right. (*b*) A vertical stretch does not change the output signals since the dominant paths involving optical excitation transfer do not change. On the other hand, a horizontal stretch greatly changes the output signal. (*c*) For an applied strain, the changes are initially small, but the output from L2 increases as S1 approaches L2.

assuming that the QDs are initially separated from each other by 100 nm. The output signals do *not* change due to the *vertical* stretching. This is because the distances between smaller QDs and larger QDs stay constant, and so the optical excitation transfer from smaller to larger QDs behaves constantly. On the other hand, the output signal appears differently in response to *horizontal* stretching because the smaller-to-larger dot distance strongly affects the optical excitation transfer. Figure 9(*c*) demonstrates the output signal in response to *strain*, which induces horizontal displacement of the QDs located on the upper row, as denoted in the inset. As the strain increases, the output signals initially do not exhibit substantial changes. However, when the strain reaches around 50 nm, the output from L1 decreases and that from L2 increases. This is because, as the strain increases, S1 gets closer to L2, whereas the distance between S1 and L1 remains constant. Therefore, an optical excitation initially located in S1 is more likely to be transferred to L2, not just to L1. L2 also accepts an optical excitation from S2. Therefore, the behavior observed in figure 9(*c*) is also a clear manifestation of the networking effects of optical near-fields.

An experimental demonstration was conducted by using CdSe/ZnS spherical QDs dispersed in a flexible substrate formed of polydimethylsiloxane (PDMS) [96]. The PDMS substrate was provided by the Dai Nippon Printing Co. Ltd, Japan. In this experiment, we fabricated two kinds of samples: the first one, which we will call sample R (resonant), contained a mixture of two kinds of QDs whose diameters were, respectively, 8.2 nm and 8.7 nm, referred to as QD_S and QD_L, respectively. Such a combination of smaller and larger QDs satisfies the conditions for optical excitation transfer discussed in section 2.1.4, and this has been experimentally demonstrated [73]. The other sample, called sample NR (non-resonant), also consisted of two different-sized QDs, with diameters of 7.7 and 8.7 nm. The QD with a diameter of 7.7 nm is referred to as $QD_{S'}$. Such a combination of QDs does not satisfy the above-mentioned conditions for optical excitation transfer. We mixed 5 mL of each QD solution, dispersed them on a 2 cm × 2 cm square PDMS substrate, and allowed them to dry naturally at room temperature. The average distances between QDs were estimated to be 5–10 nm. The idea of the experiment was to observe the changes in the photoluminescence spectra of sample R and sample NR in response to induced mechanical deformation. If sample R exhibited a significant deformation-dependence, it would clearly be attributed to the effects of the reconfiguration of optical near-field interactions.

Each sample was excited with a He–Cd laser (wavelength 325 nm) with a power density of 5 mW cm^{-2}. The sample was set on an aperture formed at the side of a vacuum desiccator and was deformed by evacuation. The air pressure was fixed to ∼0.07 MPa to achieve a 20% in-plane compression ratio of the substrate, which was geometrically determined from the size of the aperture and the depth of the flexed substrate, bringing the dispersed QDs closer to each other. The emission spectra of sample R and sample NR, observed by a spectrometer (JASCO, CT-25TP), are, respectively, shown in figures 10(*a*) and (*b*). The fitted curves have peak wavelengths corresponding to the emission from QD_S, $QD_{S'}$ and QD_L.

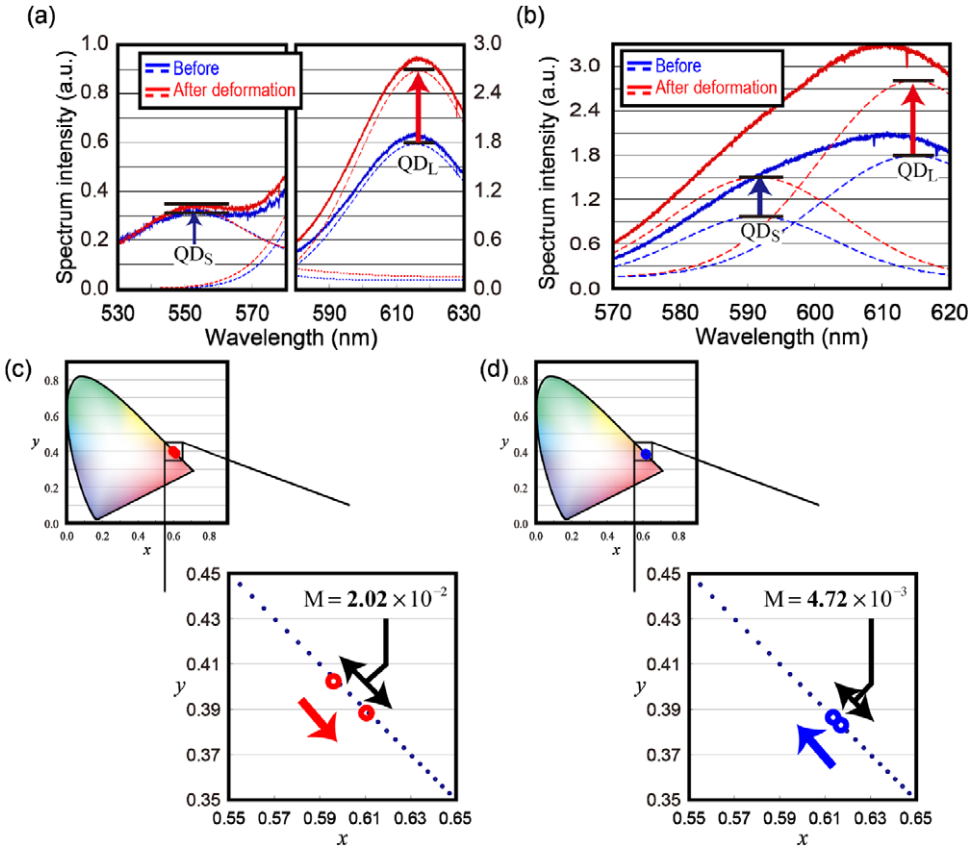

Figure 10. Experimental demonstration of reconfigurable optical near-field network by quantum-dot mixture embedded in a flexible substrate (PDMS). (*a*) Photoluminescence spectra from sample R in which smaller and larger QDs, which are energetically resonant, are embedded. Due to the induced deformation, the intensity corresponding to QD_L selectively increases, indicating the induced optical excitation transfer, that is to say, reconfiguration of the optical near-field interactions. (*b*) Photoluminescence from sample NR, which also contains two kinds of QDs which are energetically non-resonant with each other. The intensities corresponding to QD_L and QD_S both increase uniformly, suggesting that optical excitation transfer is not induced due to deformation. (*c*) Evaluation of the spectral change of the sample R in a chromatic diagram and (*d*) that of the sample NR.

The intensities of the spectra were increased by the induced deformation of the substrate because the numbers of QDs per unit area increased. Regarding sample R, the increase of the emission intensity corresponding to QD_S was suppressed because the average distance between QD_S and QD_L was shortened, which enhanced the optical excitation transfer from QD_S to QD_L. On the other hand, the spectra for sample NR increased uniformly, indicating that the changes are purely based on the QD density increase, whereas no optical excitation transfer is induced. The induced spectral change can also be represented as a position change in a chromaticity diagram, as shown in figure 10(*c*). Sample R revealed a larger shift in the diagram than sample NR, although the absolute amount of the change was small. However, this finding suggests various potential applications based on reconfiguration of optical near-field interactions, ranging from touch displays, color rendering for displays and solid-state lighting, to sensing, amusement, etc.

2.3. Time-domain performance and functions

2.3.1. Timing asymmetry. One of the most important attributes from an information processing perspective is the dynamic properties of nanophotonic devices in the time domain. In particular, a fundamental characteristic of optical devices and systems is skew, which is the difference in the arrival timing among multiple input channels [97, 98]. Elucidating the dynamic properties of nanophotonic devices will have implications for novel system architectures. In this section, we examine the timing dependence inherent in optical excitation transfer [99]. Specifically, we theoretically analyze the dynamic behavior of a two-input nanophotonic switch composed of three quantum dots described in section 2.1.5 while assuming arrival-time differences, or skew, between the two inputs.

We analyze the dynamic behavior of the system based on the density matrix formalism shown in section 2.1.1, assuming optical near-field interactions between these three dots, as well as external inputs to QD_S and QD_L. Since there are a total of six energy levels (namely, S_1 in QD_S, M_1 and M_2 in QD_M, and L_1, L_2 and L_3 in QD_L), the number of different states occupying those energy levels is 2^6 (=64). Our main interest is in the timing difference between the two inputs, and so the external Hamiltonian is given by

$$H_{\mathrm{ext}}(t) = \mathrm{IN_S}(t) \times (R^{\dagger}_{\mathrm{S_1}} + R_{\mathrm{S_1}}) + \mathrm{IN_L}(t) \times (R^{\dagger}_{\mathrm{L_1}} + R_{\mathrm{L_1}}), \quad (11)$$

where $\mathrm{IN}_S(t)$ and $\mathrm{IN}_L(t)$ specify the duration and the amplitude of the external input light applied to QD_S and QD_L. The

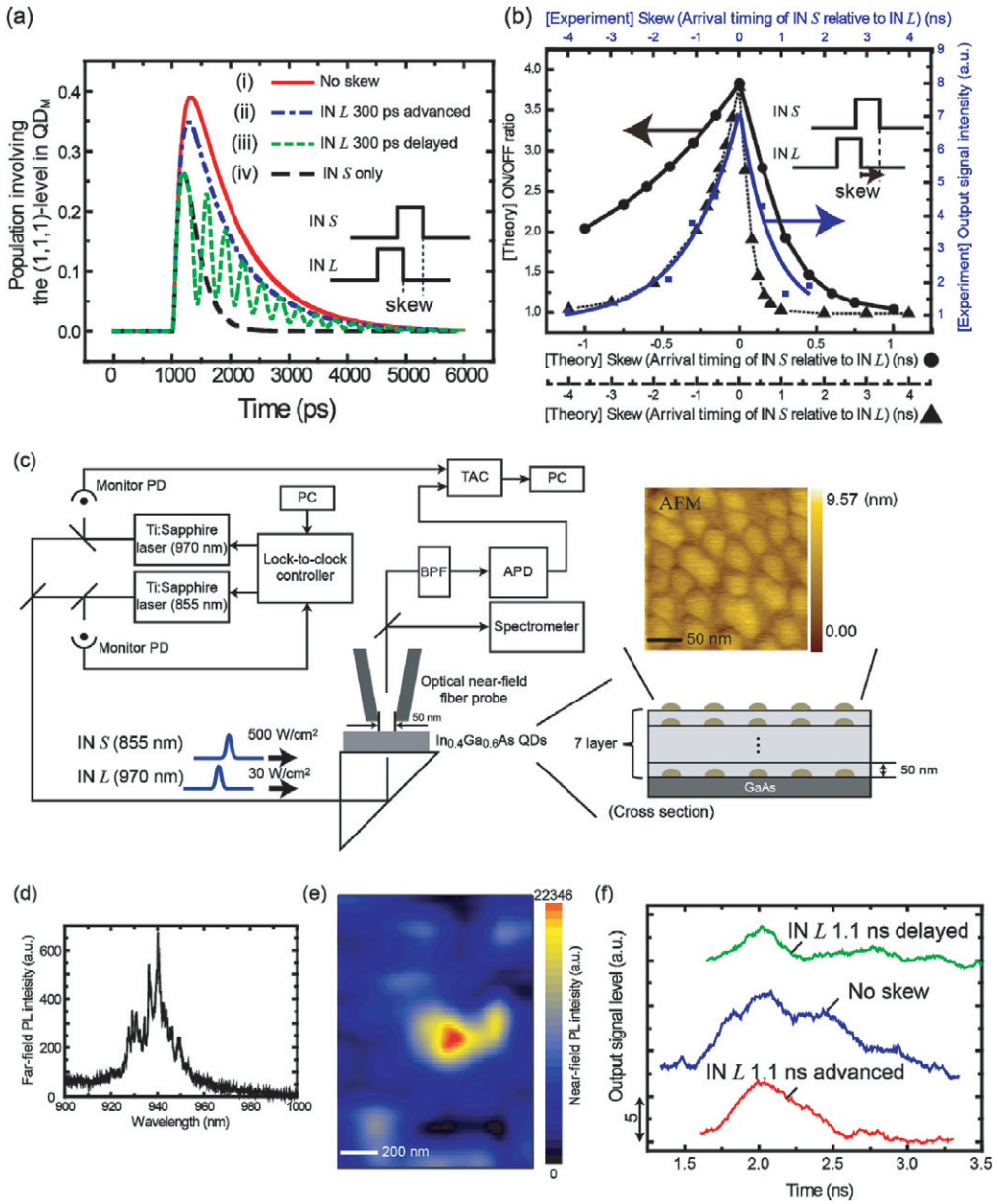

Figure 11. Time-domain performance of optical excitation transfer. (*a*) Time evolution of the output population, that is, the population involving the (1,1,1)-level in QD_M, depending on the arrival-timing difference, or skew, between IN *S* and IN *L*. (*b*) (Theory, ● and ▲) ON/OFF ratio of the output of the AND-gate as a function of the skew between the two input signals predicted by theoretical calculations. The skew ranges corresponding to the circular and triangular marks are, respectively $\{-1$ to 1 ns$\}$ and $\{-4$ to 4 ns$\}$ (Experiment, ■). Output signal intensity as a function of the skew between the two input signals obtained experimentally by near-field spectroscopy of an InGaAs stacked QD device. (*c*) Experimental setup and devices. (*d*) Far-field photoluminescence spectrum of the sample. (*e*) Spatial distribution of the near-field intensity obtained by a near-field fiber probe tip. (*f*) Time evolution of the output signal when the arrival timing of IN *L* relative to IN *S* is −1.1 ns, 0 ns and +1.1 ns.

matrices $R_i^\dagger$ ($i = \mathrm{S}_1, \mathrm{L}_1$) and R_i are, respectively, creation and annihilation operators regarding the energy levels S_1 and L_1.

We assume a rectangular-shaped input signal for both $\mathrm{IN}_S(t)$ and $\mathrm{IN}_L(t)$, and then characterize the output population related to the radiation from QD_M, i.e., the population involving the (1,1,1)-level of QD_M (M_1). We assume the following parameter values for evaluation: (i) inter-dot optical near-field interaction $U^{-1} = 100$ ps, (ii) sublevel relaxation $\Gamma^{-1} = 10$ ps and (iii) radiative decay times $\gamma_L^{-1} = 1$ ns, $\gamma_M^{-1} = 2^{3/2} \times 1 \approx 2.83$ ns and $\gamma_S^{-1} = 2^3 \times 1 = 8$ ns. The durations of both $\mathrm{IN}_S(t)$ and $\mathrm{IN}_L(t)$ are set to 2 ps.

Figure 11(*a*) shows the evolution of the population in the output dot under the assumption that (i) there is no skew between the two inputs (solid, blue), (ii) IN *L* is advanced by 300 ps relative to IN *S* (dashed–dotted, red), (iii) IN *L* is delayed by 300 ps relative to IN *S* (dotted, green), and (iv) only IN *S* is provided (dashed, black). Comparing cases (i) and (iv), we find that the former exhibits a larger population than the latter, which demonstrates behavior typical of a logical AND gate. Note that case (ii) exhibits an output population comparable to that of case (i). On the other hand, in case (iii), the curve of the population evolution is greatly deteriorated

compared with case (i) due to the optical nutation effect introduced in section 2.1.5. Case (iv) should, as an AND gate, exhibit a lower population; however, due to the limited radiation lifetime in QD_L, a non-zero output population still appears.

Next, we evaluate the ON/OFF ratio of the output signal as a function of skew, which is the difference between the arrival times of IN *S* and IN *L*. The ON/OFF ratio is estimated as the time integral of the output population when both IN *L* and IN *S* are applied (ON state), divided by the time integral of the output population when only IN *S* is applied (OFF state). The circular marks in figure 11(*b*) represent the ON/OFF ratio as a function of skew ranging from −1 to 1 ns, and the triangular marks represent that for skew ranging from −4 to 4 ns. The AND gate shows tolerance to the delay of IN *S*: a delay of nearly 1000 ps in IN *S* provides an ON/OFF ratio greater than 2. Since the duration of the input signal is 2 ps, the system can tolerate a skew much longer than the duration of the input signals. On the other hand, the gate operation cannot tolerate a delay of IN *L* relative to IN *S*. This is due to the fact that state filling of QD_L is crucial for the optical excitation transfer from QD_S to QD_M. Therefore, an early (rather than late) arrival of IN *L* is preferred when AND-gate-like behavior is intended.

We experimentally examined the skew properties involving optical excitation transfer via optical near-field interactions based on InGaAs QDs and a near-field spectroscopy setup with a two-channel short-pulse system (figure 11(*c*)). Stacked InGaAs QD devices fabricated by molecular-beam epitaxy (MBE) based on the Stranski–Krastanow (S–K) growth mode [100] were used in the experiment. The inset in figure 11(*c*) shows a schematic cross-sectional diagram of the InGaAs device sample used in the experiment, where seven layers of InGaAs QDs with an inter-layer distance of 50 nm were fabricated on a GaAs substrate. The inset in the top-right corner of figure 11(*c*) shows a surface profile image of the device captured with an atomic force microscope (AFM). The average diameter and height of the QDs were around 50 nm and 5.5 nm, respectively.

Stacked, self-organized QD systems, based on the S–K growth mode in lattice-mismatched materials, have been used in investigating the interactions among QDs [101–104]. In the case of optical excitation transfer via optical near-field interactions, the inter-layer QD distances, corresponding to barrier layers, should be thick enough that the wave functions representing the electronic states of the two QDs do not overlap but should be thin enough that the optical near-field interactions exist [16]; 50 nm satisfies this requirement. Using such stacked QDs, we have demonstrated logic gate operations based on optical near-field interactions [24]. In precisely controlling the size of the quantum dots layer-by-layer, Akahane *et al* developed stacked InAs QDs with InGaAlAs spacer layers on an InP(3 1 1)B substrate by employing a strain compensation technique [105, 106], which provides layer-by-layer size-controlled stacked quantum nanostructures. The device used in our experiment was, however, intentionally chosen to use InGaAs QDs on a GaAs substrate, where large inter-layer strain remains compared with InAs QDs on an InP substrate [105], leading to non-uniformity in the QD sizes. One reason is that the feasible operating wavelengths ($<1.0\,\mu$m) of the optical near-field experimental apparatus described below are well-matched with InGaAs QDs, whereas InP-based QDs requires wavelengths of greater than 1.0 μm, which are not well-matched. Another reason is that, as demonstrated in the spatial intensity distribution observed by near-field spectroscopy, described below, the inhomogeneity of the dot size of the InGaAs QDs enabled inter-dot optical excitation transfer, and we searched for spatial positions where the InGaAs QDs work as AND gates.

The two-channel input signals, IN *S* and IN *L*, were, respectively, applied to the sample by optical pulses generated by two Ti : sapphire lasers with wavelengths of 855 nm and 970 nm. These two lasers were synchronized by a lock-to-clock controller. The pulse duration of both input channels was 2 ps, and their repetition rate was 80 MHz. The average optical powers in the IN *S* and IN *L* channels radiated onto the sample were 500 W cm^{-2} and 30 W cm^{-2}, respectively, which were sufficiently low to avoid multiphoton processes in the sample. One of the input beams, namely, the IN *S* channel at 855 nm, was sampled by a monitoring photodetector and was fed back to the lock-to-clock controller for the purpose of electrical timing control of the 855 nm pulses. This allowed a relative timing difference to be produced between IN *S* and IN *L* for the skew evaluation described below. The QD sample under study was placed on a prism, and the two input beams were radiated onto the sample from the back side (facing the substrate).

The photoluminescence of the sample was obtained from the front side (facing the top layer of QDs) by an optical near-field fiber probing tip with a diameter of 50 nm, which conveyed the sampled light to a spectrometer and an avalanche photodiode (APD). Figure 11(*d*) shows a far-field photoluminescence spectrum of the sample measured at 48.8 K, showing inhomogeneous broadening corresponding to the size distributions in the sample. This allowed us to investigate the optical excitation transfer in the region where the transfer conditions were satisfied in the sample. The near-field intensity distribution of the output signal, corresponding to the radiation from QD_M, was obtained by the spectrometer as the integrated photoluminescence between 945 and 955 nm. Figure 11(*e*) shows the near-field intensity distribution for irradiation with 855 nm light, corresponding to the output wavelength. The distribution exhibits spatial position dependence, indicating that energy transfer occurs among the QDs.

To evaluate the skew dependence, we employed a time-correlated single-photon counting method [107]. The photoluminescence of the sample obtained by a near-field probing tip was first filtered by a band-pass filter (945–955 nm) to select the output signal, and was detected by an APD. At the same time, input optical pulses at 970 nm (IN *L* channel) were monitored by a photodiode. These two signals were provided to a time-to-amplitude converter (TAC) to characterize the time evolution of the output signal. This evaluation was repeated while modifying the relative timing difference between IN *S* and IN *L* using the lock-to-clock laser system described earlier.

Figure 11(*f*) demonstrates three time evolutions of the output signal, detected through the TAC, when the arrival timings of IN L relative to IN S were −1.1 ns, 0 ns and +1.1 ns, respectively. (These three signal traces are represented with different offsets in figure 11(*f*) so that we can clearly observe the differences.) The output signal exhibited a higher level when there was no skew between the inputs. The output signal decreased due to the timing difference between IN L and IN S, but it was more robust to the early arrival of IN L rather than the delay of IN L, as theoretically discussed above.

We characterized the output signal intensity as the time integral of the output signal for a duration between 0 and 3 ns. The output signal intensity depended on the skew, as indicated by the squares in figure 11(*b*). We observed that they exhibited asymmetric responses with respect to the arrival timing of IN S and IN L, showing good agreement with the behavior predicted by the theory discussed earlier.

Finally, we make a few remarks regarding the content discussed in this section. First, elucidating the dynamic properties of nanophotonic devices in this way has implications for novel system architectures. For example, resistance to a skew that is much longer than the duration of input signals opens up the possibility of *asynchronous* architectures [108] based on optical excitation transfer. Such architectures are especially useful in situations where the implementation of clock signals poses problems. Asynchronous circuits have been well known for their robustness to timing fluctuations, and in recent years this idea has been extended to the design of asynchronous cellular automata [109]. The probabilistic nature of optical near-field interactions, the limited distances over which these interactions take place, and the array-like structures of QDs that are in the realm of achievable fabrication technology together constitute a promising basis for the practical realization of such architectures. Furthermore, the asymmetric properties in timing dependence in optical excitation transfer indicate the ability to recognize the order of the incoming signals, which is an important principle of information processing in the human brain called spike timing dependent plasticity (STDP) [46]. Various approaches for implementing STDP are currently being investigated, for example, by using vertical cavity surface emitting lasers (VCSELs) [110], or phase change materials via electrical wires [111]. Optical near-field interactions could break through the limitations inherent in these methods, such as the diffraction limit of light and interconnection bottlenecks due to wires [112].

Second, the resistance to timing skew of the order of nanoseconds reveals that a nanophotonic system could suffer from the problem of lower bit rate (a 100 Mbps regime), although strict timing management could provide Gbps performance [16]. The bit rate also depends on the energy dissipation in the system, as well as the SNR of the detectors and the number of photons per time slot, as discussed in section 2.1.3. A unified, total performance evaluation of nanophotonic systems taking into account architectural, energy dissipation, reliability and dynamic properties will be an important theme for future research.

To implement more-advanced nanophotonic devices, Akahane *et al* developed a method of stacking InAs QDs using a strain compensation scheme where spacer layers with a lattice constant slightly smaller than that of the substrate are used to embed the QD layers. Using this method, 150 InAs QD layers were successfully stacked without any degradation in QD quality [106], leading to the implementation of a versatile arrangement of QDs within a device. Another approach to size- and position-controlled realization of nanophotonic devices includes DNA-based self-assembly technologies [37, 113]. We have recently developed a self-assembly method of linearly aligning ZnO quantum dots with the help of DNA as a size-controlled template [114]. With these architectural and experimental insights and technologies, we will continue to broaden our understanding of optical near-field interactions and utilize them for information processing and communications applications.

2.3.2. Pulsation. Generating an optical pulse train is one of the most important functionalities required for optical systems. Conventional principles of optical pulse generation are based on optical energy build-up in a cavity whose size is much larger than the optical wavelength; thus, the volume and the energy efficiency of the entire system have serious limitations. For nanophotonic applications, novel principles should be developed on the nanometer scale. Shojiguchi *et al* theoretically investigated the possibility of generating superradiance in N two-level systems interacting with optical near-fields [115]. This approach, however, requires precise control of the initial states, which is not straightforward to implement. Here, we theoretically demonstrate a mechanism of optical pulsation based on optical near-field interactions pumped by continuous-wave (CW) light irradiation [116]. With an architecture composed of two subsystems each of which involves energy transfer based on optical near-field interactions, we observe pulsation in the populations based on a model system using a density matrix formalism. The details of the theoretical elements of this paper will be found in [116].

As discussed in section 2.1.5, when the lower level of QD_L is populated by an external input, the optical excitation occurring in QD_S cannot be transferred to QD_L because the lower energy level in QD_L is populated, which is called the state filling effect. Putting it another way, the population of the (1,0)-level in QD_S is changed by the external input applied to L_1 in QD_L. Optical pulsation based on optical excitation transfer comes from the idea that the externally applied change induced in L_1 can be provided in a self-induced manner by S_1 with a certain timing delay. If QD_S is irradiated with continuous input light, such a change should repeat with a certain period; that is, a pulsed signal should result.

We consider two quantum-dot systems, each of which consists of one smaller and one larger QD, as shown in figure 12(*a*). One system, called *system 1* hereafter, is represented by one smaller dot (QD_C) and one larger dot (QD_G). A CW input is provided to the upper level of QD_C. The optical near-field interaction between QD_C and QD_G is denoted by U_{CG}. Another system, called *system 2*, provides a delay time by the multiple use of smaller and larger dots, as

already experimentally realized in [74]. However, modeling the delay caused by multiple QDs makes the discussion of pulsation mechanisms unnecessarily complicated; thus, we assume an arbitrary delay time applied to the input signal of system 2, denoted by Δ, followed by the last two quantum dots in the delay system, namely, a smaller QD (QD_A) and a larger QD (QD_B), as indicated in figure 12(*a*). Here, QD_A accepts radiation from QD_C in system 1; that is, the change of the states in QD_C is transferred to QD_A. The optical near-field interaction between QD_A and QD_B is denoted by U_{AB}. The output from QD_B then influences the lower energy level of QD_G. We described the details of the above modeling based on a density matrix formalism. For example, regarding system 1, there are in total three energy levels (namely, C_1 in QD_C, and G_1 and G_2 in QD_G). The radiative relaxation rates from C_1 and G_1 are, respectively, given by γ_C and γ_G. Then we rigorously derived the quantum master equations for system 1 and system 2, respectively [116].

We assume the following typical parameter values based on experimental observations of energy transfer observed in ZnO quantum dots [72]: inter-dot optical near-field interactions (144 ps), sublevel relaxation (10 ps), and radiative decay times of the smaller dot (443 ps) and the large dot (190 ps). Also, we assume 1 ns for the delay Δ in system 2 in figure 12(*a*). Figure 12(*b*) demonstrates an example of the evolution of the populations involving the lower level of QD_G (G_1) for different CW input light amplitudes, where optical pulsation is successfully observed with appropriate input light amplitudes, as summarized in figure 12(*c*). The period of the pulsation, or frequency, depends on the input CW light amplitude, which is one of the indications that the pulsation is based on optical excitation transfer among the QDs, as shown in figure 12(*d*).

To observe such an effect more clearly, figure 12(*e*) shows the parameter dependences on the inter-dot interactions between QD_C and QD_G (U_{CG}) and the radiation lifetime of QD_C (γ_C). The squares and circles in figure 12(*e*) indicate the peak-to-peak value of the pulsations in populations as a function of U_{CG} and the radiation lifetime of QD_C, respectively. To seek the origin of such behavior, we investigate the virtually isolated system 1, namely, an independent system composed only of QD_C and QD_G. Figure 12(*f*) represents the steady-state populations involving the lower level of QD_G (G_1) as a function of the radiation lifetime of QD_C. Increasing the radiation lifetime of QD_C allows an excitation generated in QD_C to be transferrable during that lifetime, thus increasing the possibility of a transition to QD_G, shown by the circles in figure 12(*f*). On the other hand, increasing the inter-dot interaction time, namely, weakening the inter-dot interaction, degrades the population in QD_G, as shown by the squares in figure 12(*f*). Here we should note that the pulsation vanishes, in figure 12(*e*), when U_{CG}^{-1} is larger than 230 ps, corresponding to a population in G_1 of around 0.02 in figure 12(*f*). In figure 12(*f*), the pulsation also vanishes when γ_C^{-1} is smaller than 300 ps, which also corresponds to a population in G_1 of around 0.02 in figure 12(*f*). This agreement, or unified understanding, of two different parameter dependences indicates that the energy transfer via optical near-field interactions plays a crucial role in optical pulsation at the nanometer scale.

3. Hierarchical architectures in nanophotonics

There are multiple physical scales, that is to say, a hierarchy, between the macroscale world and the atomic-scale world, as schematically shown in figure 13(*a*). The scales at the larger- and smaller-extremes are, respectively, governed by propagating light and electron interactions. Between those two extremes, typically in scales ranging from a few nanometers to a size equal to the light wavelength, optical near-field interactions play a crucial role. This section introduces some basic theoretical treatments of hierarchy in optical near-field interactions and their applications.

Before entering into the details, there are some remarks that should be made about the hierarchy inherent in nanophotonics. As mentioned in the introduction, the electronic near-fields, utilized in STM and related nanotechnologies, correspond simply to the evanescent tails of electronic waves in bulk crystal since no structures of electronic subwavelength size are available for usual condensed matter, and thus the correlation length of an electron is constant. In contrast, the scale-dependent nature of optical near-fields is a unique physical property and may provide functions that complement those offered by electronics. Also, as schematically indicated in figure 13(*a*), propagating light and optical near-fields can co-exist. This means that, while preserving the optical response function regarding propagating light, additional functions—or 'added-value'—can be simultaneously implemented by way of optical near-fields. As argued in the introduction, there is a well-established solid foundation for optical system design with respect to propagating light. We consider that basic theories and design methodologies taking account of optical near-fields should also be developed to significantly enhance optical systems.

This section first introduces three theories for describing hierarchy in nanophotonics (section 3.1). The first one is based on dipole–dipole interactions, the second is based on a Yukawa potential of optical near-fields, and the last one is based on an angular spectrum representation of electromagnetic fields. Section 3.2 discusses the design of hierarchy by engineering means, such as arrangements of nanoparticles and shape-engineered metal nanostructures. Section 3.3 presents some hierarchical optical devices that have been demonstrated experimentally.

3.1. Fundamentals

3.1.1. Theory of hierarchy based on dipole–dipole interactions. This section describes a physical model of optical near-field interactions based on dipole–dipole interactions [75]. Suppose that a probe, which is modeled by a sphere of radius r_P, is placed close to a sample to be observed, which is modeled as a sphere of radius r_S. The inset in figure 13(*b*) shows three different sizes for the probe and the sample. When they are illuminated by incident light whose

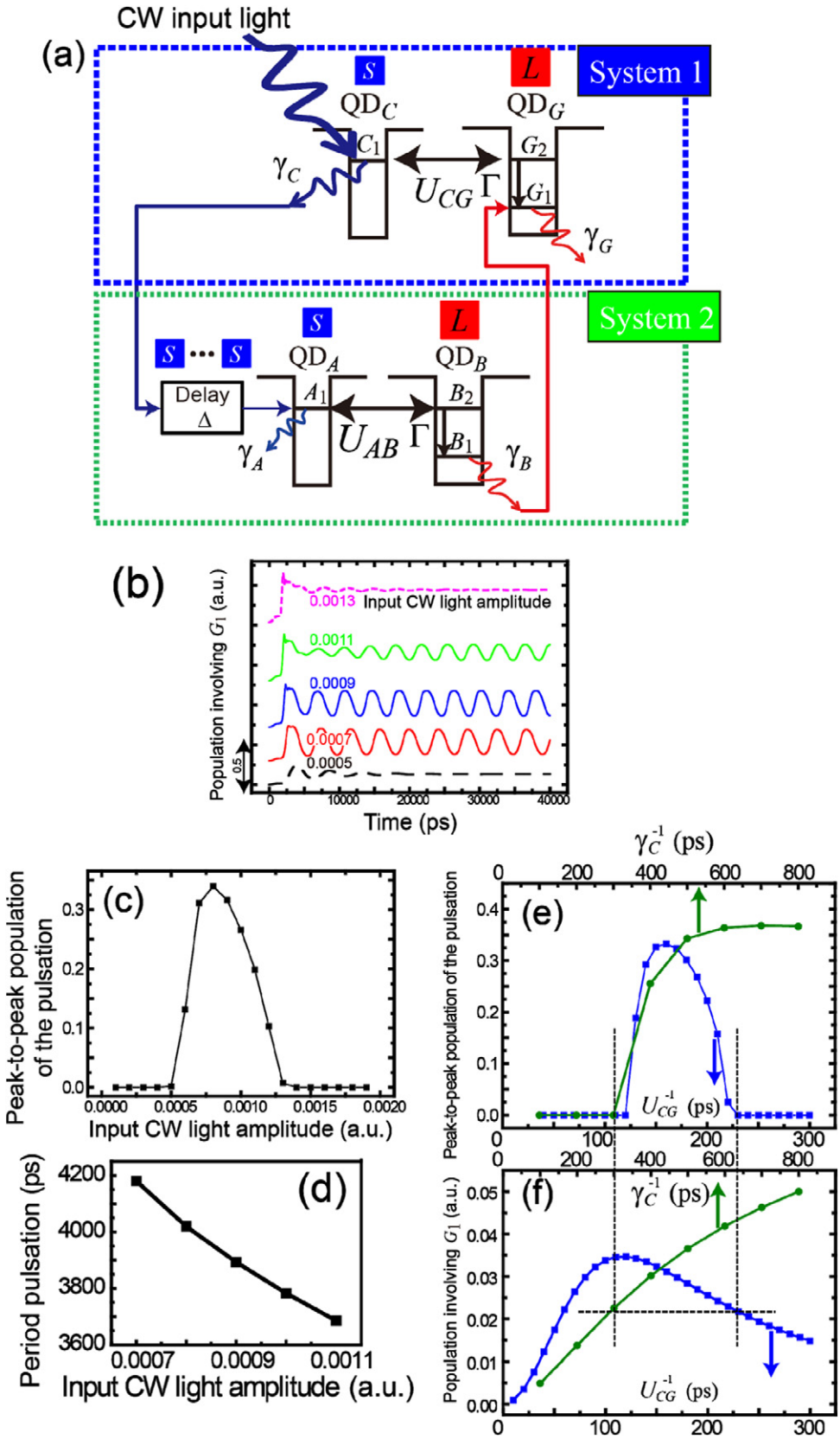

Figure 12. (*a*) System architecture of pulsation composed of two subsystems each of which provides optical excitation transfer from QD_S to QD_L. (*b*) Evolution of population in the lower energy level of QD_G with different CW input light amplitudes, where pulsations are observed in suitable parameter ranges. (*c*) Peak-to-peak population of pulsation versus input CW light amplitude. (*d*) The period of pulsation depends on the input CW light amplitude. Parameter dependences on inter-dot optical near-field interactions and the radiation lifetime, showing (*e*) peak-to-peak population related to the pulsation, and (*f*) populations involving G_1.

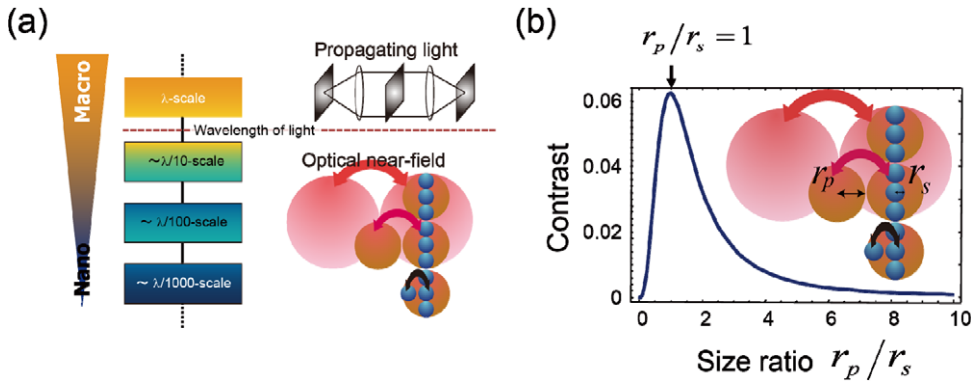

Figure 13. (*a*) Hierarchy in optical near-field interactions and hierarchical nanophotonic architecture. (*b*) Signal contrast as a function of the ratio of the radii of the sample and the probe based on dipole–dipole interactions.

electric field is $\boldsymbol{E}_0$, electric dipole moments are induced in both the probe and the sample; these moments are, respectively, denoted by $\boldsymbol{p}_\mathrm{P} = \alpha_\mathrm{P}\boldsymbol{E}_0$ and $\boldsymbol{p}_\mathrm{S} = \alpha_\mathrm{S}\boldsymbol{E}_0$. The electric dipole moment induced in the sample, $\boldsymbol{p}_\mathrm{S}$, then generates an electric field, which changes the electric dipole moment in the probe by an amount $\Delta\boldsymbol{p}_\mathrm{P} = \Delta\alpha_\mathrm{P}\boldsymbol{E}_0$. Similarly, $\boldsymbol{p}_\mathrm{P}$ changes the electric dipole moment in the sample by $\Delta\boldsymbol{p}_\mathrm{S} = \Delta\alpha_\mathrm{S}\boldsymbol{E}_0$. These electromagnetic interactions are called dipole–dipole interactions.

The scattering intensity induced by these electric dipole moments is given by

$$I = |\boldsymbol{p}_\mathrm{P} + \Delta\boldsymbol{p}_\mathrm{P} + \boldsymbol{p}_\mathrm{S} + \Delta\boldsymbol{p}_\mathrm{S}|^2 \approx (\alpha_\mathrm{P} + \alpha_\mathrm{S})^2|E_0|^2 + 4\Delta\alpha(\alpha_\mathrm{P} + \alpha_\mathrm{S})|E_0|^2, \quad (12)$$

where $\Delta\alpha = \Delta\alpha_\mathrm{S} = \Delta\alpha_\mathrm{P}$ [75]. The second term in equation (12) shows the intensity of the scattered light generated by the dipole–dipole interactions, containing the information of interest, which is the relative difference between the probe and the sample. The first term in equation (12) is the background signal for the measurement. Therefore, the ratio of the second term to the first term in equation (12) corresponds to a signal contrast, which will be maximized when the sizes of the probe and the sample are the same ($r_\mathrm{P} = r_\mathrm{S}$), as shown in figure 13(*b*). Thus, one can see a scale-dependent physical hierarchy in this framework, where a small probe, say $r_\mathrm{P} = D/2$ where D is a constant, can nicely resolve objects with a comparable resolution, whereas a large probe, say $r_\mathrm{P} = 3D/2$, cannot resolve detailed structure but can resolve structure with a resolution comparable to the probe size. Therefore, although a large diameter probe cannot detect smaller-scale structure, it could detect certain features associated with its scale.

3.1.2. Theory of hierarchy based on Yukawa potential. Hierarchy in optical near-field interactions can also be derived by way of a Yukawa potential, introduced in equation (9). Suppose that there is a spherical probe with radius a_P and a sample with radius a_S. The near-field optical potential is then given by

$$V(r) = \sum_{i=S}^{P} \frac{\exp(-\pi r/a_i)}{r}. \quad (13)$$

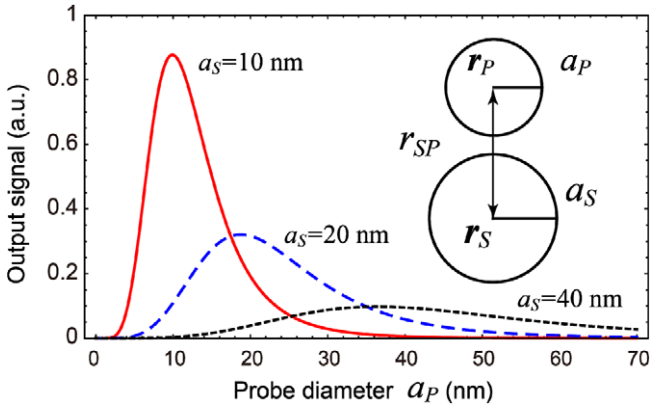

Figure 14. Hierarchy in optical near-field interactions derived via Yukawa potential.

The scattered signal obtained from the probe–sample interaction is then given by

$$I(r_\mathrm{SP}) \equiv \left|\iint \nabla_{r_\mathrm{P}} V(|\boldsymbol{r}_\mathrm{P} - \boldsymbol{r}_\mathrm{S}|) d^3r_\mathrm{S} d^3r_\mathrm{P}\right|^2 \propto \left[a_\mathrm{P}^3\left\{\frac{a_\mathrm{S}}{a_\mathrm{P}}\cosh\left(\frac{\pi a_\mathrm{S}}{a_\mathrm{P}}\right) - \frac{1}{\pi}\sinh\left(\frac{\pi a_\mathrm{S}}{a_\mathrm{P}}\right)\right\} \times \left(\frac{1}{r_\mathrm{SP}} + \frac{a_\mathrm{P}}{\pi r_\mathrm{SP}^2}\right)\exp\left(-\frac{\pi r_\mathrm{SP}}{a_\mathrm{P}}\right)\right]^2 \quad (14)$$

where the center positions of the probe and the sample are, respectively, $\boldsymbol{r}_\mathrm{S}$ and $\boldsymbol{r}_\mathrm{P}$, and the distance between $\boldsymbol{r}_\mathrm{S}$ and $\boldsymbol{r}_\mathrm{P}$ is given by r_SP. The detailed derivation of equation (14) is found in [117]. Assuming a constant sample radius, we evaluate how the output signal depends on the probe radius. Here the output signal is defined by the quantity given by equation (14) divided by the square of the total volume of the sample and the probe, that is $(a_\mathrm{P}^3 + a_\mathrm{S}^3)^2$, so that the evaluation is made in the dimension of per unit area. The solid, dashed, and dotted curves in figure 14, respectively, represent the output signal when the sample radius is by 10 nm, 20 nm and 40 nm. The peak of the output signal is obtained when the probe size is comparable to the sample size, which is consistent with the finding shown in the previous section (section 3.1.1).

3.1.3. Theory of hierarchy based on angular spectrum. In this section, we introduce an electromagnetic theory based

on an angular spectrum representation [118, 119] to describe hierarchy in optical near-fields [120]. This approach allows an analytical treatment, while giving an intuitive picture of the localization of optical near-fields, and represents the relationship between the arrangements of dipoles and the resulting electric fields at certain positions in optical near-field interactions at different scales of observation since it describes electromagnetic fields as a superposition of evanescent waves with different decay lengths and corresponding spatial frequencies for an assumed planar boundary.

Suppose that there is an oscillating electric dipole, $\boldsymbol{d}^{(k)} = (d^{(k)} \cos\phi^{(k)}, 0)$, on the xz plane oriented parallel to the x-axis whose phase is specified by $\phi^{(k)}$. Also note that the physical scale under study is smaller than the wavelength of light but larger than the scale governing electron interactions, typically around 1 nm.

Now, consider the electric field of radiation observed at a position displaced from the dipole by $\boldsymbol{R} = (r_{||}^{(k)} \cos\varphi^{(k)}, z^{(k)})$. The angular spectrum representation of the z-component of the optical near-field is given by

$$E_z(\boldsymbol{R}) = \left(\frac{\mathrm{i}K^3}{4\pi\varepsilon_0}\right)\int_1^\infty \mathrm{d}s_{||}\frac{s_{||}}{s_z} f_z(s_{||}, \boldsymbol{d}^{(1)}, \ldots, \boldsymbol{d}^{(N)}), \quad (15)$$

where

$$f_z(s_{||}, \boldsymbol{d}^{(1)}, \ldots, \boldsymbol{d}^{(N)}) = \sum_{k=1}^{N} d^{(k)} s_{||}\sqrt{s_{||}^2 - 1}\cos(\phi^{(k)} - \varphi^{(k)}) J_1 \times \left(Kr_{||}^{(k)} s_{||}\right)\exp\left(-Kz^{(k)}\sqrt{s_{||}^2 - 1}\right). \quad (16)$$

Here, $s_{||}$ is the spatial frequency of an evanescent wave propagating parallel to the x-axis, and $J_n(x)$ represents Bessel functions of the first kind. Here the term $f_z(s_{||}, \boldsymbol{d}^{(1)}, \ldots, \boldsymbol{d}^{(N)})$ is called the angular spectrum of the electric field.

Now, assume that there are two dipoles whose phases differ from each other by π, and consider the angular spectrum of the electric field at a position equidistant to those dipoles and away from the x-axis by distance Z (figure 15(a)). The distance between the dipoles, given by G, represents the spatial fine/coarse structure of the material. Here, G and Z indicate distances in units of wavelength. If the angular spectrum contains higher spatial frequency components, it means that the electric field is localized at that position to the extent given by that spatial frequency. In order to evaluate localization at different scales (Z) and associate it with the spatial structure of the material (G), the spatial frequency that gives the maximum of the angular spectrum is noted; this is called the 'representative spatial frequency' (RSF). Figure 15(b) shows the RSF as a function of the distance Z, as well as its dependence on G; this diagram gives a quantitative, intuitive picture of the hierarchy in the subwavelength regime.

For instance, first note the RSF when Z is 1/5. The RSF exhibits nearly equal values for all cases $G = 1/5$, 1/10 and 1/20. This indicates that the degrees of localization of the electric field at this scale ($Z = 1/5$) are comparable and do not depend on the fine structure of the dipoles. Second, at $Z = 1/10$, the RSF values for $G = 1/10$ and 1/20 are nearly equal, but the value for $G = 1/5$ is small. This means that at this scale, $G = 1/10$ and 1/20 exhibit comparable degrees of localization but that for $G = 1/5$ deteriorates. Third, at $Z = 1/20$, these three cases exhibit different degrees of localization. As just described, the propagation of locality can be treated intuitively and explicitly by using the angular spectrum representation.

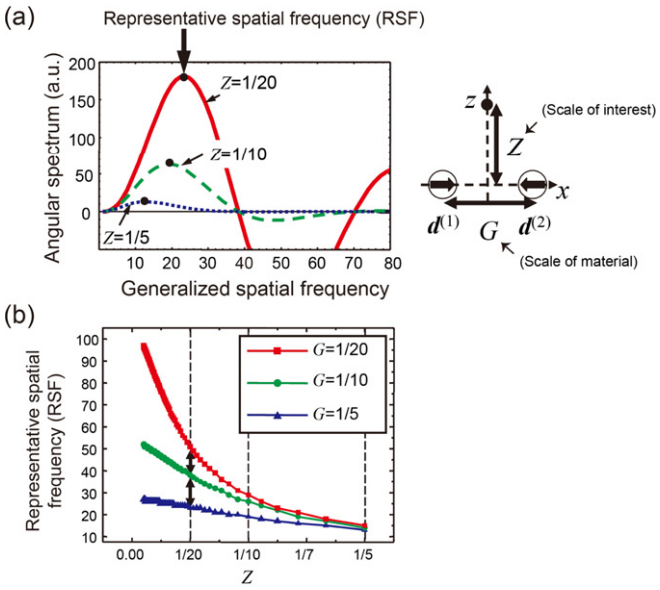

Figure 15. Hierarchy in optical near-field interactions derived via angular spectrum representation. (a),(b) Relation between the scale of the material and the scale of interest, and its angular spectrum representation.

The analysis shown above leads to the possibility of designing a system in which the electric field exhibits a desired hierarchical response based on the fact that, as demonstrated, the orientations of the dipoles and their spatial arrangement are correlated with the localization of optical near-fields at each scale. We introduce such a principle of synthesis of hierarchy using a model shown in figure 16(a).

Regarding a system composed of two closely located dipoles, we pay attention to the z-components of the electric fields at the position equidistant to the two dipoles and slightly away from the x-axis. A logical ZERO or ONE level is defined when the z-component of the electric field is weak or strong, respectively. An in-phase dipole pair yields a logical ZERO level, and that with a phase difference of π gives a logical ONE level, as schematically shown in figure 16(a-1) and (a-2), respectively, by considering the electrical lines of force.

Now, suppose that there are two closely spaced dipole pairs (that is, four dipoles in total). The dipoles $\boldsymbol{d}^{(1)}$ and $\boldsymbol{d}^{(2)}$ are oriented in the same direction, and the other dipole pair, $\boldsymbol{d}^{(3)}$ and $\boldsymbol{d}^{(4)}$, are both oriented oppositely to $\boldsymbol{d}^{(1)}$ and $\boldsymbol{d}^{(2)}$, as shown in figure 16(b). At a position close to the x-axis equidistant from $\boldsymbol{d}^{(1)}$ and $\boldsymbol{d}^{(2)}$, such as at the position A_1 in figure 16(b), the electric field is weak (logical ZERO) because, at such a finer scale, $\boldsymbol{d}^{(1)}$ and $\boldsymbol{d}^{(2)}$ dominate the fields at A_1. The same argument applies to the position A_2, which is equidistant to $\boldsymbol{d}^{(3)}$ and $\boldsymbol{d}^{(4)}$. On the other hand, consider the observation at an intermediate position between the dipole pairs, such as the position B in figure 16(c). From this position, the four dipoles

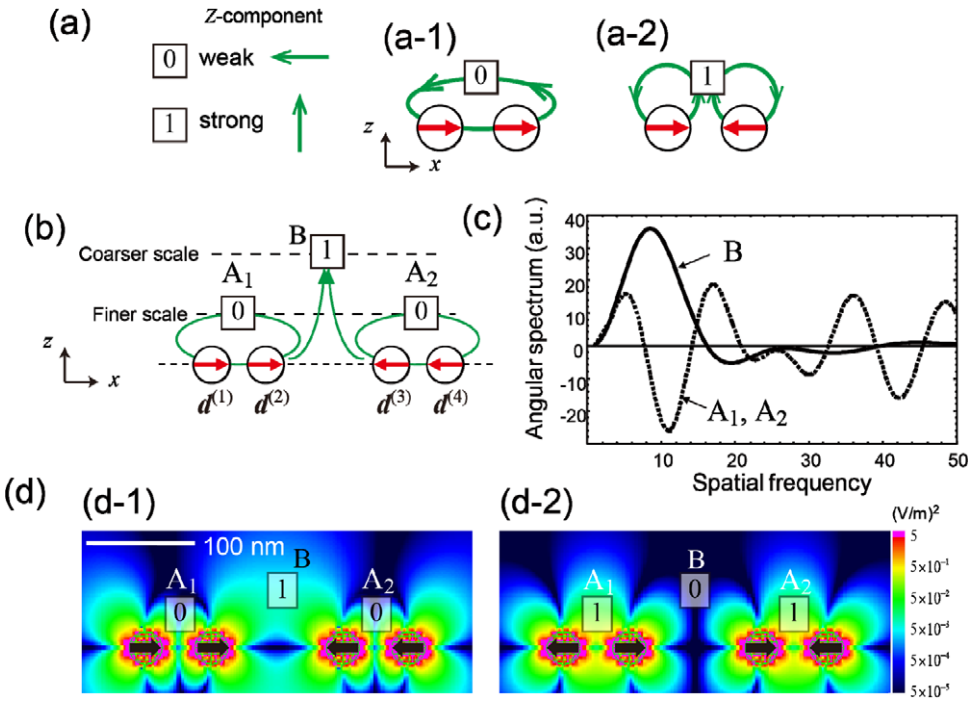

Figure 16. (*a*) Two dipoles and their associated electric fields. (*a*-1) A pair of in-phase dipoles yields a logical ZERO level in its vicinity, whereas (*a*-2) a pair of anti-phase dipoles gives a logical ONE level. (*b*) Two pairs of dipoles can provide logical ZERO level at the smaller scale and logical ONE level at the larger scale. (*c*) Behavior manifested by angular spectrum representation. (*d*) Numerical demonstrations of two cases.

effectively appear to be two dipoles that are oriented in opposite directions to each other, because the fine structure of the dipole pairs cannot have any effect due to the hierarchical property suggested by the analysis shown in figure 15(*b*), leading to a logical ONE level at B. The angular spectrum can clearly represent such scale-dependent localization/non-localization of light, as demonstrated in figure 16(*c*). The dashed curves in figure 16(*c*) show the angular spectrum with respect to A_1 and A_2, which are oscillating as a function of spatial frequency, meaning that light is not localized. The integral of the angular spectrum, which is correlated with the field intensity at that point, is low. On the other hand, the solid curve in figure 16(*c*) is the angular spectrum regarding B which exhibits a single peak, indicating that the electric field is localized to a degree determined by its spectral width, so that a logical ONE is retrievable at that position.

Numerical simulations were performed based on finite-difference time-domain (FDTD) methods to see how they agree with the theoretical analysis based on the angular spectrum. Four silver nanoparticles (radius of 15 nm) containing a virtual oscillating light source were assumed in order to simulate dipole arrays. The first and the second layers were located 40 nm and 80 nm away from the dipole plane, respectively. The operating wavelength was 488 nm. The electric fields obtained at A_1, A_2 and B agree with the combinations of the first- and second-layer signals to be retrieved, as shown in figure 16(*d*-1).

In fact, arbitrary combinations of logical levels are achievable by properly arranging the dipoles. Figure 16(*d*-2) shows another case where A_1 and A_2 exhibit a logical ONE, whereas B exhibits a logical ZERO, which is the opposite response to the one shown in figure 16(*d*-1).

It should also be noted that these two examples are examples of realizing an 'unscalable' hierarchy, where the information obtained at a coarser scale is *not* the average of the information obtained at finer scales. We can synthesize a hierarchy based on these theoretical elements and inherent physical principles of optical near-fields. In section 3.4, we will discuss an information-theory analysis of hierarchical optical systems.

3.2. Design and synthesis of hierarchy by engineering means

3.2.1. Hierarchy based on nanoparticles. Based on the hierarchical mechanism demonstrated in the previous section, a hierarchical information retrieval system has been constructed. Consider, for example, a maximum of N nanoparticles distributed in a region of subwavelength scale. Those nanoparticles can be nicely resolved by a scanning near-field microscope if the size of its fiber probe tip is comparable to the size of individual nanoparticles (sections 3.1.1 and 3.1.2). In this way, the *first-layer* information associated with each distribution of nanoparticles is retrievable, corresponding to 2^N-different codes. By using a larger-diameter fiber probe tip instead, although the distribution of the particles cannot be resolved, a mean-field feature with a resolution comparable to the size of the probe can be extracted, namely, the number of particles within an area comparable to the size of the fiber probe tip. Thus, *second-layer* information associated with the number of particles, corresponding to $(N + 1)$ different signal levels, is retrievable. Therefore, one can access different sets of signals, 2^N or $N + 1$, depending on the scale of observation. This leads to hierarchical memory retrieval by associating this

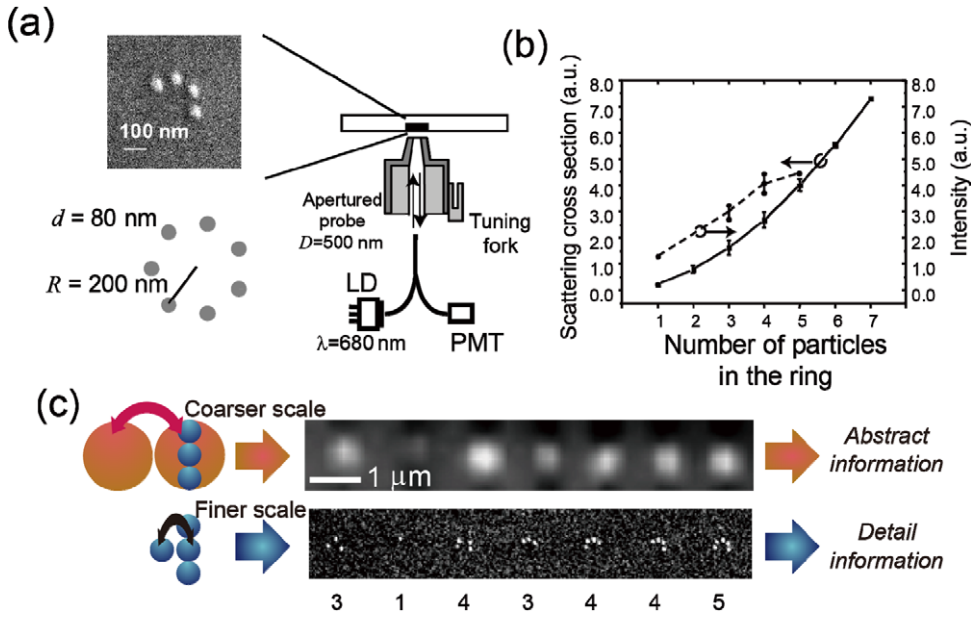

Figure 17. Hierarchical information retrieval or hierarchical information hiding. (*a*) Experimental setup. Each section of the material consists of small particles. (*b*) Calculated scattering cross-sections depending on the number of particles in each section (square marks), and peak intensity of each section in the intensity profile of images shown in (*c*) (circular marks). (*c*) SEM image of an Au particle array and intensity pattern captured by a fiber probe with a 500 nm diameter aperture.

information hierarchy with the distribution and the number of nanoparticles using an appropriate coding strategy. For example, in encoding N-bit information, (N-1)-bit signals can be encoded by distributions of nanoparticles while associating the remaining 1-bit with the number of nanoparticles. Details of encoding/decoding strategies can be found in [121].

Simulations were performed assuming ideal isotropic metal particles to see how the second-layer signal varies depending on the number of particles by using a FDTD simulator. Here, 80 nm diameter particles are distributed over a 200 nm radius circular grid at constant intervals, as shown in figure 17(*a*). The solid circles in figure 17(*b*) show calculated scattering cross-sections as a function of the number of particles. A linear correspondence to the number of particles was observed. This result supports the simple physical model described above.

In order to experimentally demonstrate such principles, an array of Au particles, each with a diameter around 80 nm, was distributed over a SiO_2 substrate in a 200 nm radius circle. These particles were fabricated by a liftoff technique using electron-beam (EB) lithography with a Cr buffer layer. Each group of Au particles was separated by 2 μm. A scanning electron microscope (SEM) image is shown in figure 17(*c*) in which the values below indicate the number of particles within each group. In order to illuminate all Au particles in each group and collect the scattered light from them, a near-field scanning optical microscope (NSOM) with a large-diameter-aperture (500 nm) metalized fiber probe was used in an illumination-collection setup. The light source used was a laser diode with an operating wavelength of 680 nm. The distance between the substrate and the probe was maintained at 750 nm. Figure 17(*c*) shows an intensity pattern captured by the probe, from which the second-layer information is retrieved. The solid squares in figure 17(*b*) indicate the peak intensity of each section, which increased linearly. These results show the validity of hierarchical memory retrieval from nanostructures.

3.2.2. Shape-engineered nanostructures for polarization control in nanophotonic systems. Shape-engineering of nanostructures is one of the most useful means to implement nanoscale photonic systems. There is a vast number of design parameters associated with the geometries of nanostructures, including their size, shape, layout, etc. In order to obtain the intended functionalities by engineering such a variety of degrees-of-freedom, design methodologies and intuitive physical pictures are important. In this section, by taking an example of polarization control in the optical near-field and far-field, we discuss one example of design-related issues in nanophotonics. In particular, we focus on the problem of rotating the plane of polarization. Polarization in the optical near-field is an important factor in the operation of nanophotonic devices [25]. Polarization in the far-field is, of course, important for various applications; nanostructured devices have already been employed, for instance, in so-called wire-grid polarizers [122, 123].

In attacking the design issues involving geometry, we introduce the concepts of *elemental shape* and *layout*, to analyze and synthesize the optical responses brought about by nanostructures [124]. The concepts of elemental shape and layout are physically related, respectively, to the electrical current induced in the metal nanostructure and the electric fields, that is, the optical near-fields, induced between individual elements of the metal nanostructure, which helps in understanding the induced optical responses. For example, it will help to determine whether a particular optical response originates from the shape of the nanostructure itself, that is to say, the elemental shape factor, or from the positional

relations between individual elements, that is to say, the layout factor. Such analysis will also help in the design of more complex structures, including multi-layer three-dimensional nanostructures. In fact, the design concept demonstrated below leads to demonstrations of interesting applications (hierarchical hologram and lock-and-key), shown in section 3.3. Also, what should be noted, particularly in the case of multi-layer systems, is that the optical near-fields appearing between individual elemental shapes, including their hierarchical properties, strongly affect the resultant optical response. This indicates that the properties of the system are not obtained by a superposition of the properties of individual elements, in contrast to optical antennas, whose behavior is explained by focusing on factors associated with individual elements [125].

We assume that the nanostructures are located on an *xy*-plane and are irradiated with linearly polarized light from the direction of the normal. We first assume that the nanostructure has a regular structure on the *xy*-plane; in other words, it has no fine structure along the *z*-axis. Here we consider the concepts of *elemental shape* and *layout*, introduced above, to represent the whole structure. Elemental shape refers to the shape of an individual structural unit, and the whole structure is composed of a number of such units having the same elemental shape. Layout refers to the relative positions of such structural units. Therefore, the whole structure is described as a kind of convolution of elemental shape and layout.

We begin with the following two example cases that exhibit contrasting properties in their optical near-field and far-field responses. One is what we call an *I-shape*, which exhibits a strong electric field only in the optical near-field regime, while showing an extremely small far-field electric field. The other is what we call a *Z-shape*, which exhibits a weak near-field electric field, while showing a strong far-field electric field. They are schematically shown in the first row in figure 18. In the case of the I-shape, the elemental shape is a rectangle. Such rectangular units are arranged with the same interval horizontally (along the *x*-axis) and vertically (along the *y*-axis), but every other row is horizontally displaced by half of the interval. In the case of the *Z*-shape, the element shape is like the letter 'Z', and they are arranged regularly in the *xy*-plane as specified by the layout shown in the second row in figure 18.

We calculate the optical responses in both the near-field and far-field based on a FDTD method [126, 127]. As the material, we assume gold, which has a refractive index of 0.16 and an extinction ratio of 3.8 at a wavelength of 688 nm [128]. Representative geometries of the I-shape and Z-shape structures in the *xy*-plane are shown in the left column in figure 18. The width (line width) of the structures is 60 nm, and the thickness is 200 nm. The light source, operating at a wavelength of 688 nm, is placed 500 nm away from one of the surfaces of the structures. We assume periodic boundary conditions at the edges in the *x*- and *y*-directions and perfectly matched layers in the *z*-direction.

We pay attention to the electric field intensity of *y*-polarized output light from *x*-polarized input light. The near-field electric field intensity is nearly 2000 times higher

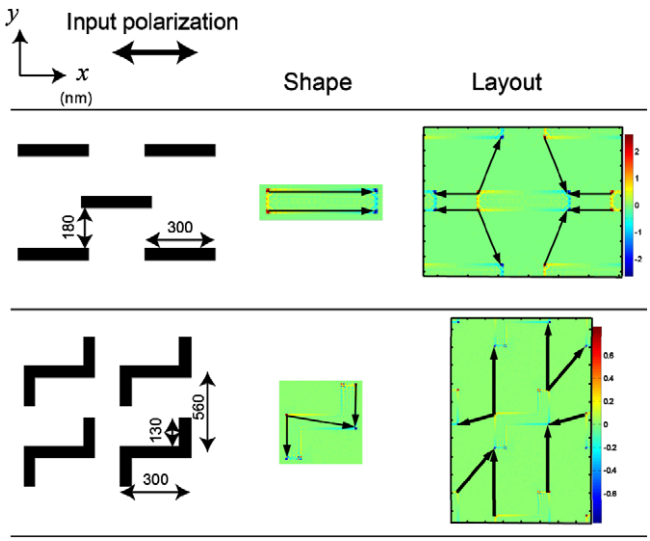

Figure 18. Charge distributions induced in the I-shape and the Z-shape structures with *x*-polarized input light. The arrows in the column 'shape' are associated with the induced electric currents within the elemental shapes, and those in the column 'layout' are associated with near-fields among elemental shapes.

with the I-shape than with the Z-shape. The far-field electric field intensity, on the other hand, is around 200 times higher with the Z-shape than with the I-shape. We explain the physical mechanism of these contrasting optical responses in the near- and far-fields using an intuitive framework. We derive the distribution of induced electron charge density (simply referred to as charge hereafter) by calculating the divergence of the electric fields to analyze the relation between the shapes of the structures and their resultant optical responses. Figure 18 shows such charge distributions for I-shape and Z-shape structures.

First, the images shown in the column denoted by 'shape' represent the distributions of charges at each unit, namely, charges associated with the elemental shape. The images in the column denoted by 'layout' show the distributions of charges at elemental shapes and their surroundings. We can extract positions at which induced electron charge densities exhibit a local maximum and a local minimum. Then, we can derive two kinds of vectors connecting the local maximum and local minimum, which we call flow vectors. One is a vector existing inside an elemental shape, denoted by dashed arrows, which is physically associated with an electric current induced in the metal. The other vector appears between individual elemental shapes, denoted by solid arrows, which is physically associated with near-fields between elemental shapes. We call the latter ones inter-elemental-shape flow vectors.

From those flow vectors, first, in the case of the I-shape structure, we note that:

(i) Within an elemental shape, the flow vectors are parallel to the *x*-axis. (There is no *y*-component in the vectors.)
(ii) At the layout level, flow vectors that have *y*-components appear. Also, flow vectors that have *y*-components are in opposite directions between neighboring elemental shapes.

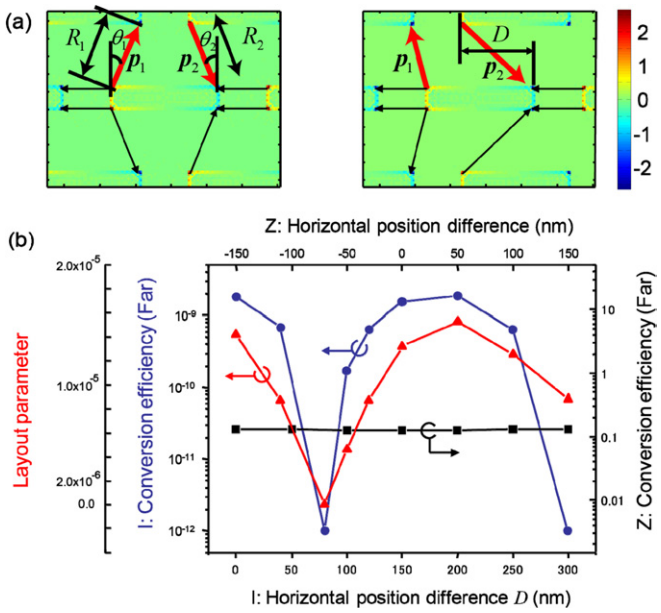

Figure 19. Dependence of polarization conversion efficiency on the layout. (*a*) Current distributions and inter-elemental-shape flow vectors for an I-shape structure when $D = 80$ nm (left) and $D = 200$ nm (right). (*b*) The I-shape structure exhibits stronger dependence on layout than the Z-shape structure does.

From these facts, the y-components of the flow vectors are arranged in a quadrupole manner, which agrees with the very small radiation in the far-field. Also, these suggest that the appearance of y-components in the flow vectors originates from the layout factor, not from the elemental shape factor. This indicates that the polarization conversion capability of the I-shape structure is layout-sensitive, which will be explored in more detail later.

Second, in the case of the Z-shape structure, we note that:

(i) In the elemental shape, y-components of the flow vectors appear.
(ii) In the layout, we can also find y-components in the flow vectors. Also, at the layout level, the y-components of all vectors are in the same direction.

In complete contrast to the I-shape structure, the Z-shape structure has y-components in the flow vectors arranged in a dipole-like manner, leading to strong y-polarized light in the far-field. Also, the ability to convert x-polarized input light to y-polarized output light in the far-field primarily originates from the elemental shape factor, not from the layout factor.

As indicated above, the polarization conversion from x-polarized input light to y-polarized output light with the I-shape structure originates from the layout factor. Here, we modify the layout while keeping the same elemental shape, and we evaluate the resulting conversion efficiencies.

In figure 19, we examine such layout dependences by changing the horizontal displacement of elemental shapes between two consecutive rows, indicated by the parameter D in figure 19(*a*). The far-field polarization conversion efficiency at the wavelength of 688 nm as a function of D is indicated by the circles in figure 19(*b*). Although it exhibits very small values for the I-shape structure, it has a large variance depending on the layout: a maximum value of around 10^{-9} when D is 200 nm, and a minimum value of around 10^{-12} when D is 80 nm, a difference of three orders of magnitude. On the other hand, the Z-shape structure exhibits an almost constant conversion efficiency with different horizontal positional differences, as indicated by the squares in figure 19(*b*), meaning that the Z-shape structure is weakly dependent on the layout factor.

To account for such a tendency, we represent the I-shape structure by two inter-elemental-shape flow vectors denoted by $\boldsymbol{p}_1$ and $\boldsymbol{p}_2$ in figure 19(*a*). Here, R_i and θ_i, respectively, denote the length of $\boldsymbol{p}_i$ and its angle relative to the y-axis. All of the inter-elemental-shape flow vectors are identical to those two vectors and their mirror symmetric vectors. Physically, a flow vector with a large length and a large inclination to the y-axis contributes weakly to the y-components of the radiation. Therefore, the term $\cos\theta_i/R_i^2$ will affect the radiation. Together with the quadrupole-like layout, we define the following metric

$$\left|\cos\theta_1/R_1^2 - \cos\theta_2/R_2^2\right|, \tag{17}$$

which is denoted by the triangles in figure 19(*b*); it agrees well with the conversion efficiency of the I-shape structure.

3.3. Hierarchical optical elements

3.3.1. Hierarchical hologram. Holography, which generates natural three-dimensional images, is one of the most common anti-counterfeiting techniques [129]. In the case of a volume hologram, the surface is ingeniously formed into microscopic periodic structures that diffract incident light in specific directions. A number of diffracted light beams can form an arbitrary three-dimensional image. Generally, these microscopic structures are recognized as being difficult to duplicate, and therefore holograms have been widely used in the anti-counterfeiting of bank notes, credit cards, etc. However, conventional anti-counterfeiting methods based on the physical appearance of holograms are nowadays not completely secure [130]. Nanophotonic solutions, utilizing light–matter interactions on the nanoscale, would provide higher anti-counterfeiting capability and would potentially enable other novel applications, such as artifact-metric systems [131].

A hierarchical hologram works in both optical far-fields and near-fields, the former being associated with conventional holographic images, and the latter being associated with the optical intensity distribution based on a nanometric structure that is accessible only via optical near-fields. In principle, a structural change occurring at the subwavelength scale does not affect the optical response function, which is dominated by propagating light. Therefore, the visual aspect of the hologram is not affected by such a small structural change on the surface. Additional data can thus be written by engineering structural changes in the subwavelength regime so that they are only accessible via optical near-field interactions without having any influence on the optical response obtained via the conventional far-field light. By applying this hierarchy, new functions can be added to conventional holograms.

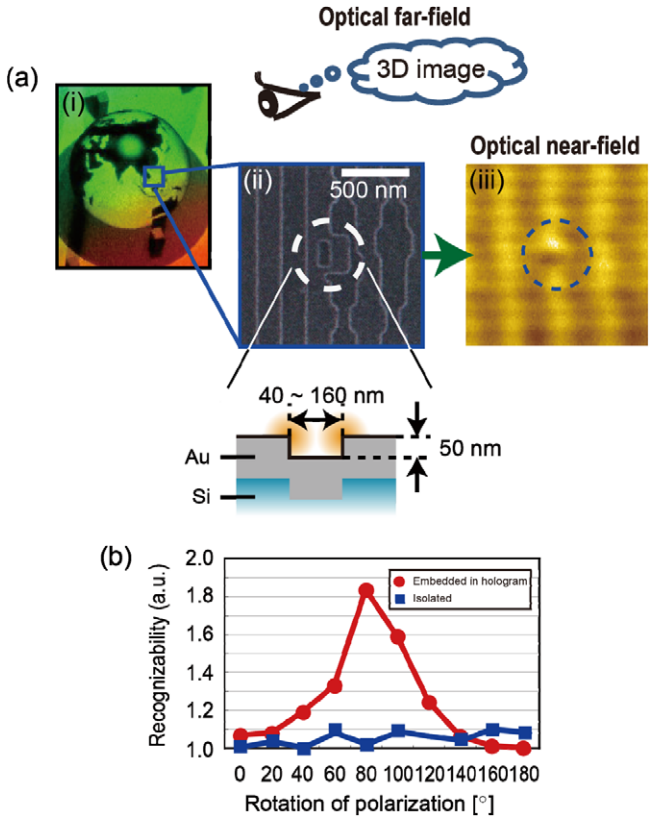

Figure 20. (*a*) Hierarchical hologram based on the different optical responses obtained in the optical far-field and the optical near-field. A nanostructure is embedded in the original grating structure of the hologram. (*b*) Evident polarization dependence in optical near-field results based on the surrounding structures.

There are at least two strategies for realizing a hierarchical hologram.

One strategy is to apply nanometric structural changes to the surface structure of a conventional hologram. In [47], a thin metal layer is coated on a conventional hologram and diffraction grating, followed by nanostructure patterning by a focused ion-beam machine. Additional information corresponding to the fabricated nanostructures is successfully retrieved while preserving the macroscopic view of the original hologram or the diffraction efficiency of the diffraction grating.

The other strategy, employed in the case of embossed holograms composed of diffraction gratings, is to locally engineer the original hologram pattern from the beginning, that is, to embed nanostructures *within* the original pattern of the hologram [27]. In this case, since the original hologram is basically composed of one-dimensional grating structures, evident polarization dependence is obtained in retrieving the nanostructures via optical near-fields, as detailed below. There are some additional benefits with this approach: One is that we can fully utilize the existing industrial facilities and fabrication technologies that have been developed for conventional holograms, yet providing additional information in the hologram. Another is that the polarization dependence facilitates the readout of nanostructures via optical near-fields, as mentioned below.

As shown in figure 20(*a*), we created a sample device to experimentally demonstrate retrieval of the nanostructures embedded within an embossed hologram. The entire device structure, whose size was 15 mm × 0 mm, was fabricated by EB lithography on a Si substrate, followed by sputtering a 50 nm thick Au layer.

As indicated in figure 20(*a*,i), we can observe a three-dimensional image of the Earth reconstructed from the device. More specifically, the device was based on the design of *Virtuagram*®, developed by Dai Nippon Printing Co. Ltd., Japan, which is a high-definition computer-generated hologram composed of binary-level one-dimensional modulated gratings, as shown in the SEM image in figure 20(*a*,ii). Within the device, we slightly modified the shape of the original structure of the hologram so that the nanostructural change was accessible only via optical near-field interactions. Square- or rectangle-shaped structures, whose associated optical near-fields correspond to the additional, or hidden, information, were embedded in the original hologram structures. The unit size of the nanostructures ranged from 40 to 160 nm. Note that the original hologram was composed of arrays of one-dimensional grid structures, spanning along the vertical direction in figure 20(*a*,ii). To embed the nanophotonic codes, the grid structures were partially modified in order to implement the nanophotonic codes. Nevertheless, the grid structures remained topologically continuously connected along the vertical direction. On the other hand, the nanostructures were always isolated from the original grid structures. These geometrical characteristics provide interesting polarization dependence.

The input light induces oscillating surface charge distributions due to the coupling between the light and electrons in the metal. Note that the original 1D grid structures span along the vertical direction. The y-polarized input light induces surface charges along the vertical grids. Since the grid structure continuously exists along the y-direction, there is no chance for the charges to be concentrated. However, in the area of the embedded nanophotonic code, we can find structural discontinuity in the grid; this results in higher charge concentrations at the edges of the embedded nanostructure. On the other hand, the x-polarized input light sees structural discontinuity along the horizontal direction due to the vertical grid structures, as well as in the areas of the embedded nanostructures. It turns out that charge concentration occurs not only in the edges of the embedded nanostructures but also at other horizontal edges of the environmental grid structures. When square-shaped nanophotonic codes are *isolated* in a uniform plane, both x- and y-polarized input light have equal effects on the nanostructures. These mechanisms indicate that the nanostructures embedded in holograms could exploit these polarization dependences.

In the experimental demonstration, optical responses in near-mode observation were detected using a NSOM operated in an illumination-collection mode with an optical fiber tip having a radius of curvature of 5 nm. The observation distance between the tip of the probe and the sample device was set at less than 50 nm. The light source used was a laser diode (LD) with an operating wavelength of 785 nm, and scattered light was detected by a photomultiplier tube (PMT).

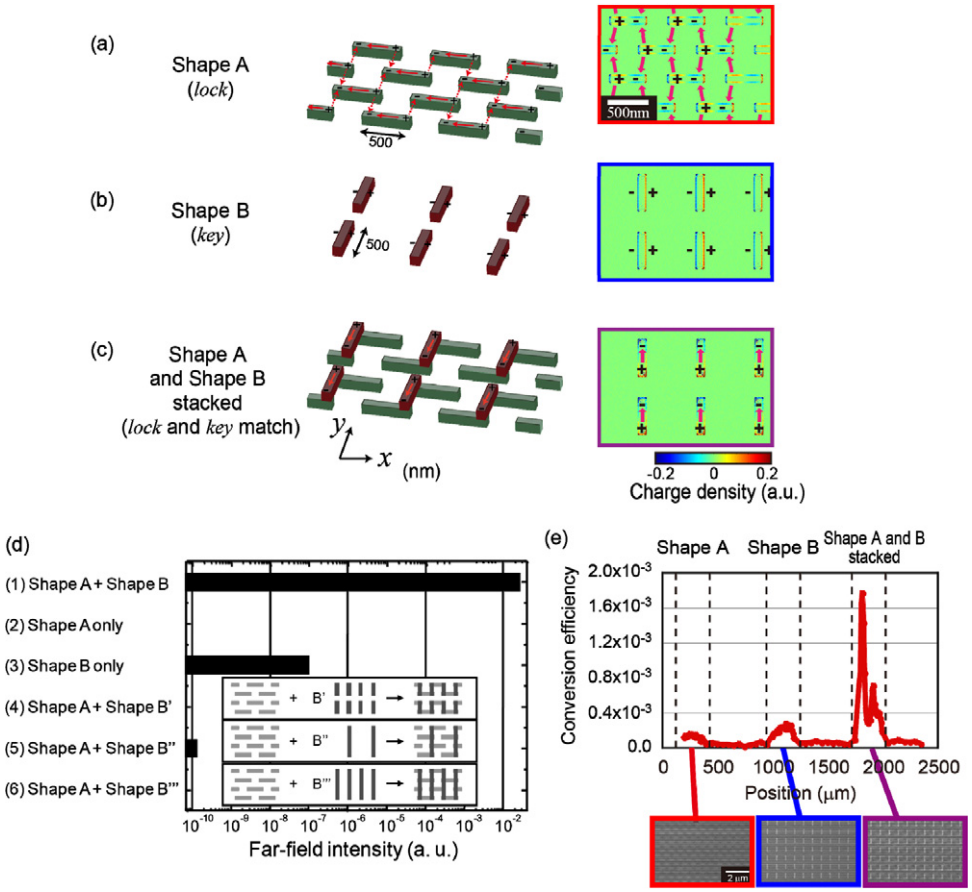

Figure 21. (*a*)–(*c*) Shapes and the associated distributions of induced charge density. (*a*) Shape A, (*b*) shape B and (*c*) the stacked structure of shapes A and B. (*d*) Comparison of calculated far-field intensity for various combinations of shapes. Far-field intensity appears strongly only when shape A matches the appropriate shape B. (*e*) Measured polarization conversion efficiency for three areas of the fabricated device. Conversion efficiency exhibited a larger value specifically in the areas where the stacked structure of shapes A and B was located. SEM images of each area are also shown.

We examined NSOM images in the vicinity of nanostructures that were embedded in the hologram and nanostructures that were not embedded in the hologram using light from a linearly polarized radiation source, with polarizations rotated by 0° to 180° at 20° intervals. In the case of nanostructures embedded in the hologram, clear polarization dependence was observed. To quantitatively evaluate the polarization dependence of the embedded nanophotonic code, we adopted a figure-of-merit (FoM) that we call *recognizability* for the observed NSOM images [27], indicating the relative intensity compared with the surroundings.

The square and circular marks in figure 20(*b*), respectively, show the recognizability of isolated nanostructures and those embedded in the hologram. Clear polarization dependence is observed in the case of the nanostructures embedded in the holograms, facilitating near-field information retrieval.

3.3.2. Lock-and-key. We take the concept of elemental shape and layout and their associated polarization discussed in section 3.2.1 and apply it to realize an application that we call a 'lock-and-key', meaning that access is granted only when a lock is matched with an appropriate key. More specifically, the lock and the key are, respectively, realized by two-dimensional planar nanostructures. The output signal, which is defined later below, appears only when a 'lock' structure matches its partner 'key' structure.

As an example, suppose that a lock is given the I-shape structure discussed in section 3.2.1, which we call 'shape A' hereafter. Recall that shape A exhibits very small far-field radiation in its y-component for x-polarized input light. Surface charges are concentrated at the horizontal edges of each of the rectangular units. The relative phase difference of the oscillating charges between the horizontal edges is π, which is schematically represented by the + and − marks in figure 21(*a*). Now, consider the y-component of the far-field radiation from shape A, which is associated with the charge distributions induced in the rectangle. When we draw arrows from the + marks to the − marks along the y-axis, we find that adjacent arrows are always directed oppositely, indicating that the y-component of the far-field radiation is externally small. In other words, shape A behaves as a quadrupole regarding the y-component of the far-field radiation. It should also be noted that near-field components exist in the vicinity of the units in shape A.

With this fact in mind, we put the other metal nanostructure, shape B, on top of shape A for the purpose of acting as the key for the lock. Through the optical near-fields in the vicinity of shape A, surface charges are induced

on shape B. What should be noted here is that the arrows connecting the + and − marks along the y-axis are now aligned in the same direction, and so the y-component of the far-field radiation appears; that is, the stacked structure of shape A and shape B behaves as a dipole (figure 21(c)). Also, shape A and shape B need to be closely located to invoke such effects since the optical near-field interactions between shape A and shape B are critical. In other words, far-field radiation appears only when shape A and shape B are correctly stacked; that is to say, a *quadrupole–dipole transform* is achieved through shape-engineered nanostructures and their associated optical near-field interactions.

In figure 21(d), the output signals are evaluated when differently shaped structures are, respectively, located on top of shape A, instead of shape B. With shape B′, shape B′′, and shape B′′′, which are, respectively, represented in the insets of figure 21(d), the output signals do not appear, as shown from the fourth to the sixth rows in figure 21(d), since the condition necessary for far-field radiation is not satisfied with those shapes; namely, the correct *key* is necessary to unlock the *lock* [132].

We fabricated structures consisting of (i) shape A only, (ii) shape B only, and (iii) shape A and shape B stacked. Although the stacked structure should ideally be provided by combining the individual single-layer structures, in the experiment described here, the stacked structure was integrated in a single sample as a solid two-layer structure to avoid the experimental difficulty in precisely aligning the individual structures mechanically. The fabrication process was detailed in [26]. The lower side in figure 21(e) also shows SEM images of fabricated samples of (i), (ii) and (iii). Because the stacked structure was fabricated as a single sample, the gap between shape A and shape B was fixed at 200 nm. The performance was evaluated in terms of the polarization conversion efficiency by radiating x-polarized light on each of the areas (i), (ii) and (iii) and measuring the intensity of the y-component in the transmitted light. The light source was a laser diode with an operating wavelength of 690 nm. Figure 21(e) shows the polarization conversion efficiency as a function of the position on the sample, where it exhibited a larger value specifically in the areas where the stacked structure of shapes A and B was located, which agrees well with the theoretically predicted and calculated results shown in figure 21(d).

3.4. Information-theory analysis of hierarchy in nanophotonics

This section presents an information-theory approach to hierarchical nanophotonic systems [133]. As mentioned briefly in the introduction, information-theory analysis [134] is well established, for example, in assessing and improving the performance figures of optical communications [135]. Information-theory analysis also sheds light on the behavior of a wide range of optical devices and systems [136, 137]. The application of information-theory methods to nanotechnology is found, for instance, in molecular communications based on material transfer [138] and in molecular biology [139].

As already discussed in section 3.1.3, hierarchical nanophotonic systems have been assessed by angular spectrum analysis of optical near-fields. From an information-based standpoint, the hierarchical nanophotonic system is modeled as a communication medium that connects input and output symbols and also suffers from environmental disturbances, as schematically shown in figure 22(a). Concrete applications represented by such a model will include, for instance, optical storage systems where the input and output, respectively, correspond to write and retrieve processes. Here, at each level of the hierarchy, we formulate mutual information that quantitatively reveals the relation between the physics associated with the hierarchy in optical near-fields, as well as possible environmental disturbances affecting the system locally or globally, and the capabilities of the system for information processing and communications. In other words, our aim here is to understand the hierarchical structure of nanophotonic systems from a cross-cutting standpoint, including their electromagnetic, logical and information-theory aspects.

As discussed in section 3.1.3, one of the two first-layer signals, the electric field at $F^{(1)}$, primarily depends on the dipole pair $\boldsymbol{d}^{(1)}$ and $\boldsymbol{d}^{(2)}$, and the other, the electric field at $F^{(2)}$, is dominated by the dipole pair $\boldsymbol{d}^{(3)}$ and $\boldsymbol{d}^{(4)}$. The second-layer signal is determined by the two pairs of dipoles. These dependence structures are schematically shown in figure 22(b). With such a hierarchical mechanism, a total of eight different signal combinations, or symbols, can be achieved by appropriately orienting the four dipoles [120], as summarized in figure 22(c), where the eight symbols are denoted by $a_i (i = 0, \ldots, 7)$, each of which refers to a three-bit sequence whose first element represents the digit obtained at the second layer (S), and whose second and third elements refer to the digits obtained at the first layer ($F^{(1)}$ and $F^{(2)}$). Corresponding dipole orientations are also indicated in the right-hand side of figure 22(b).

The input and output signals are, as introduced already, three-bit sequences; a total of eight symbols for the input and output symbols are, respectively, denoted by $A = \{a_i\}$ and $B = \{b_i\}$, where $i = 0, \ldots, 7$. The output symbol b_i should represent the same three-bit sequence given by the input symbol a_i if there is no error from the input to the output. The probability of the input symbol a_i is given by $P(a_i)$. The probability of the output symbol b_i, given by $P(b_i)$, depends on the input symbol probability $P(a_i)$, and the transition matrix T that represents the relation between the input and output and is given by

$$\begin{pmatrix} P(b_0) \\ \vdots \\ P(b_7) \end{pmatrix} = T \begin{pmatrix} P(a_0) \\ \vdots \\ P(a_7) \end{pmatrix}, \tag{18}$$

where the elements of T are given by $t_{ij} = P(b_i|a_j)$, which is the probability of the output b_i conditioned on the input a_j.

The matrix T is affected by environmental disturbances. We will introduce two representative disturbance models for the analysis. The first is the case where the environmental disturbance has an explicit spatial structure, or what we call a *near-field* disturbance. The second is the case where the disturbance selectively couples to the dipole arrangement, or what we call a *far-field* disturbance. Here, in considering

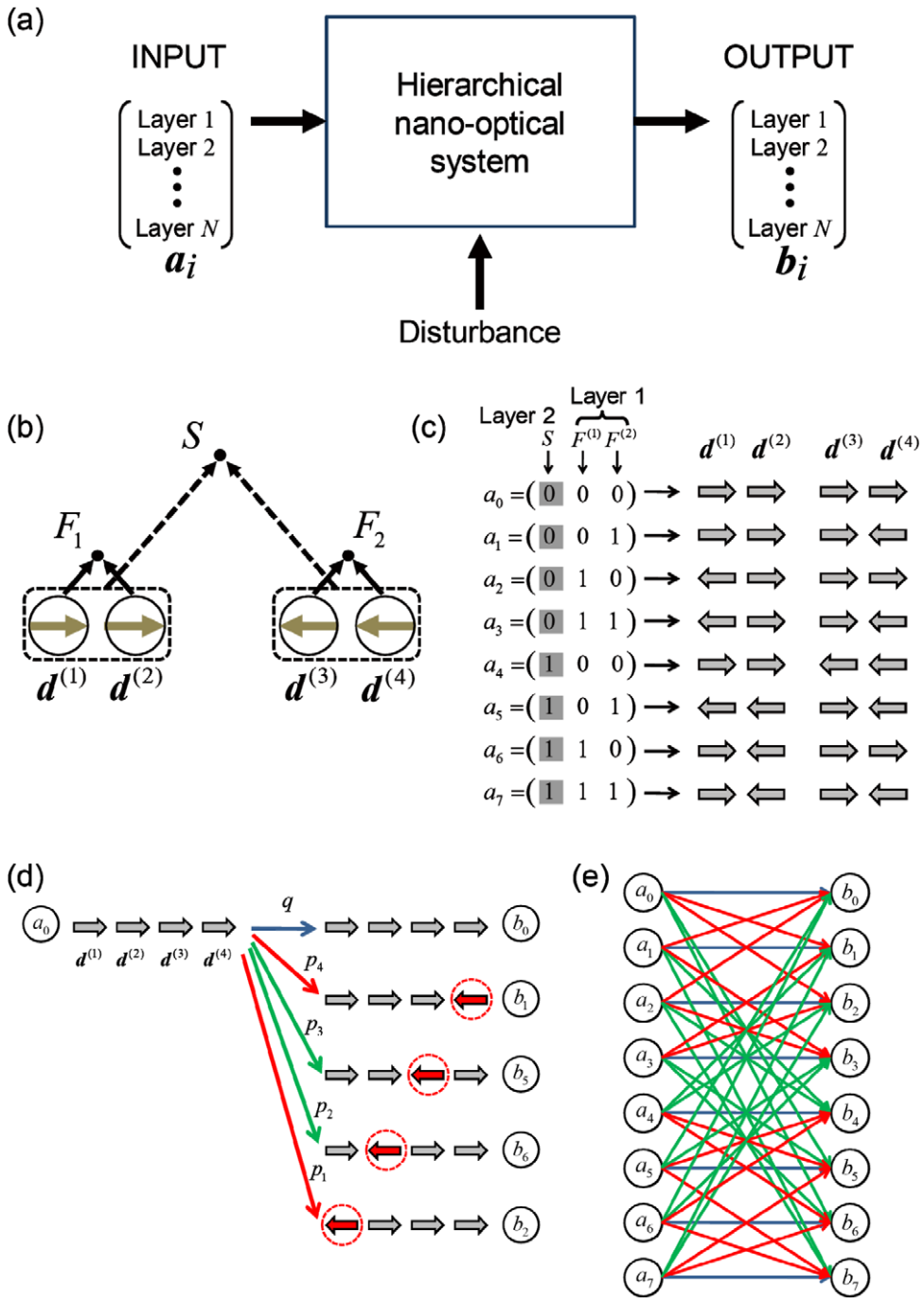

Figure 22. (*a*) A system diagram for studying information-theory aspects of hierarchical nano-optical systems. (*b*) Dependence structure between the dipole pairs and the logical levels in the first layer (F_1 and F_2) and the second layer (S). (*c*) List of a total of eight bit sequences, or symbols, and their corresponding dipole arrangements. (*d*) Model of an environmental disturbance that locally affects each of the dipoles. The phase of dipole $\boldsymbol{d}^{(i)}$ can be flipped with probability p_i. (*e*) The relation between the input symbols a_i and the output ones b_j.

the interactions between the disturbance and the system under study, we take into account the optical selection rule that the far-field optical radiation cannot be coupled to energy levels specified by even quantum number(s), or quadrupole(s).

Near-field disturbance. We assume an environmental disturbance that modifies the status of each spatial position in the system locally. In other words, here we assume a *near-field* environmental disturbance that locally disturbs the polarizations of each of the dipoles. Suppose that the phase of at most one of the four dipoles could be flipped, that is, changed by 180°. Let the probability of such a phase flip occurring for the dipole $\boldsymbol{d}^{(i)}$ be given by p_i. In the case of input symbol a_0, for example, whose corresponding four dipoles are all in-phase, as shown in figure 22(*d*), the phase of the first dipole $\boldsymbol{d}^{(1)}$ is flipped, which yields output symbol b_2 with probability p_1. When the second dipole $\boldsymbol{d}^{(2)}$ is flipped, the resulting output symbol is b_6. The error-free probability is given by $q = 1 - \sum_{i=1}^{4} p_i$. All transitions from input symbols to output ones are derived as schematically represented in figure 22(*e*),

where possible changes from an input to an output symbol are indicated by arrows.

It is technically possible to further generalize the effects of disturbances in this model, such as arbitrary phase flips occurring in the dipoles. However, this leads to an unnecessarily complex situation and makes it hard to understand how the local change in the system affects the information capacity. As a first step, simple position-dependent errors clearly reveal the relation between the physical consequences and their impact on layer-dependent information-theory measures, which is the primary concern of this section.

The mutual information $I(A;B)$ represents the quantity of the data transmitted through the system, which is equal to the amount of remaining uncertainty of data A on condition that the output B is measured, namely, $I(A;B) = H(A) - H(A|B)$, where $H(A)$ is the entropy of the input and $H(A|B)$ is the entropy of the input conditioned on the output. It is calculated by

$$I(A;B) = \sum_{i=0}^{N-1}\sum_{j=0}^{N-1} P(a_i, b_j)\log_2 \frac{P(a_i, b_j)}{P(a_i)P(b_j)}, \tag{19}$$

where the joint probability of input a_i and output b_j is given by $P(a_i, b_j) = t_{j,i}P(a_i)$ [32]. N indicates the number of symbols.

We further introduce a representative spatial structure of environmental disturbances so that the error probabilities affecting dipoles located at the edge and the center are different; that is, the error probability for the dipoles $\boldsymbol{d}^{(1)}$ and $\boldsymbol{d}^{(4)}$ is given by p_{E}, namely $p_1 = p_4 = p_{\mathrm{E}}$, whereas that for $\boldsymbol{d}^{(2)}$ and $\boldsymbol{d}^{(3)}$ is given by $p_{\mathrm{C}} = p_2 = p_3$. The error-free probability is given by $q = 1 - 2p_{\mathrm{E}} - 2p_{\mathrm{C}}$. As described in section 3.1.3, the four-dipole model is intended to represent the mixture of the coarse-scale structure and the fine-scale structure. In the present model, the two center dipoles dominate the second-layer information, meaning that those two play the major role in coarser scale structures. Therefore, the position-dependent errors denoted by p_{C} and p_{E} are physically associated with errors occurring in coarse-scale structures and in the fine-scale structures, respectively. If those dipoles with designated orientations are implemented by means of shape-engineered nanostructures, the error would physically correspond to fabrication errors occurring at either coarser or finer scales.

Now, we assume that the input symbol probability is uniform; that is, $P(a_i) = 1/8 (i = 0, \ldots, 7)$. The mutual information is evaluated as a function of p_{E} and p_{C}. For example, $p_{\mathrm{E}} = 9/100$ and $p_{\mathrm{C}} = 1/100$ yields 1.92 bits of mutual information.

We analyze the mutual information regarding each of the layers separately to see how the spatial structure of the local system disturbance affects the transmission capability for each of the layers. Let the input symbols for the left-hand side of the first layer be $f_0^{(1)}$ and $f_1^{(1)}$, which, respectively, mean logical 0 and 1. Since $f_0^{(1)}$ and $f_1^{(1)}$are, respectively, equivalent to the input symbol of either one of $F_0^{(1)} = \{a_0, a_1, a_4, a_5\}$ and $F_1^{(1)} = \{a_2, a_3, a_6, a_7\}$, the probability of input symbol $f_i^{(1)}$ is given by

$$P(f_i^{(1)}) = \sum_{a_j \in F_i^{(1)}} P(a_j). \tag{20}$$

Likewise, we denote the output symbols as $g_0^{(1)}$ and $g_1^{(1)}$, which are equivalent to either of the output symbols $G_0^{(1)} = \{b_0, b_1, b_4, b_5\}$ and $G_1^{(1)} = \{b_2, b_3, b_6, b_7\}$, respectively. The joint probability of inputs $f_i^{(1)}$ and $g_j^{(1)}$ is then derived as

$$P(f_i^{(1)}, g_j^{(1)}) = \sum_{a_s \in F_i^{(1)}}\sum_{b_t \in G_j^{(1)}} P(b_t|a_s)P(a_s), \tag{21}$$

which leads to mutual information for the left-hand bit of the first layer, given by

$$I_{F^{(1)}}(A;B) = \sum_{i=0}^{1}\sum_{j=0}^{1} P(f_i^{(1)}, g_j^{(1)})\log_2 \frac{P(f_i^{(1)}, g_j^{(1)})}{P(f_i^{(1)})P(g_j^{(1)})}. \tag{22}$$

Secondly, let the symbols of the second layer be s_0 and s_1. The symbols s_0 and s_1, respectively, correspond to either one of the input symbols $S_0 = \{a_0, a_1, a_2, a_3\}$ and $S_1 = \{a_4, a_5, a_6, a_7\}$. Similarly, the corresponding output symbols are defined by t_0 and t_1. The mutual information for the second layer is given by

$$I_S(A;B) = \sum_{i=0}^{1}\sum_{j=0}^{1} P(s_i, t_j)\log_2 \frac{P(s_i, t_j)}{P(s_i)P(t_j)}. \tag{23}$$

Here we quantitatively compare the mutual information given by equations (22) and (23) assuming the same error probabilities. With fewer errors in the center and more errors at the periphery, for instance $p_{\mathrm{C}} = 1/100$ and $p_{\mathrm{E}} = 9/100$, $I_{F^{(1)}}(A;B)$ yields 0.53 bit, whereas $I_S(A;B)$ yields 0.86 bit, indicating that the second layer has a larger information transmission efficiency than the first layer. On the other hand, with more errors in the center and fewer errors at the periphery, for instance $p_{\mathrm{C}} = 9/100$ and $p_{\mathrm{E}} = 1/100$, $I_{F^{(1)}}(A;B)$ yields 0.53 bit, whereas $I_S(A;B)$ yields 0.32 bit, showing that the quantity of information for the first layer is unchanged, whereas that for the second layer is severely degraded. With the condition that the error-free probability be kept constant at 0.8, $I_{F^{(1)}}(A;B)$ and $I_S(A;B)$ are, respectively, shown by the dashed line A and the solid line B as functions of p_{C} in figure 23, where $I_{F^{(1)}}(A;B)$ stays constant, whereas $I_S(A;B)$ takes larger values as p_{C} gets smaller. This is due to the fact that the second-layer information depends on the two center dipoles. On the other hand, the left-hand bit at the first layer depends on both $\boldsymbol{d}^{(1)}$ and $\boldsymbol{d}^{(2)}$; therefore, $I_{F^{(1)}}(A;B)$ yields a constant value as long as $p_1 + p_2$ is constant.

Far-field disturbance. We consider another type of environmental disturbance involving *far-field* radiation applied to nanoscale optical systems. Here, the optical selection rule that the far-field optical radiation cannot be coupled to energy levels specified by even quantum number(s) or quadrupole(s) [17, 140] should be taken into account in considering the interactions between the disturbance and the system under study.

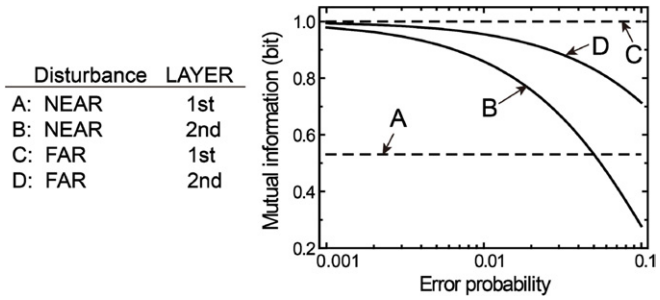

Figure 23. Scale-dependent mutual information. Mutual information $I(A;B)$ at the first layer and the second layer is evaluated for two types of disturbances.

The physical model consisting of multiple dipoles is, in fact, not directly compatible with such quantum optical properties. However, we consider that the following assumptions approximately describe their principal characteristics in order to understand their impact on information-theory measures. They are:

(i) When the phases of $\boldsymbol{d}^{(1)}$ and $\boldsymbol{d}^{(2)}$ are the same, both phases can be flipped with probability p. Similarly, when the phases of $\boldsymbol{d}^{(3)}$ and $\boldsymbol{d}^{(4)}$ are the same, they can be flipped with probability p. The error-free probability is given by $q = 1 - p$.

(ii) When all of the dipoles have the same phase, they can be flipped with probability p. The error-free probability is given by $q = 1 - p$.

(iii) When the combinations of [$\boldsymbol{d}^{(1)}$ and $\boldsymbol{d}^{(2)}$] and/or [$\boldsymbol{d}^{(3)}$ and $\boldsymbol{d}^{(4)}$] have opposite phases, we assume that the far-field radiation serving as the system disturbance cannot be coupled to the dipoles, and so no phase flips occur.

For instance, for the case of input symbol a_0, all of the dipoles are arranged in the same directions, and they can all be coupled to the environmental disturbance; that is, item (ii) above will apply. However, from a logical point of view, flipping all of the dipoles does not affect the information of any bits to be retrieved at the output. In other words, the input symbol a_0 is always connected to output symbol b_0. For the case of input symbol a_1, $\boldsymbol{d}^{(1)}$ and $\boldsymbol{d}^{(2)}$ are in dipole arrangement, whereas $\boldsymbol{d}^{(3)}$ and $\boldsymbol{d}^{(4)}$ are in quadrupole arrangement. The dipoles $\boldsymbol{d}^{(1)}$ and $\boldsymbol{d}^{(2)}$ can be flipped with probability p, which results in the output symbol b_5.

The mutual information for the first layer and the second layer are, respectively, evaluated following equations (21) and (22). As indicated by the dashed line C in figure 23, the mutual information for the first layer $I_{F^{(1)}}(A;B)$ is always 1, indicating that the system is completely resistant to the disturbances in the first layer. This is due to the fact that the environmental disturbance transforms the input symbols $F_0^{(1)} = \{a_0, a_1, a_4, a_5\}$ into the output symbols $G_0^{(1)}$, and the input symbols $F_1^{(1)} = \{a_2, a_3, a_6, a_7\}$ into the output symbols $G_1^{(1)}$, where the left-hand bit at the first layer remains the same. On the other hand, the mutual information for the second layer $I_S(A;B)$ decreases as the error probability increases, as shown in the solid curve in figure 23. Since the second-layer signal depends on the pairs of dipoles, it could be disturbed in situations where the left- and the right-hand dipole pairs are a combination of a dipole arrangement and a quadrupole one.

The mutual information for the entire system can be improved by biasing the input symbol probability distribution, whose maximum is defined as the channel capacity, given by $C = \max_{p(a_i)} I(A;B)$. With the error probability $p = 2/10$, the maximum mutual information, i.e., the channel capacity, is 2.68 bit when the probability distribution is given by $P(a_0) = P(a_3) = P(a_4) = P(a_7) = 0.16$, $P(a_1) = P(a_2) = P(a_5) = P(a_6) = 0.09$, which is obtained by a full search in the parameter space. On the other hand, the mutual information with a uniform input symbol distribution $P(a_i) = 1/8$ $(i = 0, \ldots, 7)$ yields 2.64 bits. Although the increase of the channel capacity by changing the probability distribution is, in this particular case, just 0.04 bit, such a consideration may lead to design strategies that can fully utilize the capacity of such hierarchical systems.

4. Stochastic approach to nanophotonics

A stochastic understanding of physical phenomena is important in physics in general [40] and should provide fundamental insights and enable interesting novel applications for nanophotonics too. This section reviews two topics regarding a stochastic approach to nanophotonics: one is stochastic modeling of material formation involving optical near-field processes (section 4.1), and the other is stochastic computing, or more specifically solution searching, by exploiting the unique stochastic spatio-temporal dynamics inherent in nanophotonics (section 4.2).

4.1. Stochastic processes in light-assisted nanomaterial formation

Precision control of the geometrical features of materials on the nanometer scale, such as their sizes and positions, are important factors in obtaining the intended functionalities of nanophotonic devices and systems in which multiple nanostructures interact via optical near-fields [16], and also for plasmonic devices [141]. For example, the sizes of QDs should be well-controlled to ensure that the quantized energy levels between adjacent QDs are resonant, to facilitate efficient optical near-field interactions, as discussed in section 2.2.1 [35]. Arrays of nanoparticles are important in various applications, such as nanophotonic devices [16], optical far-field to near-field converters [89] and plasmonic light transmission lines [142].

To satisfy such requirements, light-assisted, self-organized nanostructure fabrication principles and techniques have been developed [49, 50]. One example is the sol–gel synthesis of ZnO quantum dots (QDs) using photo-induced desorption, which yields reduced fluctuations in QD diameter [49]. Another example of light-assisted nanostructure fabrication is metal sputtering with light irradiation which produces self-organized, size- and position-controlled metal nanoparticle chains [50]. In addition to the superior ability in regulating the geometries of nanostructures, these light-assisted, self-organized fabrication techniques are relatively simple in their experimental setups and have superior

production throughput compared with, for instance, scanning-based methods, such as those based on electron beams [143] or scanning probes [144].

The physical mechanisms behind light-assisted nanostructure formation have been attributed to material desorption [49, 145, 146] or plasmon resonance between light and matter. However, stochastic physical processes are also present, as observed in the experimental data discussed below. Also, we consider that a stochastic approach is indispensable to take account of the emergence of ordered structures and the wide range of phenomena observed on the nanoscale in general [147, 148]. For example, Söderlund *et al* demonstrated log-normal size distributions in particle growth processes with a simple statistical model [147], and Kish *et al* demonstrated the log-normal distribution of single-molecule fluorescence bursts in micro- and nano-fluidic channels based on a stochastic analysis [148]. Also, a study [149] of the stochastically driven growth of self-organized structures indicates that the spatio-temporal distribution functions have a key role in controlling the shape and width of size distributions within the formations. Cutting the log tails of such distribution functions can contribute to narrower size distributions.

In light of this background, we approach light-assisted nanofabrication from a stochastic standpoint. Taking account of light-assisted processes, we build stochastic models that reproduce tendencies consistent with experimental observations. Through such considerations, we obtain critical insights into order formation on the nanometer scale, which will contribute to the design of nanophotonic devices and systems.

4.1.1. Light-assisted size-regulation of nanoparticles. First, we characterize the light-assisted, self-organized ZnO quantum dot formation, which was experimentally demonstrated in [49], with a stochastic approach. We first briefly review the experimental observations. In making ZnO QDs, synthetic methods using liquid solutions are advantageous because of their need for simple facilities and their high productivity [150] compared with other techniques [151, 152]. In conventional sol–gel methods [150], however, the size of the QDs fluctuates by as much as 25%. Liu *et al* demonstrated a light-assisted sol–gel method that reduced the QD diameter fluctuations [49]. When light with a photon energy higher than the bandgap energy is radiated during the ZnO QD formation process, electron–hole pairs could trigger an oxidation–reduction reaction in the QDs, causing the ZnO atoms depositing on the QD surface to be desorbed. In addition, such desorption is induced with a high probability when the formed QDs reach a particular diameter. This light-dependent QD size regulation has also been reported in other material systems, such as CdSe [145] and Si [146].

The insets in figures 24(*a*) and (*b*), respectively, show transmission electron microscope (TEM) images of fabricated ZnO QDs without and with CW light illumination at a wavelength of 325 nm with a power density of 8 mW cm^{-2} [49]. Figures 24(*a*) and (*b*), respectively, summarize the incidence rate of nanoparticles as a function of their diameter, whose fluctuations decreased from 23% to 18% with light irradiation. In particular, note that the diameter distributions are different between these two cases. Without light illumination (figure 24(*a*)), it exhibits behavior similar to a normal distribution. In contrast, with light irradiation, the distribution is skewed; in particular, the incidences at larger diameters decreased (figure 24(*b*)). We investigate this different behavior by means of stochastic modeling.

First, in the absence of light illumination, we represent the formation process with a statistical pile-up model, as schematically shown in figure 24(*e*). An elemental material that constitutes a nanoparticle is represented by a square-shaped block. Such blocks are grown, or stacked one on another, with a piling success probability p; accordingly, the piling fails with a probability of $1 - p$. In other words, if we let the height of the pile at step t be $s(t)$, the piling probability is given by

$$\begin{aligned} P\left[s(t+1) = s(t) + 1 | s(t)\right] &= p, \\ P\left[s(t+1) = s(t) | s(t)\right] &= 1 - p. \end{aligned} \tag{24}$$

Since this is equivalent to a random walk with drift, after repeating this process with an initial condition $s(0) = 0$, the resultant heights of the piles exhibit a normal distribution, as shown in figure 24(*c*). Specifically, the statistics shown in figure 24(*c*) were obtained by repeating 10 000 steps for 100 000 different trials.

On the other hand, we model the effect of light irradiation in the formation process in the stochastic model as follows. As described above, since the material desorption is likely to be induced at a particular nanoparticle diameter, we consider that the piling success rate p is a function of the diameter, namely the height of the pile. For simplicity, we consider that p, which represents the deposition success probability, decreases linearly beyond a certain total pile height, as schematically shown in figure 24(*f*). In other words, the material desorption is more likely to be induced beyond a certain pile size due to the resonant effect mentioned above. That is, the probability p in equation (22) is replaced with the following size-dependent probability:

$$p(s(t)) = \begin{cases} c & s(t) \leqslant R, \\ c - \alpha s(t) & s(t) > R, \end{cases} \tag{25}$$

where c and α are constants. With such a stochastic model, the resultant incidence distributions of the piles is skewed or reduced at larger sizes. In the calculated results shown in figure 24(*d*), we assume $c = 1/2$ and $\alpha = 1/250$. The numerical results obtained through the statistical modeling are consistent with the experimental observations.

4.1.2. Light-assisted nanoparticle array formation. Yatsui *et al* demonstrated the self-organized formation of an ultralong array of nanoparticles based on near-field optical desorption (figures 25(*a*) and (*b*)) [50]. We first briefly describe the experimental observations. With conventional radio-frequency (RF) sputtering, aluminum was deposited on a glass substrate. A 100 nm wide and 30 nm deep groove was formed in the substrate, as schematically shown in figure 25(*c*). Also,

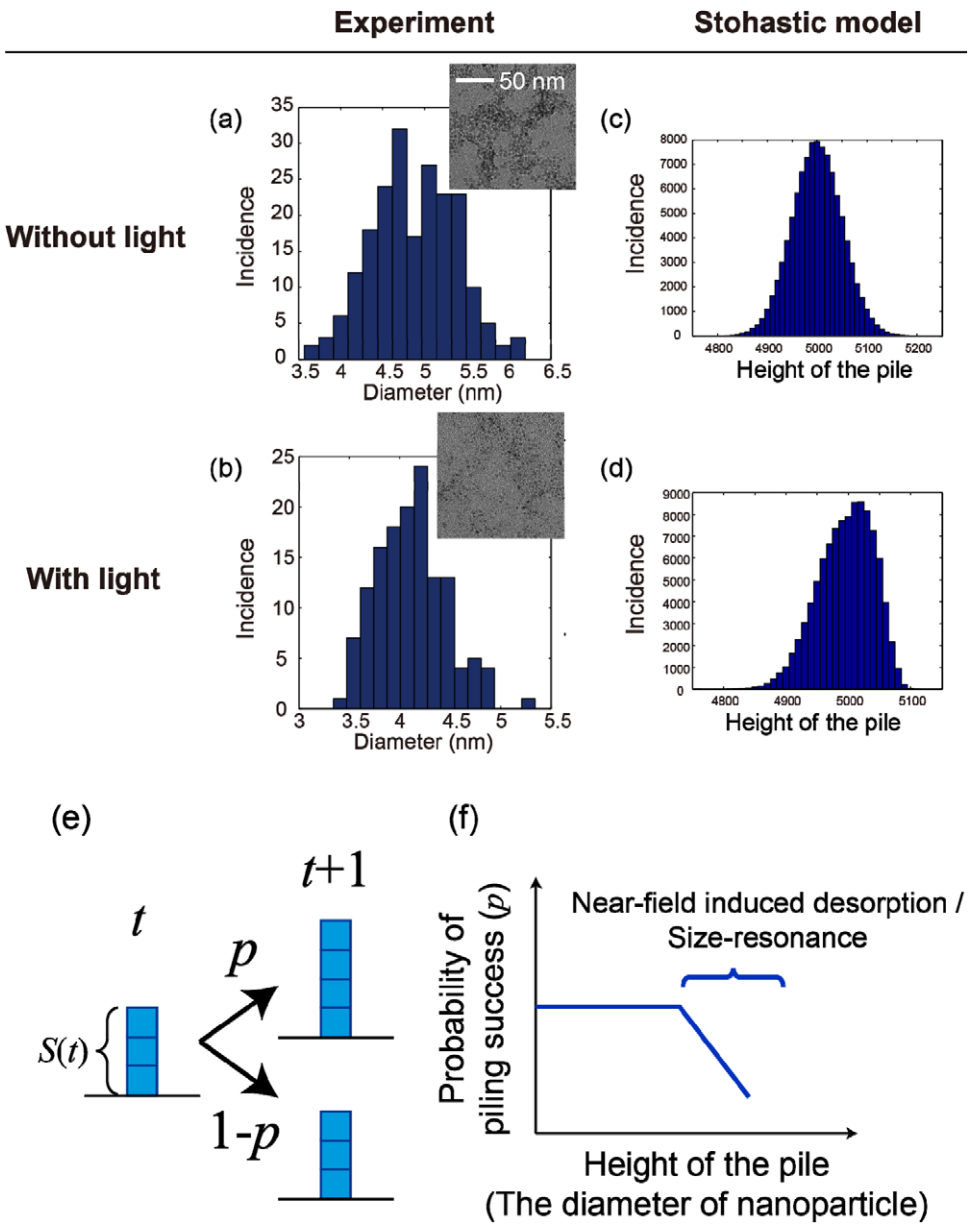

Figure 24. Incidence patterns of the diameters of fabricated ZnO quantum dots (QDs) formed by a sol–gel method (*a*) without light irradiation and (*b*) with light irradiation. Insets in (*a*) and (*b*) are transmission electron microscope images of QDs without and with light irradiation, respectively. (*c*),(*d*) Incidence patterns of the size distribution generated with the proposed stochastic model. The patterns are consistent with the experimental observations in (*a*) and (*b*). (*e*) A stochastic model of light-assisted nanoparticle formation. The growth of the QD is characterized with a one-dimensional pile-up model. The success of the piling depends on probability p. (*f*) The effect of light irradiation is modeled by a decrease in the probability p beyond a certain pile height, which corresponds to the diameter of the nanoparticle in the experiment.

the substrate was illuminated with light linearly polarized perpendicularly to the direction of the groove during the RF sputtering. Thanks to the well-defined edge of the groove, a strong optical near-field was generated in its vicinity.

A metallic nanoparticle has strong optical absorption because of plasmon resonance that depends strongly on the particle size [153–155]. This can induce desorption of a deposited metallic material when it reaches the resonant diameter [156, 157]. It turns out that as the deposition of the metallic material proceeds, the growth is governed by a tradeoff between deposition and desorption, which determines the particle diameter, depending on the photon energy of the incident light. Consequently, an array of metallic nanoparticles is aligned along the groove. While radiating CW light with a photon energy of 2.33 eV (wavelength: 532 nm) during the deposition of aluminum, 99.6 nm diameter, 27.9 nm separation nanoparticles were formed in a region as long as 100 μm, as shown in figure 25(*a*).

As described above, the origin of the size regulation of the nanoparticles was attributed to the resonance between the nanoparticles and the illuminated light, similarly to the case discussed in section 4.1.1. At the same time, we consider that although this physical mechanism indeed plays a crucial role, it is not enough to explain the formation of the uniformly

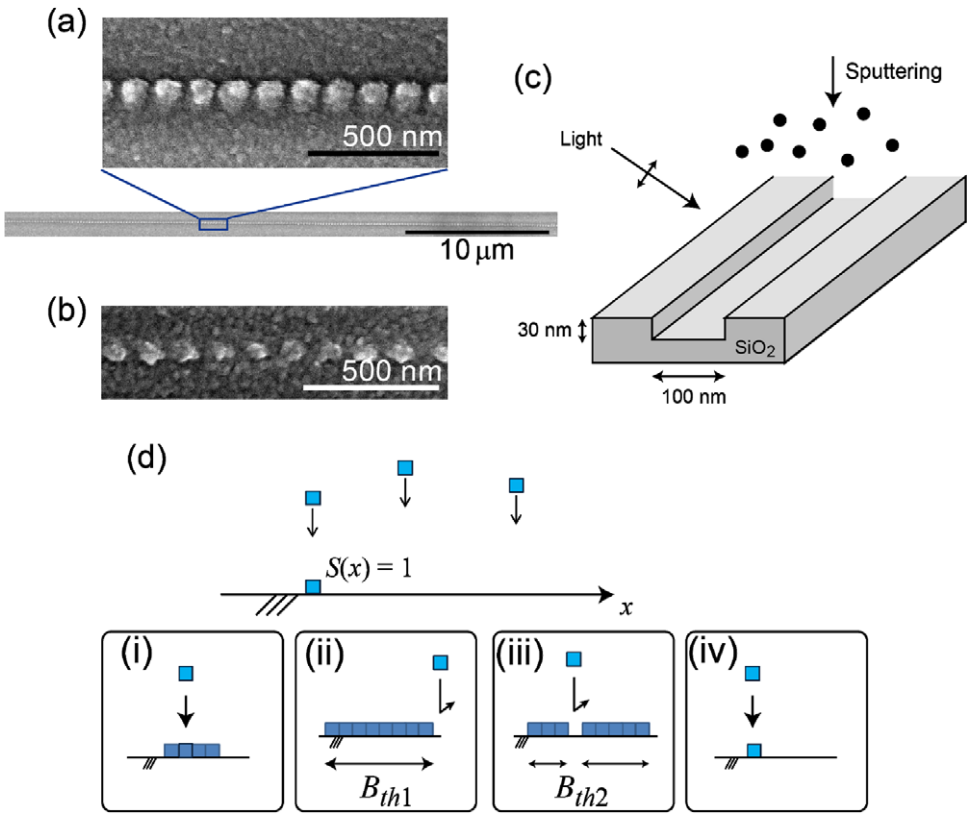

Figure 25. An array of uniform-diameter, uniform-separation Al nanoparticles is self-organized along a groove, with (*a*) 2.33 eV light irradiation and (*b*) 2.62 eV light irradiation. (*c*) Schematic diagram of the experimental setup of Al sputtering on a SiO_2 substrate in which a 100 nm wide, 30 nm deep groove is formed. During the sputtering, the substrate is irradiated with light having a polarization perpendicular to the direction of the groove. (*d*) A stochastic model of the nanoparticle array formation. A one-dimensional array in which an elemental block could be deposited at position x. (i)–(iv) Rules for successful deposition at a randomly chosen position x. (i) When the position belongs to one of the clusters, the cluster is maintained. (ii) Deposition is inhibited next to a cluster whose size is larger than B_{th1}. (iii) Deposition is inhibited at a position where the block sees clusters at both the left- and right-hand sides and when the total size of both clusters is larger than B_{th2}. (iv) In other cases, deposition at the position succeeds.

formed array structure. To explain such an observation, we need to extend the stochastic model described in section 4.1.1 as follows.

In the modeling, we assume a one-dimensional horizontal system that mimics the groove on the substrate; it consists of an array of N pixels identified by an index i ranging from 1 to N. An elemental material to be deposited onto the system, experimentally by the RF sputtering described above, is schematically represented by a square-shaped block (figure 25(*d*)). The initial condition is a flat structure without any blocks.

At every iteration cycle, the position at which a block arrives, denoted by x, is randomly chosen. We determine the success of the deposition at x by the following rules. We denote the occupation by a block at position x of the groove by $S(x)$; $S(x) = 1$ when a block occupies a position x, and $S(x) = 0$ when there is no block at position x. Also, we use the term 'cluster' to mean multiple blocks consecutively located along the groove. We also call a single, isolated block in the system a 'cluster'.

(i) When the randomly chosen position x belongs to one of the cluster(s), namely, $S(x) = 1$, we maintain $S(x) = 1$ (figure 25(*d*,i)).

(ii) Even if $S(x) = 0$, when the chosen position x belongs to a 'neighbor' of a cluster with a size greater than a particular number B_{th1}, the deposition is inhibited. That is, we maintain $S(x) = 0$ (figure 25(*d*,ii)).

(iii) Even if $S(x) = 0$, when the chosen position x has blocks at both its left and right sides and the total number of connected blocks is greater than B_{th2}, the deposition is inhibited. That is, we maintain $S(x) = 0$ (figure 25(*d*,iii)).

(iv) In other cases, the deposition at position x succeeds; namely, $S(x) = 1$ (figure 25(*d*,iv)).

The rules (ii) and (iii) correspond to the physical effect of the resonance between the material and the light illumination that facilitates desorption of the particle. The optical near-field intensity in the vicinity of a nanostructure follows a Yukawa function which depends on the material size, as discussed in section 3.1.2. Therefore, the optical near-fields promote material desorption, or in effect, inhibit material deposition, beyond a certain size of nanoparticles, which is characterized as rule (ii) above. Also, even when a single cluster size is small, meaning that the corresponding near-fields are small, when several such clusters are located in close proximity, a material desorption effect should be induced overall. Such an effect is represented as rule (iii) above. One remark here is

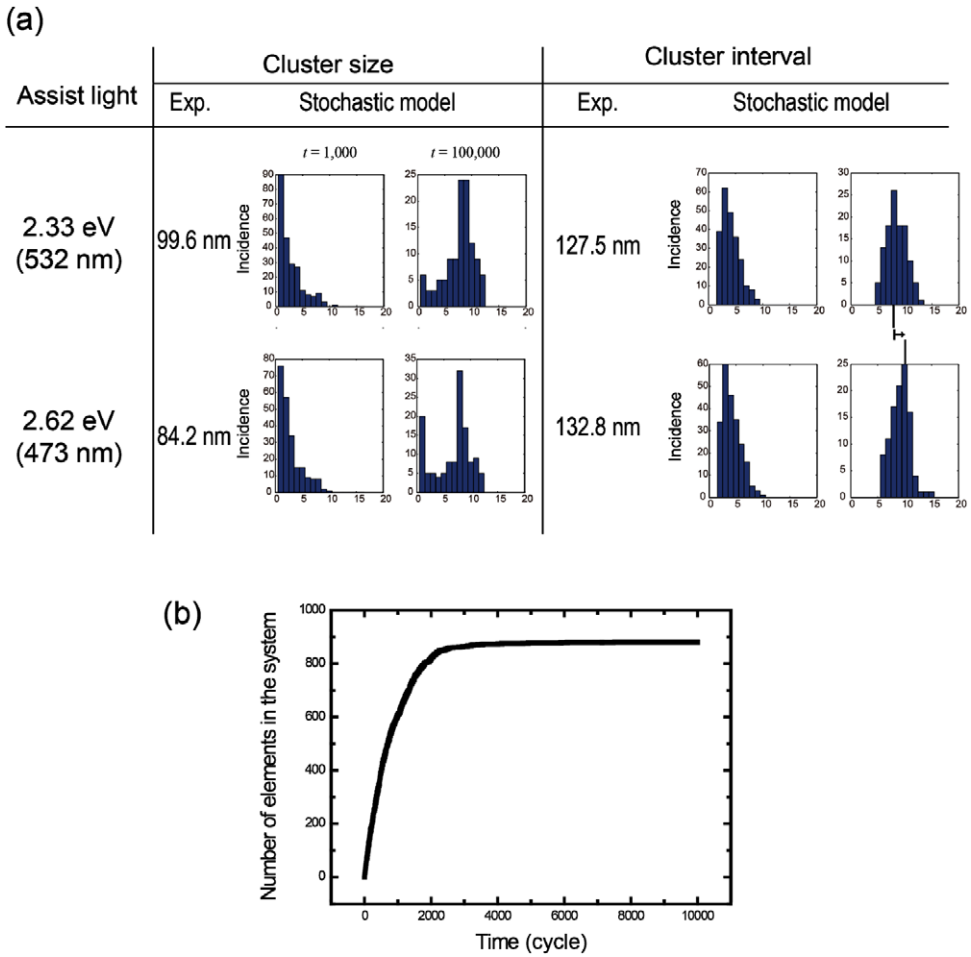

Figure 26. (*a*) Evolution of the cluster size and the cluster interval based on a stochastic model. Both the size and the interval converged to incidence patterns that exhibited maxima at a particular value, which reproduced the experimentally observed size- and separation-controlled formation of a nanoparticle array. The interval of the nanoparticles is greater with higher photon energy. By modifying rule (ii) of the stochastic model, the cluster interval increases, which is consistent with the experimental observations. (*b*) Evolution of the number of elements in the stochastic model. After cycle $t = 3000$, the number of elements is stable, meaning that the system is getting into a steady state in a self-organized manner.

that we do not pile more than two blocks at a single position x; that is to say, $S(x)$ takes binary values only, since our concern is how the clusters are formed in the 1D system.

Figure 26(*a*) shows the results of a numerical demonstration assuming a 1D array with $N = 1000$. As statistical values in the simulations, we evaluated the incidence of the cluster size and the center-to-center interval between two neighboring clusters. Figure 26(*a*) summarizes the evolution of these two values at $t = 1000$ and $t = 100\,000$. In the numerical calculations, for the threshold values in rules (ii) and (iii), we assumed $B_{\mathrm{th1}} = 8$ and $B_{\mathrm{th2}} = 12$, respectively. We clearly observed that the size and the interval converged to representative values, which is consistent with the experimental observations shown in figure 25(*a*). Furthermore, we evaluate the total number of elemental blocks contained in the system as a function of elapsed time in the stochastic simulation. As shown in figure 26(*c*) it converges to a constant value beyond around 3000 iteration cycles, which is another indication that a self-organized process emerges based on optical near-field processes. Since the present modeling includes some parameters, this does not strictly exhibit so-called self-organized criticality [41]. However, we consider that the convergence to a uniformly sized, uniformly separated 1D pattern is indeed a kind of self-organized critical phenomenon.

Moreover, as reported in [50], a similar experiment was conducted with a higher photon energy of 2.62 eV (473 nm) and an optical power of 100 mW, which resulted in the formation of 84.2 nm diameter, 48.6 nm separation nanoparticles (figure 25(*b*)). As summarized in the experimental results indicated in figure 26(*a*), the diameter is slightly reduced and the nanoparticle distance is enlarged compared with the previous case of lower photon energy (2.33 eV (532 nm)). The reduced diameter of the nanoparticles is attributed to the fact that the higher photon energy leads to desorption at smaller diameters [49, 153]. The larger separation between adjacent nanoparticles is, however, not obviously explained.

We presume that a stronger light–matter resonance is induced at a higher photon energy, which more strongly induces material desorption, or inhibits the deposition of materials, in the neighboring clusters. We can take account

of this effect by modifying the stochastic model described above. Instead of blocking the deposition at the neighboring positions by rule (ii), we consider that distant neighbors are also inhibited:

(ii′) Even if $S(x) = 0$, when x sees a cluster with a size greater than a particular number B_{th1}, within an area (a) between $x - 3$ and $x - 1$ or (b) between $x + 1$ and $x + 3$, the deposition is inhibited. That is, we maintain $S(x) = 0$.

While preserving B_{th1} and B_{th2} values with the previous example, the cluster size statistics evolve as shown in figure 26(*a*). At the iteration cycles $t = 1000$ and 100 000, the incidences of single-sized clusters are large. This is due to the strict inhibition rule (ii′) above, which reduces the chance of clusters growing. Treating such a single-sized cluster as an artifact, or a virtually ignorable element, in the system, we evaluate the cluster-to-cluster interval except for single-sized clusters. The cluster interval converges to a maximum of 10, as shown in figure 26(*a*), which is larger than the previous case, which converged to 8. This is consistent with the experimental observations. Finally, we make one remark about the dimensions of the models concerned in this paper. We consider that the 1D models described above characterize the physical principles behind the experimental demonstrations of ZnO QD formation and the Al nanoparticle array formation.

4.1.3. Light-assisted morphology formation. We previously reported in [21] that a unique granular Ag film was formed by depositing Ag particles on the electrode of a photovoltaic device composed of P3HT and ZnO under light illumination (wavelength $\lambda = 660$ nm) while reversely biasing the P3HT/ZnO p–n junction. The resultant device generated a photocurrent at wavelengths as long as 670 nm, which is longer than the long-wavelength cut-off ($\lambda_c = 570$ nm) of P3HT. In other words, light-assisted fabrication yields photosensitivity in a frequency regime where there is conventionally zero response. Such an effect is attributed to a phonon-assisted near-field process, as discussed in [21]. Similar phenomena have been observed in other material systems [19, 20].

One important concern is to investigate the relevance between the induced characters associated with the material after the light-assisted fabrication process and the resultant emergent optical properties. But before obtaining such crucial insights, here we address the character of the resultant morphology of the devices and elucidate the physical mechanism of the pattern formation in the first place. We analyzed the morphological character of Ag clusters, and in order to understand the principles behind the formation process, we constructed a stochastic model involving the geometrical character of the material, its associated optical near-fields, and the materials that flow in and out of the system.

The device structure is summarized as follows [21]. A schematic cross-section of the device structure is shown in figure 27(*a*). A P3HT layer about 50 nm thick was used as a p-type semiconductor material, and a ZnO film about 200 nm thick was used as an n-type semiconductor. P3HT is commonly used as a hole-conduction component [158]. In the experiment [21], photocurrent generation in a ZnO thin

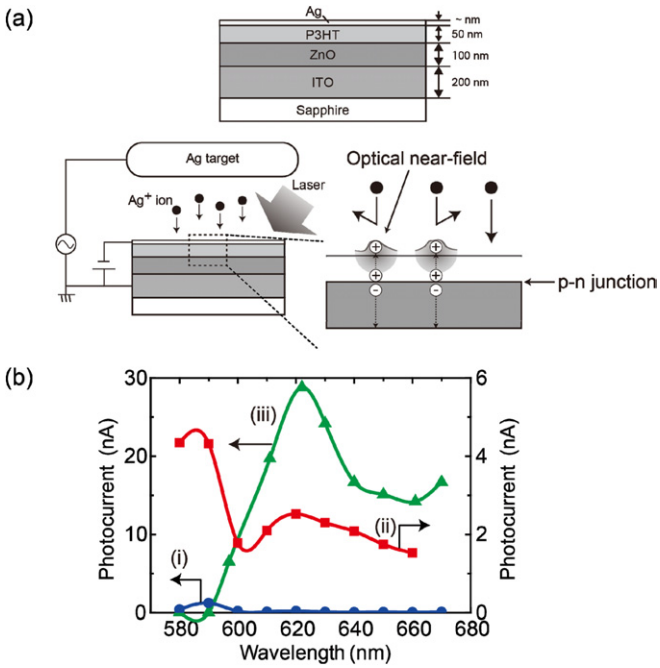

Figure 27. (*a*) (Top) cross-sectional structure of a photovoltaic device made of P3HT and ZnO sandwiched by Ag and ITO electrodes. (Bottom) a schematic diagram of the Ag sputtering process under laser light irradiation and application of a reverse-bias dc voltage. A close-up of the Ag deposition/repulsion at the surface due to the phonon-assisted optical near-field process. (*b*) Photocurrent generation in devices (i)–(iii) in a longer wavelength region, where the normal device, case (i), exhibited almost no sensitivity, whereas the other two showed evident photocurrent generation.

film was evaluated at wavelengths longer than the cut-off wavelength $\lambda_c = 570$ nm, which falls within the wavelength range where the ZnO thin film is transparent ($\lambda = 400$ nm). An ITO film about 200 nm thick and an Ag film a few nanometers thick were used as the two electrodes. In the previously reported experiment [21], thin films of these materials were deposited on a sapphire substrate in series. As a result, a multi-layered film with an area of 30 mm^2 was formed on the sapphire substrate. At the last stage of the fabrication process, Ag was deposited on the Ag thin film, which is the key process in differentiating the resultant performance in terms of photocurrent generation. Figure 27(*a*) schematically illustrate the experimental setup used in [21] and the corresponding processes. Briefly, the Ag is deposited by RF sputtering under light illumination while applying a reverse-bias dc voltage, $V_b = -1.5$ V, to the P3HT/ZnO p–n junction. The wavelength of the incident light is 660 nm, longer than the cut-off wavelength of P3HT. Under light illumination, an optical near-field is locally generated on the Ag surface, which induces a coherent phonon at the p–n junction, leading to the generation of a virtual exciton–phonon–polariton. This then generates an electron–hole pair at the p–n junction. The electron and hole are separated from each other by the reverse-bias voltage. The positive hole is attracted to the Ag film, which makes the Ag film positively charged.

Since the sputtered Ag is positively ionized by passing through the argon plasma or due to the collision of the argon

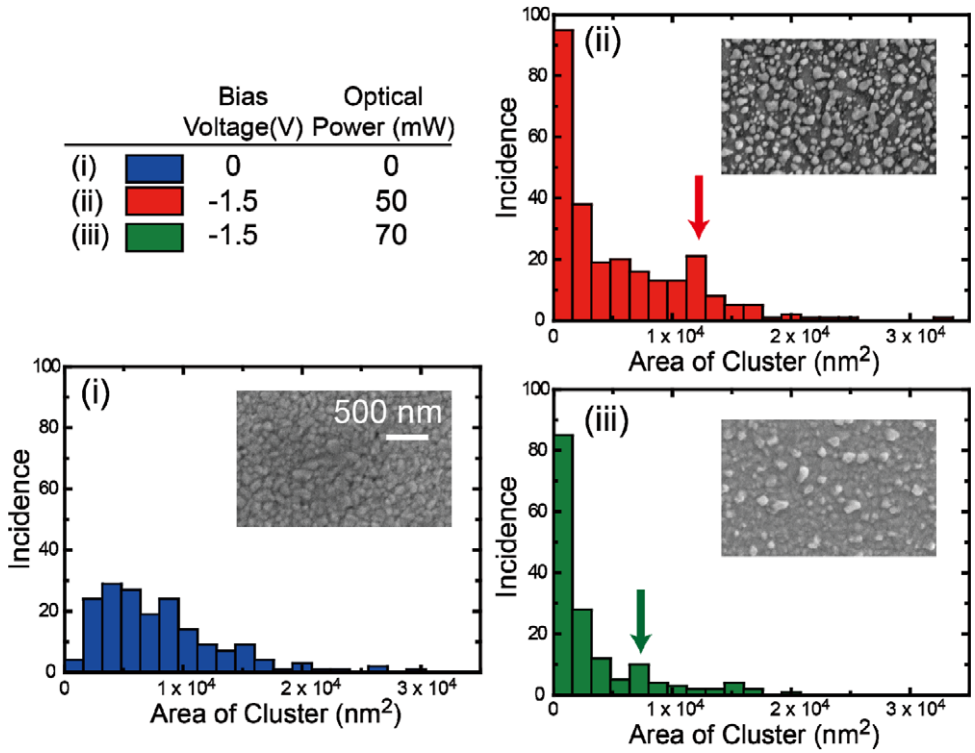

Figure 28. SEM images of the surfaces of the Ag electrodes and the incidence patterns of the cluster areas. (i) No dc bias ($V_b = 0$), no light irradiation ($P = 0$), (ii) $V_b = -1.5$ V, $P = 50$ mW and (iii) $V_b = -1.5$ V, $P = 70$ mW.

plasma with the Ag-target used for RF sputtering [159], these positively ionized Ag particles are repulsed from the positively charged area of the Ag film where the positive holes have been injected, as schematically shown in figure 27(*a*). This means that the subsequent deposition of Ag is suppressed in the area where optical near-fields are efficiently induced. The processes described here lead to the unique granular structure of the Ag film formed in a self-organized manner, which is the primary focus of the stochastic modeling. Five kinds of devices are discussed in [21], with different combinations of reverse-bias voltage and incident light power. In the work described in this paper, we analyzed the following three devices, or cases: (i) $V_b = 0$ and $P = 0$, (ii) $V_b = -1.5$ V and $P = 50$ mW, and (iii) $V_b = -1.5$ V and $P = 70$ mW. Figure 28 shows SEM images of the Ag film surfaces for cases (i)–(iii). It is evident that unique surface morphologies were obtained in cases (ii) and (iii) with the light irradiation. As summarized in figure 27(*b*), photocurrents were generated in cases (ii) and (iii) in the longer wavelength range, where case (i) exhibited no response.

Figure 28 represents the incidence pattern as a function of the size of the Ag clusters, obtained by analyzing the SEM images. A number of small clusters were observed in cases (ii) and (iii), but some of them were large. Also, as depicted by arrows in figures 28(ii) and (iii), the incidence showed a local maximum at a particular cluster size. Also note that the maximum appeared at a larger size with lower power light irradiation. On the other hand, case (i) exhibited a different incidence pattern of the cluster area, showing a representative (mode) size of around 5×10^3 nm^2. In other words, we can see evident differences in the surface morphologies between the fabrication processes with and without light irradiation and a reverse dc bias.

Taking account of the physical processes of the material formation described above, we constructed a simple stochastic model that preserves the essential characteristics. First we consider a two-dimensional (2D) $M \times M$ square grid cell structure Λ_M where a cell, also called a pixel, is specified by $P = (p_x, p_y) \in \Lambda_M$. In each cell, a variable $h(P) \in \{0, 1\}$ is assigned so that areas where the Ag film surface has bumps are represented by $h(P) = 1$, and areas where the surface is flat are represented by $h(P) = 0$. In figure 29(*a*), the pixels with $h(P) = 1$ are indicated by black cells, whereas those with $h(P) = 0$ are indicated by white ones. We simulate the material deposition process as follows.

Initially, we assume a completely flat surface, namely, $h(P) = 0$ for all $P \in \Lambda_M$. First, we randomly choose a cell P in the 2D grid structure and let a particle arrive at P. Second, we determine if the particle successfully lands on a cell or is repulsed, that is, deflected, out of the system, by taking account of the positively charged Ag to be sputtered and the holes that could appear on the Ag film surface. We calculate a *pseudo-footprint* denoted by Q_P, defined below, in order to evaluate this effect in the stochastic modeling.

If the calculated value of Q_P is smaller than or equal to a threshold Z, and if the flat surface condition is satisfied ($h(P) = 0$), an arriving particle is able to land on the cell P; that is, $h(P) = 0 \rightarrow h(P) = 1$. In contrast, if Q_P is larger than Z, the arriving particle is deflected outside the system, representing repulsion between the positively charged Ag particle and the positively charged clusters on the surface due to the reverse bias. If Q_P is smaller than or equal to

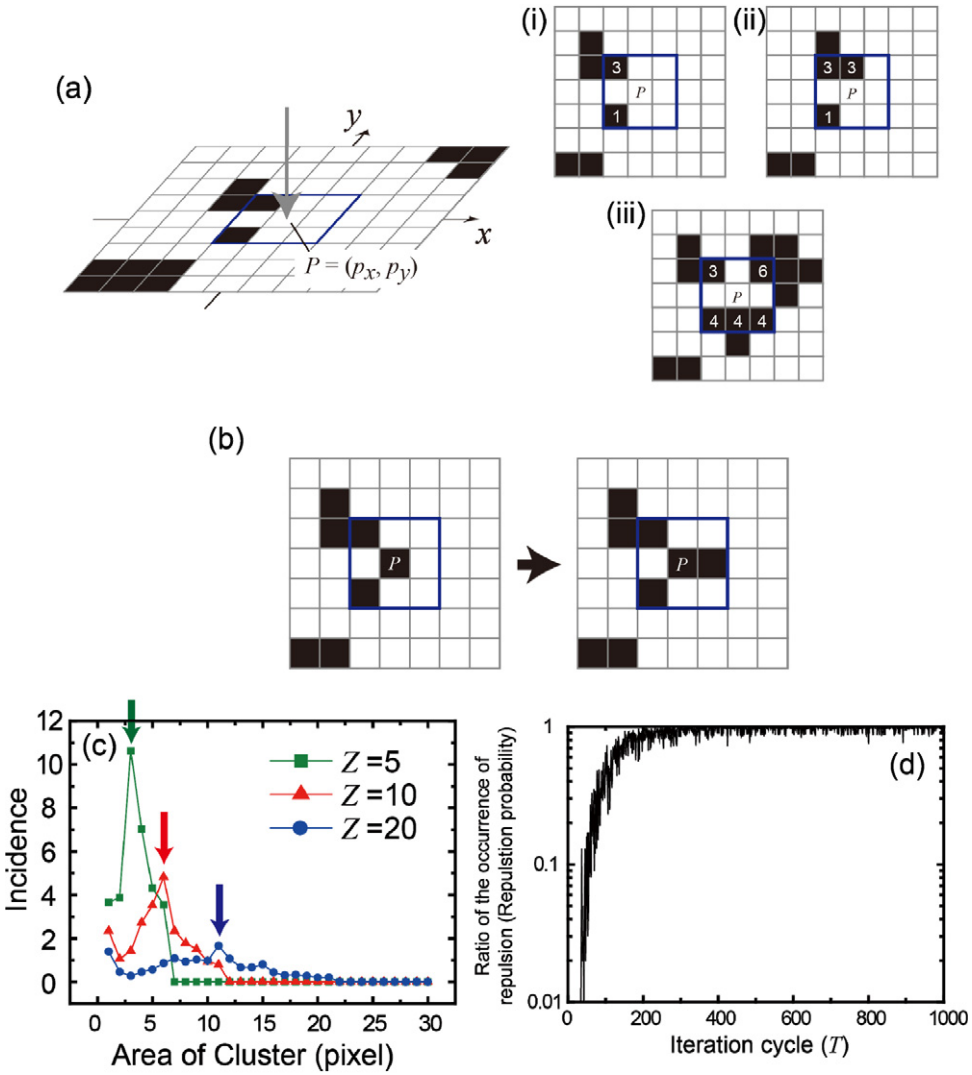

Figure 29. (*a*) A two-dimensional (2D) grid cell structure used to model the stochastic pattern formation process. (i)–(iii): Examples for calculating the *pseudo-footprint* for a cell P. (*b*) Simulating a drift process when the pseudo-footprint at cell P is less than the threshold value but cell P is occupied. (*c*) Incidence pattern as a function of cluster area, with threshold Z as a parameter. The model produces behavior consistent with the experimental observations. (*d*) Evolution of the ratio of the occurrence of repulsion. The value becomes stable after cycle $t = 300$, representing self-organized pattern formation.

Z but the point P is already occupied ($h(P) = 1$), the arriving particle will sit in a free, randomly chosen neighbor, representing a drift process.

The pseudo-footprint metric in each square grid cell corresponds to the sum of the areas of its eight neighbors. More precisely, the pseudo-footprint at P is given by

$$Q_P = \sum_{i=\{-1,0,1\}, j=\{-1,0,1\}} S_P^{(i,j)}, \tag{26}$$

where $S_P^{(i,j)}$ represents the total number of occupied cells, or area, connected to the cell $(p_x + i, p_y + j)$ either in the horizontal (x) or vertical (y) neighbors, as schematically shown in figure 29(*a*). For example, in the case shown in figure 29(*a*,i), the area of the top-left corner is $S_P^{(-1,+1)} = 3$, and that of the bottom-left one is $S_P^{(-1,-1)} = 1$. Therefore, based on equation (26), the pseudo-footprint is given by $Q_P = S_P^{(-1,+1)} + S_P^{(-1,-1)} = 4$. In another example shown in figure 29(*a*,ii), the areas are given by $S_P^{(-1,+1)} = 3$, $S_P^{(0,+1)} = 3$ and $S_P^{(-1,-1)} = 1$, which yields $Q_P = S_P^{(-1,+1)} + S_P^{(0,+1)} + S_P^{(-1,-1)} = 7$. In another example shown in figure 29(*a*,iii), $Q_P = \sum_{i,j} S_P^{(i,j)} = 21$.

When an arriving Ag particle is not repulsed from the system, but the point P is occupied, the particle lands in a randomly chosen neighboring cell. The left-hand side of figure 29(*b*) represents one such example where $Q_P = 4$. Suppose that this Q_P is smaller than the threshold Z. Since the point P is occupied, a free neighboring cell is randomly chosen along the x- or y-direction. For example, the system is updated as shown in the right-hand side of figure 29(*b*), where a newly arriving particle lands to the right of the point P, in other words, $h(p_x + 1, p_y) = 0 \rightarrow h(p_x + 1, p_y) = 1$. Such a rule represents the drift process occurring on the Ag film surface.

By iteratively applying the stochastic process described above in a repeated manner for T cycles from a flat initial state, a variety of resultant spatial patterns were generated.

They also depended on the threshold Z. By setting the size of the grid to 16×16 cells, that is, $M = 16$ for the region Λ_M, while setting the threshold at $Z = 10$ and the number of cycles $T = 300$, a variety of spatial patterns are generated based on the stochastic model. To examine the statistical properties, the incidence pattern of the mean number of each cluster in N different samples was evaluated, as shown in figure 29(c), where the number of iteration cycles was $T = 1000$ and the number of trials was $N = 100$. Squares, triangles and circles, respectively, represent the incidence of the clusters in the system with different thresholds $Z = 5$, 10 and 20.

The incidence pattern exhibited different characters depending on the threshold value ($Z = 5$, 10, 20): with smaller Z, the cluster area yielding the local maximum incidence shifted towards a smaller value in figure 29(c), which agrees with the experimentally observed character shown in figure 28, where larger optical light irradiation produced smaller clusters (peaks are indicated by arrows). In other words, higher-power light irradiation more likely induces repulsion, leading to a local maximum at a smaller cluster area for the clusters formed on the surface. This supports the physical interpretation that the pseudo-footprint appropriately represents the repulsion due to the optical near-field effect. That is to say, the pseudo-footprint reflects the positive holes, and an associated optical near-field localized around a cluster, or spatial inhomogeneity, is induced. In considering the self-organized pattern formation, figure 29(d) characterizes the ratio of the occurrence of repulsion at cycle T among $N = 100$ trials. In other words, it shows the time evolution of the probability of repulsion. The probability increases as the iteration cycle increases; a repulsion probability of 0.8 or higher was observed after the iteration cycle reached around 300. Since the present stochastic model includes a threshold value Z, strictly speaking, it does not exhibit so-called self-organized criticality [41]. However, a flat surface converges to various kinds of patterns in a self-organized manner while exhibiting common statistical properties, which is as a kind of self-organized critical phenomenon due to near-field effects inherent in the stochastic model described above.

In summary, in photovoltaic devices made by exploiting an optical phonon-assisted near-field process exhibiting unique photocurrent generation, we analyzed the surface morphology of the Ag electrode of the fabricated devices and constructed a stochastic model to explain the fundamental physical process of the material formation. The numerical simulation results exhibited behavior consistent with the experimental results.

4.2. Solution searching

Another aspect of the stochastic nature inherent in nanophotonics is its application to novel computing devices and architectures [160]. Nature-inspired architectures are attracting significant attention in various research areas, such computational neurosciences, stochastic-based computing and noise-based logic, and spatio-temporal computation dynamics [53], in order to benefit from the superior attributes of nature and living systems.

Among this research, Aono *et al* demonstrated 'amoeba-based computing' tasks, such as solving the constraint satisfaction problem (CSP) [53] and the TSP [55], by utilizing the spatio-temporal oscillatory dynamics of the photoresponsive amoeboid organism Physarum combined with external optical feedback control. These demonstrations indicate that spatio-temporal stochastic dynamics can be utilized for obtaining solutions for problems which today's von-Neumann-architecture computers cannot deal with efficiently. Such stochastic dynamics could originate from nanometer-scale interactions between light and matter [91]. In particular, it should be noted that the optical excitation transfer between quantum nanostructures mediated by optical near-field interactions, discussed in section 2, is fundamentally probabilistic, as indicated by the quantum master equations. Until energy dissipation is induced, an optical excitation simultaneously interacts with potentially transferable destination quantum dots in the resonant energy level. Such a probabilistic behavior can be used for the function of solution searching and exploration. In addition, the optical energy transfer has been shown to be 10^4-times more energy efficient than that of the bit-flip energy required in conventional electrically wired devices (section 2.1.3) [70].

We investigate the spatio-temporal dynamics inherent in optical excitation transfer. Furthermore, we demonstrate that it can be utilized for solving a CSP. The optical excitation transfer depends on the existence of resonant energy levels between the quantum dots or the state filling effect occurring at the destination QDs (section 2.1.5). Such a spatial and temporal mechanism yields different evolutions of energy transfer patterns combined with certain feedback mechanisms. In contrast to biological substrates, optical energy transfer is implemented by highly-controlled engineering means for designated structures. The operating speed of such optical-near-field mediated QD systems, which is in the order of nanoseconds when we are concerned with radiative relaxation processes, is also significantly faster than ones based on biological organisms, which is in the order of seconds or minutes [53].

In addition, we should emphasize that the concept and the principles discussed here are fundamentally different from those of conventional optical computing or optical signal processing, which are limited by the abilities of propagating light. The concept and the principles are also different from the quantum computing paradigm where the superposition of all possible states is exploited to lead to a correct solution. The optical near-field-mediated energy transfer is a coherent process, indicating that an optical excitation could be transferred to all possible destination QDs via a resonant energy level, but such coherent interaction between QDs results in a unidirectional energy transfer by means of an energy dissipation process occurring in the larger dot. Thus, our approach paves the way to another computation paradigm in which both coherent and dissipative processes are exploited.

Here we assume one smaller quantum dot, denoted by QD_S, and four larger quantum dots, denoted by QD_{L1}, QD_{L2}, QD_{L3} and QD_{L4}, as shown in figure 30(a). The smaller and larger QDs are resonant with each other. Figure 30(b) shows representative parameterizations associated with the system; for example, the (1,0)-level in the smaller QD is denoted by

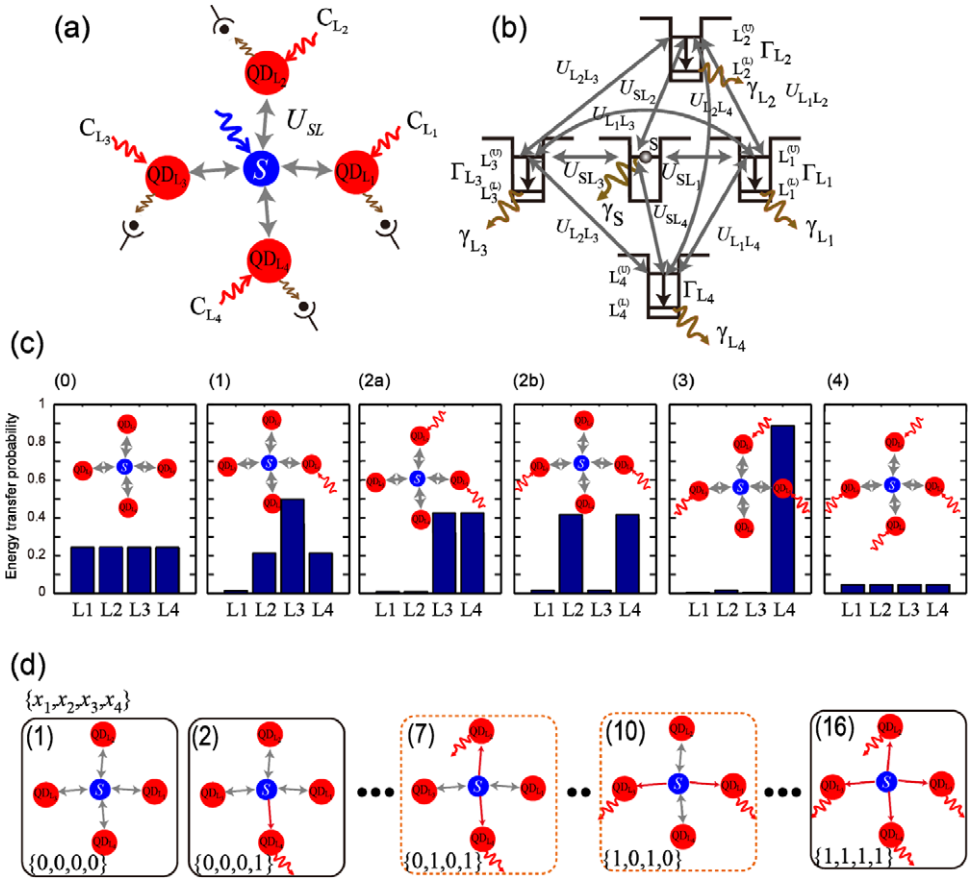

Figure 30. (*a*) Architecture of the optical-energy-transfer-based system for solving the constraint satisfaction problem studied in this paper and composed of a smaller quantum dot and four larger quantum dots and (*b*) its energy diagram. Radiation from the larger quantum dots is detected. Control light is used for inducing state filling in the larger quantum dots. (*c*) Energy transfer probabilities calculated as time integrals of the populations depending on the state filling of the larger dots, shown in (*a*). There are a total of six different spatial arrangements of the induced state filling, excluding the symmetries. (*d*) There are a total of 2^4 (=16) different combinations of binary values in the given problem. The correct solutions are the state numbers (7) and (10), where $\{x_1, x_2, x_3, x_4\}$ are, respectively, given by {0,1,0,1} and {1,0,1,0}.

S, and the (1,1)-level in $\mathrm{QD}_{\mathrm{L}_i}$ is denoted by $\mathrm{L}_i^{(\mathrm{U})}$. These levels are resonant with each other and are connected by inter-dot interactions denoted by U_{SL_i} $(i = 1, \ldots, 4)$. The lower level in $\mathrm{QD}_{\mathrm{L}_i}$, namely, the (1,0)-level, is denoted by $\mathrm{L}_i^{(\mathrm{L})}$, which could be filled via the sublevel relaxation denoted by Γ_{L_i} from $\mathrm{L}_i^{(\mathrm{U})}$. The radiations from the S and L_i levels are, respectively, represented by the relaxation constants γ_{S} and γ_{L_i}. We call the inverse of those relaxation constants the radiation lifetime in the following. We also assume that the photon radiated from the lower level of $\mathrm{QD}_{\mathrm{L}_i}$ can be separately captured by photodetectors. The channels of control light, denoted by C_{L_i}, can induce a state filling effect at $\mathrm{L}_i^{(\mathrm{L})}$. Summing up, figure 30(*a*) schematically represents the architecture of the system to be studied in this paper for solving a CSP.

In the numerical calculation, we assume $U_{\mathrm{SL}i}^{-1} = 100\,\mathrm{ps}$, $\Gamma_i^{-1} = 10\,\mathrm{ps}$, $\gamma_{\mathrm{L}i}^{-1} = 1\,\mathrm{ns}$ and $\gamma_{\mathrm{S}}^{-1} = 2.92\,\mathrm{ns}$ as a typical parameter set. If there is no state filling in the system, an optical excitation sitting initially at S can be transferred to any one of $\mathrm{QD}_{\mathrm{L1}}$ to $\mathrm{QD}_{\mathrm{L4}}$ with the same probability, as demonstrated in figure 30(*c*,0), which is the time integral of the population involving the energy level $\mathrm{L}_i^{(L)}$. If $\mathrm{QD}_{\mathrm{L1}}$ suffers from state filling, on the other hand, the initial excitation at S is more likely to be transferred to $\mathrm{QD}_{\mathrm{L2}}$, $\mathrm{QD}_{\mathrm{L3}}$ or $\mathrm{QD}_{\mathrm{L4}}$, as shown in figure 30(*c*,1). Looking at the results more closely, the probability of transfer to $\mathrm{QD}_{\mathrm{L3}}$ is higher than the probabilities of transfer to $\mathrm{QD}_{\mathrm{L2}}$ and $\mathrm{QD}_{\mathrm{L4}}$ by considering the geometrical arrangements of the system. A detailed discussion is found in [160]. Additionally, the energy transfer probabilities in the presence of two, three or four state filling are summarized in figure 30(*c*). The energy transfer probability, given by the integral of the population divided by a constant gain factor, is indeed a FoM indicating the trend of optical energy transfer from the smaller quantum dot to the four larger ones. It does *not* obey the conservation law of probability, namely, the summation of the transition probability to $\mathrm{QD}_{\mathrm{L}_i}$ is not unity. Instead, we see that the energy transfer to $\mathrm{QD}_{\mathrm{L}_i}$ occurs if a random number generated uniformly between 0 and 1 is less than the transition probability to $\mathrm{QD}_{\mathrm{L}_i}$.

The idea for problem solving is to control optical energy transfer by controlling the destination QD by using control light in an adequate feedback mechanism. We assume that photon radiation, or observation, from the energy level $\mathrm{L}_i^{(\mathrm{L})}$ is equivalent to a binary value x_i resulting in a logical 1 level, whereas no observation of a photon means $x_i = 0$.

We consider the following CSP as an example regarding an array of N binary-valued variables x_i ($i = 1, \ldots, N$). The constraint is that $x_i = \mathrm{NOR}(x_{i-1}, x_{i+1})$ should be satisfied for all i. That is, variable x_i should be consistent with a logical NOR operation of the two neighbors. For $i = 0$ and N, the constraints are, respectively, given by $x_1 = \mathrm{NOR}(x_N, x_2)$ and $x_N = \mathrm{NOR}(x_{N-1}, x_1)$. We call this problem the 'NOR problem' hereafter in this paper. Taking account of the nature of an individual NOR logic operation, one important inherent characteristic is that if $x_i = 1$ then its two neighbors should both be zero, or $x_{i-1} = x_{i+1} = 0$. Recall that a photon radiated, or observed, from the energy level $\mathrm{L}_i^{(L)}$ corresponds to a binary value $x_i = 1$, whereas the absence of an observed photon means $x_i = 0$. Therefore, $x_i = 1$ should mean that the optical energy transfer to both $\mathrm{L}_{i-1}^{(L)}$ and $\mathrm{L}_{i+1}^{(L)}$ is prohibited so that $x_{i-1} = x_{i+1} = 0$ is satisfied. Therefore, the feedback or control mechanism is as follows:

[Control mechanism] If $x_i = 1$ at the cycle t, then the control light beams C_{i-1} and C_{i+1} are turned on at the cycle $t = t + 1$.

In the case of $N = 4$, there are in total 2^4 optical energy transfer patterns from the smaller dot to larger ones. In this case, variables satisfying the constraints do exist, and they are given by $\{x_1, x_2, x_3, x_4\} = \{0, 1, 0, 1\}$ and $\{1,0,1,0\}$, which we call 'correct solutions'. Figure 30(d) schematically represents some of the possible states where the states (7) and (10), respectively, correspond to the correct solutions.

We now make a few remarks regarding the NOR problem. One is about potential deadlock, analogous to Dijkstra's '*dining philosophers problem*', as already argued by Aono *et al* in [53]. Starting with an initial state $x_i = 0$ for all i, and assuming a situation where optical energy is transferred to all larger QDs, we observe photon radiation from all energy levels $\mathrm{L}_i^{(L)}$, namely, $x_i = 1$ for all i. Then, based on the feedback mechanism shown above, all control light beams are turned on. If such a feedback mechanism perfectly inhibits the optical energy transfer from the smaller QD to the larger ones at the next step $t + 1$, the variables then become $x_i = 0$ for all i. This leads to all control light beams being turned off at $t + 2$. In this manner, all variables constantly repeat a periodic switching between $x_i = 0$ and $x_i = 1$ in a synchronized manner. Consequently, the system can never reach the correct solutions. However, as indicated in figure 30(c), the probability of optical energy transfer to larger dots is in fact not zero even when all larger QDs are illuminated by control light, as shown in figure 30(c(4)). Also, even for a non-illuminated destination QD, the energy transfer probability may not be exactly unity. Such a stochastic behavior of the optical energy transfer is a key role in solving the NOR problem. This nature is similar to the demonstrations in amoeba-based computing [53] where fluctuations of chaotic oscillatory behavior involving spontaneous symmetry breaking in the amoeboid organism guarantees such a critical property.

The operating dynamics cause one pattern to change to another one in every iteration cycle. Thanks to the stochastic nature, each trial could exhibit a different evolution of the energy transfer patterns. In particular, the transition probability, shown in figure 30(c), affects the behavior of the transitions. Therefore, we introduce a gain factor (G) to be multiplied by the energy transfer probability summarized in figure 30(c).

The curves in figure 31(a) represent the evolution of the output appearance from $\mathrm{QD}_{\mathrm{L}_i}$, namely, the ratio of the incidence when $x_i = 1$ among 1000 trials evaluated at each cycle. The curves in figure 31(b) characterize the ratio of the appearance of the state that corresponds to the correct solutions: {0,1,0,1} (state 7) and {1,0,1,0} (state 10), respectively. When we closely examine the evolutions of x_i in figure 31(a), we can see that the pair x_1 and x_3 exhibit similar behavior, as do the pair x_2 and x_4. Also, the former pair exhibit larger values, whereas the latter pair show smaller values, and vice versa. This corresponds to the fact that correct solutions are likely to be induced as the iteration cycle increases.

Such a tendency is more clearly represented when we evaluate the time-averages of the characteristics in figures 31(a) and (b). Figure 31(c) shows the evolutions of the ratio of the incidences when $x_i = 1$, and figure 31(d) shows the ratios of state (7) and state (10) averaged over every five cycles. We can clearly observe a similar tendency to the one described above. Also, we should emphasize that, thanks to the probabilistic nature of the system, the states of correct solutions appear in an interchangeable manner. This is a clear indication of the fact that the probabilistic nature of the system autonomously seeks the solutions that satisfy the constraints of the NOR problem; the state-dependent probability of energy transfer plays a critical role in this. In other words, it should be emphasized that a non-local correlation is manifested in the evolution of x_i; for instance, when the system is in state (7), {0,1,0,1}, the probabilities of energy transfer to $\mathrm{QD}_{\mathrm{L1}}$ and $\mathrm{QD}_{\mathrm{L3}}$ are equally comparably low (due to state filling), whereas those to $\mathrm{QD}_{\mathrm{L2}}$ and $\mathrm{QD}_{\mathrm{L4}}$ are equally comparably high, indicating that the probability of energy transfer to an individual $\mathrm{QD}_{\mathrm{L}_i}$ has inherent spatial patterns or non-local correlations. At the same time, the energy transfer to each $\mathrm{QD}_{\mathrm{L}_i}$ is indeed probabilistic; therefore, the energy transfer probability to, for instance, $\mathrm{QD}_{\mathrm{L1}}$ is not zero even in state (7), and thus, the state could transition from state (7) to state (10), and vice versa. In fact, starting with the initial condition of state (7), the ratio of the output appearance from $\mathrm{QD}_{\mathrm{L1}}$ and the ratio of the correct solutions evolve as shown in figures 31(e) and (f), where states (7) and (10) occur equally in the steady state at around 20 time cycles. Figure 31(g) evaluates the accuracy rate, which is the number of correct solutions among 1000 different trials at $t = 100$, as a function of the gain factor. We can see that a gain of 2.5 provides the highest accuracy rate.

We make two final remarks to conclude this section. The first is about the relevance to a satisfiability (SAT) problem. In the case of $N = 4$, solving the NOR problem demonstrated above is equivalent to solving the following satisfiability problem instance given in a conjunctive normal form:

$$f(x_1, x_2, x_3, x_4) = (\neg x_1 \vee \neg x_2) \wedge (\neg x_1 \vee \neg x_4) \wedge (\neg x_2 \vee \neg x_3) \wedge (\neg x_3 \vee \neg x_4) \wedge (x_1 \vee x_2 \vee x_3) \wedge (x_1 \vee x_2 \vee x_4) \wedge (x_1 \vee x_3 \vee x_4) \wedge (x_2 \vee x_3 \vee x_4). \quad (27)$$

Since the maximum number of literals in clauses in equation (27) is three, this is an instance of a so-called 3SAT problem [161]. We presume that such a SAT problem could be

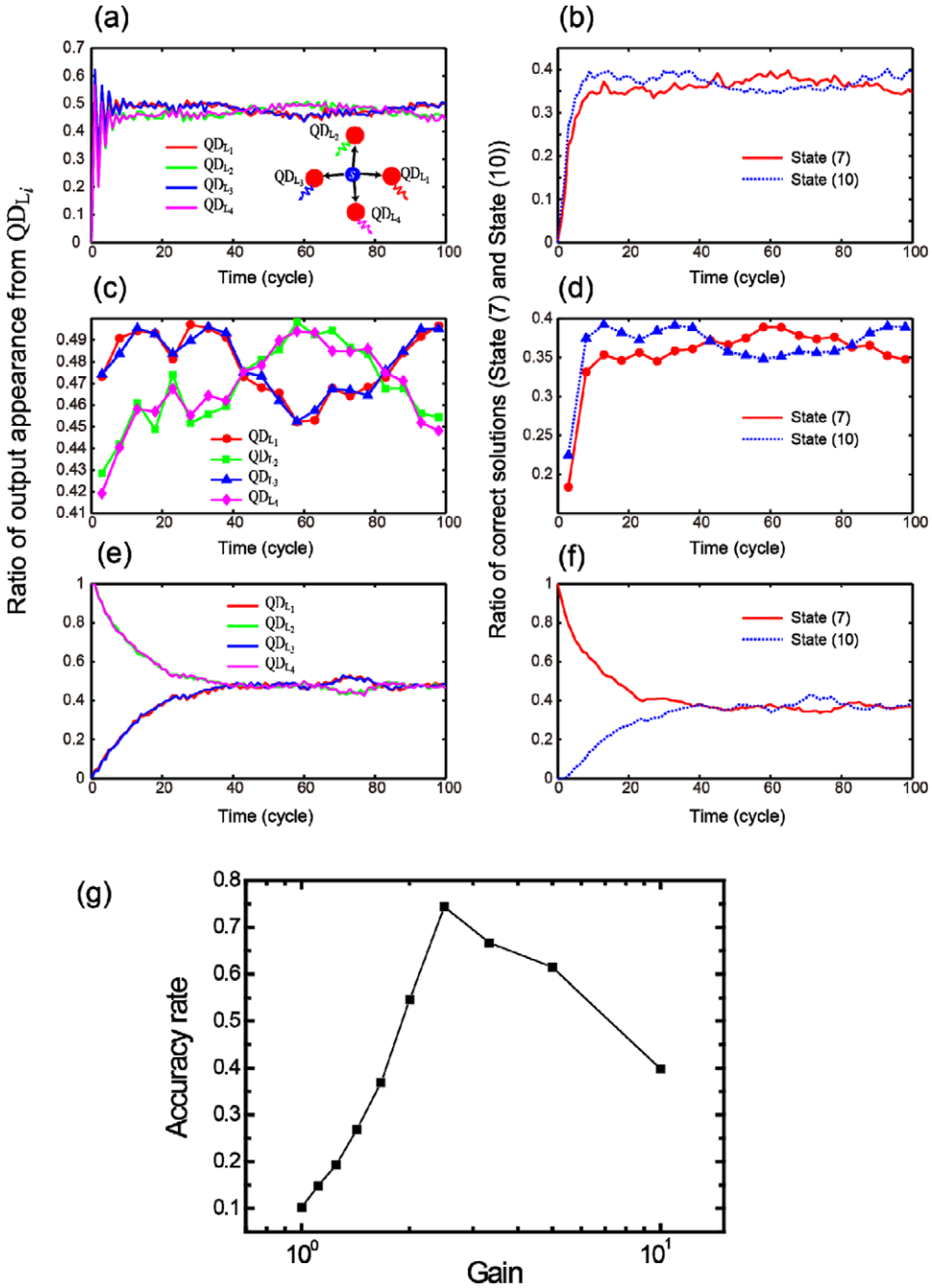

Figure 31. (*a*) The evolution of the ratio of the output appearance from QD_{L_i}, or $x_i = 1$, and (*b*) the ratio of the state corresponding to the correct solutions with the initial state of $\{x_1, x_2, x_3, x_4\} = \{0, 0, 0, 0\}$. (*c*),(*d*) Time-averaged traces of (*b*) and (*c*), respectively. (*e*) The evolution of the ratio of the output appearance from QD_{L_i}, or $x_i = 1$, and (*f*) the ratio of the state corresponding to correct solutions with the initial state $\{x_1, x_2, x_3, x_4\} = \{0, 1, 0, 1\}$. (*g*) Calculated accuracy rate, or the ratio of the number of correct states among all trials, as a function of the gain factor.

dealt with by variants of our optical-near-field–mediated systems developed in the future [162]. SAT is an important non-deterministic polynomial-time complete (NP-complete) problem, indicating that no fast algorithm has been found yet [161]. We consider that nanophotonic principles could potentially provide a new way to solve such computationally demanding problems.

The second remark is about the implementation of optical energy transfer for such stochastic computing applications. As mentioned in the introduction, the latest notable features are the rapid advancements made in nanomaterials for optical energy transfer [24, 25, 37, 74, 163]. Among various technologies, for example, Akahane *et al* successfully demonstrated energy transfer in multi-stacked InAs QDs where layer-by-layer QD size control has been accomplished [163]. Adequate QD size control also allows optical coupling between optical far-fields and optically-allowed energy levels in a quantum dot mixture, which could help to solve the interfacing issues of the system, as demonstrated in section 2.1.4. Research in the field of nanodiamonds may also be of promise in implementing

the architecture of the present study [164, 165]; near-field applications of nanodiamonds have already been demonstrated by Cuche *et al* in [12].

5. Conclusion and future outlook

In this paper, we have discussed nanophotonics from the standpoint of information physics. In particular, we highlighted optical excitation transfer involving optical near-field interactions, hierarchical properties inherent in optical near-fields, and the stochastic nature of nanophotonics. Design issues and applications were theoretically and experimentally investigated, together with a presentation of theoretical fundamentals and formalisms.

Finally, we make a few remarks on the future prospects of research and development in nanophotonics from an information physics, or system-level, viewpoint. We consider that future research and development will be roughly grouped into three categories.

The first category concerns further investigation of basic and emergent properties in nanophotonics. This paper addresses and resolves some of these concerns, such as unidirectionality of optical excitation transfer, the lower bound of energy dissipation, networks of optical near-fields and their associated associated spatio-temporal dynamics, and the theory of hierarchy. However, there are plenty of unresolved issues. For instance, the randomness of nanostructures and their resultant information-related performance measures, such as information capacity [166], should be further investigated while taking account of localized and hierarchical properties of near-field interactions. In addition, scalability and adequate information representations for nanophotonic systems should be further investigated in the future. For example, the scalability of the solution searching discussed in section 4.2 would be important in terms of both purely theoretical standpoints and physical implementations.

The second category involves design-related concerns in nanophotonics. This paper presented a theoretical approach to networks of near-field interactions, shape-engineered nanostructures, etc, for the purpose of extracting and/or optimizing intended functions by utilizing optical excitation transfer and the hierarchical nature of nanophotonics. The multipole nature of optical near-fields, for instance, has been applied to the demonstration of a 'lock-and-key' relation between two nanostructures, as described in section 3.3.2. The degrees-of-freedom available on the nanoscale, however, are in fact much more abundant and should be thoroughly investigated; these include magnetic field, electron spin and so on. For instance, magnet-chiral effects [167] and energy transfer in diluted magnet semiconductors [79] suggest the importance of including a discussion of spin in the treatment of optical near-fields. Besides, as discussed in section 4.1, morphology in nanoscale material provides interesting functions, such as light emission from indirect-type semiconductors (e.g. silicon) [20]. It has been suggested that coherent coupling between phonons and optical near-fields lies behind such phenomena [168]. Solid theoretical schemes, including ones that offer systematic design frameworks for realizing versatile materials and functionalities, should be investigated. Computational approaches that can unify the first-principles calculations of matter and localized electromagnetic phenomena are also demanded [57, 169].

The third category concerns applications. Logic operations (section 2.1.5), interconnects (section 2.1.4), and stochastic computing (section 4.2) exploit optical excitation transfer. Hierarchical information retrieval (section 3.2.1) and hierarchical optical elements (such as hierarchical holograms; section 3.3) based on the hierarchical properties inherent in optical near-fields have been described. In addition to these information-related applications, an information physics approach provides the foundations and principles for other applications, such as energy or nanofabrication. For instance, networks of optical near-field interactions have been applied to the analysis of photodetection (section 2.2), and a stochastic approach has an impact on the fabrication of nanostructures (section 4.1.1) and energy devices (section 4.1.2). Further applications of nanophotonics are expected, and an information physics approach will be fundamental for conceiving novel applications and putting them into practice.

Through these inter- and cross-disciplinary investigations covering optical, material, and information sciences, as well as considering applications that will provide new value via state-of-the-art technologies, we hope to convey the excitement and sense of wonder that emerges, and to harness the fruits of these investigations to pave the way to a new research area of physical and information sciences and technologies.

Acknowledgments

The authors would like to thank many collaborators for illuminating discussions over several years, in particular T Kawazoe, T Yatsui, W Nomura, H Hori, K Kobayashi, K Akahane, N Yamamoto, T Inoue, F Peper, K Leibnitz, M Hoga, Y Ohyagi, L B Kish, C Lienau, E Runge, S Huant and S-J Kim.

References

[1] Yariv A and Yeh P 2006 *Photonics: Optical Electronics in Modern Communication* (New York: Oxford University Press)
[2] Tucker R S, Parthiban R, Baliga J, Hinton K, Ayre R W A and Sorin W V 2009 Evolution of WDM optical IP networks: a cost and energy perspective *J. Lightwave Technol.* **27** 243–52
[3] Ryhänen T, Uusitalo M A, Ikkala O, Kärkkäinen A 2010 *Nanotechnologies for Future Mobile Devices* (Cambridge: Cambridge University Press)
[4] Narukawa Y, Kawakami Y, Fujita S, Fujita S and Nakamura S 1997 Recombination dynamics of localized excitons in In0.20Ga0.80N-In0.05Ga0.95N multiple quantum wells *Phys. Rev.* B **55** R1938–41
[5] Naruse M, Tate N, and Ohtsu M 2012 Optical security based on near-field processes at the nanoscale *J. Opt.* **14** 094002
[6] Javidi B 2005 *Optical and Digital Techniques for Information Security* (New York: Springer)
[7] Ohtsu M, Kobayashi K, Kawazoe T, Sangu S and Yatsui T 2002 Nanophotonics: design, fabrication, and operation of

nanometric devices using optical near fields *IEEE J. Sel. Top. Quantum Electron.* **8** 839–62
[8] National Research Council 2008 *Nanophotonics: Accessibility and Applicability* (Washington, DC: National Academies Press)
[9] MONA (Merging Optics and Nanotechnologies Association) consortium 2008 *A European Roadmap for Photonics and Nanotechnologies*
[10] Ohtsu M and Hori H 1999 *Near-Field Nano-Optics* (New York: Kluwer/Plenum)
[11] Pohl D W and Courjon D (ed) 1993 *Near Field Optics* (Dordrecht: Kluwer)
[12] Cuche A, Drezet A, Sonnefraud Y, Faklaris O, Treussart F, Roch J-F and Huant S 2009 Near-field optical microscopy with a nanodiamond-based single-photon tip *Opt. Express* **17** 19969–80
[13] Nishida T, Matsumoto T, Akagi F, Hieda H, Kikitsu A and Naito K 2007 Hybrid recording on bit-patterned media using a near-field optical head *J. Nanophoton.* **1** 011597
[14] Naya M, Tsurusawa I, Tani T, Mukai A, Sakaguchi S and Yasutani S 2005 Near-field optical photolithography for high-aspect-ratio patterning using bilayer resist *Appl. Phys. Lett.* **86** 201113
[15] Tojo S and Hasuo M 2005 Oscillator-strength enhancement of electric-dipole-forbidden transitions in evanescent light at total reflection *Phys. Rev.* A **71** 012508
[16] Ohtsu M, Kawazoe T, Yatsui T and Naruse M 2008 Nanophotonics: application of dressed photons to novel photonic devices and systems *IEEE J. Sel. Top. Quantum Electron.* **14** 1404–17
[17] Ohtsu M, Kobayashi K, Kawazoe T, Yatsui T and Naruse M 2008 *Principles of Nanophotonics* (Boca Raton, FL: Taylor and Francis)
[18] Kawazoe T, Kobayashi K and Ohtsu M 2005 The optical nano-fountain: a biomimetic device that concentrates optical energy in a nanometric region *Appl. Phys. Lett.* **86** 103102
[19] Fujiwara H, Kawazoe T and Ohtsu M 2010 Nonadiabatic multi-step excitation for the blue–green light emission from dye grains induced by the near-infrared optical near-field *Appl. Phys.* B **98** 283–9
[20] Kawazoe T, Mueed M A and Ohtsu M 2011 Highly efficient and broadband Si homojunction structured near-infrared light emitting diodes based on the phonon-assisted optical near-field process *Appl. Phys.* B **104** 747–54
[21] Yukutake S, Kawazoe T, Yatsui T, Nomura W, Kitamura K and Ohtsu M 2010 Selective photocurrent generation in the transparent wavelength range of a semiconductor photovoltaic device using a phonon-assisted optical near-field process *Appl. Phys.* B **99** 415–22
[22] Kawazoe T, Ohtsu M, Akahane K and Yamamoto N 2012 Si homojunction structured near-infrared laser basedon a phonon-assisted process *Appl. Phys.* B **107** 659–63
[23] Aeschlimann M, Bauer M, Bayer D, Brixner T, Javier F, de Abajo G, Pfeiffer W, Rohmer M, Spindler C and Steeb F 2007 Adaptive subwavelength control of nano-optical fields *Nature* **446** 301–4
[24] Kawazoe T, Ohtsu M, Aso S, Sawado Y, Hosoda Y, Yoshizawa K, Akahane K, Yamamoto N and Naruse M 2011 Two-dimensional array of room-temperature nanophotonic logic gates using InAs quantum dots in mesa structures *Appl. Phys.* B **103** 537–46
[25] Yatsui T, Sangu S, Kawazoe T, Ohtsu M, An S J, Yoo J and Yi G-C 2007 Nanophotonic switch using ZnO nanorod double-quantum-well structures *Appl. Phys. Lett.* **90** 223110
[26] Tate N, Sugiyama H, Naruse M, Nomura W, Yatsui T, Kawazoe T and Ohtsu M 2009 Quadrupole–dipole transform based on optical near-field interactions in engineered nanostructures *Opt. Express* **17** 11113–21
[27] Tate N, Naruse M, Yatsui T, Kawazoe T, Hoga M, Ohyagi Y, Fukuyama T, Kitamura M and Ohtsu M 2010 Nanophotonic code embedded in embossed hologram for hierarchical information retrieval *Opt. Express* **18** 7497–505
[28] Drezet A, Genet C, Laluete J-Y and Ebbesen T W 2008 Optical chirality without optical activity: how surface plasmons give a twist to light *Opt. Express* **16** 12559–70
[29] Ueno K, Mizeikis V, Juodkazis S, Sasaki K and Misawa H 2005 Optical properties of nanoengineered gold blocks *Opt. Lett.* **30** 2158–60
[30] International Technology Roadmap for Semiconductors, http://public.itrs.net/
[31] Peper F 2009 Nanocomputers *Encyclopedia of Complexity and Systems Science* vol 14 (New York: SpringerScience+Business Media) pp 5859–89
[32] Cover T M and Thomas J A 1991 *Elements of Information Theory* (Hoboken, NJ: Wiley)
[33] Goodman J W 2004 *Introduction To Fourier Optics* (Greenwood Village, CO: Roberts & Company)
[34] Miller D A B 2007 Fundamental limit for optical components *J. Opt. Soc. Am.* B **24** A1–18
[35] Naruse M, Kawazoe T, Ohta R, Nomura W and Ohtsu M 2009 Optimal mixture of randomly dispersed quantum dots for optical excitation transfer via optical near-field interactions *Phys. Rev.* B **80** 125325
[36] Naruse M, Yatsui T, Hori H, Kitamura K and Ohtsu M 2007 Generating small-scale structures from large-scale ones via optical near-field interactions *Opt. Express* **15** 11790–7
[37] Pistol C, Dwyer C and Lebeck A R 2008 Nanoscale optical computing using resonance energy transfer logic *IEEE Micro* **28** 7–18
[38] Pistol C, Chongchitmate W, Dwyer C and Lebeck A R 2010 Architectural implications of nanoscale integrated sensing and computing *IEEE Micro* **30** 110–20
[39] Catrysse P B and Fan S 2010 Nano-patterned metallic films for use as transparent conductive electrodes in optoelectronic devices *Nano Lett.* **10** 2944
[40] Van Kampen N G (ed) 2007 *Stochastic Processes in Physics and Chemistry* (Amsterdam: Elsevier)
[41] Bak P, Tang C and Wiesenfeld K 1988 Self-organized criticality *Phys. Rev.* A **38** 364
[42] Naruse M, Kawazoe T, Yatsui T, Tate N and Ohtsu M 2011 A stochastic modeling of morphology formation by optical near-field processes *Appl. Phys.* B **105** 185–90
[43] Naruse M, Liu Y, Nomura W, Yatsui T, Aida M, Kish L B and Ohtsu M 2012 Stochastic processes in light-assisted nanoparticle formation *Appl. Phys. Lett.* **100** 193106
[44] Sangu S, Kobayashi K, Shojiguchi A, Kawazoe T and Ohtsu M 2003 Excitation energy transfer and population dynamics in a quantum dot system induced by optical near-field interaction *J. Appl. Phys.* **93** 2937–45
[45] Hori H 2001 Electronic and electromagnetic properties in nanometer scales *Optical and Electronic Process of Nano-Matters* ed M Ohtsu (Dordrecht: Kluwer) pp 1–55
[46] Markram H, Lubke J, Frotscher M and Sakmann B 1997 Regulation of synaptic efficacy by coincidence of postsynaptic APs and EPSPs *Science* **275** 213–5
[47] Tate N, Nomura W, Yatsui T, Naruse M and Ohtsu M 2008 Hierarchical hologram based on optical near- and far-field responses *Opt. Express* **16** 607–12
[48] Naruse M, Yatsui T, Nomura W, Hirose N and Ohtsu M 2005 Hierarchy in optical near-fields and its application to memory retrieval *Opt. Express* **13** 9265–71
[49] Liu Y, Morishima T, Yatsui T, Kawazoe T and Ohtsu M 2011 Size control of sol–gel-synthesized ZnO quantum dots

using photo-induced desorption *Nanotechnology* **22** 215605
[50] Yatsui T, Nomura W and Ohtsu M 2005 Self-assembly of size- and position-controlled ultralong nanodot chains using near-field optical desorption *Nano Lett.* **5** 2548
[51] Amari S and Kasabov N (ed) 1998 *Brain-like Computing and Intelligent Information Systems* (Singapore: Springer)
[52] Kish L B 2009 Noise-based logic: Binary, multi-valued, or fuzzy, with optional superposition of logic states *Phys. Lett.* A **373** 911–8
[53] Aono M, Hara M and Aihara K 2007 Amoeba-based neurocomputing with chaotic dynamics *Commun. ACM* **50** 69–72
[54] Nakagaki T, Yamada H and Toth A 2000 Maze-solving by an amoeboid organism *Nature* **407** 470
[55] Aono M, Zhu L and Hara M 2011 Amoeba-based neurocomputing for 8-city traveling salesman problem *Int. J. Unconventional Comput.* **7** 463–80
[56] Leibnitz K and Murata M 2010 Attractor selection and perturbation for robust networks in fluctuating environments *IEEE Network* **24** 14–18 (Special Issue on Biologically Inspired Networking)
[57] Tamura H, Mallet J-M, Oheim M and Burghardt I 2009 *ab initio* study of excitation energy transfer between quantum dots and dye molecules *J. Phys. Chem.* C **113** 7548
[58] Imahori H 2004 Giant multiporphyrin arrays as artificial light-harvesting antennas *J. Phys. Chem.* B **108** 6130–43
[59] Rebentrost P, Mohseni M, Kassal I, Lloyd S and Aspuru-Guzik A 2009 Environment-assisted quantum transport *New J. Phys.* **11** 033003
[60] Förster T 1948 Zwischenmolekulare Energiewanderung und Fluoreszenz (Intermolecular energy migration and fluorescence) *Ann. Phys.* **2** 55–75
[61] Crooker S A, Hollingsworth J A, Tretiak S and Klimov V I 2002 Spectrally resolved dynamics of energy transfer in quantum-dot assemblies: towards engineered energy flows in artificial materials *Phys. Rev. Lett.* **89** 186802
[62] Scholes G D and Fleming G R 2000 On the mechanism of light harvesting in photosynthetic purple bacteria: B800 to B850 energy transfer *J. Phys. Chem.* B **104** 1854–68
[63] Kubo M, Mori Y, Otani M, Murakami M, Ishibashi Y, Yasuda M, Hosomizu K, Miyasaka H, Imahori H and Nakashima S 2007 Ultrafast photoinduced electron transfer in directly linked porphyrin–ferrocene dyads *J. Phys. Chem.* A **111** 5136–43
[64] Kawazoe T, Kobayashi K, Lim J, Narita Y and Ohtsu M 2002 Direct observation of optically forbidden energy transfer between CuCl quantum cubes via near-field optical spectroscopy *Phys. Rev. Lett.* **88** 067404
[65] Itoh T, Furumiya M, Ikehara T and Gourdon C 1990 Size-dependent radiative decay time of confined excitons in CuCl microcrystals *Solid State Commun.* **73** 271–4
[66] Carmichael H J 1999 *Statistical Methods in Quantum Optics 1* (Berlin: Springer)
[67] Ingold G-L and Nazarov Y V 1992 Charge tunneling rates in ultrasmall junctions*Single Charge Tunneling* ed H Grabert and M H Devoret (New York: Plenum) pp 21–107
[68] Naruse M, Hori H, Kobayashi K and Ohtsu M 2007 Tamper resistance in optical excitation transfer based on optical near-field interactions *Opt. Lett.* **32** 1761–3
[69] Kocher P, Jaffe J and Jun B 1998 Introduction to differential power analysis and related attacks *Cryptography Research* http://www.cryptography.com/resources/whitepapers/DPATechInfo.pdf
[70] Naruse M, Hori H, Kobayashi K, Holmstrom P, Thylen L and Ohtsu M 2010 Lower bound of energy dissipation in optical excitation transfer via optical near-field interactions *Opt. Express* **18** A544–53
[71] Kawazoe T, Kobayashi K, Sangu S and Ohtsu M 2003 Demonstration of a nanophotonic switching operation by optical near-field energy transfer *Appl. Phys. Lett.* **82** 2957–9
[72] Yatsui T, Jeong H and Ohtsu M 2008 Controlling the energy transfer between near-field optically coupled ZnO quantum dots *Appl. Phys.* B **93** 199–202
[73] Nomura W, Yatsui T, Kawazoe T and Ohtsu M 2007 The observation of dissipated optical energy transfer between CdSe quantum dots *J. Nanophoton.* **1** 011591
[74] Nomura W, Yatsui T, Kawazoe T, Naruse M and Ohtsu M 2010 Structural dependency of optical excitation transfer via optical near-field interactions between semiconductor quantum dots *Appl. Phys.* B **100** 181–7
[75] Ohtsu M and Kobayashi K 2004 *Optical Near Fields* (Berlin: Springer)
[76] Haykin S 1983 *Commun. Syst.* (New York: Wiley)
[77] Kish L B 2004 Moore's law and the energy requirement of computing versus performance *IEE Proc. Circuits Devices Syst.* **151** 190–4
[78] Naruse M, Kawazoe T, Sangu S, Kobayashi K and Ohtsu M 2006 Optical interconnects based on optical far- and near-field interactions for high-density data broadcasting *Opt. Express* **14** 306–13
[79] Ohmori K, Kodama K, Muranaka T, Nabetani Y and Matsumoto T 2010 Tunneling of spin polarized excitons in ZnCdSe and ZnCdMnSe coupled double quantum wells *Phys. Status Solidi* c **7** 1642–4
[80] Seufert J, Bacher G, Schömig H, Forchel A, Hansen L, Schmidt G and Molenkamp L W 2004 Spin injection into a single self-assembled quantum dot *Phys. Rev.* B **69** 035311
[81] Naruse M, Holmström P, Kawazoe T, Akahane K, Yamamoto N, Thylén L and Ohtsu M 2012 Energy dissipation in energy transfer mediated by optical near-field interactions and their interfaces with optical far-fields *Appl. Phys. Lett.* **100** 241102
[82] Nomura W, Yatsui T, Kawazoe T, Naruse M, Runge E, Lienau C and Ohtsu M 2012 Direct observation of optical excitation transfer based on resonant optical near-field interaction *Appl. Phys.* B **107** 257–62
[83] Himeno A, Kato K and Miya T 1998 Silica-based planar lightwave circuits *IEEE J. Selected Top. Quantum Electron.* **4** 913–24
[84] Li B, Qin Y, Cao X and Sivalingam K M 2001 Photonic packet switching: architectures and performance *Opt. Networks Mag.* **2** 27–39
[85] Wang X and Wada N 2007 Spectral phase encoding of ultra-short optical pulse in time domain for OCDMA application *Opt. Express* **15** 7319–26
[86] Guilfoyle P S and McCallum D S 1996 High-speed low-energy digital optical processors *Opt. Eng.* **35** 436-442
[87] Yatsui T, Kourogi M and Ohtsu 2001 M Plasmon waveguide for optical far/near-field conversion *Appl. Phys. Lett.* **79** 4583–5
[88] Takahara J, Suguru Y, Hiroaki T, Morimoto A and Kobayashi T 1997 Guiding of a one-dimensional optical beam with nanometer diameter *Opt. Lett.* **22** 475–7
[89] Nomura W, Ohtsu M and Yatsui T 2005 Nanodot coupler with a surface plasmon polariton condenser for optical far/near-field conversion *Appl. Phys. Lett.* **86** 181108
[90] Akers S B 1978 Binary decision diagram *IEEE Trans. Comput.* **C-27** 509–16
[91] Naruse M, Miyazaki T, Kawazoe T, Sangu S, Kobayashi K, Kubota F and Ohtsu M 2005 Nanophotonic computing based on optical near-field interactions between quantum dots *IEICE Trans. Electron.* **E88-C** 1817–23
[92] Franzl T, Klar T A, Schietinger S, Rogach A L and Feldmann J 2004 Exciton recycling in graded gap nanocrystal structures *Nano Lett.* **4** 1599–1603

[93] Klar T A, Franzl T, Rogach A L and Feldmann J 2005 Super-efficient exciton funneling in layer-by-layer semiconductor nanocrystal structures *Adv. Matter.* **17** 769–73

[94] Naruse M, Runge E, Kobayashi K and Ohtsu M 2010 Efficient optical excitation transfer in layered quantum dot nanostructures networked via optical near-field interactions *Phys. Rev.* B **82** 125417

[95] Tate N, Naruse M, Nomura W, Kawazoe T, Yatsui T, Hoga M, Ohyagi Y, Sekine Y, Fujita H and Ohtsu M 2011 Demonstration of modulatable optical near-field interactions between dispersed resonant quantum dots *Opt. Express* **19** 18260–71

[96] Tung Y C and Kurabayashi K 2005 Nanoimprinted strain-controlled elastomeric gratings for optical wavelength tuning *Appl. Phys. Lett.* **86** 161113

[97] Naruse M, Mitsu H, Furuki M, Iwasa I, Sato Y, Tatsuura S and Tian M 2003 Femtosecond timing measurement and control using ultrafast organic thin films *Appl. Phys. Lett.* **83** 4869–71

[98] Keeler G A, Nelson B E, Agarwal D and Miller D A B 2000 Skew and jitter removal using short optical pulses for optical interconnection *IEEE Photon. Technol. Lett.* **12** 714–6

[99] Naruse M, Peper F, Akahane K, Yamamoto N, Kawazoe T, Tate N and Ohtsu M 2012 Skew dependence of nanophotonic devices based on optical near-field interactions *ACM J. Emerging Technol. Comput. Syst.* **8** 4:1–4:12

[100] Akahane K, Kawamura T, Okino K, Koyama H, Lan S, Okada Y, Kawabe M and Tosa M 1998 Highly packed InGaAs quantum dots on GaAs(3 1 1)B *Appl. Phys. Lett.* **73** 3411

[101] Xu Z Y, Lu Z D, Yang X P, Yuan Z L, Zheng B Z, Xu J Z, Ge W K, Wang Y, Wang J and Cang L L 1996 Carrier relaxation and thermal activation of localized excitons in self-organized InAs multilayers grown on GaAs substrates *Phys. Rev.* B **54** 11528–31

[102] Heitz R, Mukhametzhanov I, Chen P and Madhukar A 1998 Excitation transfer in self-organized asymmetric quantum dot pairs. *Phys. Rev.* B **58** R10151–4

[103] Mazur Y I, Wang Z M, Tarasov G G, Xiao M, Salamo G J, Tomm J W, Talalaev V and Kissel H 2005 Interdot carrier transfer in asymmetric bilayer InAs/GaAs quantum dot structures *Appl. Phys. Lett.* **86** 063102

[104] Kagan C R, Murray C B, Nirmal M and Bawendi M G 1996 Electronic energy transfer in CdSe quantum dot solids *Phys. Rev. Lett.* **76** 1517–20

[105] Akahane K, Ohtani N, Okada Y and Kawabe M 2002 Fabrication of ultra-high density InAs-stacked quantum dots by strain-controlled growth on InP(3 1 1)B substrate *J. Cryst. Growth* **245** 31–6

[106] Akahane K, Yamamoto N and Tsuchiya M 2008 Highly stacked quantum-dot laser fabricated using a strain compensation technique *Appl. Phys. Lett.* **93** 041121

[107] Becker W 2005 *Advanced Time-correlated Single Photon Counting Techniques* (Berlin: Springer)

[108] Hauck S 1995 Asynchronous design methodologies: an overview *Proc. IEEE* **83** 69–93

[109] Lee J, Adachi S, Peper F, Mashiko S 2005 Delay-insensitive computation in asynchronous cellular automata *J. Comput. Syst. Sci.* **70** 201–20

[110] Hurtado A, Schires K, Henning I D and Adams M J 2012 Investigation of vertical cavity surface emitting laser dynamics for neuromorphic photonic systems *Appl. Phys. Lett.* **100** 103703

[111] Kuzum D, Jeyasingh R G D, Lee B and Wong H-S P 2012 Nanoelectronic programmable synapses based on phase change materials for brain-inspired computing *Nano Lett.* **12** 2179–86

[112] Konishi M, Santo H, Hongo Y, Tajima K, Hosoi M and Saiki T 2010 Ultrafast amorphization in $Ge_{10}Sb_2Te_{13}$ thin film induced by single femtosecond laser pulse *Appl. Opt.* **49** 3470–3

[113] Warner M G and Hutchison J E 2003 Linear assemblies of nanoparticles electrostatically organized on DNA scaffolds *Nature Mater.* **2** 272–7

[114] Yatsui T, Ryu Y, Morishima T, Nomura W, Kawazoe T, Yonezawa T, Washizu M, Fujita H and Ohtsu M 2010 Self-assembly method of linearly aligning ZnO quantum dots for a nanophotonic signal transmission device *Appl. Phys. Lett.* **96** 133106

[115] Shojiguchi A, Kobayashi K, Sangu S, Kitahara K and Ohtsu M 2003 Superradiance and dipole ordering of an N two-level system interacting with optical near fields *J. Phys. Soc. Japan.* **72** 2984–3001

[116] Naruse M, Hori H, Kobayashi K, Kawazoe T and Ohtsu M 2011 Pulsation Optical pulsation mechanism based on optical near-field interactions *Appl. Phys.* B **102** 717–23

[117] Kobayashi K, Sangu S and Ohtsu M 2003 Quantum theoretical approach to optical near-fields and some related applications *Progress in Nano-Electro-Optics: I* ed M Ohtsu (Berlin: Springer) pp 119–57

[118] Wolf E and Nieto-Vesperinas M 1985 Analyticity of the angular spectrum amplitude of scattered fields and some of its consequences *J. Opt. Soc. Am.* A **2** 886–9

[119] Inoue T and Hori H 2005 Quantum theory of radiation in optical near field based on quantization of evanescent electromagnetic waves using detector mode *Progress in Nano-Electro-Optics: IV* ed M Ohtsu (Berlin: Springer) pp 127–99

[120] Naruse M, Inoue T and Hori H 2007 Analysis and synthesis of hierarchy in optical near-field interactions at the nanoscale based on angular spectrum *Japan. J. Appl. Phys.* **46** 6095–103

[121] Naruse M, Yatsui T, Nomura W, Hirose N and Ohtsu M 2005 Hierarchy in optical near-fields and its application to memory retrieval *Opt. Express* **13** 9265–71

[122] Xu M, Urbach H, de Boer D and Cornelissen H 2005 Wire-grid diffraction gratings used as polarizing beam splitter for visible light and applied in liquid crystal on silicon *Opt. Express* **13** 2303

[123] Wang J J, Walters F, Liu X, Sciortino P and Deng X 2007 High-performance, large area, deep ultraviolet to infrared polarizers based on 40 nm line/78 nm space nanowire grids *Appl. Phys. Lett.* **90** 061104

[124] Naruse M, Yatsui T, Hori H, Yasui M and Ohtsu M 2008 Polarization in optical near- and far-field and its relation to shape and layout of nanostructures *J. Appl. Phys.* **103** 113525

[125] Crozier K B, Sundaramurthy A, Kino G S and Quate C F 2003 Optical antennas: resonators for local field enhancement *J. Appl. Phys.* **94** 4632–42

[126] Yee K 1966 Numerical solution of initial boundary value problems involving maxwell's equations in isotropic media *IEEE Trans. Antennas Propagat.* **14** 302

[127] Taflove A and Hagness S C 2005 *Computational Electrodynamics: The Finite-Difference Time-Domain Method* (Boston, MA: Artech House)

[128] Lynch D W and Hunter W R 1985 Comments on the optical constants of metals and an introduction to the data for several metals *Handbook of Optical Constants of Solids* ed E D Palik (San Diego, CA: Academic) pp 275–367

[129] van Renesse R L 2005 *Optical Document Security* (Boston, MA: Artech House)

[130] McGrew S P 1990 Hologram counterfeiting: problems and solutions *Proc. SPIE* **1210** 66–76

[131] Matsumoto H and Matsumoto T 2003 Clone match rate evaluation for an artifact-metric system *IPSJ J.* **44** 1991–2001
[132] Naruse M, Yatsui T, Kawazoe T, Tate N, Sugiyama H and Ohtsu M 2008 Nanophotonic matching by optical near-fields between shape-engineered nanostructures *Appl. Phys. Exp.* **1** 112101
[133] Naruse M, Hori H, Kobayashi K, Ishikawa M, Leibnitz K, Murata M, Tate N and Ohtsu M 2009 Information theoretical analysis of hierarchical nano-optical systems in the subwavelength regime *J. Opt. Soc. Am.* B **26** 1772–9
[134] Shannon C E 1948 A mathematical theory of communications *Bell. Syst. Tech. J.* **27** 379–423
Shannon C E 1948 *Bell. Syst. Tech. J.* **27** 623–56
[135] Mitra P P and Stark J B 2001 Nonlinear limits to the information capacity of optical fibre communications *Nature* **411** 1027–30
[136] Neifeld M A and Lee M 2008 Information theoretic framework for the analysis of a slow-light delay device *J. Opt. Soc. Am.* B **25** C31–8
[137] Oittinen P and Saarelma H 1986 Average mutual information as a quality measure in imaging processes *J. Opt. Soc. Am.* A **3** 897–901
[138] Eckford A W 2007 Achievable information rates for molecular communication with distinct molecules *Bio-Inspired Models of Network, Information and Computing Systems (Budapest)* pp 313–5
[139] Yu R C, Pesce C G, Colman-Lerner A, Lok L, Pincus D, Serra E, Holl M, Benjamin K, Gordon A and Brent R 2008 Negative feedback that improves information transmission in yeast signaling *Nature* **456** 755–61
[140] Tang Z K, Yanase A, Yasui T, Segawa Y and Cho K 1993 Optical selection rule and oscillator strength of confined exciton system in CuCl thin films *Phys. Rev. Lett.* **71** 1431–4
[141] Ozbay E 2006 Plasmonics: merging photonics and electronics at nanoscale dimensions *Science* **311** 189–93
[142] Sweatlock L A, Maier S A, Atwater H A, Penninkhof J J and Polman A 2005 Highly confined electromagnetic fields in arrays of strongly coupled Ag nanoparticles *Phys. Rev.* B **71** 235408
[143] Ishikawa T, Kohmoto S and Asakawa K 1998 Site control of self-organized InAs dots on GaAs substrates by *in situ* electron-beam lithography and molecular-beam epitaxy *Appl. Phys. Lett.* **73** 1712–814
[144] Yatsui T, Kawazoe T, Ueda M, Yamamoto Y, Kourogi M and Ohtsu M 2002 Fabrication of nanometric single zinc and zinc oxide dots by the selective photodissociation of adsorption-phase diethylzinc using a nonresonant optical near field *Appl. Phys. Lett.* **81** 3651–3
[145] Torimoto T, Murakami S, Sakuraoka M, Iwasaki K, Okazaki K, Shibayama T and Ohtani B 2006 Photochemical fine-tuning of luminescent color of cadmium selenide nanoparticles: fabricating a single-source multicolor luminophore *J. Phys. Chem.* B **110** 13314–8
[146] Koyama H and Koshida N 1993 Photo-assisted tuning of luminescence from porous silicon *J. Appl. Phys.* **74** 6365–7
[147] Söderlund J, Kiss L B, Niklasson G A and Granqvist C G 1998 Lognormal size distributions in particle growth processes without coagulation *Phys. Rev. Lett.* **80** 2386–8
[148] Kish L L, Kameoka J, Granqvist C G and Kish L B 2011 Log-normal distribution of single molecule fluorescence bursts in micro/nano-fluidic channels *Appl. Phys. Lett.* **99** 143121
[149] Kertesz J and Kiss L B 1990 The noise spectrum in the model of self-organised criticality *J. Phys. A: Math. Gen.* **23** L433
[150] Meulenkamp E A 1998 Synthesis and Growth of ZnO Nanoparticles *J. Phys. Chem.* B **102** 5566–72
[151] Besner S, Kabashin A V, Winnik F M and Meunier M 2008 Ultrafast laser based 'green' synthesis of non-toxic nanoparticles in aqueous solutions *Appl. Phys.* A **93** 955–9
[152] Wu H Z, Qiu D J, Cai Y J, Xu X L, Chen N B 2002 Optical studies of ZnO quantum dots grown on Si(0 0 1) *J. Cryst. Growth* **245** 50–5
[153] Yatsui T, Takubo S, Lim J, Nomura W, Kourogi M and Ohtsu M 2003 Regulating the size and position of deposited Zn nanoparticles by optical near-field desorption using size-dependent resonance *Appl. Phys. Lett.* **83** 1716–8
[154] Wokaun A, Gordon J P, Liao P F 1982 Radiation damping in surface-enhanced Raman scattering *Phys. Rev. Lett.* **48** 957–60
[155] Boyd G T, Rasing T, Leite J R R and Shen Y R 1984 Local-field enhancement on rough surfaces of metals, semimetals, and semiconductors with the use of optical second-harmonic generation *Phys. Rev.* B **30** 519–26
[156] Bosbach J, Martin D, Stietz F, Wenzel T and Träger F 1999 Laser-based method for fabricating monodisperse metallic nanoparticles *Appl. Phys. Lett.* **74** 2605–7
[157] MacDonald K F, Fedotov V A, Pochon S, Ross K J, Stevens G C, Zheludev N I, Brocklesby W S and Emel'yanov V I 2002 Optical control of gallium nanoparticle growth *Appl. Phys. Lett.* **80** 1643–5
[158] Bredol M, Matras K, Szatkowski A, Sanetra J and Prodi-Schwab A 2009 P3HT/ZnS: a new hybrid bulk heterojunction photovoltaic system with very high open circuit voltage *Sol. Energy Mater. Sol. Cells* **93** 662–6
[159] Joo J 2000 Ionization enhancement in ionized magnetron sputter deposition *J. Vac. Sci. Technol.* **18** 23–9
[160] Naruse M, Aono M, Kim S -J, Kawazoe T, Nomura W, Hori H, Hara M and Ohtsu M 2012 Spatiotemporal dynamics in optical energy transfer on the nanoscale and its application to constraint satisfaction problems *Phys. Rev.* B **86** 125407
[161] Korte B and Vygen J 2012 *Combinatorial Optimization: Theory and Algorithms* (Berlin: Springer)
[162] Aono M, Naruse M, Kim S-J, Wakabayashi M, Hori H, Ohtsu M and Hara M 2013 Amoeba-inspired nanoarchitectonic computing: solving intractable computational problems using nanoscale photoexcitation transfer dynamics *Langmuir* in press
[163] Akahane K, Yamamoto N, Naruse M, Kawazoe T, Yatsui T and Ohtsu M 2011 Energy transfer in multi-stacked InAs quantum dots *Japan. J. Appl. Phys.* **50** 04DH05
[164] Dumeige Y, Treussart F, Alleaume R, Gacoin T, Roch J-F and Grangier P 2004 Photo-induced creation of nitrogen-related color centers in diamond nanocrystals under femtosecond illumination *J. Lumin.* **109** 61–7
[165] Mohan N, Tzeng Y-K, Yang L, Chen Y-Y, Hui Y Y, Fang C-Y, Chang H-C 2010 Sub-20-nm fluorescent nanodiamonds as photostable biolabels and fluorescence resonance energy transfer donors *Adv. Mater.* **22** 843–7
[166] Skipetrov S E 2003 Information transfer through disordered media by diffuse waves *Phys. Rev.* E **67** 036621
[167] van Tiggelen B A, Lacoste D, Rikken G L J A 2000 Magneto-optics with diffuse light *Physica* B **279** 13–16
[168] Tanaka Y and Kobayashi K 2007 Spatial localization of an optical near field in one-dimensional nanomaterial system *Physica* E **40** 297–300
[169] Yasuike T and Nobusada K 2009 Photoinduced coherent adsorbate dynamics on a metal surface: nuclear wave-packet simulation with quasi-diabatic potential energy curves using an open-boundary cluster model approach *Phys. Rev.* B **80** 035430

Appl. Phys. B (2013) 110:293–297
DOI 10.1007/s00340-012-5285-1

Applied Physics B
Lasers and Optics

RAPID COMMUNICATION

Nanophotonic droplet: a nanometric optical device consisting of size- and number-selective coupled quantum dots

Naoya Tate · Yang Liu · Tadashi Kawazoe · Makoto Naruse · Takashi Yatsui · Motoichi Ohtsu

Received: 23 October 2012 / Accepted: 9 November 2012 / Published online: 14 December 2012

Abstract Although recent advances in fabrication technologies have allowed the realization of highly accurate nanometric devices and systems, most approaches still lack uniformity and mass-production capability sufficient for practical use. We have previously demonstrated a novel technique for autonomously coupling heterogeneous quantum dots to induce particular optical responses based on a simple phonon-assisted photocuring method in which a mixture of quantum dots and photocurable polymer is irradiated with light. The cured polymer sequentially encapsulates coupled quantum dots, forming what we call a *nanophotonic droplet*. Recently, we found that each quantum dot in the mixture is preferably coupled with other quantum dots of similar size due to a size resonance effect of the optical near-field interactions between them. Moreover, every nanophotonic droplet is likely to contain the same number of coupled quantum dots. In this paper, we describe the basic mechanisms of autonomously fabricating nanophotonic droplets, and we examine the size- and number-selectivity of the quantum dots during their coupling process. The results from experiments show the uniformity of the optical properties of mass-produced nanophotonic droplets, revealed by emission from the contained coupled quantum dots, due to the fundamental characteristics of our method.

N. Tate (✉) · Y. Liu · T. Kawazoe · T. Yatsui · M. Ohtsu
The University of Tokyo, 2-11-16 Yayoi,
Bunkyo-ku, Tokyo 113-8656, Japan
e-mail: tate@nanophotonics.t.u-tokyo.ac.jp

M. Naruse
National Institute of Information and Communications
Technology, 4-2-1 Nukui-kita, Koganei, Tokyo, 184-8795, Japan

1 Introduction

Various fabrication technologies have been actively developed for realizing novel devices and systems that operate on the nanometric scale, and some of them have become commercially available [1–4]. Especially in the case nanophotonic devices [5] that operate based on optical near-field interactions between nanometric components, they must be fabricated by precisely combining and aligning nanometric components to exhibit the intended optical functions [6–9]. In order to develop the concepts and achievements of such nanometric devices and systems to a practical level where they can be employed in various applications, mass-production while maintaining uniform quality is essential.

Self-assembly is one promising method of realizing mass-production of nanometric devices [10–13]. Previously, we reported an all-autonomous technique for producing *nanophotonic droplets* [14]. A nanophotonic droplet is formed of coupled heterogeneous quantum dots (QDs) encapsulated by locally cured photocurable polymer. Encapsulation of selected micro- or nano-materials is an effective approach for preparing an isolated system from its surroundings, as well as realizing stability and durability [15–17]. During the process of fabricating nanophotonic droplets, incident light having a lower photon energy than the curing energy of the polymer is radiated. The incident light induces a phonon-assisted process [18–21], namely, multistep excitation, which cures the polymer via activated phonon levels. This process occurs only when heterogeneous QDs come close to each other. In this paper, we focus on the QD-coupling process and experimentally verified the size- and number-selectivity during the process due to the optical near-field interactions between QDs, which determines the uniformity of the optical properties

of mass-produced nanophotonic droplets. First, we briefly review the basics of the phonon-assisted photocuring method, whose details have been published in [14]. Then, we describe experiments conducted to reveal the characteristic features of the coupling process by measuring the optical properties of individual nanophotonic droplets.

2 Basics of producing a nanophotonic droplet

An optical near-field can be described with the concept of a dressed photon (DP), which is a quasi-particle representing the coupled state of a photon and an electron in a nanometric space [22]. A DP can excite a multi-mode phonon in a nanometric material and can then couple with this phonon [18–21]. The quasi-particle representing this coupled state has been named a dressed-photon-phonon (DPP). In our proposed method for producing nanophotonic droplets, we utilize the DPP for coupling heterogeneous QDs in a solution with a photocurable polymer and encapsulating them in the photocured polymer. In order to induce the photocuring process in a self-assembled manner, the mixture in the solution, in which QDs freely float, exhibiting Brownian motion, is irradiated with assisting light.

The principle of our proposed method is schematically shown in Fig. 1. We assume a mixture containing two types of QDs, QD_A and QD_B, and a photocurable polymer, and the mixture is irradiated with assisting light having photon energy $h\nu_{assist}$. The transition energies of QD_A and QD_B are $E_{A.bg}$ and $E_{B.bg}$, respectively, and the activation energy of the photocurable polymer is $E_{poly.act}$. When the energies satisfy the condition $E_{A.bg} < h\nu_{assist} < E_{poly.act} < E_{A.bg}$, the following process can be induced. If the numbers of QDs, or in other words, their volume densities, in the mixture are not sufficiently high and they rarely encounter each other, only QD_A spontaneously emits visible light by absorbing the assisting light. In this case, no subsequent physical or chemical reaction occurs. On the other hand, if the density is sufficiently high that the QDs can frequently encounter each other, multistep energy excitation of the photocurable polymer occurs due to DPP interactions between neighboring QD_A and QD_B, and the photocurable polymer is subsequently cured, as shown in the upper diagram in Fig. 1. Moreover, further irradiation with the assisting light induces multistep excitation of QD_B due to DPP interactions with the neighboring QD_A. Subsequently, QD_B spontaneously emits light with a higher photon energy than the assisting light, and the photocurable polymer in the surroundings is locally cured by absorption of the emitted light. As a result, the cured polymer encapsulates the coupled-QDs, preventing further combination or separation of the encapsulated QDs.

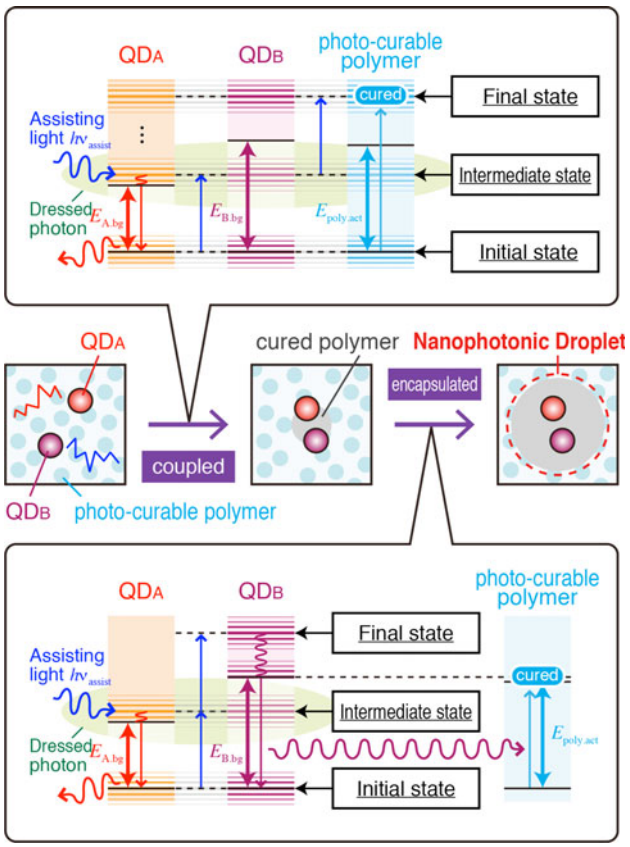

Fig. 1 Schematic diagram of process of fabricating a nanophotonic droplet based on phonon-assisted photocuring

Since the spatial distribution of the DPP energy generated on the surface of the QDs is expressed by a Yukawa function [23], the separation between the two QDs is theoretically defined by the Yukawa function. Moreover, the encapsulated coupled-QDs are necessarily composed of heterogeneous QDs, because the above sequence is induced only when QD_A and QD_B encounter each other. Descriptions of the electronic transitions via such a coupled state induced by the assisting light have been previously described in a recent report by the authors [14].

Here, we describe the size resonance effect of optical near-field interactions [24]. Because induced optical near-fields are localized around nanometric structures, and the scale of their spatial distribution is comparable to the size of the structure, as described by the Yukawa function [23], the energy of the optical near-field interactions between two nanometric structures is expected to be maximized when the sizes of the two structures are similar. From the theoretical formulation in [24], when two nanometric particles with diameters r_A and r_B come close to each other, as shown in Fig. 2a, the intensity of the size resonance effect, $I(d_{AB})$, between the two is given by

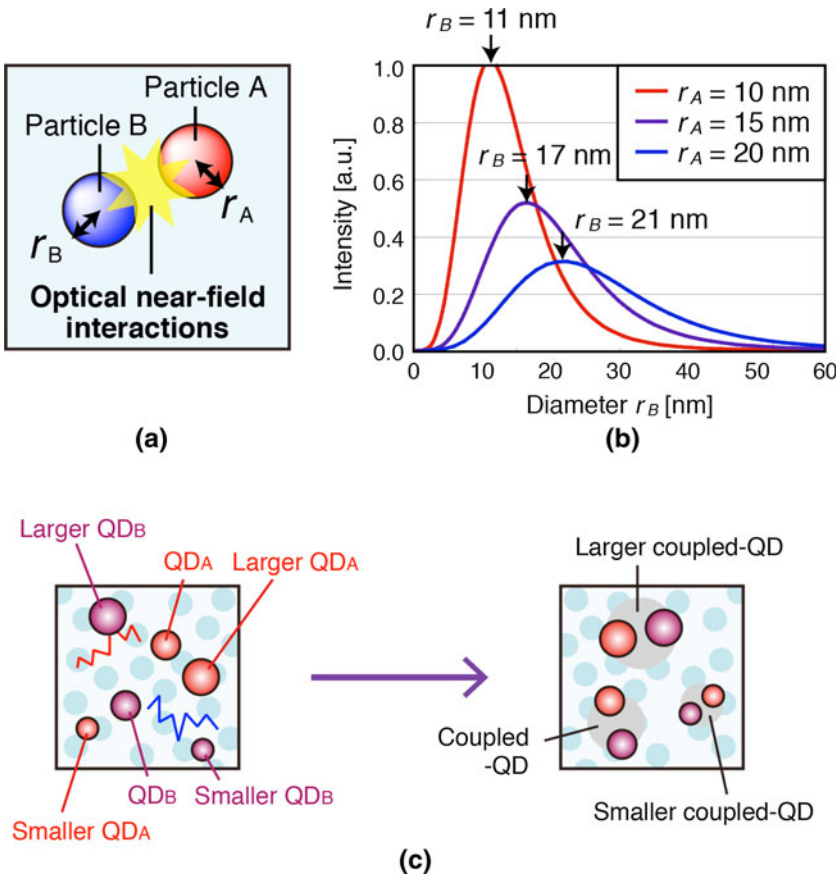

Fig. 2 **a** Schematic diagram of optical near-field interactions between two nanometric particles, and **b** intensity of optical near-field interactions between particles of various sizes. **c** Schematic diagram of size-selective coupling during fabrication of nanophotonic droplet due to the size resonance effect

$$I(d_{\mathrm{AB}}) = A\left[r_{\mathrm{A}}^3\left\{\frac{r_{\mathrm{B}}}{r_{\mathrm{A}}}\cosh\left(\frac{r_{\mathrm{B}}}{r_{\mathrm{A}}}\right) - \sinh\left(\frac{r_{\mathrm{B}}}{r_{\mathrm{A}}}\right)\right\} \times\left(\frac{1}{d_{\mathrm{AB}}} + \frac{r_{\mathrm{A}}}{d_{\mathrm{AB}}^2}\right) \times \exp\left(-\frac{d_{\mathrm{AB}}}{r_{\mathrm{A}}} - 1\right)\right]^2, \quad (1)$$

where d_{AB} is the distance between the two particles, and A is a proportionality constant. Figure 2b plots the normalized intensity of the optical near-field interactions in the cases where $r_{\mathrm{A}} = 10$, 15, and 20 nm. As shown, other particles with similar sizes, namely, $r_{\mathrm{B}} = 11$, 17, and 21 nm, respectively, are likely to produce more intense interactions.

Because our phonon-assisted curing method is fundamentally induced by the optical near-field interactions between two heterogeneous QDs, QDs with similar sizes are assumed to be preferably coupled with each other due to this size resonance effect, as schematically shown in Fig. 2c. Moreover, encapsulation of the coupled-QDs begins almost as soon as the QDs are coupled. This means that each nanophotonic droplet is likely to contain only one pair of coupled-QDs. Because actual QDs necessarily exhibit a size distribution, and their size distribution causes inhomogeneous emission properties, such size- and number-selectivity of the QDs during the nanophotonic droplet fabrication process is expected to result in uniform emission spectra and emission intensity of mass-produced nanophotonic droplets.

3 Experimental demonstrations

In order to demonstrate the uniformity of nanophotonic droplets, first we experimentally produced and extracted nanophotonic droplets by our proposed method. Specifically, as $\mathrm{QD_A}$ and $\mathrm{QD_B}$ in Fig. 1, we used solutions of CdSe-QDs and ZnO-QDs, which emit visible and ultraviolet (UV) light, respectively. These QD solutions were mixed with a UV-curable polymer and irradiated with visible assisting light whose photon energy was high enough to excite excitons in the CdSe-QDs but too low to excite excitons in the ZnO-QDs and the UV-curable polymer. Figure 3 shows the energy conditions for the following experiment. We used commercially available CdSe-QDs (Ocean Optics, *Evidot*) and ZnO-QDs prepared by sol–gel synthesis using photo-induced desorption [25]. The QD solutions were then dispersed in a UV-curable polymer (NORLAND, *NOA 65*) and irradiated with assisting light emitted from a 120-mW laser diode with a photon energy of 2.71 eV. These conditions fulfilled the previously described energy conditions for inducing the

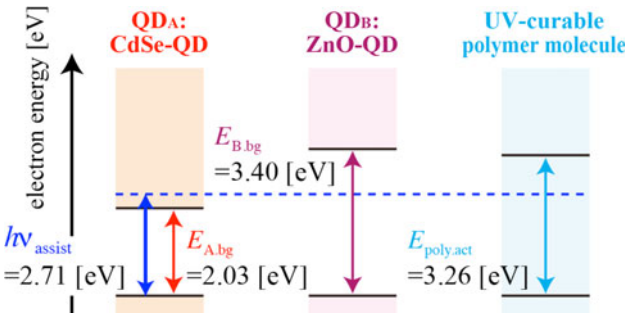

Fig. 3 Energy diagram of the experimental conditions

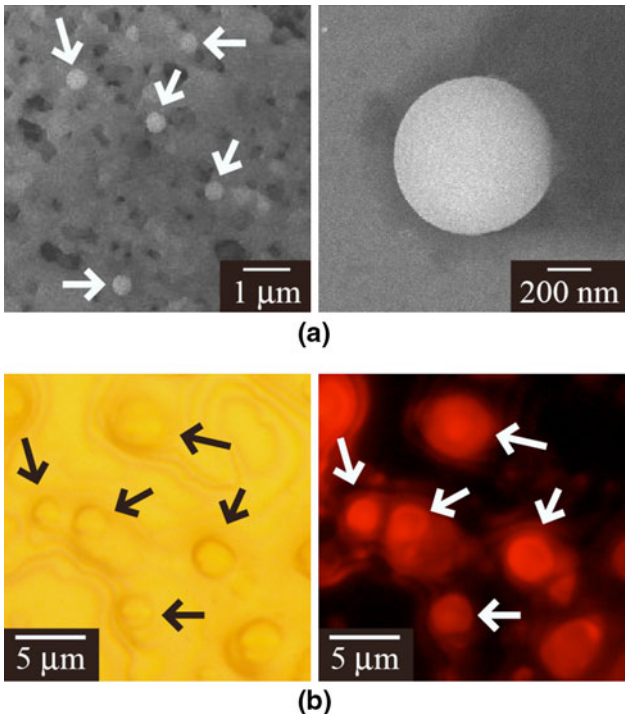

Fig. 4 **a** SEM images and **b** microscope images of mass-produced nanophotonic droplets

sequential process of the phonon-assisted photocuring method. The total amount of the mixed solution was limited to 50 μL to maintain spatially uniform illumination. This volume contained about 10^{14} CdSe-QDs and about 10^{12} ZnO-QDs.

Under these experimental conditions, the QDs can be assumed to encounter each other at a sufficiently high frequency to induce the phonon-assisted photocuring. After irradiation with the assisting light, the mixture was separated into cured and uncured materials by centrifugation at 10,000 rpm for 5 min. The extracted cured material, which was assumed to contain a large number of nanophotonic droplets, was dispersed in a toluene solution and uniformly spin-coated on a Si substrate. Figure 4a, b show SEM images and microscope images of materials irradiated with assisting light for 30 and 90 min, respectively. As shown, with the shorter irradiation time, nanophotonic droplets with quite similar sizes were successfully obtained. The diameter of each nanophotonic droplet was about 500 nm. With the longer irradiation time, the nanophotonic droplets increased in size to micrometer level and were successfully observed in the microscope images, as shown in Fig. 4b. The images on the left- and right-hand sides show a sample under white-light and UV-light illumination, respectively. As shown in the image on the right-hand side, each nanophotonic droplet exhibited emission from the contained CdSe-QDs.

In order to compare multiple emission spectra of individual nanophotonic droplets, we constructed a two-dimensional map of the emission spectra of samples obtained with a micro-spectrophotometer (NFGP-740, JASCO, Japan). Samples were irradiated by a laser diode with a photon energy of 3.06 eV. The spatial resolution of the experimental setup was expected to be less than 200 nm. Figure 5a shows a two-dimensional emission image of aggregated nanophotonic droplets. The inset represents a bright-field image under white-light illumination. The individual emission spectra of nanophotonic droplets A, B, C, and D indicated in Fig. 5a are respectively plotted in Fig. 5b.

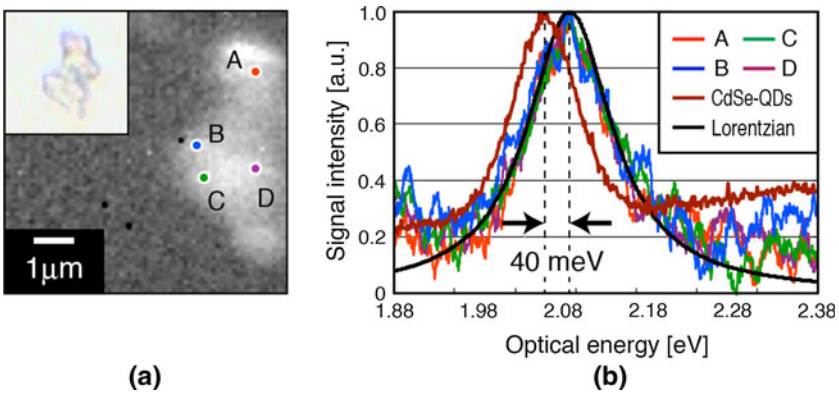

Fig. 5 **a** Obtained emission image of aggregated nanophotonic droplets. **b** Emission spectra of multiple nanophotonic droplets, collectively observed emission spectrum of CdSe-QDs, and a Lorentzian fitted curve

As shown, the heights and widths of the emission spectra are quite similar to each other. Because they can be simply fitted by a single Lorentzian, which is generally applied to approximate the emission spectrum of a single illuminant, it is considered that the nanophotonic droplets contain single CdSe-QDs of similar size and coupled ZnO-QDs. This demonstrates the uniformity of the optical properties of mass-produced nanophotonic droplets.

We also measured the collectively observed emission spectrum of multiple CdSe-QDs, as shown in Fig. 5b. The sample was prepared by mixing a solution of CdSe-QDs and a UV-curable polymer, and was directly spin-coated on a substrate without any irradiation with assisting light. There was a 40 meV difference between the peak optical energy in the spectra of the individual nanophotonic droplets and the collective CdSe-QDs. Such a large difference is due to not only re-absorption of emission within the collective CdSe-QDs, but also size-selectivity during the coupling process between CdSe-QD and ZnO-QD. The result indicates that ZnO-QDs preferably coupled with *smaller* CdSe-QDs in the mixture and revealed such uniformity in their emission spectra.

4 Summary

In this paper, we described the uniformity of the optical properties of mass-produced nanophotonic droplets, made possible by a novel fabrication process based on optical near-field interactions between nanometric components. From the results of our experimental demonstrations, we verified that such uniformity was physically ensured by the size-selectivity during the QD-coupling process, and that each nanophotonic droplet contained the same number of QDs, exhibiting the expected homogeneity. These findings show the fundamental features of our proposed method, where we can obtain a large number of nanophotonic droplets with homogeneous optical properties with an all-autonomous fabrication process. Our method can be easily applied to various applications where novel nanophotonics and nanotechnologies are required for further practical development.

Acknowledgments A part of this work was supported by the Research and Development Program for Innovative Energy Efficiency Technology funded by the New Energy and Industrial Technology Development Organization (NEDO), Japan.

References

1. M.T. Bohr, IEEE Trans. Nanotechnol. **1**, 56–62 (2002)
2. J. Melngailis, A.A. Mondelli, I.L. Berry III, R. Mohondro, J. Vacuum Sci. Technol. B (Microelectron. Nanometer Struct.) **16**, 927–957 (1998)
3. C.A. Mirkin, S.H. Hong, L. Demers, Chem. Phys. Chem. **2**, 37–39 (2001)
4. J.G. Chase, B.W. Smith, J. Intell. Mater. Syst. Struct **12**, 807–817 (2001)
5. M. Ohtsu, T. Kawazoe, T. Yatsui, M. Naruse, IEEE J. Sel. Top. Quantum Electron. **14**, 1404–1417 (2008)
6. T. Kawazoe, K. Kobayashi, S. Sangu, M. Ohtsu, Appl. Phys. Lett. **82**, 2957–2959 (2003)
7. T. Kawazoe, K. Kobayashi, K. Akahane, M. Naruse, N. Yamamoto, M. Ohtsu, Appl. Phys. B Lasers Opt. **84**, 243–246 (2006)
8. W. Nomura, T. Yatsui, M. Ohtsu, Appl. Phys. B Lasers Opt. **84**, 257–259 (2006)
9. N. Tate, H. Sugiyama, M. Naruse, W. Nomura, T. Yatsui, T. Kawazoe, M. Ohtsu, Opt. Express **17**, 11113–11121 (2009)
10. B.Q. Wei, R. Vajtai, Y. Jung, J. Ward, R. Zhang, G. Ramanath, P.M. Ajayan, Nature **416**, 495–496 (2002)
11. B.A. Parviz, D. Ryan, G.M. Whitesides, IEEE Trans. Adv. Packag. **26**, 233–241 (2003)
12. Y.I. Mazur, Z.M. Wang, G.G. Tarasov, M. Xiao, G.J. Salamo, J.W. Tomm, V. Talalaev, H. Kissel, Appl. Phys. Lett. **86**, 063102 (2005)
13. M.P. Stoykovich, M. Müller, S. Ouk Kim, H.H. Solak, E.W. Edwards, J.J. de Pablo, P.F. Nealey, Science **308**, 1442–1446 (2005)
14. N. Tate, Y. Liu, T. Kawazoe, M. Naruse, T. Yatsui, M. Ohtsu, Appl. Phys. B Lasers Opt. doi:10.1007/s00340-012-5249-5 (online first 2012)
15. Y. Zhou, Z.L. Wang, Z.R. Ma, Y. Ebina, K. Takada, T. Sasaki, Curr. Nanosci. **3**, 155–160 (2007)
16. N. Murase, M. Ando, AIST Today **10**, 10 (2010)
17. H. Ren, S. Xu, D. Ren, S.-T. Wu, Opt. Exp. **19**, 1985–1990 (2011)
18. S. Yukutake, T. Kawazoe, T. Yatsui, W. Nomura, K. Kitamura, M. Ohtsu, Appl. Phys. B Lasers Opt. **99**, 415–422 (2010)
19. H. Fujiwara, T. Kawazoe, M. Ohtsu, Appl. Phys. B **98**, 283–289 (2010)
20. T. Kawazoe, M.A. Mueed, M. Ohtsu, Appl. Phys. B **104**, 747–754 (2011)
21. K. Kitamura, T. Kawazoe, M. Ohtsu, Appl. Phys. B **107**, 293–299 (2012)
22. T. Kawazoe, K. Kobayashi, S. Takubo, M. Ohtsu, J. Chem. Phys. **122**(024715), 1–5 (2005)
23. M. Ohtsu Eds., *Progress in Nano-Electro-Optics II* (Springer, Berlin, 2004)
24. S. Sangu, K. Kobayashi, M. Ohtsu, J. Microsc. **202**, 279–285 (2001)
25. Y. Liu, T. Morishima, T. Yatsui, T. Kawazoe, M. Ohtsu, Nanotechnology **22**(215605), 1–5 (2011)

Unveiling the mechanisms of dressed-photon–phonon etching based on hierarchical surface roughness measure

Makoto Naruse,[1,a)] Takashi Yatsui,[2] Wataru Nomura,[2] Tadashi Kawazoe,[2] Masaki Aida,[3] and Motoichi Ohtsu[2]

[1]*Photonic Network Research Institute, National Institute of Information and Communications Technology, 4-2-1 Nukui-kita, Koganei, Tokyo 184-8795, Japan*
[2]*Department of Electrical Engineering and Information Systems/Nanophotonics Research Center, School of Engineering, The University of Tokyo, 2-11-16 Yayoi, Bunkyo-ku, Tokyo 113-8656, Japan*
[3]*Tokyo Metropolitan University, 6-6 Asahigaoka, Hino, Tokyo 191-0065, Japan*

(Received 17 December 2012; accepted 7 February 2013; published online 20 February 2013)

Dressed-photon–phonon (DPP) etching is a disruptive technology in planarizing material surfaces because it completely eliminates mechanical contact processes. However, adequate metrics for evaluating the surface roughness and the underlying physical mechanisms are still not well understood. Here, we propose a two-dimensional hierarchical surface roughness measure, inspired by the Allan variance, that represents the effectiveness of DPP etching while conserving the original two-dimensional surface topology. Also, we build a simple physical model of DPP etching that agrees well with the experimental observations, which clearly shows the involvement of the intrinsic hierarchical properties of dressed photons, or optical near-fields, in the surface processing.
 [http://dx.doi.org/10.1063/1.4793233]

Nanophotonics, which exploits light–matter local interactions on the nanometer scale, has been intensively investigated from a variety of aspects, ranging from fundamental science, such as atom/molecule and optical near-field interactions[1] and spectroscopy,[2] to a number of practical applications, including information security,[3] computing,[4] the environment and energy,[5] and healthcare,[6] to name a few. What we particularly address in this letter is nanofabrication involving optical near-field processes.[7,8]

The idea is to induce a nanofabrication process, either in the form of material desorption or deposition, selectively in a region where optical near-fields are present. Nowadays, the optical near-field is understood as a virtual photon coupled with an excited electron, called a dressed photon (DP). DPs can interact with phonons in the crystal lattice structure of nanomaterials in a coherent manner.[7] The combined coupled state of a DP and a coherent phonon, which is referred to as dressed-photon–phonon (DPP), has a higher energy than those of the DP and the incident photon.[7] Therefore, a DPP can induce photochemical reactions even under irradiation with a low photon energy at which photochemical reactions are conventionally inactive.[8,9] Such a process has been called a phonon-assisted process and has been applied to numerous demonstrations, including photochemical vapor deposition,[10] photolithography,[11] the generation of smaller-scale structures using larger-scale templates via optical near-fields,[12] and energy up-conversion devices,[13] among others.

In particular, the DPP-based surface etching, or flattening, proposed by Yatsui *et al.*, which planarizes the surfaces of devices without any mechanical contact processes, is an interesting and industrially important technique.[8,9,14,15] It selectively induces photochemical reactions in regions on a surface where DPPs are excited, namely, in the vicinity of regions possessing fine-scale rough structures, leading to reduced surface roughness. Planarization of surfaces is important for various devices such optical elements,[8] solid-state materials, such as silicon wafers, diamonds,[9] and so on.

There are, however, several unsolved, important issues associated with DPP etching. The first concerns a suitable metric for evaluating the surface roughness. Conventionally, the roughness average, R_a, defined as the average of the absolute values of the deviation from the average height, has been widely used. However, by definition, R_a depends on the size of the region-of-interest (ROI). Furthermore, with such a measure, the effects provided by DPPs are concealed, and so it has been difficult to obtain physical insights into the underlying mechanisms which would serve to reveal the ultimate limitations of the method and to improve/optimize fabrication processes.

In fact, with a view to resolving these issues, we have previously proposed a parametric statistical spectrum analysis method for evaluating surfaces flattened by DPP etching.[15] Furthermore, in Ref. 9, we developed another measure, namely, the standard deviation of the height differences of two adjacent areas averaged over every l pixels, inspired by the Allan variance[16] that is widely applied in evaluating the stability of time-domain signals. Specifically, letting $\overline{z_k^{(l)}}$ be the average height over every l pixels, the measure was defined as $R(l) = \sqrt{\left\langle \left(\overline{z_{k+1}^{(l)}} - \overline{z_k^{(l)}} \right)^2 / 2 \right\rangle}$. These methods allowed us to see the reduction in surface roughness correlated with spatially finer/coarser structures.[9,15]

Nevertheless, important concerns still remain. One is that both of the above-mentioned methods must convert the original two-dimensional (2D) surface profile data to one-dimensional (1D) data, on which the analysis is made. Namely, the topology inherent in the experimental data is destroyed, which is a large impediment to gaining an accurate physical understanding of the mechanisms involved. By overcoming these weaknesses, we will be able understand

[a)]E-mail: naruse@nict.go.jp.

the fundamental mechanisms of DPP etching, as well as the physical and technological limitations.

In this letter, we propose a metric for evaluating surface roughness while preserving the original topology, what we call the *two-dimensional, hierarchical surface roughness measure*, or THM for short. Furthermore, taking into consideration the intrinsic hierarchical properties of dressed photons, we propose a simple physical model representing the principal attributes of DPP etching. The resultant data agree well with experiments.

We first review the principles of DPP etching proposed by Yatsui *et al.*[8] The surface of a device to be etched is irradiated with a light beam. If the surface is rough, DPPs will be generated in the vicinity of the corresponding rough structures, and photochemical reactions can be induced selectively in the regions where the DPPs are generated.[8,9] More specifically, in the case of the experiments described below, chlorine gas (Cl_2) is filled in the space around the device to be processed, and chlorine radicals ($Cl^{\bullet}$) are selectively produced from the Cl_2 gas in the regions where DPPs are generated. The $Cl^{\bullet}$ then reacts with and etches the material, decreasing the local surface roughness, or bumps. Once the rough structures are eliminated, the DPPs will disappear, thus automatically terminating the photochemical reaction process. This physical principle is schematically shown in Fig. 1(a). In the experiment, the device under study was a (001) GaN substrate, which was subjected to 30 min of irradiation with continuous-wave (CW) light having a wavelength of 532 nm in a chlorine gas (Cl_2) atmosphere at 200 Pa. Figures 1(b) and 1(c), respectively, show surface profile images taken by an atomic force microscope (AFM) before and after the etching process. The surface heights were measured at 256×256 equally spaced sampling points in a $5\,\mu\text{m} \times 5\,\mu\text{m}$ area. The value of R_a decreased from 0.23 nm to 0.14 nm.

Now, assume that the height of a surface profile is given by $h(i,j)$, where the indexes (i,j) specify the position among $N \times N$ sampling points. Both i and j are positive integers ranging from 1 to N. The idea of the proposed measure, THM, is (1) to evaluate the average height over $l \times l$ pixels (denoted by $h_P^{(l)}$); (2) to see how $h_P^{(l)}$ differs from the average height of its four neighbors, namely, the north ($h_N^{(l)}$), south ($h_S^{(l)}$), east ($h_E^{(l)}$), and west ($h_W^{(l)}$) areas; and then (3) to calculate the variance of such differences in the entire region of the sample. A schematic illustration of $h_P^{(l)}$ is shown in Fig. 2(a). As a function of the scale parameter, or the size of the local area (l), the THM is defined by

$$\sigma_{2D}^2(l) = \left\langle \left(h_P^{(l)} - \left(\frac{h_N^{(l)} + h_S^{(l)} + h_E^{(l)} + h_W^{(l)}}{4} \right) \right)^2 \right\rangle, \quad (1)$$

where $\langle\ \rangle$ means taking the average over all areas of a given sample. For simplicity, we assume that N and l are both powers of 2. When the size of a single local area is given by $l = 2^k$, there are in total $N/2^k \times N/2^k$ areas at the corresponding scale, and the average height in an area specified by (s,t), corresponding to $h_P^{(l)}$ in Eq. (1), is given by

$$h^{(l)}(s,t) = \sum_{m=1\cdots,l,\ n=1,\cdots,l} h(l \times (s-1) + m, l \times (t-1) + n)/l^2. \quad (2)$$

Here, $h_N^{(l)}$, $h_S^{(l)}$, $h_E^{(l)}$, and $h_W^{(l)}$, respectively, correspond to $h^{(l)}(s,t+1)$, $h^{(l)}(s,t-1)$, $h^{(l)}(s+1,t)$, and $h^{(l)}(s-1,t)$. The indexes s and t are natural numbers ranging from 1 to $N/2^k$.

In an experimental demonstration using GaN as the sample, N was 256, and we used scale parameters l of 1, 2, 4, 8, 32, and 64 pixels, corresponding to physical lengths of about 19.5, 39.0, 78.1, 156.2, 312.5, 625, and 1250 nm, respectively. Figures 2(b) and 2(c) schematically represent the scale- and position-dependent metric $E_P^{(l)} = h_P^{(l)} - (h_N^{(l)} + h_S^{(l)} + h_E^{(l)} + h_W^{(l)})/4$, which we call the *hierarchical etching score* (HES), before and after the optical processing, respectively. As demonstrated in Fig. 3(a), we can clearly see that the

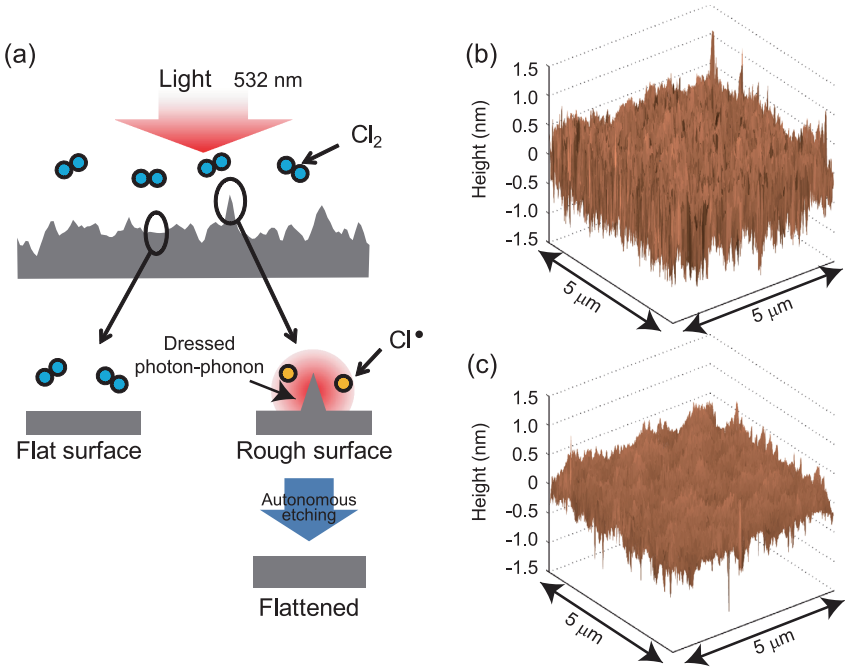

FIG. 1. (a) Schematic illustration of the dressed-photon–phonon etching. ((b) and (c)) Surface height profiles of a (001) GaN substrate (b) before and (c) after 30-min irradiation with CW light at a wavelength of 532 nm in a Cl_2 atmosphere at 200 Pa. The roughness average, R_a, decreased from 0.23 nm to 0.14 nm.

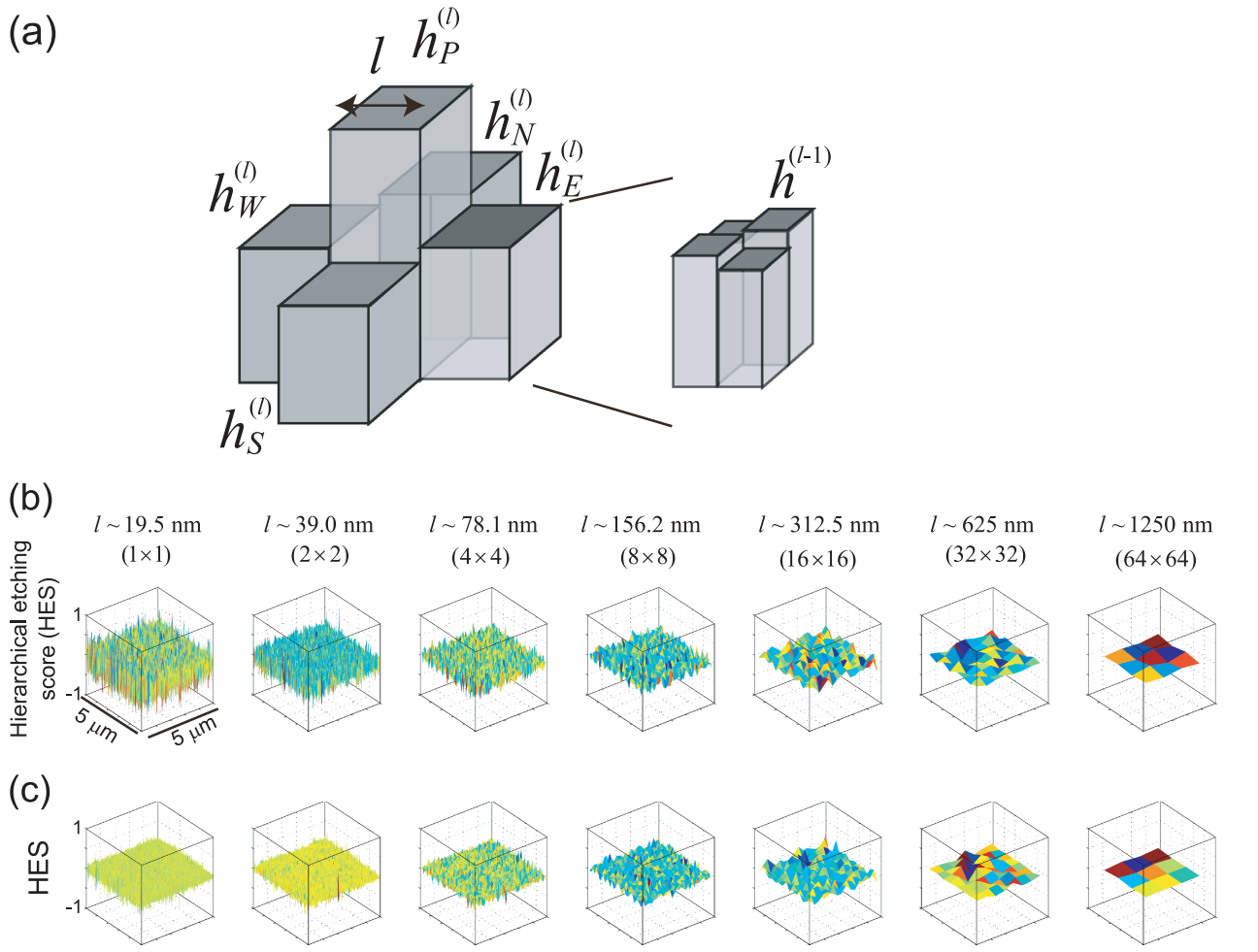

FIG. 2. (a) Schematic diagram of the proposed two-dimensional hierarchical surface roughness measure (THM). ((b) and (c)) The two-dimensional distribution of the HES ($E_P^{(l)}$) (b) before and (c) after the DPP etching.

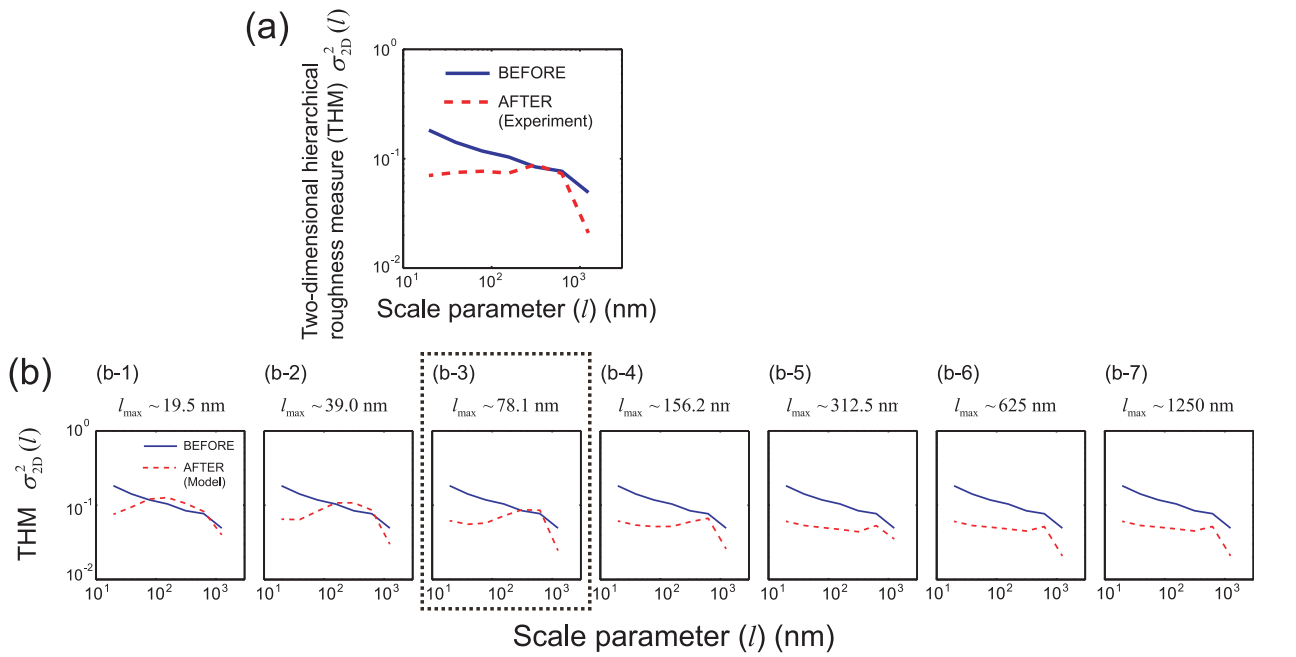

FIG. 3. (a) The THM, $\sigma_{2D}^{(l)}$, based on experimental results for GaN surfaces. (b) Evaluation of THM, $\sigma_{2D}^{(l)}$, with respect to the calculated surface profiles derived through the proposed DPP etching model for different values of the maximum physical scale, l_{max}.

dashed curve, which is the THM of the surface after DPP etching, is reduced compared with the solid curve, which is the THM of the surface before the etching.

As mentioned above, the surface etching is autonomously induced at locations where the DPPs are generated by the roughness of the sample under study. We may envisage a physical picture in which etching is preferentially induced in regions where a tiny bumps exist. Namely, the etching may be dominated by the HES of the tiniest scale, $E_P^{(1)}$, concerning the surface roughness at the tiniest scale. Based on such a picture, we can construct a physical model of the DPP etching as follows:

(a) Calculate the HES *at the tiniest scale*, $E_P^{(1)} = h_P^{(1)} - (h_N^{(1)} + h_S^{(1)} + h_E^{(1)} + h_W^{(1)})/4$, at each of the positions of a given device.
(b) Find the position that gives the maximum $E_P^{(1)}$. Decrease the height of that position by an amount Δ_h.
(c) Repeat the process until all values calculated at step (a) above are smaller than a certain threshold value.

We applied the above surface etching strategy to the original, unpolished surface profile of the GaN device. Through such modeling, the resultant surface roughness indeed decreased as compared with the original one, but the resulting THM, $\sigma_{2D}^2(l)$, was as shown in Fig. 3(b-1), which did *not* agree with the experimental reality shown in Fig. 3(a).

We should consider that this is clear evidence that the DPP etching does *not* depend only on the finer structures. In fact, dressed photons, or optical near-fields, appear in a hierarchical manner depending on the spatial fine/coarse structures.[17,18] Suppose that there are two spheres whose radii are, respectively, given by a_P and a_S (Fig. 4(a)). The near-field optical potential is given by[18]

$$V(r) = \sum_{i=S}^{P} \frac{\exp(-\pi r/a_i)}{r}. \tag{3}$$

The scattered signal obtained from the interaction between these two spheres is given by

$$I(r_{SP}) \equiv \left| \int\int \nabla_{r_P} V(|\boldsymbol{r}_P - \boldsymbol{r}_S|) d^3 r_S d^3 r_P \right|^2 \propto \left[a_P^3 \left\{ \frac{a_S}{a_P} \cosh\left(\frac{\pi a_S}{a_P}\right) - \frac{1}{\pi} \sinh\left(\frac{\pi a_S}{a_P}\right) \right\} \left(\frac{1}{r_{SP}} + \frac{a_P}{\pi r_{SP}^2} \right) \exp\left(-\frac{\pi r_{SP}}{a_P} \right) \right]^2, \tag{4}$$

where the center positions of the two spheres are, respectively, given by $\boldsymbol{r}_S$ and $\boldsymbol{r}_P$, and the distance between $\boldsymbol{r}_S$ and $\boldsymbol{r}_P$ is given by r_{SP}.[18] We can consider that a_S represents the surface roughness, whereas a_P indicates the size of the environment, containing chlorine radicals that could interact with the surface roughness. The effect of the interactions involving these two spheres is defined by the quantity given by Eq. (4) divided by the square of the total volume of the two spheres, so that the evaluation is made in the dimension of per unit area. The solid, dotted, and dashed curves in Fig. 4(a) indicate the normalized quantity given by Eq. (4) divided by $(a_P^3 + a_S^3)^2$, which represents the strength of the interaction between the two spheres, as a function of a_P when a_S is given by 10, 20, and 40 nm, respectively. Notice that the peak of the signal is obtained when the sizes of the two spheres are comparable. It turns out that, by regarding a_S as the spatial fine/coarse surface roughness of the structure, the interaction may be stronger at a coarser scale, rather than at a finer scale, when the roughness of the sample dominates on a large scale. Therefore, we should modify the DPP etching model by taking into account the hierarchical attributes of dressed photons, so that the surface flatness is evaluated on multiple scales, and a reduction in surface roughness may be induced in a region that gives the maximum HES. Specifically:

(a′) Calculate the HES, $E_P^{(1)} = h_P^{(1)} - (h_N^{(1)} + h_S^{(1)} + h_E^{(1)} + h_W^{(1)})/4$, at each of the regions of a given device *and* at multiple scales: $l = 1, 2, 4, \cdots, l_{\max}$. The maximum scale considered is given by $l_{\max}$.
(b′) Find the area that gives the maximum $E_P^{(l)}$ among all of the calculated positions and scales. Decrease the height of the corresponding area by an amount Δ_h.
(c′) Repeat the process until all values calculated at step (a′) are smaller than a certain threshold value.

In this model, we modify the maximum scale to be considered, $l_{\max}$, in step (a′) and investigate the physical scales that affect the surface etching. The threshold at step (c′) was assumed to be sufficiently small and was set at 0.1. Figure 3(b) shows the THM, $\sigma_{2D}^2(l)$, for different values of $l_{\max}$,

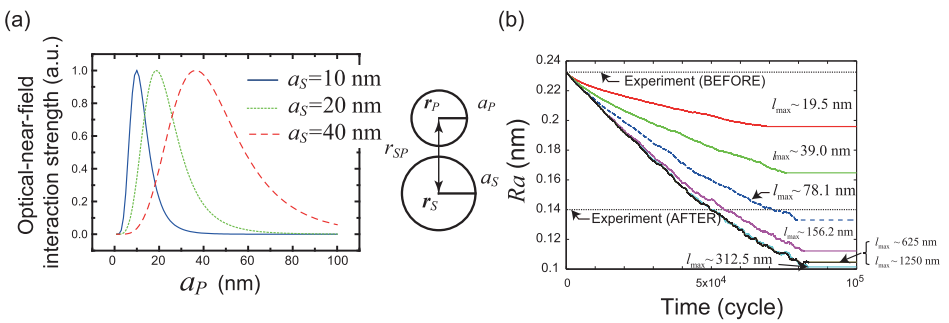

FIG. 4. (a) The hierarchical nature of near-field interactions based on two-sphere model where the radii are, respectively, given by a_S and a_P. (b) Simulated time evolution of the roughness average (R_a) with respect to the maximum physical scale in the DPP etching model.

namely, 1, 2, 4, 8, 16, 32, and 64. We can see that the resultant $\sigma_{2D}^2(l)$ is consistent with the experimental demonstrations shown in Fig. 3(b-1) when l_{max} is 4, corresponding to a physical length of 78.1 nm. Also, Fig. 4(b) shows the simulated time evolution of R_a depending on different l_{max} values. The resultant R_a in the experiment was 0.14 nm, whereas the converged R_a obtained through the modeling was 0.13 nm when l_{max} was 78.1 nm. This is another indication of the consistency between the proposed model and the experiment. These results suggest that the hierarchical properties of dressed photons inevitably affect the surface etching. With this model, we can predict the converged surface characteristics and the achievable flatness of given initial surfaces.

Finally, we remark on the converged surface characteristics. Minimizing the HES to zero, in the best case, indicates that the height at a particular area is equal to the average of its surrounding areas. This is exactly the property of the so-called harmonic functions, which are solutions of Laplace's equations.[19] What is particularly different from the conventional harmonic functions is that the solutions should minimize the HES at multiple scales (not just at a single scale). Nevertheless, such considerations inspired by harmonic functions support the fact that completely flat surfaces may *not* be the only converged pattern of DPP etching.

In conclusion, we proposed a two-dimensional hierarchical surface roughness measure (THM) for evaluating the surface roughness of a surface planarized by DPP etching. Taking into account the intrinsic hierarchical properties of dressed photons, we built a simplified physical model of the DPP etching, which agreed well with the experimental demonstration. It clearly demonstrates that the DPP etching involves multi-scale structures of the rough surface being processed. This study has unveiled one fundamental mechanism of nanofabrication, and we consider that the method described here will help to predict the achievable performance of nanofabrication and to optimize fabrication processes.

A part of this work was supported by Grants-in-Aid for Scientific Research from the Japan Society for the Promotion of Science, the Advanced Low Carbon Technology Research and Development Program of the Japan Science and Technology Agency, the Research and Development Program of Innovative Energy Efficiency Technology of the New Energy and Industrial Technology Development Organization, and a research grant (Basic Research) from the TEPCO Memorial Foundation.

[1]S. Tojo and M. Hasuo, Phys. Rev. A **71**, 012508 (2005).
[2]M. Aeschlimann, M. Bauer, D. Bayer, T. Brixner, F. Javier, G. de Abajo, W. Pfeiffer, M. Rohmer, C. Spindler, and F. Steeb, Nature **446**, 301 (2007).
[3]M. Naruse, N. Tate, and M. Ohtsu, J. Opt. **14**, 094002 (2012).
[4]M. Naruse, M. Aono, S.-J. Kim, T. Kawazoe, W. Nomura, H. Hori, M. Hara, and M. Ohtsu, Phys. Rev. B **86**, 125407 (2012).
[5]T. Franzl, T. A. Klar, S. Schietinger, A. L. Rogach, and J. Feldmann, Nano Lett. **4**, 1599 (2004).
[6]C. Pistol, C. Dwyer, and A. R. Lebeck, IEEE MICRO **28**, 7 (2008).
[7]A. Sato, Y. Tanaka, F. Minami, and K. Kobayashi, J. Lumin. **129**, 1718 (2009).
[8]T. Yatsui, K. Hirata, W. Nomura, Y. Tabata, and M. Ohtsu, Appl. Phys. B. **93**, 55 (2008).
[9]T. Yatsui, W. Nomura, M. Naruse, and M. Ohtsu, J. Phys. D **45**, 475302 (2012).
[10]T. Kawazoe, K. Kobayashi, S. Takubo, and M. Ohtsu, J. Chem. Phys. **122**, 024715 (2005).
[11]H. Yonemitsu, T. Kawazoe, K. Kobayashi, and M. Ohtsu, J. Lumin. **122–123**, 230 (2007).
[12]M. Naruse, T. Yatsui, H. Hori, K. Kitamura, and M. Ohtsu, Opt. Express **15**, 11790 (2007).
[13]H. Fujiwara, T. Kawazoe, and M. Ohtsu, Appl. Phys. B **98**, 283 (2010).
[14]T. Yatsui, K. Hirata, Y. Tabata, Y. Miyake, Y. Akita, M. Yoshimoto, W. Nomura, T. Kawazoe, M. Naruse, and M. Ohtsu, Appl. Phys. B **103**, 527 (2011).
[15]M. Naruse, T. Yatsui, W. Nomura, K. Hirata, Y. Tabata, and M. Ohtsu, J. Appl. Phys. **105**, 063516 (2009).
[16]D. W. Allan, Proc. IEEE **54**, 221 (1966).
[17]M. Naruse, T. Inoue, and H. Hori, Jpn. J. Appl. Phys., Part 1 **46**, 6095 (2007).
[18]K. Kobayashi, S. Sangu, and M. Ohtsu, "Quantum theoretical approach to optical near-fields and some related applications," in *Progress in Nano-Electro-Optics I*, edited by M. Ohtsu (Springer-Verlag, Berlin, 2003), pp. 119–157.
[19]L. C. Evans, *Partial Differential Equations* (American Mathematical Society, Providence, 2010).

Appl. Phys. B (2013) 110:39–45
DOI 10.1007/s00340-012-5249-5

Applied Physics B
Lasers and Optics

Fixed-distance coupling and encapsulation of heterogeneous quantum dots using phonon-assisted photo-curing

Naoya Tate · Yang Liu · Tadashi Kawazoe · Makoto Naruse · Takashi Yatsui · Motoichi Ohtsu

Received: 16 August 2012 / Revised: 5 September 2012 / Published online: 25 November 2012

Abstract We propose a novel method of coupling heterogeneous quantum dots at fixed distances and capsulating the coupled quantum dots by utilizing nanometric local curing of a photo-curable polymer caused by multistep electronic transitions based on a phonon-assisted optical near-field process between quantum dots. Because the coupling and the capsulating processes are triggered only when heterogeneous quantum dots floating in a solution closely approach each other to induce optical near-field interactions between them, the distances between the coupled quantum dots are physically guaranteed to be equal to the scale of the optical near fields. To experimentally verify our idea, we fabricated coupled quantum dots, consisting of CdSe and ZnO quantum dots and a UV-curable polymer. We also measured the photoluminescence properties due to the quantum-dot coupling and showed that the individual photoluminescences from the CdSe and ZnO quantum dots exhibited a trade-off relationship.

1 Introduction

The field of nanophotonics has seen rapid progress in recent years. Nanophotonics exploits the local interactions between nanometer-scale particles via optical near fields in order to meet the requirements of future optical technologies [1]. An optical near field can also be described as a dressed photon (DP), which is a quasi-particle representing the coupled state of a photon and an electron in a nanometric space [2]. By using the energy transfer between semiconductor quantum dots (QDs) via DPs, novel nanophotonic devices and systems have been realized. Useful features such as compactness and low-energy consumption have been experimentally demonstrated [3–7].

A fundamental issue in implementing practicable nanophotonic devices and systems that consist of coupled QDs is the design and assembly of an appropriate nanometric setup using QDs to induce the intended optical near-field interactions and corresponding optical far-field responses [8]. Although there have been several reports of self-assembled QD systems based on crystal growth [9–12], coupling of heterogeneous QDs is not straightforward due to their physical incompatibilities. Achieving more diverse types of coupling and the corresponding optical properties requires self-assembling methods for coupled-QD devices consisting of heterogeneous QDs. Moreover, in recent work by the authors, self-assembling techniques for implementing nanophotonic devices and systems utilizing optical near-field interactions have been studied with the aim of producing an assembled structure that is the optimal nanometric structure for each application [13–16].

Our proposed method utilizes nanometric local curing of a photo-curable polymer solution via an induced phonon-assisted process caused by optical near-field interactions between heterogeneous QDs in order to fix their separation and to capsulate coupled QDs in individual grains of cured polymer. We present the principle of our novel photo-curing method for coupling heterogeneous QDs and report the photo response characteristics of coupled QDs obtained in an experiment for verifying the proposed idea.

N. Tate (✉) · Y. Liu · T. Kawazoe · T. Yatsui · M. Ohtsu
The University of Tokyo, 2-11-16 Yayoi, Bunkyo-ku, Tokyo 113-8656, Japan
e-mail: tate@nanophotonics.t.u-tokyo.ac.jp

M. Naruse
National Institute of Information and Communications Technology, 4-2-1 Nukui-kita, Koganei, Tokyo 184-8795, Japan

2 Principle of phonon-assisted photo-curing

We have demonstrated that a DP can excite a multi-mode phonon in a nanometric material, and excited phonon states can couple with each other [14, 16–18]. The quasi-particle representing this coupled state has been named a dressed-photon-phonon (DPP). In our proposed photo-curing method, we use the DPP for fixing heterogeneous QDs in a solution of a photo-curable polymer. In order to induce photo-curing in a self-assembled manner, the mixture in the solution, in which the QDs freely float due to Brownian motion, is irradiated with assisting light. Specifically, we used CdSe- and ZnO-QDs dispersed in toluene and ethanol, respectively. These QDs emit visible and ultraviolet (UV) light, respectively. These solutions were mixed with a UV-curable polymer, and the mixture was irradiated with visible assisting light whose photon energy was sufficiently high to excite excitons in the CdSe-QDs but too low to do so in the ZnO-QDs and the photo-curable polymer.

An overview of our proposed method is given here. If the number of QDs, or in the other words, their volume density, is sufficiently high for the QDs to frequently encounter each other, multistep excitation of the ZnO-QDs occurs due to DPP interactions with neighboring CdSe-QDs. Subsequently, the ZnO-QDs spontaneously emit UV light, and the UV-curable polymer in their surroundings is locally cured by absorbing the emitted UV light. As a result, the separation between the CdSe-QDs and ZnO-QDs is fixed, and the cured polymer capsulates the QDs. This completes the phonon-assisted photo-curing. The spatial distribution of the DPP energy generated on the surface of the QDs governs the volume of the capsulated QDs, which is expressed by a Yukawa function [19]. Moreover, the coupled QDs to be capsulated must be composed of heterogeneous QDs, CdSe and ZnO-QDs in this case, because the above sequence is induced only when the CdSe and ZnO-QDs encounter each other. On the other hand, if the density is not sufficiently high in the mixture and they rarely encounter each other, only the CdSe-QDs spontaneously emit visible light by absorbing the assisting light. In this case, no physical or chemical reactions occur subsequently. The electronic transitions related to the phonon-assisted photo-curing are explained in the following:

When a solution containing a mixture of QD_A (CdSe-QDs of size a_A), QD_B (ZnO-QDs of size a_B), and a photocurable polymer is irradiated with assisting light, the two types of QDs form a coupled state due to interactions mediated by dressed-photon-phonons (DPPs) when the distance between them, r_{AB}, is equal to a_A or a_B or less. In general, the state of the nanomaterial related to the DPP-mediated interaction can be described by the direct product of the electron state and the phonon state, $|E;el\rangle \otimes |E;phonon\rangle \otimes$. Here, $|E;el\rangle$ and $|E;phonon\rangle$, respectively, represent the states of an electron and a phonon having energy E. When the distance between the QDs and the polymer molecules, r_{QP}, becomes sufficiently smaller than r_{AB}, in other words, when $r_{QP} \leq r_{AB}$, the polymer molecules exist in the DPP field at the surfaces of both QDs. Therefore, the polymer molecules also form a coupled state with both QDs. On the other hand, when $r_{QP} > r_{AB}$, the polymer molecules exist outside the DPP field. In this case, the polymer molecules do not form a coupled state with both QDs via the DPP-mediated interaction. In these two cases, transition processes Process 1 and Process 2 shown in Figs. 1 and 2 occur. Fixing of the distance between the two QDs via Process 1, and capsulation of the coupled QDs by curing of the polymer molecules in the vicinity via Process 2 proceed in a self-organized manner. These transition processes will be described below.

2.1 Process 1

First, the case where $r_{QP} \leq r_{AB}$ will be described. In this case, it is not just the two QDs but also the polymer molecules that interact via the DPP to form a coupled state. The photocuring process in this case is composed of two steps, as shown in Fig. 1.

2.1.1 Step 1

The initial ground state is the ground state of the coupled QDs and polymer molecule, $|E_{A.g}, E_{B.g}, E_{Poly.g}; el\rangle \otimes |E_{A.thermal}, E_{B.thermal}, E_{poly.thermal}; phonon\rangle$. Here, $E_{poly.g}$ and $E_{poly.thermal}$ represent the intrinsic energy of the electronic ground state of the polymer molecules, and the intrinsic energy taking into account the phonon distribution in the thermal equilibrium state. This coupling is brought about by the DPPs, and the initial coupled state transitions to the intermediate state $C'_1|E'_{A.ex}, E_{B.g}, E_{poly.g}; el\rangle \otimes |E'_{A.ex}, E_{B.thermal}, E_{poly.thermal}; phonon\rangle + C'_2|E_{A.g}, E_{B.g}, E_{poly.g}; el\rangle \otimes |E_{A.thermal}, E'_{B.ex}, E_{poly.thermal}; phonon\rangle + C'_3|E_{A.g}, E_{B.g}, E_{poly.g}; el\rangle \otimes |E_{A.thermal}, E_{B.thermal}, E'_{poly.ex}; phonon\rangle$ $\left(\text{where } |C'_1|^2 + |C'_2|^2 + |C'_3|^2 = 1\right)$ which is a superposition of the individual states in cases where an exciton exists in QD_A, QD_B, or the polymer molecule. Here, $E_{poly.ex'}$ represents the intrinsic energy of the excited state of the phonons in the polymer molecules, which have an energy equal to the photon energy of the assisting light, $h\nu_{assist}$. Because this intermediate state is electronic-dipole forbidden, the contribution of the DPPs is indispensable in this transition.

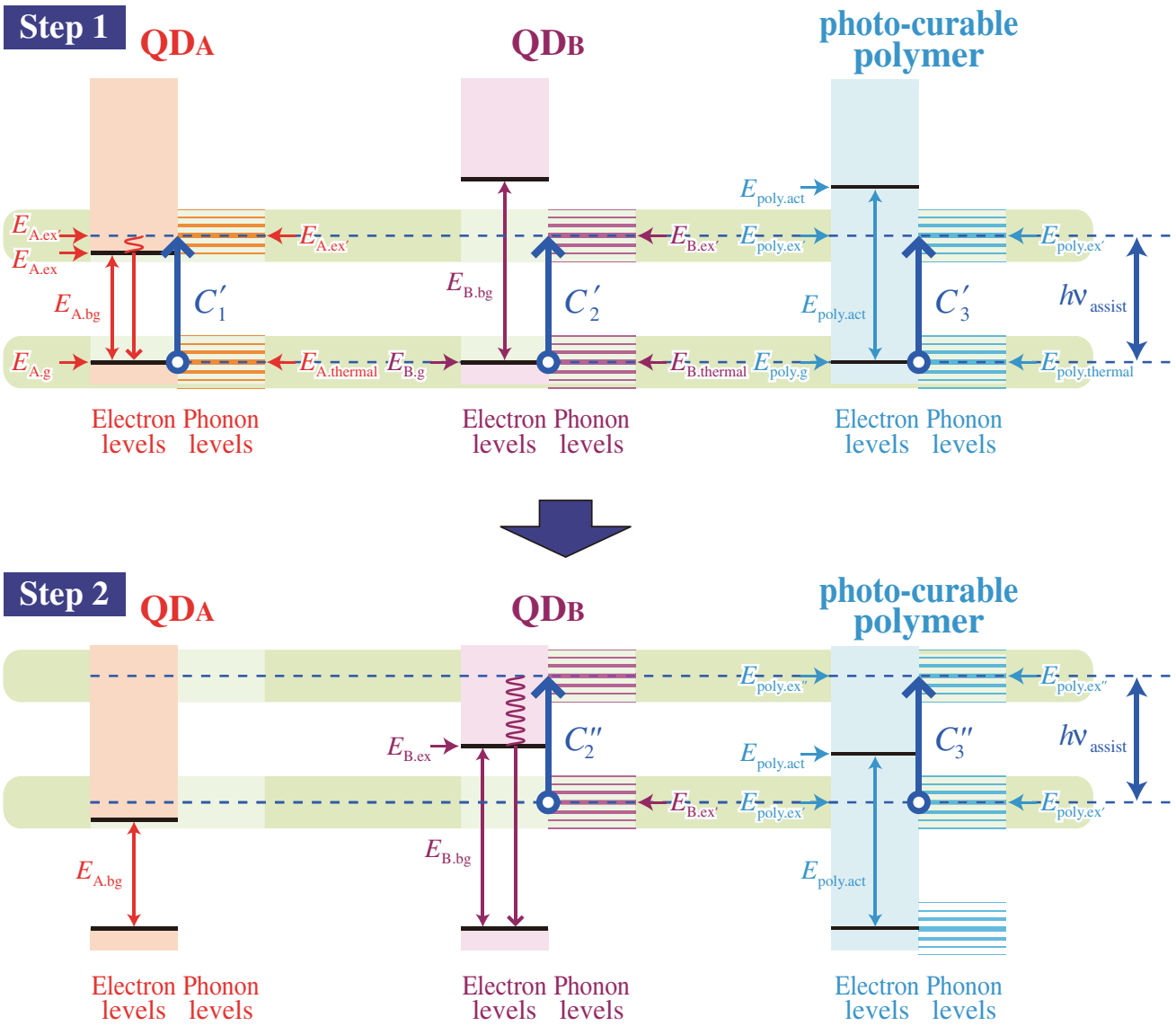

Fig. 1 Process 1 of the phonon-assisted QD-coupling method at the case of $r_{QP} \leq r_{AB}$

2.1.2 Step 2

In the intermediate state, from the state where an exciton exists in QD_A, a photon having a photon energy equal to the transition energy in QD_A, $E_{A.trans}$ ($= E_{A.ex} - E_{A.g}$) is generated by spontaneous emission. Here, the transition energies of the two QDs, $E_{A.trans}$ and $E_{B.trans}$, have the relationship $E_{A.trans} < h\nu_{assist} < E_{B.trans}$ ($=E_{B.ex} - E_{B.g}$). Because the energy $E_{A.trans}$ is smaller than the activation energy of the polymer molecule, $E_{poly.act}$, in other words, the energy difference between the excited state and the ground state, $E_{poly.ex} - E_{poly.g}$, this light does not contribute to the photocuring process. Therefore, the case where an exciton exists in QD_B or the polymer molecule will be considered below. In other words, in Step 2, the coupling of the two QDs and the polymer in the intermediate state is further excited by the assisting light and they transition to the final state $C''_2|E_{A.g}, E''_{B.ex}, E_{poly.g}; el\rangle \otimes |E_{A.thermal}, E''_{B.ex}, E_{poly.thermal}; phonon\rangle + C''_3|E_{A.g}, E_{B.g}, E_{poly.ex''}; el\rangle \otimes |E_{A.thermal}, E_{B.thermal}, E_{poly.ex''}; phonon\rangle$ (where $|C''_1|^2 + |C''_2|^2 + |C''_3|^2 = 1$), in which an exciton exists in either the QD_B or the polymer molecule. Here, because the energy $E_{poly.ex''}$, which represents the intrinsic energy of the exited state in the polymer molecule, is larger than the activation energy $E_{poly.act}$, the polymer is cured. Because this final state is electronic-dipole allowed, the transition from the intermediate state to the final state can be brought about by propagating light, not just the DPP. This curing fixes the distance between the two QDs.

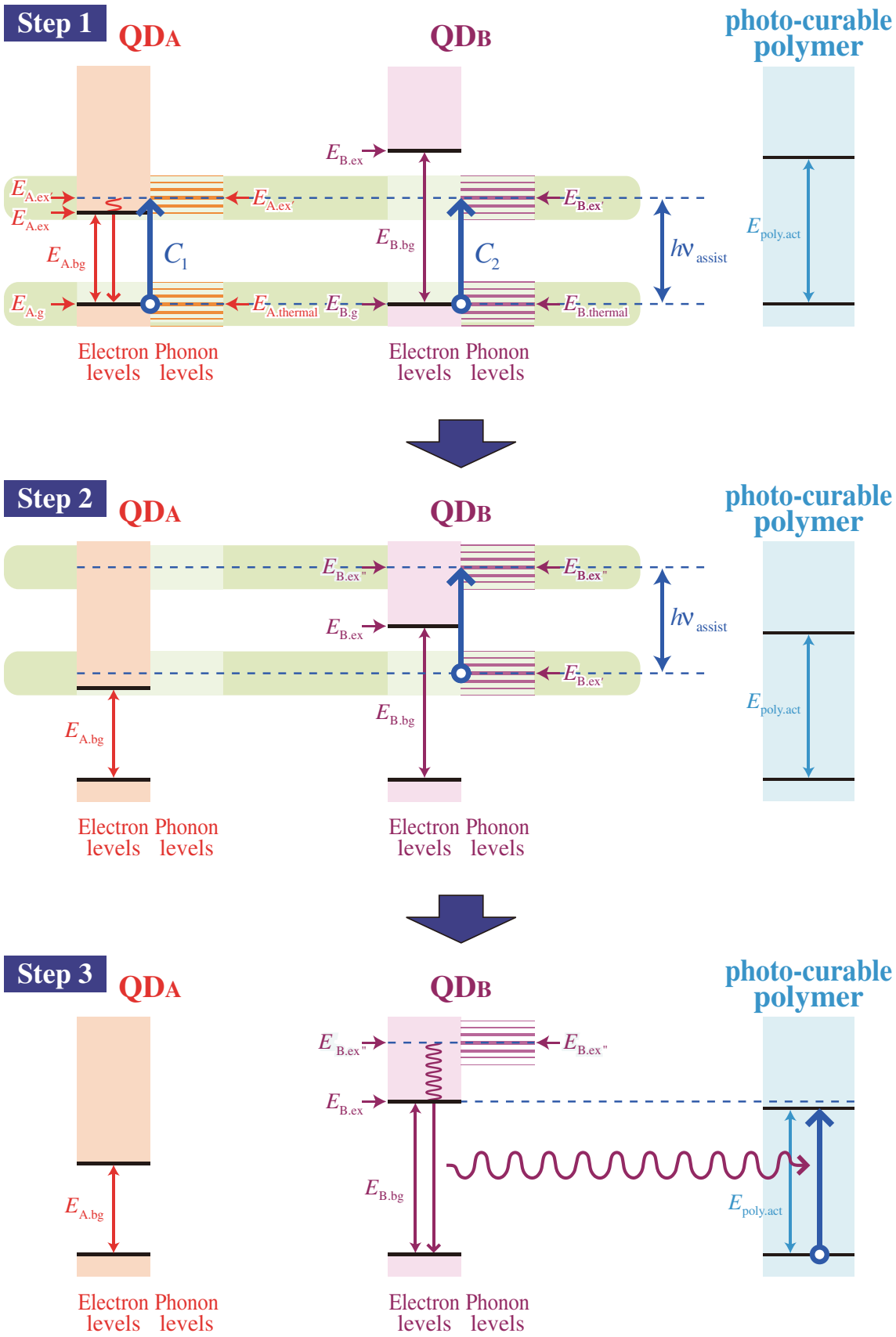

Fig. 2 Process 2 of the phonon-assisted QD-coupling method at the case of $r_{QP} > r_{AB}$

2.2 Process 2

Next, the case where $r_{QP} > r_{AB}$ will be described. The state in which the two QDs are coupled via the DPP-mediated interaction is represented by $|E_A, E_B; el\rangle \otimes |E_A, E_B; phonon\rangle$. Here, E_A and E_B represent the intrinsic energies of QD_A and QD_B, respectively. The photocuring process in this case is composed of the following three steps, as shown in Fig. 2.

2.2.1 Step 1

The initial state is the ground state of the coupled QD_A and QD_B, $|E_{A.g}, E_{B.g}; el\rangle \otimes |E_{A.thermal}, E_{B.thermal}; phonon\rangle$. Here, $E_{A.g}$ and $E_{B.g}$ are the intrinsic energies of the electronic ground states of QD_A and QD_B, and $E_{A.thermal}$ and $E_{B.thermal}$ represent the intrinsic energies taking account of the thermal equilibrium distribution. The two QDs are excited by DPPs and transition to the intermediate state $C_1|E_{A.ex'}, E_{B.g}; el\rangle \otimes |E_{A.ex'}, E_{B.thermal}; phonon\rangle + C_2|E_{A.g}, E_{B.g}; el\rangle \otimes |E_{A.thermal}, E_{B.ex'}; phonon\rangle$ (where $|C_1|^2 + |C_2|^2 = 1$). Here, $|E_{A.ex'}, E_{B.g}; el\rangle \otimes |E_{A.ex'}, E_{B.thermal}; phonon\rangle$ is the state where an exciton exists in QD_A and $|E_{A.g}, E_{B.g}; el\rangle \otimes |E_{A.thermal}, E_{B.ex'}; phonon\rangle$ is the state where an exciton exists in QD_B. The energies $E_{A.ex'}$ and $E_{B.ex'}$ represent the intrinsic energies of the excited states of the electron or phonon in QD_A and QD_B, respectively, which have energies equal to the photon energy of the assisting light, $h\nu_{assist}$, as shown in Fig. 2. Because this intermediate state is electronic-dipole forbidden, the contribution of the DPP is essential in this transition.

After the transition described above, the exciton in QD_A relaxes from the state $|E_{A.ex'}, E_{B.g}; el\rangle \otimes |E_{A.ex'}, E_{B.thermal}; phonon\rangle$ to the lowest excited state $|E_{A.ex}, E_{B.g}; el\rangle \otimes |E_{A.ex}, E_{B.thermal}; phonon\rangle$ within a short time. Then, light having a photon energy corresponding to the transition energy of QD_A, $E_{A.trans}$, is generated by a spontaneous emission process; however, as with Process 1, this light does not contribute to the photocuring process.

2.2.2 Step 2

Similar to above, because the spontaneous emission from the state in which the exciton exists in QD_A does not contribute to the photocuring process, only the transition from the state $|E_{A.g}, E_{B.g}; el\rangle \otimes |E_{A.thermal}, E_{B.ex'}; phonon\rangle$ in which an exciton exists in QD_B will be described here. In other words, in Step 2, the two QDs in the intermediate state are excited by the assisting light and transition to the final state $|E_{A.g}, E_{B.ex''}; el\rangle \otimes |E_{A.thermal}, E_{B.ex''}; phonon\rangle$. Here, the energy $E_{B.ex''}$ ($>E_{B.ex'}$) represents the intrinsic energy possessed by the excited state in QD_B. Because this final state is electronic-dipole allowed, this transition can be induced by propagating light, not just the DPP.

2.2.3 Step 3

After being excited to the final state described above, the exciton in QD_B relaxes to the lowest excited state $|E_{A.g}, E_{B.ex}; el\rangle \otimes |E_{A.thermal}, E_{B.ex}; phonon\rangle$ within a short time. Then, propagating light having a photon energy corresponding to the transition energy $E_{B.trans}$ of QD_B is generated by a spontaneous emission process. Because $E_{B.trans}$ is sufficiently larger than the activation energy of the polymer molecules, $E_{poly.act}$, the polymer molecules absorb the propagating light generated in this way, becoming excited. The generated propagating light is a spherical wavefront, and therefore, the probability of absorption by the polymer molecules in the vicinity of the two QDs is higher than the probability of absorption at a distance. Therefore, the polymer is cured close to the two QDs, and capsulation of the two QDs thus proceeds.

3 Experimental results

Figure 3 shows the energy conditions for an experiment conducted to verify the proposed method. These conditions fulfill the previously described energy conditions for inducing the sequential process of the phonon-assisted photo-curing. We used commercially available CdSe-QDs (Ocean Optics; *Evidot*) and ZnO-QDs prepared by sol–gel synthesis using photo-induced desorption [15]. The QD solutions were then dispersed in a UV-curable polymer (NORLAND; *NOA 65*) and irradiated with assisting light emitted from a 120 mW laser diode with a photon energy of 2.71 eV. The total amount of the mixed solution was limited to 50 μL to maintain spatially uniform illumination. This volume contained about 10^{14} CdSe-QDs and about 10^{12} ZnO-QDs. Under these experimental conditions, the QDs can be assumed to encounter each other at a

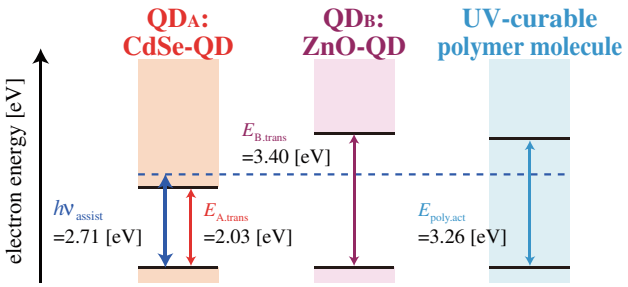

Fig. 3 Practical energy conditions of the materials used for the experimental verification: two heterogeneous QDs, CdSe-QDs and ZnO-QDs, and a UV-curable polymer (Norland, *NOA 65*)

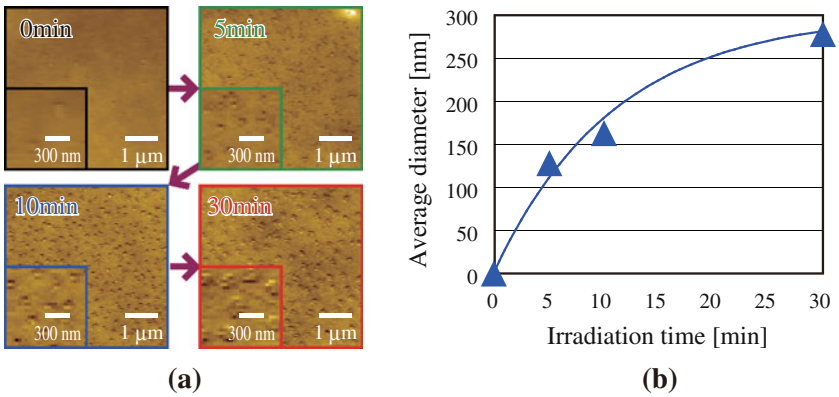

Fig. 4 **a** AFM images of the sample dispersed on a Si substrate and irradiated for 30 min. **b** Growth of the grain structures depended on the irradiation time of the assisting light. The *solid line* represents theoretically predicted values

sufficiently high frequency to induce the phonon-assisted photo-curing.

First, we verified the effect of the phonon-assisted process by direct observation of the locally cured polymer material. During irradiation of the assisting light, the polymer material in the mixture continued to be cured in a self-organized manner, as we previously described, and the volume of the cured polymer in which coupled QDs were capsulated increased. Figure 4a shows observed AFM images of a sample on a Si substrate after irradiation with the assisting light for 0–30 min. As shown, a number of spherical grains, which were formed of locally cured polymer capsulating coupled QDs, were observed. As summarized in Fig. 4b, the average diameter of the grains increased as the irradiation time of the assisting light increased, and then saturated, as represented by the solid line. The saturated diameter was determined by both the rate of occurrence of the phonon-assisted process and the energy absorption rate of the polymer material.

Second, photoluminescence (PL) spectral properties of the coupled QDs capsulated in the photo-cured grains were investigated. By irradiating the grains with 3.82 eV excitation light from a He-Cd laser, whose photon energy was sufficiently high to excite both CdSe and ZnO-QDs, as shown in Fig. 5, the preferred DP energy transfer from ZnO-QDs to CdSe-QDs is expected to occur only in the case where these two are coupled. As a result of this transfer, the decreases and increases in the PL intensities from these QDs are expected to vary in an anti-correlated manner. That is, the PL intensity from the CdSe-QDs increases while that from the ZnO-QDs decreases. We measured the relation between irradiation time of the assisting light used for capsulation and the PL intensities from both QDs. Because the surrounding polymer mostly absorbs the PL light emitted from the excited state of an exciton in the ZnO-QDs, we measured the emission intensities from the defect levels in the ZnO-QDs, which are proportional to that from the excited state.

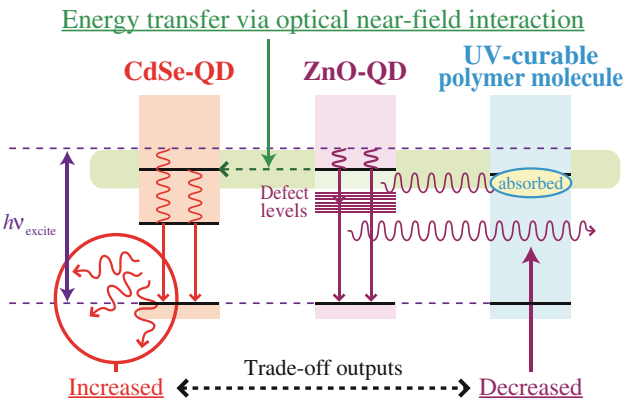

Fig. 5 Preferred optical energy transfer from ZnO-QD to CdSe-QD by irradiation with excitation light. The trade-off of the emission intensity, where the intensity of the CdSe-QDs increases and that of the ZnO-QDs decreases, can be induced only when the QDs are coupled to each other

Figure 6a shows the obtained emission spectra of the coupled QDs capsulated using various irradiation times of the assisting light. The left- and right-hand spectra, whose peak energies were lower and higher than 2.34 eV, represent PL from the lowest excitation level of the CdSe-QDs and the defect levels in the ZnO-QDs, respectively. The peak energies of the two spectra were 2.21 and 2.61 eV, respectively. As summarized in Fig. 6b, the expected decrease and increase in emission intensities from the CdSe- and ZnO-QDs in an anti-correlated manner were successfully observed. These results indicate that coupled QDs selectively consisted of both CdSe and ZnO-QDs, and that the number of coupled QDs gradually increased during irradiation with the assisting light.

4 Summary

We have described the principle of a phonon-assisted self-organized photo-curing method for fixing the separation between heterogeneous QDs and capsulating them. The

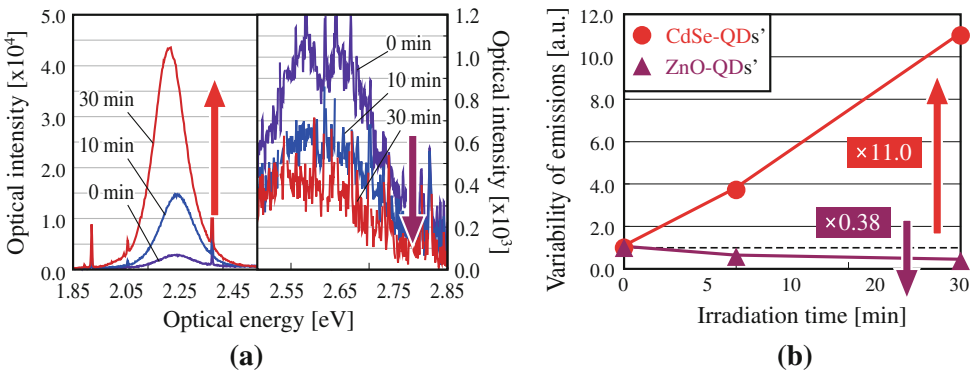

Fig. 6 **a** Emission spectra of several samples formed with various irradiation times of the assisting light. The left and right-hand spectra represent PL from the lowest excited level of the CdSe-QDs and defect levels in the ZnO-QDs, respectively. **b** The *plotted* variabilities of the emission intensities from the CdSe and ZnO-QDs

proposed method utilizes a phonon-assisted excitation process between QDs and a photo-curable polymer. We verified the effectiveness of our technique via an experiment using sample solutions containing CdSe-QDs, ZnO-QDs, and a UV-curable polymer. Moreover, we observed the expected characteristic optical responses of the sample, demonstrating the validity of our idea.

Under the conditions used in our experiment, the coupling processes, Processes 1 and 2 described above, contributed to fixing the separation between the QDs and capsulating them, respectively. Further experiments conducted under various conditions will be required to reveal the differences in the characteristics of the coupled QDs fabricated by each process. Moreover, it is expected that further studies will confirm the discussion in our recent research work [6], namely, that the most appropriate combination ratio of multiple heterogeneous QDs for inducing optical near-field interactions is not necessarily one-to-one, but one-to-many.

Acknowledgments A part of this work was supported by the Global Center of Excellence (G-COE) "Secure-Life Electronics", Special Coordination Funds for Promoting Science and Technology sponsored by the Ministry of Education, Culture, Sports, Science and Technology (MEXT), Japan, and the Strategic Information and Communications R&D Promotion Programme (SCOPE) sponsored by the Ministry of Internal Affairs and Communications (MIC).

References

1. M. Ohtsu, K. Kobayashi, T. Kawazoe, T. Yatsui, M. Naruse (eds.), *Principles of Nanophotonics* (Taylor and Francis, Boca Raton, 2008)
2. T. Kawazoe, K. Kobayashi, S. Takubo, M. Ohtsu, J. Chem. Phys. **122**, 024715 (2005)
3. T. Kawazoe, K. Kobayashi, S. Sangu, M. Ohtsu, Appl. Phys. Lett. **82**(18), 2957 (2003)
4. T. Kawazoe, K. Kobayashi, M. Ohtsu, Appl. Phys. Lett. **86**(10), 103102 (2005)
5. W. Nomura, T. Yatsui, T. Kawazoe, M. Ohtsu, J. Nanophotonics **1**, 011591 (2007)
6. M. Naruse, K. Leibnitz, F. Peper, N. Tate, W. Nomura, T. Kawazoe, M. Murata, M. Ohtsu, Nano Commun. Netw. **2**(4), 189 (2011)
7. T. Kawazoe, M. Ohtsu, S. Aso, Y. Sawado, Y. Hosoda, K. Yoshizawa, K. Akahane, N. Yamamoto, M. Naruse, Appl. Phys. B **103**(3), 537 (2011)
8. T. Kawazoe, K. Kobayashi, J. Lim, Y. Narita, M. Ohtsu, Phys. Rev. Lett. **88**(6), 067404 (2002)
9. Z.Y. Xu, Z.D. Lu, X.P. Yang, Z.L. Yuan, B.Z. Zheng, J.Z. Xu, Phys. Rev. B **54**(16), 11528 (1996)
10. R. Heitz, I. Mukhametzhanov, P. Chen, A. Modhukar, Phys. Rev. B **58**(16), R10151 (1998)
11. A. Polimeni, A. Patane, M. Henini, L. Eaves, P.C. Main, Phys. Rev. B **59**(7), 5064 (1999)
12. YuI Mazur, ZhM Wang, G.G. Tarasov, M. Xiao, G.J. Salamo, J.W. Tomm, V. Talalaev, H. Kissel, Appl. Phys. Lett. **86**(6), 063102 (2005)
13. T. Yatsui, K. Hirata, W. Nomura, Y. Tabata, M. Ohtsu, Appl. Phys. B **93**(5), 55 (2008)
14. S. Yukutake, T. Kawazoe, T. Yatsui, W. Nomura, K. Kitamura, M. Ohtsu, Appl. Phys. B Lasers Opt. **99**(3), 415 (2010)
15. Y. Liu, T. Morishima, T. Yatsui, T. Kawazoe, M. Ohtsu, Nanotechnology **22**(21), 215605 (2011)
16. T. Kawazoe, M.A. Mueed, M. Ohtsu, Appl. Phys. B **104**(4), 747 (2011)
17. H. Fujiwara, T. Kawazoe, M. Ohtsu, Appl. Phys. B **98**(2–3), 283 (2010)
18. K. Kitamura, T. Kawazoe, M. Ohtsu, Appl. Phys. B **107**(2), 293 (2012)
19. M. Ohtsu (ed.), *Progress in Nano-Electro-Optics II* (Springer, Berlin, 2003)

Effects of laser irradiation on the self-assembly of MnAs nanoparticles in a GaAs matrix

Pham Nam Hai,[1,a)] Wataru Nomura,[1,a)] Takashi Yatsui,[1,2] Motoichi Ohtsu,[1,2] and Masaaki Tanaka[1,2]
[1]*Department of Electrical Engineering and Information Systems, The University of Tokyo, 7-3-1 Hongo, Bunkyo-ku, Tokyo 113-8656, Japan*
[2]*Nanophotonics Research Center, The University of Tokyo, 7-3-1 Hongo, Bunkyo-ku, Tokyo 113-8656, Japan*

(Received 26 July 2012; accepted 17 October 2012; published online 6 November 2012)

We investigate the effects of laser irradiation on the self-assembly of MnAs nanoparticles during solid-phase decomposition in a GaAs matrix. It is found that laser irradiation suppresses the growth of MnAs nanoparticles from small to large size, and that the median diameter D_1 in the size distribution of small MnAs nanoparticles depends on the incident photon energy E following $D_1 \sim E^{-1/5}$. We explain this behavior by the desorption of Mn atoms on the MnAs nanoparticle surface due to resonant optical absorption, in which incident photons excite intersubband electronic transitions between the quantized energy levels in the MnAs nanoparticles. © *2012 American Institute of Physics*. [http://dx.doi.org/10.1063/1.4765355]

Ferromagnetic metallic nanoparticles embedded in a semiconductor matrix are attractive because of their possible applications in nano-scale spintronic devices, such as nano-scale magnetic memory and single-electron spin transistor.[1] Besides, ferromagnetic metallic nanoparticles can exhibit rich quantum phenomena, such as spin-dependent transport, Coulomb blockade, and quantum-size effects. A model system of ferromagnetic granular materials is MnAs nanoparticles embedded in a GaAs matrix (here referred to as GaAs:MnAs). This system can be obtained by thermal annealing of (Ga,Mn)As alloy at high temperature (500–600 °C).[2] When annealing (Ga,Mn)As at around 500 °C, zinc-blende (ZB) MnAs nanoparticles are formed in a GaAs matrix due to solid-phase decomposition.[3] Subsequent annealing at higher temperature (>550 °C) results in more chemically stable MnAs nanoparticles of hexagonal (Hex) NiAs-type phase.[4] The ZB MnAs nanoparticles have been shown to exhibit spin-induced electromotive force and huge magnetoresistance,[5] while the Hex MnAs nanoparticles have been shown to be good spin injectors/detectors[6–8] and to have quite long spin-relaxation time.[9] Controlling the size of MnAs nanoparticles during solid-phase decomposition is very important for realistic applications. In a previous study, we have shown that the size and the distance between MnAs nanoparticles can be controlled to some extent by utilizing the thermodynamic spinodal decomposition technique.[10] However, statistical fluctuation of the particle size still remains. A more effective technique to actively control the particle size is highly required.

It is known that laser irradiation can induce desorption of atoms on the surfaces of nanoparticles or thin films due to optical resonant absorption.[11,12] In such a process, a nanoparticle is electronically excited by, for example, surface plasmon absorption. The absorbed energy is transferred from the electronic system to the atomic system on the surface, which is then spent for atomic desorption. Since the resonant photon energy depends on the particle size, laser-induced desorption can be used to fabricate very homogeneous nanoparticles during gas-phase deposition,[13] and to control the particle size during liquid-phase self-assembly of nanoparticles.[14,15] However, such phenomena in solid-phase self-assembly of nanoparticles have not been investigated so far. In this letter, we report on the effects of laser irradiation on the self-assembly of MnAs nanoparticles during solid-phase decomposition in a GaAs matrix. We show that laser irradiation can suppress the growth of MnAs nanoparticles from small to large size, and that the median diameter D_1 in the size distribution of very small nanoparticles depends on the incident photon energy E as $D_1 \sim E^{-1/5}$. We explain this relationship by resonant optical absorption, in which incident photons excite intersubband electronic transitions between the quantized energy levels in the MnAs nanoparticles. Our result shows that laser-irradiation can be used for active control of the size of nanoparticles during solid-phase self-assembly.

Our experimental procedure is as follows. A 6 nm-thick $(Ga_{0.8},Mn_{0.2})As$ layer was grown by low-temperature molecular beam epitaxy on a 0.5 mm-thick GaAs semiconductor wafer at 234 °C. Then, a 2.1 nm-thick AlAs layer and a 3 nm-thick GaAs cap layer were successively grown on the top of the $(Ga_{0.8},Mn_{0.2})As$ thin film. These layers prevent diffusion of Mn atoms to the surface during subsequent high temperature thermal annealing (HTTA). Next, a 10 nm-thick SiO_2 cap layer was deposited on the top by sputtering to prevent As evaporation during HTTA. Then, the wafer was cleaved into small samples with size of about 1 cm × 1 cm. These small samples were mounted on a 5 cm × 5 cm stainless-steel holder by indium solder and loaded into a vacuum chamber equipped with a heater (~1200 W) and glass windows for laser irradiation, as illustrated in Fig. 1(a). Two thermocouples, one is in contact with the stainless-steel holder and the other is in contact with the heater, were used to monitor the temperature of the samples and the heater. In the following, temperature means the sample temperature if not explicitly stated. The samples were thermally annealed and irradiated by lasers following the sequence shown in

[a)]P. N. Hai and W. Nomura contribute equally to this work.

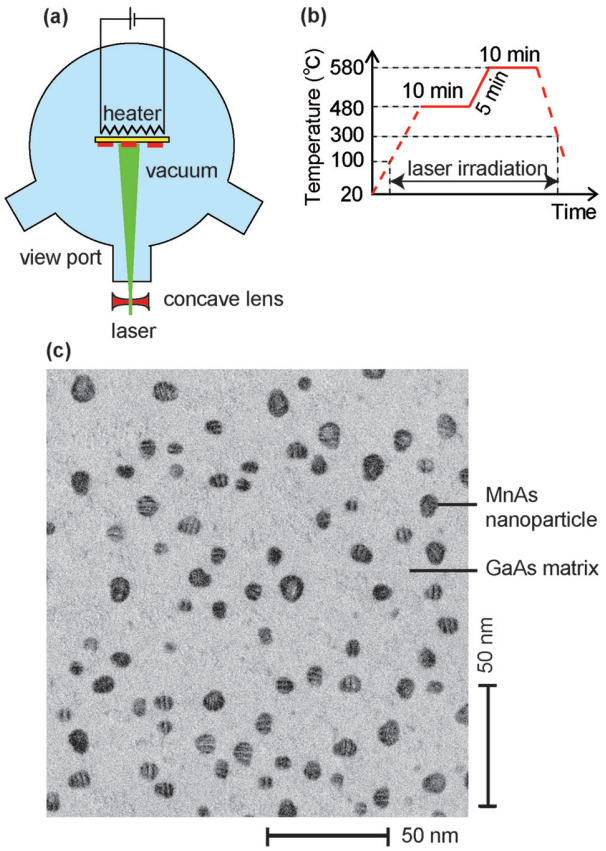

FIG. 1. (a) Schematic illustration of our experiment setup. (b) Experimental sequence of thermal annealing and laser irradiation for solid-phase formation of MnAs nanoparticles in a GaAs matrix. (c) Representative transmission electron microscopy image of a sample which was annealed under laser irradiation with a wavelength of 671 nm and a photon flux of 4×10^{18} cm^{-2} s^{-1}.

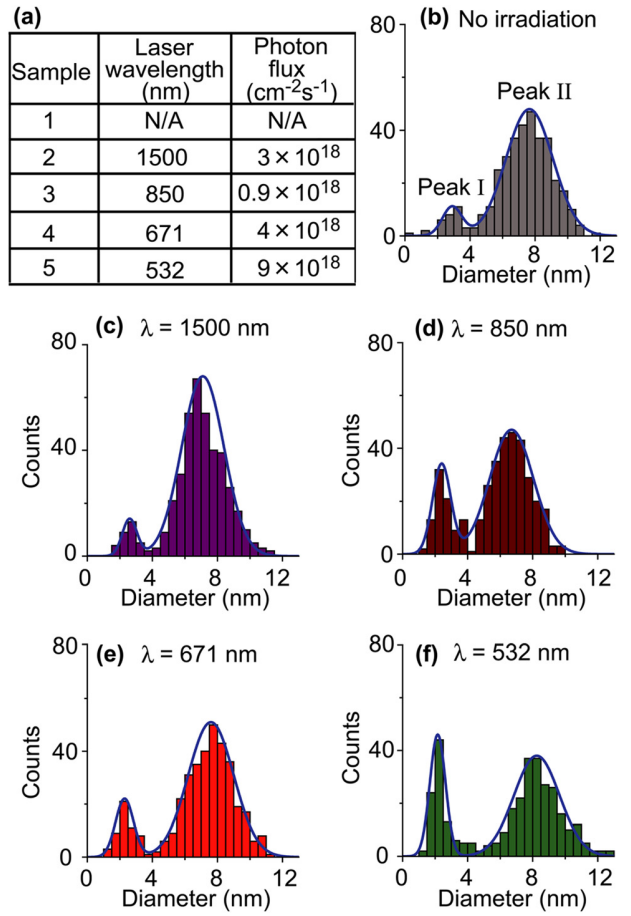

Sample	Laser wavelength (nm)	Photon flux (cm^{-2}s^{-1})
1	N/A	N/A
2	1500	3×10^{18}
3	850	0.9×10^{18}
4	671	4×10^{18}
5	532	9×10^{18}

FIG. 2. (a) Sample number, and corresponding laser wavelength and photon flux. (b) Particle diameter (D) distribution of sample 1 (annealed without laser irradiation.) (c)-(f) Particle diameter distributions of samples 2-5 (irradiated by laser light with wavelength $\lambda = 1500$, 850, 671, and 532 nm, respectively.) Solid curves are Gaussian fittings.

Fig. 1(b). The samples were first heated up to 480 °C and then kept at 480 °C for 10 min. A feedback control loop of the heater power is used to keep the temperatures of the heater and the holder constant. During this annealing, solid-phase spinodal decomposition occurred and very small ZB MnAs nanoparticles (2–3 nm) were formed.[5] After that, the samples were heated up to 580 °C. During this final heating, the ZB MnAs nanoparticles continue to grow and reach their final sizes. Finally, the samples were kept at 580 °C for 10 min. At this final stage, the ZB MnAs nanoclusters are transformed to more chemically stable Hex MnAs nanoclusters, which can be easily observed by transmission electron microscopy (TEM). During this thermal annealing, we irradiated the samples with solid-state lasers with wavelength $\lambda = 1500$, 850, 671, and 532 nm. Figure 2(a) shows the sample number, the corresponding laser wavelength λ, and the incident photon flux F. Figure 1(c) shows a representative TEM image of sample 4, which was annealed under irradiation of a laser with $\lambda = 671$ nm and $F = 4 \times 10^{18}$ cm^{-2} s^{-1}. The size distributions of MnAs nanoparticles were investigated by TEM images with areas of 0.36×0.36 μm^2.

Figure 2(b) shows the distribution of particle diameter D of sample 1, which was annealed without laser irradiation. There is a large peak (noted as peak II) at 7.65 nm, corresponding to the mean diameter due to spinodal decomposition.[10] During spinodal decomposition process, the driving force of particle formation is the reduction of thermodynamic free energy. There is also a very small peak (noted as peak I) at 2.90 nm, on which we will discuss later. Next, we investigate the particle diameter distributions of samples 2-5 (Figs. 2(c)–2(f)), which are irradiated by laser light with $\lambda = 1500$, 850, 671, and 532 nm, respectively. A striking feature in the distributions of the irradiated samples is that peak I is strongly enhanced. This enhancement of peak I can be more clearly seen in Fig. 3(a), in which the normalized peak heights (peak count/total count) of peak I and II of samples 2-5 are shown (filled rectangles and circles, respectively). With increasing the photon energy, the height of peak I is gradually increased, while that of peak II is gradually decreased. That is, the number of very small nanoparticles increases while the number of larger nanoparticles decreases due to laser irradiation. For $\lambda = 532$ nm, peak I is even higher than peak II. This result clearly indicates that laser irradiation *suppresses* the growth of MnAs nanoparticles from small to large size, which is consistent with the laser-induced desorption of atoms on the surfaces of nanoparticles.[11,15]

Let us discuss on the possibility of heating effect on the particle growth due to laser irradiation. To estimate the temperature increase at the sample surface due to laser irradiation, we solved the thermal diffusion equation assuming that the thermal conductivity of GaAs substrates at 480–580 °C is $\sim$0.1 WK^{-1} cm^{-1} (Ref. 16), and the stainless-steel holder is

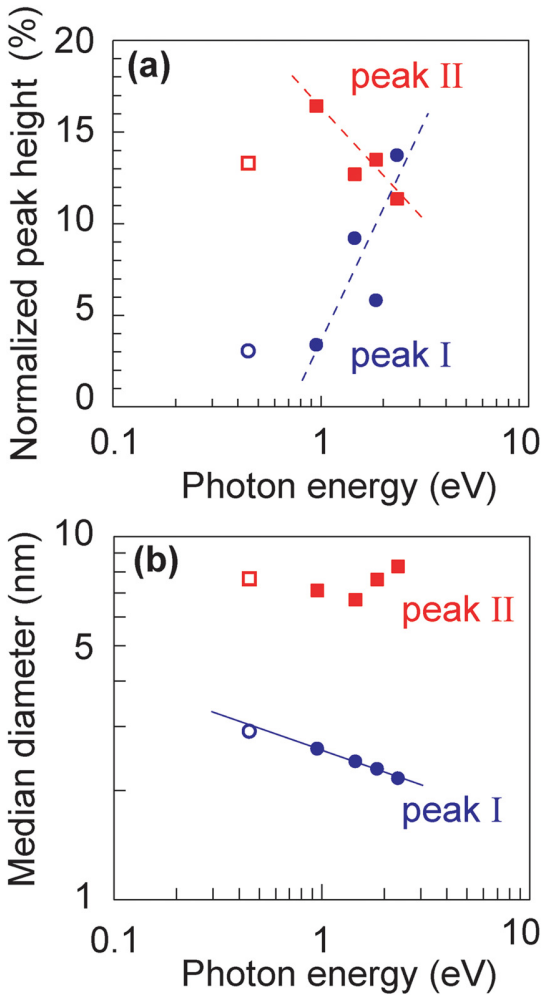

FIG. 3. Photon energy (E) dependence of (a) the normalized peak height and (b) the median diameters D_1 and D_2 of peak I ($D \sim 2$–3 nm) and peak II ($D \sim 7$ nm), respectively. Filled circles and rectangles are data of peak I and peak II for samples 2-5, respectively. Blank circles and rectangles are the data of sample 1 with a defined "background" photon energy of 0.45 eV corresponding to the peak of the black-body radiation spectrum of the heater (1050 K). Dashed lines in (a) are guides for the eyes. Solid line in (b) shows the relationship $D_1 \sim E^{-1/5}$.

a heat sink due to the feedback control of the heater power. We estimated that the sample surface temperature is increased by only 2 °C even for the largest incident optical power density of 3.5 W cm^{-2} for sample 5. Furthermore, in the case of solid-phase decomposition, the increase of temperature should *enhance* the growth of particles with larger size, rather than suppress it. This is because the thermodynamic free energy gain (loss) due to absorption (desorption) of Mn atoms from (to) the GaAs matrix increases with increasing temperature.[10] As a result, if heating due to laser irradiation is dominant, the absorption rate of Mn atoms should increase, while the desorption rate should decrease with increasing temperature, resulting in larger nanoparticles. This was indeed experimentally observed in previous reports.[4,17] Therefore, the suppression of particle growth observed in our experiment cannot be explained by the heating effect. (Note that the temperature-dependence of solid-phase decomposition is significantly different from that of gas-phase formation of nanoparticles. In gas-phase formation of nanoparticles, the energy loss due to desorption is temperature-independent. Thus, the desorption rate can increase with increasing temperature due to larger thermal excitation.)

Figure 3(b) shows the median diameters D_1 and D_2 of peak I and II as a function of photon energy E, where D_1 and D_2 were estimated by fitting the size distributions to Gaussian functions. Data of samples 2-5 are shown by filled rectangles (peak II) and circles (peak I). One can see that peak I can be fitted by the relation $D_1 \sim E^{-1/5}$ (solid line). This result shows that we can control the size of small nanoparticles by changing the laser photon energy. Interestingly, by defining a "background" photon energy of 0.45 eV corresponding to the peak of the black-body radiation spectrum of the heater (1050 K) for sample 1, we found that the median diameter of peak I of sample 1 also agrees with the above relation (blank circle). We suggest that peak I of sample 1 may occur due to optical absorption of the black-body radiation from the heater.

The E-dependence of D_1 can be understood by the resonant optical absorption process; for each E, there is an optimum resonant size D_r of nanoparticles at which photon energy is strongly absorbed. The rate equation for nanoparticle growth in this process is given by $dV/dt = \alpha S - \beta V F$, where $V = \frac{1}{6}\pi D^3$ is the particle volume, $S = \pi D^2$ is the particle surface area, and α, β are proportional coefficients. Note that α is a constant as long as D is small, and β is a strong function of D which reflects the resonant absorption process. At equilibrium, $dV/dt = 0$, the particle size is a solution of

$$\beta(D) = \frac{6\alpha}{FD}. \tag{1}$$

We can see that as long as $\beta(D)$ is close to a delta-function of D at the resonant size D_r, i.e., $\beta(D) \sim \delta(D - D_r)$, solutions of Eq. (1) are always very close to D_r and do not depend much on F, which is good for robust control of the nanoparticle size. This resonant optical absorption effect explains the systematic E-dependence of D_1. In contrast, D_2 shows no systematic E-dependence. However, the change of D_2 is indeed related to that of D_1, because Mn atoms that dissolved back to the matrix from the surface of small particles due to the laser-induced desorption effect can participate in the growth of large particles.[18]

The blue shift of optical resonant energy of absorption in very small nanoparticles ($D \sim 3$ nm) with decreasing the particle size has been observed for Ag nanoparticles, and is usually explained by the size-dependence of plasmon resonance energy due to the quantum-size effect of nanoparticles.[19] Using a simple model of free electrons in a cubic box with sides L and infinite surface potential, Genzel *et al.* have shown that the plasmon frequency ω_P for a small nanoparticle is modified as[19]

$$\omega_P{}^2 = \omega_M{}^2 + \frac{\pi}{2}\left(\frac{v_F}{2L/\pi}\right)^2 - \left(y + \frac{v_F}{2L/\pi}\right)^2. \tag{2}$$

Here, ω_M is the surface plasmon frequency without damping, v_F is the Fermi velocity, and y is the damping frequency. The size-dependent plasmon resonant absorption effect, however, cannot describe our results due to the following reasons. First, Eq. (2) predicts that $E = \hbar\omega_P$ depends on L at most by

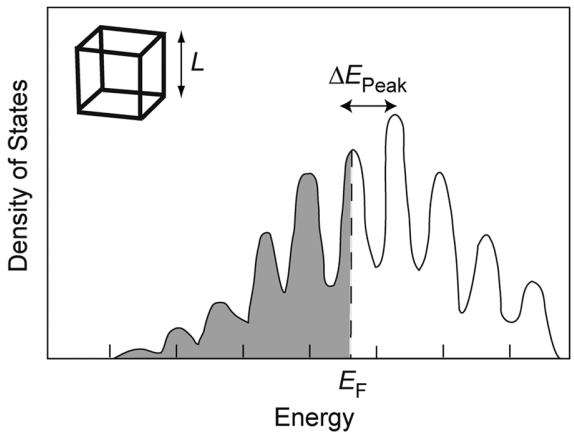

FIG. 4. DOS of a cubic-shaped nanoparticle with size of L (inset) and large surface potential (see Ref. 21). DOS shows periodic delta-function-like peaks. The intersubband electronic transition energy between these peaks ΔE_{Peak} can explain our experimental results.

$\sim 1/L$ rather than $1/L^5$. Lushnikov and Simonov also calculated Eq. (2) by taking into account the electron-electron interactions and reached a more complicated relation, but the L-dependence of E is not much different from that of Eq. (2).[20] Second, the change of the plasmon resonant energy is of the order of 0.1 eV (Refs. 19 and 20), while our results show the change in photon energy of the order of 1 eV. Third, ω_{P} decays not to zero but to the classical surface plasmon frequency $\sqrt{\omega_{\mathrm{M}}{}^2 - \gamma^2}$ for large L.

Beside the resonant surface plasmon excitation, it has been predicted that there are also resonant intersubband electronic excitations due the quantized electron energies in very small nanoparticles.[19] Bachelet *et al.* have calculated the density of states (DOS) for a very small cubic nanoparticle with sides L, which is shown in the inset of Fig. 4.[21] They have shown that DOS in very small nanoparticles with high surface potential can have many periodic delta-function-like peaks, as illustrated in Fig. 4. In such a cube, electronic energies are quantized due to the quantum size effect. A DOS peak occurs at an energy level E_{Peak} with a high degree of degeneracy. Resonant optical absorptions corresponding to the intersubband electronic transition between those DOS peaks can occur below or above the surface plasmon frequency.[19] Unlike the plasmon energy $\hbar\omega_{\mathrm{P}}$, the intersubband electronic transition energy ΔE_{Peak} rapidly decays to zero as the particle size increases, which can explain our result. Next, we estimate the order of ΔE_{Peak}. In Ref. 21, a value of $\Delta E_{\mathrm{Peak}} \sim 1.5\xi$ is predicted for a particle with size of 125 atoms, where ξ is the overlap integral energy between electron wavefunctions of adjacent atoms. Taking a reasonable value of $\xi \sim 1$ eV for metallic nanoparticles, ΔE_{Peak} is about 1.5 eV for a particle of 125 atoms. In fact, sample 4 with very small MnAs nanoparticles with a mean size of 139 Mn atoms has resonant photon energy of 1.85 eV, which is in good agreement with the above expected value. Last but not least, it is shown that DOS peaks come mostly from the electronic states near the particle surface. This suggests that the intersubband electronic excitation would occur near the surface, and the energy transfer process from the electronic system to the atomic system at the surface may be effective.

In conclusion, we have shown that laser irradiation can suppress the growth of MnAs nanoparticles from small to large size, and that the median diameter D_1 of very small nanoparticles depends on the incident photon energy E as $D_1 \sim E^{-1/5}$. We explain this behavior by the desorption of Mn atoms on the MnAs nanoparticle surface due to resonant optical absorption, in which incident photons excite intersubband electronic transitions between the quantized energy levels in MnAs nanoparticles. Our result gives hints to the control of the self-assembly process of very small metallic nanoparticles during solid-phase decomposition.

This work was partly supported by Grant-in-Aids for Scientific Research including Specially Promoted Research, Global COE Program (C04), Project for Developing Innovation Systems of MEXT, FIRST Program of JSPS, and the research grant (Basic Research) from The TEPCO Memorial Foundation, Japan.

[1]P. N. Hai, S. Sugahara, and M. Tanaka, Jpn. J. Appl. Phys., Part 1 **46**, 6579 (2007).
[2]J. De Boeck, R. Oesterholt, A. Van Esch, H. Bender, C. Bruynseraede, C. Van Hoof, and G. Borghs, Appl. Phys. Lett. **68**, 2744 (1996).
[3]M. Yokoyama, H. Yamaguchi, T. Ogawa, and M. Tanaka, J. Appl. Phys. **97**, 10D317 (2005).
[4]A. Kwiatkowski, D. Wasik, M. Kamińska, R. Bożek, J. Szczytko, A. Twardowski, J. Borysiuk, J. Sadowski, and J. Gosk, J. Appl. Phys. **101**, 113912 (2007).
[5]P. N. Hai, S. Ohya, M. Tanaka, S. E. Barnes, and S. Maekawa, Nature **458**, 489 (2009).
[6]P. N. Hai, M. Yokoyama, S. Ohya, and M. Tanaka, Appl. Phys. Lett. **89**, 242106 (2006).
[7]P. N. Hai, K. Takahashi, M. Yokoyama, S. Ohya, and M. Tanaka, J. Magn. Magn. Mater. **310**, 1932 (2007).
[8]P. N. Hai, Y. Sakata, M. Yokoyama, S. Ohya, and M. Tanaka, Phys. Rev. B **77**, 214435 (2008).
[9]P. N. Hai, S. Ohya, and M. Tanaka, Nat. Nanotechnol. **5**, 593 (2010).
[10]P. N. Hai, S. Yada, and M. Tanaka, J. Appl. Phys. **109**, 73919 (2011).
[11]W. Hoheisel, K. Jungmann, M. Vollmer, R. Weidenauer, and F. Trager, Phys. Rev. Lett **60**, 1649 (1988).
[12]I. Lee, J. E. Parks II, T. A. Callcott, and E. T. Arakawa, Phys. Rev. B **39**, 8012 (1989).
[13]T. Yatsui, W. Nomura, and M. Ohtsu, Nano Lett. **5**, 2548 (2005).
[14]Y. Liu, T. Morishima, T. Yatsui, T. Kawazoe, and M. Ohtsu, Nanotechnology **22**, 215605 (2011).
[15]M. Naruse, Y. Liu, W. Nomura, T. Yatsui, M. Aida, L. B. Kish, and M. Ohtsu, Appl. Phys. Lett. **100**, 193106 (2012).
[16]J. S. Blakemore, J. Appl. Phys. **53**, R123 (1982).
[17]M. Moreno, A. Trampert, B. Jenichen, L. Däweritz, and K. H. Ploog, J. Appl. Phys. **92**, 4672 (2002).
[18]See supplementary material at http://dx.doi.org/10.1063/1.4765355 for further analysis of E-dependence of D_2.
[19]L. Genzel, T. P. Martin, and U. Kreibig, Z. Phys. B **21**, 339 (1975).
[20]A. A. Lushnikov and A. J. Simonov, Z. Phys. **270**, 17 (1974).
[21]G. B. Bachelet, F. Bassani, M. Bourg, and A. Julg, J. Phys. C **16**, 4305 (1983).

IOP PUBLISHING JOURNAL OF PHYSICS D: APPLIED PHYSICS

J. Phys. D: Appl. Phys. **45** (2012) 475302 (4pp) doi:10.1088/0022-3727/45/47/475302

Realization of an atomically flat surface of diamond using dressed photon–phonon etching

Takashi Yatsui[1,2], **Wataru Nomura**[1], **Makoto Naruse**[3] **and Motoichi Ohtsu**[1]

[1] School of Engineering, University of Tokyo, Bunkyo-ku, Tokyo 113-8656, Japan
[2] Advanced Low Carbon Technology Research and Development Program (ALCA), Japan Science and Technology Agency, Kawaguchi-shi, Saitama 332-0012, Japan
[3] National Institute of Information and Communications Technology, 4-2-1 Nukui-kita, Koganei, Tokyo 184-8795, Japan

E-mail: yatsui@ee.t.u-tokyo.ac.jp

Received 20 August 2012, in final form 4 October 2012
Published 30 October 2012
Online at stacks.iop.org/JPhysD/45/475302

Abstract
We obtained an atomically flat diamond surface following dressed photon–phonon (DPP) etching using 3.81 eV light and O_2 gas. We obtained a surface roughness (R_a) of 0.154 nm for Ib-type (1 1 1) diamond and 0.096 nm for Ib-type (1 0 0) diamond. To evaluate the surface roughness, we grouped the surface into bins of width l and introduced the standard deviation of the height difference function for a given separation l, which allowed us to determine the height variation of the surface. Based on the calculation of standard deviation, the conventional adiabatic photochemical reaction did not remove the small surface features, while DPP etching decreased the surface roughness for all length scales.

(Some figures may appear in colour only in the online journal)

Realization of ultra-flat diamond substrate surfaces is required for a variety of future applications, including light-emitting devices [1], power devices [2] and quantum communication [3]. Although mechanical polishing has been used to flatten the surfaces, there are difficulties due to the hardness of diamond. We have developed a non-contact self-organized near-field etching [4] capable of producing atomically flat diamond.

The optical near-field is a virtual photon coupled with an excited electron. The quasiparticle representing this coupled state has been called a dressed photon (DP) with a greater amount of energy than a free photon due to the contribution from the energy of the coupled electron. The DP has been theoretically described by assuming a multipolar quantum electrodynamic Hamiltonian in a Coulomb gauge and single-particle states in a finite nano-system [5]. After a unitary transformation and some simple calculations, the creation and annihilation operators of the DP are expressed as the sum of the operators of the free photon and an electron–hole pair. The DP also interacts with the crystal lattice structure of nanomaterials by coupling with the multimodes of the phonons. As a result, the DP can couple with the phonons in a coherent state [6], and the combined coupled state of DP and coherent phonon quasiparticle, referred to as a dressed photon and phonon (DPP), has a higher energy than the DP or the incident free photon. Numerous experiments have been reported, in which the results were explained by DPP theory, including photochemical vapour deposition [7], photolithography [8], visible-light water splitting [9], photovoltaic devices [10] and energy up-conversion devices [11]. Based on these theoretical studies and experiments, we succeeded in realizing an Ångström-scale flattened glass substrate [4]. Here, we apply this method to a diamond substrate.

When non-focused propagating light is irradiated on the substrate, a DPP is generated at the protrusions of the substrate (figure 1(*a*)). If the dissociation energy, E_d, of the etching gas is higher than the photon energy, E, of the propagating light, the conventional adiabatic photochemical reaction of the gas is avoided. However, due to the higher energy of the DPP, the etching gas is selectively dissociated at the protrusions on the surface (figure 1(*b*)). The dissociated etching gas

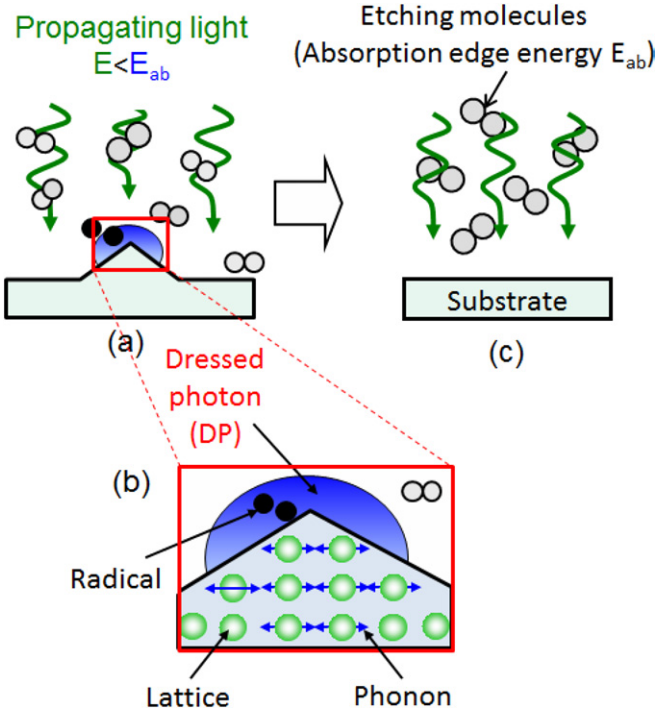

Figure 1. Schematic of DPP etching. (*a*) Etching gas (absorption edge energy E_{ab}) is selectively photodissociated at the protrusions and the activated etching gas atoms etch away the protrusions. (*b*) Magnified schematic of (*a*). (*c*) DPP etching automatically stops when the substrate becomes sufficiently flat.

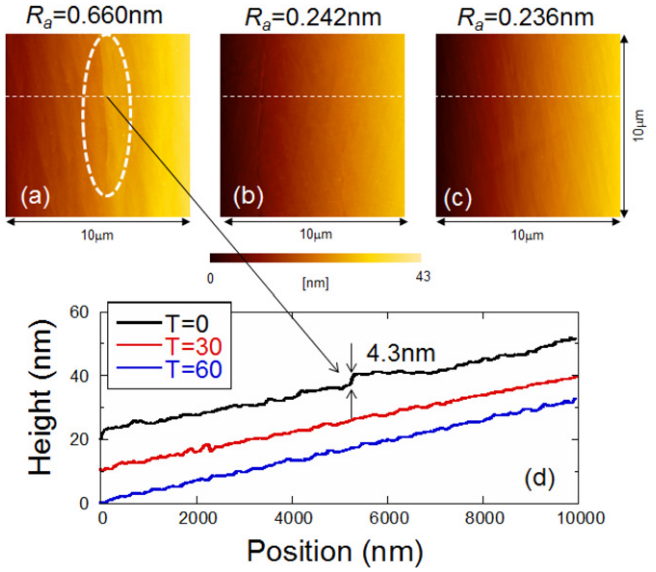

Figure 2. Typical AFM images of the Ib-type diamond (1 1 1) substrate with a 10 μm × 10 μm scanning area. Etching time T: (*a*) 0 min (before etching), (*b*) 30 min and (*c*) 60 min with a surface roughness R_a of (*a*) 0.660 nm, (*b*) 0.242 nm and (*c*) 0.236 nm, respectively. (*d*) Cross-sectional profile along the white dashed lines in (*a*)–(*c*).

then etches away the surface features, and the etching process automatically stops when the surface becomes flat (figure 1(*c*)).

We used O_2 gas to perform DPP etching on a diamond substrate, which has a dissociation energy of 5.12 eV (E_d) [12]. A continuum wave He–Cd laser with a wavelength of 325 nm (3.81 eV) and an excitation power of 0.8 W cm^{-2} was used to dissociate the O_2 gas through a DPP reaction, inducing the oxygen radical O* to produce an ultra-flat surface. This photon energy is lower than E_d, so that the conventional O_2 adiabatic photochemical reaction is avoided. Note that a laser power density of the order of W cm^{-2} is 10^{15} times smaller than that of multiple photon processing using an ultra-short pulse laser [13]. Therefore, the DPP etching process did not originate from a conventional multiple photon excitation process [14].

We used a single-crystalline diamond substrate grown under high pressure and high temperature [15]. We performed the DPP etching under atmosphere conditions using a Ib-type (absorption band edge of 3.02 eV) diamond (1 1 1) substrate prepared by cleaving. The surface roughness, R_a, was evaluated using an atomic force microscope (AFM), in which all images were obtained using tapping mode and a cantilever with a 15 nm tip diameter. Figures 2(*a*)–(*c*) show typical AFM images with a 10 μm × 10 μm of scanning area before DPP etching, after 30 min of etching and after 60 min of etching, respectively. The scanned area was 256 × 256 pixels with a spatial resolution of 40 nm. The R_a value before etching was 0.660 nm (figure 2(*a*)), comparable to the reported value of the ultra-flat substrate [16]. We confirmed that the standard deviation of R_a for figure 2(*a*) was small (0.0022) through 20 times repeated measurements. Hence, we considered that the change in the R_a value due to the change in the shape of the cantilever apex could be excluded. By comparing figures 2(*a*)–(*c*), we found that the R_a value decreased to 0.236 nm after 60 min of DPP etching. The cross-sectional profiles along the white dashed lines in figures 2(*a*)–(*c*) show that a large step (4.3 nm) was observed in figure 2(*a*) (before DPP etching); however, as shown inside the dashed white ellipse, flat surfaces without a large step were obtained after DPP etching (figures 2(*b*) and (*c*)). We also obtained AFM images with a 5 μm × 5 μm scanning area. Figures 3(*a*), (*b*) and (*c*) correspond to figures 2(*a*), (*b*) and (*c*), respectively. The scanned area was 256 × 256 pixels with a spatial resolution of 20 nm, which was comparable to the tip diameter of the cantilever. These smaller scanning area images were confirmed to have similar R_a decreases (from 0.457 to 0.154 nm). In addition, we compared the cross-sectional profile of the bump indicated as A–A′ in figure 3(*a*) and C–C′ in figure 3(*c*) (see figure 3(*d*)). This revealed a drastic reduction in height (from 11.32 to 5.82 nm) and a full-width at half-maximum (FWHM) from 103 to 83 nm. These results support the DPP etching and show flattening of the surface, as described above.

Figure 3(*e*) shows the cross-sectional profiles of figures 3(*a*)–(*c*), showing the decrease in the surface roughness. Additionally, 60 min DPP etching resulted in an ultra-flat surface with atomic steps. Based on the (1 1 1) crystal plane of the substrate, we calculated the size of each step in units of the lattice spaces, a, as 0.206 nm. The dashed horizontal lines in figure 3(*f*) show the average height of each terrace. The average heights were not exactly the same but close to integer multiples of a, because the height was an average value along each step as long as 200 nm, indicating that the observed flat terraces were atomic steps of the diamond (1 1 1) plane.

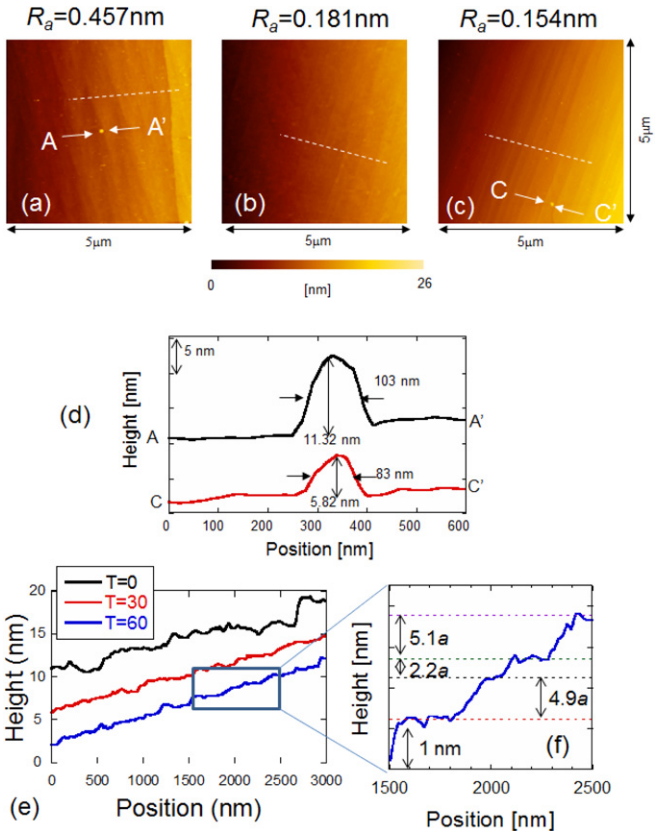

Figure 3. Typical AFM images of the Ib-type diamond (1 1 1) substrate with 5 μm × 5 μm scanning area. Etching time T: (*a*) 0 min (before etching), (*b*) 30 min and (*c*) 60 min with a surface roughness, R_a, of (*a*) 0.457 nm, (*b*) 0.181 nm and (*c*) 0.154 nm, respectively. (*d*) Cross-sectional profile along A–A′ in figure (*a*) and C–C′ in (*c*). (*e*) Cross-sectional profiles of (*a*)–(*c*). (*f*) Magnified profile of (*e*).

The parameter R_a is an arithmetic average of the absolute values of the surface height deviations measured from the best-fitting plane (as shown in the blue dashed line in figures 4(*a*) and (*b*)), which was used to produce AMF images with tilt compensation using the third-order least-squares method. The R_a value is given by

$$R_a = \frac{1}{L}\int_0^L |z(x)|\mathrm{d}x \cong \frac{1}{n}\sum_{i=1}^{n} |z(x_i)|,$$

where $|z(x_i)|$ are the absolute values measured from the best-fitting plane and L is the evaluation length. Physically, dx corresponds to the spatial resolution in the measurement of $f(x)$ and n is the number of pixels in the measurement; $n = L/\mathrm{d}x$. This gives information about the surface roughness, but it is the average value of the roughness for an entire region. Consequently, we calculated the standard deviation of the height difference function $R(l)$ $(=\sqrt{\langle(\overline{z_{k+1}} - \overline{z_k})^2/2\rangle})$, figure 4(*b*)) [17], where l is the bin size and separation, z is the height and $\overline{z_k}$ is the average z value of the bin. Using $R(l)$, we found contributions of different length scales to the overall surface roughness. The scanned area of all images was 256 × 256 pixels with a spatial resolution of 20 nm.

Curves $T_{0\_3.81}$ and $T_{60\_3.81}$ in figure 4(*c*) represent the $R(l)$ at etching times of 0 and 60 min, respectively. These results

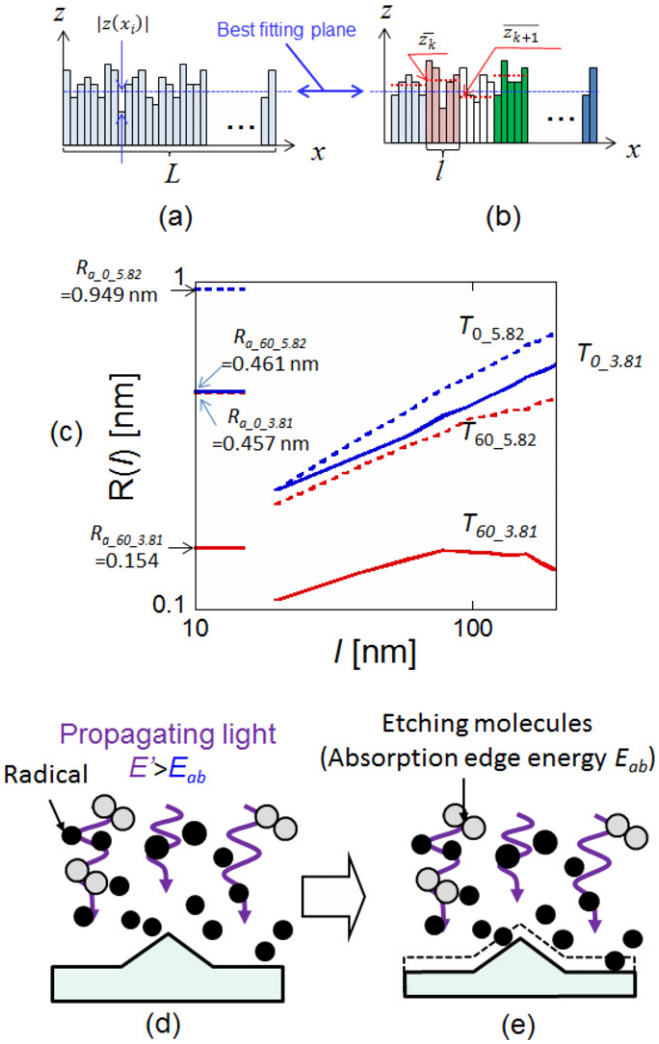

Figure 4. Schematic of (*a*) surface roughness R_a and (*b*) standard deviation $R(l)$. (*c*) Calculated values of $R(l)$. T_{0_325} (0 min), T_{30} (30 min) and T_{60} (60 min). (*d*), (*e*) Schematic of the conventional adiabatic photochemical etching.

indicated that the value of $R(l)$ decreased for all values of l. The order of magnitude of the $R(l)$ values was comparable to the R_a values, and $R(l)$ decreased as the R_a value decreased. We also performed conventional photochemical etching using 5.82 eV light (λ = 213 nm, 20 Hz, pulse width = 5 ns), with a photon energy higher than E_d of 5.12 eV. This induced an adiabatic photochemical reaction in the gas. Etching for 60 min with 5.82 eV light resulted in a drastic decrease in the surface roughness from 0.949 nm (R_a_0_5.82) to 0.461 nm (R_a_60_5.82). However, by comparing the $R(l)$ curves for 5.82 eV etch, $T_{0\_5.82}$ (0 min) and $T_{60\_5.82}$ (60 min) in figure 4(*c*), we found that $R(l)$ remained unchanged for l = 20 nm. Because the tip of the protrusion on the substrate had a larger surface area and a higher etching rate, we expected a reduction in surface roughness. However, 5.82 eV light induced the adiabatic photochemical reaction of the gas (figure 4(*d*)), which did not selectively etch the protrusions. Thus, etching with 5.82 eV light did not change the profiles of the nano-scale surface roughness (figure 4(*e*)).

We performed DPP etching using IIa-type (absorption band edge of below 5.50 eV [18]) diamond (1 1 1) with a

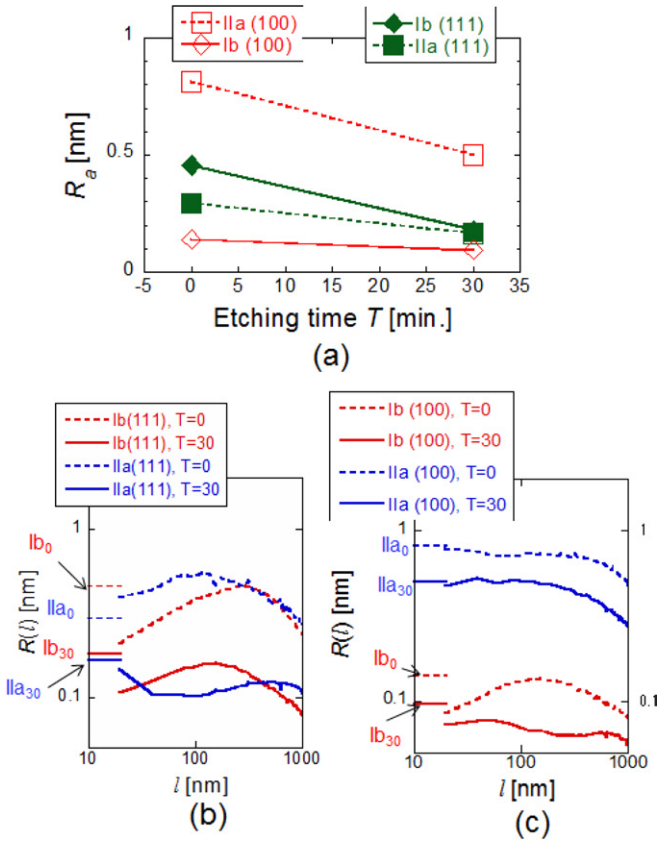

Figure 5. (*a*) Dependence of R_a values on the etching time T with 3.81 eV light. (*b*) Calculated values of $R(l)$ for the (1 1 1) substrate. (*c*) Calculated values of $R(l)$ for the (1 0 0) substrate.

continuum wave He–Cd laser with a wavelength of 325 nm (3.81 eV) and an excitation power of 0.8 W cm^{-2}. Figure 5(*a*) shows the decrease in R_a from 0.294 to 0.166 nm. In addition, DPP etching was performed on a diamond (1 0 0) substrate. The (1 0 0) substrate was also grown under high-pressure and high-temperature conditions. The (1 0 0) substrate was mechanically polished by a conventional method before DPP etching, so that it had a flat surface with R_a less than 1.0 nm. This value was comparable to the ultra-flat surface prepared by ion implantation after mechanical polishing [19]. Using those (1 0 0) substrates, we found the decrease in the R_a value after a 30 min DPP etch (see figure 5(*a*)). Although the initial R_a for IIa-type (1 0 0) was as high as 0.813 nm, the rate of decrease in the R_a value for IIa-type (1 0 0) (10.4×10^{-3} nm min^{-1}, open squares in figure 5(*a*)) was comparable to the rate for Ib-type (1 1 1) (9.2×10^{-3} nm min^{-1}, solid diamonds in figure 5(*a*)). The minimum R_a value of 0.096 nm was obtained for Ib-type (1 0 0) following a 30 min DPP etching. Figures 5(*b*) and (*c*) show the calculated $R(l)$ values, indicating that the DPP etch decreased $R(l)$ for all value of l.

In conclusion, we performed DPP etching on a diamond substrate. Using 3.81 eV light and O_2 gas, we obtained an atomically flat surface with a surface roughness R_a of 0.154 nm (Ib-type (1 1 1)) and 0.096 nm (Ib-type (1 0 0)). By introducing the standard deviation, $R(l)$, we found that the conventional adiabatic photochemical reaction did not remove the smallest surface features, while DPP etching decreased the surface roughness for all length scales. Because DPP etching is a non-contact method and does not cause damage due to polishing, it will improve the electrical and optical performance in a variety of applications. DPP etching can be applied not only to flat but also to three-dimensional surfaces including convex, concave and periodic profiles [20].

References

[1] Makino T, Tokuda N, Kato H, Kanno S, Yamasaki S and Okushi H 2008 *Phys. Status Solidi* a **205** 2200
[2] Denisenko A and Kohn E 2005 *Diamond Relat. Mater.* **14** 491
[3] Gruber A, Dräbenstedt A, Tietz C, Fleury L, Wrachtrup J and von Borczyskowski C 1997 *Science* **276** 2012
[4] Yatsui T, Hirata K, Nomura W, Tabata Y and Ohtsu M 2008 *Appl. Phys.* B **93** 55
[5] Kobayashi K, Sangu S, Ito H and Ohtsu M 2000 *Phys. Rev.* A **63** 013806
[6] Sato A, Tanaka Y, Minami F and Kobayashi K 2009 *J. Lumin.* **129** 1718
[7] Kawazoe T, Kobayashi K, Takubo S and Ohtsu M 2005 *J. Chem. Phys.* **122** 024715
[8] Yonemitsu H, Kawazoe T, Kobayashi K and Ohtsu M 2007 *J. Lumin.* **122–123** 230
[9] Le T H H, Mawatari K, Pihosh Y, Kawazoe T, Yatsui T, Ohtsu M, Tosa M and Kitamori T 2011 *Appl. Phys. Lett.* **99** 213105
[10] Yukutake S, Kawazoe T, Yatsui T, Nomura W, Kitamura K and Ohtsu M 2010 *Appl. Phys.* B **99** 415
[11] Kawazoe T, Fujiwara H, Kobayashi K and Ohtsu M 2009 *IEEE J. Sel. Top. Quantum Electron.* **15** 1380
[12] Keilin D and Hartree E F 1950 *Nature* **165** 543
[13] Miyaji G and Miyazaki K 2008 *Opt. Exp.* **16** 16265
[14] Kawata S, Sun H-B, Tanaka T and Takada K 2001 *Nature* **412** 697
[15] Sumiya H, Toda N and Satoh S 2002 *J. Cryst. Growth* **237–239** 1281
[16] Tokuda N, Umezawa H, Kato H, Ogura M, Gonda S, Yamabe K, Okushi H and Yamasaki S 2009 *Appl. Phys. Express* **2** 055001
[17] Allan D W 1966 *Proc. IEEE* **54** 221
[18] Clark C, Dean P and Harris P 1964 *Proc. R. Soc. Lond.* A **277** 312
[19] Tran Thi T N, Fernandez B, Eon D, Gheeraert E, Härtwig J, Lafford T, Perrat-Mabilon A, Peaucelle C, Olivero P and Bustarret E 2011 *Phys. Status Solidi* a **208** 2057
[20] Yatsui T, Hirata K, Tabata Y, Miyake Y, Akita Y, Yoshimoto M, Nomura W, Kawazoe T, Naruse M and Ohtsu M 2011 *Appl. Phys.* B **103** 527

Appl. Phys. B (2012) 108:707–711
DOI 10.1007/s00340-012-5151-1

Applied Physics B
Lasers and Optics

RAPID COMMUNICATION

Controlling the size of ZnO quantum dots using the dressed photon–phonon-assisted sol–gel method

Y. Liu · T. Yatsui · M. Ohtsu

Received: 7 July 2012 / Published online: 15 September 2012

Abstract We developed a sol–gel method using the dressed photon–phonon (DPP) process. DPPs are selectively exited in nanoscale structures at photon energies that are lower than the bandgap energy, which allows one to increase the growth rate of smaller ZnO quantum dots (QDs). Thus, we obtained a smaller size variance of ZnO QDs. The growth rate was proportional to the power of the light used for DPP excitation. The results were confirmed using a rate equation that accounted for the concentration of the sol–gel solution.

Recently, techniques involving ZnO quantum dots (QDs) have been used to produce nanoscale optical devices known as nanophotonic devices [1, 2]. By using nanophotonic devices, one can decrease the device size beyond the diffraction limit of light and achieve novel functionality unattainable using conventional photonic devices. Furthermore, nanophotonic devices reduce power consumption and achieve energy savings. We have demonstrated AND gate [3–5], NOT gate [6], nanoscale optical energy transfer devices [7], and nanoscale light-harvesting nanofountains [8] as nanophotonic devices.

Several semiconductor materials, including CuCl [1, 3, 8], InAs [5, 6], and CdCe [7, 9], have been used for nanophotonic devices. In particular, ZnO is a promising candidate because of its large exciton binding energy and good optical properties at room temperature [10, 11]. To achieve high-performance nanophotonic devices, the size of ZnO QDs must be accurately controlled to decrease the size variance and resonate the discrete exciton energy level of QDs. A sol–gel method that synthesizes ZnO QDs in liquid solution is advantageous because it allows high productivity and size control. However, when using conventional sol–gel synthesis, the size variance of ZnO QDs exceeds 20 % [12].

Previous studies have proposed the photoetching-assisted sol–gel method to decrease the size variance via He–Cd laser light irradiation ($\lambda = 325$ nm, photon energy = 3.81 eV), in which the photon energy is higher than the bandgap of ZnO QDs ($\lambda = 380$ nm, photon energy = 3.26 eV) to selectively etch large ZnO QDs [13]. Here, we propose the dressed photon–phonon (DPP)-assisted sol–gel method for realizing further size control and decreasing the size variance. Although the irradiating light was not absorbed by the nano-structures, the irradiated photon can couple with the material excitations including the electrons in the nano structures. The coupled state of photon and material excitation is considered as a dressed photon (DP) [2]. Because DPs exist in nanostructures, they can couple with multiple modes of phonons in ZnO precursors to generate a DPP state [14, 15]. The DPP state can activate phonon energy levels that are optically forbidden using conventional propagating light. Thus, chemical reactions can occur via multistep excitation using light irradiation in which the phonon energy is lower than the reaction energy [16, 17]. Figure 1a, b shows schematic diagrams of the growth processes for the conventional sol–gel process and the DPP-assisted sol–gel method, respectively. In the sol–gel method, particle growth proceeds by the dehydration reaction between $ZnOH^-$ in solution and

Y. Liu (✉) · T. Yatsui · M. Ohtsu
Department of Electrical Engineering and Information Systems, School of Engineering, The University of Tokyo, Tokyo 113-8656, Japan
e-mail: ryu@nanophtonics.t.u-tokyo.ac.jp

T. Yatsui · M. Ohtsu
Nanophotonics Research Center, The University of Tokyo, Tokyo 113-8656, Japan

OH^- on the ZnO QD surface ($Zn–OH + ZnOH^- \rightarrow ZnO + H_2O$). Figure 1e shows that for conventional sol–gel synthesis, the solution must be heated until the energy of the molecules is higher than the potential energy barrier of the dehydration reaction. However, for DPP-assisted sol–gel synthesis, one can induce growth via multistep excitation of the DPP generated in the vicinity of ZnO QDs. In other words, the required potential energy is reduced by the DPP process, resulting in an increase in the size of the ZnO QDs (Fig. 1b). Figure 1d shows that the size distribution of the ZnO QDs is Gaussian owing to the thermal equilibrium of the chemical reaction. For the conventional sol–gel method, one can increase the growth rate by increasing the temperature of the growth solution. However, the size distribution is not affected because the heat is applied equally to all ZnO QDs. In contrast to the conventional process, the DPP-assisted process excites the DPP state in smaller QDs selectively; thus, the size variance is expected to decrease, resulting in an asymmetric size distribution (Fig. 1e). Based on the DPP-assisted sol–gel method, we successfully controlled the size and decreased the size variance of ZnO QDs.

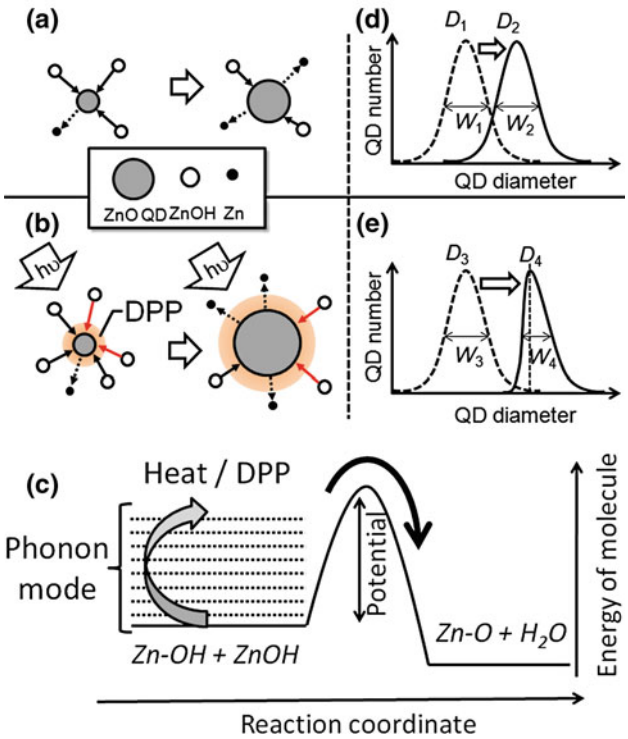

Fig. 1 **a** Mechanism of ZnO QD growth for the conventional sol–gel method. **b** Time transition of the size distribution for QDs synthesized by the conventional sol–gel method. *Dashed curve* size distribution of ZnO QDs in the early phase of growth. W1 is the half-bandwidth of the distribution. *Solid line* size distribution of ZnO QDs at growth saturation. W2 is the half-bandwidth of the distribution. $W_1 \cong W_2$. **c** Mechanism of ZnO QD growth for the DPP-assisted sol–gel method. **d** Time transition of the size distribution for QDs synthesized by the DPP-assisted sol–gel method. *Dashed curve* size distribution of ZnO QDs in the early phase of growth. W3 is the half-bandwidth of the distribution. *Solid line* size distribution of ZnO QDs at growth saturation. W4 is the half-bandwidth of the distribution. $W_1 \cong W_2$

For the sol–gel synthesis of ZnO QDs, 1.1 g of zinc acetate dehydrate and 0.29 g of lithium hydroxide monohydrate were dissolved in ethanol (50 mL) separately, and the two solutions were mixed at 273 K [12]. In conventional sol–gel synthesis, ZnO QDs grow due to the dehydration reaction between the precursors (ZnOH) and hydroxyl groups on the ZnO QD surface as heat energy is absorbed from the growth solution [12, 18]. The growth rate of ZnO QDs is proportional to the concentration of $ZnOH^-$ ([ZnOH]) because higher [ZnOH] increases the probability of dehydration. In addition, desorption also occurs during particle growth. Desorption is induced by the hydrolysis reaction between Zn deposited on the ZnO QD core and H_2O in the growth solution. The probability of hydrolysis is proportional to the H_2O concentration in the growth solution. The H_2O molecules are generated when ZnOH is deposited on the ZnO QD core; therefore, the H_2O concentration is inversely proportional to [ZnOH]. Thus, the desorption rate is also inversely proportional to [ZnOH] [12, 19, 20]. For these reasons, the particle growth rate can be determined by the deposition rate (α [ZnOH]) and desorption rate (α $[ZnOH]^-$), and QD growth can be controlled by the trade-off between deposition and desorption. In contrast, the DPP-assisted sol–gel method has a higher ZnO QD growth rate than the conventional method because the dehydration reaction is accelerated by the DPP state. To verify this principle, we synthesized ZnO QDs by semiconductor laser light irradiation ($\lambda = 671$ nm, 1.85 eV < 3.26 eV), which induced DPPs during ZnO QD growth. Also, the DPP intensity was proportional to the power of the irradiating light; therefore, an increase in size can be expected for light of higher intensity.

To analyze the growth rate, we measured the absorption edge wavelength of the ZnO QDs and calculated the diameter using the relationship between diameter and absorption edge wavelength [13, 21]. The circles in Fig. 2 show the relationship between growth time and QD diameter. The growth rate depended on the power of the irradiating light, and the saturation diameter of the ZnO QDs was proportional to the irradiation power. We successfully controlled the growth rate and size of the ZnO QDs using the DPP-assisted sol–gel method. Based on these results, we analyzed the growth rate quantitatively using a rate equation that accounts for the rates of deposition and desorption. The growth rate was determined by deposition via heat energy, desorption, and DPP-assisted deposition:

1. Deposition by heat energy: The rate of deposition by heat energy is proportional to the amount of ZnOH to

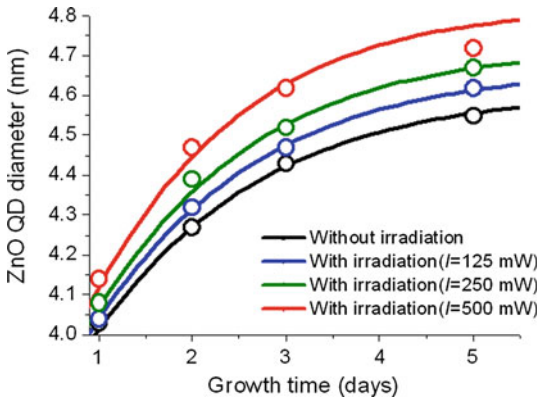

Fig. 2 Relationship between irradiation power and growth rate. Without irradiation: ZnO QDs synthesized without irradiation; with 125 mW irradiation: ZnO QDs synthesized with irradiation ($\lambda = 671$ nm, $I = 125$ mW); with 250 mW irradiation: ZnO QDs synthesized with irradiation ($\lambda = 671$ nm, $I = 250$ mW); with 500 mW irradiation: ZnO QDs synthesized with irradiation ($\lambda = 671$ nm, $I = 500$ mW). I is the power of the irradiating light

be deposited on the QD surface. Therefore, the rate is proportional to the surface area of the ZnO QDs (αr^2: r is the radius of the QD) and [ZnOH].

2. Desorption: The desorption rate is also proportional to the surface area of the ZnO QDs. However, desorption occurs readily as [ZnOH] decreases; therefore, the desorption rate is inversely proportional to [ZnOH].
3. DPP-assisted deposition: The rate of deposition induced by the DPP state is proportional to the power of the irradiating light that induces the DPP process. DPP-assisted deposition occurs via a two-step transition from the phonon energy level. The second step of the transition, from the phonon energy level to the deposition energy level, is a conventional adiabatic transition, and the probability of the second step is more than 10^6 times higher than that of the first step, from ground level to the phonon energy level [22, 23].

Considering (1)–(3), the rate equation was determined as

$$\frac{dr^3}{dt} = \alpha[\mathrm{ZnOH}]r^2 - \beta\frac{1}{[\mathrm{ZnOH}]}r^2 + \gamma I, \quad (1)$$

where r is the radius of the QD and I is the power of the irradiating light. The first to third terms on the right side represent (1)–(3) described above. [ZnOH] can be represented as $[\mathrm{ZnOH}] = 1 - \kappa r^3$, where [ZnOH] decreases in proportion to the volume of the ZnO QDs. α, β, γ, and κ are proportionality constants.

We fitted Eq. (1) to the experimental values. In the case of conventional particle growth without light irradiation ($I = 0$ mW), the third term representing DPP-assisted deposition could be ignored. Furthermore, [ZnOH] could be considered equal to zero for particle growth saturation when the QD diameter was 4.65 nm. Thus, the values of κ, α, and β were found to be 9.95×10^{24}, 1.95×10^{-9}, and 1.50×10^{-9}, respectively, by fitting Eq. (1) to the experimental values for the case without light irradiation. Next, by fitting to the experimental values for $I = 125$ mW (green curve in Fig. 2), γ_{125} mW was 1.38×10^{-9}, γ_{250} mW was 1.41×10^{-9} for $I = 250$ mW, and γ_{500} mW was 1.32×10^{-9} for $I = 500$ mW. Thus, the values agreed well, validating the model and indicating that particle size can be controlled by light intensity.

To observe the effect of the DPP state, one must decrease the probability of deposition by heat energy and increase the probability of desorption. Therefore, we synthesized ZnO QDs by diluting [$ZnOH^-$] in the growth solution. As a result, the growth rate became slower and the saturation size became smaller compared with the conventional method. DPP-assisted deposition, however, was not affected by [$ZnOH^-$]. Therefore, the probability of DPP-assisted deposition became dominant, and the increase in the growth rate was observed clearly. Figure 3 shows the growth rate for 500 mW light irradiation using solutions of the conventional [$ZnOH^-$] and an eightfold-diluted concentration. The growth rate, ΔD, can be defined as

$$\Delta D = (D_{\text{with irradiation}} - D_{\text{without irradiation}})/D_{\text{without irradiation}} \times 100, \quad (2)$$

where $D_{\text{without irradiation}}$ is the diameter of the ZnO QDs synthesized without irradiation and $D_{\text{with irradiation}}$ is the diameter of the ZnO QDs synthesized with irradiation. We confirmed that the growth rate using the eightfold-diluted concentration (red solid curve) was larger than that using the conventional concentration (black solid curve). For ZnO QDs grown for 7 days, the growth rate was 3.7 % with the conventional concentration and 10.6 % using the

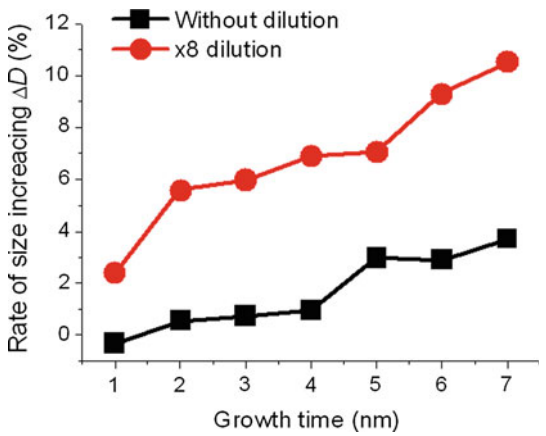

Fig. 3 Relationship between the growth rate and the concentration of the growth solution. Without dilution: increasing growth rate with the conventional concentration; 8× dilution: increasing growth rate with the eightfold-diluted concentration

eightfold-diluted concentration. This suggests that DPP-assisted deposition was dominant, causing the growth acceleration to be more pronounced.

We observed ZnO QDs by transmission electron microscopy (TEM) to analyze the size distribution. Figure 4a, b shows TEM images of ZnO QDs grown for 7 days with and without light irradiation using the conventional and the eightfold-diluted solutions, respectively. The lattice fringes of ZnO QDs can be identified very clearly in the magnified images. The lattice spacings were estimated to be 0.252 nm (without irradiation) and 0.250 nm (with irradiation), which agreed well with the lattice spacing of ZnO QDs along the *c*-axis, confirming high-quality single-crystal growth. Figure 4c, d shows the size distributions measured using binarized TEM images in Fig. 4a, b, respectively. Table 1 summarizes the average size and size distribution of the ZnO QDs. The average diameter for QDs grown without irradiation was 3.1 nm and increased to 3.6 nm with light irradiation. Table 1 also shows that the full-width at half-maximum (FWHM) of the size distribution was 0.88 nm for ZnO QDs grown without irradiation and 0.79 nm for ZnO QDs grown with irradiation. This result indicates that the size variance decreased from 28 to 21 % by introducing DPP-assisted deposition, confirming highly accurate particle size control. For strong, local DPPs the accelerated growth affects smaller ZnO QDs, more so than larger ZnO QDs. To confirm this phenomenon, we compared the size distributions of ZnO QDs synthesized by each method. The blue curve in Fig. 4c is a Gaussian fit to the size distribution of ZnO QDs synthesized without irradiation. The fitting agreed well (97 %) with the size distribution of ZnO QDs with diameters smaller than the average experimental diameter. We confirmed that the size distribution of ZnO QDs synthesized by the conventional sol–gel method is a Gaussian curve, as shown in Fig. 1d, while the red dashed curve in Fig. 4d is a Gaussian fit to the size distribution of ZnO QDs synthesized with irradiation, indicating diameters larger than the average experimental diameter, with an agreement of only 77 %. We confirmed that the growth rate of smaller ZnO QDs synthesized by the DPP-assisted sol–gel method was accelerated selectively, as indicated by the asymmetric size distribution shown in Fig. 1e).

We developed a sol–gel method using DPP-induced deposition for size-controlled ZnO QDs and successfully controlled the QD size and size variance. Growth via DPP-assisted deposition was induced by irradiation with light in which the photon energy was lower than the bandgap of ZnO QDs during growth. Thus, the ZnO QDs synthesized by DPP-induced deposition were larger than those synthesized by the conventional sol–gel method. We analyzed changes in the deposition rate based on light irradiation power using a theoretical model and a rate equation that accounted for the concentration of the growth solution. The

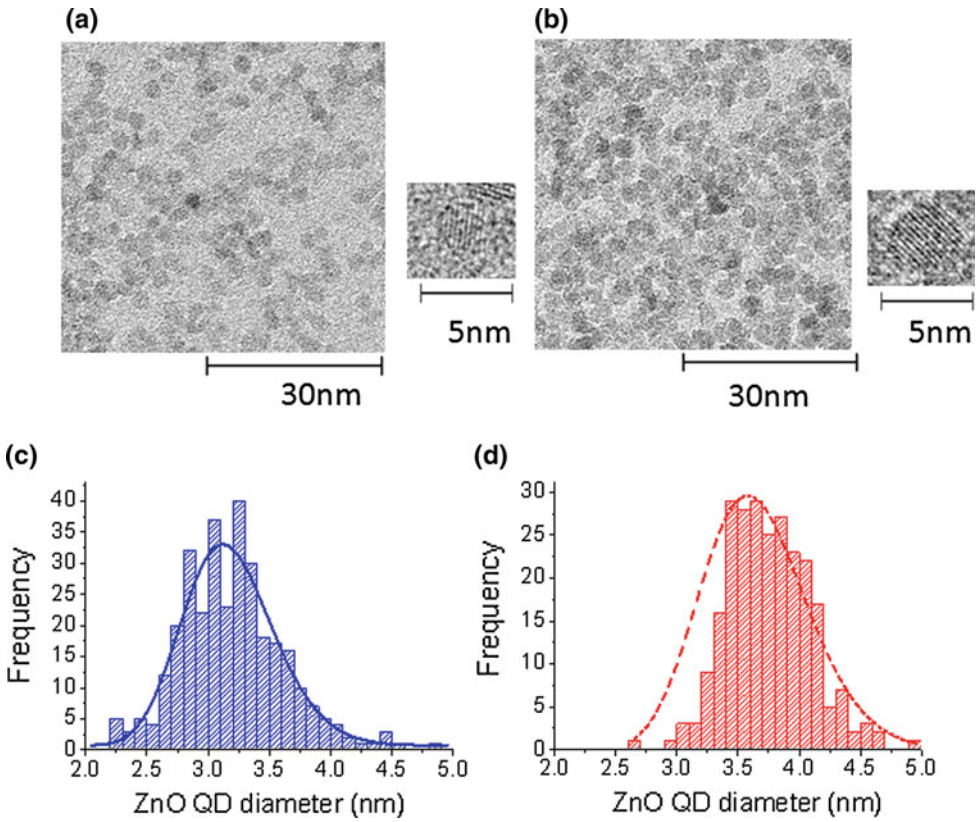

Fig. 4 **a** TEM image of ZnO QDs deposited without light irradiation. **b** TEM image of ZnO QDs deposited with 325 nm laser irradiation. The insets show the respective magnified images. The scale bars in the magnified images are 5 nm. **c** Size distribution of ZnO QDs grown without light irradiation. **d** Size distribution of ZnO QDs grown with 325 nm laser irradiation

Table 1 Average size and size variance of ZnO QDs for respective growth conditions FWHM: full-width at half-maximum

	QD diameter(nm)	FWHM of distribution (nm)	Variance (%)
Without irradiation	3.1	0.88	28
With irradiation	3.6	0.79	21

results agreed well with the experimental data. The size of the ZnO QDs was successfully controlled by the power of the irradiating light; therefore, accelerated growth can be expected using irradiating light of higher intensity. In addition to DPP-assisted deposition, a further decrease in the size variance can be achieved using the photoetching-assisted sol–gel method to selectively etch larger ZnO QDs.

Acknowledgments This work was partially supported by The University of Tokyo Global COE Program "Secure-Life Electronics", Project for Developing Innovation Systems of the Ministry of Education, Culture, Sports, Science and Technology (MEXT), Grant-in-Aid for Young Scientists (A) from MEXT, and by a research grant (Basic Research) from The TEPCO Memorial Foundation.

References

1. T. Kawazoe, K. Kobayashi, J. Lim, Y. Narita, M. Ohtsu, Phys. Rev. Lett. **88**, 067404 (2002)
2. M. Ohtsu, T. Kawazoe, T. Yatsui, M. Naruse, IEEE J. Sel. Top. Quantum Electron. **14**, 1404 (2008)
3. T. Kawazoe, K. Kobayashi, S. Sangu, M. Ohtsu, Appl. Phys. Lett. **82**, 2957 (2003)
4. T. Yatsui, S. Sangu, T. Kawazoe, M. Ohtsu, S.J. An, J. Yoo, G.-C. Yi, Appl. Phys. Lett. **90**, 223110 (2007)
5. T. Kawazoe, M. Ohtsu, S. Aso, Y. Sawado, Y. Hosoda, K. Yoshizawa, K. Akahane, N. Yamamoto, M. Naruse, Appl. Phys. B **103**, 537 (2011)
6. T. Kawazoe, K. Kobayashi, K. Akahane, M. Naruse, N. Yamamoto, M. Ohtsu, Demonstration of nanophotonic NOT gate using near-field optically coupled quantum dots. Appl. Phys. B **84**, 243 (2006)
7. W. Nomura, T. Yatsui, T. Kawazoe, M. Ohtsu, J. Nanophotonics **1**, 011591 (2007)
8. T. Kawazoe, K. Kobayashi, M. Ohtsu, Appl. Phys. Lett. **86**, 103102 (2005)
9. W. Nomura, T. Yatsui, T. Kawazoe, M. Naruse, M. Ohtsu, Appl. Phys. B **100**, 181 (2010)
10. T. Yatsui, H. Jeong, M. Ohtsu, Appl. Phys. B **93**, 199 (2008)
11. T. Yatsui, Y. Ryu, T. Morishima, W. Nomura, T. Kawazoe, T. Yonezawa, M. Washizu, H. Fujita, M. Ohtsu, Appl. Phys. Lett. **96**, 133106 (2010)
12. E.A. Meulenkamp, J. Phys. Chem. B **102**, 5566 (1998)
13. Y. Liu, T. Morishima, T. Yatsui, T. Kawazoe, M. Ohtsu, Nanotechnology **22**, 215605 (2011)
14. Y. Tanaka, K. Kobayashi, J. Microsc. **299**, 228 (2008)
15. K. Kobayashi, A. Sato, T. Yatsui, T. Kawazoe, M. Ohtsu, Appl. Phys. Express **2**, 075504 (2009)
16. T. Yatsui, K. Hirata, Y. Tabata, Y. Miyake, Y. Akita, M. Yoshimoto, W. Nomura, T. Kawazoe, M. Naruse, M. Ohtsu, Appl. Phys. B **103**, 527 (2011)
17. T. Yatsui, T. Kawazoe, M. Ueda, Y. Yamamoto, M. Kourogi, M. Ohtsu, Appl. Phys. Lett. **81**, 3651 (2002)
18. C.J. Brinker, G.W. Scherer, *Sol-Gel Science* (Academic Press, San Diego, 1990)
19. J. Garside, R. Janssen-van Rosmalen, P. Bennema, J. Cryst. Growth **29**, 353 (1975)
20. J. Garside, Industrial crystallization from solution. Chem. Eng. Sci. **40**, 3 (1985)
21. L. Zhang, L.W. Yin, C. Wang, N. Lun, Y. Qi, Appl. Mater. Interfaces **2**, 1769 (2010)
22. T. Kawazoe, H. Fujiwara, K. Kobayashi, M. Ohtsu, IEEE J. Sel. Top. Quantum Electron. **15**, 1380 (2009)
23. T. Kawazoe, K. Kobayashi, S. Takubo, M. Ohtsu, J. Chem. Phys. **122**, 024715 (2005)

Spatiotemporal dynamics in optical energy transfer on the nanoscale and its application to constraint satisfaction problems

Makoto Naruse,[1,2,*] Masashi Aono,[3] Song-Ju Kim,[3] Tadashi Kawazoe,[2,5] Wataru Nomura,[2,5] Hirokazu Hori,[4] Masahiko Hara,[3] and Motoichi Ohtsu[2,5]

[1]*Photonic Network Research Institute, National Institute of Information and Communications Technology, 4-2-1 Nukui-kita, Koganei, Tokyo 184-8795, Japan*

[2]*Nanophotonics Research Center, Graduate School of Engineering, The University of Tokyo, 2-11-16 Yayoi, Bunkyo-ku, Tokyo 113-8656, Japan*

[3]*Flucto-order Functions Research Team, RIKEN Advanced Science Institute, 2-1, Hirosawa, Wako, Saitama 351-0198, Japan*

[4]*Interdisciplinary Graduate School of Medicine and Engineering, University of Yamanashi, Takeda 4-3-11, Kofu, Yamanashi 400-8511, Japan*

[5]*Department of Electrical Engineering and Information Systems Graduate School of Engineering, The University of Tokyo, 2-11-16 Yayoi, Bunkyo-ku, Tokyo 113-8656, Japan*

(Received 22 May 2012; revised manuscript received 10 July 2012; published 5 September 2012)

Nature-inspired devices and architectures are attracting considerable attention for various purposes, including developing novel computing based on spatiotemporal dynamics, exploiting stochastic processes for computing, and reducing energy dissipation. This paper demonstrates that the optical energy transfer between quantum nanostructures mediated by optical near-field interactions occurring at scales far below the wavelength of light could be utilized for solving constraint satisfaction problems (CSPs). The optical energy transfer from smaller quantum dots to larger ones, which is a quantum stochastic process, depends on the existence of resonant energy levels between the quantum dots or a state-filling effect occurring at the larger quantum dots. Such a spatiotemporal mechanism yields different evolutions of energy transfer patterns in multi-quantum-dot systems. We numerically demonstrate that optical energy transfer processes can be used to solve a CSP. The work described in this paper is a first step in showing the applicability and potential of nanometer-scale optical near-field processes toward solving computationally demanding problems.

DOI: 10.1103/PhysRevB.86.125407 PACS number(s): 78.67.−n, 05.10.−a, 05.30.−d

I. INTRODUCTION

There is great demand for novel computing devices and architectures that can overcome the limitations of conventional technologies based solely on electron transfer, in terms of reducing power dissipation, solving computationally demanding problems, and so on.[1] Also, nature-inspired architectures are attracting significant attention from various research arenas, such as brainlike computing and computational neurosciences,[2] stochastic-based computing and noise-based logic,[3] and spatiotemporal computation dynamics.[4]

Among these research topics, Nakagaki *et al*. showed that a single-celled amoebalike organism, a plasmodium of the true slime mold *Physarum polycephalum,* is capable of finding the minimum-length solutions between two food sources.[5] Also, Aono *et al*. demonstrated "amoeba-based computing," such as solving a constraint satisfaction problem (CSP) (Ref. 4) and the traveling salesman problem (TSP),[6] by utilizing the spatiotemporal oscillatory dynamics of the photoresponsive amoeboid organism *Physarum* combined with external optical feedback control. Aside from such experimental demonstrations, Leibtnitz *et al*. showed an algorithm for selecting the most suitable and robust network by utilizing fluctuations inspired by biological experiments where the speed of fluorescence evolution of proteins in bacteria is observed to have a positive correlation with the phenotypic fluctuation of fluorescence over clone bacteria.[7]

These demonstrations indicate that we can utilize the inherent spatial and temporal dynamics appearing in physical processes in nature for novel computing architectures and applications. Such arguments should also be applicable to nanometer-scale light-matter interactions. In fact, Naruse *et al*. demonstrated nanophotonic computing based on optical near-field processes at scales below the wavelength of light.[8] In particular, energy transfer between quantum nanostructures mediated by optical near-field interactions, detailed in Sec. II, plays a crucial role. Optical near-field interactions, which are described by a Yukawa-type potential, have realized energy transfer that involves conventionally dipole-forbidden energy levels. Its theoretical foundation has been explained by the dressed photon model,[9] and the process has been experimentally demonstrated in various quantum nanostructures such as InGaAs,[10] ZnO,[11] CdSe,[12] etc. In particular, Kawazoe *et al*. recently demonstrated room-temperature optical energy transfer using two-layer InGaAs quantum dots (QDs).[13] In addition, the optical energy transfer has been shown to be 10^4 times more energy efficient than that of the bit-flip energy required in conventional electrically wired devices.[14]

This article theoretically demonstrates that optical energy transfer between quantum dots mediated by optical near-field interactions can be utilized for solving a CSP. The optical energy transfer from smaller quantum dots to larger ones depends on the existence of resonant energy levels between the quantum dots or a state-filling effect occurring at the destination quantum dots. Also, as indicated by the quantum master equations, the energy transfer process is fundamentally probabilistic. Such a spatiotemporal mechanism yields different evolutions of energy transfer patterns combined with certain feedback mechanisms, similarly to the evolution of the shape of *Physarum* demonstrated by Aono *et al*. in

Ref. 4. At the same time, in contrast to biological organisms, optical energy transfer is implemented by highly controlled engineering means for designated structures, such as semiconductor quantum nanostructures based on, for instance, molecular beam epitaxy[15] or DNA-based self-assembly.[16] The operating speed of such optical-near-field–mediated quantum-dot systems, which is on the order of nanoseconds when radiative relaxation processes are involved, is significantly faster than those based on biological organisms, which is on the order of seconds or minutes.[4,6] The energy efficiency,[14] as indicated already above, and the possibility of room-temperature operation[13] are also strong motivations behind the investigations described in this paper. Other interesting nanomaterials, such as nanodiamonds,[17,18] could be considered in the implementation aside from semiconductor quantum dots. In addition, we should emphasize that the concept and the principles discussed in this paper are fundamentally different from those of conventional optical computing or optical signal processing, which are limited by the properties of propagating light.[19] The concept and principles are also different from the quantum computing paradigm where a superposition of all possible states is exploited so as to lead to a correct solution.[20] The optical-near-field–mediated energy transfer is a coherent process, suggesting that an optical excitation could be transferred to all possible destination QDs via a resonant energy level, but such coherent interaction between QDs results in a unidirectional energy transfer by an energy dissipation process occurring in the larger dot, as described in Sec. II. Thus, our approach opens up the possibility of another computing paradigm where both coherent and dissipative processes are exploited.

This paper is organized as follows. Section II characterizes state-dependent optical energy transfer via optical near-field interactions. Section III formulates the satisfiability problem studied in this paper, followed by an example demonstration. Section IV concludes the paper.

II. STATE-DEPENDENT OPTICAL ENERGY TRANSFER VIA OPTICAL NEAR-FIELD INTERACTIONS FOR SOLVING A CONSTRAINT SATISFACTION PROBLEM (CSP)

A. Energy transfer between quantum dots mediated by optical near-field interactions

First, we briefly review the fundamental principles of optical energy transfer involving optical near-field interactions.[9,21] We begin with the interaction Hamiltonian between an electron-hole pair and an electric field, which is given by

$$\hat{H}_{\rm int} = -\int d^3r \sum_{i,j=e,h} \hat{\psi}_i^{\dagger}(\mathbf{r}) e\mathbf{r}\cdot\mathbf{E}(\mathbf{r})\hat{\psi}_j(\mathbf{r}), \qquad (1)$$

where e represents the electron charge, $\hat{\psi}_i^{\dagger}(\mathbf{r})$ and $\hat{\psi}_j(\mathbf{r})$ are, respectively, creation and annihilation operators of either an electron ($i,j=e$) or a hole ($i,j=h$) at position $\mathbf{r}$, and $\mathbf{E}(\mathbf{r})$ is the electric field.[22] In usual light-matter interactions, $\mathbf{E}(\mathbf{r})$ is a constant since the electric field of diffraction-limited propagating light is homogeneous on the nanometer scale. Therefore, we can derive optical selection rules by calculating the dipole transition matrix elements. As a consequence, in the case of spherical quantum dots, for instance, only transitions to states specified by $l=m=0$ are allowed, where l and m are the orbital angular momentum quantum number and magnetic quantum number, respectively. In the case of optical near-field interactions, on the other hand, due to the large spatial inhomogeneity of the localized optical near fields at the surface of nanoscale material, an optical transition that violates conventional optical selection rules is allowed. Detailed theory and experimental details can be found in Ref. 23.

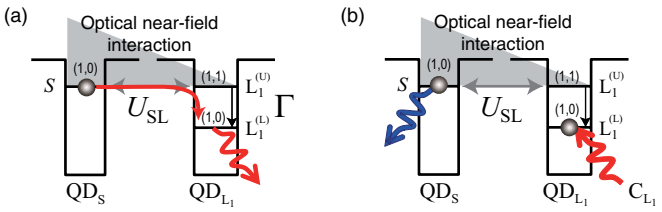

FIG. 1. (Color online) (a) Optical energy transfer between quantum dots mediated by optical near-field interactions. (b) State filling induced at the lower energy level in the larger dot by control light.

Here, we assume two spherical quantum dots whose radii are R_S and R_L, which we call QD_S and QD_{L_1}, respectively, as shown in Fig. 1(a). The energy eigenvalues of states specified by quantum numbers (n,l) are given by

$$E_{nl} = E_g + E_{ex} + \frac{\hbar^2\alpha_{nl}^2}{2MR^2} \quad (n=1,2,3,\ldots), \qquad (2)$$

where E_g is the band-gap energy of the bulk semiconductor, E_{ex} is the exciton binding energy in the bulk system, M is the effective mass of the exciton, and α_{nl} are determined from the boundary conditions, for example, as $\alpha_{n0}=n\pi$, $\alpha_{11}=4.49$. According to Eq. (2), there exists a resonance between the level with quantum number (1,0) in QD_S, denoted by S in Fig. 1(a), and that with quantum number (1,1) in QD_{L_1}, denoted by $L_1^{(U)}$, if $R_L/R_S = 4.49/\pi \approx 1.43$. Note that the (1,1) level in QD_{L_1} is a dipole-forbidden energy level. However, optical near fields allow this level to be populated by excitation.[23] Therefore, an exciton in the (1,0) level in QD_S could be transferred to the (1,1) level in QD_{L_1}. In QD_{L_1}, due to the sublevel energy relaxation with a relaxation constant Γ, which is faster than the near-field interaction, the exciton relaxes to the (1,0) level, denoted by $L_1^{(L)}$, from where it radiatively decays. Also, because the radiation lifetime of quantum dots is inversely proportional to their volume,[24] finally we find unidirectional optical excitation transfer from QD_S to QD_{L_1}.

In the optical excitation transfer discussed above, the energy dissipation occurring in the destination quantum dot determines the unidirectionality of energy transfer. Therefore, when the lower energy level of the destination quantum dot is filled with another excitation (called "state filling"), an optical excitation occurring in a smaller QD can not move to a larger one. As a result, the optical excitation will go back and forth between these dots (optical nutation) and will finally decay from the smaller QD, as schematically shown in Fig. 1(b). This suggests two different patterns of optical energy transfer, which appear depending on the occupation of the destination quantum dots. Another mechanism for realizing two different states is to induce resonance or nonresonance

between QD_S and QD_{L_1} due to many-body effects; details of this are discussed in Ref. 13.

B. Architecture for solving a constraint satisfaction problem: State-dependent energy transfer

To solve a constraint satisfaction problem (CSP) by using the optical energy transfer introduced in Sec. II A, we design an architecture where a smaller QD is surrounded by multiple larger QDs. In this paper, we assume four larger QDs, labeled QD_{L_1}, QD_{L_2}, QD_{L_3}, and QD_{L_4} as indicated in Fig. 2(a). Figure 2(c) shows representative parametrizations associated with the system. The (1,0) level in QD_S is denoted by S, and the (1,1) level in QD_{L_i} is denoted by $L_i^{(U)}$. These levels are resonant with each other and are connected by interdot interactions denoted by U_{SL_i} ($i = 1, \ldots, 4$). It should also be noted that

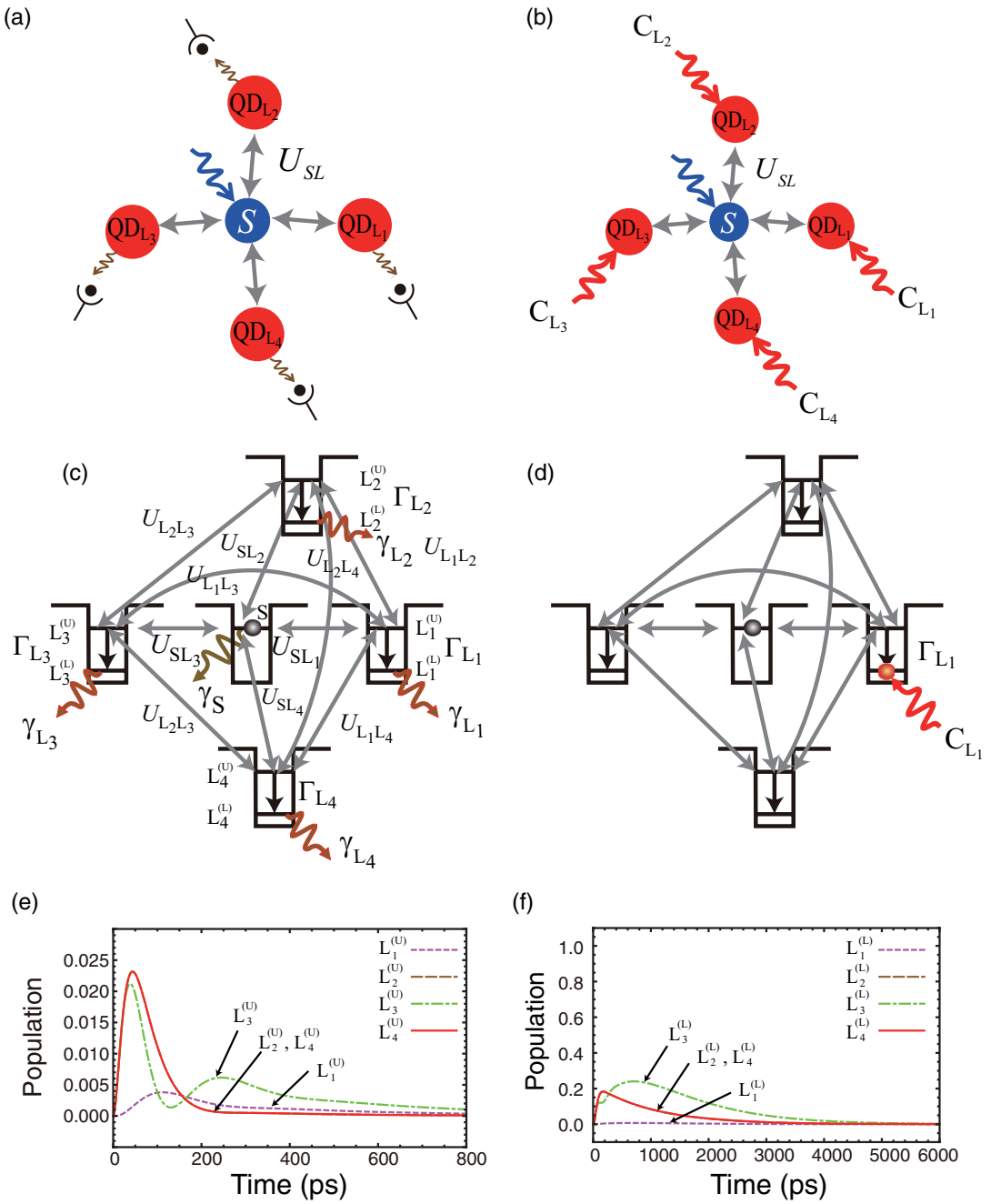

FIG. 2. (Color online) Architecture of the optical-energy-transfer–based satisfiability solver studied in this paper and energy diagram of a system composed of a smaller quantum dot and four larger quantum dots. (a) Radiation from the larger quantum dots is detected. (b) Control light for inducing state filling in the larger quantum dots. (c) Energy diagram and parametrization of the system. (d) A schematic diagram showing state filling induced at the lower energy level in QD_{L_1}. (e), (f) The effect of state filling induced in the lower energy level in QD_{L_1}. (e) Population evolutions for the upper energy levels in QD_{L_i} ($i = 1, \ldots, 4$) with two initial excitons: one exciton sits in S and the other sits in the lower energy level in QD_{L_1}. (f) Population evolutions for the lower energy levels in QD_{L_i} ($i = 1, \ldots, 4$) with one initial exciton in S while inducing a 100-times increase in the sublevel relaxation lifetime $\Gamma_{L_1}^{-1}$.

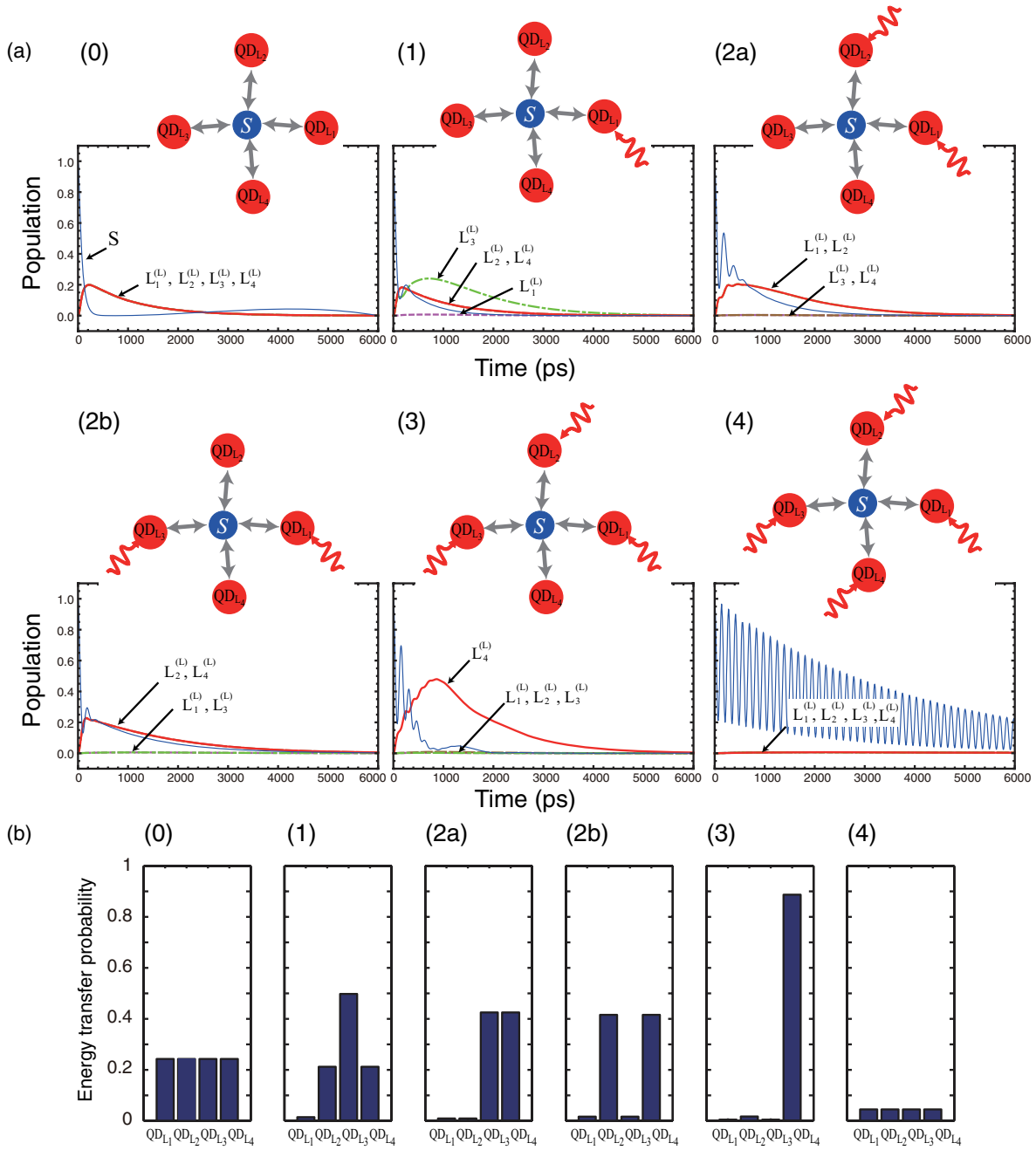

FIG. 3. (Color online) (a) Population evolutions for the lower energy levels in QD_{L_i} ($i = 1, \ldots, 4$) depending on the state filling induced at the larger dots. (b) Estimated energy transfer probabilities calculated as time integrals of the populations shown in (a).

optical near-field interactions between the (1,1) levels in QD_{L_i} and QD_{L_j} ($i \neq j$) are indicated by $U_{L_iL_j}$ in Fig. 3(c), which will be described in detail later below. Note that the interactions $U_{L_iL_j}$ are not shown in Figs. 2(a) and 2(b), nor are other illustrations regarding the architecture of the QD system in this paper, in order to avoid too much complexity in the figures. The lower level in QD_{L_i}, namely, the (1,0) level, is denoted by $L_i^{(L)}$, which could be filled via the sublevel relaxation from $L_i^{(U)}$ ($i = 1, \ldots, 4$), denoted by Γ_{L_i}. The radiations from the S and L_i levels are, respectively, represented by the relaxation constants γ_S and γ_{L_i} ($i = 1, \ldots, 4$). In the following discussion, we call the inverse of the relaxation constant the radiation lifetime. We also assume that the photons radiated from the lower levels of QD_{L_i} can be separately captured by photodetectors, as schematically shown in Fig. 2(a). In addition, as introduced in Sec. I, we assume control light, denoted by C_{L_i} in Fig. 2(b), so as to induce the state-filling effect at $L_i^{(L)}$. Summing up, Figs. 2(a) and 2(b) schematically represent the architecture of the system studied in this paper for solving a CSP. In this section, we characterize the basic behavior of optical energy transfer in the system shown in Figs. 2(a) and 2(b).

First, we suppose that the system initially has one exciton in S. From the initial state, through the interdot interactions U_{SL_i}, the exciton in S could be transferred to $L_i^{(U)}$ ($i = 1, \ldots, 4$).

Also, interactions exist between $L_i^{(U)}$, which are represented by $U_{L_iL_j}$. Accordingly, we can derive quantum master equations in the density matrix formalism.[23,25] The interaction Hamiltonian is given by

$$H_{\rm int} = \begin{pmatrix} 0 & U_{SL_1} & U_{SL_2} & U_{SL_3} & U_{SL_4} \\ U_{SL_1} & 0 & U_{L_1L_2} & U_{L_1L_3} & U_{L_1L_4} \\ U_{SL_2} & U_{L_1L_2} & 0 & U_{L_2L_3} & U_{L_2L_4} \\ U_{SL_3} & U_{L_1L_3} & U_{L_2L_3} & 0 & U_{L_3L_4} \\ U_{SL_4} & U_{L_1L_4} & U_{L_2L_4} & U_{L_3L_4} & 0 \end{pmatrix}. \quad (3)$$

The interdot near-field interactions are given by a Yukawa-type potential

$$U = \frac{A\exp(-\mu r)}{r}, \quad (4)$$

where r denotes the distance between the QDs, and A and μ are constants.[9,23]

The relaxation regarding these five states is described by

$$N_\Gamma = \begin{pmatrix} \frac{\gamma_S}{2} & 0 & 0 & 0 & 0 \\ 0 & \frac{\Gamma_{L_1}}{2} & 0 & 0 & 0 \\ 0 & 0 & \frac{\Gamma_{L_2}}{2} & 0 & 0 \\ 0 & 0 & 0 & \frac{\Gamma_{L_3}}{2} & 0 \\ 0 & 0 & 0 & 0 & \frac{\Gamma_{L_4}}{2} \end{pmatrix}. \quad (5)$$

The Liouville equation for the system is then

$$\frac{d\rho(t)}{dt} = -\frac{i}{\hbar}[H_{\rm int}, \rho(t)] - N_\Gamma\rho(t) - \rho(t)N_\Gamma, \quad (6)$$

where $\rho(t)$ is the density matrix with respect to the five energy levels and $\hbar$ is Planck's constant divided by 2π. Similarly, we can derive differential equations with respect to the lower level of the larger dot $L_i^{(L)}$, which is populated by the relaxations from the upper energy levels with constants Γ_{L_i}, which radiatively decay with relaxation constants γ_{L_i}. In the numerical calculation, we assume $U_{SL_i}^{-1} = 100$ ps, $\Gamma_i^{-1} = 10$ ps, $\gamma_{L_i}^{-1} = 1$ ns, and $\gamma_S^{-1} = (R_L/R_S)^3 \times \gamma_{L_i}^{-1} \approx 2.92$ ns as a typical parameter set. For instance, in the experimental demonstrations based on a CdSe/ZnS core-shell QD shown in Ref. 26, the radiation lifetime of a CdSe/ZnS quantum dot with a diameter of 2.8 nm (larger QD) was measured to be 2.1 ns, which is close to the radiation lifetimes in the above parameter set. Also, the interaction time between smaller and larger quantum dots via optical near fields was estimated to be 135 ps in Ref. 26, which is also close to the above interdot interaction time.

The interactions between larger QDs, $U_{L_iL_j}$, could be obtained by referring to the geometry of the system, which is schematically shown in Figs. 2(a) and 2(b), and the Yukawa-type potential given by Eq. (4). For simplicity, we assume that these interaction times are the same as those between smaller and larger QDs, namely, $U_{L_1L_2}^{-1} = U_{L_2L_3}^{-1} = U_{L_3L_4}^{-1} = U_{L_1L_4}^{-1} = 100$ ps. On the other hand, the interactions between nonadjacent QDs, for example, the interaction between QD_{L_1} and QD_{L_3}, are considered to be weaker with regard to the geometry and the distance dependence given by Eq. (4). In this study, we assume that $U_{L_1L_3}^{-1} = U_{L_2L_4}^{-1} = 1000$ ps. Based on the above modeling and parametrizations, the calculated populations are represented in Fig. 3(a,0), where short-dashed (magenta), long-dashed (brown), dashed-dotted (green), and solid (red) curves, respectively, correspond to populations involving $L_1^{(L)}$, $L_2^{(L)}$, $L_3^{(L)}$, and $L_4^{(L)}$, which are relevant to the radiation from the larger QDs. The population with respect to S is also indicated by a thin solid curve (blue) in Fig. 3(a,0). Since the interdot optical near-field interactions between QD_S and QD_{L_i} are uniform, and the relaxation constants are also uniform for QD_{L_i}, the population evolutions exhibit the same patterns for QD_{L_i} ($i = 1, \ldots, 4$), as shown in Fig. 3(a,0).

Second, we consider situations where one or more of the larger QDs are subjected to state filling by the control light C_{L_i} ($i = 1, \ldots, 4$). Suppose, for example, that the control light C_{L_1} induces state filling at the energy level $L_1^{(L)}$, as schematically shown in Fig. 2(d). In order to take account of such state filling, we calculate the population evolutions with an initial state in which one exciton sits at S and another one is located at $L_1^{(L)}$. Based on a similar formalism to that described in Eqs. (3)–(6), we derive master equations for the two-exciton system, and combine them with those for the one-exciton system.[21] In order to characterize the differences of excitation transfer from QD_S to QD_{L_i} ($i = 1, \ldots, 4$), we evaluate the populations for the upper energy levels in QD_{L_i}, that is $L_1^{(U)}$ ($i = 1, \ldots, 4$). As shown in the solid curves in Fig. 2(e), the populations for $L_2^{(U)}$, $L_3^{(U)}$, and $L_4^{(U)}$ mostly exhibit larger values compared with that for $L_1^{(U)}$, which is shown by the dashed curve. This is a clear indication that optical energy is more likely to be transferred to QD_{L_2}, QD_{L_3}, and QD_{L_4} than to QD_{L_1}.

Another way of describing such an effect in the quantum master equations introduced above is by inducing a significant increase in the sublevel relaxation lifetime that corresponds to the QD_{L_i} subjected to state filling by the control light; more specifically, we assume that $\Gamma_{L_i}^{-1}$ increases by a factor of 1000 due to the control light C_{L_i}. Figure 2(f) characterizes the population evolutions associated with the energy levels in the system when the control light C_{L_1} is switched on. The population for $L_1^{(L)}$, shown by the dashed curve, stays at a lower level, whereas the populations for $L_2^{(L)}$, $L_3^{(L)}$, and $L_4^{(L)}$ increase. That is, Fig. 2(f) also shows that optical energy is more likely be transferred to QD_{L_2}, QD_{L_3}, and QD_{L_4} than to QD_{L_1}, which is consistent with the tendency shown in Fig. 2(e).

Looking at Figs. 2(e) and 2(f) in more detail, the populations for $L_2^{(U)}$ and $L_4^{(U)}$ exhibit different evolutions compared with that of $L_3^{(U)}$; this is because QD_{L_3} is located at the opposite side of QD_{L_1} where the control light is induced. Furthermore, the populations for $L_2^{(U)}$ and $L_4^{(U)}$ initially exhibit larger values compared with that for $L_3^{(U)}$; such behavior is also consistent in Figs. 2(e) and 2(f). Therefore, in the rest of this paper, we take the approach of inducing increases in $\Gamma_{L_i}^{-1}$ by using the control light C_{L_i}.

Figure 3(a) summarizes the population evolutions with respect to different numbers of control light beams. Figure 3(a,1) is the same as Fig. 2(f), as already explained, corresponding to the situation where $L_1^{(L)}$ is subjected to state filling. Figures 3(a,2a) and 3(a,2b) show the populations when two levels among $L_i^{(L)}$ are subjected to state filling. The relative position of the two QDs subjected to control light are different between Figs. 3(a,2a) and 3(a,2b). Figure 3(a,3) shows the

populations when three levels among $L_i^{(L)}$ are subjected to state filling. The energy transfer preferentially flows into the larger dots that are not subjected to state filling with the control light. When all of the larger dots are subjected to state filling, the exciton sitting in the level S initially goes back and forth among the levels S and $L_i^{(U)}$ and decays from the level S, as observed by the solid thin curve in Fig. 3(a,4). The differences in the population evolutions shown in Fig. 3(a) depending on the control light C_{L_i} suggest differences in energy transfer probabilities from the smaller source dot to the larger destination dots. Taking account of such differences, we assume that the energy transfer probability to QD_{L_i} is correlated with the integrals of the populations for $L_i^{(L)}$, as summarized in Fig. 3(b). More specifically, the transition probabilities shown in Fig. 3(b) are the numerical integrations of the populations between 0 and 20 ns divided by a factor of 1000. Note that such population integrals are indeed figures-of-merit (FoM) indicating the trend of optical energy transfer from the smaller quantum dot to the four larger dots. That is, they do *not* satisfy the law of conservation of probability, namely, the sum of the transition probabilities to QD_{L_i} $(i = 1, \ldots, 4)$ is not unity. Instead, we see that the energy transfer to QD_{L_i} occurs if a uniformly generated random number between 0 and 1 is less than the transition probability to QD_{L_i} shown in Fig. 3(b); for example, in the case of Fig. 3(b,3), the energy transfer to QD_{L_4} is induced with high likelihood, whereas the transfers to QD_{L_1}, QD_{L_2}, and QD_{L_3} are induced with lower probability.

The idea for problem solving is to control the optical energy transfer by controlling the destination quantum dot with control light in an adequate feedback mechanism. We assume that a photon radiated, or observed, from the energy level $L_i^{(L)}$ is equivalent to a binary value x_i having a logical level 1, whereas the absence of an observed photon means $x_i = 0$.

To end this section, we make one remark about "nonlocal" properties of the system. The interaction Hamiltonian includes distant interactions $U_{L_1L_3}$ and $U_{L_2L_4}$, not just interactions between adjacent dots. In that sense, a "nonlocal" nature has been treated in this study. Furthermore, we consider that the state-filling-dependent population differences summarized in Fig. 3 also manifest a nonlocal property. The initial exciton sitting in QD_S can be transferred to the upper energy levels of the larger QD via optical near-field interactions. Seemingly, the exciton immediately senses the vacancy in the destination, or larger, QD, and exhibits different energy transfer patterns. For instance, in the case of Fig. 3(a,3), the probability of energy transfer to QD_{L_4} is significantly higher than in the other cases. This can be viewed as a "nonlocal" property in the sense that it is a consequence of the character of the system as a whole.

III. APPLICATION TO SOLVING A CONSTRAINT SATISFACTION PROBLEM

A. Problem formation

We consider the following constraint satisfaction problem as an example regarding an array of N binary-valued variables $x_i \in \{0,1\}\,(i = 1, \ldots, N)$. The constraint is that $x_i = \mathrm{NOR}(x_{i-1}, x_{i+1})$ should be satisfied for all i. That is, variable x_i should be consistent with a logical NOR operation of the two neighbors. For $i = 1$ and N, the constraints are respectively given by $x_1 = \mathrm{NOR}(x_N, x_2)$ and $x_N = \mathrm{NOR}(x_{N-1}, x_1)$. We call this problem the "NOR problem" hereafter in this paper. Taking account of the nature of an individual NOR operation, one important inherent character is that, if $x_i = 1$ then its two neighbors should be both zero ($x_{i-1} = x_{i+1} = 0$). Recall that a photon radiated, or observed, from the energy level $L_i^{(L)}$ corresponds to a binary value $x_i = 1$, whereas the absence of an observed photon means $x_i = 0$. Therefore, $x_i = 1$ should mean that the optical energy transfer to both $L_{i-1}^{(L)}$ and $L_{i+1}^{(L)}$ is prohibited so that $x_{i-1} = x_{i+1} = 0$ is satisfied. Therefore, the feedback or control mechanism is as follows: *Control mechanism*. If $x_i = 1$ at cycle t, then the control light beams C_{i-1} and C_{i+1} are turned on at cycle $t = t + 1$. An example scheme is illustrated in Fig. 4.

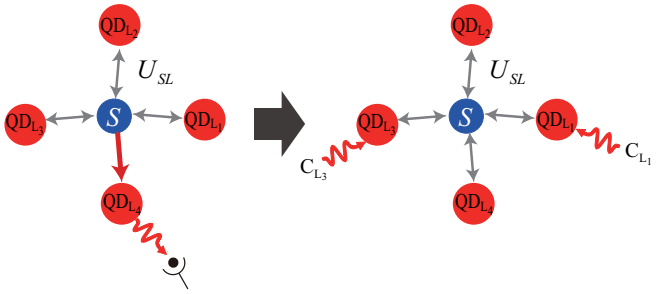

FIG. 4. (Color online) A schematic representation of the feedback mechanism. When the radiation from QD_{L_4} is detected in cycle t, control light beams C_{L_1} and C_{L_3}, which are in channels adjacent to QD_{L_4}, are switched on.

In the case of $N = 4$, variables satisfying the constraints do exist, and they are given by $\{x_1, x_2, x_3, x_4\} = \{0,1,0,1\}$ and $\{1,0,1,0\}$, which we call "correct solutions." There are a few remarks that should be made regarding the NOR problem. One is about the potential deadlock, analogous to Dijkstra's "dining philosophers problem," as already argued by Aono *et al.* in Ref. 4. Starting with an initial state $x_i = 0$ for all i, and assuming a situation where optical energy is transferred to all larger QDs, we observe photon radiation from all energy levels $L_i^{(L)}$ $(i = 1, \ldots, N)$, namely, $x_i = 1$ for all i. Then, based on the feedback mechanism shown above, all control light beams are turned on. If such a feedback mechanism perfectly inhibits the optical energy transfer from the smaller QD to the larger ones at the next step $t + 1$, the variables then go to $x_i = 0$ for all i. This leads to all control light beams being turned off at $t + 2$. In this manner, all variables constantly repeat periodic switching between $x_i = 0$ and 1 in a synchronized manner. Consequently, the system can never reach the correct solutions. However, as indicated in Fig. 3(b), the probability of optical energy transfer to larger dots is in fact not zero even when all larger QDs are illuminated by control light, as shown in Fig. 3(b,4). Also, even for a nonilluminated destination QD, the energy transfer probability may not be exactly unity. Such a stochastic behavior of the optical energy transfer is a key role in solving the NOR problem. This nature is similar to the demonstrations in the amoeba-based computer,[4] where fluctuations of chaotic oscillatory behavior

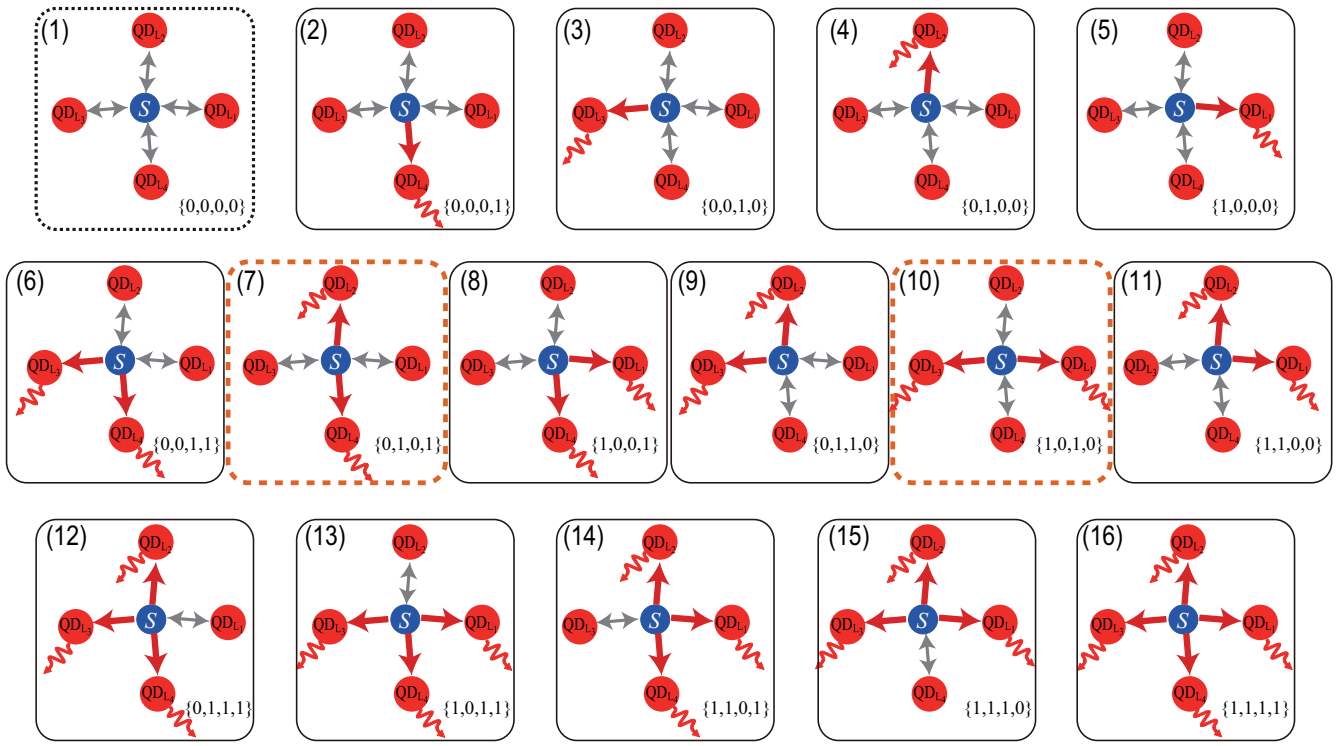

FIG. 5. (Color online) Schematic representation of all possible states of the system. States (7) and (10) correspond to the correct solutions.

involving spontaneous symmetry breaking in the amoeboid organism guarantees such a critical property. In fact, Aono *et al*. experimentally demonstrated solving the NOR problem when $N = 8$ using amoeba and the feedback mechanism shown above.[4]

B. Demonstration

In the case of $N = 4$, there are in total $2^4 = 16$ optical energy transfer patterns from the smaller dot to the larger ones, as schematically summarized in Fig. 5. The numbers shown in the lower-right corner of each inset indicate the corresponding variables $\{x_1,x_2,x_3,x_4\}$. The correct solutions correspond to states (7) and (10) in Fig. 5, marked by dashed boxes. The operating dynamics cause one pattern to change to another one in every iteration cycle. Thanks to the stochastic nature discussed in Secs. II B and III A, each trial could exhibit a different evolution of the energy transfer patterns. In particular, the transition probability, shown in Fig. 3(b), affects the behavior of the transitions. Therefore, we introduce a gain factor (G) to be multiplied by the energy transfer probability summarized in Fig. 3(b).

Figure 6 summarizes the incidences of states for 1000 trials evaluated at $t = 1$, 2, 3, 50, and 100 when $G = 2.5$. The initial state is $\{x_1,x_2,x_3,x_4\} = \{0,0,0,0\}$, meaning that there is no energy transfer to larger dots [state (1) in Fig. 5]. The incidences of states (7) and (10), which are the correct solutions, grow as the iteration cycle increases. The detailed

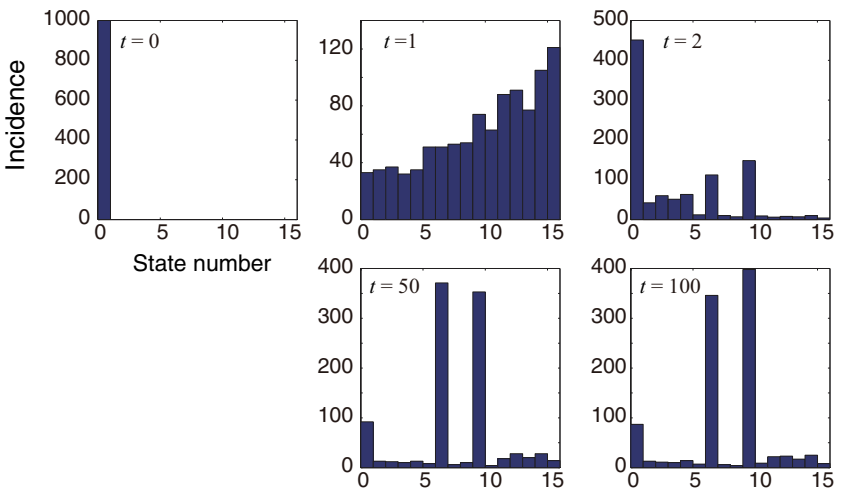

FIG. 6. (Color online) The evolution of incidence patterns of the states among 1000 trials when the gain factor is 2.5. The incidences corresponding to the correct solutions increase as the iteration cycle increases.

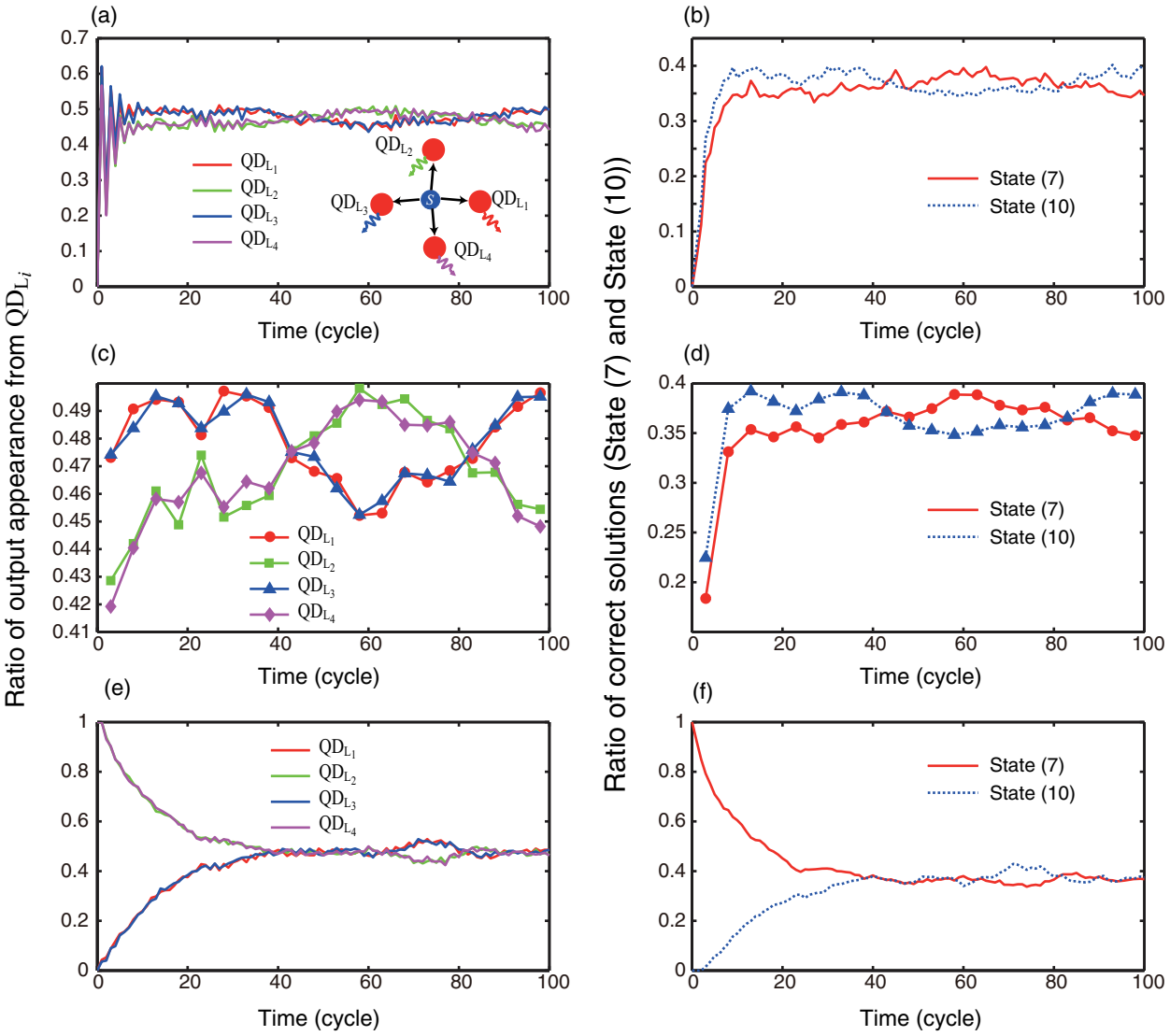

FIG. 7. (Color online) (a) The evolution of the ratio of the output appearance from QD_{L_i}, or $x_i = 1$, and (b) the ratio of the state corresponding to the correct solutions with the initial state (1) in Fig. 5. (c), (d) Time-averaged traces of (b) and (c), respectively. (e) The evolution of the ratio of the output appearance from QD_{L_i}, or $x_i = 1$, and (f) the ratio of the state corresponding to correct solutions with the initial state of (7) in Fig. 5.

behavior of the system is characterized in Figs. 7(a) to 7(d). The curves in Fig. 7(a) represent the evolution of the output appearance from QD_{L_i}, namely, the ratio of the incidence when $x_i = 1$ among 1000 trials evaluated at each cycle. Similarly, the solid and dotted curves in Fig. 7(b) characterize the ratio of the appearance of states (7) and (10), respectively. When we closely examine the evolutions of x_i in Fig. 7(a), we can see that the pair x_1 and x_3 exhibit similar behavior, as do the pair x_2 and x_4. Also, the former pair exhibits larger values when the latter pair shows smaller values, and vice versa. This corresponds to the fact that correct solutions, that is, {0,1,0,1} [state (7)] and {1,0,1,0} [state (10)], are likely to be induced as the iteration cycle increases, as shown in Fig. 6.

Such a tendency is more clearly represented when we evaluate the time averages of the characteristics in Figs. 7(a) and 7(b). Figure 7(c) shows the evolution of the ratio of the incidences when $x_i = 1$, and Fig. 7(d) shows the ratios of states (7) and (10) averaged over every five cycles. We can clearly observe a similar tendency to the one described above. Also, we should emphasize that, thanks to the probabilistic nature of the system, the states of correct solutions appear in an interchangeable, or in an anticorrelated, manner. This is a clear indication of the fact that the probabilistic nature of the system autonomously seeks the solutions that satisfy the constraints of the NOR problem; the state-dependent probability of energy transfer plays a critical role in this. In other words, it should be emphasized that a nonlocal correlation is manifested in the evolution of x_i ($i = 1, \ldots, 4$); for instance, when the system is in state (7), i.e., {0,1,0,1}, the probabilities of energy transfer to QD_{L_1} and QD_{L_3} are equally comparably low (due to state filling), whereas those to QD_{L_2} and QD_{L_4} are equally comparably high, indicating that the probability of energy transfer to an individual QD_{L_i} has inherent spatial patterns or nonlocal correlations. At the same time, the energy transfer

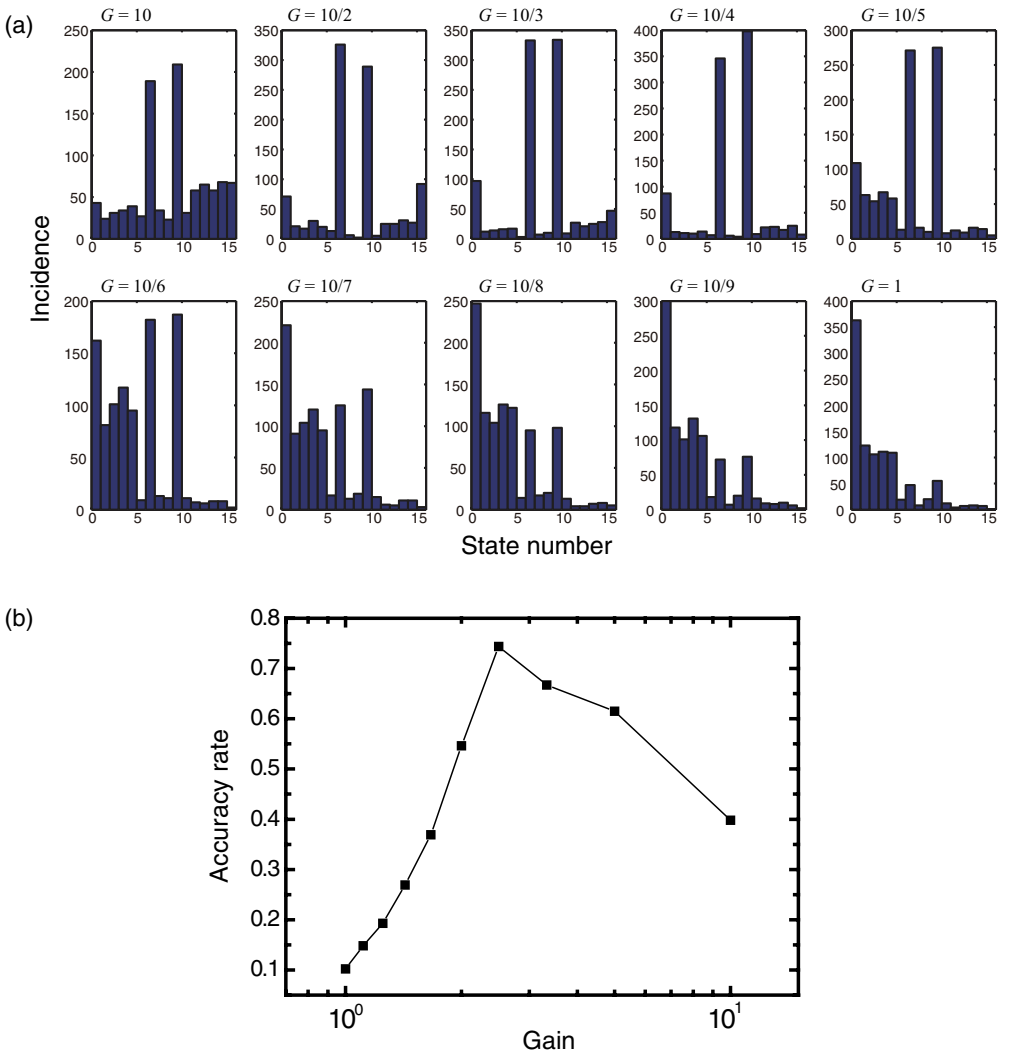

FIG. 8. (Color online) (a) The incidence patterns of the states for different gain factors at the cycle $t = 100$. (b) Calculated accuracy rate, or the ratio of the number of correct states among all trials. The accuracy rate is maximized when the gain factor is 2.5.

to each QD_{L_i} is indeed probabilistic; therefore, the energy transfer probability to, for instance, QD_{L_1} is not zero even in state (7), and thus, the state could transition from state (7) to state (10), and vice versa. In fact, starting with the initial condition of state (7), the ratio of the output appearance from QD_{L_1} and the ratio of the correct solutions evolve as shown in Figs. 7(e) and 7(f), where states (7) and (10) occur equally in the steady state around time cycles after 20.

Figure 8(a) summarizes the incidence patterns at $t = 100$ for 1000 trials as a function of the gain factor ranging from 1 to 10. As shown in the upper-left corner of Fig. 8(a), too high a gain always results in incorrect solutions; this is because energy transfers to larger dots are always induced even when state filling is induced. On the other hand, as shown in the lower-right corner of Fig. 8(a), too low a gain also results in a high incidence of incorrect solutions, indicating that the energy transfer is too strictly inhibited by the control light. Figure 8(c) evaluates the accuracy rate, which is the number of correct solutions among 1000 different trials at $t = 100$, as a function of the gain factor. We can see that a gain of 2.5 provides the highest accuracy rate.

Finally, we make two remarks relevant to this study. The first remark is about the relevance to a satisfiability (SAT) problem. In the case of $N = 4$, solving the NOR problem demonstrated above is equivalent to solving the following satisfiability problem instance given in a conjunctive normal form:

$$\begin{aligned} f(x_1,x_2,x_3,x_4) = {} & (\neg x_1 \vee \neg x_2) \wedge (\neg x_1 \vee \neg x_4) \\ & \times \wedge (\neg x_2 \vee \neg x_3) \wedge (\neg x_3 \vee \neg x_4) \\ & \times \wedge (x_1 \vee x_2 \vee x_3) \wedge (x_1 \vee x_2 \vee x_4) \\ & \times \wedge (x_1 \vee x_3 \vee x_4) \wedge (x_2 \vee x_3 \vee x_4). \end{aligned} \quad (7)$$

Since the maximum number of literals in clauses in Eq. (7) is three, this is an instance of a so-called 3SAT problem.[27] We presume that such a SAT problem could be dealt with by variants of our optical-near-field–mediated systems developed in the future.[28] SAT is an important nondeterministic polynomial-time complete (NP-complete) problem, indicating that no fast algorithm has been found yet.[27] We consider that nanophotonic principles could potentially provide a new way to solve such computationally demanding problems.

The second remark is about implementation of optical energy transfer for such stochastic computing applications. As mentioned in the Introduction, the latest notable features are the rapid advancements in nanomaterials for optical energy transfer.[10–16] Among various technologies, for example, Akahane *et al.* successfully demonstrated energy transfer in multistacked InAs QDs,[29] where layer-by-layer QD size control has been accomplished.[13] Adequate QD size control also allows optical coupling between optical far fields and optically allowed energy levels in a quantum-dot mixture,[30] which could help to solve the interfacing issues of the system. Research in the field of nanodiamonds may also be of promise in implementing the architecture of this study;[17,18] near-field applications of nanodiamonds have already been demonstrated by Cuche *et al.* in Ref. 31.

IV. SUMMARY

In summary, we have demonstrated that energy transfer between quantum nanostructures based on optical near-field interactions occurring at scales far below the wavelength of light has the potential to solve a constraint satisfaction problem. The optical energy transfer from smaller quantum dots to larger ones, which is a quantum stochastic process, depends on the existence of resonant energy levels between the quantum dots or a state-filling effect occurring at the destination quantum dots. We exploit these unique spatiotemporal mechanisms in optical energy transfer to solve a constraint satisfaction problem, and numerically demonstrated that the NOR problem is successfully solved. As indicated in the Introduction, the concept and the principles demonstrated in this paper are based on both coherent and dissipative processes on the nanoscale, which is not the case with conventional optical, electrical, and quantum computing paradigms. The inherently nonlocal nature is also a unique attribute provided by the optical-near-field–mediated optical energy transfer. This paper paves the way for applying nanometer-scale optical near-field processes to solving computationally demanding applications and suggests a new computing paradigm.

ACKNOWLEDGMENT

This work was supported in part by the Strategic Information and Communications R&D Promotion Programme (SCOPE) of the Ministry of Internal Affairs and Communications, and Grants-in-Aid for Scientific Research from the Japan Society for the Promotion of Science.

*naruse@nict.go.jp

[1] *International Technology Roadmap for Semiconductors*, 2009 Edition, Emerging Research Devices.
[2] *Brain-like Computing and Intelligent Information Systems,* edited by S. Amari and N. Kasabov (Springer, Singapore, 1998).
[3] L. B. Kish, Phys. Lett. A **373**, 911 (2009).
[4] M. Aono, M. Hara, and K. Aihara, Commun. ACM **50**, 69 (2007).
[5] T. Nakagaki, H. Yamada, and A. Toth, Nature (London) **407**, 470 (2000).
[6] M. Aono, L. Zhu, and M. Hara, Int. J. Unconventional Comput. **7**, 463 (2011).
[7] K. Leibnitz and M. Murata, IEEE Network, Special Issue on Biologically Inspired Networking **24**, 14 (2010).
[8] M. Naruse, T. Miyazaki, T. Kawazoe, S. Sangu, K. Kobayashi, F. Kubota, and M. Ohtsu, IEICE Trans. Electron. **E88-C**, 1817 (2005).
[9] M. Ohtsu, T. Kawazoe, T. Yatsui, and M. Naruse, IEEE J. Sel. Top. Quantum Electron. **14**, 1404 (2008).
[10] T. Kawazoe, K. Kobayashi, K. Akahane, M. Naruse, N. Yamamoto, and M. Ohtsu, Appl. Phys. B **84**, 243 (2006).
[11] T. Yatsui, S. Sangu, T. Kawazoe, M. Ohtsu, S. J. An, J. Yoo, and G.-C. Yi, Appl. Phys. Lett. **90**, 223110 (2007).
[12] W. Nomura, T. Yatsui, T. Kawazoe, M. Naruse, and M. Ohtsu, Appl. Phys. B **100**, 181 (2010).
[13] T. Kawazoe, M. Ohtsu, S. Aso, Y. Sawado, Y. Hosoda, K. Yoshizawa, K. Akahane, N. Yamamoto, and M. Naruse, Appl. Phys. B **103**, 537 (2011).
[14] M. Naruse, H. Hori, K. Kobayashi, P. Holmström, L. Thylén, and M. Ohtsu, Opt. Express **18**, A544 (2010).
[15] K. Akahane, N. Yamamoto, and M. Tsuchiya, Appl. Phys. Lett. **93**, 041121 (2008).
[16] C. Pistol, C. Dwyer, and A. R. Lebeck, IEEE Micro. **28**, 7 (2008).
[17] Y. Dumeige, F. Treussart, R. Alleaume, T. Gacoin, J.-F. Roch, and P. Grangier, J. Lumin. **109**, 61 (2004).
[18] N. Mohan, Y.-K. Tzeng, L. Yang, Y.-Y. Chen, Y. Y. Hui, C.-Y. Fang, and H.-C. Chang, Adv. Mater. **22**, 843 (2010).
[19] H. J. Caulfield and S. Dolev, Nat. Photonics **4**, 261 (2010).
[20] D. P. DiVincenzo, Science **270**, 255 (1995).
[21] M. Naruse, T. Kawazoe, R. Ohta, W. Nomura, and M. Ohtsu, Phys. Rev. B **80**, 125325 (2009).
[22] H. Haug and S. W. Koch, *Quantum Theory of the Optical and Electronic Properties of Semiconductors* (World Scientific, Singapore, 2004).
[23] M. Ohtsu, K. Kobayashi, T. Kawazoe, T. Yatsui, and M. Naruse, *Principles of Nanophotonics* (Taylor and Francis, Boca Raton, 2008).
[24] T. Itoh, M. Furumiya, T. Ikehara, and C. Gourdon, Solid State Commun. **73**, 271 (1990).
[25] H. J. Carmichael, *Statistical Methods in Quantum Optics 1* (Springer, Berlin, 1999).
[26] W. Nomura, T. Yatsui, T. Kawazoe, and M. Ohtsu, J. Nanophotonics **1**, 011591 (2007).
[27] B. Korte and J. Vygen, *Combinatorial Optimization: Theory and Algorithms* (Springer, Berlin, 2012).
[28] M. Aono, S.-J. Kim, L. Zhu, M. Naruse, M. Ohtsu, H. Hori, and M. Hara, The 2012 International Symposium on Nonlinear Theory and its Applications (NOLTA 2012) (to be published).
[29] K. Akahane, N. Yamamoto, M. Naruse, T. Kawazoe, T. Yatsui, and M. Ohtsu, Jpn. J. Appl. Phys. **50**, 04DH05 (2011).
[30] M. Naruse, T. Kawazoe, S. Sangu, K. Kobayashi, and M. Ohtsu, Opt. Express **14**, 306 (2006).
[31] A. Cuche, A. Drezet, Y. Sonnefraud, O. Faklaris, F. Treussart, J.-F. Roch, and S. Huant, Opt. Express **17**, 19969 (2009).

[II] PRESENTATIONS

IN INTERNATIONAL CONFERENCES

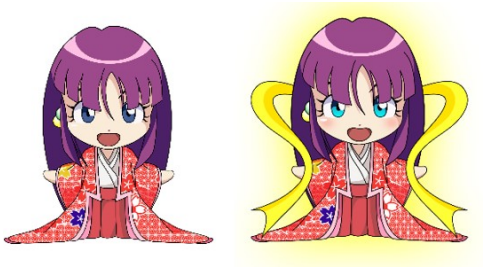

WIO 2013 Chairs Schedule July, 2013

	Monday, 15	Tuesday, 16	Wednesday, 17	Thursday, 18	Friday, 19
Session Chairs:	**Bahram Javidi**	**Toyohiko Yatagai**	**Manuel Martínez Corral**	**Osamu Matoba**	**Artur Carnicer**
9:00-9:30	**Chang Yeong Kim** (Samsung) New challenges for the future 3d tv Keynote session	**Jean-Christophe Olivo-Marin (Institut Pasteur)** Mathematical Microscopy	**O. Matoba (Kobe University)** Assessment of fast recording in parallel phase-shifting digital holography	**Pierre Marquet** (EPFL) Exploring neural transmembrane water movements with digital holographic microscopy : relevance to functional brain imaging	**Juan Campos** (UAB) Building polarimeters with liquid crystal cells
9:30-10:00	**Bahram Javidi** (U.Connecticut) 3D Imaging and Visualization- An Overview of Recent Advances	**Mahalanobis Abhijit** *(Lockheed Martin)* Adaptive Compressive Sensing for efficient target detection	**Toralf Scharf** (EPFL) From achromatic microlenses to submicron focusing: Physical optics at the micro-scale	**Zeev Zalevsky** (BINA) Super resolved configurations in Microscopy	**Filiberto Pla** (U. Jaume I) One-class classificatio n techniques in image recogni- tion problems
10:00-10:40	Coffee break				
Session Chairs:	**Rodríguez-Ramos**	**Mahalanobis Abhijit**	**Enrique Tajahuerce**	**Pierre Marquet**	**Juan Campos**
10:40-11:10	**Marc Pollefeys** (ETH Zurich) Multi-View 3D Imaging	**Enrique Tajahuerce** (U. Jaume I) Single-pixel hyperspectral imaging polarimeter for full Stokes parameter measurement	**Rafael Rebolo** (IAC) Challenges in Astrophysical Imaging	**Makoto Naruse** (NICT) Information Systems based on Optical Near-Field Processes at the Nanoscale	**Jesper Glückstad** (Danmarks Tekniske U.) Optimal light coupling and tracking for wave-guided optical waveguides (WOWs)
11:10-11:40	**Naomi Inoue** (NICT) Glasses-free 3D Display Systems Being Developed at NICT	**Adrian Stern** (Ben Gurion U.) Hyprespectral Compressive Imaging	**Manuel Martínez** (UV) Algorithms for transforming an integral photography into a plenoptic picture	**Takashi Kakue** (Chiba U.) Fast computation of image-reconstruction process of high-speed parallel phase-shifting digital holography	**Artur Carnicer** (U. Barcelona) Realizable highly focused beams with arbitrary polarization
11:40-12:10	**Jinwoong Kim** (ETRI) Holographic video system: issues and approaches	**Masahiro Yamaguchi** (Tokyo IT) Color and multispectral image analysis for quantitative pathology	**Rodríguez-Ramos** (ULL) Plenoptic wavefront tomography	**Yasuhiro Awatsuji** (Kyoto IT) Digital holographic spectroscopy using spectral estimation tech.	**Rafael Pérez Jiménez** (ULPGC) Optical Communication s

12:10-14:00	Lunch				
Session Chairs:	**Jinwoong Kim**	visit to the Teide Astrophysical Observatory	**Adrian Stern**	**Jung-Young Son**	**Filiberto Pla**
14:00-14:30	**Toyohiko Yatagai** (Utsunomiya U.) Multi-Wavelength Doppler Phase Shifting Interferometry		**Jung-Young Son (Konyang University-ETRI)** Problems in Current Electro-Holographic Display	**Pascal Picart** (Univ Lemans) Digital Color Holography Applied to Acoustics and Mechanics	**Salvador Bosch** (U. Barcelona) Increasing the dynamic range of a point diffraction interferometer by simultaneous processing of local interferograms. Applications in ophthalmic optics
14:30-15:00	**Eriko Watanabe (UEC)** High-precision microscopic phase imaging without phase unwrapping		**Poster session**	**Miguel Alonso (Univ. of Rochester)** The connection between rays and waves	**Inocencio R. Martín Benenzuela (ULL)** Upconversion emission in rare earth doped materials under near infrared excitation using silica microspheres as focusing lenses And CLOSING
15:00-15:40	Coffee break		Coffee break		
Session Chairs:	**Eriko Watanabe**			**Miguel Alonso**	
15:40-16:10	**Corinne Fournier** (U. Saint-Etienne) Dictionary size reduction for a faster object recognition in digital holography			**Majid Ebrahim-Zadeh** (ICFO) Nonlinear Light Sources: New Advances	

Dressed photon science and technology for novel devices, fabrications, and energy conversion systems

M. OHTSU
Department of Electrical Eng. and Information Systems, Graduate School of Eng., the Univ. of Tokyo, also with Nanophotonics Research Center, the Univ. of Tokyo
ohtsu@ee.t.u-tokyo.ac.jp

Abstract: This presentation reviews the theoretical picture of dressed photons used to describe the electromagnetic interactions between nanometric particles located in close proximity to each other. The coupling between a dressed photon and multi-mode coherent phonons is also presented. Applications of this novel process to innovative optical devices, fabrication technologies, and energy conversion are demonstrated.

1. Introduction

Dressed photon (DP) science and technology utilize the electromagnetic fields localized in nanometric space. These fields have been named optical near-fields due to their non-propagating features. The principles and concepts of DP science and technology are quite different from those of conventional wave-optical technology encompassing photonic crystals, plasmonics, metamaterials, silicon photonics, and quantum-dot photonic devices. This is because these devices use propagating light even though the materials or particles used may be nanometer-sized. The theoretical picture of DP has been proposed to describe the electromagnetic interactions between nanometric particles located in close proximity to each other. The optical near-field is a virtual cloud of photons that always exists around an illuminated nanometric particle. A real photon (, i.e., conventional propagating scattered light) can be emitted from an electron in an illuminated nanometric particle. Independently of the real photon, another photon is emitted from the electron, and this photon can be reabsorbed within a short duration. This photon, i.e., a virtual photon, is nothing more than the optical near-field, and its energy is localized at the surface of the nanometric particle. Since the virtual photon remains in the proximity of the electron, it can couple with the electron in a unique manner. This coupled state (DP) is a quasiparticle from the standpoint of photon energy transfer. It is the DP that carries the material excitation energy.

2. Principles

The DP has been theoretically described by assuming a multipolar quantum electrodynamic Hamiltonian in a Coulomb gauge in a finite nano-system [1]. After a unitary transformation, the creation and annihilation operators of the DP are expressed as the sum of the operators of the real photon and an electron–hole pair. A real nanometric material is composed not only of electrons but also of a crystal lattice. In this case, after a DP is generated on an illuminated nanometric particle, its energy can be exchanged with the crystal lattice. By this exchange, the crystal lattice can excite the vibration mode coherently, creating a multi-mode coherent phonon state. As a result, the DP and the coherent phonon can form a coupled state (dressed-photon – phonon: DPP). The creation operator of the DPP is expressed as the product of the creation operator of the DP and a displacement operator of the phonon, which represents the creation of the coherent phonon state [2]. This coupled state is a quasi-particle and is generated only when the particle size is small enough to excite the crystal lattice vibration coherently.

3. Application

Three examples for application to energy conversion are reviewed in this presentation: (1) Up-conversion from optical to optical energy by using organic dye particles[3]. (2) Conversion from optical to electrical energy by taking an organic thin film photovoltaic device as an example[4]. (3) Conversion from electrical to optical energy by taking a LED as an example. Novel LED[5], a laser[6], an optical-electrical relaxation oscillator[7], and a photo-detector with optical gains[8] will be demonstrated by using indirect transition-type semiconductors (Si, SiC, and GaP), which are fabricated and operated by DPP. It should also be noted that Si has low toxicity and no concerns about depletion of resources. These notable features, realized by using DP science and technology, are advantageous for energy saving and environmental protection for future society.

Biography (http://uuu.t.u-tokyo.ac.jp/eng/)

Motoichi Ohtsu received the Dr. E. degrees in electronics engineering from the Tokyo Institute of Technology, Tokyo in 1978. He was appointed a Research Associate, an Associate professor, a Professor at the Tokyo Institute of Technology. From 1986 to 1987, while on leave from the Tokyo Institute of Technology, he joined the Crawford Hill Laboratory, AT&T Bell Laboratories, Holmdel, NJ. In 2004, he moved to the University of Tokyo as a professor. He has been the leader of several Japanese national projects for academia-industry collaborations. He has written over 509 papers and received 83 patents. He is the author, co-author, and editor of 62 books, including 27 in English In 2000, he was appointed as the President of the IEEE LEOS Japan Chapter. From 2000, he is an executive director of the Japan Society of Applied Physics. He is a Fellow of the Optical Society of America, and a Fellow of the Japan Society of Applied Physics. He is also a Tandem Member of the Science Council of Japan. He has been awarded 14 prizes from academic institutions, including the Issac Koga Gold Medal of URSI in 1984, the Japan IBM Science Award in 1988, two awards from the Japan Society of Applied Physics in 1982 and 1990, the Inoue Science Foundation Award in 1999, the Japan Royal Medal with a Purple Ribbon from the Japanese Government in 2004, H. Inoue Award from JST in 2005, the Distinguished Achievement Award from the IEICE of Japan in 2007, Julius Springer Prize for Applied Physics in 2009, and Fuji-Sankei Business Eye Award in 2012.

Spatiotemporal optical energy transfer in randomly distributed quantum dots system

Wataru NOMURA[1], Takashi YATSUI[1], Tadashi KAWAZOE[1], Makoto NARUSE[2], and Motoichi OHTSU[1]

[1] School of Engineering, The University of Tokyo, and The Nanophotonics Research Center, The University of Tokyo, Bunkyo-ku, Tokyo, Japan 113-8656
[2] National Institute of Information and Communications Technology, 4-2-1 Nukui-kita, Koganei, Tokyo, Japan 184-8795
nomura@nanophotonics.t.u-tokyo.ac.jp

1. Background: An optical energy transfer based on optical near-field interactions can be suppressed by exciting the destination quantum dot (QD). Based on this principle, the nanophotonic device which acts as all optical switch was developed [1]. Recently, the concept of a novel computing by utilizing fluctuation of optical near-field energy transfer was proposed [2]. On the other hand, we have developed long range optical energy transfer using randomly distributed QD system [3]. Here, we successfully demonstrated a spatiotemporal control of optical energy transfer with suppression of optical near-field energy transfer in randomly distributed QD system.
2. Experiment: We prepared two types of CdSe/ZnS core-shell QDs, designated as QDS and QDL. The ground state of the exciton in QDS was resonant with the first excited state in QDL. Using e-beam lithography and lift-off technique, these QDs were deposited in structures as shown in Fig.1 on a silica substrate. The QDSs and QDLs were randomly and closely dispersed in green and orange regions in Fig. 1, respectively. We measured the emission intensity IA of QDS from an edge of QDS structure named A, during exciting QDS by irradiating the center of QDS structure (shown as white dotted circle in Fig. 1) with UV laser light. We evaluated the variation of IA, with irradiating the other edge of QDS structure, B or C with = 589 nm laser to excite QDL.
3. Result: Figure 2 shows the obtained variation of IA with irradiation of B or C. IA increased in 2.8 % with irradiating B due to suppression of optical energy transfer by exciting QDL in B. However, IA shows no significant variation with irradiating C because there were no QDL in region C. This result indicated the spatiotemporal control of optical energy transfer can be realized by suppression of optical near-field energy transfer.

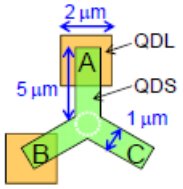

Fig. 1 Schematic image of an experimental sample. Green and orange regions show QDS and QDL structure, respectively.

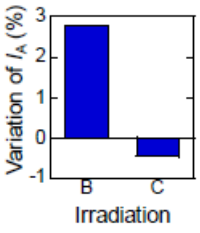

Fig. 2 The variation of I_A with irradiating B or C.

Acknowledgement This work has been partly supported by The New Energy and Industrial Technology Development Organization(NEDO) Project “Development of Next-generation High-performance Technology for Photovoltaic Power Generation System”.

Reference

[1] M. Ohtsu, T. Kawazoe, T. Yatsui, and M. Naruse, “Nanophotonics: Application of Dressed Photons to Novel Photonic Devices, andSystems,” IEEE J. of Selected Topics in Quantum Electronics, 14, 1404 (2008)
[2] Makoto Naruse, Masashi Aono, Song-Ju Kim, Tadashi Kawazoe, Wataru Nomura, Hirokazu Hori, Masahiko Hara, and Motoichi Ohtsu,“Spatiotemporal dynamics in optical energy transfer on the nanoscale and its application to constraint satisfaction problems,” Phys. Rev. B,86, 125407 (2012)
[3] W. Nomura, T. Yatsui, T. Kawazoe, M. Naruse, and M. Ohtsu, “Structural dependency of optical excitation transfer via optical nearfieldinteractions between semiconductor quantum dots, ” Appl. Phys. B, 100, 181 (2010)

Phonon-assisted photo-curing method for autonomous formation of Nanophotonic Droplets

Naoya TATE[1], Yang LIU[1], Tadashi KAWAZOE[1], Makoto NARUSE[2], Takashi YATSUI[1], and Motoichi OHTSU[1]
[1] The University of Tokyo
[2] National Institute of Information and Communications Technology
tate@nanophotonics.t.u-tokyo.ac.jp

Abstract: We have demonstrated a novel technique for autonomously coupling heterogeneous quantum dots to induce particular optical responses based on a simple phonon-assisted photocuring method in which a mixture of quantum dots and photocurable polymer is irradiated with light. The cured polymer sequentially encapsulates coupled quantum dots, forming what we call a Nanophotonic Droplet. The Nanophotonic Droplets exhibited quite homogeneous sizes, shapes, and optical properties due to their characteristic formation process.

Various fabrication technologies have been actively developed for realizing novel devices and systems that operate on the nanometric scale. Among these technologies, self-assembly is one promising method of achieving mass-production of nanometric devices. Previously, we reported an all-autonomous technique for producing *Nanophotonic Droplets* [1], which are coupled heterogeneous quantum dots (QDs) encapsulated by locally cured photocurable polymer. In this technique, a mixture of QDs and photocurable polymer is irradiated with incident light having a lower photon energy than the curing energy of the polymer, inducing a phonon-assisted process [2], namely, multistep excitation, which cures the polymer via excited phonon levels. The important point is that this process occurs only when heterogeneous QDs of similar size come close to each other. In this paper, we describe the basic mechanisms of autonomously fabricating Nanophotonic Droplets, and we discuss their optical properties using the results of experimental demonstrations.

In order to experimentally demonstrate the formation of Nanophotonic Droplets, first we produced nanophotonic droplets by our proposed method and extracted them. Specifically, we used solutions of CdSe-QDs and ZnO-QDs, which emit visible and ultraviolet (UV) light, respectively. Figure 1(a) shows SEM images and microscope emission images of Nanophotonic Droplets formed by irradiating the solutions with assisting light having a wavelength of 532 nm for 30 minutes. The individual emission spectra of four Nanophotonic Droplets A, B, C, and D indicated in Fig. 1(a) are respectively plotted in Fig. 1(b). As shown, similar-sized spherical regions of cured polymer were successfully obtained, and the microspectroscopy results demonstrate the uniformity of the optical properties of the produced Nanophotonic Droplets.

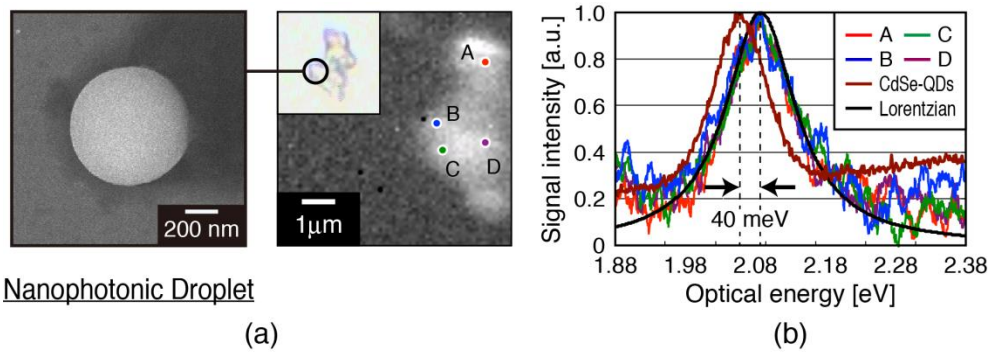

Fig. 1. (a) SEM image and microscope emission image of a single (left) and aggregated (right) Nanophotonic Droplets. (b) Emission spectra of multiple Nanophotonic Droplets, due to emission from the contained CdSe-QDs.

These findings show the fundamental features of our proposed method, where we can obtain a large number of Nanophotonic Droplets with homogeneous optical properties by using an all-autonomous fabrication process. Our method can be easily used in various applications where the further development of novel nanophotonic devices and nanotechnologies will be required.

A part of this work was supported by the Research and Development Program for Innovative Energy Efficiency Technology funded by the New Energy and Industrial Technology Development Organization (NEDO), Japan.

References

[1] N. Tate, et al., Appl. Phys. B, DOI: 10.1007/s00340-012-5249-5, Online First (2012).
[2] T. Kawazoe, et al., Journal of Selected Topics in Quantum Electronics, **15**, Issue 5, pp. 1380-1386 (2009).

THz coherent phonon generation using dressed-photon–phonons in a Si homojunction-structured LED

Naoki WADA[1], Minh Anh TRAN[1], Tadashi KAWAZOE[1,2], and Motoichi OHTSU[1,2]
[1] Dept. Eng., The Univ. Tokyo
[2] Nanophotonics Research Center, The Univ. Tokyo
wada@nanophotonics.t.u-tokyo.ac.jp

Abstract: A novel Si-LED was fabricated based on dressed photons. Signals of several THz were observed, originating from sidebands in the emission spectra. The contribution of dressed-photon–phonons to the THz-signal generation was analyzed by pump–probe spectroscopy using femtosecond light pulses.

Infrared and visible LEDs have been realized by using indirect-transition-type Si bulk crystals based on the principles of dressed-photon–phonons [1,2]. A novel optical and electrical relaxation oscillator has also been developed by using these LEDs [3]. Their EL emission spectral peaks originate from the photon energy irradiated during the process of annealing. Furthermore, they have several sidebands which are due to the contribution of coherent phonons, as shown in Fig. 1 [2]. In the present study, we succeeded in generating a THz signal from a Si-LED and confirmed that LO phonons contributed to the signal generation. The mechanisms of light emission from the Si-LED were analyzed for application to novel monochromatic or broadband Si-LEDs.

In order to observe a THz coherent phonon signal [3] from our homo pn-junction Si-LED, we measured the temporal evolution of the reflectivity, induced by coherent phonon excitation, by pump–probe spectroscopy using 15 fs optical pulses at a wavelength of 800 nm. Figure 2 shows the spectral profile derived from Fourier transformation of the acquired signals. The transformed signals had frequency components at 20 THz, 40 THz, and 60 THz (83 meV, 165 meV, and 248 meV), originating from the coherent phonons. Among them, the signal at 60 THz corresponds to the separation between the sidebands of the Si-LED fabricated by using the same Si substrate, as is shown in Fig. 1 [2], from which we confirmed the generation of coherent phonons of higher sidebands and the correspondence with the EL spectrum of the Si-LED.

By referring to conventional pump–probe spectroscopic studies of phonons [4], the experimental results obtained here demonstrate that the sidebands of the EL emission originated from optical phonons and, furthermore, suggest that the intensities of the sidebands can be controlled by controlling the spectral properties of coherent phonons. Since the present Si-LED was fabricated by phonon-assisted annealing by injecting current while irradiating the device with laser light [1], it is expected that the emission sidebands due to phonons will be suppressed or enhanced by irradiating the Si crystal with a pair of optical pulses having a time difference that is inversely proportional to the phonon frequency [5]. With this method, it should be possible not only to realize highly efficient monochromatic emission but also white-light emission.

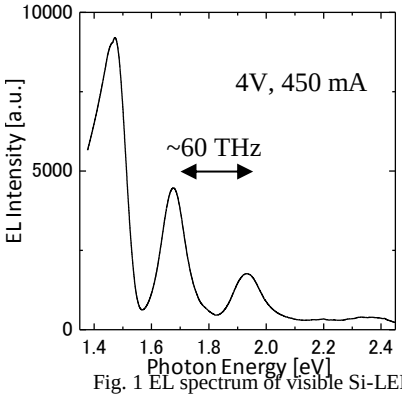

Fig. 1 EL spectrum of visible Si-LED

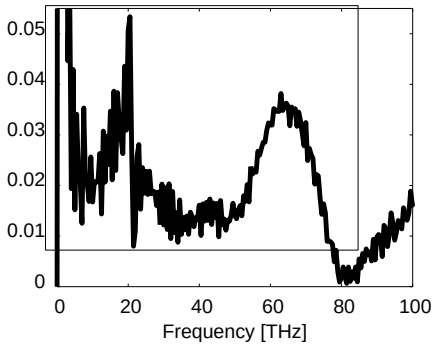

Fig. 2 Transformed THz spectral profiles.

References

[1] T. Kawazoe, M. A. Mueed, and M. Ohtsu, Appl. Phys. B **104**, 747-754 (2011).
[2] A. M. Tran, M. Yamaguchi, T. Kawazoe, and M. Ohtsu, "Silicon blue light emitting diode," Optics & Photonics Japan 2012 (Tokyo, Japan, Oct.).
[3] N. Wada, T. Kawazoe, and M. Ohtsu, Appl. Phys. B **108**, 25-29 (2012).
[4] A. V. Kuznetsov and C. J. Stanton, Phys. Rev. Lett. **73**, 3243-3246 (1994).
[5] T. Mishina, Y. Iwazaki, Y. Masumoto, and M. Nakayama, Solid State Commun. **107**, 281-284 (1998).

Si photodetectors with optical gain using dressed-photon–phonons

Hajime TANAKA[1], Tadashi KAWAZOE[1,2], and Motoichi OHTSU[1,2]
[1] Dept. Eng., The Univ. of Tokyo
[2] Nanophotonics Research Center, The Univ. of Tokyo
tanaka@nanophotonics.t.u-tokyo.ac.jp

Abstract: A novel infrared Si photodetector was fabricated by annealing using current injection and infrared light irradiation. A drastic increase in detection sensitivity was found for incident light whose photon energy was lower than the bandgap energy of Si. This was attributed to optical gain due to stimulated emission via phonon energy levels.

Infrared photodetectors (PDs) are used in a wide range of applications, including optical fiber communication systems. Composite semiconductors (e.g., InSb and InGaAs) with low bandgap energy, Eg, are typically used for PDs. However, a serious problem is the difficulty of integrating them with Si electronic devices due to lattice mis-matching [1]. In order to solve this problem, we realized a novel Si-PD that exhibits high detection sensitivity to incident light with a photon energy lower than Eg of Si [2].

After impurities (boron) were doped into the Si crystal to form a homo pn-junction, the crystal was annealed with Joule heat caused by current injection. During this process, the Si crystal surface was irradiated with laser light, inducing stimulated emission which controlled the diffusion of the boron. A diode laser with a wavelength of 1.32 μm was used as a light source for the irradiation. Curve A in Fig. 1 shows the wavelength dependence of the detection sensitivity of a Si-PD fabricated by annealing with an injected current density of 1.3 A/cm^2 and irradiation with laser light power of 120 mW. This curve shows that the fabricated Si-PD was sensitive even in the wavelength range longer than the cut-off wavelength λc (= 1.11 μm), which is inversely proportional to Eg. Furthermore, its sensitivity was higher than that of a commercially available Si-PD used for comparison (Hamamatsu, S3590; curve B).

By injecting a forward bias current, much higher sensitivity was obtained in the wavelength region longer than λc. Closed circles, squares, and triangles in Fig. 1 represent the measured sensitivity with forward bias current densities of 10 A/cm^2, 3.5 A/cm^2, and 1 A/cm^2, respectively. The closed circle at 1.32 μm shows that the sensitivity was as high as 0.04 A/W. This was achieved due to a unique spatial distribution of impurities (boron) autonomously formed at the pn-junction by the annealing. Furthermore, at 1.16 μm, the sensitivity and the quantum efficiency were as high as 3.1 A/W and 336 %, respectively, due to the optical gain caused by stimulated emission via dressed-photon–phonons.

Curve A in Fig. 2 shows the relation between the incident photon energy and the detection sensitivity of the Si-PD at a forward bias current density of 10 A/cm^2, normalized by that at 1 A/cm^2. For comparison, curve B is the EL spectrum of a Si-LED fabricated using the same annealing method by irradiating 1.32 μm-wavelength light [3]. In curve B, the peak at 0.94 eV originates from the photon energy of the light irradiated in the annealing process. The two peaks at the left are LO phonon sidebands, whose separation is 53 meV. By comparing with curve B, it was found that curve A contains two LO phonon sidebands at higher photon energy. From these sidebands, it is concluded that the optical gain giving a

drastic increase in the detection sensitivity of the Si-PD is due to stimulated emission by the dressed-photon–phonons.

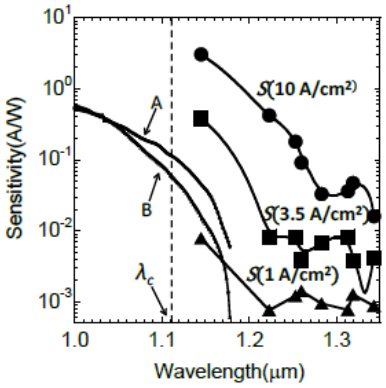

Fig. 1 Sensitivity of the Si-PD.

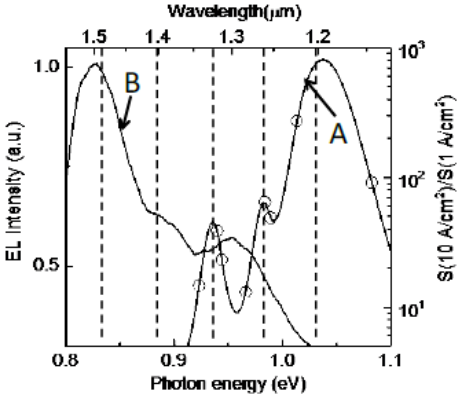

Fig. 2 A: Detection sensitivity of the Si-PD

References

[1] M. E. Groenert, C. W. Leitz, A. J. Pitera, V. Yang, H. Lee, R. J. Ram, E. A. Fitzgerald, J. Appl. Phys., 93, 362-367 (2003).
[2] H. Tanaka, T. Kawazoe, and M. Ohtsu, Appl. Phys. B, 108, 51-56 (2012).
[3] T. Kawazoe, M. A. Mueed, and M. Ohtsu, Appl. Phys. B, 104, 747-754 (2011).

EL emission with the higher photon energy than the bandgap energy from a Silicon homojunction LED based on dressed photon-phonons

Maiku YAMAGUCHI[1], Minh Anh TRAN[1], Tadashi KAWAZOE[1,2], and Motoichi OHTSU[1,2]
[1] Dept. Eng., The Univ. Tokyo
[2] Nanophotonics Research Center, The Univ. Tokyo
yamaguchi@nanophotonics.t.u-tokyo.ac.jp

Abstract: A novel Si-LED was fabricated by using a dressed photon-assisted annealing. It emits the light of the photon energy larger than the bandgap energy. By the successful observation of the phonon sidebands in the emission spectrum, magnitude of the exciton-phonon interaction was estimated.

Slicon, an indirect transition-type semiconductor, has never been used for active optical devices such as LED because of its extremely low emission efficiency. Since Si is high in its crystal quality and low price, a lot of methods have been proposed for realizing LEDs in order for integration with electronic ICs. However, the fatal problems have never been solved, which originated from the indirect transition. In order to solve these problems, the authors have invented the novel annealing which is assisted by dressed photons (the quasi-particle representing the coupled state of a photon and an electron-hole pair) and succeeded in realizing the high efficiency LED with a homo pn-junction bulk crystal of Si [1].

Since the dressed photons create novel phonon energy levels by combining phonons in the crystal [2], the probability of recombination of electron and hole increased via these energy levels even though the semiconductor is indirect transition-type. In order to form a unique distribution of the impurities (borons) in the Si crystal for efficient generation of the dressed photons, the crystal was annealed by injecting the current while the surface was irradiated by the light. The LED fabricated by this annealing emits the light efficiently, and moreover, the emitted photon energy is determined not by the bandgap energy E_g (=1.12 eV) of Si but by the photon energy of the light irradiated in the process of annealing. It means that the emission wavelength can be controlled by the wavelength of the irradiated light. Although the previous study has realized the Si LED with the emission photon energy lower than E_g [1], the present study obtained the higher emission photon energy than E_g by modifying the method of annealing.

After ion-implantation of borons to the As-doped n-type Si crystal to form the homo pn-junction, the 65 mA-current was injected for annealing while the laser light of 1 W-power (photon energy hv_{anneal} =1.4 eV, wavelength=890 nm) was irradiated for one hour. The solid curve in Fig. 1 shows the EL spectrum emitted from the fabricated Si-LED, which shows the high intensity emission peak at hv_{anneal} (=1.4 eV). On its left side, two more peaks are seen, which are confirmed to be the phonon sidebands because the separation (55 meV) between the peaks is equivalent to the

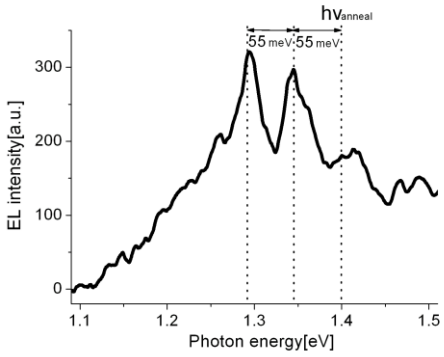

Fig.1 EL emission spectra

LO phonon energy.

The intensity of the phonon sideband can be expressed by a Poisson-distribution function with the Huang-Phys factor *S* and the intensity of the zero-phonon line. Here, the Huang-Phys factor *S* in the Poisson-distribution function represents the magnitude of interaction between excitons and phonons. By fitting this function to the measured EL spectral profile, the value of *S* was found to be 1.82. This value is about 100 times larger than that in the conventional bulk Si crystal, by which the strong interaction between the excitons hole and phonons induced by the dressed photon was confirmed.

In summary, we succeeded in fabricating a Si LED with the emitted photon energy higher than E_g. The origin of the sidebands in the EL spectra was confirmed to be the contribution of the dressed photon-phonons.

References

[1]T. Kawazoe, M. A. Mueed, and M. Ohtsu, Appl. Phys. B, **104**, 747-754 (2011).
[2]T. Kawazoe, K. Kobayashi, S. Takubo, and M. Ohtsu, J. Chem. Phys. **122**, 024715 1-5 (2005).

Highly efficient SiC homojunction structured white- and UV- LEDs based on the dressed photon-assisted process

Tadashi KAWAZOE, Ayako MIZUSHIMA, Kiyomi MATSUE, and Motoichi OHTSU
Department of Electrical Engineering and Information Systems, Graduate School of Engineering, The University of Tokyo, 2-11-16 Yayoi, Bunkyo-ku, Tokyo 113-8656, Japan
kawazoe@ee.t.u-tokyo.ac.jp

Abstract: We fabricated highly efficient white- and UV-LEDs using Silicon carbide (SiC) driven by dressed photons created at the inhomogeneous domain boundary in a homojunction bulk SiC crystal.

1. Introduction

Recently, Silicon carbide (SiC) has attracted attention as a material for high power electric devices. However, SiC is unsuitable for electroluminescence material. Because, SiC is an indirect-transition type semiconductor and therefore, it has been difficult to develop an efficient light emitting diode(LED) for the practical use[1]. On the other hand, according to recent research by the authors, the emission efficiency of SiC has been increased by employing annealing using dressed photons, a technique known as dressed-photon–assisted annealing. This annealing method has already been applied to silicon (Si), an indirect-transition type semiconductor, to realize high-efficiency p–n homojunction-structured LEDs, lasers, and IR photodetectors using bulk Si crystal [2-4].

In this study, we have fabricated and operated a p-n homojunction-structured SiC LED that emits at room temperature by applying dressed-photon–assisted annealing. The principle of the annealing technique, the device fabrication method, and the characteristics of the fabricated devices are described in the presentation.

2. Fabrication

The followings are the fabrication processes: 1**.** A p-n homojunction was formed by the ion implanting method to a n-type bulk SiC wafer. 2. The electrodes on the SiC wafer with a p-n himojunction were fabricated by the sputtering method. 3. The devices were singulated from the SiC wafer with the electrodes. 4. The devices were annealed by Joule heating brought by a forward bias current under the laser irradiation condition (dressed photon–assisted annealing). Here, we used 532-nm (*hv*=2.33eV) laser with the power of 10 mW for the annealing.

3. Device Characters

Figure 1 shows the EL spectra from the SiC LED driven by the constant (0.4mA,8.6V) and pulse (duration; 50μs,100Hz) currents, respectively. At the pulse current operation, The emission peak appeared at photon energy was 3.13 eV in UV region. Figure 2 shows the injection current dependence of the EL power. The quantum efficiency of the LED was about 1% at the pulse current operation.

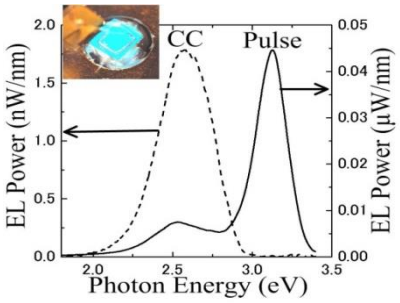

Fig.1. EL spectra from the fabricated

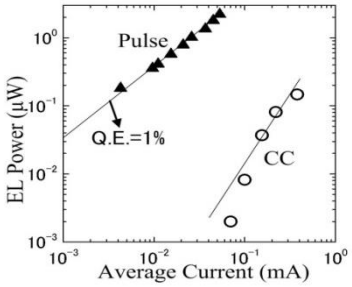

Fig.2. EL power vs. injection currents.

4. Acknowledgment

A part of this study has been supported by "Development of Next-generation High-performance Technology for Photovoltaic Power Generation System Project" of The New Energy and Industrial Technology Development Organization (NEDO) since 2012.

[1] A. Galeckas, J. Linnros, and M. Lindstedt, Materials Science and Engineering B **102**, (2003), pp 304-307.
[2] T. Kawazoe, M. A. Mueed, and M. Ohtsu, Appl. Phys. B-Lasers and Optics, **104**, (20119, pp747-754.
[3] T. Kawazoe, M. Ohtsu, K. Akahane, and N. Yamamoto, Appl. Phys. B-Lasers and Optics, **107**, (2012), pp. 659-663.
[4] H. Tanaka, T. Kawazoe, and M. Ohtsu, Appl. Phys. B-Lasers and Optics, **108**, (2012), pp. 51-56.

Emission from a dipole-forbidden energy state in a GaAs quantum ring induced by near-field interaction with a fiber probe

T. YATSUI[1], W. NOMURA[1], T. MANO[2], H. MIYAZAKI[2], K. SAKODA[2], T. KAWAZOE[1], and M. OHTSU[1]

[1]University of Tokyo, [2]National Institute for Materials Science (NIMS)

yatsui@ee.t.u-tokyo.ac.jp

Abstract: Enhanced emission intensity from a dipole-forbidden state in a GaAs quantum ring was observed, using the near-field interaction induced by the close proximity of an aperture fiber probe tip to quantum ring. A significant decrease in the decay time of the emission was confirmed using time-resolved photoluminescence spectroscopy.

To reduce the size of photonic devices below the diffraction limit, we have proposed nanophotonic devices[1] that consist of semiconductor quantum structures. In a nanophotonic device, the dipole-forbidden energytransition can reduce the size of the device beyond the diffraction limit of light and achieve unidirectional energy transfer, which is unattainable in conventional photonic devices. The dipole-forbidden energy transition originates from an exchange of virtual photons between resonant energy states. The use of virtual photons activates dipole-forbidden energy states. Although emission from the dipole-forbidden energy state cannot be detected in the far field (FF), it can be utilized when the nanoparticle and detector are in close proximity. Here, we report direct observation of emission from an optically forbidden level in GaAs quantum ring using the nearfield (NF) interaction induced by a fiber probe.

The GaAs quantum ring structure was fabricated using the droplet epitaxy technique[2] (see Figs. 1(a) and 1(b)). We performed time-resolved NF photoluminescence (PL) spectroscopy using an apertured fiber probe. Figure 1(c) shows the time-resolved PL spectra obtained at a 725-nm wavelength for the ground state of the GaAs quantum ring; the curves correspond to spectra obtained with probe-to-sample distances of d > 1 m (FF), d ~ 5nm (NF1), d ~ 10nm (NF2), and the conventional FF (FF'). Table 1 shows the respective decay times, τ. Although the emission peak at 725 nm originated from the dipole-forbidden state, the results indicated that the decay time decreased to almost half that of FF spectrum, due to the close proximity of the fiber probe to the quantum ring. These results were attributed to NF interaction between the probe tip and the quantum ring to activate the dipole-forbidden energy state[3].

Table 1. Decay time τ

	τ (ps)
NF1 (d ~5nm)	305
NF2 (d ~10nm)	305
FF (d > 1μm)	330
FF'	580

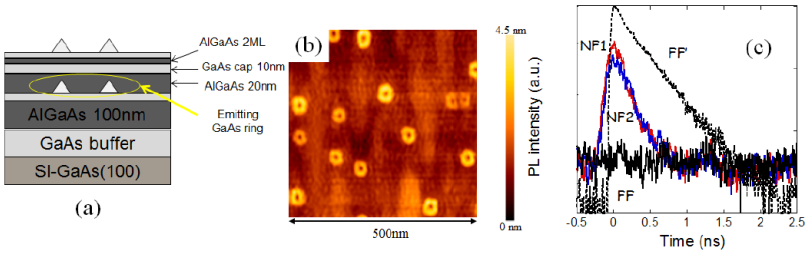

Fig. 1 (a) Schematic diagram of the GaAs ring structure. (b) Atomic force microscopy (AFM) image of the fabricated GaAs ring. (c) Time-resolved photoluminescence (PL) intensity. NF1 and NF 2: near-field PL spectra using NF spectroscopy. FF: Far-field spectra using NF spectroscopy. FF': FF spectra using conventional spectroscopy.

Acknowledgements

This work was financially supported by The New Energy and Industrial Technology Development Organization (NEDO) Project "Development of Next-generation High-performance Technology for Photovoltaic Power Generation System"

1. M. Ohtsu, T. Kawazoe, T. Yatsui and M. Naruse, IEEE J. Select. Top. Quant. Electron. **14** (6), 1404-1417 (2008).
2. T. Mano, T. Kuroda, S. Sanguinetti, T. Ochiai, T. Tateno, J. Kim, T. Noda, M. Kawabe, K. Sakoda, G. Kido and N. Koguchi, Nano Lett. **5** (3), 425-428 (2005).
3. T. Yatsui, M. Tsuji, Y. Liu, T. Kawazoe and M. Ohtsu, Appl. Phys. Lett. **100** (22), 223110 (2012).

Dressed photon phonon assisted electroluminescence mechanism in Si homojunction visible LED

Minh Anh Tran[1], Maiku Yamaguchi[1], Tadashi Kawazoe[1,2], Motoichi Ohtsu[1,2]
[1] Dept. Eng., The Univ. Tokyo, [2] Nanophotonics Research Center, The Univ. Tokyo
minh@nanophotonics.t.u-tokyo.ac.jp

Abstract: We succeeded in fabrication of a novel Si visible light emitting diode (LED) by using dressed photon phonon annealing. By studying emission intensity-voltage characteristic of the device, the dressed photon phonon assisted electroluminescence mechanism was clarified.

Our research group has achieved the first homojunction structured Si light emitting diode (LED) in the world which showed electroluminescent in the visible region at room temperature by using the dressed photon annealing process [1, 2]. In visible wavelength region, whose photon energy is significantly higher than band gap energy, the emission spectrum of this novel Si LED features of three peaks: One peak at photon energy of 3.1 eV (λ=400 nm, corresponding to blue color) and two other peaks at 2.1 eV and 2.0 eV (λ= 590 nm and λ= 620 nm, corresponding to red color) as shown in Fig. 1. In this paper, we studied the relationship between emission intensity and forward bias voltage to clarify the light emitting mechanism.

The emission intensity-voltage relationships at the blue region (peak 3.1 eV) and red region (2.0 eV) are plotted as blue curve and red curve respectively in Fig. 2. When the voltage of 2.5 V the red curve starts rising up and results as a change in slope of the curve. This corresponds to the emission of the light in red color wavelength. Furthermore, at a voltage of about 4 V, there exists a kink in the red curve while the blue curve also changes its slope. This changing point corresponds to the start of blue light emission.

This relationship confirms the electroluminescence mechanism that we have proposed in [2] and illustrated in Fig. 3. Since a dressed photon strongly coupled with coherent phonons, the transition between the phonon coupled electronic levels (horizontal lines) appears if the existence probability of the dressed photon resonant to the transition energy is sufficiently high. Now let the voltage loss due to Schottky and parasite circuit resistance be about 1~1.5 V. Therefore, when a voltage of 3 V applied, the highest energy injected electrons is about 2 eV. Thus of density of electrons relaxed at L-point in the conduction band started rising. Via the interaction with phonon (demonstrated as arrow a), the emission at transition with the photon energy of 2.0 eV appears. This transition corresponds to the change in slope of the red curve in Fig. 2.

After the dressed photon annealing process, almost all the domains of B in Si become suitable to generate dressed photon whose photon energy corresponds to the irradiating light at the annealing (λ=400nm, photon energy 3.1 eV) [2]. Therefore, when an adequate forward bias was applied, the energy of injected electrons became larger than 3.1 eV, thus the emission at transition with phonon energy of 3.1 eV appeared. This transition is indicated by arrow b in Fig. 3, corresponding to the change in slope of the blue curve in Fig. 2. Especially, a kink in red curve is observed at the start of blue emission. It is because a part of injected electrons have been caught to the radiative recombination, thus the density of electrons down to L-point becomes fewer and results as a decrease of emission intensity in red region.

In summary, our proposed dressed photon phonon assisted electroluminescence mechanism has explained thoroughly the emission intensity-voltage characteristic of the novel Si homojunction visible LED.

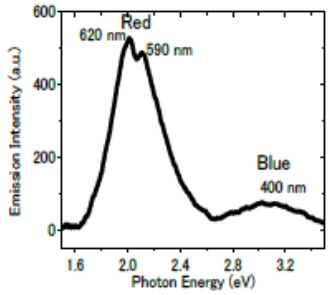

Fig. 1 EL spectrum of visible Si LED

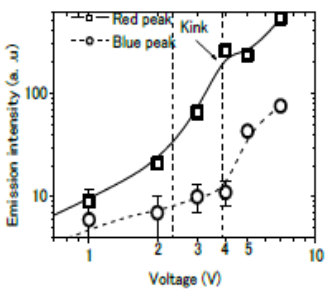

Fig. 2 Peak intensity and voltage relationship

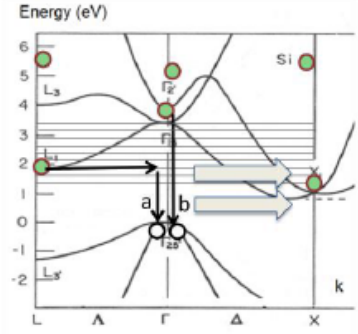

Fig. 3 Dressed photon phonon assisted electroluminescence mechanism

References
[1] T. Kawazoe, M. A. Mueed, and M. Ohtsu, Appl. Phys. B **104**, 747-754 (2011).
[2] A. M. Tran, M. Yamaguchi, T. Kawazoe, and M. Ohtsu, "Silicon blue light emitting diode," Optics & Photonics Japan 2012 (Tokyo, Japan, Oct. 2012).

ZnO quantum structure based nanophotonic device

T. Yatsui[1,2,a)], M. Ohtsu[1,2], and G.-C. Yi[3]

[1] *School of Engineering, University of Tokyo, Bunkyo-ku, Tokyo, 113-8656 Japan*

[2] *The Nanophotonics Research Centre, University of Tokyo, Bunkyo-ku, Tokyo, 113-8656 Japan*

[3] *National Creative Research Initiative Centre for Semiconductor Nanorods and Department of Physics and Astronomy, Seoul National University, Seoul, Gwanak-gu, 151-747 Republic of Korea*

a) Electronic mail: yatsui@ee.t.u-tokyo.ac.jp

To miniaturize the photonic device below the diffraction limit of light, we have proposed nanophotonic devices [1], which consists of quantum dots (QDs) and it can be realized by controlling energy levels in QDs. One representative device studied is a nanophotonic switch using CuCl [2], in which switching dynamics are controlled by a dipole-forbidden optical near field energy transfer among resonant energy levels in QDs. ZnO is a promising material for realizing room-temperature nanophotonic devices, due to the large exciton binding energy [3]. The progress of ZnO studies were supported by the recent achievements in the fabrication of nanorod heterostructures [4]. This paper reviews recent progress of nanophotonic device using one-dimensionally aligned ZnO nanorod multiple-quantum-well structures (MQWs). We demonstrated switching dynamics by a dipole-forbidden optical energy transfer among resonant exciton states [5]. We also observed a superradiance, i.e., a cooperative spontaneous emission [6]. Our findings provide criteria for designing nanoscale synergetic devices without the use of an external cavity.

Acknowledgements

This work was financially supported by a Grant-in-Aid for Young Scientists (A) and Challenging Exploratory Research from MEXT, and by The New Energy and Industrial Technology Development Organization (NEDO) Project “Development of Next-generation High-performance Technology for Photovoltaic Power Generation System”.

References

1. M. Ohtsu, K. Kobayashi, T. Kawazoe, S. Sangu, and T. Yatsui, IEEE J. Select. Top. Quant. Electron. **8**, 839 (2002).
2. T. Kawazoe, K. Kobayashi, S. Sangu, and M. Ohtsu, Appl. Phys. Lett. **82**, 2957 (2003).
3. A. Ohtomo, K. Tamura, M. Kawasaki, T. Makino, Y. Segawa, Z. K. Tang, G. K. L. Wong, Y. Matsumoto, and H. Koinuma, Appl. Phys. Lett. **77**, 2204 (2000).
4. W. I. Park, S. J. An, J. L. Yang, G.-C. Yi, S. Hong, T. Joo, and M. Kim, J. Phys. Chem. B **108**, 15457 (2004).
5. T. Yatsui, S. Sangu, T. Kawazoe, M. Ohtsu, S. J. An, J. Yoo, and G.-C. Yi, Appl. Phys. Lett., **90**, 223110 (2007).
6. T. Yatsui, A. Ishikawa, K. Kobayashi, A. Shojiguchi, S. Sangu, T. Kawazoe, M. Ohtsu, J. Yoo, G.-C. Yi, Appl. Phys. Lett., **100**, 233118 (2012).

4B-2

Intelligence by Nanophotonics: Solution Searching and Information Security Applications

Makoto Naruse[1,†], Naoya Tate[2], Masashi Aono[3], Song-Ju Kim[4], and Motoichi Ohtsu[2]

1 Photonic Network Research Institute, National Institute of Information and Communications Technology, 4-2-1 Nukui-kita, Koganei, Tokyo 184-8795, Japan

2 Department of Electrical Engineering and Information Systems / Nanophotonics Research Center, Graduate School of Engineering, The University of Tokyo, 2-11-16 Yayoi, Bunkyo-ku, Tokyo 113-8656, Japan

3 Earth-Life Science Institute, Tokyo Institute of Technology, 2-12-1-1E-1 Ookayama, Meguro-ku, Tokyo 152-8550, Japan

4 WPI Center for Materials Nanoarchitectonics, National Institute for Materials Science, 1-1 Namiki, Tsukuba, Ibaraki 305-0044, Japan

E-mail: †naruse@nict.go.jp

Abstract Nanophotonics has been extensively studied with the aim of unveiling and exploiting light–matter interactions that occur at a scale below the diffraction limit of light. From the viewpoint of information, novel architectures, design and analysis principles, and even novel computing paradigms should be considered so that we can fully benefit from the potential of nanophotonics for various applications. In this paper, we first present some fundamental and emergent attributes associated with optical excitation transfer mediated by optical near-field interactions. Toward achieving a computing paradigm that surpasses the classical von Neumann architecture, we describe stochastic solution searching, which exploits the spatiotemporal dynamics of optical excitation transfer. Second, we show information security applications based on near-field processes together with their theoretical and experimental foundations. We consider that a common feature across all of these demonstrations is the extraction of "*intelligent*" functions and behaviors from an information-based standpoint while exploiting unique properties offered by light and matter interactions in the nanometer-scale.

Keyword Nanophotonics, optical near-field, nanostructure, nanotechnology, information and communications technology, solution search, optical security.

1. Introduction

Nanophotonics has been extensively studied with the aim of unveiling and exploiting light–matter interactions that occur at a scale below the diffraction limit of light, and recent progress made in experimental technologies—both in nanomaterial fabrication and characterization—is driving further advancements in the field [1]. From the viewpoint of information, on the other hand, novel architectures, design and analysis principles, and even novel computing paradigms should be considered so that we can fully benefit from the potential of nanophotonics [2]. This paper examines intelligent functions based on nanophotonics. More specifically, we present some fundamental and emergent information properties that stem from optical excitation transfer mediated by optical near-field interactions and the hierarchical properties inherent in optical near-fields. First, toward achieving a computing paradigm that surpasses the classical von Neumann architecture, we describe stochastic solution searching, which exploits the spatiotemporal dynamics of optical excitation transfer [3,4]. Second, we show information security applications based on near-field applications together with their theoretical and experimental foundations [5].

2. Solution Searching by Nanophotonics

There is great demand for novel computing devices and architectures that can overcome the limitations of conventional technologies based solely on electron transfer, in terms of reducing power dissipation, solving computationally intractable problems, and so on [6]. Also, nature-inspired architectures are attracting significant attention from various research areas, such as brain-like

computing and computational neurosciences [7], stochastic-based computing and noise-based logic [8], and spatiotemporal computation dynamics [9].

Among these research topics, Aono *et al.* demonstrated "amoeba-based computing" by utilizing the spatiotemporal oscillatory dynamics of the photoresponsive amoeboid organism Physarum combined with external optical control to solve a constraint satisfaction problem (CSP) [9] and the traveling salesman problem (TSP) [10]. Besides such experimental demonstrations, Leibtnitz *et al.* showed an algorithm for selecting the most suitable and robust network by utilizing fluctuations, inspired by biological experiments where the speed of fluorescence evolution of proteins in bacteria is observed to have a positive correlation with the phenotypic fluctuation of fluorescence over clone bacteria [11].

These demonstrations indicate that we can utilize the inherent spatial and temporal dynamics appearing in physical processes in nature for novel computing architectures and applications. Such arguments should also be applicable to nanometer-scale light–matter interactions. In fact, Naruse *et al.* demonstrated nanophotonic computing based on optical near-field processes at scales below the wavelength of light [12]. In particular, energy transfer between quantum nanostructures mediated by optical near-field interactions plays a crucial role. Optical near-field interactions, which are described by a Yukawa-type potential, have been used to realize energy transfer that involves conventionally dipole-forbidden energy levels. Its theoretical foundation has been explained by the dressed photon model [1], and the process has been experimentally demonstrated in various quantum nanostructures, such as InGaAs [13], ZnO [14], and CdSe [15]. In particular, Kawazoe *et al.* recently demonstrated room-temperature optical energy transfer using two-layer InGaAs quantum dots (QDs) [16]. In addition, the optical energy transfer has been shown to be 10^4-times more energy efficient than that of the bit-flip energy required in conventional electrically wired devices [17].

We demonstrated that a network of optical energy transfers between quantum dots mediated by optical near-field interactions can be utilized for solving the CSP [2], the satisfiability problem (SAT) [3], and the multi-armed bandit problem (BP) [18], which is a decision making problem. The optical energy transfer from smaller quantum dots to larger ones depends on the existence of resonant energy levels between the quantum dots or a state-filling effect occurring at the larger destination quantum dots. Also, the energy transfer process is fundamentally probabilistic. Such a stochastic spatiotemporal mechanism yields different evolutions of energy transfer patterns combined with certain control mechanisms, which we call bounceback control, similarly to the evolution of the shape of Physarum demonstrated by Aono *et al.* in Ref. [9]. At the same time, in contrast to biological organisms, optical energy transfer is implemented by highly controlled engineering means for designated structures, such as semiconductor quantum nanostructures fabricated by molecular beam epitaxy [19] or DNA-based self-assembly [20], etc. The operating speed of such optical-near-field–mediated quantum dot systems, which is on the order of nanoseconds when radiative relaxation processes are involved, is significantly faster than those based on biological organisms, which is on the order of seconds or minutes [9,10]. The energy efficiency [17], as indicated already above, and the possibility of room-temperature operation [16] are also strong motivations behind the investigations. In addition, we should emphasize that the concept and the principles are fundamentally different from those of conventional optical computing or optical signal processing, which are limited by the properties of propagating light [21]. The concept and principles are also different from the quantum computing paradigm where a superposition of all possible states is exploited to lead to a correct solution [22]. The optical-near-field–mediated energy transfer is a coherent process, suggesting that an optical excitation could be transferred to all possible destination QDs via a resonant energy level, but such a coherent interaction between QDs results in a unidirectional energy transfer by an energy dissipation process occurring in the larger dot. Thus, our approach opens up the possibility of another computing paradigm where both coherent and dissipative processes are exploited.

3. Optical Security by Nanophotonics

Optics has been playing crucial roles in security applications ranging from authentication and watermarks to anti-counterfeiting [23]. However, since the fundamental physical principle involves optical far-fields, or propagating light, diffraction of light causes severe difficulties, for example, in device scaling and system integration. Moreover, conventional security technologies in use today have been facing increasingly stringent

demands to safeguard against threats such as counterfeiting of holograms [24], requiring innovative physical principles and technologies to overcome their limitations. Nanophotonics, which utilizes interactions between light and matter at the nanometer scale via optical near-field interactions, can break through the diffraction limit of conventional propagating light. Moreover, we can make use of the hierarchical nature in optical near-field interactions, which is one of the unique attributes nanophotonics, paving the way for novel security functionalities [25].

For instance, we have demonstrated a "*hierarchical hologram*" that works in both optical far-fields and near-fields, the former being associated with conventional holographic images, and the latter being associated with the optical intensity distribution originating from a nanometric structure embedded in the hologram, which is accessible only via optical near-fields [26,27]. In other words, information hiding can be realized by using optical near-fields and nanofabrication technologies. Also, authentication functions have been theoretically and experimentally demonstrated by using two shape-engineered nanostructures and their associated optical near-fields [28]. In this system, the two nanostructures respectively work as a *lock* and *key*, where authenticity is guaranteed by the nanoscale-precision shapes of the structures.

4. Conclusion

In summary, we examined some intelligent functions based on optical near-field interactions occurring at scales below the wavelength of light has the potential to solve solution searching and decision making problems. More specifically, we demonstrated solving a constraint satisfaction problem, a satisfiability problem, and a multi-armed bandit problem. The key is that nanostructured matter in the form of quantum dots are networked via optical near-fields; optical energy transfer from smaller quantum dots to larger ones, which is a quantum stochastic process, depends on the existence of resonant energy levels between the quantum dots or a state-filling effect occurring at the destination quantum dots. We exploit these unique spatiotemporal mechanisms in optical energy transfer to solve solution searching and decision making problems. Also we showed some security applications based on optical near-field processes that achieve information hiding and authentication functions.

Acknowledgements

Part of this work was supported in part by SCOPE of the Ministry of Internal Affairs and Communications and Grant-in-Aid for scientific research from the Japan Society for the Promotion of Science.

References

[1] M. Ohtsu, T. Kawazoe, T. Yatsui, and M. Naruse: Nanophotonics: Application of Dressed Photons to Novel Photonic Devices, and Systems, IEEE J. Sel. Top. Quantum Electron, 14, 1404-1417, 2008.

[2] M. Naruse, N. Tate, M. Aono, and M. Ohtsu: Information physics fundamentals of nanophotonics, Reports on Progress in Physics, Vol. 76, pp. 056401 1-50, April 2013.

[3] M. Naruse, M. Aono, S.-J. Kim, T. Kawazoe, W. Nomura, H. Hori, M. Hara, and M. Ohtsu, "Spatiotemporal dynamics in optical energy transfer on the nanoscale and its application to constraint satisfaction problems," Phys. Rev. B, vol. 86, no. 12, pp. 125407 1-10, September 2012.

[4] M. Aono, M. Naruse, S.-J. Kim, M. Wakabayashi, H. Hori, M. Ohtsu, M. Hara: Amoeba-inspired Nanoarchitectonic Computing: Solving Intractable Computational Problems using Nanoscale Photoexcitation Transfer Dynamics, Langmuir, in press DOI: 10.1021/la400301p

[5] M. Naruse, N. Tate, and M. Ohtsu: Optical security based on near-field processes at the nanoscale, Journal of Optics, 14, 094002 1-13, 2012.

[6] International Technology Roadmap for Semiconductors, 2009 Edition, Emerging Research Devices.

[7] S. Amari and N. Kasabov, eds., Brain-like Computing and Intelligent Information Systems, Springer, Singapore, 1998.

[8] L. B. Kish: Noise-based logic: Binary, multi-valued, or fuzzy, with optional superposition of logic states, Phys. Lett. A, 373, 911-918, 2009.

[9] M. Aono, M. Hara, K. Aihara: Amoeba-based neurocomputing with chaotic dynamics, Communications of the ACM, 50, pp. 69-72, 2007.

[10] L. Zhu, M. Aono, S.-J. Kim, M. Hara: Amoeba-based computing for traveling salesman problem: Long-term correlations between spatially separated individual cells of Physarum polycephalum, BioSystems, 112, 1-10, 2013.

[11] K. Leibnitz and M. Murata: Attractor selection and perturbation for robust networks in fluctuating environments, IEEE Network, 24, 14-18, 2010.

[12] M. Naruse, T. Miyazaki, T. Kawazoe, S. Sangu, K. Kobayashi, F. Kubota, and M. Ohtsu: Nanophotonic Computing Based on Optical Near-Field Interactions between Quantum Dots, IEICE Trans. Electron., E88-C, 1817-1823, 2005.

[13] T. Kawazoe, K. Kobayashi, K. Akahane, M. Naruse, N. Yamamoto, and M. Ohtsu: Demonstration of nanophotonic NOT gate using near-field optically coupled quantum dots, Appl. Phys. B, 84, 243-246, 2006.

[14] T. Yatsui, S. Sangu, T. Kawazoe, M. Ohtsu, S. J. An, J. Yoo, and G.-C. Yi, Nanophotonic switch using ZnO nanorod double-quantum-well structures, Appl. Phys. Lett., 90, 223110 1-3, 2007.

[15] W. Nomura, T. Yatsui, T. Kawazoe, M. Naruse, and

M. Ohtsu: Structural dependency of optical excitation transfer via optical near-field interactions between semiconductor quantum dots, Appl. Phys. B, 100, 181-187, 2010.

[16] T. Kawazoe, M. Ohtsu, S. Aso, Y. Sawado, Y. Hosoda, K. Yoshizawa, K. Akahane, N. Yamamoto, and M. Naruse: Two-dimensional array of room-temperature nanophotonic logic gates using InAs quantum dots in mesa structures, Appl. Phys. B, 103, 537-546, 2011.

[17] M. Naruse, H. Hori, K. Kobayashi, P. Holmström, L. Thylén, and M. Ohtsu: Lower bound of energy dissipation in optical excitation transfer via optical near-field interactions, Opt. Express, 18, A544-A553, 2010.

[18] S.-J. Kim, M. Naruse, M. Aono, M. Ohtsu, M. Hara: Technical Digest of The First International Workshop on Information Physics and Computing in Nano-scale Photonics and Materials (IPCN), Orleans, France, 2012, Paper Number IPCN1-14.

[19] K. Akahane, N. Yamamoto, and M. Tsuchiya: Highly stacked quantum-dot laser fabricated using a strain compensation technique," Appl. Phys. Lett., 93, 041121 1-3, 2008.

[20] C. Pistol, C. Dwyer, and A. R. Lebeck: Nanoscale Optical Computing Using Resonance Energy Transfer Logic, IEEE Micro, 28, 7-18, 2008.

[21] H. J. Caulfield and S. Dolev: Why future supercomputing requires optics, Nature Photonics, 4, 261-263, 2010.

[22] D. P. DiVincenzo, Quantum Computation, Science, 270, 255-261, 1995.

[23] B. Javidi: Optical and Digital Techniques for Information Security, New York, Springer, 2005.

[24] S. P. McGrew: Hologram counterfeiting: problems and solutions, Proc. SPIE, 1210, 66-76, 1990.

[25] M. Naruse, T. Inoue, and H. Hori: Analysis and Synthesis of Hierarchy in Optical Near-Field Interactions at the Nanoscale Based on Angular Spectrum, Jpn. J. Appl. Phys., 46, 6095-6103, 2007.

[26] N. Tate, W. Nomura, T. Yatsui, M. Naruse, and M. Ohtsu: Hierarchical hologram based on optical near- and far-field responses, Opt. Express, 16, 607-612, 2008.

[27] N. Tate, M. Naruse, T. Yatsui, T. Kawazoe, M. Hoga, Y. Ohyagi, T. Fukuyama, M. Kitamura, and M. Ohtsu: Nanophotonic code embedded in embossed hologram for hierarchical information retrieval, Opt. Express, 18, 7497-7505, 2010.

[28] N. Tate, H. Sugiyama, M. Naruse, W. Nomura, T. Yatsui, T. Kawazoe, and M. Ohtsu: Quadrupole–Dipole Transform based on Optical Near-Field Interactions in Engineered Nanostructures, Opt. Express, 17, 11113-11121, 2009.

Dressed photon science and applications

Motoichi Ohtsu
Graduate School of Engineering, the University of Tokyo,
2-11-16 Yayoi, Bunkyo-ku, Tokyo 113-8656, Japan,
also with Nanophotonics Research Center, The University of Tokyo,
2-11-16 Yayoi, Bunkyo-ku, Tokyo 113-8656, Japan,
E-mail: ohtsu@ee.t.u-tokyo.ac.jp

Dressed photon (DP) science and technology exploits the electromagnetic field localized in nanometric space. The principles and concepts of DP science and technology are quite different from those of conventional wave-optical technology encompassing photonic crystals, plasmonics, metamaterials, silicon photonics, and quantum-dot photonic devices. This is because these devices use propagating light even though the materials or particles used may be nanometer-sized. The theoretical picture of DP has been proposed to describe the electromagnetic interactions between nanometric particles located in close proximity to each other. The DP is a virtual cloud of photons that exists around an illuminated nanometric particle. Independently of the real photon, a virtual photon is emitted from the electron, and this photon can be re-absorbed within a short duration. Since the virtual photon remains in the proximity of the electron, it can couple with the electron in a unique manner. This coupled state (DP) is a quasi-particle from the standpoint of photon energy transfer.

The DP has been theoretically described by assuming a multipolar quantum electrodynamic Hamiltonian in a Coulomb gauge in a finite nano-system [1]. A real nanometric material is composed not only of electrons but also of a crystal lattice. In this case, the DP energy can be exchanged with the crystal lattice. By this exchange, the crystal lattice can excite the vibration mode coherently, creating a multi-mode coherent phonon state. As a result, the DP and the coherent phonon can form a coupled state (dressed-photon – phonon: DPP) [2]. This coupled state is a quasi-particle and is generated only when the particle size is small enough to excite the crystal lattice vibration coherently. Several examples for application to energy conversion will be reviewed as are shown by Fig.1 [3-6]. A part of this work was supported by the "Development of Next-generation High-performance Technology for Photovoltaic Power Generation System" Program, NEDO, Japan.

References

[1] K. Kobayashi, S. Sangu, H. Ito, and M. Ohtsu, Phys. Rev. A 63, 013806 (2001).
[2] Y. Tanaka and K. Kobayashi, Journal of Microscopy 229, 228(2008)
[3] T. Kawazoe, H. Fujiwara, K. Kobayashi, and M. Ohtsu, J. of Selected Topics in Quantum

Electron. 15, 1380 (2009).
[4] S. Yukutake, T. Kawazoe, T. Yatsui, W. Nomura, K. Kitamura, and M. Ohtsu, Appl. Phys. B 99, 415 (2010).
[5] T. Kawazoe, A. Mueed, and M. Ohtsu, Appl. Phys. B 104,747 (2011).
[6] T. Kawazoe, M. Ohtsu, K. Akahane, and N. Yamamoto, Appl. Phys. B 107, 659 (2012).

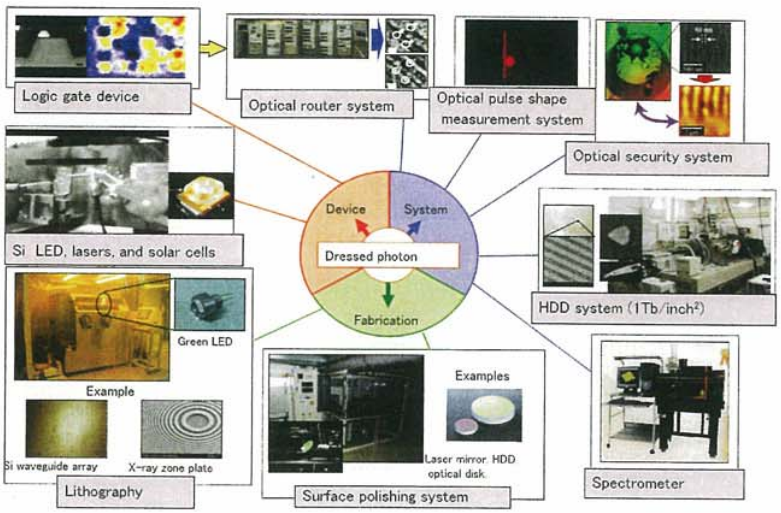

Fig.1 Examples of application

Motoichi Ohtsu received the Dr. E. degrees in electronics engineering from the Tokyo Institute of Technology, Tokyo in 1978. He was appointed a Research Associate, an Associate professor, a Professor at the Tokyo Institute of Technology. From 1986 to 1987, while on leave from the Tokyo Institute of Technology, he joined the Crawford Hill Laboratory, AT&T Bell Laboratories, Holmdel, NJ. In 2004, he moved to the University of Tokyo as a professor. He has been the leader of several Japanese national projects for academia-industry collaborations. He has written over 509 papers and received 83 patents. He is the author, co-author, and editor of 62 books, including 27 in English In 2000, he was appointed as the President of the IEEE LEOS Japan Chapter. From 2000, he is an executive director of the Japan Society of Applied Physics. He is a Fellow of the Optical Society of America, and a Fellow of the Japan Society of Applied Physics. He is also a Tandem Member of the Science Council of Japan. He has been awarded 14 prizes from academic institutions, including the Issac Koga Gold Medal of URSI in 1984, the Japan IBM Science Award in 1988, two awards from the Japan Society of Applied Physics in 1982 and 1990, the Inoue Science Foundation Award in 1999, the Japan Royal Medal with a Purple Ribbon from the Japanese Government in 2004, H. Inoue Award from JST in 2005, the Distinguished Achievement Award from the IEICE of Japan in 2007, Julius Springer Prize for Applied Physics in 2009, and Fuji-Sankei Business Eye Award in 2012.

Emission from a Dipole-Forbidden Energy State in a GaAs Quantum-Ring Induced by Dressed Photon

T. Yatsui[1], W. Nomura[1], T. Mano[2], H. Miyazaki[2], K. Sakoda[2], T. Kawazoe[1], and M. Ohtsu[1]
1 University of Tokyo, 2 National Institute for Materials Science (NIMS)
Author e-mail address: yatsui@ee.t.u-tokyo.ac.jp

Abstract: A significant decrease in the decay time of the emission from a dipole-forbidden state in a GaAs quantum-ring was observed, using the near-field interaction induced by the close proximity of an apertured fiber probe tip.
OCIS codes: (180.4243) Near-field microscopy; (230.5590) Quantum-well, -wire and -dot devices

To reduce the size of photonic devices below the diffraction limit, we have proposed nanophotonic devices [1] that consist of semiconductor quantum structures. In a nanophotonic device, the dipole-forbidden energy-transition can reduce the size of the device beyond the diffraction limit of light and achieve unidirectional energy transfer, which is unattainable in conventional photonic devices [2, 3]. The dipole-forbidden energy transition originates from an exchange of virtual photons between resonant energy states. The use of virtual photons activates dipole-forbidden energy states. Although emission from the dipole-forbidden energy state cannot be detected in the far field (FF), it can be utilized when the nanoparticle and detector are in close proximity. Here, we report direct observation of emission from an optically forbidden level in GaAs quantum ring using the near-field (NF) interaction induced by a fiber probe.

The GaAs quantum ring structure was fabricated using the droplet epitaxy technique [4]. As shown in Figs. 1(a). emitting GaAs quantum-ring is below the GaAs cap layer with 10 nm, and top GaAs quantum-ring layer is inactive layer to confirm the position of quantum-ring structure (Fig. 1(b)). We performed time-resolved NF photoluminescence (PL) spectroscopy using an apertured fiber probe (aperture diameter of 50 nm). Figure 2 shows the time-resolved PL spectra obtained at a 725-nm wavelength for the ground state of the GaAs quantum ring; the curves correspond to spectra obtained with probe-to-sample distances of $d > 1$ μm (FF), $d \sim 5$nm (NF1), $d \sim 10$nm (NF2), and the conventional FF (FF'). Table 1 shows the respective decay times, τ. Although the emission peak at 725 nm originated from the dipole-forbidden state, the results indicated that the decay time decreased to almost half that of FF spectrum, due to the close proximity of the fiber probe to the quantum ring. These results were attributed to NF interaction between the probe tip and the quantum ring to activate the dipole-forbidden energy state [5].

Because the decay time of the dipole-forbidden state is 10^6 times longer than that of the dipole-active state [6], the dipole-forbidden state can be used to realize novel devices such as optical buffer memory and signal-transmission devices.

References

[1] M. Ohtsu, T. Kawazoe, T. Yatsui, and M. Naruse, "Nanophotonics: Application of Dressed Photons to Novel Photonic Devices and Systems," *IEEE J. Select. Top. Quant. Electron.*, vol. 14, pp. 1404-1417, 2008.
[2] T. Kawazoe, K. Kobayashi, S. Sangu, and M. Ohtsu, "Demonstration of a nanophotonic switching operation by optical near-field energy transfer," *Appl. Phys. Lett.*, vol. 82, pp. 2957-2959, May 5 2003.
[3] T. Yatsui, S. Sangu, T. Kawazoe, M. Ohtsu, S. J. An, J. Yoo, *et al.*, "Nanophotonic switch using ZnO nanorod double-quantum-well structures," *Appl Phys Lett*, vol. 90, p. 223110, 2007.
[4] T. Mano, T. Kuroda, S. Sanguinetti, T. Ochiai, T. Tateno, J. Kim, *et al.*, "Self-assembly of concentric quantum double rings," *Nano Lett.*, vol. 5, pp. 425-428, 2005.
[5] T. Yatsui, M. Tsuji, Y. Liu, T. Kawazoe, and M. Ohtsu, "Emission from a dipole-forbidden energy state in a ZnO quantum dot induced by a near-field interaction with a fiber probe," *Appl. Phys. Lett.*, vol. 100, p. 223110, 2012.
[6] C. Garcia, B. Garrido, P. Pellegrino, R. Ferre, J. A. Moreno, J. R. Morante, *et al.*, "Size dependence of lifetime and absorption cross section of Si nanocrystals embedded in SiO2," *Applied Physics Letters*, vol. 82, pp. 1595-1597, Mar 2003.

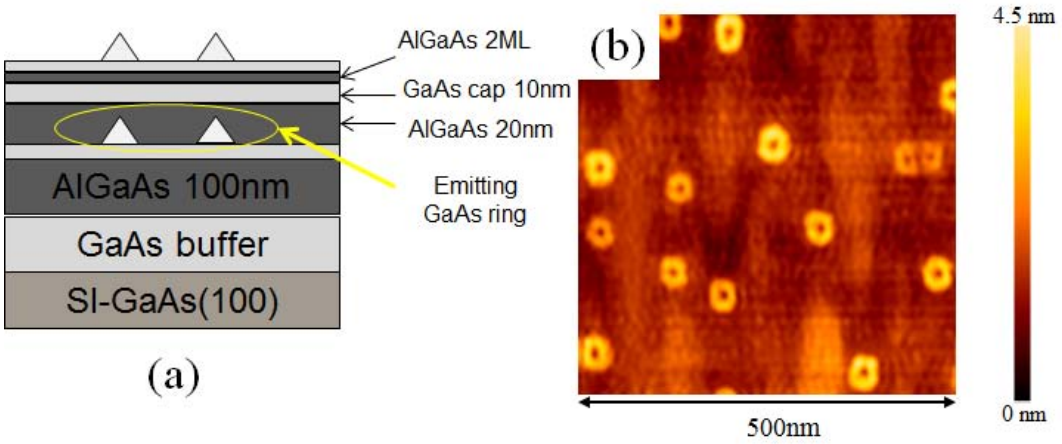

Fig. 1 (a) Schematic diagram of the GaAs ring structure. (b) Atomic force microscopy (AFM) image of the fabricated GaAs ring.

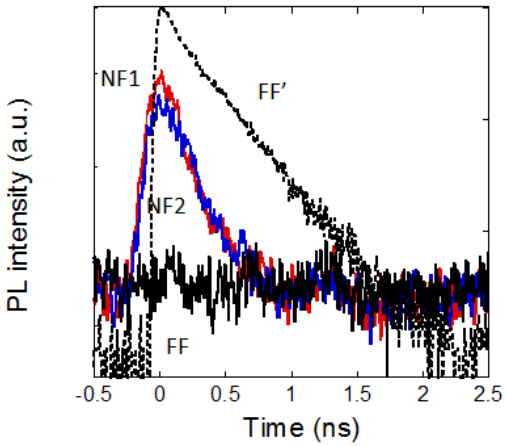

Fig. 2 Time-resolved photoluminescence (PL) intensity. NF1 and NF 2: near-field PL spectra using NF spectroscopy. FF: Far-field spectra using NF spectroscopy. FF': FF spectra using conventional spectroscopy.

Table 1. Decay time τ

	τ (ps)
NF1 (d ~5nm)	305
NF2 (d ~10nm)	305
FF (d > 1μm)	330
FF'	580

Dressed photons for energy conversion

Motoichi Ohtsu
Graduate School of Engineering, the University of Tokyo,
2-11-16 Yayoi, Bunkyo-ku, Tokyo 113-8656, Japan,
also with Nanophotonics Research Center, The University of Tokyo,
2-11-16 Yayoi, Bunkyo-ku, Tokyo 113-8656, Japan,
E-mail: ohtsu@ee.t.u-tokyo.ac.jp

The principles and concepts of dressed photon (DP) science and technology are quite different from those of conventional wave-optical technology encompassing photonic crystals, plasmonics, metamaterials, silicon photonics, and quantum-dot photonic devices. This is because these devices use propagating light even though the materials or particles used may be nanometer-sized. The theoretical picture of DP has been proposed to describe the electromagnetic interactions between nanometric particles located in close proximity to each other. The DP is a virtual cloud of photons that always exists around an illuminated nanometric particle. Since the virtual photon remains in the proximity of the electron, it can couple with the electron in a unique manner. This coupled state (DP) is a quasi-particle from the standpoint of photon energy transfer.

The DP has been theoretically described by assuming a multipolar quantum electrodynamic Hamiltonian in a Coulomb gauge in a finite nano-system [1]. The creation and annihilation operators of the DP are expressed as the sum of the operators of the real photon and an electron–hole pair. A real nanometric material is composed not only of electrons but also of a crystal lattice. In this case, after a DP is generated on an illuminated nanometric particle, its energy can be exchanged with the crystal lattice. By this exchange, the crystal lattice can excite the vibration mode coherently, creating a multi-mode coherent phonon state. As a result, the DP and the coherent phonon can form a coupled state (dressed-photon – phonon: DPP) [2]. This coupled state is a quasi-particle and is generated only when the particle size is small enough to excite the crystal lattice vibration coherently.

Two examples for application to energy conversion will be reviewed: (1) Up-conversion of optical energy [3]. (2) Conversion from electrical to optical energy by taking a LED as an example. Novel LED[4] and a laser[5] will be demonstrated by using indirect transition-type silicon crystals, which are fabricated and operated by DPP.

A part of this work was supported by the "Development of Next-generation High-performance Technology for Photovoltaic Power Generation System" Program, NEDO, Japan.

References

[1] K. Kobayashi, S. Sangu, H. Ito, and M. Ohtsu, Phys. Rev. A 63, 013806 (2001).

[2] Y. Tanaka and K. Kobayashi, Journal of Microscopy 229, 228(2008)

[3] T. Kawazoe, H. Fujiwara, K. Kobayashi, and M. Ohtsu, J. of Selected Topics in Quantum Electron. 15, 1380 (2009).

[4] T. Kawazoe, A. Mueed, and M. Ohtsu, Appl. Phys. B 104,747 (2011).

[5] T. Kawazoe, M. Ohtsu, K. Akahane, and N. Yamamoto, Appl. Phys. B 107, 659 (2012).

Motoichi Ohtsu received the Dr. E. degrees in electronics engineering from the Tokyo Institute of Technology, Tokyo in 1978. He was appointed a Research Associate, an Associate professor, a Professor at the Tokyo Institute of Technology. From 1986 to 1987, while on leave from the Tokyo Institute of Technology, he joined the Crawford Hill Laboratory, AT&T Bell Laboratories, Holmdel, NJ. In 2004, he moved to the University of Tokyo as a professor. He has been the leader of several Japanese national projects for academia-industry collaborations. He has written over 509 papers and received 83 patents. He is the author, co-author, and editor of 62 books, including 27 in English In 2000, he was appointed as the President of the IEEE LEOS Japan Chapter. From 2000, he is an executive director of the Japan Society of Applied Physics. He is a Fellow of the Optical Society of America, and a Fellow of the Japan Society of Applied Physics. He is also a Tandem Member of the Science Council of Japan. He has been awarded 14 prizes from academic institutions, including the Issac Koga Gold Medal of URSI in 1984, the Japan IBM Science Award in 1988, two awards from the Japan Society of Applied Physics in 1982 and 1990, the Inoue Science Foundation Award in 1999, the Japan Royal Medal with a Purple Ribbon from the Japanese Government in 2004, H. Inoue Award from JST in 2005, the Distinguished Achievement Award from the IEICE of Japan in 2007, Julius Springer Prize for Applied Physics in 2009, and Fuji-Sankei Business Eye Award in 2012.

Concepts of dressed photon science and technology

Motoichi Ohtsu
Graduate School of Engineering, the University of Tokyo,
2-11-16 Yayoi, Bunkyo-ku, Tokyo 113-8656, Japan,
also with Nanophotonics Research Center, The University of Tokyo,
2-11-16 Yayoi, Bunkyo-ku, Tokyo 113-8656, Japan,
E-mail: ohtsu@ee.t.u-tokyo.ac.jp

Dressed photon (DP) science and technology exploits the electromagnetic field localized in nanometric space. This fields has been named optical near-fields due to its non-propagating features. The principles and concepts of DP science and technology are quite different from those of conventional wave-optical technology encompassing photonic crystals, plasmonics, metamaterials, silicon photonics, and quantum-dot photonic devices. This is because these devices use propagating light even though the materials or particles used may be nanometer-sized. The theoretical picture of DP has been proposed to describe the electromagnetic interactions between nanometric particles located in close proximity to each other. The DP is a virtual cloud of photons that always exists around an illuminated nanometric particle. Independently of the real photon (, i.e., conventional propagating scattered light), a virtual photon is emitted from the electron, and this photon can be re-absorbed within a short duration. Since the virtual photon remains in the proximity of the electron, it can couple with the electron in a unique manner. This coupled state (DP) is a quasi-particle from the standpoint of photon energy transfer.

The DP has been theoretically described by assuming a multipolar quantum electrodynamic Hamiltonian in a Coulomb gauge in a finite nano-system [1]. The creation and annihilation operators of the DP are expressed as the sum of the operators of the real photon and an electron–hole pair. A real nanometric material is composed not only of electrons but also of a crystal lattice. In this case, after a DP is generated on an illuminated nanometric particle, its energy can be exchanged with the crystal lattice. By this exchange, the crystal lattice can excite the vibration mode coherently, creating a multi-mode coherent phonon state. As a result, the DP and the coherent phonon can form a coupled state (dressed-photon – phonon: DPP) [2]. This coupled state is a quasi-particle and is generated only when the particle size is small enough to excite the crystal lattice vibration coherently.

Three examples for application to energy conversion will be reviewed: (1) Up-conversion of optical energy [3]. (2) Conversion from optical to electrical energy [4]. (3) Conversion from electrical to optical energy by taking a LED as an example. Novel LED [5]

and a laser[6] will be demonstrated by using indirect transition-type semiconductors (Si, SiC, and GaP), which are fabricated and operated by DPP.

A part of this work was supported by the "Development of Next-generation High-performance Technology for Photovoltaic Power Generation System" Program, NEDO, Japan.

References

[1] K. Kobayashi, S. Sangu, H. Ito, and M. Ohtsu, Phys. Rev. A 63, 013806 (2001).

[2] Y. Tanaka and K. Kobayashi, Journal of Microscopy 229, 228(2008)

[3] T. Kawazoe, H. Fujiwara, K. Kobayashi, and M. Ohtsu, J. of Selected Topics in Quantum Electron. 15, 1380 (2009).

[4] S. Yukutake, T. Kawazoe, T. Yatsui, W. Nomura, K. Kitamura, and M. Ohtsu, Appl. Phys. B 99, 415 (2010).

[5] T. Kawazoe, A. Mueed, and M. Ohtsu, Appl. Phys. B 104,747 (2011).

[6] T. Kawazoe, M. Ohtsu, K. Akahane, and N. Yamamoto, Appl. Phys. B 107, 659 (2012).

Motoichi Ohtsu received the Dr. E. degrees in electronics engineering from the Tokyo Institute of Technology, Tokyo in 1978. He was appointed a Research Associate, an Associate professor, a Professor at the Tokyo Institute of Technology. From 1986 to 1987, while on leave from the Tokyo Institute of Technology, he joined the Crawford Hill Laboratory, AT&T Bell Laboratories, Holmdel, NJ. In 2004, he moved to the University of Tokyo as a professor. He has been the leader of several Japanese national projects for academia-industry collaborations. He has written over 509 papers and received 83 patents. He is the author, co-author, and editor of 62 books, including 27 in English In 2000, he was appointed as the President of the IEEE LEOS Japan Chapter. From 2000, he is an executive director of the Japan Society of Applied Physics. He is a Fellow of the Optical Society of America, and a Fellow of the Japan Society of Applied Physics. He is also a Tandem Member of the Science Council of Japan. He has been awarded 14 prizes from academic institutions, including the Issac Koga Gold Medal of URSI in 1984, the Japan IBM Science Award in 1988, two awards from the Japan Society of Applied Physics in 1982 and 1990, the Inoue Science Foundation Award in 1999, the Japan Royal Medal with a Purple Ribbon from the Japanese Government in 2004, H. Inoue Award from JST in 2005, the Distinguished Achievement Award from the IEICE of Japan in 2007, Julius Springer Prize for Applied Physics in 2009, and Fuji-Sankei Business Eye Award in 2012.

Dressed-photon Nanopolishing for Extreme Ultraviolet Mask Substrate Defect Mitigation

Ranganath Teki*[a], Arun John Kadaksham[a], Frank Goodwin[a], Takashi Yatsui[b,c] and Motoichi Ohtsu[b]

[a]SEMATECH, Albany, New York, U.S.A.
[b]Nanophotonics Research Center, University of Tokyo, Tokyo, Japan
[c]Advanced Low Carbon Technology Research and Development Program (ALCA), Japan Science and Technology Agency, Saitama, Japan.

ABSTRACT

Although the quality of extreme ultraviolet (EUV) mask substrates has improved by continuous refinement of the polishing processes, the yield of defect-free blanks is still very low. Dressed-photon nanopolishing (DPNP) is a novel vapor phase, photo-chemical, non-contact etching process that has been shown to locally smooth bumps and pits to below 1 nm in height/depth while not affecting the surface roughness. DPNP is based on the concept of a dressed photon, which is a quasi-particle in the optical near field of a surface that can couple with lattice phonons in nanometric regions (< 100 nm). When illuminated with light of a suitable wavelength, such coupled states are generated on a nanometrically rough material surface and impart sufficient energy to an etchant gas to enable its dissociation and etching in the rough regions only. DPNP can be the last polishing step on EUV substrates to eliminate any remnant pits and/or embedded particles on the surface to yield potentially defect-free substrates.

Keywords: EUV, mask substrate, defectivity, roughness, flatness, CMP, dressed-photon, DPNP

1. INTRODUCTION

The defectivity of EUV mask blanks remains a significant obstacle in the realization of EUV lithography. About two-thirds of the defects are present on the substrate[1] and remain difficult to repair after multilayer deposition. These defects are mostly below ~70 nm in size[2] and are pits, scratches or particles composed of chemical mechanical planarization (CMP) and/or cleaning residues, storage adders, etc. Over the past few years, mask suppliers have been able to gradually improve the quality of the substrates to meet the above specifications, but the yield is still poor. Here we describe a novel dry etching process DPNP which can smooth pits and bumps on the substrate without increasing the surface roughness. DPNP etches according to local nanoscale surface curvature based on the optical near-field effect. Unlike CMP, DPNP is a non-contact process and does not add pits while polishing. We present the results of DPNP polishing on bumps and pits on doped substrates and show its potential to etch defects to < 1 nm in height/depth. We look at the effect of DPNP on surface roughness and evaluate process-induced defectivity and cleaning chemistries to address that. DPNP can potentially be the last polishing step on EUV substrates to eliminate any remnant pits and/or embedded particles on the surface, and thus enable a route to obtain low-defectivity EUV substrates with higher yields.

1.1. EUV substrate requirements

EUV mask substrates, made of titania-doped fused silica, are manufactured using a flame-hydrolysis process[3] where high purity precursor gases react in high-temperature flame burners and settle as SiO_2 and TiO_2 soot particles on a large boule, which undergoes a complex motion in x, y, z and θ in order to make the glass as homogeneous as possible. The substrates are cut from the boule into the required dimensions and then undergo a series of (iterative) polishing steps to reach the required specifications. The substrates ideally require ~0.05 nm root mean square (RMS) surface roughness, sub-30 nm peak-valley flatness, and no defects larger than 1 nm in height/depth. It appears that the requirements, particularly roughness and flatness, are not hard to reach by themselves, but very difficult to achieve along with defectivity. This is something similar to the infamous resist-line edge roughness (LER)-sensitivity (RLS) triangle for

* Ranganath.Teki@sematech.org ; Phone: (518) 649-1058

Extreme Ultraviolet (EUV) Lithography IV, edited by Patrick P. Naulleau, Proc. of SPIE Vol. 8679, 86790F

photoresists[4], in which the three metrics (triangle corners) of resolution, LER and sensitivity are interrelated and very hard to lower simultaneously. In a similar sense, the three parameters of defectivity (D), roughness (R), and flatness (F) are interconnected and very hard to optimize at the same time—resulting in a DRF triangle for EUV mask substrates/blanks. This mainly arises from the global/local polishing/cleaning processes required to take substrates toward the needed specifications and will be discussed later in this article (see Figure 5).

1.2. Effect of substrate roughness

The multilayer (and hence substrate) roughness, depending on the spatial frequency, impacts the imaging and inspection of EUV masks. The low spatial frequency (1/1 mm to 1/10 µm) roughness (LSFR) impacts the pattern shift and overlay, while the medium spatial frequency (1/10 µm to 1/250 nm) roughness (MSFR) impacts the pattern shift as well as random phase variation (LER) and the high spatial frequency (1/250 nm to 1/50 nm) roughness (HSFR) impacts the loss in reflectivity and inspection sensitivity[5]. While the LSFR can be compensated during e-beam writing, the MSFR and the HSFR need to be minimized during the mask/substrate processing.

The impact of roughness on LER has been studied by the EUV community. As per simulations the mask replicated surface roughness, which typically originates from the substrate and propagates through conformal multilayer deposition, must be limited to 0.05 nm to meet current LER targets for the 22 nm and 16 nm half-pitch (HP) lithography nodes[6,7]. Experimental results from the NXE 3100 at 27 nm HP lines/spaces showed an impact from mask surface roughness in terms of resist 3σ-LER only when the roughness values exceeded 0.3 nm RMS[8]. Thus, there is currently a lack of consensus on the impact of roughness on LER, and the required range is anywhere between 0.05-0.3 nm RMS.

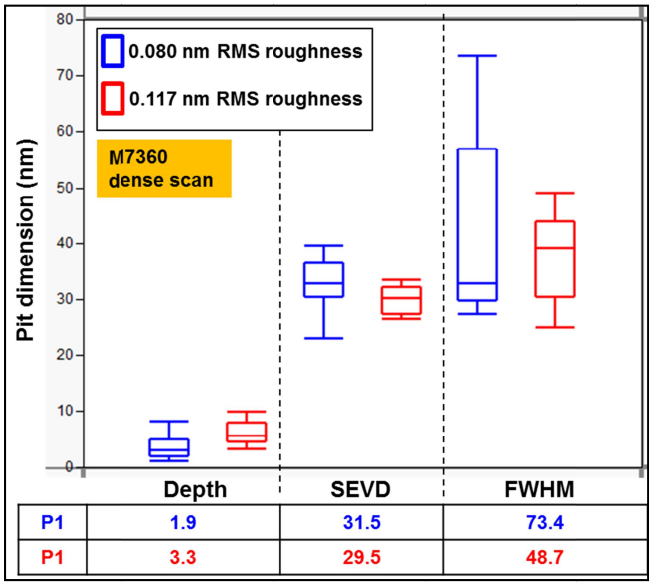

	Depth	SEVD	FWHM
P1	1.9	31.5	73.4
P1	3.3	29.5	48.7

Figure 1: Dimensions of the 10 smallest pit defects detected by the M7360 on two substrates with different surface RMS roughness. At lower roughness the inspection tool is able to catch shallower and wider defects.

It is well known that higher surface roughness impacts the inspection sensitivity on both substrates and mask blanks by increasing the rate of false counts. We looked at the impact of HSFR on inspection sensitivity and substrate size on the Lasertec M7360 tool. We measured the surface roughness of a substrate and characterized the 10 smallest pit type defects picked up by the M7360 on a Veeco D9000 atomic force microscope (AFM). Then we intentionally roughened the surface using a HF-based cleaning recipe, as a result of which the HSFR increased from 0.08 nm to 0.12 nm RMS. Again, we characterized the smallest 10 pit defects picked up on the M7360. Looking at the distribution of pit depth, full width at half maxima (FWHM) and spherically equivalent volume diameter (SEVD) in Figure 1, one can see that at lower roughness the tool is able to pick up defects which are shallower and wider. This makes sense intuitively since such defects are more likely to be lost in the background noise of higher surface roughness. As an example, the dimensions of two pit defects (both of pixel size 1) are listed at the bottom of Figure 1. The two defects are of similar

SEVD (~30 nm), but the depth of the defect picked up at the lower roughness is only 1.9 nm and the FWHM is 73.4 nm, while the depth of the defect picked up at the higher roughness is greater (3.3 nm) and the FWHM smaller (48.7 nm). This indicates that as the HSFR roughness increases, the inspection noise increases and inspection sensitivity is reduced. Although, it remains to be determined if such small (shallow and wide) defects are an issue from the point of defect printability, missing such defects on the inspection tool means that they cannot be addressed in a repair/repair verification cycle using an aerial image metrology system (AIMS) and subsequently will not be picked up until they print on the wafer. Therefore, inspection sensitivity sets the tightest requirements on the surface roughness and will drive the need for lower surface roughness on EUV substrates.

But, there is also a downside to lowering the surface roughness on the substrates. There appears to be a connection between the substrate roughness and defectivity. When comparing fused silica substrates with average HSFR values of 0.07 nm RMS and 0.10 nm RMS, it was observed that substrates with lower roughness values had on average 30% more scratches and 90% more pits, as compared to the substrates with higher roughness[9]. This can be attributed to the increased complexity of CMP polishing/cleaning required to drive down the roughness, resulting in increased defect counts. So it is critical that we determine the right level of roughness required from a LER and inspection sensitivity (for a given HP node) point of view, and not polish the substrates to below that level.

2. DPNP TECHNOLOGY

2.1. Principle and mechanism

The concept of dressed-photons was first introduced by Prof. Ohtsu who established the Nanophotonics Engineering Organization (NPEO) to help develop the technology. When a surface is illuminated with light, an optical near field—a virtual cloud of photons—is generated. In the case of visible light illumination (photon energy ~2 eV), the size of the near field is estimated to be ~100 nm. Dressed photon is a term used to designate a quasi-particle made of a coupled state of above-virtual photon and a lattice electron. The dressed photon has a higher energy than a free photon due to the contribution of the material excitation energy. The dressed photon can couple with lattice phonons only in nanometric regions, which are small enough to excite the crystal lattice vibration coherently. This coupling, called dressed photon-coherent phonon (DP-CP) coupling, represents a dressed photon carrying the coherent phonon energy[10]. In macro-scale regions, the vibration is incoherent, and thus the energy is dissipated as heat.

In DPNP, the substrate surface is exposed to a laser wavelength measuring 532 nm along with flowing Cl_2 gas, which has an absorption wavelength of 400 nm. Since the energy provided is less than the absorption energy of Cl_2, the gas does not dissociate on its own. On the illuminated surface, DP-CPs are generated at the tips of bumps (nanoscale roughness) and then exchanged between the surface and the Cl_2 molecules in the vicinity (see Figure 2). This exchange provides the extra energy needed for the dissociation of the Cl_2 molecule into Cl* radicals which etch the glass surface[11]. It is important to remember that this exchange—and hence dissociation—occurs only in region of bumps, and only these regions are selectively etched by the radicals, while no etching occurs in the flat/smooth areas.

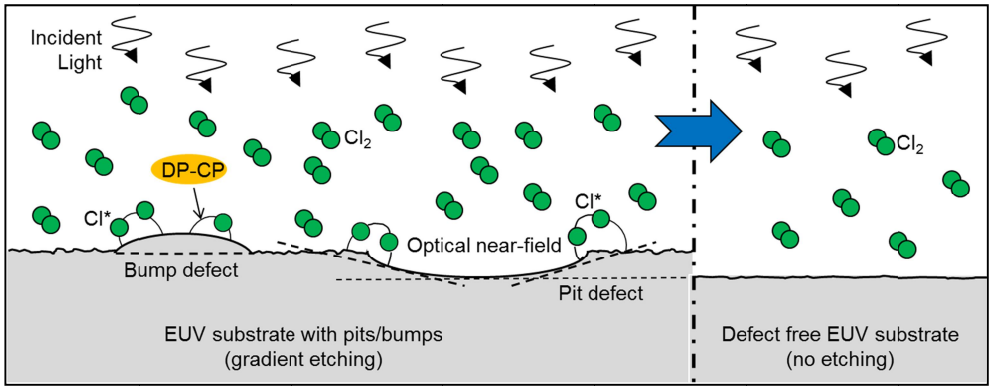

Figure 2: Schematic depicting gradient etching of the substrate bumps and pits due to the presence of optical near field; the etching stops once the surface is smooth.

Moreover, the etching will automatically stop when the region/surface has become smooth enough to stop generating DP-CPs. For smoothing pits, the proposed mechanism is based on the fact that the edges of a pit will appear as a bump to the isotropic etchant gas-so the edges would get etched and the pit would become wider and wider until rendered unprintable. Typical process parameters are laser wavelength and power, etchant gas pressure and flow rate and beam exposure time and intensity[12].

2.2. Experimental details

Low-thermal expansion material (LTEM) substrates made of titania-doped fused silica were first inspected at SEMATECH on the Lasertec M7360 inspection tool to estimate the initial defect count. Selected pit and bump type defects were then punch marked (four punch marks in a diamond shape, 5 µm from the defect). Additional punch marks and "+" signs were milled into the substrate surface to enable alignment of the substrate on the dynamic force microscope (DFM) at NPEO. Select defects were scanned on the DFM at NPEO to estimate defect dimensions, including depth/height and width, and then marked with a blank sharpie to identify the defect location.

The DPNP tool essentially consisted of an inductively coupled plasma tool modified to insert a laser head from the top port. The laser used was a solid-state diode-pumped laser with a wavelength of 532 nm and an output power of 2 W. The beam spot is oval shaped and roughly 2 mm in X and 4 mm in Y. The substrate was manually placed in the DPNP tool and adjusted to place the defect directly under the path of the laser beam. Then it was exposed to Cl_2 gas at a chamber pressure of 100 Pa along with the laser beam for 10–30 minutes. The defects were re-scanned on the DFM to measure the change in the dimensions of the defect.

2.3. Results

Figure 3 shows a representative result both before and after DPNP processing on a substrate bump and pit in the same DFM scan area. This proves that DPNP can smooth both a pit and a bump type defect at the same process conditions. A bump type defect with an initial height 4.7 nm was reduced to 1.3 nm, and a pit type defect was reduced in depth from 15.1 nm to 5.9 nm after 20 minutes of processing. Additional results have been obtained that demonstrate that DPNP smoothed a bump defect 4 nm high and a pit defect 10 nm deep to less than 1 nm of variation from the baseline surface. This indicates the capability of DPNP to smooth defects to below the printable level on EUV mask substrates.

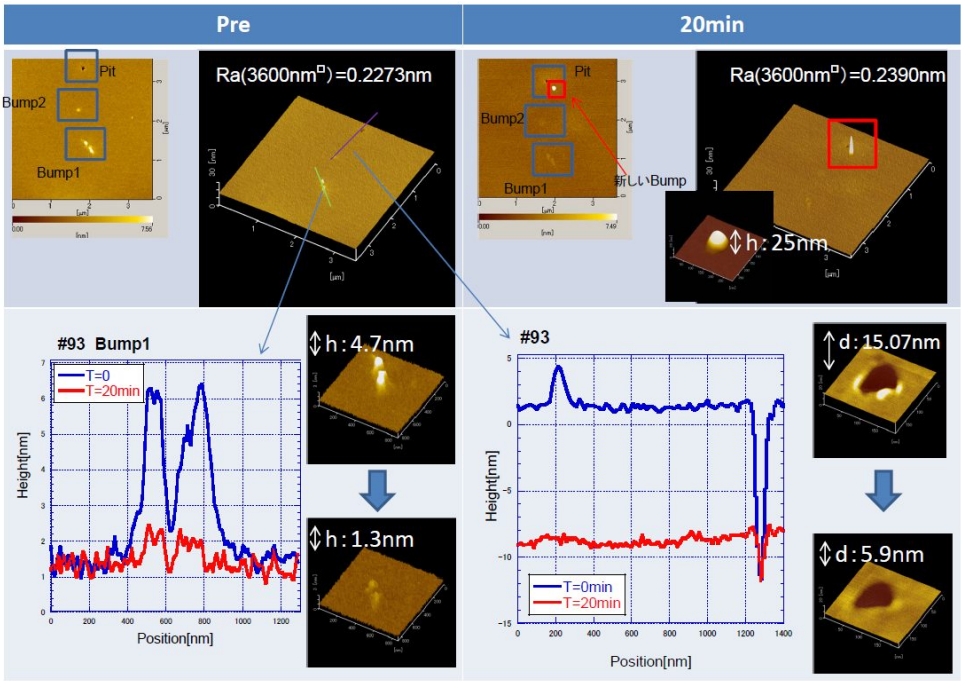

Figure 3: DFM scans showing simultaneous etching of both bump and pit type defects with DPNP polishing.

It was found that after being exposed to DPNP the substrates had a huge number of process adders, prompting isolation tests to help determine their source. Six different clean substrates were inspected on the M7360 and then shipped to NPEO. The substrates went through the following schemes: 1) remain in shipping Pozzetta box, 2) open in NPEO clean room and put back in shipping box, 3) place in DPNP tool and put back in shipping box, 4) expose to Cl_2 gas only for 30 minutes and put back in shipping box, 5) expose to laser beam for 30 minutes and put back in shipping box, and lastly 6) expose to DPNP process (combination of laser exposure and Cl_2 gas passage) for 30 minutes and put back in shipping box. All the substrates were returned to SEMATECH for re-inspection on the M7360. Even though all the substrates showed some particle adders, the number of adders on the substrate exposed to the process was exponentially larger compared to any of the other substrates: the defect counts increased from ~10 over 142×142 mm^2 area to almost ~100,000 over 5×5 mm^2 area (see Figure 4). When scanning the substrate on the AFM, these particle adders were found to be about 2–7 nm in height and 100–200 nm in width. When this substrate was subjected to the standard substrate cleaning process, all of these small particles were removed, leaving only some large particle adders. This indicates that the likely source of these small sized adders is etching residue from DPNP. The composition of these particles is yet to be determined.

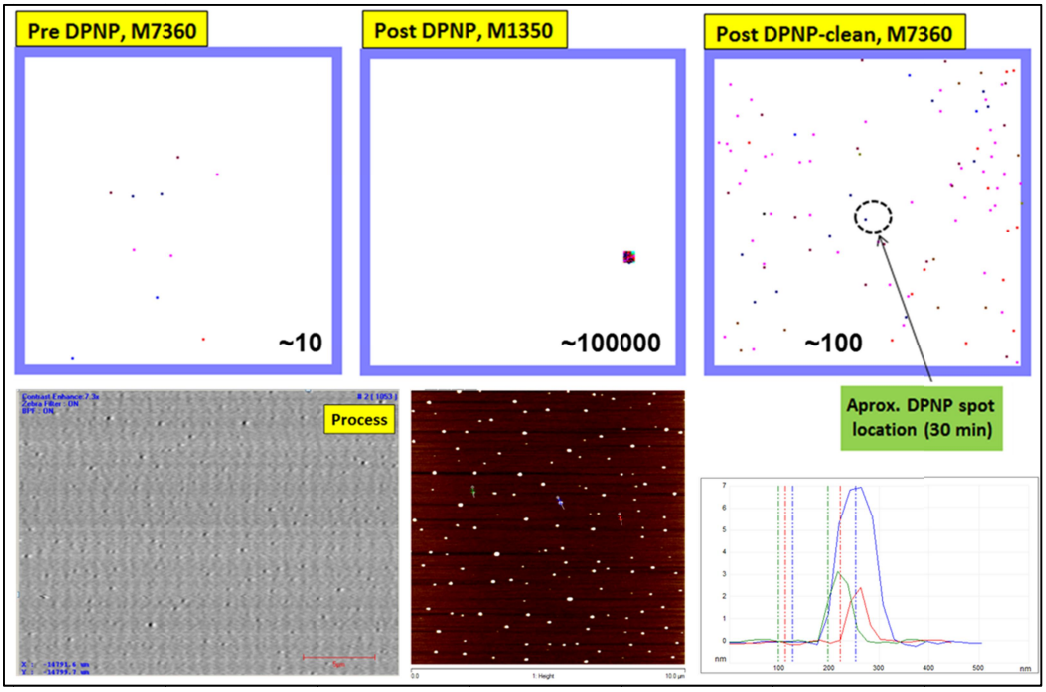

Figure 4: Inspection maps showing the defectivity on the substrate before DPNP, after DPNP and after cleaning (top row). M7360 review image and AFM scan/section showing the presence of small adder particles from DPNP polishing (bottom row).

3. DPNP FOR EUV

3.1. CMP vs. DPNP

CMP is the best known technique to globally polish the substrates to the required roughness levels (< 0.1 nm RMS), but it is an inherently random process based on contact between the surface and slurry particles/polishing pad that invariably adds defects while lowering the roughness. On current substrates these pits and scratches are typically less than 10 and 2 nm in depth[13], respectively. CMP employs slurry particles and other additives to polish the surface, which must be cleaned away after polishing. The post-CMP cleaning, while removing the particles, adds to the substrate defectivity due to megasonic cavitation-induced pitting, if not carefully controlled[14]. The CMP removal rate of such thick substrates cannot be accurately controlled uniformly over the entire surface, resulting in some degradation of substrate flatness. Also, CMP has no end-point detection capability, in the sense the polishing continues until it is externally stopped. Moreover, its roughness is limited by the size of the slurry particles and the roughness of the polishing pad used. DPNP,

on the other hand, is a more controllable process that can achieve atomic scale roughness. It is a self-limiting process where once the surface is smooth enough the etching stops on its own. Another major advantage of DPNP is that it is a non-contact process, so it does not create new pit/scratch type defects on the substrate surface, unlike CMP. One area where CMP holds an advantage over DPNP is the extent of anisotropic etching-CMP is highly anisotropic (it removes vertically downwards), while the anisotropy in DPNP etching depends on the size and curvature of the surface features.

3.2. DPNP in the overall process flow

Once the EUV substrate material is cut into the required shape and size, it undergoes a series of local and global polishing steps to achieve the required roughness and flatness levels. One such possible flow is depicted in Figure 5. Here the first step would be a local polishing process named magneto-rheological finishing (MRF), which because of its stable removal rates and help of numerical control and sophisticated computer algorithms, can very deterministically and accurately correct for surface figure[15,16]. It has been shown to achieve sub-30 nm peak-valley flatness over the entire 142×142 mm^2 substrate area[9]. Since MRF is a directional shear based polishing process, it leaves unidirectional grooves in its wake, and the lowest surface roughness produced by MRF is in the range of 0.2 to 0.3 nm RMS. Local polishing also makes post-MRF cleaning of the substrate difficult, resulting in high defectivity.

The next step would be a global polish like CMP which can bring down the roughness to sub-0.1 nm levels. Since the EUV substrate is very thick, it is very hard to control the removal rate over different areas of the surface (no local pressure variations) and CMP invariable worsens the flatness of the substrate to some degree. One might need to go back to MRF local polishing to correct for the flatness, and then return to a milder CMP process to keep the flatness and roughness levels within acceptable limits. The defectivity from CMP is intrinsically coupled to the post-CMP cleaning process. Since CMP requires the addition of small solid abrasive and other particles in order to polish, all these particles need to be removed after the CMP process.

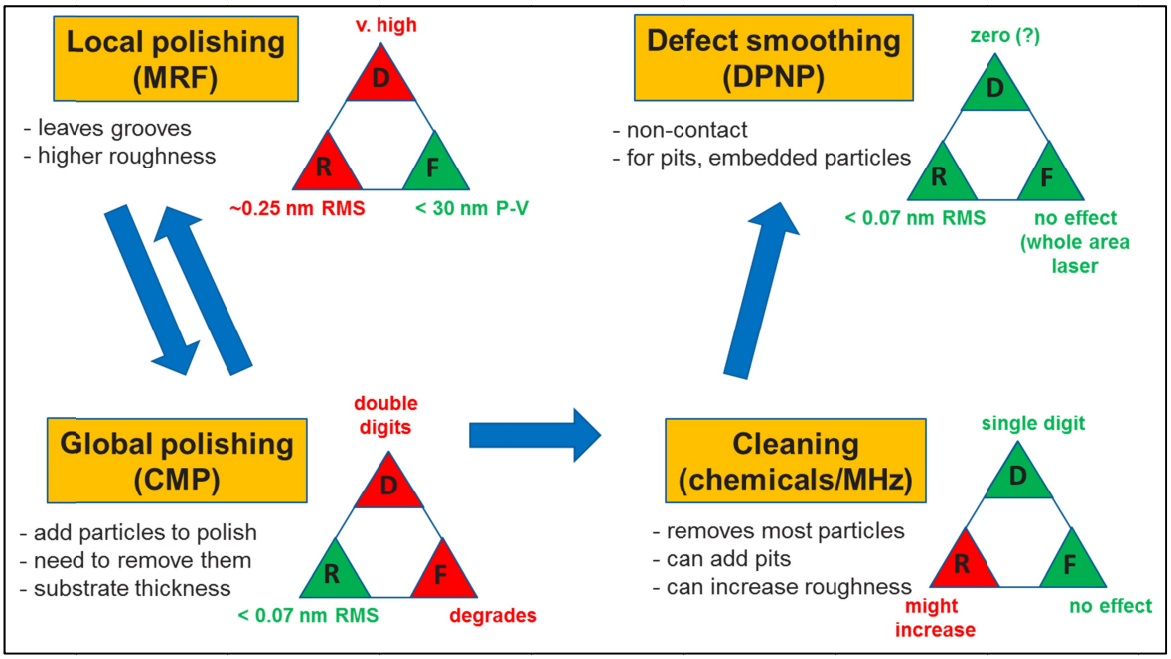

Figure 5: A possible overall process flow for EUV substrates showing the sequence of local/global polishing and cleaning, with DPNP being the final polishing step.

The post-CMP cleaning typically employs a combination of SC1 ($NH_4OH + H_2O_2$) and SPM ($H_2SO_4 + H_2O_2$) based chemistries for removing metallic and organic contaminants, respectively. The cleaning also employs megasonic irradiation to provide sufficient force to dislodge the particles, which can create pits due to cavitation collapse on the surface. If the particles are too strongly adhered to the surface, the surface itself might need to be slightly etched using a HF-based chemistry to undercut the contact between the particle and the underlying glass surface. The downside of using

HF is that the surface roughness of the substrates increases by a slight amount[17]. Quality substrates and proper post-CMP cleaning can remove most of the particles on the surface without the generation of many pits.

DPNP can potentially be the last superfine polishing step in the polishing process flow. The advantage is that it is a non-contact process and doesn't increase the roughness or impact the flatness (for laser exposure over the full substrate area) while smoothing any remaining pits or particles on the substrate. This is particularly important in case of any embedded particles, since in normal cleaning process removing an embedded particle results in a pit defect in its wake, while in DPNP the particle is smoothed to the surface level only. DPNP needs to be coupled with a mild cleaning step (likely without megasonic irradiation) to remove the etching residues added.

4. SUMMARY

EUV substrates require the development of a tightly integrated global/local polishing/cleaning processing in order to simultaneously meet the three coupled requirements of defectivity, roughness and flatness. DPNP is a novel dry etching process based on the optical near-field effect and achieves gradient-based selective etching on fused silica and doped fused silica substrates. It has been shown to completely smooth pit and particle defects to less than 1 nm in depth or height and has potential to be the final polishing process step for EUV substrates. To take the DPNP technology to a commercial scale requires the expansion of the laser exposure field to the full substrate area and proper integration with the overall polishing/cleaning process flow.

ACKNOWLEDGEMENTS

The authors would like to express their gratitude to T. Murakami from NPEO for facilitating the entire project. We would also like to thank the following people at SEMATECH for helping with the AFM measurements and FIB/SEM milling: T. Owen, J. Underwood, B. Halliday, M. Maloney, N. Lethbridge, L. Gwenden, E. Maillet and E. Stinzianni.

REFERENCES

[1] Huh, S.-M., Rastegar, A., Wurm, S., Goldberg, K., Mochi I., Nakajima, T., Kisimoto, M. and Komakine M., "Study of real defects on EUV blanks and a strategy for EUV mask inspection", 26th European Mask and Lithography Conference Proc. SPIE **7545** (2010)

[2] Teki, R., JohnKadaksham, A., House, M., Harris-Jones, J., Ma, A., Babu, S. V., Hariprasad, A., Dumas, P., Jenkins, R., Provine, J., Richmann, A., Stowers, J., Meyers, S., Dietze, U., Kusumoto, T., Yatsui, T., Ohtsu, M. and Goodwin, F., "Alternative Smoothing Techniques to Mitigate EUV Substrate Defectivity", Proc. of SPIE **8322**, 83220B (2012)

[3] Rosch, W., Beall, L., Maxon, J., Sabia, R. and Sell, R., "Corning ULE® glass can meet P-37 specifications", Proc. of SPIE **6517**, 651724 (2007)

[4] Gronheid, R. and Leeson, M. J., "Extreme ultraviolet interference lithography as applied to photoresist studies", J. Micro/Nanolith. MEMS MOEMS **8(2),** 021205 (2009)

[5] Seo, H.-S., Huh, S.-M., Lee, S.-Y., Kim, T.-G., Kim, S.-S. and Jeon, C.-U., "EUVL mask blank requirements toward high volume manufacturing", International Symposium on EUVL, Brussels, Belgium, October 4 2012

[6] Naulleau, P. P., George, S. A. and McClinton, B. M., "Mask roughness and its implications for LER at the 22- and 16-nm nodes", Proc. Of SPIE **7636**, 76362H-1 (2010)

[7] George, S. A., Naulleau, P. P., Salmassi, F., Mochi, I., Gullikson, E. M., Goldberg, K. A. and Henderson, E. H., "Extreme ultraviolet mask substrate roughness effects on lithographic patterning," J. Vac. Sci. Technol. B **28(6),** C6E23 (2010)

[8] Vaglio-Pret, A., Gronheid, R., Younkin, T. R., Leeson, M. J. and Yan, P.-Y., " Impact of EUV Mask Surface Roughness on LER", Proc. of SPIE **8322**, 83220N (2012)

[9] Teki, R., JohnKadaksham, A., Ma, A., Goodwin, F., Yatsui, T., Ohtsu, M., Hariprasad, A., Lagudu, U. R. K., Babu, S. V., Dumas, P. and Jenkins, R., "Material- and polishing-induced defectivity on EUV mask substrates," International Symposium on EUVL, Brussels, Belgium, October 4 2012

[10] Ohtsu, M. (ed.), Progress in Nanophotonics 1, Nano-Optics and Nanophotonics, Springer-Verlag Berlin, Heidelberg, 2-6 (2011)

[11] Yatsui, T., Nomura, W., Ohtsu, M., Hirata, K. and Tabata, Y., "Realization of an ultra-flat silica surface with angstrom-scale average roughness using nanophotonic polishing", Proc. Lasers and Electro-optics **20**, 1 (2008)

[12] Yatsui, T., Nomura, W., Naruse, M. and Ohtsu, M., "Realization of an atomically flat surface of diamond using dressed photon–phonon etching", J. Phys. D: Appl. Phys. **45**, 475302 (2012)

[13] Teki, R., JohnKadaksham, A., Harris-Jones, J., Stinzianni, E. and Goodwin, F., "Understanding polishing induced surface defectivity on EUV mask fused silica substrates", Glass & Optical Materials Division Annual Meeting, St. Louis, MO, U. S. A., May 23 2012

[14] Kapila, V., Deymier, P. A., Shende, H., Pandit, V., Raghavan, S. and Eschbach, F. O., "Megasonic cleaning, cavitation, and substrate damage: an atomistic approach", Proc. of SPIE **6283**, 628324 (2006)

[15] Golini D., Kordonski, W. I., Dumas P. and Hogan, S. J., "Magnetorheological finishing (MRF) in commercial precision optics manufacturing", Proc. SPIE **3782**, 80 (1999)

[16] Polllicove, H. and Golini, D., "Deterministic manufacturing processes for precision optical surfaces", Key Engineering Materials **238-239**, 53 (2003)

[17] JohnKadaksham, A., Teki, R., Harris-Jones, J. and Lin, C. C., "Preparation of substrates for EUV Blanks using an etch clean process to meet HVM challenges", Proc. of SPIE **8522**, 852216 (2012)

EVENT DETAILS

INFORMATION SYSTEMS BASED ON OPTICAL NEAR-FIELD PROCESSES AT THE NANOSCALE

Speaker: Makoto Naruse, National Institute of Technology, Tokyo

Department: Electrical Engineering

Location: Bowen Hall Auditorium 222

Date/Time: Wednesday, January 16, 2013, 3:00 p.m. - 4:00 p.m.

Nanophotonics has been extensively studied with the aim of unveiling and exploiting light–matter interactions that occur at a scale below the diffraction limit of light, and recent progress made in experimental technologies—both in nanomaterial fabrication and characterization—is driving further advancements in the field. From the viewpoint of information, on the other hand, novel architectures, design and analysis principles, and even novel computing paradigms should be considered so that we can fully benefit from the potential of nanophotonics. This talk will briefly review information physics aspects of nanophotonics. More specifically, we present some fundamental and emergent information properties that stem from optical excitation transfer mediated by optical near-field interactions and the hierarchical properties inherent in optical near-fields. We theoretically and experimentally investigated aspects such as unidirectional signal transfer, energy efficiency, and networking effects, as well as applications such as optical securities. A stochastic analysis of light-assisted material formation is also mentioned, where an information-based approach provides a deeper understanding of the phenomena involved, such as self-organization. Furthermore, the spatio-temporal dynamics of optical excitation transfer and its inherent stochastic attributes are utilized for solution searching, paving the way to a novel computing paradigm that exploits coherent and dissipative processes in nanophotonics.

Makoto Naruse1,2, Naoya Tate2,3, Masashi Aono4, and Motoichi Ohtsu2,3
Photonic Network Research Institute, National Institute of Information and Communications Technology, 4-2-1 Nukui-kita, Koganei, Tokyo 184-8795, Japan
https://sites.google.com/site/makotonaruseweb/
Nanophotonics Research Center, Graduate School of Engineering, The University of Tokyo, 2-11-16 Yayoi, Bunkyo-ku, Tokyo 113-8656, Japan
http://www.npc.t.u-tokyo.ac.jp/index_e.html
Department of Electrical Engineering and Information Systems, Graduate School of Engineering, The University of Tokyo, 2-11-16 Yayoi, Bunkyo-ku, Tokyo 113-8656, Japan
http://uuu.t.u-tokyo.ac.jp/eng/index.html
RIKEN Advanced Science Institute, 2-1, Hirosawa, Wako, Saitama 351-0198, Japan
http://arn.local.frs.riken.jp/~aono/

Optical security based on optical near-field processes

Makoto Naruse[1,2], Naoya Tate[2,3], and Motoichi Ohtsu[2,3]

[1] *National Institute of Information and Communications Technology, 4-2-1 Nukui-kita, Koganei, Tokyo 184-8795, Japan*

[2] *Nanophotonics Research Center, School of Engineering, The University of Tokyo, 2-11-16 Yayoi, Bunkyo-ku, Tokyo 113-8656, Japan*

[3] *Department of Electrical Engineering and Information Systems, School of Engineering, The University of Tokyo, 2-11-16 Yayoi, Bunkyo-ku, Tokyo 113-8656, Japan*

Abstract

Optics has been playing crucial roles in security applications ranging from authentication and watermarks to anti-counterfeiting. However, conventional security technologies in use today have been facing increasingly stringent demands to safeguard against threats such as counterfeiting of holograms, requiring innovative physical principles and technologies to overcome their limitations. Nanophotonics, which utilizes interactions between light and matter at the nanometer scale via optical near-field interactions, can break through the diffraction limit of conventional propagating light. Moreover, nanophotonics has

some unique physical attributes, such as localized optical energy transfer and the hierarchical nature of optical near-field interactions, which pave the way for novel security functionalities. This talk reviews physical principles and describes some experimental demonstrations of systems based on nanophotonics, with respect to security applications such as tamper resistance against non-invasive and invasive attacks, hierarchical information retrieval, hierarchical holograms, authentication, and traceability.

2012 International Symposium on Nonlinear Theory and its Applications
NOLTA2012, Palma, Majorca, Spain, October 22-26, 2012

Network of Energy Transfer on the Nanoscale and its Application to Solving Constraint Satisfaction Problems

Makoto Naruse[1], Masashi Aono[2], Horikazu Hori[3], Masahiko Hara[2], and Motoichi Ohtsu[4]

1 Photonic Network Research Institute, National Institute of Information and Communications Technology, 4-2-1 Nukui-kita, Koganei, Tokyo 184-8795, Japan
2 Flucto-order Functions Research Team, RIKEN Advanced Science Institute, 2-1, Hirosawa, Wako, Saitama 351-0198, Japan
3 Interdisciplinary Graduate School of Medicine and Engineering, University of Yamanashi, Takeda 4-3-11, Kofu, Yamanashi 400-8511, Japan
4 Department of Electrical Engineering and Information Systems and Nanophotonics Research Center, Graduate School of Engineering, The University of Tokyo, 2-11-16 Yayoi, Bunkyo-ku, Tokyo 113-8656, Japan
Email: naruse@nict.go.jp, masashi.aono@riken.jp, hirohori@yamanashi.ac.jp, masahara@riken.jp, ohtsu@ee.t.u-tokyo.ac.jp

Abstract–This paper demonstrates that a network of optical energy transfer between quantum nanostructures mediated by optical near-field interactions, occurring at scales far below the wavelength of light, could be utilized for solving constraint satisfaction problems (CSPs). The optical energy transfer, from smaller quantum dots to larger ones, a quantum stochastic process, depends on the existence of resonant energy levels between the quantum dots or a state-filling effect occurring at the larger quantum dots. Such a spatial and temporal mechanism yields different evolutions of energy transfer patterns in multi-quantum-dots systems. We numerically demonstrate that optical energy transfer processes can solve a CSP. We consider such an approach pave the way for a novel computation paradigm beyond those of conventional optical or quantum computations.

1. Introduction

Novel computing devices and architectures are highly demanded to overcome the limitations of conventional ones that are based solely on electron transfer in terms of reducing power dissipation, solving computationally demanding problems, and so on. Also, nature-inspired architectures are attracting significant attention from various research arenas such computational neurosciences, stochastic-based computing and noise-based logic, and spatio-temporal computation dynamics [1].

Among these research, Aono et al. demonstrated the "amoeba-based computing", such as solving constraint satisfaction problem (CSP) [1], the traveling salesman problem (TSP), by utilizing the spatio-temporal oscillatory dynamics of the photoresponsive amoeboid organism Physarum combined with external optical feedback control. These demonstrations indicate that we can utilize inherent spatial and temporal dynamics for novel computing architectures and applications; such arguments should be applicable for nanometer-scale light and matter interactions [2]. In particular, energy transfer between quantum nanostructures mediated by optical near-field interactions plays a crucial role; its theoretical foundation has been given in the dressed photon model [3] and experimentally demonstrated in various quantum nanostructures [4-6] including room temperature operations [6]. Besides, the optical energy transfer has been shown to be 10^4-times more energy efficient than that of a bit-flip energy required in conventional electrically wired devices [7].

This paper theoretically demonstrates that optical energy transfer between quantum dots mediated by optical near-field interactions is utilized for solving a CSP. The optical energy transfer depends on the existence of resonant energy levels between the quantum dots (QDs) or the state filling effect occurring at the destination QDs. Also, as indicated by the quantum master equations, the energy transfer process is fundamentally probabilistic. Such a spatial and temporal mechanism yields different evolutions of energy transfer patterns combined with certain feedback mechanisms. In contrast to biological substrates, optical energy transfer is implemented by highly-controlled engineering means for designated structures. The operating speed of such optical-near-field mediated QD systems, which is in order of nanosecond when we concern with radiative relaxation processes, is also significantly faster than the ones based on biological organisms, which is in orders of seconds or minutes [1]. In addition, we should emphasize that the concept and the principles discussed in this paper is fundamentally different from those of conventional optical computing or optical signal processing which are limited by the abilities of propagating light. The concept and the principles are also different from quantum computing paradigm where superposition of all possible states is exploited so that it leads to a collect solution. The optical near-field-mediated energy transfer is a coherent process, indicating that an optical excitation could be transferred to all possible destination QDs via a resonant energy level, but such coherent interaction between QDs results in an

unidirectional energy transfer by an energy dissipation process occurring in the larger dot. Thus, our approach paves another computation paradigm where both coherent and dissipative processes are exploited.

2. State-dependent Optical Energy Transfer via Near-Field Interactions for Solving a Constraint Satisfaction Problem (CSP)

Here we assume two spherical quantum dots whose radii are R_S and R_L, which we call QD_S and QD_{L1}, respectively, as shown in Fig. 1(a). There exists a resonance between the level of quantum number (1,0) of QD_S, denoted by S in Fig. 1(a), and that of quantum number (1,1) of QD_{L1}, marked by $L_1^{(U)}$. Note that the (1,1)-level of QD_{L1} is a dipole-forbidden energy level. However, optical near-fields allow this level to be populated by excitation. Therefore, an exciton in the (1,0)-level in QD_S could be transferred to the (1,1)-level in QD_{L1}. In QD_{L1}, due to the sublevel energy relaxation with a relaxation constant Γ, which is faster than the near-field interaction, the exciton relaxes to the (1,0)-level, denoted by $L_1^{(L)}$, from where it radiatively decays. Therefore, we find uni-directional optical excitation transfer from QD_S to QD_{L1}.

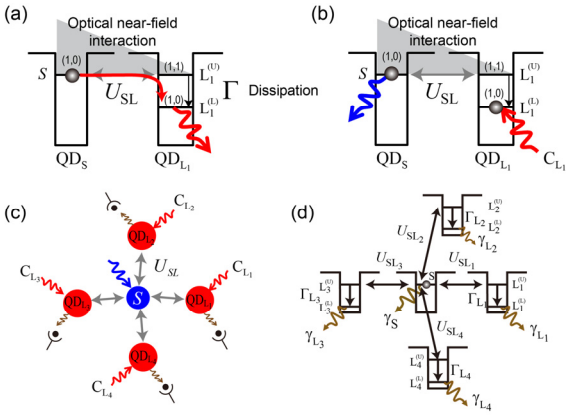

Fig. 1 (a,b) Optical energy transfer between QD mediated by near-field interaction. (c,d) Architecture of optical-energy-transfer-based problem solver studied in this paper.

When the lower energy level of the destination quantum dot is filled with another excitation (called "state filling"), an optical excitation occurring in a smaller QD cannot move to a larger one. This suggests two different patterns of optical energy transfer appear depending on occupation of the destination quantum dots (Fig. 1(b)).

Toward solving a constraint satisfaction problem (CSP) using optical energy transfer, we design an architecture where a smaller QD are surrounded by multiple larger QDs. In this paper, we assume four larger QDs each of which is labeled with QD_{L1}, QD_{L2}, QD_{L3}, QD_{L4} as indicated in Fig. 1(c). Fig. 1(d) shows representative parameterizations associated with the system. The (1,0)-level in QD_S is denoted by S, and the (1,1)-level in QD_{Li} is denoted by $L_i^{(U)}$. These levels are resonant with each other and are connected by inter-dot interactions denoted by U_{SLi} (i=1,...,4). The lower level in QD_{Li}, namely the (1,0)-level, is denoted by $L_i^{(L)}$, which could be filled via the sublevel relaxation denoted by Γ_{Li} from $L_i^{(U)}$. The radiations from the S and L_i levels are respectively represented by the relaxation constants γ_S and γ_{Li}. We call the inverse of those relaxation constants the radiation lifetime in the following. We also assume that the photon radiated from the lower level of QD_{Li} can be separately captured by photodetectors. In addition, we assume control lights, denoted by C_{Li} in Fig. 1(c), so that they could induce state filling effect at $L_i^{(L)}$. Summing up, Fig. 1(c) and (d) schematically represent the architecture of the system to be studied in this paper for solving a CSP.

First, we suppose that the system initially has one exciton in S. From the initial state, through the inter-dot interactions U_{SLi}, the exciton in S could be transferred to $L_i^{(U)}$ (i=1,...,4). Correspondingly, we can derive quantum master equations in the density matrix formalism [8]. The Liouville equation for the system is then given by

$$\frac{d\rho(t)}{dt} = -\frac{i}{\hbar}[H_{\text{int}}, \rho(t)] - N_\Gamma \rho(t) - \rho(t) N_\Gamma \quad (1)$$

where $\rho(t)$ is the density matrix with respect to the five energy levels, H_{int} is interaction Hamiltonian, and N_Γ indicates relaxations. In the numerical calculation, we assume U_{SLi}^{-1}=100 ps, Γ_i^{-1}=10 ps, γ_{Li}^{-1}=1 ns and γ_S^{-1}~2.92 ns as a typical parameter set [8].

Based on the above modeling and parameterizations, we can calculate populations involving $L_1^{(L)}$, $L_2^{(L)}$, $L_3^{(L)}$, and $L_4^{(L)}$ which are relevant to the radiation from the larger QDs. Also, when QD_{Li} suffers from state filling by control lights C_{Li}, the energy transfer from the QD_S to QD_{Li} behaves differently.

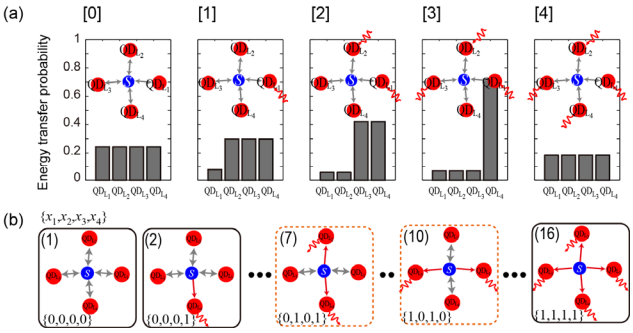

Fig. 2 (a) Estimated energy transfer probability depending on the control light beam(s). (b) Schematic representation of possible states of the system. States (7) and (10) correspond to the correct solutions.

We assume that the energy transfer probability to QD_{Li} is correlated with the integral of the populations with respect to $L_i^{(L)}$ as summarized in Fig. 2(a). We should notice that such integral of populations are indeed a figure-of-merit (FoM) indicating the trend of optical

energy transfer from smaller one to the four larger dots; it does *not* hold the conservation law of the probability, namely, the summation of the transition probability to QD_{Li} is not unity. Instead, we see that the energy transfer to QD_{Li} occurs if a random number generated uniformly between 0 and 1 is less than the transition probability to QD_{Li} shown in Fig. 2(a); for example in the case of Fig. 2(a,[3]), the energy transfer to QD_{L4} is highly likely induced whereas the transfer to QD_{L1}, QD_{L2}, and QD_{L3} are less likely induced.

The idea for the problem solving is to control optical energy transfer by controlling the destination QD by control lights in an adequate feedback mechanisms. We assume that a photon radiation, or observation, from the energy level $L_i^{(L)}$ is equivalent that a binary value x_i results in a logical 1 level, while no observation of photon means x_i =0.

3. Application to Solving a Constraint Satisfaction Problem

We consider the following constraint satisfaction problem as an example regarding an array of N binary-valued variables x_i (i=1,...,N). The constraint is that x_i =NOR(x_{i-1},x_{i+1}) should be satisfied for all i. That is, variable x_i should be consistent with a logical NOR operation of the two neighbors. For i=0 and N, the constraints are respectively given by x_1=NOR(x_N,x_2) and x_N=NOR(x_{N-1},x_1). We call this problem the "NOR problem" hereafter in this paper. Taking account of the nature of an individual NOR logic operation, one important inherent character is that if x_i=1 then its two neighbors should be both zero x_{i-1}=x_{i+1}=0. Recall that a photon radiated, or observed, from the energy level $L_i^{(L)}$ corresponds to a binary value x_i=1, whereas the absence of an observed photo means x_i=0. Therefore, x_i=1 should mean that the optical energy transfer to both $L_{i-1}^{(L)}$ and $L_{i+1}^{(L)}$ is prohibited so that x_{i-1}=x_{i+1}=0 is satisfied. Therefore, the feedback or control mechanism is that;

[Control mechanism] If x_i=1 at cycle t, then the control light beams C_{i-1} and C_{i+1} are turned on at cycle t=t+1.

In the case of N=4, there are in total 2^4 optical energy transfer patterns from the smaller dot to larger ones. In this case, the variables satisfying the constraints do exist, and they are given by {x_1, x_2, x_3, x_4}={0,1,0,1} and {1,0,1,0}, which we call "correct solutions". Fig. 2(b) schematically represent some of the possible states where the state (7) and (10) respectively corresponding to the correct solutions.

There are a few remarks regarding the NOR problem. One is about the potential deadlock, analogous to Dijkstra's "dining philosophers problem", as already argued by Aono et al. in Ref. [1]. Starting with an initial state x_i=0 for all i, and assuming a situation where optical energy is transferred to all larger QDs, we observe photon radiation from all energy levels $L_i^{(L)}$, namely, x_i=1 for all i. Then, based on the feedback mechanism shown above, all control light beams are turned on. If such a feedback mechanism perfectly inhibits the optical energy transfer from the smaller QD to the large ones at the next step t+1, the variables then go to x_i=0 for all i. This leads to all control light beams being turned off at t+2. In this manner, all variables constantly repeat a periodic switching between x_i=0 and x_i=1 in a synchronized manner. Consequently, the system can never reach the correct solutions. However, as indicated in Fig. 2(a), the probability of optical energy transfer to larger dots is in fact not zero even when all larger QDs are illuminated by control lights as shown in Fig. 2(a,[4]). Also, even for a non-illuminated destination QD, the energy transfer probability may not be exactly unity. Such a stochastic behavior of the optical energy transfer is a key role in solving the NOR problem. This nature is similar to the demonstrations in the amoeba-based computer [1] where fluctuations of chaotic oscillatory behavior involving spontaneous symmetry breaking in the amoeboid organism guarantees such a critical property.

The operating dynamics cause one pattern to change to another one in every iteration cycle. Thanks to the stochastic nature, each trial could exhibit a different evolution of the energy transfer patterns. In particular, the transition probability, shown in Fig. 2(a), affects the behavior of the transitions. Therefore, we introduce a gain factor (G) to be multiplied by the energy transfer probability summarized in Fig. 2(a).

The curves in Fig. 3(a) represent the evolution of the output appearance from QD_{Li}, namely, the ratio of the incidence when x_i=1 among 1,000 trials evaluated at each cycle. The curves in Fig. 3(b) characterizes the ratio of the appearance of the state that corresponding to the correct solutions; {0,1,0,1} (state 7) and {1,0,1,0} (state 10), respectively. When we closely examine the evolutions of x_i in Fig. 3(a), we can see that the pair x_1 and x_3 exhibit similar behavior and as do the pair x_2 and x_4. Also, the former pair exhibit larger values the latter pair show smaller values, and vice versa. This corresponds to the fact that correct solutions are likely to be induced as the iteration cycle increases.

Such a tendency is more clearly represented when we evaluate the time-averages of the characteristics in Fig. 3(a) and (b). Fig. 3(c) shows the evolutions of the ratio of the incidences when x_i=1, and Fig. 3(d) shows the ratios of State (7) and State (10) averaged over every 5 cycles. We can clearly observe a similar tendency to the one described above. Also, we should emphasize that, thanks to the probabilistic nature of the system, the states of correct solutions appear in an interchangeable manner. This is a clear indication of the fact that the probabilistic nature of the system autonomously seeks the solutions that satisfy the constraints of the NOR problem; the state-dependent probability of energy transfer plays the critical role in this. In other words, it should be emphasized that a non-local correlation is manifested in the evolution of x_i; for instance, when the system is in State (7), {0,1,0,1}, the probabilities of energy transfer to QD_{L1} and QD_{L3} are equally comparably low (due to state filling), whereas

those to QD_{L2} and QD_{L4} are equally comparably high, indicating that the probability of the energy transfer to an individual QD_{Li} has inherent spatial patterns or non-local correlations. At the same time, the energy transfer to each QD_{Li} is indeed probabilistic; therefore, the energy transfer probability to, for instance, QD_{L1} is not zero even in the State (7), and thus, the state could transition from State (7) to State (10), and vice versa. In fact, starting with the initial condition of State (7), the ratio of output appearance from QD_{L1} and the ratio of the correct solutions evolve as shown in Fig. 3(e) and (f) where States (7) and (10) occur equally in the steady state around time cycles around 20.

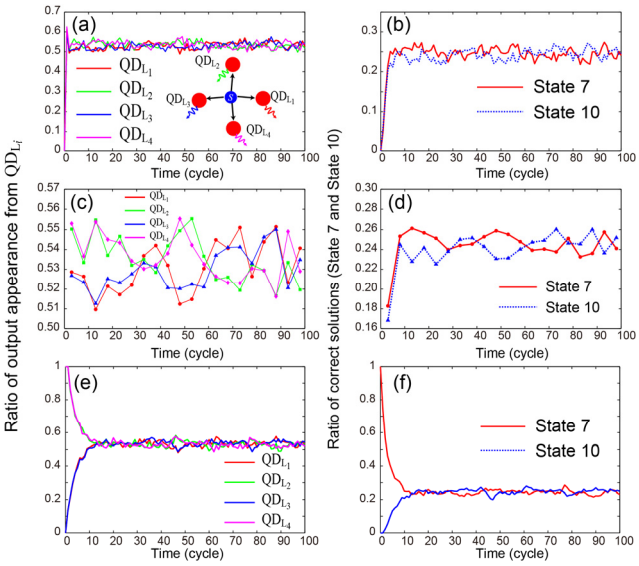

Fig. 3 (a) The evolution of the ratio of the output appearance from QD_{Li}, and (b) the ratio of the state corresponding to correct solutions. (c,d) Time-averaged traces (b) and (c), respectively. (e) The evolution of the ratio of the output appearance from QD_{Li}, and (f) the ratio of the state corresponding to correct solutions with the initial state (7).

Fig. 4 evaluates the accuracy rate, which is the number of correct solutions among 1000 different trials at t =100, as a function of the gain factor. We can see that gain of 2.5 provides the highest accuracy rate.

4. Conclusion

In summary, we have demonstrated that energy transfer between quantum nanostructures based on optical near-field interactions occurring at scales far below the wavelength of light has the potential to solve a constraint satisfaction problem. The optical energy transfer from smaller quantum dots to larger ones, which is a quantum stochastic process, depends on the existence of resonant energy levels between the quantum dots or a state-filling effect occurring at the destination quantum dots. We exploit these unique spatiotemporal mechanism in optical energy transfer to solve a constraint satisfaction problem, and numerically demonstrated that the NOR problem is successfully solved.

Acknowledgments

This work was supported in part by the Strategic Information and Communications R&D Promotion Programme (SCOPE) of the Ministry of Internal Affairs and Communications, and Grants-in-Aid for Scientific Research from the Japan Society for the Promotion of Science.

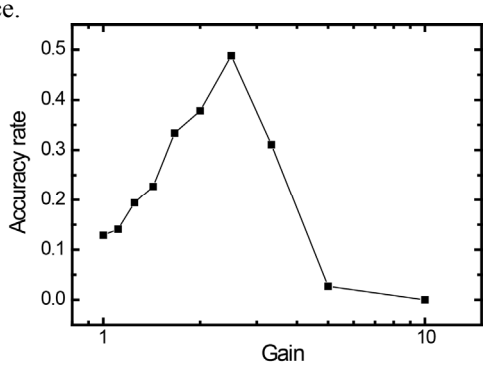

Fig. 4 Calculated accuracy rate, or the ratio of the number of correct states among all trials. The accuracy rate is maximized when the gain factor is 2.5.

References

[1] M. Aono, M. Hara, K. Aihara, "Amoeba-based neurocomputing with chaotic dynamics," Communications of the ACM 50, 69–72 (2007).

[2] M. Naruse, T. Miyazaki, T. Kawazoe, S. Sangu, K. Kobayashi, F. Kubota, M. Ohtsu, "Nanophotonic computing based on optical near-field interactions between quantum dots," IEICE Transaction on Electronics E88-C, 1817–1823 (2005).

[3] M. Ohtsu, T. Kawazoe, T. Yatsui, M. Naruse, "Nanophotonics: Application of Dressed Photons to Novel Photonic Devices and Systems," IEEE J. Sel. Top. Quantum Electron. 14 1404–1417 (2008).

[4] T. Kawazoe, et al, "Demonstration of nanophotonic NOT gate using near-field optically coupled quantum dots," Appl. Phys. B 84, 243–246 (2006).

[5] W. Nomura, et al., "Structural dependency of optical excitation transfer via optical near-field interactions between semiconductor quantum dots," Appl. Phys. B 100, 181-187 (2010).

[6] T. Kawazoe, et al., "Two-dimensional array of room-temperature nanophotonic logic gates using InAs quantum dots in mesa structures," Appl. Phys. B 103, 537–546 (2011).

[7] M. Naruse, H. Hori, K. Kobayashi, P. Holmström, L. Thylén, and M. Ohtsu, "Lower bound of energy dissipation in optical excitation transfer via optical near-field interactions," Opt. Express 18, A544–A553 (2010).

[8] M. Naruse, T. Kawazoe, R. Ohta, W. Nomura, and M. Ohtsu, "Optimal mixture of randomly dispersed quantum dots for optical excitation transfer via optical near-field interactions," Phys. Rev. B 80, 125325 1–7 (2009).

2012 International Symposium on Nonlinear Theory and its Applications
NOLTA2012, Palma, Majorca, Spain, October 22-26, 2012

Amoeba-inspired SAT Solver

Masashi Aono†, Song-Ju Kim†, Liping Zhu‡, Makoto Naruse£,
Motoichi Ohtsu§, Hirokazu Hori¶, Masahiko Hara†

†Flucto-order Functions Research Team, RIKEN Advanced Science Institute,
‡Tokyo Tech-RIKEN International School, Tokyo Institute of Technology,
2-1, Hirosawa, Wako, Saitama 351-0198, Japan
£Photonic Network Research Institute, National Institute of Information and Communications Technology,
4-2-1 Nukui-kita, Koganei, Tokyo 184-8795, Japan
§Graduate School of Engineering, The University of Tokyo,
2-11-16 Yayoi, Bunkyo-ku, Tokyo 113-8656, Japan
¶Interdisciplinary Graduate School of Medical and Engineering, University of Yamanashi,
Kofu 400-8511, Japan
Email: masashi.aono@riken.jp

Abstract—We propose a biologically-inspired computing algorithm called "AmoebaSAT" for solving an NP-complete combinatorial optimization problem, the Boolean satisfiability problem (SAT). AmoebaSAT is a hybrid of two dynamics; chaotic oscillatory dynamics for exploring the state space are combined with spatiotemporal control dynamics for bouncing back logically-false state transitions. For the former, we employ the logistic map as a unit for generating chaotic fluctuation. The control principle of the latter that we call "bounceback control" is designed to stabilize a state only when it represents a solution, i.e., a satisfiable assignment. We show that, for some benchmark problem instances, AmoebaSAT finds a solution faster than a well-known algorithm called "WalkSAT", which is considered to be one of the fastest algorithms.

1. Introduction

There has been growing interest in biologically-inspired algorithms for solving computationally demanding problems in a fashion similar to search dynamics of various biological systems such as neural networks, evolutionary processes, ants, and swarms [1]. AmoebaSAT extracts the essence of spatiotemporal oscillatory dynamics of a single-celled amoeboid organism, the true slime mold *Physarum polycephalum*, which is capable of searching for a solution to some optimization problems [2]. When placed under our previously studied spatiotemporal control which applies aversive light stimuli locally and dynamically depending on the shape of the organism, the organism exhibits chaotic oscillatory dynamics and finds a solution to the traveling salesman problem by changing its shape into the optimal one for which the area of the body is maximized and the risk of being illuminated is minimized [3]. Inspired by this scheme, we define AmoebaSAT as a hybrid of chaotic oscillatory dynamics and spatiotemporal control dynamics.

The SAT is the problem of determining if a given Boolean formula of N variables $x_i \in \{0\ (false), 1\ (true)\}$ ($i \in I = \{1, 2, \cdots, N\}$) is "satisfiable", i.e., there exists at least one particular assignment of true values to the variables such that it makes the entire formula *true*. Many decision problems and optimization problems can be transformed into instances of the SAT. Thus, SAT solvers are potentially applied to a wide range of practical purposes such as software and hardware design, planning, constraint optimization, and automatic inference.

The SAT is a basis of hard computational problems, as it is the first problem shown to be NP-complete [4]. No algorithm is known to solve the NP-complete problem in a practically tractable time. Indeed, the number of possible assignments 2^N grows exponentially as a function of N.

A "conjunctive normal form (CNF)" of a Boolean formula is the *AND* ($\wedge$) of a series of *clauses*, where each *clause* is the *OR* ($\vee$) of *literals*, and each *literal* is either a variable x_i or its negation $\neg x_i$. The SAT is called "k-SAT" when the formula is a CNF whose *clause* contains at most k variables. 3-SAT is NP-complete whereas 2-SAT is not.

In this study, we formulate AmoebaSAT so that it can be applied to k-SAT. For 20-variable 3-SAT benchmark instances that are available online [6], we compare the performance of AmoebaSAT with that of a widely-studied randomized algorithm for k-SAT, called WalkSAT [5].

2. Models

2.1. AmoebaSAT

2.1.1. Assignment

Given an N-variable formula, AmoebaSAT is defined as a discrete-time-state dynamical system consisting of $2 \cdot N$ units, each of which is labeled with $(i, v) \in I \times \{0, 1\}$ and is an analogy of a pseudopod-like branch of the amoeboid organism. Let $X_{i,v}(t)$ be a displacement of resources in each

unit at time step t. If $X_{i,v} > 0$, we consider that unit (i, v) has "abundant" resources and the system assigns the value v to the ith variable, i.e., $x_i = v$. Accordingly, a *system state* $X = (X_{1,0}, X_{1,1}, X_{2,0}, X_{2,1}, \cdots, X_{N,0}, X_{N,1})$ is mapped to an *assignment* $x = (x_1, x_2, \cdots, x_N)$ as follows:

$$x_i = \begin{cases} 0 & (\text{if } X_{i,0} > 0 \text{ and } X_{i,1} \leq 0), \\ 1 & (\text{if } X_{i,0} \leq 0 \text{ and } X_{i,1} > 1), \\ \text{undefined} & (\text{otherwise}). \end{cases} \quad (1)$$

Consider a four-variable 3-SAT instance, $(x_1 \vee \neg x_2) \wedge (\neg x_2 \vee x_3 \vee \neg x_4) \wedge (x_1 \vee x_3) \wedge (x_2 \vee \neg x_3) \wedge (x_3 \vee \neg x_4) \vee (\neg x_1 \vee x_4)$ in which a "*solution*" $(x_1, x_2, x_3, x_4) = (1, 1, 1, 1)$ uniquely exists. This formula is represented as a set $F = \{\{1, -2\}, \{-2, 3, -4\}, \{1, 3\}, \{2, -3\}, \{3, -4\}, \{-1, 4\}\}$ by replacing x_i and $\neg x_i$ in the formula with i and $-i$, respectively.

2.1.2. Bounceback control dynamics

To make an entire formula *true*, every *clause* needs to be *true* because all the *clauses* in a CNF are connected with *AND* operators. Now, let us focus on a *clause* $(x_1 \vee \neg x_2)$. To make this *clause* "true", if x_1 is $false$, then x_2 should NOT be *true*. Therefore, we introduce the following operation that we call "bounceback control dynamics": If $X_{1,0}(t) > 0$, resource supply to unit $(2, 1)$ is suppressed by applying inhibitory stimulus at the next step $t+1$ as $S_{2,1}(t+1) = 1$. Likewise, scanning all *clauses*, we determine if the inhibitory stimuli are applied ($S_{i,v} = 1$) or not ($S_{i,v} = 0$). For a set-theoretical form F of the given formula, these bounceback control dynamics are written as follows:

$$S_{i,v}(t+1) = \begin{cases} 1 & (\text{if } (B \ni (P, Q) \text{ such that } Q \ni (i, v)) \\ & \quad \text{and (for all } (j, u) \in P,\ X_{j,u}(t) > 0)), \\ 0 & (\text{otherwise}), \end{cases} \quad (2)$$

where

$$B = Intra \cup Inter \cup Contra \quad (3)$$

is a set of bounceback rules whose element (P, Q) is taken as "if all units in P are resource-abundant at t, then suppress all units in Q at $t + 1$".

Intra prohibits each variable x_i to take two values 0 and 1 at a time, i.e., it maintains intra-variable consistency. For each $i \in I$, we append the following element in *Intra*:

$$Intra \ni (\{(i, v)\}, \{(i, 1 - v)\}). \quad (4)$$

Inter defines inter-variable inhibitory coupling. For each *variable* $i \in I$ in each *clause* $C \in F$, we append the following element in *Inter*:

$$Inter \ni \begin{cases} (P, \{(i, 0)\}) & (\text{if } C \ni i), \\ (P, \{(i, 1)\}) & (\text{if } C \ni -i), \end{cases} \quad (5)$$

where, for each $j \neq i$, P includes the following element:

$$P \ni \begin{cases} (j, 0) & (\text{if } C \ni j), \\ (j, 1) & (\text{if } C \ni -j). \end{cases} \quad (6)$$

Some rules in *Inter* may imply that neither 0 nor 1 can be assigned to a variable. To avoid these contradictions, for each $i \in I$, we build *Contra* by checking *Inter* as follows:

$$\begin{aligned} &\text{If } (P, \{(i, 0)\}) \in Inter \text{ and } (P', \{(i, 1)\}) \in Inter, \\ &\text{then } Contra \ni (P \cup P', P \cup P'). \end{aligned} \quad (7)$$

Intra, *Inter*, and *Contra* of F are shown in Table 1. These rules are determined in a polynomial time $poly(N \cdot M)$, where M is the number of *clauses*.

Table 1: Bounceback rules determined by F.

B	P (if abundant at t)	Q (suppressed at $t + 1$)
Intra	$\{(1, 0)\}$	$\{(1, 1)\}$
	$\{(1, 1)\}$	$\{(1, 0)\}$
	$\{(2, 0)\}$	$\{(2, 1)\}$
	$\{(2, 1)\}$	$\{(2, 0)\}$
	$\{(3, 0)\}$	$\{(3, 1)\}$
	$\{(3, 1)\}$	$\{(3, 0)\}$
	$\{(4, 0)\}$	$\{(4, 1)\}$
	$\{(4, 1)\}$	$\{(4, 0)\}$
Inter	$\{(2, 1)\}$	$\{(1, 0)\}$
	$\{(1, 0)\}$	$\{(2, 1)\}$
	$\{(3, 0), (4, 1)\}$	$\{(2, 1)\}$
	$\{(2, 1), (4, 1)\}$	$\{(3, 0)\}$
	$\{(2, 1), (3, 0)\}$	$\{(4, 1)\}$
	$\{(3, 0)\}$	$\{(1, 0)\}$
	$\{(1, 0)\}$	$\{(3, 0)\}$
	$\{(3, 1)\}$	$\{(2, 0)\}$
	$\{(2, 0)\}$	$\{(3, 1)\}$
	$\{(4, 1)\}$	$\{(3, 0)\}$
	$\{(3, 0)\}$	$\{(4, 1)\}$
	$\{(4, 0)\}$	$\{(1, 1)\}$
	$\{(1, 1)\}$	$\{(4, 0)\}$
Contra	$\{(1, 1), (3, 0)\}$	$\{(1, 1), (3, 0)\}$
	$\{(1, 0), (2, 0)\}$	$\{(1, 0), (2, 0)\}$
	$\{(1, 0), (3, 1)\}$	$\{(1, 0), (3, 1)\}$
	$\{(2, 1), (4, 0)\}$	$\{(2, 1), (4, 0)\}$
	$\{(2, 0), (4, 1)\}$	$\{(2, 0), (4, 1)\}$
	$\{(3, 0), (4, 0)\}$	$\{(3, 0), (4, 0)\}$
	$\{(1, 1), (2, 1), (3, 0)\}$	$\{(1, 1), (2, 1), (3, 0)\}$
	$\{(2, 0), (2, 1), (4, 1)\}$	$\{(2, 0), (2, 1), (4, 1)\}$
	$\{(3, 0), (3, 1), (4, 1)\}$	$\{(3, 0), (3, 1), (4, 1)\}$

2.1.3. Chaotic oscillatory dynamics

The dynamics of the units are given as follows:

$$X_{i,v}(t+1) = \begin{cases} X_{i,v}(t) + 1 & (\text{if } (R_{i,v}(t) = 1 \text{ and } |X_{i,v}(t)| < 2) \\ & \quad \text{or } X_{i,v}(t) \leq -2\ ), \\ X_{i,v}(t) - 1 & (\text{if } (R_{i,v}(t) = 0 \text{ and } |X_{i,v}(t)| < 2) \\ & \quad \text{or } 2 \leq X_{i,v}(t)\ ), \end{cases} \quad (8)$$

where $R_{i,v} \in \{0, 1\}$ represents "resource supply" and $X_{i,v} \in \{-2, -1, 0, 1, 2\}$. The following function of the external

stimulus $S_{i,v}$ and internal fluctuation $f_{i,v}$ determines if the resource is supplied ($R_{i,v} = 1$) or bounced back ($R_{i,v} = 0$) :

$$R_{i,v}(t) = \begin{cases} sgn(f_{i,v}(t) - 1 + \beta_+) & (\text{if } S_{i,v}(t) = 1), \\ sgn(1 - f_{i,v}(t) - \beta_-) & (\text{if } S_{i,v}(t) = 0), \end{cases} \quad (9)$$

where $sgn(r) = 1$ if $r > 0$, otherwise 0, and β_+ and β_- are parameters for adjusting the occurrences of errors in stimulus response. Namely, the larger the β_+, the more the resource is likely to be supplied, even though it should be suppressed when $S_{i,v} = 1$. The larger the β_-, the less the resource is likely to supplied, despite the absence of the inhibitory stimulus ($S_{i,v} = 0$). We fix these parameters at $\beta_+ = 0$ and $\beta_- = 0.25$ in this study, because these values were confirmed to be the optimal. The internal fluctuation $f_{i,v}$ is generated by the following logistic map

$$f_{i,v}(t+1) = 4 \cdot f_{i,v}(t) \cdot (1 - f_{i,v}(t)), \quad (10)$$

which produces chaotic behavior.

2.1.4. Solution search process

The pseudocode for AmoebaSAT is given as follows.

```
INPUT:    A k-SAT formula F.
OUTPUT:   A satisfiable assignment or "not found"
BEGIN:    Determine B (bounceback rules) of F
          according to Eqs. (3), (4), (5), (6) and (7);
          FOR (i, v) = (1, 0) to (N, 1)
          Set X_{i,v} = 0, R_{i,v} = 0, and S_{i,v} = 0;
          Choose f_{i,v} ∈ [0.0, 1.0] randomly; END FOR
          REPEAT:
          Obtain an assignment x from X by Eq. (1);
          IF x satisfies F THEN RETURN x;
          ELSE      FOR (i, v) = (1, 0) to (N, 1)
                    Update X_{i,v}, R_{i,v}, f_{i,v}, and S_{i,v}
                    according to Eqs. (8), (9), (10),
                    and (2), respectively; END FOR
          END IF
          UNTIL:    Run out of time;
          RETURN:   "not found";
END:
```

A *system state* X is "stabilizable" if the following condition holds for all units (i, v): If $X_{i,v}(t) > 0$ then $S_{i,v}(t) = 0$, or if $X_{i,v}(t) \leq 0$ then $S_{i,v}(t) = 1$. This is because, in a unit where the above condition is not met, in response to $S_{i,v}(t)$, $sgn(X_{i,v}(t+1))$ may differ from $sgn(X_{i,v}(t))$, thus X is unstable. We designed the bounceback control dynamics so that only satisfiable *assignments* (*solutions*) can be stabilizable. In fact, among all possible states, we can confirm that only the states mapped to the solution are stabilizable.

In the example of the solution search process shown in Fig.1, we can confirm that the solution was found after 41 iterations and was likely to be stabilized, where the black arrow indicates the time step when first the inverted binary sequences of $S_{i,v}$ matched with the solution.

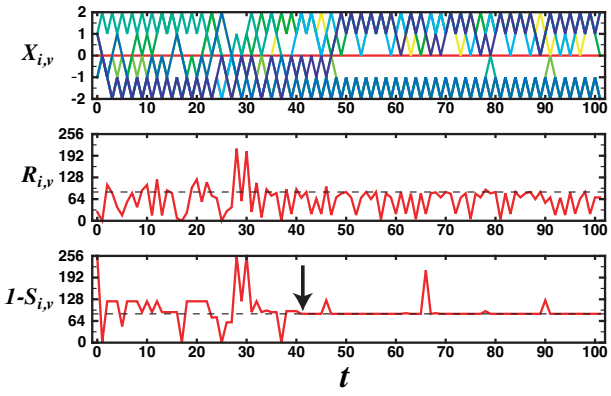

Figure 1: Time evolution of AmoebaSAT solving the four-variable instance given in the text. For $X_{i,v}$, the time series data of 8 units were shown in different colors. For $R_{i,v}$, the binary sequences of 8 units were transformed into a decimal number series, where the solution $(x_1, x_2, x_3, x_4) = (1, 1, 1, 1)$ mapped to 85 was indicated by the black broken line. For $S_{i,v}$, the binary sequences were first inverted (i.e., $S_{i,v} \mapsto 1 - S_{i,v}$), then expressed in a decimal number.

2.2. WalkSAT

WalkSAT is a stochastic local search algorithm which finds a solution with a reasonably large probability after taking a fairly small number of iterations [5].

```
INPUT:    A k-SAT formula F
OUTPUT:   A satisfiable assignment or "not found"
BEGIN:    Choose an assignment x randomly;
          REPEAT:
          IF A satisfies F THEN RETURN x;
          ELSE      Choose a clause C randomly
                    from among unsatisfied clauses;
                    Choose a variable x_i randomly
                    from among C's variables;
                    Update x by flipping x_i;
          END IF
          UNTIL:    Run out of time;
          RETURN:   "not found";
END:
```

In [5], the average number of iterations required for finding a solution was estimated as an exponential function $(2(k-1)/k)^N poly(N)$. Thus, for 3-SAT, WalkSAT requires an average of $(4/3)^N poly(N)$ iterations and is one of the fastest algorithms.

3. Results

The SATLIB website provides benchmark instances [6]. We used a test set of "Uniform Random-3-SAT", which is a family of 3-SAT instance distributions obtained by randomly generating 3-literal CNF formulae. The test set

"uf20-91" contains 1000 instances, each of which is a 20-*variable*-91-*clause* formula. In this study, we focused on 54 instances in the test set, each of which has 8 solutions.

We evaluated the performances of AmoebaSAT and WalkSAT by counting the number of iterations that each algorithm required for finding a solution. For each instance, we performed 500 trials of Monte Carlo simulations.

As shown in Fig. 2, for all instances, AmoebaSAT finds a solution faster than WalkSAT. The average numbers of iterations of the former and latter were approximately 374 and 1173, respectively. The performance of WalkSAT varies wildly depending on instances. Also, it fluctuates greatly depending on trials, as indicated by error bars. In contrast, AmoebaSAT is robust in exhibiting its high performance.

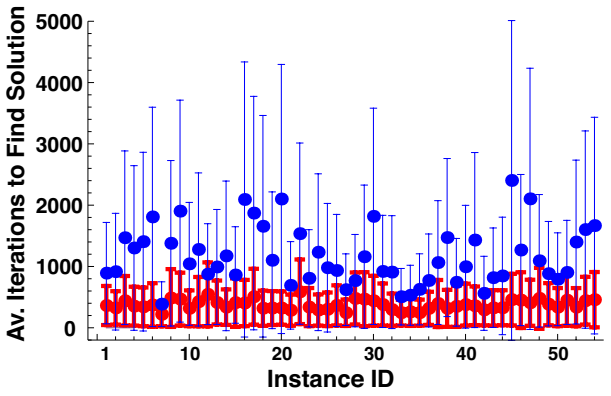

Figure 2: Performance comparison between AmoebaSAT (red) and WalkSAT (blue). For each of 54 benchmark instances, the number of iterations required for finding a solution was averaged over 500 trials, where error bar indicates standard deviation.

4. Discussion and Conclusion

In this study, we demonstrated that AmoebaSAT exhibits its powerful search ability for solving the SAT in a concurrent fashion. AmoebaSAT is a hybrid of chaotic oscillatory dynamics and spatiotemporal control dynamics. We evaluated a modified version of AmoebaSAT in which the chaotic fluctuation Eq. (10) was replaced with random fluctuation (uncorrelated white noise). Compared with the original version, the performance of the modified version degraded significantly, which was even worse than that of WalkSAT. In some previous studies [7, 8], the usefulness of chaotic dynamics for optimization has already been demonstrated with chaotic neural network models and local search algorithms. Why are chaotic fluctuations more powerful than random fluctuations? Some authors reported that negative temporal correlations in chaotic dynamics produce the powerful search abilities [9, 10]. We will examine whether the same applies to AmoebaSAT.

We emphasize that AmoebaSAT is designed to run on some physical substrates that are capable of implementing similar spatiotemporal dynamics, for example, optical energy transfer dynamics between quantum dots mediated by optical near-field interactions [11]. When implemented using these dynamics with spatial and temporal correlations, AmoebaSAT will exhibit its maximum power for larger-sized instances owing to its highly concurrent nature.

References

[1] R. Poli, J. Kennedy, T. Blackwell, "Particle swarm optimization. An overview," *Swarm Intelligence*, vol.1(1), pp.33–57, 2007.

[2] M. Aono, M. Hara, K. Aihara, "Amoeba-based neurocomputing with chaotic dynamics," *Communications of the ACM*, vol.50(9), pp.69–72, 2007.

[3] M. Aono, Y. Hirata, M. Hara, K. Aihara, "Amoeba-based chaotic neurocomputing: Combinatorial optimization by coupled biological oscillators," *New Generation Computing*, vol.27, pp.129–157, 2009.

[4] M. R. Garey, D. S. Johnson, "Computers and Intractability: A Guide to the Theory of NP-Completeness," W. H. Freeman and co., New York, 1979.

[5] U. Schoning, "A probabilistic algorithm for *k*-SAT and constraint satisfaction problems," *Proc. 40th Symposium on Foundations of Computer Science*, pp.410–414, 1999.

[6] H. H. Hoos, T. Stutzle, "SATLIB: An online resource for research on SAT," *Proc. SAT2000*, pp.283-292, IOS Press, 2000. Benchmark instances are available online at http://www.cs.ubc.ca/ hoos/SATLIB/benchm.html

[7] K. Aihara, T. Takabe, M. Toyoda, "Chaotic neural networks," *Phys. Lett. A*, vol.144, pp.333–340, 1990.

[8] M. Hasegawa, T. Ikeguchi, K. Aihara, "Combination of chaotic neurodynamics with the 2-opt algorithm to solve traveling salesman problems," *Phys. Rev. Lett.*, vol.79(12), pp.2344–2347, 1997.

[9] M. Hasegawa, K. Umeno, "Solvable performance of optimization neural networks with chaotic noises and stochastic noise with negative correlation," *Lecture Notes in Computer Science*, vol.4984, pp.693–702, Springer, 2008.

[10] K. Umeno, "Performance of chaotic Monte Carlo computation and chaos codes for communications: Theory and experiments," *AIP Conf. Proc.*, vol.1339, pp.197–209, 2011.

[11] M. Naruse, M. Aono, S. -J. Kim, T. Kawazoe, W. Nomura, H. Hori, M. Hara, M. Ohtsu, "Spatiotemporal dynamics in optical energy transfer on the nanoscale and its application to constraint satisfaction problems," submitted.

INFRARED–VISIBLE LIGHT CONVERSION USING DCM DYE MICROGRAINS EMBEDDED IN A RESIN SHEET AND APPLICATION TO AN IR SENSOR CARD

Paper # M1001

Tadashi Kawazoe[1], Tohru Fujita[2], Hiroyasu Fujiwara[2], Minoru Niigaki[2], and Motoichi Ohtsu[1]

[1] Electrical Engineering and Information Systems, The University of Tokyo, Bunkyo-ku, Tokyo, 113-8656, Japan
[2] Central Research Labs., Hamamatsu Photonics KK, Hamakita, Japan

Abstract

We report high-efficiency visible light emission (λ=600–690 nm) from aggregated 4-dicyanomethylene-2-methyl-6-p-dimethylaminostyryl-4H-pyran (DCM) dye micrograins excited by infrared light (λ_{ex} = 805 nm). The light-emitting regions were localized at the surfaces and edges of the micrograins, where the optical near-field was more intense. This has been theoretically explained by exciton−phonon polaritons, *i.e.*, the dressed photon model, in which an electron is excited due to a multistep transition via an intermediate phonon state coupled with a localized exciton polariton (a dressed photon). The lifetime (about 1 ps) of the intermediate state has been measured by the pump–probe method. We prepared a resin sheet containing the DCM and identified the origin of the intermediate state as an O-H stretching vibration mode, by time-resolved Raman spectroscopy using a 10 fs pulsed laser as an excitation light source. As the molecules aggregated, the emission efficiency with visible light excitation (λ<550 nm) decreased, *i.e.*, concentration quenching, whereas the emission efficiency with infrared excitation increased. This is because a broad O-H phonon band with strong oscillator strength is created by hydrogen bonds among the molecules, acting as an efficient intermediate phonon state for the multistep transition. An IR sensor card was also demonstrated.

Introduction

It has been found that optical near-fields, which are described as quanta of dressed photons, can excite coherent phonons on the surface of a nanometric particle. These excited coherent phonons form a coupled state which is called a virtual exciton-phonon-polariton[1]. This coupled state is used in the nonadiabatic excitation process, by which electron-hole pairs can be created in the semiconductor or the molecule even though the incident photon energy is lower than the band-gap energy E_g. This is because the energies of both the dressed photon E_{dp} and the induced phonon E_{phon} contribute to this electron-hole pair generation, *i.e.*, $E_{dp}+E_{phon}>E_g$. Previous theoretical studies support the possibility of exciting electrons by a two-step transition process for creating electron-hole pairs.

So far, we demonstrate unique phenomena and novel devices using the nonadiabatic excitation process [2-7]. Here, the visible light emission (λ=600–690 nm) from aggregated 4-dicyanomethylene-2-methyl-6-p-dimethylaminostyryl-4H-pyran (DCM) dye micrograins excited by infrared light (λ_{ex} = 805 nm) is reviewed. And we discuss the This phenomenon is applicable to the efficient frequency up-conversion device.

Experimental Results

So far the lifetime (about 1 ps) of the intermediate state has been measured by the pump–probe method [4] with the time resolution of 100 fs. In this paper, we prepared a resin sheet containing the DCM and identified the origin of the intermediate state as an O-H stretching vibration mode, by time-resolved Raman spectroscopy using a 10 fs pulsed laser with 800-nm wavelength as an excitation light source.

Figure 1 shows a experimental result of the pump–probe method with the time resolution of 10fs. The pump-probe signal intensity is proportional to the density of occupied intermediate states. Clear oscillatory structures appeared in the signal. We identified these origins as coherent phonons of an O-H stretching and a hydrogen-bonded O-H stretching vibration modes through their frequency and band width. These phonon modes were considered essential to the intermediate states in the frequency up-conversion process, because amplitudes of these phonon mode were proportional to the frequency up-conversion efficiency. As the molecules aggregated, the emission efficiency with visible light excitation (λ<550 nm) decreased, *i.e.*, concentration quenching, whereas the emission efficiency with infrared

excitation increased. This is because a broad O-H phonon band with strong oscillator strength is created by hydrogen bonds among the molecules, acting as an efficient intermediate phonon state for the multistep

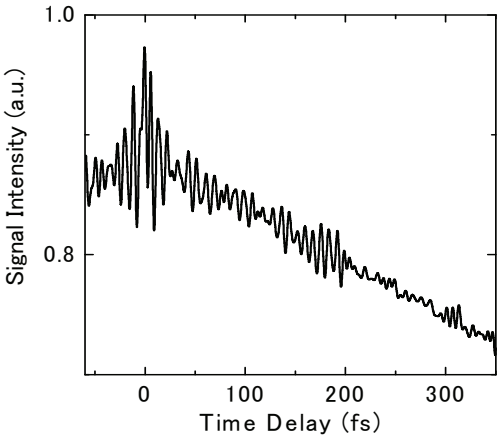

transition.

Fig.1. The experimental result of pump-probe method using a 10 fs pulsed laser as an excitation light source.

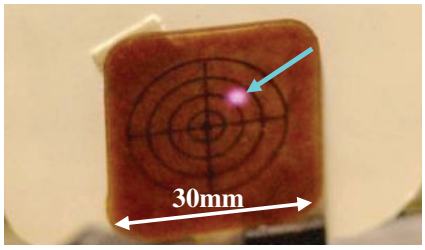

Fig.2. The demonstration as an IR sensor card using the resin sheet containing the aggregated DCM dye micrograins.

Figure 2 shows a photograph of the resin sheet containing the aggregated DCM dye micrograins demonstrated as an IR sensor card. The red bright spot (shown by an arrow) appears emitting visible red light at position illuminated by the infrared light (λ=900 nm).

Acknowledgement

This work was supported by a New Energy and Industrial Technology Development Organization (NEDO) project.

References

[1] Kawazoe T., Kobayashi K., Takubo S. & Ohtsu M., Nonadiabatic photodissociation process using an optical near field (2005) J. Chem. Phys. **122**, 024715.

[2] Kawazoe T., Fujiwara H., Kobayashi K., & Ohtsu M., Visible Light Emission From Dye Molecular Grains via Infrared Excitation Based on the Nonadiabatic Transition Induced by the Optical Near Field (2009) IEEE, J. Sel. Top. Quant. Electron., 15, 1380.

[3] Fujiwara H., Kawazoe T., & Ohtsu M., Nonadiabatic multi-step excitation for the blue-green light emission from dye grains induced by the near-infrared optical near-field (2010) Applied Physics B-Lasers and Optics 98 pp.283.

[4] Fujiwara H., Kawazoe T., & Ohtsu M., Nonadiabatic nondegenerate excitation by optical near-field and its application to optical pulse-shape measurement (2010) Appl. Phys. B- Lasers and Optics, 100, pp. 85

[5] Kawazoe T., Mueed M.A., & Ohtsu M., Si homojunction structured near-infrared laser based on a phonon-assisted process (2011) Appl. Phys. B 104, pp747.

[6] Kitamura K., Kawazoe T., & Ohtsu M., Homojunction-structured ZnO light-emitting diodes fabricated by dressed-photon assisted annealing (2012) Appl. Phys. B 107, pp293.

[7] Kawazoe T., Ohtsu M., Akahane K. & Yamamoto N., Si homojunction structured near-infrared laser based on a phonon-assisted process (2012). Appl. Phys. B 107, pp659.

Tadashi Kawazoe. He received the Ph.D. degree in physics from University of Tsukuba, Tsukuba, Japan, in 1996. He has studied optical nonlinearities in quantum dots at University of Tsukuba. In 2000, he has been with Japan Science and Technology Corporation, Japan. In 2007, he joined the University of Tokyo as a projected associated professor. His current research interests are in the nanophotonic device.

1.3μM-BAND SI PHOTODETECTORS WITH OPTICAL GAINS FABRICATED BY DRESSED PHOTON ASSISTED ANNEALING

Paper #M1105

Hajime Tanaka[1], Tadashi Kawazoe[1,2] , and Motoichi Ohtsu[1,2]

[1]Department of Electrical Engineering and Information Systems, Graduate School of Engineering,The University of Tokyo, 2-11-16 Yayoi, Bunkyo-ku, Tokyo 113-8656, Japan
[2]Nanophotonics Research Center, Graduate School of Engineering, The University of Tokyo,2-11-16 Yayoi, Bunkyo-ku, Tokyo 113-8656, Japan

Abstract

We fabricated a novel photodetector by subjecting a Si crystal having a p–n homojunction to phonon-assisted annealing. The photosensitivity of this device for incident light having a wavelength of 1.16 μm or greater was about three-times higher than that of a reference Si-PIN photodiode. The photosensitivity for incident light with a wavelength of around 1.32 μm was increased by applying a forward current. When the forward current density was 10 A/cm^2, the device showed photosensitivities of 3.1 A/W at a wavelength of 1.14 μm and 0.10 A/W at 1.32 μm. The photosensitivity at 1.32 μm is at least 4000-times higher than the zero-bias photosensitivity. This remarkable increase was due to the manifestation of optical amplification cause by the forward current injection. For a forward current density of 9 A/cm^2, the small-signal gain coefficient of the optical amplification was 2.2×10^{-2}, and the saturation power was 7.1×10^2 mW.

Introduction

Silicon (Si) is an abundant material in the Earth's crust and has low toxicity, and is thus widely used as a material for electronic and optical devices. For example, Si photodetectors (Si-PDs) are widely used photoelectric conversion devices; however, their photosensitivity limit at the long-wavelength side is limited by the bandgap energy, E_g, of Si (1.12 eV) [1], and the photosensitivity drops rapidly at wavelengths above 1.11 μm. Because of this, materials such as Ge [2], InGaAsP [3], and InGaAs [4] that have a smaller E_g than Si have been used in optical fiber communications. However, there are some drawbacks with these materials. For example, Ge photodetectors have a large dark current, and cooling is required in many cases. InGaAs photodetectors suffer from problems such as the use of highly toxic metal-organic materials in their fabrication, high cost, and so forth. Recently, depletion of resources, such as In, has also been a problem. If the photosensitivity limit of Si-PDs could be extended past the 1.11 μm wavelength into the near-infrared region at 1.3 μm and above, these problems could be overcome. An additional benefit of Si-PDs is their high compatibility with electronic devices. For this reason, photoelectric conversion devices exploiting effects observed in Si, such as mid-bandgap absorption [5–7], surface-state absorption [8, 9], internal photoemission absorption [10, 11], and two-photon absorption [12, 13], have been reported in the literature. However, in the case of mid-bandgap absorption, for example, the photosensitivity at a wavelength of 1.3 μm is limited to only 50 mA/W [5].

In this research, we realized a novel Si-PD with increased photosensitivity. We applied the same fabrication method and light emission principle of a silicon light emitting diode (Si-LED) based on a phonon-assisted process that we previously proposed [14, 15]. Specifically, while radiating light, Joule-heat annealing was performed to control the spatial distribution of the impurity (boron) concentration in a Si crystal in a self-organized manner, to efficiently generate dressed photons. The photocurrent of the novel Si-PD fabricated by this method was varied by a stimulated emission process driven by the incident light. Because this stimulated emission process caused optical amplification, the photosensitivity of this Si-PD was remarkably increased. The operating principle of the Si-PD is described in Section 2, the fabrication method is described in Section 3, device characterization and evaluation results are presented in Section 4, and the paper concludes with Section 5.

2. Operating Principle

The operating principle of the Si-PD fabricated in this research is based on a phonon-assisted process caused by dressed photons [16–20]. A dressed photon is a quasi-particle representing a coupled state between a photon and an electron at the nanoscale. The phonon-assisted process originates in the property of a dressed photon to couple with a phonon. By using this property, it is possible to create an electron–hole pair via a two-

step excitation even with photons having an energy smaller than the bandgap energy, E_g, of the semiconductor. Therefore, the Si-PD can exhibit photosensitivity even for infrared light with a photon energy smaller than E_g. This principle has already been applied to photochemical vapor deposition [16], photovoltaic devices [17], photolithography [18], subnanometer polishing of a glass surface [19], optical frequency up-conversion [20], and other applications.

Electrons in the Si-PD experience a two-step excitation via processes (1) and (2) described below. (These processes (1) and (2), as well as processes (1') and (2') described later, are the same as those in the Si-LED previously proposed by the authors; for details, refer to Ref. [14] and Fig. 1 therein.)

(1) First step: The electron is excited from the initial ground state $\left|E_g;el\right\rangle\otimes\left|E_{ex_{thermal}};phonon\right\rangle$ to intermediate state $\left|E_g;el\right\rangle\otimes\left|E_{ex};phonon\right\rangle$. Here, $\left|E_g;el\right\rangle$ represents the ground state (valence band) of the electron, and $\left|E_{ex_{thermal}};phonon\right\rangle$ and $\left|E_{ex};phonon\right\rangle$ respectively represent the excited state of the phonon determined by the crystal lattice temperature and the excited state of the phonon determined by the dressed photon energy. The symbol $\otimes$ represents the direct product of the ket vectors. Because this is an electric-dipole–forbidden transition, a dressed photon is essential for the excitation.

(2) Second step: The electron is excited from the intermediate state $\left|E_g;el\right\rangle\otimes\left|E_{ex};phonon\right\rangle$ to the final state $\left|E_{ex};el\right\rangle\otimes\left|E_{ex'};phonon\right\rangle$. Here, $\left|E_{ex};el\right\rangle$ represents the excited state (conduction band) of the electron, and $\left|E_{ex'};phonon\right\rangle$ represents the excited state of the phonon. Because this is an electric-dipole–allowed transition, the electron is excited not only by the dressed photon but also by propagating light. After this excitation, the phonon in the excited state relaxes to a thermal equilibrium state having an occupation probability determined by the crystal lattice temperature, which completes excitation to the electron excited state $\left|E_{ex};el\right\rangle\otimes\left|E_{ex_{thermal}};phonon\right\rangle$.

Because a phonon is involved in the above excitation of the electron, this excitation process is known as a phonon-assisted process [16–20]. When light having a photon energy smaller than E_g is incident on the Si-PD, electrons are excited by the two-step excitation described above, generating a photocurrent. Photosensitivity to this incident light is manifested by means of the above process.

Note that applying a forward current to the Si-PD causes the two-step stimulated emission described by processes (1') and (2') below [17].

(1') First step: When a forward current is applied, an electron is injected from the external circuit to the conduction band, and therefore, the state $\left|E_{ex};el\right\rangle\otimes\left|E_{ex_{thermal}};phonon\right\rangle$ is the initial state. During this time, driven by a dressed photon generated in the p–n junction of the Si-PD by the incident light, the electron transitions from the initial state $\left|E_{ex};el\right\rangle\otimes\left|E_{ex_{thermal}};phonon\right\rangle$ to an intermediate state $\left|E_g;el\right\rangle\otimes\left|E_{ex};phonon\right\rangle$, creating a dressed photon and propagating light via stimulated emission. Because Si is an indirect-transition–type semiconductor, there are almost no transitions caused by spontaneous emission.

(2') Second step: The electron transitions from the intermediate state $\left|E_g;el\right\rangle\otimes\left|E_{ex};phonon\right\rangle$ to a final state $\left|E_g;el\right\rangle\otimes\left|E_{ex'};phonon\right\rangle$, causing stimulated emission. Because this is an electric-dipole–forbidden transition, only a dressed photon is generated. After this transition, the phonon in the excited state relaxes to a thermal equilibrium state determined by the crystal lattice temperature, which completes the transition to the electron ground state $\left|E_g;el\right\rangle\otimes\left|E_{ex_{thermal}};phonon\right\rangle$.

Here, if the electron number densities occupying the initial state $\left|E_{ex};el\right\rangle\otimes\left|E_{ex_{thermal}};phonon\right\rangle$ and the intermediate state $\left|E_g;el\right\rangle\otimes\left|E_{ex};phonon\right\rangle$, n_{ex} and n_{inter}, satisfy the Bernard–Duraffourg inversion condition ($n_{ex} > n_{inter}$) [21], the number of photons created by stimulated emission exceeds the number of photons annihilated by absorption. In other words, optical amplification occurs. Because the amplified light brings about processes (1') and (2') again via dressed photons, the photosensitivity of the Si-PD in the case where a forward current is applied far exceeds

the photosensitivity based on only processes (1) and (2).

3. Fabrication method

To realize the optical amplification described in Section 2, it is essential to efficiently generate dressed photons in the p–n junction of the Si-PD. To do so, we adopted a Si-LED fabrication method that we previously proposed [14]. In this method, Joule-heat annealing was performed while radiating 1.32 μm-wavelength light.

First, an n-type silicon substrate with an electrical resistivity of 10 Ω·cm and a thickness of 625 μm, doped with arsenic (As), was used as the Si-PD material. This substrate was doped with boron (B) via ion implantation to form a p layer. For the B doping, the implantation energy was 700 keV , and the ion dose density was 5×10^{13} cm^{-2}. After forming a p–n homojunction in this way, an indium tin oxide (ITO) film with a thickness of 150 nm was deposited at the p-layer side, a chromium film and an aluminum film with thicknesses of 5 nm and 80 nm were deposited at the n-substrate side, all by RF sputtering, and these were used as positive and negative electrodes. Then, the silicon substrate with these electrodes attached was diced with a dicer to form a single Si-PD. The area was about 2 mm^2.

Next, annealing was performed by applying a forward current to the Si-PD to generate Joule heating, causing the B to diffuse and changing the spatial distribution of the B concentration. During this time, the device was irradiated, from the ITO electrode side, with laser light having a photon energy smaller than E_g of Si (E_g of 0.9 eV, corresponding to a wavelength of 1.32 μm, and optical power of 120 mW). This induced the phonon-assisted process, which controlled the B diffusion due to the annealing. As a result, a B concentration with a spatial distribution suitable for efficiently generating dressed photons was formed in a self-organized manner.

The above method is the same as the method of fabricating Si-LEDs previously reported by the authors [14, 15]. Here, however, in order to make use of the stimulated emission process described in Section 2 for the Si-PD to be fabricated, it is necessary to make the probability of generating stimulated emission larger than the probability of generating spontaneous emission. To do so, the forward current density for annealing was kept smaller than that in Ref. [14], namely, 1.3 A/cm^2. Determining the number of injected electrons per unit time and per unit area on this basis gives a value of 8.1×10^{18} $s^{-1}\cdot cm^{-2}$, which corresponds to the probability of generating spontaneous emission. On the other hand, the probability of generating stimulated emission corresponds to the number of photons per unit time and per unit area, which is 3.9×10^{19} $s^{-1}\cdot cm^{-2}$ in the case of the laser power mentioned above (120 mW). Comparing this with the number of injected electrons confirms that the probability of generating stimulated emission is sufficiently large.

When performing Joule-heat annealing under laser irradiation in practice, the surface temperature of the Si-PD, measured by thermography, showed a temporal variation similar to Fig. 2(c) in Ref. [14]. Specifically, immediately after applying the forward current, the surface temperature rose to 40.7 °C, then dropped due to the generation of stimulated emission and dissipation of its associated Joule energy, and reached an almost stable temperature (38.6 °C) after about 10 minutes, at which point the annealing was completed.

4. Device characterization

In this section we present the results of evaluating the spectral sensitivity characteristics, the current–voltage characteristics, the current dependency of the photosensitivity, and the optical amplification characteristics of the fabricated device.

4.1 Spectral sensitivity characteristics

First, we measured the spectral sensitivity characteristics when a forward current was not applied to the device. Photoelectric conversion in this case is based on the two-step excitation described by processes (1) and (2) in Section 2. As the light source, we used a xenon lamp, for wavelength selection we used a monochromator, and for photocurrent detection we used a lock-in amplifier. The optical power at each wavelength was measured with an InGaAs photodiode (Hamamatsu Photonics, G8370). The measurement wavelength range was 1.00–1.20 μm. The spectral sensitivity characteristics measured in the infrared region are shown by curves A to C in Fig. 1. Curve A shows the values obtained with a Si-PD fabricated by annealing using the phonon-assisted process described in Section 3. For comparison, curve B shows values obtained with a Si-PD fabricated without annealing. Curve C shows the values obtained with a Si-PIN photodiode (Hamamatsu Photonics, S3590) used as a

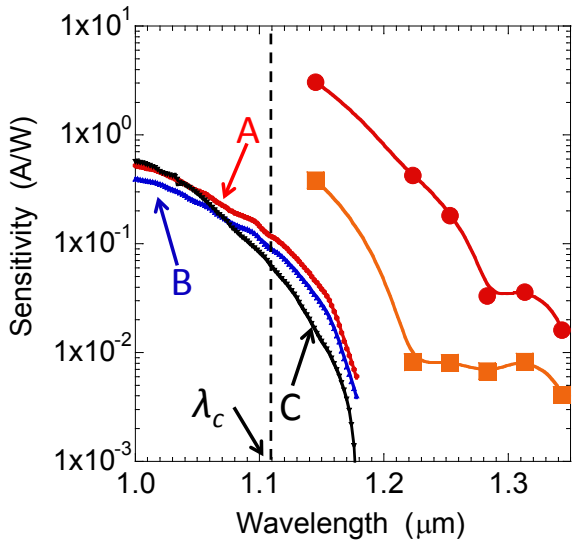

Fig. 1

Wavelength dependency of photosensitivity. Curve A: device fabricated by phonon-assisted annealing. Curve B: device fabricated without annealing. Curve C: commercially available photodiode (S3590, Hamamatsu Photonics). The red circles and orange squares show the photosensitivity to incident light (wavelength 1.14–1.34 μm) for forward current densities of 10 A/cm^2 and 3.5 A/cm^2, respectively.

reference. Comparing curves A and C, the photosensitivities of both of them were reduced in the wavelength region longer than a cutoff wavelength λ_c = 1.11 μm determined by E_g of Si, although in curve A the reduction was more gentle, and at wavelengths above 1.16 μm, the photosensitivity was about three-times higher than that of curve C. In addition, the photosensitivity values for curve A were larger than the values for curve B. This was due to the spatial distribution of the B concentration being controlled in a self-organized manner so that dressed photons are efficiently generated by annealing using the phonon-assisted process. Also, the higher photosensitivity values for curve B compared with the values for curve C indicates that dressed photons are readily generated inside the Si-PD compared with the case of curve C, as a result of implantation of a high concentration of B.

Because Joule-heat annealing was performed while radiating 1.32 μm-wavelength light for fabricating the Si-PD (see Section 3), when light having the same wavelength (1.32 μm) is incident on the device, it is expected that the photosensitivity will be selectively increased. This wavelength-selective photosensitivity increase and, in addition, a photosensitivity increase around this wavelength have already been observed in the case of photovoltaic devices that we developed using the phonon-assisted process [17]. Therefore, the photosensitivity for incident light with a wavelength of around 1.32 μm (1.14–1.34 μm) in particular is discussed in the following. We made a constant forward current flow in the device and evaluated the photosensitivity for incident light with a wavelength of 1.14–1.34 μm. Photoelectric conversion in this case involved not only the two-step excitation described by processes (1) and (2) in Section 2, but also processes (1') and (2'); however, the contribution of the latter was sufficiently large. A Ti-sapphire laser was used as the light source, an optical parametric oscillator was used for wavelength modulation, and the output beam was made incident on the Si-PD after being intensity-modulated with a chopper. We obtained the current variation $\Delta I = V / R$ from the ratio of the voltage variation V produced at that time and the resistance R of the Si-PD, and we divided this by the incident light power P to obtain the photosensitivity $\Delta I / P$. The results are indicated by the red circles and the orange squares in Fig. 1. These are the measured values for cases where the forward current densities of the fabricated Si-PD were 10 A/cm^2 and 3.5 A/cm^2, respectively. The higher photosensitivity at higher forward current was due to the higher stimulated emission gain, as well as the higher number of recombining electrons. The photosensitivity for the current density of 10 A/cm^2 was 3.1 A/W at a wavelength of 1.14 μm, and the quantum efficiency was 330%. This photosensitivity was 66-times higher than that of curve A, showing the zero-bias photosensitivity. It was confirmed that the operating principle of the Si-PD was not light absorption but stimulated emission, from the fact that the quantum efficiency was over 100%. The photosensitivity for the current density of 10 A/cm^2 was 0.036 A/W at a wavelength of 1.32 μm, which was 4.4-times higher than that for the current density of 3.5 A/cm^2. The photosensitivity of one of the devices fabricated by the same process described in Section 3 was 0.10 A/W at a wavelength of 1.32 μm, which was at least 4000-times higher than the zero-bias photosensitivity. This photosensitivity (0.10 A/W) is as much as two-times higher than the case using mid-bandgap absorption [5–7] described in Section 1, demonstrating that we achieved our objective of increasing the photosensitivity. This value shows the same large values as curve C at a wavelength of 1.09 μm. This photosensitivity is sufficiently high for use in long-distance optical fiber communication systems [22].

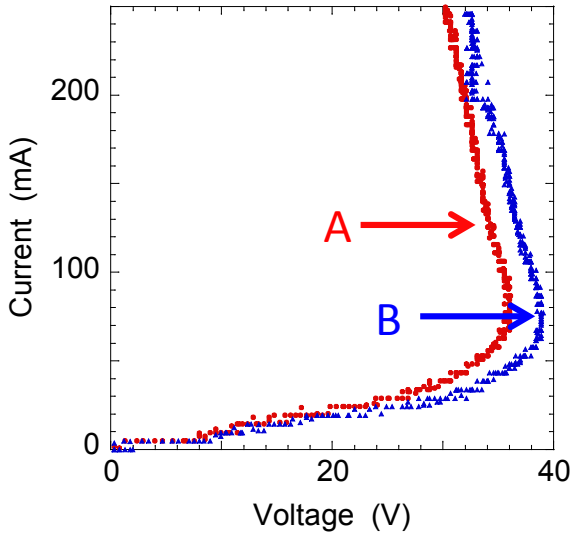

Fig. 2

Current–voltage characteristics. Curves A and B are measurement results obtained with and without light irradiation.

4.2 Current–voltage characteristics

First, we measured the current–voltage characteristics for cases where the Si-PD was irradiated and not irradiated with 1.32 μm-wavelength, 120 mW-power laser light. The measurement results are shown by curves A and B in Fig. 2. Both curves show negative-resistance characteristics at forward currents of 80 mA and higher, similarly to the case of a Si-LED (see Fig. 4 in Ref. [14]). Also, curve A is shifted toward lower voltages compared with curve B. This shift was particularly remarkable when the forward current was 30 mA and higher. The reason for this is that the electron number density in the conduction band is reduced because a population inversion occurs around a forward current of 30 mA, consuming electrons for stimulated emission, and as a result, the voltage required for injecting the same number of electrons is decreased. On the other hand, when the forward current is increased further, the amount of shift is reduced. This is because the probability of stimulated emission recombination driven by spontaneous emission is increased as the forward current increases, and as a result, the voltage drop due to stimulated emission recombination caused by incident light becomes relatively small.

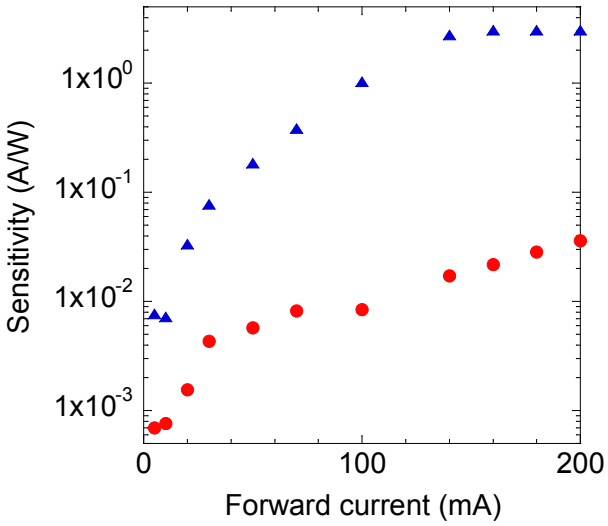

Fig. 3

Current dependency of photosensitivity. The blue triangles and red circles are for wavelengths of 1.14 μm and 1.32 μm, respectively.

4.3 Current dependency of photosensitivity and optical amplification characteristics

First, we measured the current dependency of the photosensitivity of the Si-PD. The measurement results are shown by the blue triangles and the red circles in Fig. 3. These are measured values for incident light with wavelengths of 1.14 μm and 1.32 μm, respectively. The increase in photosensitivity with increasing forward current is due to the higher number of recombining electrons. At 5–20 mA, the photosensitivity increased rapidly with increasing forward current, because the number of electrons for stimulated emission recombination was smaller. The increase in photosensitivity became more moderate, and the photosensitivity at a wavelength of 1.14 μm was saturated at a forward current higher than 140 mA. This is because the number of electrons for stimulated emission recombination did not increase very much as the spontaneous emission increased with increasing forward current, as referred to above in the current–voltage characteristics. The photosensitivity at a wavelength of 1.32 μm may be also saturated if the forward current increases further.

Next, we measured the relationship between the incident light power P and the current variation ΔI. For this measurement, we used forward current densities of 60 mA/cm^2 and 9 A/cm^2, and we varied the incident light power by using neutral density filters. In a

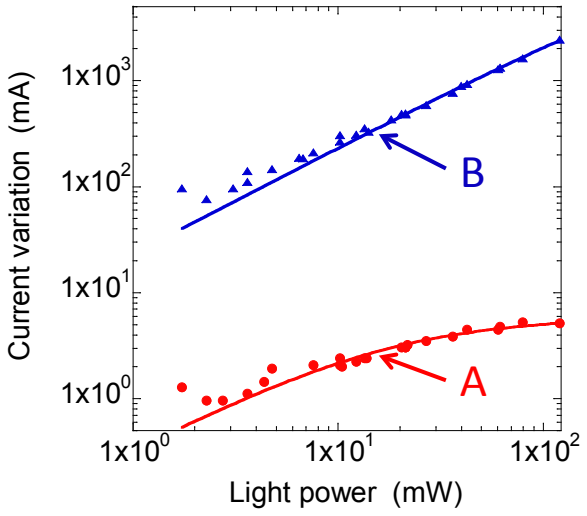

Figure 4

Relationship between incident light power (wavelength 1.32 μm) and current variation. Curves A and B are for forward current densities of 60 mA/cm^2 and 9 A/cm^2, respectively.

conventional Si-PD, only absorption of light is used for photoelectric conversion. In our Si-PD, however, because stimulated emission is also used, the current variation ΔI depends on the number of electron–hole pairs that recombine due to stimulated emission and is given by $\Delta I = (eP/h\nu)(G-1)$. Here, e is the electron charge, $h\nu$ is the photon energy, and G is the stimulated emission gain.

The relationship between the incident light power at a wavelength of 1.32 μm and the current variation ΔI is shown in Fig. 3. Similarly to Fig. 1, the red circles and blue triangles show the measurement results for forward current densities of 60 mA/cm^2 and 9 A/cm^2, respectively. For the forward current density of 60 mA/cm^2, ΔI saturated as the incident light power increased, whereas for the forward current density of 9 A/cm^2, ΔI did not saturate but continued to increase linearly. The curves A and B show calculation results fitted to the experimental results using the above relationship $\Delta I = (eP/h\nu)(G-1)$. The stimulated emission gain G depends on the incident light power as $\exp\left[g/(1+P/P_s)\right]$ [23], where g is the small-signal gain coefficient, and P_s is the saturation power. For the fitted results, these values were $g = 3.2 \times 10^{-4}$ and $P_s = 17$ mW in the case of curve A, and $g = 2.2 \times 10^{-2}$ and $P_s = 7.1 \times 10^2$ mW in the case of curve B. The increases in g and P_s as the forward current increased were due to the increasing number of electrons recombining. The experimental values and calculated values showed good agreement in Fig. 3, confirming that the remarkable increase in photosensitivity shown by the red circles and blue triangles in Fig. 1 was due to optical amplification as a result of stimulated emission.

5. Conclusion

We fabricated a new photodetector by subjecting a Si crystal having p–n homojunction to a phonon-assisted annealing process. For incident light with a wavelength of 1.16 μm and higher, this device showed a photosensitivity about three-times higher than a commercial Si-PIN photodiode used as a reference. The photosensitivity for incident light with a wavelength around 1.32 μm was increased by applying a forward current, and we obtained a photosensitivity of 0.10 A/W at a wavelength of 1.32 μm for a forward current density of 10 A/cm^2. This value is at least 4000-times greater than the zero-bias photosensitivity. We obtained a photosensitivity of 3.1 A/W at a wavelength of 1.14 μm, and the remarkable increase was due to the manifestation of optical amplification caused by the forward current injection. For a forward current density of 9 A/cm^2, the small-signal gain coefficient for optical amplification was 2.2×10^{-2}, and the saturation power was 7.1×10^2 mW.

Reference

[1] Levinshtein, M., Rumyantsev, S. & Shur, M. (1966) Handbook Series on Semiconductor Parameters, vol. 1 World Scientific

[2] Loudon, A., Hiskett, P.A. & Buller, G.S. (2002) Enhancement of the infrared detection efficiency of silicon photon-counting avalanche photodiodes by use of silicon germanium absorbing layers, Opt. Lett. 27, 219 -221

[3] Cremer, C., Emeis, N., Schier, M., Heise, G., Ebbinghaus, G. & Stoll L. (1992) Grating Spectrograph Integrated with Photodiode Array in InGaAsP/InGaAs/InP, IEEE Photonics Technol. Lett. 4, 108-110

[4] Phillips, A.F., Sweeney, S.J., Adams, A.R. & Thijs P.J.A. (1999) The Temperature Dependence of 1.3- and 1.5- μm Compressively Strained InGaAs(P)MQW Semiconductor Lasers, IEEE J. Sel.Top. Quantum Electron. 5, 401-412

[5] Carey, J.E., Crouch, C.H., Shen, M. & Mazur, E., (2005) Visible and near-infrared responsivity of femtosecond-laser microstructured silicon photodiodes, Opt. Lett. 30, 1773-1775

[6] Geis, M.W., Spector, S.J., Grein, M.E., Schulein, R.T., Yoon, J.U., Lennon, D.M., Wynn, C.M., Palmacci, S.T., Gan, F., Kärtner, F.X. & Lyszczarz, T.M., (2007) All silicon infrared photodiodes: photo response and effects of processing temperature, Opt. Express 15, 16886-16895

[7] Geis, M.W., Spector, S.J., Grein, M.E., Schulein, R.T., Yoon, J.U., Lennon, D.M., Gan, F., Kärtner, F.X. & LyszczarzI, T.M. (2007) CMOS-Compatible All-Si High-Speed Waveguide Photodiodes With High Responsivity in Near-Infrared Communication Band, IEEE Photonics Technol. Lett. 19, 152-154

[8] Baehr-Jones, T., Hochberg, M. & Scherer, A. (2008) Photodetection in silicon beyond the band edge with surface states, Opt. Express 16, 1659-1668

[9] Chen, H., Luo, X., Poon, A.W. (2009) Cavity-enhanced photocurrent generation by 1.55μm wavelengths linear absorption in a p-i-n diode embedded silicon microring resonator, Appl. Phys. Lett. 95, 171111 1-3

[10] Lee, M., Chu, C. & Wang, Y. (2001) 1.55-μm and infrared-band photoresponsivity of a Schottky barrier porous silicon photodetector, Opt. Lett. 26, 160-162

[11] Cassalino, M., Sirleto, L., Moretti, L., Gioffrè, M. & Coppola, G. (2008) Silicon resonant cavity enhanced photodetector based on the internal photoemission effect at 1.55μm: Fabrication and characterization, Appl. Phys. Lett. 92, 251104 1-3

[12] Tanabe, T., Nishiguchi, K., Kuramochi, E. & Notomi, M. (2010) All-silicon sub-Gb/s telecom detector with low dark current and high quantum efficiency on chip, Appl. Phys. Lett. 96, 101103 1-3

[13] Shi, B., Liu, X., Chen, Z., Jia, G., Cao, K., Zhang, Y., Wang, S., Ren, C. & Zhao, J. (2008) Anisotropy of photocurrent for two-photon absorption photodetector made of hemispherical silicon with (-110) plane, Appl. Phys. B 93, 873-877

[14] Kawazoe, T., Mueed, M.A., Ohtsu, M. (2011) Highly efficient and broadband Si homojunction structured near-infrared light emitting diodes based on the phonon-assisted optical near-field process, Appl. Phys. B 104, 747 -754

[15] Kawazoe, T., Ohtsu, M., Akahane, K., Yamamoto, N. (2012) Si homojunction structured near-infrared laser based on a phonon-assisted process, Appl. Phys. B 107 659-663

[16] Kawazoe T., Kobayashi K., Takubo S. & Ohtsu M. (2005) Nonadiabatic photodissociation process using an optical near field, J. Chem. Phys. 122, 024715-1-4

[17] Yukutake S., Kawazoe T., Yatsui T., Nomura W., Kitamura K. & Ohtsu, M. (2010) Selective photocurrent generation in the transparent wavelength range of a semiconductor photovoltaic device using a phonon-assisted optical near-field process, Appl. Phys. B, Lasers Opt. 99, 415-422

[18] Kawazoe, T., Ohtsu, M., Inao, Y. & Kuroda, R. (2007) Exposure dependence of the developed depth in nonadiabatic photolithography using visible optical near fields, J. Nanophotonics 1, 011595 1-9

[19] Yatsui, T., Hirata, K., Nomura, W., Tabata, Y. & Ohtsu, M. (2008) Realization of an ultra-flat silica surface with angstrom-scale average roughness using nonadiabatic optical near-field etching Appl. Phys. B 93, 55-57

[20] Kawazoe, T., Fujiwara, H., Kobayashi, K. & Ohtsu, M. (2009) Visible Light Emission From Dye Molecular Grains via Infrared Excitation Based on the Nonadiabatic Transition Induced by the Optical Near Field, IEEE J. Sel. Top. Quantum Electron. 15, 1380-1386

[21] Bernard, M.G.A. & Duraffourg, G. (1961) Laser Conditions in Semiconductors, Phys. Status Solidi 1, 699-703

[22] Schaub, J.D., Li, R., Csutak, S.M. & Campbell, J.C. (2001) High-Speed Monolithic Silicon Photoreceivers on High Resistivity and SOI Substrates, J. Lightwave Technol. 19, 272-278

[23] Saitoh T. & Mukai T. (1987) 1.5 μm GaInAsP traveling-Wave Semiconductor Laser Amplifier IEEE J. Quantum Electron. 23, 1010-1020

[24] Ashcroft N.W. & Mermin N.D. (1976) Solid State Physics, Brooks Cole, Singapore 598pp

[25] McIntyre, R.J. (1966) Multiplication Noise in Uniform Avalanche Diodes, IEEE Trans. Electron Devices 13, 164-168

Hajime Tanaka He received the B.E. in electrical engineering from the University of Tokyo in 2011

He has joined in Ohstu laboratory in 2011.

His current research field is nanophotonics.

A dressed-photon phonon etching of substrate

T. Yatsui*[1),2)] and M. Ohtsu[1)]
[1)] School of Engineering, University of Tokyo, Bunkyo-ku, Tokyo, 113-8656 Japan, [2)] Advanced Low Carbon Technology Research and Development Program (ALCA), Japan Science and Technology Agency, Kawaguchi-shi, Saitama 332-0012 Japan.

A reduction of the surface roughness (R_a) is required in various applications. R_a is formally defined as the arithmetic average of the absolute values of the surface height deviations from the best-fitting plane. Although chemical-mechanical polishing (CMP) has been used to flatten the surfaces [1], it is generally limited to reducing R_a because the polishing pad roughness is as large as 10 μm, and the polishing-particle diameters in the slurry are as large as 100 nm. We therefore developed a new polishing method that uses a dressed-photon phonon based on an autonomous phonon-assisted process, which does not use any polishing pad, with which we obtained ultra-flat silica surface with angstrom-scale average roughness (see Fig. 1) [2,3]. Since this technic uses photo-chemical reaction, it can be applicable various materials, including glass, GaN, PMMa, and diamond, and so on. In addition, this technique is a non-contact method without a polishing pad, it can be applied not only to flat substrates but also to three-dimensional substrates [4] that have convex or concave surfaces, such as micro-lenses, optical-disk, and the inner wall surface of cylinders. Furthermore, this method is also compatible with mass-production.

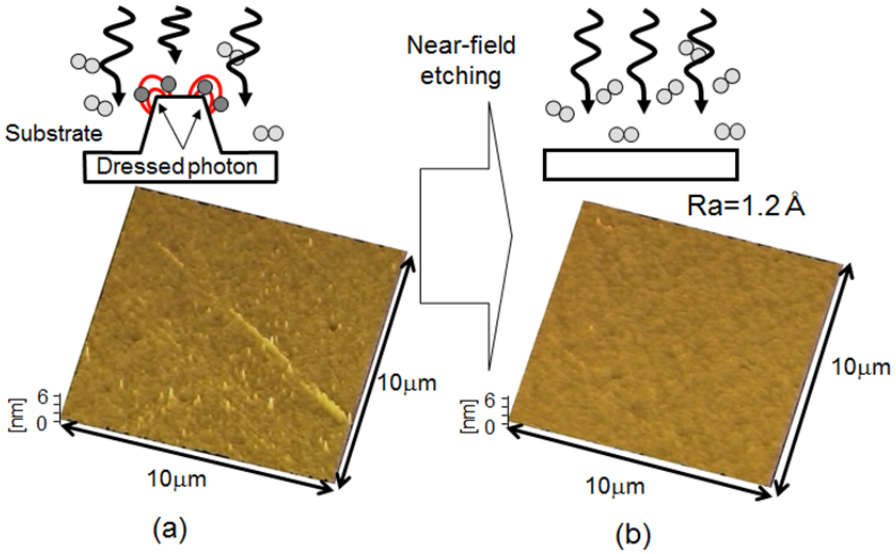

Fig. 1. Schematic of near-field etching. Atomic force microscopic images of (a) before and (b) after the dressed-photon phonon etching on glass substrate.

References:

1. L. M. Cook, J. Non-Crystalline Solids, **120**, 152 (1990).
2. T. Yatsui, K. Hirata, W. Nomura, M. Ohtsu, and Y. Tabata, Appl. Phys. B, **93**, 55 (2008).
3. T. Yatsui, K. Hirata, Y. Tabata, W. Nomura, T. Kawazoe, M. Naruse, and M. Ohtsu, Nanotechnology **21**, 355303 (2010).
4. T. Yatsui, K. Hirata, Y. Tabata, Y. Miyake, Y. Akita, M. Yoshimoto, W. Nomura, T. Kawazoe, M. Naruse, and M. Ohtsu, Appl. Phys. B, **103**, 527 (2011).

Keywords: dressed-photon phonon, ultra-flat surface, self-organized process
Corresponding author*: yatsui@ee.t.u-tokyo.ac.jp

Information Physics in Nanophotonics

Makoto Naruse[1,2], Naoya Tate[2], Masashi Aono[3], and Motoichi Ohtsu[2]
1. Photonic Network Research Institute, National Institute of Information and Communications Technology, 4-2-1 Nukui-kita, Koganei, Tokyo 184-8795, Japan
2. Nanophotonics Research Center, Graduate School of Engineering, The University of Tokyo, 2-11-16 Yayoi, Bunkyo-ku, Tokyo 113-8656, Japan
3. Flucto-order Functions Research Team, RIKEN Advanced Science Institute, 2-1, Hirosawa, Wako, Saitama 351-0198, Japan
Email: naruse@nict.go.jp

Abstract Information physics aspects of nanophotonics are examined, such as unidirectional signal transport, power dissipation, and shape-engineering of nanostructures, based on optical near-field processes. Stochastic approaches to nanophotonics, toward the realization of novel computing, are also discussed.

Nanophotonics offers ultrahigh-density device and system integration since it is based on local interactions between nanometer-scale matter and is not constrained by the diffraction limit, which is unavoidable with far-field propagating light. In addition, it provides qualitatively novel benefits over conventional optics and electronics and paves the way for a wide range of applications, including information and communication technologies, environment and energy, and so forth.

From a system architectural perspective, nanophotonics drastically changes the fundamental design rules of functional optical systems, and suitable architectures may be built to exploit this. Technological enablers in nanophotonics, such as quantum nanostructures and near-field spectroscopy, have seen rapid progress. In order to design and realize devices and systems based on nanophotonics and nanomaterials, a fundamental understanding from the viewpoint of information is indispensable. This paper briefly reviews recent research on information physics in nanophotonics, concerning (1) fundamental information properties, (2) the extremely high degree-of-freedom in the design of for nanophotonic systems, and (3) some stochastic approaches.

(1) Fundamental information properties in nanophotonics

Information-related fundamentals regarding diffraction-limited, far-field light, are well developed, such as Fourier optics for optical signal processing, optical communications theory, etc. Thus, design guidelines are available, and these help in systematic design for dedicated optical systems while revealing their performance limitations. The fundamental information-based properties of optical near-field processes on the nanoscale have to be understood, too. Based on optical energy transfer mediated by optical near-field interactions, we have been investigating (i) unidirectional signal transport [1-4], (ii) the minimum energy dissipation required for signal transport taking account of the

signal-to-noise ratio and error rate [5,6], (iii) tamper resistance [7], (iv) autonomous signal transport [8], (v) pulsation [9], (vi) summation and broadcast operations [10,11], and (vii) information theory-based capacity analysis [12], among others (Fig. 1).

(2) Extremely high degree-of-freedom in design of nanophotonic systems

One of the unique advantages of nanophotonics is the extremely high degree-of-freedom in design that is available on the nanoscale, such as the shape, size, and layout of nanomaterials, the vector and multipole nature of electromagnetic fields, and various kinds of elemental quasi-particles [13-16]. One example is a *hierarchical hologram*, which acts as a conventional hologram in the optical far-field while allowing additional information to be retrieved from embedded nanostructures, which is accessible only via the optical near-field [14]. This is a manifestation of the inherent hierarchical properties of optical near-field interactions and the multipole nature of electromagnetic fields associated with shape-engineered metal nanostructures. Also, such an abundance of design parameters is well-matched with information security applications [15]; for example, "lock-and-key" principles and experiments have been demonstrated based on metal nanostructures [16].

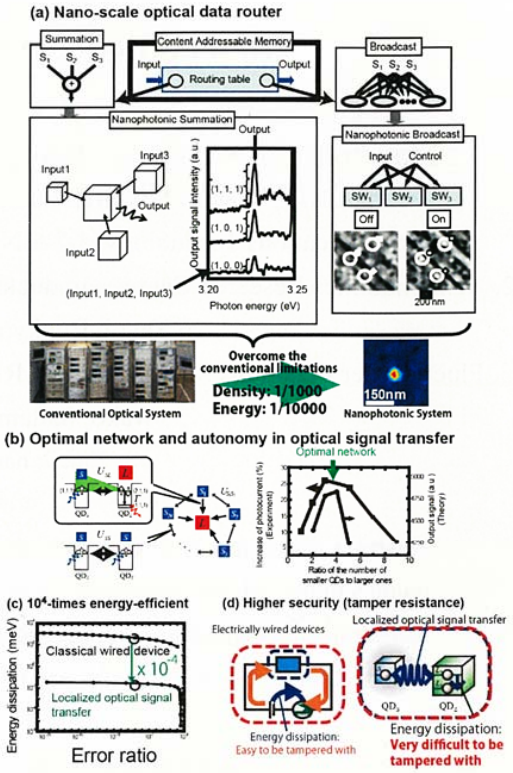

Fig. 1 Some basic functionalities based on localized energy transfer mediated by optical near-field interactions.

(3) Stochastic approach to nanophotonics

Stochastic analysis and modeling, not just the knowledge of elemental physical processes, are indispensable in understanding the various experimental data observed in nanophotonics. For example, cooperative phenomena or order formation requires stochastic analysis and modeling. One example demonstration is the stochastic understanding of light-assisted nanoparticle formation [17,18].

Stochastic approaches may also pave the way to novel computing paradigms. For instance, optical energy transfer from smaller quantum dots to larger ones via optical near-field interactions, which is a quantum stochastic process, depends on the existence of resonant energy levels between the quantum dots or a state-filling effect occurring at the destination quantum dots. We exploit these spatiotemporal mechanisms in optical energy transfer, which include both quantum and dissipative processes, for problem solving [19] (Fig. 2). The principle is uniquely inspired by nanophotonics and is quite unlike conventional optical, electrical, or quantum computing paradigms.

In summary, we briefly describe information physics aspects of nanophotonics. Further theoretical

and experimental investigations will be exciting. We consider that the interdisciplinary area of nanophotonics, nanomaterials, and information will provide new insights and a number of vitally important applications.

Acknowledgement This work was supported in part by the Strategic Information and Communications R&D Promotion Program (SCOPE) of the Ministry of Internal Affairs and Communications and by a Grant-in-Aid for Scientific Research from the Japan Society for the Promotion of Science.

References

1. M. Naruse, T. Kawazoe, R. Ohta, W. Nomura, and M. Ohtsu, Phys. Rev. B **80**, 125325 (2009).
2. M. Naruse, E. Runge, K. Kobayashi, and M. Ohtsu, Phys. Rev. B **82**, 125417 (2010).
3. M. Naruse, F. Peper, K. Akahane, N. Yamamoto, T. Kawazoe, N. Tate, and M. Ohtsu, ACM J. Emerging Technol. Computing Systems **8**, 4 (2012).
4. T. Kawazoe, M. Ohtsu, S. Aso, Y. Sawado, Y. Hosoda, K. Yoshizawa, K. Akahane, N. Yamamoto, and M. Naruse, Appl. Phys. B **103**, 537 (2011).
5. M. Naruse, H. Hori, K. Kobayashi, P. Holmström, L. Thylén, and M. Ohtsu, Opt. Express **18**, A544 (2010).
6. M. Naruse, P. Holmström, T. Kawazoe, K. Akahane, N. Yamamoto, L. Thylén, and M. Ohtsu, Appl. Phys. Lett. in press.
7. M. Naruse, H. Hori, K. Kobayashi, and M. Ohtsu, Opt. Lett. **32**, 1761 (2007).
8. M. Naruse, K. Leibnitz, F. Peper, N. Tate, W. Nomura, T. Kawazoe, M. Murata, and M. Ohtsu, Nano Commun. Networks **2**, 189 (2011).
9. M. Naruse, H. Hori, K. Kobayashi, T. Kawazoe, and M. Ohtsu, Appl. Phys. B **102**, 717 (2011).
10. M. Naruse, T. Miyazaki, F. Kubota, T. Kawazoe, K. Kobayashi, S. Sangu, M. Ohtsu, Opt. Lett. **30**, 201 (2005).
11. M. Naruse, T. Kawazoe, S. Sangu, K. Kobayashi, and M. Ohtsu, Opt. Exp. **14**, 306 (2006).
12. M. Naruse, H. Hori, K. Kobayashi, M. Ishikawa, K. Leibnitz, M. Murata, N. Tate, and M. Ohtsu, J. Opt. Soc. Am. B **26**, 1772 (2009).
13. M. Naruse, T. Yatsui, H. Hori, M. Yasui, and M. Ohtsu, J. Appl. Phys. **103**, 113525 (2008).
14. N. Tate, M. Naruse, T. Yatsui, T. Kawazoe, M. Hoga, Y. Ohyagi, T. Fukuyama, M. Kitamura, and M. Ohtsu, Opt. Exp. **18**, 7497 (2010).
15. M. Naruse, N. Tate, and M. Ohtsu, J. Optics, in press.
16. N. Tate, H. Sugiyama, M. Naruse, W. Nomura, T. Yatsui, T. Kawazoe, and M. Ohtsu, Opt. Exp. **17**, 11113 (2009).
17. M. Naruse, Y. Liu, W. Nomura, T. Yatsui, M. Aida, L. B. Kish, and M. Ohtsu, Appl. Phys. Lett. **100**, 193106 (2012).
18. M. Naruse, T. Kawazoe, T. Yatsui, N. Tate, and M. Ohtsu, Appl. Phys. B **105**, 185 (2011).
19. M. Naruse, M. Aono, H. Hori, M. Hara, and M. Ohtsu, submitted.

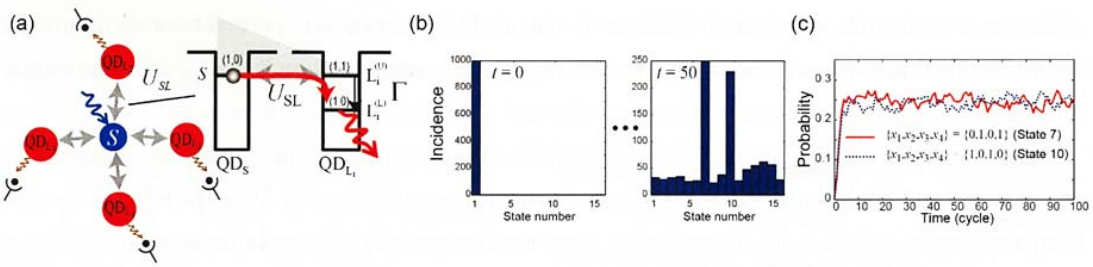

Fig. 2 (a) Architecture for solving constraint satisfaction problem based on optical energy transfer by near-field interactions. (b) Evolution of incidences of all states with an initial state (state #1) to correct solutions (state #7 and state #10). (c) Evolution of appearance probability of "correct" solutions.

IPCN1-12

Engineering of nanometric optical system based on optical near-field interactions for macro-scale applications

Naoya Tate[1], Makoto Naruse[2], Motoichi Ohtsu[1]
[1]The University of Tokyo, [2]National Institute of Information and Communication Technology
Email: tate@nanophotonics.t.u-tokyo.ac.jp

Abstract Hierarchy is one of the characteristic features of nanophotonics, a novel technology that exploits several features of optical near-fields. Here we introduce the concepts of hierarchical nanophotonic systems and experimentally verify the usability.

1. Introduction

Nanophotonics is a novel optical technology utilizing local interactions between nanometric particles via optical near-fields [1]. As shown in Fig. 1(a), the optical near-field is a virtual cloud of photons that is constantly localized around nanometric materials illuminated by incident light. Since the virtual cloud of photons is localized in a region close to the electrons in the material, it can effectively interact with the material in a unique manner. Exploiting such characteristic behaviors of optical near-fields for implementing optical devices and systems enables novel functions that would otherwise be impossible if conventional propagating light were used.

Implementation of a hierarchical system structure is one of the most appealing attributes of nanophotonics for realizing innovative devices and systems. As shown in Fig. 1(b), a hierarchical system structure is based on the fact that optical near-field interactions can be essentially distinguished from several optical phenomena based on propagating light, in which we can see the inherent hierarchy of the optical near- and far-fields. This characteristic feature has led to hierarchical optical system designs [2] where independent functions are associated with the optical near- and far-fields in the same device. Additionally, techniques for interfacing from the scale of optical near-fields to that of optical far-fields are also important for realizing further developments in nanophotonics. Such techniques are required to extract the various characteristic behaviors of optical near-field interactions as observable optical far-field functions. A fundamental aspect in realizing such a concept is the appropriate design and arrangement of the shapes and materials of nanometric components of the nanophotonic system.

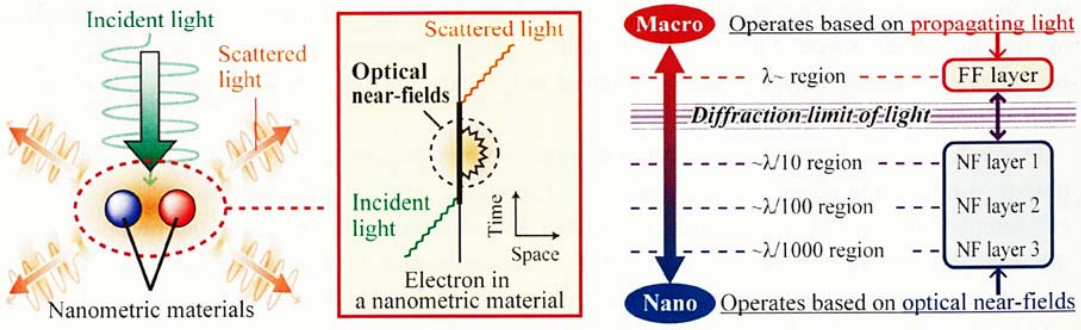

(a) (b)

Figure 1: (a) Schematic diagram of induced optical near-fields and a Feynman diagram representing their behavior. (b) Concept of nano-to-macro hierarchical structure based on nanophotonics.

Recently, we experimentally demonstrated magnified transcription of an optical near-field

distribution by using a photo-induced phase transition in a metal complex [3], polarization conversion using a quadrupole–dipole transformation based on optical near-field interactions [4], and dynamic modulation of the optical emission spectra of resonant quantum dots dispersed on a flexible substrate [5]. In this paper, we describe the concepts and experimental demonstrations of a hierarchical hologram [6,7] as a typical application of a compound system involving optical near-fields and far-fields, which was made possible by applying the inherent hierarchy of nanophotonics to a conventional optical system.

2. Hierarchical hologram

A hierarchical hologram based on the hierarchy of nanophotonics has been proposed as a demonstration of a security system [6]. The hierarchical hologram is a functionally improved version of a conventional hologram that works in both the optical far- and near-fields while maintaining the 3D visual aspect of the hologram. Figure 2(a) shows the basic concept. We defined a nanophotonic code as information embedded in the near-mode layer by a distribution of induced optical near-fields due to interactions between nanometric structures realized by nanometric shape-engineering of the original embossed hologram and retrieval probe [7]. In our concept, the conventional hologram view reconstructed by diffraction of propagating light and the nanophotonic code due to the optical near-fields are considered as *overt* and *covert* security aspects of the hierarchical hologram, respectively.

For experimental demonstration of this concept, we developed a hierarchical hologram based on the design of *Virtuagram*® developed by Dai Nippon Printing Co., Ltd., Japan, which is a high-definition computer-generated hologram composed of binary-level one-dimensional modulated gratings. Within the device, we modified the shape of the hologram structure, with a minimum feature size of 50 nm, to realize the nanophotonic code. The input light induces surface charge concentrations in the embedded nanometric structures, which are a result of optical near-field interactions between the hologram structure and the nanometric structures, allowing retrieval of the nanophotonic code only via optical near-fields in their vicinity.

We experimentally demonstrated retrieval of nanophotonic codes with embedded and isolated nanometric structures in the hologram structure. In the experimental demonstration, nanophotonic codes were retrieved by using a near-field optical microscope (NOM). The NOM was operated in an illumination-collection mode with a retrieval probe having a tip with a 5 nm radius of curvature. To quantitatively evaluate the characteristics of the near-mode retrieval, we defined a figure-of-merit called *recognizability*, which depends on the visual contrast between observed signal distributions and other light distributions in the vicinity. As shown in Fig. 2(b), the nanophotonic code embedded in the hologram successfully exhibited much greater polarization dependency and evident recognizability of the retrieved signal, whereas only slight polarization dependency was observed with an isolated code.

Presently, we are discussing an implementation of a hierarchical security system based on optical near-field-interaction–based artifact-metrics. Generally, an artifact-metrics system utilizes characteristic features of several artifacts for their authentication. The feature of our proposal is that the data observed from a security device for its authentication is physically dependent on optical near-field interactions between the device and a reader, serving as a nanophotonic code and a retrieval probe, respectively. This means that, for an attacker to attack the system, it is quite difficult to duplicate an authentic device from the observed data or to analogize accurate observed data from the device, because the observed data will drastically vary when using an only slightly different device or reader.

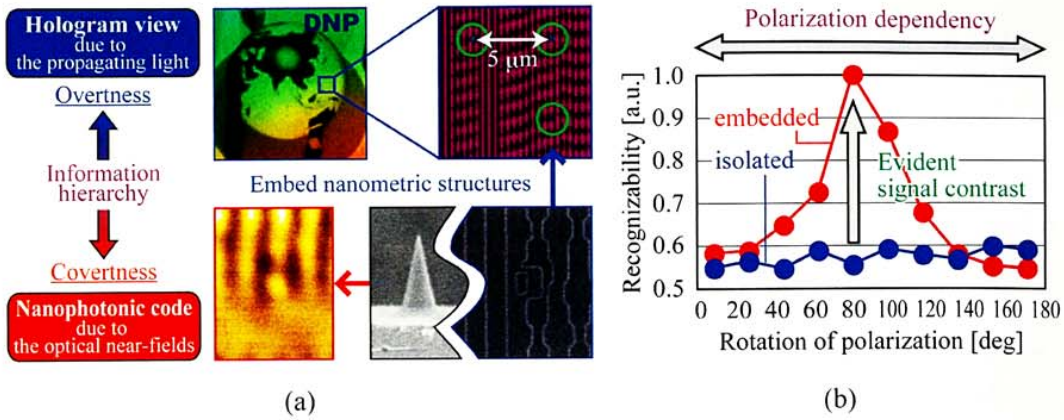

(a) (b)

Figure 2: (a) Basic concept of functional hierarchy of hierarchical hologram, and NOM image of a retrieved nanophotonic code. (b) Experimental recognizability versus polarization state of incident light.

3. Summary

Hierarchy is only one of the various features of nanophotonics. For further developments in system applications, several related nanometric phenomena should continue to be looked at more deeply, such as the behavior of photons in a nanometric space, excitation transfer and relaxation in a nanometric space, and the primary mechanisms of phonon-assisted processes. Such fundamental studies are expected to establish a new field of dressed photon science and novel system applications in the near future.

Part of this work was supported by the Research and Development Program for Innovative Energy Efficiency Technology funded by the New Energy and Industrial Technology Development Organization (NEDO) of Japan and by Strategic Information and Communications R&D Promotion Programme (SCOPE) sponsored by the Ministry of Internal Affairs and Communications (MIC).

References

1. M. Ohtsu, K. Kobayashi, T. Kawazoe, T. Yatsui, and M. Naruse (eds.), *Principles of Nanophotonics* (Taylor and Francis, 2008).

2. M. Naruse, T. Yatsui, W. Nomura, N. Hirose, and M. Ohtsu, Opt. Exp. 13, pp. 9265-9271 (2005).

3. N. Tate, H. Tokoro, K. Takeda, W. Nomura, T. Yatsui, T. Kawazoe, M. Naruse, S. Ohkoshi, and M. Ohtsu, Appl. Phys. B, 98, pp. 685-689 (2010).

4. N. Tate, H. Sugiyama, M. Naruse, W. Nomura, T. Yatsui, T. Kawazoe, M. Ohtsu, Opt. Exp. 17, pp. 11113-11121 (2009).

5. N. Tate, M. Naruse, W. Nomura, T. Kawazoe, T. Yatsui, M. Hoga, Y. Ohyagi, Y. Sekine, H. Fujita, and M. Ohtsu, Opt. Exp. 19, pp. 18260-18271 (2011).

6. N. Tate, W. Nomura, T. Yatsui, M. Naruse, and M. Ohtsu, Opt. Exp. 16, pp. 607-612 (2008).

7. N. Tate, M. Naruse, T. Yatsui, T. Kawazoe, M. Hoga, Y. Ohyagi, T. Fukuyama, M. Kitamura, and M. Ohtsu, Opt. Exp. 18, pp. 7497-7505 (2010).

IPCN1-13

Amoeba-inspired Model of Quantum Dot-based SAT Solver

Masashi Aono[1], Makoto Naruse[2], Song-Ju Kim[1],
Motoichi Ohtsu[3], Hirokazu Hori[4] and Masahiko Hara[1]

1 Flucto-Order Functions Research Team, RIKEN-HYU Collaboration Research Center, RIKEN Advanced Science Institute, 2-1 Hirosawa, Wako, Saitama 351-0198, Japan

2 Photonic Network Research Institute, National Institute of Information and Communications Technology, 4-2-1 Nukui-kita, Koganei, Tokyo 184-8795, Japan

3 Department of Electrical Engineering and Information Systems / Nanophotonics Research Center, Graduate School of Engineering, The University of Tokyo, 2-11-16 Yayoi, Bunkyo-ku, Tokyo 113-8656, Japan

4 Interdisciplinary Graduate School of Medicine and Engineering, University of Yamanashi, Kofu, Yamanashi 400-8511, Japan

Email: masashi.aono@riken.jp

Abstract We show that spatiotemporal dynamics of energy transfers among quantum dots are applied to solving the Boolean satisfiability problem when combined with control dynamics for bouncing back logically-false transitions. Our model finds a solution more efficiently than the exhaustive search method for some representative problem instances.

Can an unconventional computer with hardware exploiting its own natural processes implement some unique functions that are difficult for conventional digital computers to deal with? A promising way to answer this question would be to learn from biological organisms in terms of reducing energy consumption and solving computationally demanding problems to survive in harsh environments.

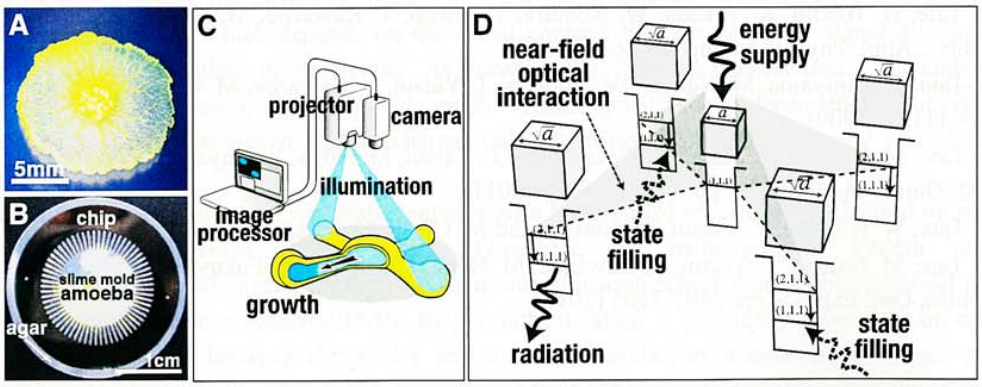

Figure 1. (A) An amoeba-like organism *P.Polycephalum*. (B) A 64-lane chip used for 8-city TSP solution. (C) Optical control system in the amoeba-based computer. (D) Optical energy transfer among quantum dots.

A plasmodium of the true slime mold *Physarum polycephalum*, a single-celled amoeba-like organism, exhibits rich spatiotemporal oscillatory dynamics and efficient resource allocation capabilities (Fig. 1A) [1]. When placed in a chip having a number of lanes (Fig. 1B), the organism inherently grows its branches inside the lanes. This is because the organism tries to occupy the entire area inside the chip to maximize the absorption of nutrients from beneath an agar plate. However, the organism withdraws its branches when illuminated by light. This photo-avoidance behavior enables us to induce the shape change of the organism when combined with an optical control system (Fig. 1C).

The author constructed an experimental system called an "amoeba-based computer", which employs the organism to search for a solution to the Traveling Salesman Problem (TSP) [2,3]. Many meta-heuristic search algorithms use uncorrelated random noise so that a wider state space can be sought; on the other hand, the organism explores the state space using fluctuations in the oscillatory movements of its branches that are spatially and temporally correlated. The optical control stimulation informs the organism the fitness of the current state determined by a recurrent neural network model. In response to external light stimuli, the organism alternates between expansion and withdrawal of its branches at each oscillation period to achieve the optimal shape for which the area of the body is maximized and the risk of being illuminated is minimized. The organism finds a high quality solution with a high probability.

In this study, we show that photoexcitation transfers among nanoscale quantum dots (QDs) based on near-field optical interactions occurring at scales far below the wavelength of light have the potential to solve a computationally demanding problem with low energy use. The near-field optical interactions have been experimentally demonstrated in various quantum nanostructures such as InGaAs, ZnO, CdSe, etc. Recently, room-temperature optical energy transfer was demonstrated using two-layer InGaAs QDs [4]. The optical energy transfer has been shown to be 10^4-times more energy efficient than that of a bit-flip energy required in conventional electrically wired devices [5].

The optical energy transfer from a smaller QD to larger ones, which is a quantum stochastic process, depends on the existence of resonant energy levels in the QDs and is inhibited by a state-filling effect occurring at the destination QDs (Fig. 1D). This photoexcitation transfer behavior shares some interesting features with that of the spatiotemporal dynamics of intracellular resource transfer behavior in the amoeboid organism (Fig. 1C) [5]. Introducing newly designed optical control dynamics for inhibiting energy transfers by state filling in a manner similar to the one used in the amoeba-based computing, we show that the QD system is applied to solving a complex computational problem.

The Boolean satisfiablitiy problem (SAT), an NP-complete combinatorial optimization problem, is the problem of determining if the N variables of a given Boolean formula can be assigned in such a way that the entire formula becomes "true". For an instance, a four-variable formula $F = (x_1 \vee \neg x_2) \wedge (\neg x_2 \vee x_3 \vee \neg x_4) \wedge (x_1 \vee x_3) \wedge (x_2 \vee \neg x_3) \wedge (x_3 \vee \neg x_4) \vee (\neg x_1 \vee x_4) = 1$, which is expressed in a conjunctive normal form (CNF), gives a uniquely-existed solution $(x_1, x_2, x_3, x_4) = (1, 1, 1, 1)$.

We employ a smaller QD and $2N$ larger QDs (Fig. 2), where each of the latter is labeled with the variable name "x_i" and its value "y". The smaller one is used for energy supply, and the energy transfer

to the larger one results in a probabilistic radiation, which represents that the QD system evaluates a validity of the assignment "x_1=y". To make the entire formula F "true", every clause needs to be "true" because all the clauses in the CNF are connected with "and" operators. Now, let us focus on $(x_1 \vee \neg x_2)$, the leftmost clause of F. To make this clause "true", if x_1 is "false", then x_2 should NOT be "true". Therefore, we introduce the following operation that we call the "bounceback control": If the number of accumulated radiations from dot x_1=*0* exceeds a certain threshold at an iteration step t, the energy transfer to dot x_2=*1* is inhibited by control light for the state-filling effect at the next step t+*1* (Fig. 2A). Likewise, we define similar operations by scanning all the clauses in F. These operations constitute control dynamics for bouncing back logically-false energy transfers. The system explores a variety of combinations of the assignments by performing the dynamic radiation behavior and finds the solution that is the only state to be stabilized after several iterations of the bounceback control (Fig. 2B).

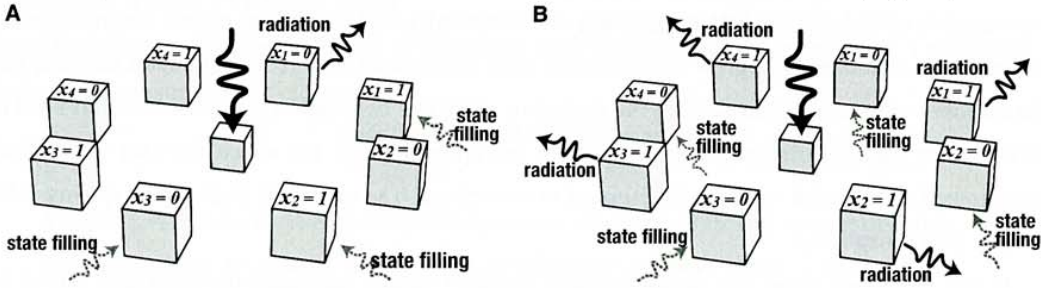

Figure 2. Quantum dot system for solving four-variable SAT. (A) An example of the application of the bounceback control. (B) System state representing the solution $(x_1, x_2, x_3, x_4) = (1, 1, 1, 1)$.

We formulate a mathematical model of the spatiotemporal dynamics of the quantum processes coupled with the bounceback control dynamics for solving the SAT. Performing Monte Carlo simulations for some instances of 2-SAT and 3-SAT, we show that our model reaches a solution within a smaller number of iterations compared with that of the exhaustive search method.

Our computing paradigm is fundamentally different from conventional optical computing or optical signal processing, which are limited by the properties of propagating light. It is also different from the quantum computing paradigm where a superposition of all possible states is exploited so as to lead to a correct solution. The optical-near-field–mediated energy transfer is a coherent process, suggesting that an optical excitation could be transferred to all possible destination QDs via a resonant energy level, but such coherent interaction between QDs results in a unidirectional energy transfer by an energy dissipation process occurring in the larger QD. Thus, our approach opens up the possibility of a new computing paradigm where both coherent and dissipative processes are exploited [6].

[1] M. Aono, et al., *Communications of the ACM* 50 (9), 69-72 (2007).

[2] M. Aono, et al., *New Generation Computing* 27, 129-157 (2009).

[3] M. Aono, et al., *Int'l J. Unconventional Computing* 7 (6), 463-480, (2011).

[4] T. Kawazoe, et al., *Appl. Phys. B* 103, 537–546 (2011).

[5] M. Naruse, et al., *Opt. Express* 18, A544–A553 (2010).

[6] M. Naruse, et al., submitted (2012).

IPCN1-14

A Model of Quantum Dot-based Decision Maker

Song-Ju Kim[1], Makoto Naruse[2], Masashi Aono[1], Motoichi Ohtsu[3] and Masahiko Hara[1]

1 Flucto-Order Functions Research Team, RIKEN-HYU Collaboration Research Center, RIKEN Advanced Science Institute, 2-1 Hirosawa, Wako, Saitama 351-0198, Japan
FTC 5F, Hanyang University, 222 Wangsimni-ro, Seongdong-gu, Seoul 133-791, Korea
2 Photonic Network Research Institute, National Institute of Information and Communications Technology, 4-2-1 Nukui-kita, Koganei, Tokyo 184-8795, Japan
3 Department of Electrical Engineering and Information Systems / Nanophotonics Research Center, Graduate School of Engineering, The University of Tokyo, 2-11-16 Yayoi, Bunkyo-ku, Tokyo 113-8656, Japan

Email: songju@riken.jp

Abstract We propose a mathematical model of an efficient decision-making system using quantum dots. The simulation results indicate that the model exhibits better performance compared with other well-known decision-making algorithms in many cases.

Recently, the interdisciplinary research area called "unconventional computation" or "natural computation" has been extensively studied to enrich or go beyond the standard models, such as Von Neumann computer architecture and Turing machine, which have dominated computer science for more than 50 years. To achieve a new kind of computing engineering inspired in nature including living organisms, these methods model their computational operations based on non-standard ways.

Our decision-making algorithm [1, 2], called the "tug-of-war model (TOW)", was also inspired by living organisms. The TOW is based on the property of a single-celled amoeba, the true slime mold *Physarum*, which maintains a constant intracellular resource volume while collecting environmental information by concurrently expanding and shrinking its branches. The conservation law entails a "nonlocal correlation" among the branches, i.e., volume increment in one branch is immediately compensated by volume decrement(s) in the other branch(es). This nonlocal correlation was shown to be useful for decision-making in our previous studies [1-5].

The multi-armed bandit problem (BP) is to determine the optimal strategy for maximizing the total reward sum with incompatible demands; either to exploit rewards that were obtained owing to already collected information or to explore new information for acquiring higher payoffs in taking risks. Consider a number of slot machines. Each of the machines has an arm which gives a player a reward with a certain probability when pulled. To maximize the total reward sum, it is necessary to judge correctly and quickly which machine has the highest reward probability. Therefore, the player should explore many machines to gather much information on which machine is the best, but should

not fail to exploit the reward from the known best machine. These requirements are not easily met simultaneously, because there is a trade-off between the "exploration" and "exploitation". Living organisms commonly encounter this "exploration–exploitation dilemma" as they should survive in the unknown world. We consider that living organisms follow some efficient method to solve the decision-making problem.

The TOW is capable of efficiently resolving this exploration–exploitation dilemma and exhibits good performances. The cumulative rate of correct selections of the TOW is higher than those of well-known algorithms such as the modified ε-greedy algorithm and modified softmax algorithm [3]. Moreover, the TOW exhibits superior flexibility in adapting to environmental changes, which is an essential property for living organisms to survive in uncertain environments. The TOW can be applicable to various fields such as the modern portfolio theory, advertising on the web, cognitive network, Monte-Carlo tree search, and so on, because BP is basic mathematical problem which relates to various stochastic phenomena.

A distinctive feature of the TOW is that it is suited for physical implementation. In fact, the TOW is a model of spatiotemporal dynamics of a physical object, i.e., an amoeboid organism. This physical implementation enable us to realize an "effective decision-maker", that is an object which can make a decision effectively. In this study, we show one of possibilities of the physical implementation of the TOW using quantum dots (QDs). Semiconductor QDs have been used for innovative nanophotonic devices [6], as well as conventional solar cells, LEDs, diode lasers, and qubits in quantum computing. We introduce a new application to "decision-making" by making use of optical energy transfer between quantum dots mediated by optical near-field interactions.

We use three kinds of cubic QDs with their side lengths of a, $\sqrt{2}a$, and $2a$, which are respectively represented by small S-, M-, and L-QD. We assume that 5 QDs are one-dimensionally arranged as "M-L-S-L-M". Thanks to the steep electric fields in the vicinity of these QDs, an optical excitation can be transferred between QDs through resonant energy levels mediated by optical near-field interactions [7, 8]. Here we should note that an optical excitation is usually transferred from smaller QDs to larger ones due to energy dissipation processes occurring at larger QDs. Also, an optical near-field interaction follows Yukawa-type potential, meaning that it could be engineered by inter-dot distances. When an optical excitation is generated at S-QD, it is transferred to the lowest energy levels in L-QDs; we observe negligible radiation from M-QDs. However, when the lowest energy levels of L-QDs are occupied by control lights, which induce state filling effects, the optical excitation at S-QD is more likely to be radiated from M-QDs [9]. Here we consider that the photon radiation either from the left M-QD or the right M-QD as the decision of selecting slot machine A and B, respectively. The intensity of control light to induce state filling at the left and right L-QDs is respectively modulated based on the resultant rewards obtained from the chosen slot machine. We call such decision-making system "QD-based tug-of-war model" (QDTOW). The QDTOW can be easily extended to N-armed (N>2) cases although we demonstrate the only 2-armed case in this study.

Figure 1 demonstrates performance (cumulative rate of correct selections) for the QDTOW

(solid line), and the well-known softmax algorithm with optimized parameter τ (dotted line) in the case where (a) P_A = 0.2 and P_B = 0.8, and (b) P_A = 0.4 and P_B = 0.6, respectively. Even with a fixed (namely, non-optimized) parameter, the performance of the QDTOW is higher than that of well-known conventional decision-making algorithm (softmax).

In summary, we demonstrate the QD-based decision maker based on optical energy transfer. Using QDs, it is possible to physically implement the TOW, which can effectively solve the BP. Thus, there is a possibility to utilize QDs as a means to realize the totally new application, i.e., "effective decision-making". Surprisingly, the performance of the QDTOW is higher than those of well-known algorithms including the original TOW in our limited simulation studies. This suggests that the efficiency of the QD-based decision maker (QDM), which will be realized experimentally in the future, could be higher than those of other systems including conventional digital computers.

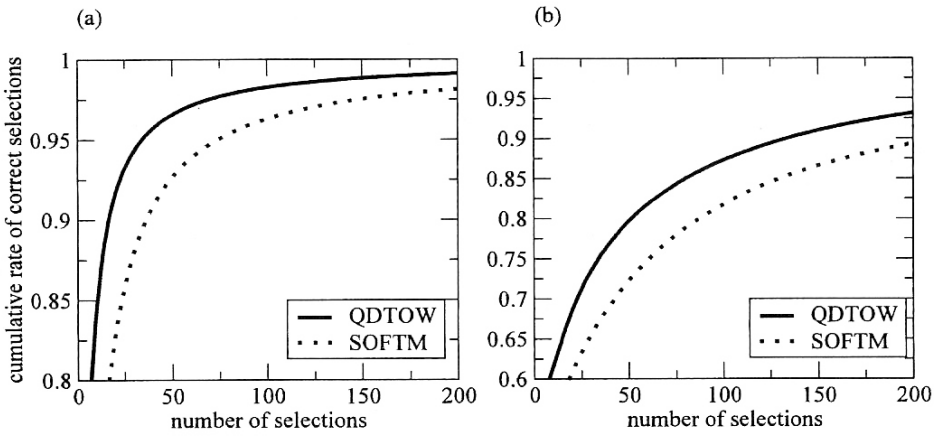

Figure 1: Cumulative rate of correct selections for the QDTOW with fixed parameter D = 50 (solid line), and the softmax algorithm with optimized parameter τ (dotted line) in the case where (a) P_A = 0.2 and P_B = 0.8, and (b) P_A = 0.4 and P_B = 0.6, respectively.

Acknowledgement

This work was supported in part by the Strategic Information and Communications R&D Promotion Program (SCOPE) of the Ministry of Internal Affairs and Communications, and Grant-in-Aid for Scientific Research from the Japan Society of the Promotion of Science.

References

[1] S. -J. Kim, M. Aono, and M. Hara: Lecture Notes in Computer Science, **5715** (2009) 289.
[2] S. -J. Kim, M. Aono, and M. Hara: Lecture Notes in Computer Science, **6079** (2010) 69.
[3] S. -J. Kim, M. Aono, and M. Hara: BioSystems, **101** (2010) 29.
[4] S. -J. Kim, M. Aono, and M. Hara: Proceedings of NOLTA 2010, 520.
[5] S. -J. Kim, E. Nameda, M. Aono, and M. Hara: Proceedings of NOLTA 2011, 176.
[6] T. Kawazoe, M. Ohtsu, S. Aso, Y. Sawado, Y. Hosoda, K. Yoshizawa, K. Akahane, N. Yamamoto, and M. Naruse: Appl. Phys. B, **103** (2011) 537.
[7] M. Ohtsu, T. Kawazoe, T. Yatsui, and M. Naruse: IEEE JSTQE, **14** (2008) 1404.
[8] W. Nomura, Y. Yatsui, T. Kawazoe, M. Naruse, and M. Ohtsu: Appl. Phys. B, **100** (2010) 181.
[9] M. Naruse, F. Peper, K. Akahane, N. Yamamoto, T. Kawazoe, N. Tate, and M. Ohtsu: ACM JETC, 8 (2012) 4.

[O79]

Realization of an ultra-flat diamond substrate using a dressed-photon phonon etching

T. Yatsui*[1,2], W. Nomura[1], M. Ohtsu[1]

[1]The University of Tokyo, Japan, [2]JST ALCA, Japan

Ultra-flat substrate surface of diamond with sub-nanometer scale roughness is required for various applications, including light emitting diode, power device, diamond cutter, and future optical computing device. To obtain a flat surface, conventional methods have used mechanical polishing. However, there are some difficulties due to the hardness of the diamond.

To overcome this difficulty, using a dressed-photon phonon (DPP), a quasiparticle representing a coupled state of photon, electron, and coherent phonon, we realized ultra-flat surface of diamond substrate. We developed self-organized DPP etching using a CW laser (3.81 eV) light source and oxygen as etching gas. Since the absorption band edge energy (5.12 eV) of oxygen is higher than the irradiation photon energy, the oxygen is selectively photodissociated at the proximity of the protrusions, where the DPP is effectively generated. The activated oxygen atoms etch away the protrusions. DPP etching automatically stop when the substrate become sufficiently flat so that DPP disappears. It was confirmed by AFM images that the DPP etching decreases the average surface roughness as small as 0.15 nm (Ib (111)) and 0.16 nm (IIa (111)).

Since this technique is based on a photochemical reaction, it is applicable to a variety of substrates. It can be applied not only to flat but also to three-dimensional surfaces including convex, concave, and periodic profiles.

Keywords: ultra-flat surface, non-contact method, dressed-photon phonon

[III] REVIEW PAPERS

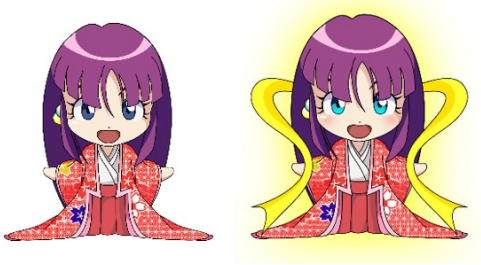

Sweden-Japan Collaboration Symposiumの開催

6月3日-4日にストックホルムセンター主催による「Sweden-Japan Collaboration Symposium “Exploring the Future of Light, Matter, and Information on the Nanoscale”」がルンド大学で開催された。

日本側は東京大学工学系研究科　大津元一教授を中心に大学や産業界から12名の研究者が、スウェーデン側はルンド大学のAnders Gustafsson教授やスウェーデン王立工科大学のLars Thylen教授などをはじめとした13人の研究者が参加し、ご自身の研究について発表をされた。ルンド大学の学生や研究者も加わり、約50名の参加を得て、活発な議論や質疑応答が行われた。

日本大使館松本書記官も参加され、両国間の重要な研究テーマとして捉えているとの共通認識のもと、今後の活動の継続・発展に向けた支援プログラムの検討などを行った。

JSPS Sweden-Japan Collaboration Symposium - June 3-4 2013
“Exploring the Future of Light, Matter, and Information on the Nanoscale”

東京大学　大津　元一
慶応大学　斎木　敏治
情報通信研究機構　成瀬　誠

ナノ寸法における光と物質の相互作用を扱う学術分野はナノフォトニクスと呼ばれ、約20年前に日本で創始された後、世界的に研究開発が活発化している。スウェーデンにおいてもナノフォトニクス研究は活発であり、日本-スウェーデンの研究交流は、2009年6月ストックホルムにて開催された第１回ワークショップ「Sweden-Japan Workshop on Nanophotonics and Related Technologies」を契機として、2011年度～2012年度のVINNOVA及びJSPSによるスウェーデン•日本二国間交流事業（共同研究）（スウェーデン側代表者Lars Thylen（スウェーデン王立工科大学（KTH））、日本側代表者大津元一（東大））、2012年6月ストックホルムでの第2回ワークショップ開催、研究者や大学院学生の相互訪問など大きく発展してきた。このような流れを受けて、日本学術振興会、ルンド大学、ＫＴＨ主催の第1回のシンポジウムが6月3日～4日に、スウェーデン南端に位置する学園都市ルンドにて開催された。

今回のシンポジウムは、シンポジウムタイトルに表象されるように、光科学、物質科学、情報・計算科学がナノ寸法という極微世界で学際融合する将来のさらなる発展を見据えながら、日本からは各分野を先導する12名の先端研究者、スウェーデン側はルンド大学、ＫＴＨ、リンショーピング大学を中心に先端研究者が結集した。ルンド大学Anders Gustafsson教授を中心に充実したプログラムを組んで下さり、ルンドの最高のシーズンで開催された。

会期中は分野を越えた新しい視点からの発表や質問が多く、議論が白熱するとともに、日本・スウェーデンの双方の研究文化の伝統や学術的厚みを相互認識することができ非常に有意義であった。今後、より一層充実した研究協力に発展させる予定である。また、日本からは産業界から2名の発表があり、ナノフォトニクスの基礎学術の発展はもちろんのこと、産業創成や社会貢献に大きく展開していることも注目を集めた。最終日はルンド郊外にバスにて一同移動し、南スウェーデンの雰囲気溢れるレストランにて、研究・文化談義と、太陽と緑が溢れる北欧の色彩と石畳の重厚な学術の街並みに一同感動した。このように有意義なシンポジウムが実現したのは、JSPSストックホルム研究連絡センター藤井義明センター長、吉澤菜穂美副センター長、二上佐和江国際協力員、JSPS東京本部の関連各位の強力なご支援によるものであり深く御礼申し上げる。また在スウェーデン日本国大使館一等書記官の松本英登様にもストックホルムよりご来臨頂き交流と意見交換することができた。この場を借りて関係各位に改めて深く御礼申し上げる。

Laser Review

ドレストフォトンを用いた新産業応用の開拓

八井 崇，大津 元一
東京大学大学院 工学系研究科（〒113-8656 東京都文京区弥生2-11-16）

Recent Progress of a Dressed Photon Technology

Takashi YATSUI and Motoichi OHTSU
School of Engineering, University of Tokyo, 2-11-16 Yayoi, Bunkyo-ku, Tokyo 113-8656

(Received October 31, 2012)

This paper describes the recent progress of dressed photon (DP) technology. DP is a novel nanometric quasi-particle representing the coupled state of a photon, an electron, and a multimode-coherent phonon. Using DP, we developed nano-scale photonic device, i.e., nanophotonic device. Here we review ZnO quantum-well structures based nanophotonic device. In addition, recent progress in ultrafine fabrication technologies using DPs is reviewed, including DP-photochemical etching and desorption, which can be used to produce angstrom-scale flat surfaces. The future outlook of these technologies is given.

Key Words: Dressed photon, Nanophotonic device, ZnO, Ultra flat surface

1. はじめに

近年，近接場光を利用することで，デバイス寸法や加工寸法が光の回折限界を超えて微小化可能となった．さらに，従来の光技術では実現不可能だった新機能，新現象が可能となっている．この新しい光技術を考える上で，近接場光は局在している光子単体とし捉えるのではなく，物質励起と光子が結合した(物質励起の衣をまとった)仮想光子(Dressed photon．以下DPと略記)と考えることが適切である(Fig. 1 (a))[1]．

DPを介したエネルギー移動を利用することにより，従来の光デバイスでは実現不可能であった全く新しい機能が実現する．この動作原理を二つの量子ドット(Quantum dots: QD)を用いて説明する(Fig. 1 (b))[2]．寸法比が1：$\sqrt{2}$のQD$_S$とQD$_L$において，QD$_S$の励起子の基底準位E_{S1}と，QD$_L$の第一励起準位E_{L2}はエネルギー的に共鳴する．なお，E_{L2}は光学禁制準位となるため従来の伝搬光では励起することができない．しかし，2つのQDを寸法サイズであるa程度に近接して配置すると，QD$_S$に励起される近接場光(局所場)によって，E_{L2}は励起可能となる．結果として，E_{S1}とE_{L2}間で近接場光エネルギー移動が発生するが，E_{L2}からE_{L1}への高速のサブレベル間緩和(散逸)が発生するために，E_{S1}に励起されたエネルギーは全てE_{L1}に移動し，E_{S1}に逆流することはない，つまり一方向なエネルギー伝送が実現する．この系に対して，(a)QD$_S$の励起子の基底準位であるE_{S1}に対して高い光子エネルギーにより励起した場合，QD$_S$とQD$_L$の間隔が充分大きい場合には，それぞれの基底準位からの発光が観測されるが，この間隔がQD$_S$の寸法と同程度になると，エネルギー的に共鳴するE_{L2}を通してE_{L1}への緩和が発生し，その結果E_{L1}からの発光しか観測されないことになる(E_{S1}での発光を観測していると非発光であるために“オフ”状態となる)．次に，(b)E_{S1}に対して高い光子エネルギーにより励起しつつE_{L1}に共鳴する光を入射すると，E_{L1}が占有されることで，E_{L2}からE_{L1}へのサブレベル緩和が抑制されるため，E_{S1}からの発光が観測される(“オン”状態)．ここで，従来光学禁制であるE_{L2}は，

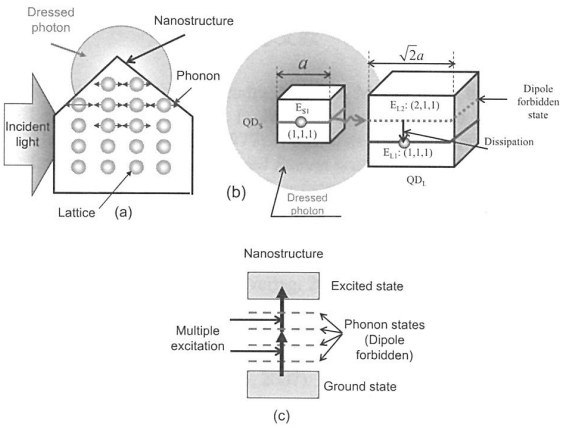

Fig. 1 (a) Schematic of generation of dressed photon. (b) Near-field energy transfer and the dissipation in the closely spaced QD$_S$. (c) Dressed photon assisted multiple excitation in nanomaterial.

隣の量子箱における局所的な電場勾配により初めて励起されるものである．つまり，このデバイスは，数nmの量子箱によって構成されているため，非常に寸法が小さいという利点だけでなく，近接場光によってのみ動作するという特長を有する．ここでは，発光さらには，このデバイスによって消費されるエネルギーはサブレベル間のエネルギー差(E_{L2}-E_{L1})のみであるために，超低消費電力であるという利点がある．以上の基本原理は，3端子に拡張され，CuCl量子箱によりスイッチング動作が実験的に確認されている[3]．

このDPは，さらに，格子振動(フォノン)とも結合しうることで，本来電気双極子禁制であるエネルギー準位にも電子，励起子が励起可能となるという重要な性質を持つ．このようにして電気双極子許容となった実在準位を介した多段階遷移が可能となるため(Fig. 1(c))，バルク材料のバンドギャップ以下の光子エネルギーを持った光が入射された場合でも，伝導帯への電子励起が可能となる．この現象は，入射光の光子エネルギーが上方変換されたことを意味する．このフォノン援用エネルギー上方変換は，実在準位を介した遷移となるため，例え入射光パワーが低い場合であっても高効率にエネルギー上方変換が実現し，第2次高調波発生のための2光子吸収過程によるエネルギー上方変換の発生効率と比較して，三桁以上高くなることが確認されている[4]．

本稿では，このDPによってもたらされる新しいデバイスおよび加工技術として，ZnO量子構造を用いたデバイス応用と，表面平坦化加工技術の進展について紹介する．

2. ZnOナノロッド量子井戸構造を用いたナノフォトニックデバイス

電子デバイスとしても良質な特性を示すZnOの光デバイスとしての特長は(1)励起子結合エネルギーが大きい(60 meV．量子構造にした場合には，110 meVまで大きくなることが報告されている)，(2)振動子強度が大きい，ことから室温において強い励起子発光強度が得られることである[5]．

本稿で紹介するZnOの量子構造は，Metalorganic Vapor Phase Epitaxy(MOVPE)法により作製されたZnOナノロッド先端に作製されている．従来，ZnOに限らず様々なナノロッドの作製は金属触媒を核としてVapor-Liquid-Solid(VLS)法により行われていたが，本手法では金属触媒を用いていないために，ナノロッド先端における金属不純物の混入の心配がなく良質な発光特性が得られている[6]．さらには，量子構造を作製するための障壁層の作製にも適しており，ナノロッドの同径方向にも欠陥が全く見られない良質な量子井戸構造の作製が可能となっている本手法により，ナノロッド先端の単一量子井戸構造とした場合でも，井戸幅に依存して強い励起子発光が観測されている[7]．この手法では，量子井戸の幅および間隔を原子層レベルでを自在に制御することができるため任意のナノフォトニックデバイス作製が可能となる．

ZnOナノロッド量子構造における近接場相互作用を観測するために，2重量子井戸(DQWs)の幅を調整し，拡い井戸幅を有する量子井戸(QW_L)の励起子第一励起準位(E_{L2})と狭い井戸幅を有する量子井戸(QW_S)の励起子基底準位(E_{S1})が共鳴する寸法でDQWsを作製した(Fig. 2 (a))．これにより，QW_Lにポピュレーションを生成させた場合でも，共鳴するエネルギー準位を介してポピュレーションが移動し，この際に失うサブバンド間エネルギーにより，励起が逆流することなくQW_Lの基底準位(E_{L1})からの発光のみ観測されることになると期待される．この際，QW_Lの第一励起準位(E_{L2})は光学禁制であるために，基底準位からの発光しか観測されないと考えられる．

この予測を確認する実験として，まず両者の井戸を励起するために，入力光としてHe-Cdレーザー(λ = 325 nm)による励起を行った．この状態で得られた近接場光スペクトル(Fig. 2 (b)の曲線NF_{off})から，362 nm付近に発光のピークを有するスペクトル(E_{L1})が観測された．QW_SとQW_Lの井戸が孤立して存在した場合には，それぞれの基底準位に対応する波長361 nmおよび362 nmでの発光ピークが観測されるが，この場合には，QW_Lの基底準位に相当するピークからの発光しか観測することができなかった．これは，先に予測したように，共鳴する励起子準位間でのエネルギー移動を示す結果であるといえる("オフ"状態に対応)．次に，このエネルギーの流れを止めるために，制御光としてE_{L1}を共鳴励起(Fig. 2 (b)の曲線$NF_{control}$．制御光はTi:Sapphireレーザーの2次高調波：波長362 nm・パルス幅2 ps)させた状況下において，He-Cdレーザー光を照射したスペクトルをFig. 2 (b)の曲線NF_{on}に示す．この結果，He-Cdレーザー単独励起では観測されなかったE_{S1}(λ = 361 nm)に相当する発光ピーク(出力光)が観測された("オン"状態に対応)．以上の結果は前述した近接場エネルギー移動制御によるナノフォトニックスイッチの基本的動作原理を実証するものである[8]．

光デバイスの微小化に伴い，出力光強度は必然的に減少してしまう．そこで，複数からなる発光体集団からの

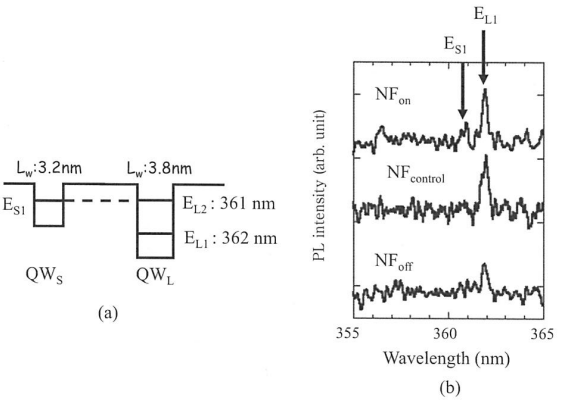

Fig. 2 (a) Schematic of DQW_S. (b) Near-field spectra. NF_{off}: Excitation with only input light, $NF_{control}$: Excitation with control pulse, and NF_{on}: Excitation both with input light and control pulse.

協調発光現象(超放射)[9]を利用したデバイスの探索を行っている．協調発光現象を利用することで，個別のナノ発光体と比較して，強い発光が短時間で得られるため，外部デバイスとのインターフェースとして利用が期待される．超放射発光については，原子系[10]や分子系[11]，さらには数多くの量子ドット集合体[12]において，数多く報告されている．しかしながら，これまでの成果の多くは，超放射を形成する発光体のうちコヒーレントに結合している個数を，密度や系全体の体積として推定しており，正確に見積もることは困難であった．

そこで，この超放射現象を観測する試料として，一次元状に緻密に配列された多重量子井戸(Fig. 3 (a)およびFig. 3 (b))を作製した．実験では，比較試料として，単一量子井戸構造を作製し，発光寿命の励起強度依存性を測定することで行った(Fig. 4 (a)およびFig. 4 (b))．その結果，超放射発光を可能とする量子井戸の数，つまり，光を介してコヒーレントに結合している量子井戸数Mを，数個の精度で見積もることに成功した[13]．

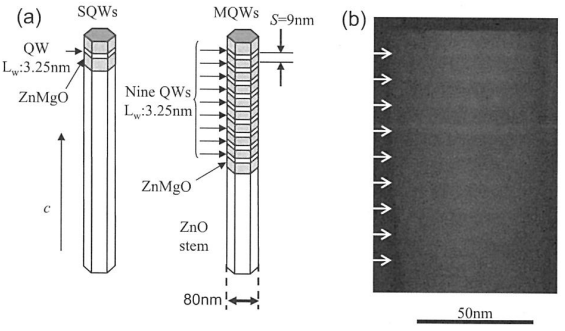

Fig. 3 Schematic of ZnO single-quantum-well structures (SQW_S) and multiple-quantum-well structures (MQW_S). (b) TEM image of MQW_S.

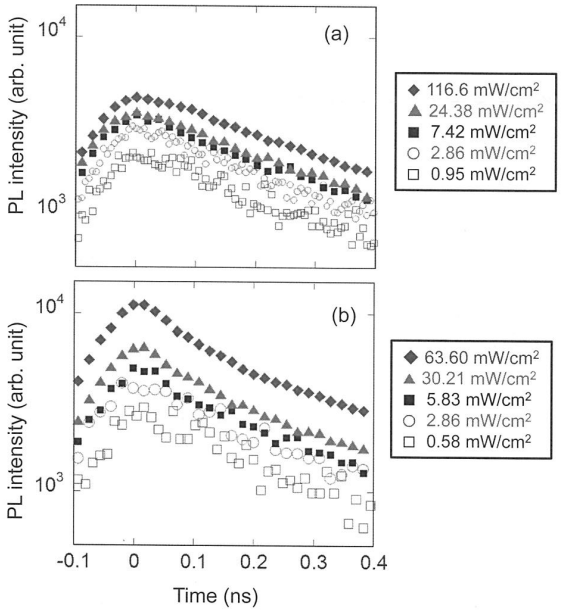

Fig. 4 Time resolved PL intensities of SQW_S and MQW_S.

3. ドレストフォトンナノポリッシング

従来の表面平坦化手法は，機械化学研磨(Chemical Mechanical Polishing: CMP)が用いられている．この手法は，研磨パットと被研磨物を機械的に接触して研磨するため，表面粗さの低減に限界があり，また研磨傷の生成を避けることができない．

上記の諸問題を解決する手法がドレストフォトンナノポリッシング(Dressed Photon Nano-Polishing: DPNP)である[14]．合成石英を用いてDPNPの詳細を述べる．合成石英のエッチングガスとしては塩素ラジカル(Cl^*：塩素分子が分解されたもの)がある．合成石英とは反応しない塩素分子(光吸収端波長400 nm)雰囲気中に基板を導入し，光(波長532 nm)を照射する(Fig. 5 (a))．

この光の波長は光吸収端波長より長いので，塩素分子に吸収されずCl^*は発生しない．一方，この光により，基板表面の局所的な凸部にDPが発生すると，フォノン援用過程によるエネルギー上方変換された光(短波長の光)によって塩素分子は分解しCl^*が発生する(Fig. 5 (a))．その結果，このCl^*が合成石英と反応し，凸構造のみがエッチングされ基板が平坦化される．そして，最終的に基板に凸部がなくなるとDPは発生しなくなるため，反応が自動的に停止し余計なエッチングを防ぐことが可能となる(Fig. 5 (b))．

上記原理を利用した合成石英平面基板の平坦化について紹介する．合成石英基板は，高出力レーザーや短波長用光源の光学素子としての利用が期待されており，高性能化のためには，R_a値を1 Å以下に低減することが望まれている．

表面粗さR_a値の評価方法には，原子間力顕微鏡(AFM)を用いた．基板エッチングのためのガスには塩素を選択し，塩素導入後のチャンバーの圧力を100 Paとした．照射光源についてはレーザー(波長532 nm)を使用した．

Fig. 6はDPNPエッチング前(Fig. 6 (a))と後(Fig. 6 (b))のAFM像の比較を示している．この比較像より表面の凹凸が低減することが明らかである．さらに，このAFM図の変化をより詳細に比較するために，それぞれの像における断面図をFig. 6 (c)に示す．この図からピーク－バレー値が近接場光エッチングによって1.2 nmから0.5 nmに減少していることが分かる．エッチング後のR_a

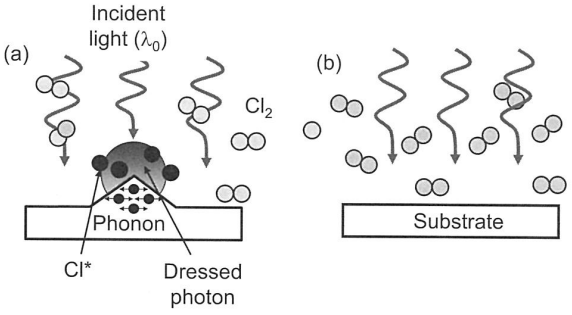

Fig. 5 Schematic of DPNP. (a) Before and (b) after DPNP.

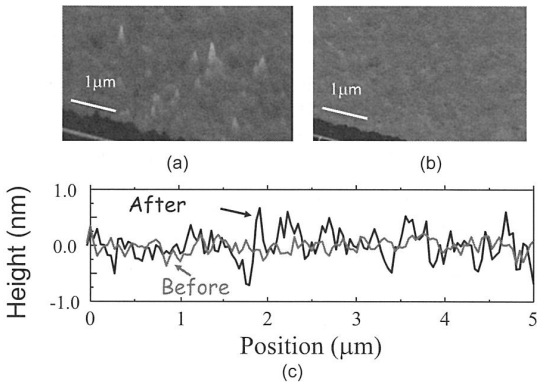

Fig. 6 AFM images of (a) before and (b) after DPNP. (c) Cross-sectional profiles of (a) and (b).

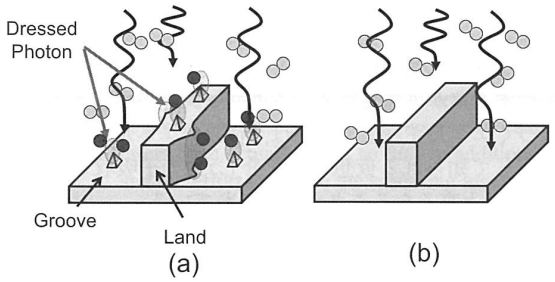

Fig. 7 Schematic of DPNP on three-dimensional substrate.

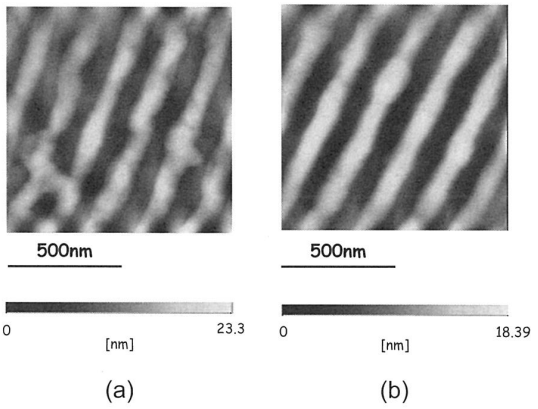

Fig. 8 AFM images of (a) before and (b) after DPNP on grating structure.

値として最小1.1 Åであった.

DPは基板表面に光が照射されていれば発生するため,平面基板以外の3次元形状を有する素子に対しても平坦化が可能であると期待される(Fig. 7 (a)およびFig. 7 (b)). 3次元構造を有する基板には,ナノインプリントにより作製されたソーダライムガラスのナノウォール基板を用いた[6]. Fig. 8 (b)は,30分間DPNPを施した後のAFM像を示す. この結果から,ランド部のR_a値は0.68 nmから0.36 nmに低減し,同様にグルーブ部のR_a値は0.76 nmから0.26 nmに低減しており,3次元構造の平坦化が実証された[15].

4. まとめと今後の展望

本稿ではZnO量子構造を用いたナノフォトニックデバイスへの応用について解説した. 本稿で述べたデバイスの特長は,半導体量子構造による「量的」に変革された微小なデバイスということだけではなく,伝搬光を用いたのでは駆動することのできない機能を持つ「質的」に変革されたデバイスということである. 今回は1次元構造による単純な構造でのエネルギー移動の観測および制御を行ったが,本構造は,結晶性・寸法の制御性にも非常に優れており,ナノフォトニックスイッチに限らず,さらに複雑で高機能なナノフォトニック機能デバイス(集光器[16]やパルス発生器[13]など)の実現に理想的な系であると考えられる.

本稿ではDPを利用することで可能となる全く新しい加工方法について紹介した. DPがナノ構造のみに局在するという特長を利用することで,従来のCMP法では到達不可能な表面性が得られることで,電子デバイス,光デバイスにおける,エネルギー利用効率の大幅な向上が期待される. さらに,本手法は光化学反応を利用したものであるため,本稿で紹介した材料意外にも応用可能である. また,従来の加工法では不可能であった,中空構造の内壁の平滑化が可能になるなど様々な応用が期待される. 上記に述べたように,DPを利用することで,従来の伝搬光を用いた光技術では原理的に実現不可能な現象が実現可能になる,つまり光技術のパラダイムシフトが達成されると期待される.

謝　辞

本研究の一部は,科学研究費助成事業(若手研究(A))(平成23年度～平成25年度),東電記念財団研究助成(基礎研究)(平成23年度～平成24年度),NEDO省エネルギー革新技術開発事業・先導研究フェーズ「近接場光エッチングを用いた光学素子用基板表面のサブナノ平坦化技術の開発」(平成20年度～平成22年度),NEDO省エネルギー革新技術開発事業・挑戦研究フェーズ「近接場光相互作用を用いた自己完結型超平坦物質形成技術の開発」(平成21年度～平成23年度)の援助の基に行われた.

本研究を遂行するにあたり,多大なる協力を頂いた有益な議論を頂いた石川 陽博士(山梨大学),小林 潔教授(山梨大学),川添 忠博士(東京大学),野村 航博士(東京大学)の各氏に深く感謝致します. 本稿で紹介させていただいたオングストローム平坦化の研究についてデータをご提供下さった多幡 能徳,平田 和也(シグマ光機(株)),基板を供給頂いた吉本 護教授(東京工業大学)の各氏に深く感謝致します.

参考文献

1) A. Sato, Y. Tanaka, F. Minami, and K. Kobayashi: J. Luminesc. **129** (2009) 1718.
2) M. Ohtsu, T. Kawazoe, T. Yatsui, and M. Naruse: IEEE J. Select. Top. Quantum. Electron. **14** (2008) 1404.

3) T. Kawazoe, K. Kobayashi, S. Sangu, and M. Ohtsu: Appl. Phys. Lett. **82** (2003) 2957.
4) T. Kawazoe, H. Fujiwara, K. Kobayashi, and M. Ohtsu: IEEE J. Select. Top. Quantum. Electron. **15** (2009) 1380.
5) H. D. Sun, T. Makino, Y. Segawa, M. Kawasaki, A. Ohtomo, K. Tamura, and H. Koinuma: J. Appl. Phys. **91** (2002) 1993; D. C. Reynolds, D. C. Look, B. Jogai, C. W. Litton, G. Cantwell, and W. C. Harsch: Phys. Rev. B **60** (1999) 2340.
6) W. I. Park, G. C. Yi, M. Y. Kim, and S. J. Pennycook: Advanced Materials **15** (2003) 526.
7) T. Yatsui, M. Ohtsu, J. Yoo, S. J. An, and G. C. Yi: Appl. Phys. Lett. 1 2002 **87** (2005).
8) T. Yatsui, S. Sangu, T. Kawazoe, M. Ohtsu, S. J. An, J. Yoo, and G.-C. Yi: Appl. Phys. Lett. **90** (2007) 223110.
9) R. H. Dicke: Phys. Rev. **93** (1954) 99.
10) H. M. Gibbs, Q. H. F. Vrehen, and H. M. J. Hikspoors: Phys. Rev. Lett. **39** (1977) 547.
11) N. Skribanowitz, I. P. Herman, J. C. MacGillivray, and M. S. Feld: Phys. Rev. Lett. **30** (1973) 309.
12) K. Miyajima, Y. Kagotani, S. Saito, M. Ashida, and T. Itoh: J. Phys: Condensed Matter **21** (2009) 195802.
13) T. Yatsui, A. Ishikawa, K. Kobayashi, A. Shojiguchi, S. Sangu, T. Kawazoe, M. Ohtsu, J. Yoo, and G. C. Yi: Appl. Phys. Lett. **100** (2012) 233118.
14) T. Yatsui, K. Hirata, W. Nomura, Y. Tabata, and M. Ohtsu: Appl. Phys. B **93** (2008) 55.
15) T. Yatsui, K. Hirata, Y. Tabata, Y. Miyake, Y. Akita, M. Yoshimoto, W. Nomura, T. Kawazoe, M. Naruse, and M. Ohtsu: Appl. Phys. B **103** (2011) 527.
16) T. Kawazoe, K. Kobayashi, and M. Ohtsu: Appl. Phys. Lett. **86** (2005) 103102.

レーザーワード

フォノン援用エネルギー上方変換(phonon assisted energy up-conversion)

近接場光は単に局在しているものと捉えるのではなく，物質励起と光子が結合した場(ドレスト光子)と考えることが適切である．このドレスト光子は，さらにコヒーレントなフォノンとも結合しうることで，従来励起不可能であった電子基底準位中のフォノン準位が励起可能となり，電気双極子許容となった実在の準位を介した多段階遷移が可能となる．このフォノン援用励起過程に基づくエネルギー上方変換は，従来のエネルギー上方変換として知られる仮想準位を介した2光子吸収と比較して3桁以上高くなることが確認されている．　(八井 崇)

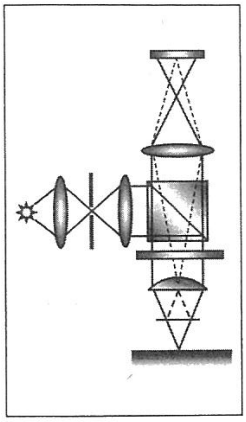

ドレスト光子の発生と基盤技術としての展開

東京大学 大学院工学系研究科及びナノフォトニクス研究センター
大津元一

1．はじめに

本特集の主旨に従い，本稿では筆者が長年携わってきた研究を通じ革新的技術の研究開発のヒントなどについて記したい。従って単なる技術紹介ではなく，主観にもとづく私見を交えた記事となることをご了承頂きたい。

光科学技術は二つに分類される。その一つは「光を道具として使う」科学技術であり，現在の光科学技術の殆どがこれに属する。すなわち光応答特性に優れた材料，デバイス，装置を研究開発する科学技術であり，それは材料科学技術の手法に基づいている。これらにより光メモリ，ホログラフィ，光源デバイス、センサなどが開発されてきた。また，光源の短波長化，短パルス化，高パワー化などの技術開発も，そのために適した材料の研究が決め手となっている。

他方，「光を研究する」科学技術も僅かながら存在する。ただしこれは波動方程式の精密解法・近似精度の向上の研究などでは決してない。また，光の量子的特性の記述と応用でもない。新しい概念と理論が必要な光を作り出し使う科学技術である。その代表例としては，レーザーが発明された前後に進展した光の量子論があり，それによりレーザー光がもたらす現象が説明されたり，量子力学理論が検証され，現在に至っている。この科学技術は光を古典論的に扱うか量子論的に扱うかという新しい概念とそれに伴う理論体系を創出した。

本稿で取り上げるのは「光を研究する」数少ない科学技術の一つである。ただしここでは上記のような「古典論 vs.量子論」ではなく，「ナノ vs.マクロ（巨視）」という対比で扱う。すなわち，ナノ寸法領域に発生するドレスト光子（dressed photon）と呼ばれる光の研究である。その際，光の量子論も必要となるが，それ以上に新概念と理論の構築が必須である。そのための基礎研究を経て，最近では多様な応用に使える基盤技術が展開されている。

下記には逐次参考文献を付記すべきであるが，膨大な数となる為，紙数の制限から本稿末尾に 5 編のみを掲げた。詳細はこれら及びその中の引用文献を参照されたい。

2．きっかけと考え方

本研究開発は「小さな光を発生させたい」という 1980 年代初頭の筆者の素朴な希望がきっかけとなって始まったので wants 型研究といえる。すなわち社会の needs に応えたり，応用の seeds を作る研究ではない。その結果生まれたのがドレスト光子と呼ばれる仮想粒子の概念である [1-3]。1990 年代冒頭にはこの仮想粒子が再現性よく発生するようになり，筆者は当時これを近接場光と命名した。これはファイバプローブ先端などの小さな物質（寸法は光波長以下）表面にしみ出し，遠方には飛んでいかない光である。その寸法は物質寸法程度なので，これを光源として使うと回折限界を超えた分解能をもつ光科学技術が可能となる。なお，「近接場光」という用語は最近では国語辞典にも掲載されている [4]。日本発の概念が文化の指標としての国語辞典に加えられたことを知り，感慨深い。

さて，ここで重要なのは近接場光の概念はニュートンの粒子説の描像，アインシュタインの光量子

説の描像とは異なること，従って「古典論 vs.量子論」の対比では扱えないことである。すなわちこれらの両説で記述するのは自由空間または巨視的物質中に存在する伝搬光にすぎず，従ってその波数 k と位置 x の不確定性 Δk，Δx の間の関係 $\Delta k \cdot \Delta x > 1$ において $\Delta x >> \lambda$（光の波長）であることから $\Delta k << k$ となり，光の波数（光子の運動量）は精度よく確定する。従って光およびそれと相互作用する物質のエネルギーは波数 k の関数により，すなわち分散関係により表される。それに対しドレスト光子では $\Delta x << \lambda$，従って $\Delta k >> k$ であり，波数，運動量は確定しない。

一方，光と物質の寸法がナノまたは巨視的である場合に分けて光科学技術をまとめると表１のようになる。この表の第二行にはナノ寸法物質を用いる光科学技術を掲載しているが，これはドレスト光子を用いるもの（項目 A）と伝搬光を用いるもの（項目 B）とを含む。その差異を見極めるには波数（運動量）が確定しているか否を調べればよい。伝搬光を用いる場合（項目 B）は波数（運動量）が確定している。これは巨視的物質を用いる従来の光科学技術と同等の「光を道具として使う」科学技術である。その代表例として，フォトニック結晶，プラズモニクス，メタマテリアル等が有り，これらの科学技術では上記の分散関係が多用されている。他方，項目 A ではドレスト光子が使われており，波数（運動量）が不確定である．言い換えるとナノ寸法領域では光の量子化のために空間に仮定する共振器が定義できないので，新概念，新理論が必要である。なお，筆者はこれを応用した技術を 1993 年に提案しナノフォトニクスと命名したが[5]，最近では項目 B の科学技術もナノフォトニクスと称する傾向が見られるので，差異を明確にするため最近では前者をドレスト光子工学と称している。以上を要するに表１中の「項目 A vs.項目 B，C」が「ナノ vs.マクロ（巨視）」の対比に他ならない。

表１　使用する光と物質の寸法による光科学技術の分類

	ドレスト光子	伝搬光
ナノ寸法物質	A ドレスト光子工学 （ナノフォトニクス）	B フォトニック結晶， プラズモニクス， メタマテリアル
巨視的寸法物質	----------	C 既存の光科学技術

ドレスト光子工学は「光」技術と言うよりも，むしろ「光・物質融合」技術と言うほうが適切である。なぜならばドレスト光子はナノ寸法物質が無いと発生しないからである。この技術の本質は，ドレスト光子とナノ寸法物質との相互作用に起因する新現象・新機能を使い，回折限界を超えるのはもちろんのこと，従来の伝搬光を使ったのでは実現しないデバイス，加工，システムを開発し，技術の質的変革を実現することである。その原理は従来の光学原理（波動，回折理論）ではなく，光科学，場の理論，凝縮系物理学の概念を統合し構築されている。

近接場光という用語はナノ寸法物質表面近傍に存在する場の空間的特性を表すには適していると思われるが，物質との相互作用，エネルギーの授受の観点からは本質を表してはいない。また，これは無限平面という特異形状の上に発生する波動であるエバネッセント光とも全く異なる。その本質についての概念を構築するには量子論的手法を使うのが便利であり，共振器が定義できない不都合を克服した理論体系が開発されている。それによるとドレスト光子とはナノ寸法領域において光子と電子とが結合した仮想粒子である。これを光子の立場からみると物質としての電子のエネルギーの衣をまとった光子と考えられるが，これがドレスト光子と呼ばれる所以である。

伝搬光がナノ寸法物質１に入射し，その結果この物質中および表面にドレスト光子が発生する場合を考える。入射する伝搬光が単一周波数（単一の光子エネルギー）であっても，この物質１中および表面に発生する光を従来の概念で表すと，共振器が定義できないことから無限のモード数の光子の重

ね合わせになる。それに対応してナノ寸法物質中の電子（及び正孔）も無限のエネルギー準位をもつと考える必要がある。すなわちドレスト光子は時間軸上および空間軸上で変調された光子といえる。従ってドレスト光子の上側波帯と，それが発生するナノ寸法物質１の近隣にあるナノ寸法物質２中の電子が共鳴すれば，ナノ寸法物質 2 はドレスト光子の上側波帯のエネルギーを吸収して励起される。これを外部から観察するとドレスト光子発生用の低周波数の伝搬光によりナノ寸法物質２が励起されるので，光周波数上方変換と考えることができる。なおナノ寸法物質中には電子のみでなく結晶格子（フォノン）も存在するが，ドレスト光子はこのフォノンとも結合する可能性を有する。これによりドレスト光子はさらにフォノンのエネルギーの衣をまとう。特にこのフォノンはナノ寸法領域においてコヒーレント状態を形成することが顕著な特徴である。その結果形成される仮想粒子としてのドレスト光子フォノンは更に多数の変調側波帯を持ち，また，フォノンのコヒーレント状態は複数のフォノン数状態を含むので，ナノ寸法物質２がドレスト光子フォノンのエネルギーを吸収するとフォノンの高いエネルギー準位に効率よく励起され，質的変革をもたらす新しい反応が促進される。

３．応用展開の事例

前節の概念・原理に関する基礎研究とともに，各種の応用技術が展開された。その概要を加工，デバイス，システムに分けて略記しよう。

3-1 加工

3-1-1 リソグラフィ

フォトマスク開口表面に発生するドレスト光子フォノンを用いて紫外線用フォトレジストを感光させるリソグラフィ装置が開発された。ここでは前節に記したようにドレスト光子フォノンがもたらす光周波数上方変換機能を用いるため，光源は可視光である。光源として仮に紫外線を用いるとドレスト光子フォノンとともにフォトマスクを通過する微弱な伝搬光により紫外線用フォトレジストが感光するので，微細パターンは描画できない。すなわち本技術では高分解能を得る為には長波長の光を使った方が有利である。これは従来の光リソグラフィ法とは逆の指針であるが，これにより大型・大消費エネルギー・高価な短波長光源が不要になった。現にこの装置の光源は発光ダイオード１個のみでありその消費電力は僅か 5W である。この装置を使い，これまでに軟 X 線用光学デバイスをはじめ多様なデバイスが作成されている。

3-1-2　立体構造表面平滑化

ドレスト光子およびドレスト光子フォノンは上記のファイバプローブ，フォトマスクなどを使わなくとも一般に物質表面のナノ寸法突起部，物質内部のナノ寸法不純物表面などに発生する。これを利用し，各種物質表面を平滑化する新しい光化学エッチング法が開発された。従来の平滑化法は希少資源の一つである酸化セリウムなどの研磨材を用いた機械化学研磨法であるが，例えばガラス表面の面粗さの研磨後の値は 0.2nm 程度に留まっていた。それに対し本方法では面粗さが約 0.1nm まで減少し，それにともない，光耐性も著しく向上した。ここでは塩素や酸素などの気体分子を用い，物質表面にこれら分子の吸収エネルギーより低い光子エネルギー（吸収端波長より長波長）を有する伝搬光を照射すると，突起部のみにドレスト光子フォノンが発生し，それが分子を解離する。解離の結果発生した活性原子が突起部を選択的にエッチングするので，光照射とともに平滑化が始まり，突起部が消滅すると終了する。すなわち自律的な加工法であり，立体構造・大面積の表面，曲面，側面など，伝搬光の到達する部位は必ず研磨される。また研磨対象もガラスなどのアモルファス物質のみでなく，結晶，樹脂，金属など多岐にわたる。この装置を使い，高パワーレーザー用の光学素子，ハードディスク，フォトマスクなどが平滑化されている。

3-2 デバイス

3-2-1 シリコン発光・受光デバイス

前項（3-1）では物質表面に発生するドレスト光子フォノンが自律的に消滅することを利用した。これに対し，物質内部のナノ寸法の不純物周囲にドレスト光子フォノンを自律的に発生させる加工法が考案された。これにより間接遷移型半導体の代表例であるシリコンが直接遷移型化し，赤外および可視発光ダイオード，レーザー，さらには広帯域フォトダイオードが世界に先駆けて開発された。従来これらの光デバイスには直接遷移型の化合物半導体が使われ，動作波長に対応するバンドギャップエネルギーをもつ半導体を探索・開発するという材料科学技術の手法が用いられてきた。これに対し本方法では動作波長は材料によらず加工の際に照射する光の光子エネルギーにより制御することができる。これは材料探索・開発・加工の科学技術からの解放を意味し，希少資源保護，自然環境保全，省エネルギーなどの観点で有利である。なお，同様な方法で高効率の太陽電池も実現している。

3-2-2 ナノ光デバイス

半導体のナノ寸法物質中の電気双極子禁制準位を利用したエネルギー移動と散逸を使い，デジタル論理演算を行うナノ光デバイスが開発された。これは特定の寸法比をもつ二つの InAs ナノ微粒子を GaAs 層中に埋め込み，メサ加工をした NOT 論理ゲートおよび AND 論理ゲートデバイスであり，室温動作する。これは回折限界を超えた小寸法とともに超低消費エネルギー（CMOS デバイスの 10^{-4}），耐タンパー性，信号伝送の自律性など，従来の光デバイスにはない性質を有している。この他，上記デバイスの原理を応用したナノ集光器，エネルギー伝送路，遅延帰還型パルス発生器など，各種デバイスが開発されている。また，このデバイスの動作原理は光エネルギー変換にも利用されている。

3-3 システム

上記（3-1），（3-2）の技術を組み合わせ，短パルス光診断装置，情報セキュリティ装置，光ルータ装置，さらには（3-2-2）のデバイスの動作特性が生体系中のエネルギー移動機構と類似していることに注目し，非ノイマン型コンピューティングが提案されている。

以上の応用展開の事例を総括すると図１のようにまとめられる。

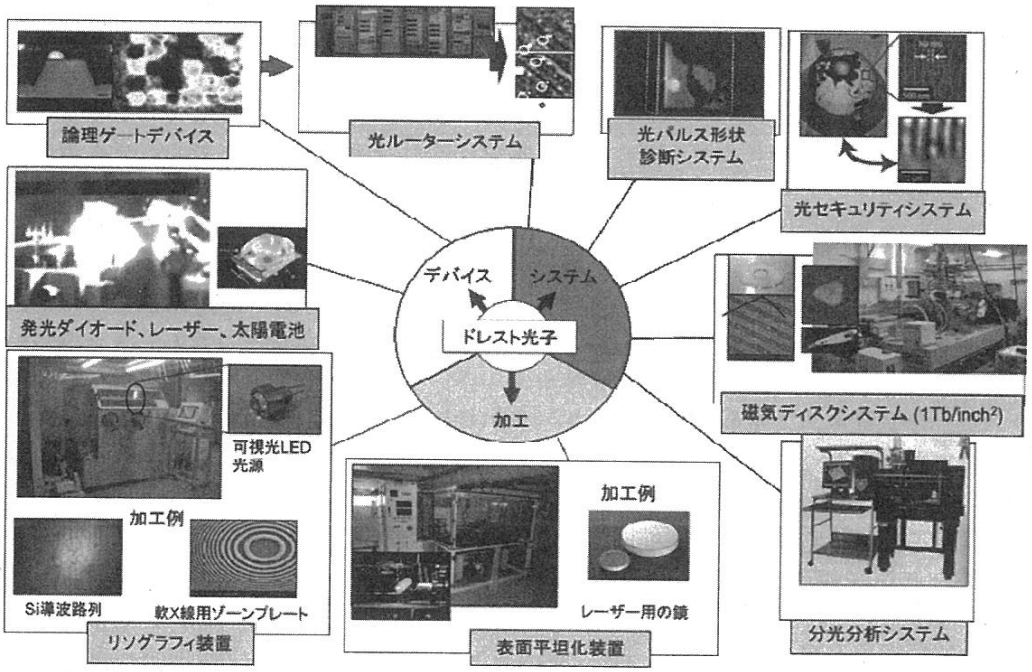

図１　これまでの応用展開の主要な事例

4．ヒントとまとめ

科学技術が社会にとって価値のある工学へと進展する為には，概念と原理が独創的であることが本質である。それに加え，その応用展開が既存技術の全てを置き換える包括的技術（generic technology）になることが必須である。この観点から本技術を概観すると，まず概念と原理が独創的であることは疑いが無い。なぜならそもそもwants型研究から開始したからである。開始当時には光の寸法をナノ化するという酔狂な提案は他にはなかった。

なお，この基礎研究を進展させる過程で，ファイバプローブやフォトマスクの使用は応用範囲を限定することがわかった。すなわちドレスト光子をファイバプローブの先端に無理して発生させることはドレスト光子を囲い飼いするようなものである。ドレスト光子はどこにでも発生するので，いわば自然に放ち，放し飼いしてその自律的発生，消滅を広域的に制御することが利用の本質である。これによって応用展開はプローブ顕微鏡といった特殊な計測技術ではなく，加工，デバイス，システムの広い分野に展開した。いわば技術の局所化ではなく大局化が実現し，包括的技術が開花した。現在すでに産学連携による実用化が進んでおり，この技術はもはや花の種の時代を過ぎ，芽，つぼみの段階に達している。今後包括的技術として大きく開花させるためには，原理の詳細をさらに研究すること，そのためにはこれまでの光科学技術では使われていない非平衡解放系の統計力学，数理科学の手法などが重要になると思われる。

本稿で取り上げた話題は新しい光科学技術の一例であるが，このような新分野を確立するためには概念・原理の独創性が必須である。そのためにいくつかの「如何に（how?）」の問いと主観的なコメントを次に列挙するが，これがヒントになれば幸いである。

(1) 流行している耳障りのよい研究課題に対し自分の研究課題を如何に遠ざけるか？（流行の研究課題と結びついた瞬間に独創性は断たれる。）
(2) 世界の研究動向を調査しそれをもとに研究課題を選ぶという方針を如何に避けるか？（研究をする前に論文や資料を読みすぎると後追い研究しかできない。）
(3) 人まねを如何に見抜くか？（「---という技術は---という人が発明した」の文中の---に入る正しい言葉を見いだすことが必要である。第一人者を標榜する人物よりも以前に，その概念を提案した真の発明者がいる場合がある。それを如何に見極めるかが，科学技術を「学ぶ」のではなく「創る」ための本質である。）
(4) 狭い研究分野を守るために研究者の仲間内で褒め合っていることを如何に見抜くか？（論文の被引用件数は必ずしも独創性の指標ではない。むしろダウンロード件数に注意すべきである。）
(5) 技術の量的変革ではなく「質的変革」を如何に追求するか？
(6) 自分の能力を補完する人と如何に協力するか？
(7) 知財の拡散を如何に防ぐか？
（概念・原理の原著論文をいち早く出版した後，応用に関する論文の出版時期を知財の観点から如何に遅らせ，さらに特許出願の内容と時期を如何に制御するか？）
(8) 独創的な研究成果を如何に既存の用語で説明し従来派にアピールするか？
（これまでの新しい概念・原理の多くは従来のものを多少手直しして創られてきた。従って従来の科学技術との接点はある。必要以上に革新性にこだわるのは邪道である。）
(9) 如何に多くの新しい実験結果を生み出すか？
（たとえばファイバプローブを用いた計測の実験結果のみを手にしている限り，ドレスト光子の概念・原理には到達しない。新しい概念・原理に関する発想は従来の議論では説明できない多数の新しい実験結果を手にした時点からわき上がってくる。）

上記の問いが示唆するように「何を（what?）研究開発するか」，よりも「如何に（how？）研究開発するか」が重要である。あえてwhat？について言えば，「何を研究しないか？」について熟考すべきである。これらをもとに，自身が多数派に巻き込まれないよう注意することが決め手となる。

本稿の第3節では光科学技術の応用展開事例を紹介した。これは大学などの基礎研究者が産業界と連携して推進すべきものである。ただし両者の間には大きな考え方の違いが有り，その溝は未だに埋まっていない。これらは両者独特の深い思い込みの差に起因するが，これらの思い込みは往々にして的を得ていない場合がある。

謝辞

筆者の能力不足を補完して頂いた内外の多くの研究者・技術者諸氏，また研究を支援して頂いた各省庁，さらに産学連携に参画頂いた企業の関係各位に深くに感謝します。なお本稿で紹介した産学連携事業による応用展開事例の多くはNPOナノフォトニクス工学推進機構の調整により実施された。

参考文献

1) M. Ohtsu, "Nanophotonics", *Progress in Nanophotonics* I, ed. by M. Ohtsu, Springer-Verlag, Berlin, 2011, pp.1-58.
2) T. Yatsui, *Nanophotonic Fabrication*, Springer-Verlag, Berlin, 2012, pp.1-124.
3) 大津元一，ドレスト光子（朝倉書店，東京，2013）
4) 松村明（編），大辞林，第3版（三省堂，東京，2006）
5) 大津元一，"ナノフォトニクスの誕生の瞬間，これまで，今後"，ナノフォトニクス創成20周年記念シンポジウム予稿集（応用物理学会・日本光学会・ナノオプティクス研究会，2012），pp.1-2.

大津元一　OHTSU, Motoichi
東京大学 大学院工学系研究科 教授（兼）ナノフォトニクス研究センター センター長
〒113-8656　東京都文京区弥生2-11-16

もし「光ロスが発生しない光学材料」が実用化されたら世の中はどう変わるのか？

八井　崇，大津 元一　　東京大学　工学系研究科

〒113-8656 東京都文京区弥生 2-11-16，Tel：03-5841-0406，Fax：03-5741-0416，E-mail： yatsui@ee.t.u-tokyo.ac.jp

1　はじめに

本稿のタイトルは，編集者の方から与えて頂いたものであるが，著者は，まさにこの「光ロスが発生しない光学材料」を実用化したいと近年取り組んできているので，その内容について紹介したい。なお，我々が光ロスを低減することを取り組んだ当初は，「光を有効活用することで省エネルギー社会を実現したい」という願いであったが，本稿で紹介する我々の成果によって，世の中をもっと変えられる可能性が産まれたのではないかと考えている。

2　光ロスとは

光学材料における光ロスは大きく分けて，吸収と散乱に分けられる。吸収を減らすために，紫外域まで透明な材料の開発が多くなされており，可視域での吸収はほぼゼロにまで近づこうとしている。しかしながら，理想的には吸収が少ない材料ができたとしても，生産コストが大きくなったり，重くなってしまって持ち運びができなくなるなど，生産性の問題から全ての用途に万能な透明材料を作るのは困難となっている。この原因は，あらゆる材料はナノ寸法以下の材料からできているためであり，表面が完全に平坦で，かつ均一な完全結晶を作ることは不可能である。その表面の凹凸な材料内部の不均一性に起因する光散乱を抑制するのは困難であるので，逆手に取って透過光を増やすことだけでも，ノート PC のバッテリーの駆動時間が飛躍的に伸びたことも知られている。

3　近接場光エッチング

著者らは，上記の光散乱を低減するために，近接場光エッチングによる表面平坦化技術を開発した。この近接場光については，近年これをデバイス，加工に用いることで，デバイス寸法や加工寸法が光の回折限界を超えて微小化可能となっている[1)]。さらに，従来の光技術では実現不可能だった新機能，新現象が可能となっている。その代表的な特長は，光学禁制遷移が可能となることである[2)]。その結果，従来光によって励起不可能であるフォノン準位を励起可能となるため，このフォノン準位を介したエネルギー上方変換が達成可能となる。この近接場光エネルギー上方変換は，実在準位を介した遷移となるため，例え入射光パワーが低い場合であっても高効率にエネルギー上方変換が実現し，第 2 次高調波発生のための 2 光子吸収過程によるエネルギー上方変換の発生効率と比較して，三桁以上高くなることが確認されている[3)]。この近接場光の特長を活かした加工技術が近接場光エッチングであり，この手法によって，原子レベルでの表面平坦化が実現している。

従来の表面平坦化手法は，機械化学研磨（Chemical Mechanical Polishing：CMP）が用いられている。この手法は，研磨パットと被研磨物を機械的に接触して研磨するため，表面粗さの低減に限界があり，また研磨傷の生成を避けることができない。さらに，より平坦化を実現するために，酸化セリウム（レアアースであるセリウムの酸化物）に代表される研磨剤を使用しているが，近年レアメタルの供給問題が大きな問題となっており，研磨剤不要の平坦化手法の開発が急務となっている。

上記の諸問題を解決する手法が近接場光エッチングである[4]。合成石英を用いて近接場光エッチングの詳細を述べる。合成石英のエッチングガスとしては塩素ラジカル（Cl*：塩素分子が分解されたもの）がある。合成石英とは反応しない塩素分子（光吸収端波長 400nm）雰囲気中に基板を導入し，光（波長 532nm）を照射する（図 1(a)）。

この光の波長は光吸収端波長より長いので，塩素分子に吸収されず Cl* は発生しない。一方，この光により，基板表面の局所的な凸部に近接場光が発生すると，フォノン援用過程によるエネルギー上方変換された光（短波長の光）によって塩素分子は分解し Cl* が発生する（図 1(a)）。その結果，この Cl* が合成石英と反応し，凸構造のみがエッチングされ基板が平坦化される。そして，最終的に基板に凸部がなくなると近接場光は発生しなくなるため，反応が自動的に停止し余計なエッチングを防ぐことが可能となる（図 1(b)）。本手法の特長としては，そもそもの目的である表面が平坦になることに加えて，機械研磨によって避けられなかった基板への損失の心配がなくなること，CMP では必要不可欠であったレアアースが不要となること，3 次元形状の平坦化に対しても平坦化が可能となること，など様々な付加価値がある。

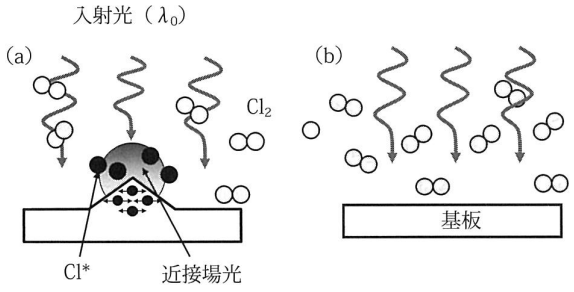

図 1　近接場光エッチングの概念図

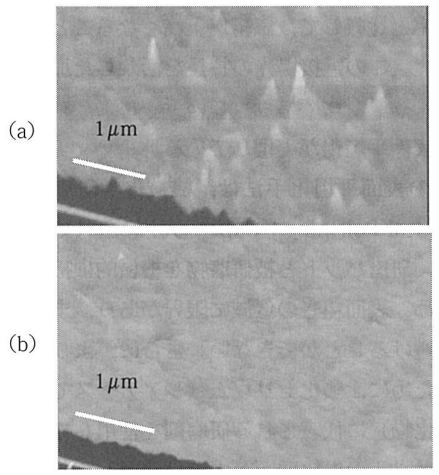

図 2　近接場光エッチング前（a）および後（b）の合成石英基板表面の AFM 像

図 2 は近接場光エッチング前（図 2(a)）と後（図 2(b)）の原子間力顕微鏡（AFM）像の比較を示している。この比較像より表面の凹凸が低減することが明らかである。エッチング後の AFM 像から得られる表面粗さ *Ra* 値として最小 1.1 Å であった。また，本技術によって平坦化された基板を用いて光学ミラーを作製したところ，世界最高のレーザー耐性を実現することに成功した。

本技術では，研磨パッドを利用していないため，平面基板のみならず，グレーティング基板の平滑化（図 3）にも成功している[5]。

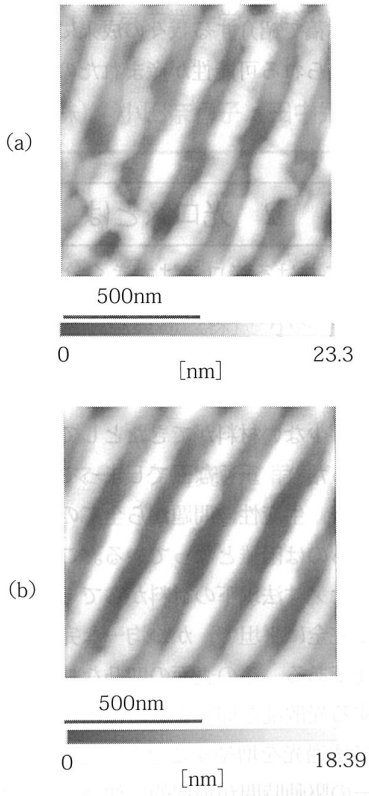

図 3　近接場光エッチング前（a）および後（b）の合成グレーティング構造基板表面の AFM 像

4　超平坦化基板の展開

本稿では近接場光を利用することで可能となる全く新しい加工方法について紹介した。近接場光がナノ構造のみに局在するという特長を利用することで，従来のCMP法では到達不可能な超平坦面が得られる。本技術によって，当初の目論見通り，光散乱によるロスが存在しない材料が実現可能となるであろう。その結果として，光の利用効率が向上するため，ディスプレイや照明などの省エネルギー化が可能となる。

さらには，派生効果として，光源の高効率化が期待される。特に極端紫外光の光源は波長が13.4nmと極端に短いため，表面凹凸の影響が可視光光源と比較して桁違いに大きくなってしまう。原子オーダーで平坦化が可能な近接場光エッチングによって，極端紫外光源に使用される光学素子が超平坦化されるため，光源の高出力化が可能となる。その結果，これを使用する半導体リソグラフィ装置のスループットが大幅に向上すると期待される。

近年，光学素子は，従来の光学機器以外での応用も盛んである。一例として，車のエンジン用点火プラグを高出力なセラミックレーザによって置き換えようという試みがなされている。着火式のプラグと比較して，光の集光によって，高効率な燃焼効率が得られるため，自動車の燃費向上が期待される。セラミック材料はガラスと比較して非常に硬いため，従来の研磨では平坦化が難しい。これを近接場光エッチングにより平坦化することで，セラミックレーザの低消費電力化が期待される。

近接場光エッチングは，元々「光学ロス」を低減することを目的に開発を進めてきていたが，本技術は多種多様な材料に適用可能であることがわかっている。その一つとして，電子材料の表面化も可能となるので，「光子」のみならず「電子」の散乱ロスも低減されると期待される。本技術の発展により，半導体デバイスの高性能化が達成されるため，さらなる省エネルギー化社会の実現が期待される。

本稿で紹介した研究は（a）NEDO　エネルギー使用合理化技術戦略的開発「近接場光エッチングを用いた光学素子用基板表面のサブナノ平坦化技術の開発」（H20-H22），（b）NEDO省エネルギー革新技術開発事業「近接場光相互作用を用いた自己完結型超平坦物質形成技術の開発」（H21-H23），（c）MEXT平成22年度レアアース等利用産業等設備導入補助金（H22-H23），（d）先端的低炭素化技術開発（ALCA）探索ステージ（H23-H24）の一環として行われたものである。

参考文献

1）M. Ohtsu, T. Kawazoe, T. Yatsui, and M. Naruse, IEEE J. Select. Top. Quant. Electron., **14**, 1404 (2008) [Invited Paper]

2）Y. Tanaka and K. Kobayashi: Physica E, **40**, 297 (2007)

3）T. Kawazoe, H. Fujiwara, K. Kobayashi, and M. Ohtsu, IEEE Journal of Selected Topics in Quantum Electronics, 15, 1380 (2009)

4）T. Yatsui, K. Hirata, W. Nomura, Y. Tabata, and M. Ohtsu, Appl. Phys. B: Lasers and Optics, **93**, 55 (2008)

5）T. Yatsui, K. Hirata, Y. Tabata, Y. Miyake, Y. Akita, M. Yoshimoto, W. Nomura, T. Kawazoe, M. Naruse, and M. Ohtsu: Appl. Phys. B-Lasers and Optics, **103**, 527 (2011)

特定非営利活動法人
ナノフォトニクス工学推進機構

ドレストフォトン表面平坦化装置

装置概要

本装置は，ナノ寸法の光であるドレストフォトンと，それがもたらすフォノン援用励起過程によって，表面凹凸を選択的に除去する，革新的な表面平坦化加工装置です．

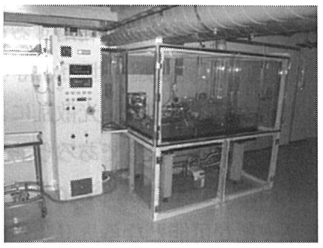

特徴

■原子寸法レベルでの基板表面平坦化が可能
■基板が平坦化されると自動的に加工が止まる自己組織的加工手法のため，使用が簡便
■非接触加工法であるため，3次元構造の側面や中空構造の内壁面などの加工が可能
■加工中リアルタイムで平坦化のモニタが計測可能

仕様

■最小表面粗さ(Ra値)：1.5A(合成石英の場合)
■一括加工可能面積：100mmφ
■標準光源：DPSSレーザ(発光波長532nm，出力光パワー2W)

加工応用例

■光学ガラス(合成石英)，結晶基板(シリコン，GaN)，プラスチック等各種基板
■平面基板，曲面基板など各種形状
■グレーティング構造の側壁
■その他(中空構造の内壁，マイクロレンズ)

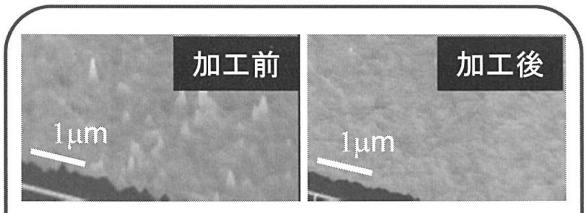

合成石英平面基板

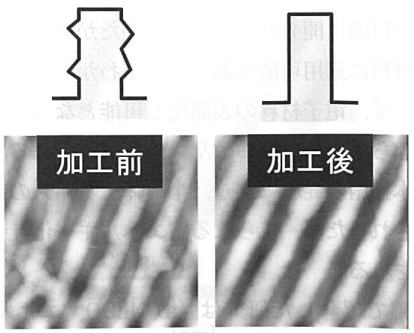

グレーティング構造のバリ取り加工
周期170nm，高さ10nm

お問い合わせ先

特定非営利活動法人　ナノフォトニクス工学推進機構　URL: http://www.nanophotonics.info/

近接場光を用いたナノ光情報システム

竪　　直也[*1]・成瀬　　誠[*2]・大津元一[*3]

1．はじめに

光が示す物理現象は，強度，波長，位相，偏光などの多様な物理量で表現され，「光情報処理」という観点において，光は多次元の情報媒体として活用される[1]．光速性，空間並列性，多次元性といった光の物理的性質を利用する光情報処理とその関連分野は，光通信技術および光記録技術を旗頭に，1980年代以来の高度情報化社会の発展を担ってきた．その一方で，いわゆる「伝搬する光」はマクロスケールにおいては波長という物理量をもつ波動であり，より一層の高速化・高密度化に加え，省エネルギー化・省資源化までが求められる現代の情報化社会への寄与においては，その回折限界という物理的制約がネックとなる．筆者らは，光情報処理の概念に対して「伝搬しない光」近接場光[2]の特性を積極的に導入することで，「伝搬する光」がもつ回折限界の問題を解決する「量的変革」と，近接場光に特有のさまざまな現象を活用することで初めて体現される特徴的な光機能を実現する「質的変革」とを二本柱に据えた「ナノ光情報システム」の確立を目指している．本稿では，近接場光の活用により実装される光機能の「階層構造」に基づいて機能するナノ光情報システムの概要について述べ，近年筆者らが取り組んできたいくつかの実装例と共に，ナノ光情報システムの応用展開の方向性について紹介する．

[*1] Naoya Tate　東京大学大学院工学系研究科電気系工学専攻　特任研究員　博士(情報科学)
[*2] Makoto Naruse　情報通信研究機構　光ネットワーク研究所　フォトニックネットワークシステム研究室　主任研究員　博士(工学)
[*3] Motoichi Ohtsu　東京大学大学院　工学系研究科電気系工学専攻・ナノフォトニクス研究センター　教授　博士(工学)
Nano-photonic Information System based on characteristic behaviors of optical near-fields

2．ナノ光情報システムの概要

近接場光は，ナノ寸法の微粒子が光励起された際にその表面極近傍に発生する局在場であり，その本質はナノ物質中の素励起の衣を纏ったフォトン「ドレスト光子(dressed photon)」の振る舞いにある(図1)[2]．近接場光の空間スケールはドレスト光子同士の交換によって物質間相互作用の影響が伝達し得る空間の大きさで定義されるため，近接場光自体は波長という概念をもたない．ドレストフォトンの振る舞いによって決定されるナノ電子系の光学応答は，素過程の連鎖を辿ることでマクロな光学応答として取り出される．このとき，ナノ電子系における光学応答は近接場光源となる個々のナノ物質の物性とその形状およびサイズに依存し，マクロスケールに至るまでの素過程の連鎖は各ナノ電子系の空間配置および系全体を取り巻く環境系との相互作用に依存している．近接場

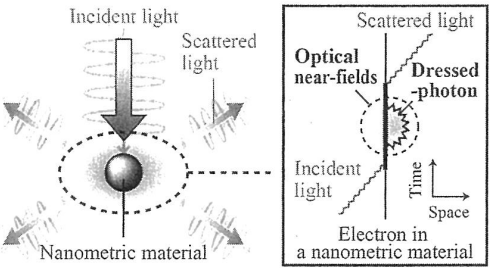

図1　ファインマン・ダイアグラムを用いた近接場光およびドレストフォトンの描像

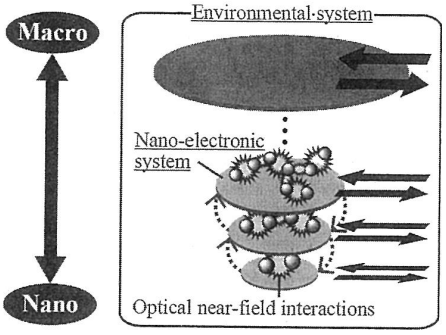

図２　階層構造に基づくナノ光情報システムの概要

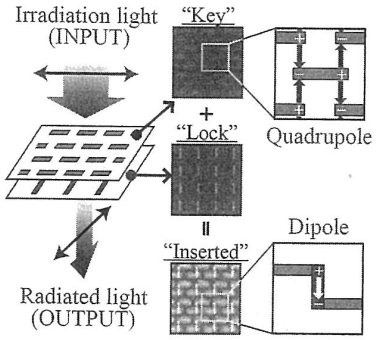

図３　電気四重極子-双極子変換に基づくナノフォトニックマッチングシステムの概要

光が示すさまざまな特徴的な性質を基礎とするナノフォトニクス[3]の要点は，まさにこのナノ電子系と環境系とを所望の機能に応じて相互に設計し活用することにある．

筆者らが提案するナノ光情報システムの概念はまさにこの要点に沿ったものであり，図２に示すように，その特徴はナノスケールからマクロスケールに至る情報空間の中でアクセス可能な情報レイヤーを複数定義した「階層構造」にある．このようなシステム構造においては微小スケールの階層で完結する作用とより大きなスケールの階層へと連鎖的に接続されていく作用とを独立に取り扱うことが可能であり，各作用にそれぞれ個別の機能を割り当てることで極めて多様な機能が多重的に集積された情報システムを実現できる[4]．特に，ナノフォトニクスの要点に基づき，構成要素となるナノ物質の寸法，形状，配置を制御することで，特異な光機能とそれらを組み合わせた階層構造の設計が可能である点が重要である[5]．

３．ナノ構造間近接場光相互作用を介した偏光変換技術に基づくナノ光認証システム

図３に示すように，ある方向に配向した直方体形状の微小構造群に対して同方向に偏光した光を照射すると各微小構造の物性に応じて表面電荷の分極が発生し，構造群全体としては図中の矢印で示されるような電気四重極子が形成される．このような構造群をもつレイヤーに対してちょうど互いの微小構造が直交するように別の構造群のレイヤーを積層すると，形成された電気四重極子が電気双極子に変換される．この変換は，光の照射により各微小構造のエッジ部分に誘起される近接場光分布を介したレイヤー間での表面電荷の移動とそれに伴う電荷分布の変化によるものである．ナノ電子系におけるこのような電気四重極子の影響は，マクロスケールにおいては互いに打ち消し合うために観測されることはないが，電気双極子に変換されることで偏光電場の放射という形で容易に観測されるようになる．マクロスケールでの光の入出力に着目すると，この電気四重極子-双極子変換はとりもなおさず光の「偏光変換」に相当する(位相制御に伴う「偏光回転」とは異なる)．

筆者らは，図３に示したような２種類の構造群をもつレイヤーをそれぞれ「鍵」と「鍵穴」に見立てた「ナノフォトニックマッチング」と称する認証システムを提案した[6]．すなわち，ある「鍵穴」構造群に対しては，それとちょうど合致する「鍵」構造群を厳密に配置しない限り，所定の偏光変換現象が観測されないという性質に基づき「鍵」構造群についての認証を実行する．原理検証実験においては，図３中のSEM画像に示すような各構造群を電子ビーム描画装置を用いて加工し，図４上に示すように各レイヤーがあらかじめ積層した形の試料を作製した[7]．このとき，各微小構造はAuで構成され，それらの寸法は100 nm×500 nm×100 nm，レイヤー間のギャップは厚み200 nmのSiO_2層で占められている．作製した試料の「鍵」構造群部分，「鍵穴」構造群部分，「鍵＋鍵穴」構造群部分に対し，それぞれ２つの偏光子を用いたクロスニコル状態で直線偏光の光

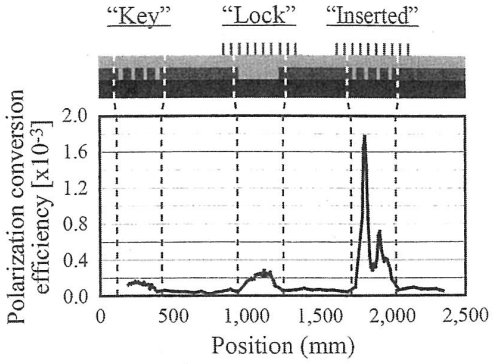

図４　試作した試料の構成とそれを用いて行った偏光変換実験の結果

を照射しつつ偏光変換された光のみを検出し，入力光強度と出力光強度の比率から光変換効率を算出した結果を図４下に示す．「鍵」構造群部分および「鍵穴」構造群部分におけるわずかな偏光変換効率の値と比較して，「鍵＋鍵穴」構造群部分においては明快な偏光変換が観測されていることがわかる．「鍵＋鍵穴」構造群部分において測定部位ごとに偏光変換効率の値にバラつきが見られるのは積層した「鍵」構造群と「鍵穴」構造群の水平方向のアライメントのずれに起因するものである．実際に「鍵＋鍵穴」構造群部分全体をSEMで観察した結果，最大で200 nm程度のずれが生じていることが確認されている．また，SiO_2層の厚みを変えて行った同様の実験において，厚みが大きくなればなるほど偏光変換効率が落ちて行くという，レイヤー間に誘起される近接場光相互作用の効果を示唆する結果も得られている[7]．

以上の結果は，精微に設計・作製された微小構造によりそれらに由来するナノ電子系における電荷の特徴的な振る舞いを「伝搬する光」の変調という明快な形で取り出せることを実証したという点において意義深い成果であると評価され，認証システムとしてのみならず，ナノスケールとマクロスケールとの間のインターフェース技術の実例として現在多様な応用展開が検討されている．

４．外部制御可能な近接場光相互作用とそれに伴うマクロ光学応答の変調

半導体量子ドットは，注入された電子や正孔およびそれらにより形成される励起子を閉じ込めることができる３次元微小構造であり，その微細構造に起因した量子的なエネルギー準位を示す．その微小性と揺らぎの少ない安定した光吸収や発光の特性から近接場光を発生させる光源としても積極的に活用されており，近接場光を介した量子ドット間のエネルギー移動を巧みに制御することで機能的な光学応答を実現する「ナノフォトニックデバイス」として論理ゲート，伝送路，スイッチといった多様な要素デバイスが試作されている[8]．近接場光に基づくエネルギー移動の基本原理について，寸法の制御された大小２つの量子構造を想定した図５を用いて説明する．このとき，小さい量子構造QD_Sと大きい量子構造QD_Lの寸法は，QD_Sにおける励起子の基底準位E_{S1}とQD_Lにける第一励起準位E_{L2}とがエネルギー的に一致するような寸法比（立方体構造の場合は$1:\sqrt{2}$）を満たすものとする．一般に，QD_LにおけるE_{L2}はその波動関数が奇関数となることから「伝搬する光」では励起することができない光学禁制な準位として扱われるが，図５上図に示すように，２つの量子構造が近接する状況においては隣に位置するQD_Sが近接場光源として働くことで形成される局所的な電場勾配により励起されることが可能になる．その結果，両量子構造のバリアー層を励

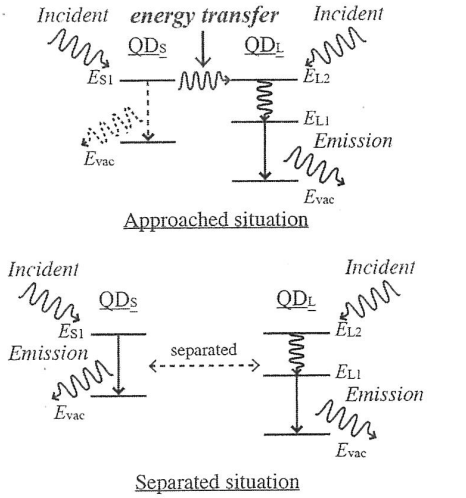

図５　近接場光を介したエネルギー移動の原理と量子構造間の距離による発光機構の差異

起した場合に E_{S1} からエネルギー的に共鳴する E_{L2} へのエネルギー移動が許容され，E_{L2} から E_{L1} への緩和に伴い QD_L からの発光が観測されると同時に，QD_S からの発光は観測されないことになる．もちろん2つの量子構造の間隔が十分離れている場合には，図5下図に示すように，両量子構造からの発光は個別に観測される．この2つの状況を区別する量子構造間の間隔は近接場光相互作用のスケールにより規定され，ちょうど各量子構造の寸法程度であることが知られている[2]．

各量子構造からの発光はそれぞれのエネルギーギャップによって決定される個別のエネルギーをもっており，図5上図および下図で示したナノ電子系における描像の差異はマクロスケールでは発光スペクトルの差異として観測される．すなわち，量子構造間の間隔をそれらの寸法程度を目安に操作することにより，量子ドット間エネルギー移動の発生頻度および自身で発光可能な2種類の量子構造の比率を制御でき，ひいてはその効果をマクロスケールでの発光スペクトルの変化として取り出すことが可能である．われわれは，シリコンゴムの一種として知られるPDMS (Polydimetylsiloxane) という柔軟性基板の表面にエネルギー的に共鳴関係および非共鳴関係にある2通りの組み合わせの CdSe/CdS 量子ドットをそれぞれ均一に散布した試料を用意し，各試料の湾曲に伴う量子ドット間エネルギー移動の変化とそれに伴う発光スペクトルの変化について検証実験を行った[9]．CdSe/CdS 量子ドットの組み合わせについては，あらかじめ共鳴関係に伴うエネルギー移動の効果が実証されている組み合わせを参考に採用した[10]．それぞれの試料の湾曲前後に計測した発光スペクトルから色度座標を同定し，色度図上での変化の様子として比較した結果を**図6**に示す．図6上図が共鳴関係にある組み合わせ，図6下図が非共鳴関係にある組み合わせを用いた場合の結果である．共鳴関係にある組み合わせにおいては色度図上で明らかな色度座標のシフトが確認でき，試料の湾曲前には近傍の量子ドットへのエネルギー移動により自身では発光できなかった量子ドットが，湾曲後は自身で発光できるようになったことによる影響が見受けられる．一方で，非共鳴関係にある組み合わせにおいては，試料の湾曲により単位面

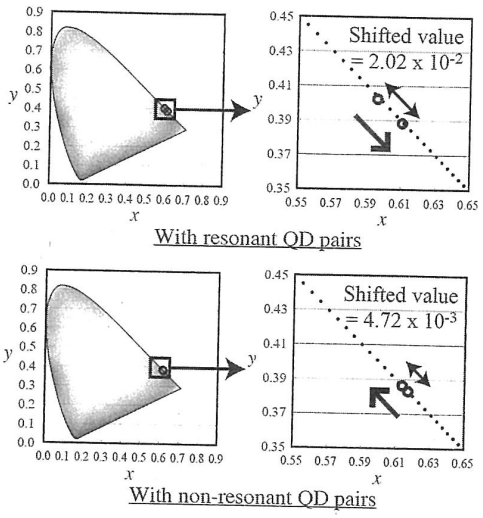

図6　試料基板の湾曲による発光特性の変化

積あたりの量子ドットの個数こそ変わるものの発光可能な量子ドットの比率自体は変わらないため，色度図上でも大きな変化は確認できない．以上の結果は，上述した階層構造において，ナノ電子系での微小変化をマクロな光学応答の明快な変調として取り出せることを近接場光を介したエネルギー移動の変調という最も典型的な形で実証したものであるといえる．

5．ナノ-マクロ間階層的光学応答を利用した階層型ホログラム

ホログラムはその見た目の特異性により，目視で簡便に判別可能なセキュリティツールとして，グラフィックアーツ等をはじめ，各種金券類，クレジットカード，ID 証明，ブランドプロテクション等に広く利用されている．一方で，ホログラムの偽造に関しては近年ホログラム構造の微細化や他技術との融合といったさまざまな対策が講じられてはいる[11]ものの，そもそもホログラムのように物理的な「見た目」に基づいて安全性が保証されるセキュリティデバイスは偽造防止という観点において原理的に必ずしも安全とはいい切れないことが指摘されている[12]．われわれは，既存のホログラムに対してその立体像の見た目を維持しながらナノ寸法の微細構造を新たに付与することで，近接場光を介することによってのみ読み出

し可能なセキュリティ情報を内包した「階層型ホログラム」を提案している[13]．本提案は，ホログラム像の見た目に寄与する「伝搬する光」と「伝搬しない光」である近接場光とではそれぞれの光学応答が原理的に独立していることを有効に利用しているという点で上述の「階層構造」の有用性をまさに体現した系となっており，ホログラム像で保証されるオバート機能と近接場光情報で保証されるコバート機能とを融合した高度な「オバート・コバート共生型セキュリティデバイス」と位置付けられる．

試作した階層型ホログラムの基本構成を図7に示す[14]．量産化に適しているという点から一般社会に広く普及しているエンボス型ホログラムは，図7右上に示すように，入射した光を所望の方向へ回折させ3次元立体像を形成するよう精微に設計された周期的な凹凸構造をもつ．試作デバイスにおいては，そのような周期構造の内部に，特徴的な近接場光分布を発生させる非周期のナノ構造を付与している．このようなナノ構造の存在は周期的な凹凸構造により回折された「伝播する光」により形成されるホログラム像の見た目には原理的に影響を及ぼさないという点により，上述の「階層構造」が保証されている．埋め込まれたナノ構造に由来する近接場光分布は「ナノフォトニックコード」と定義し，その読み出しには近接場光学顕微鏡(SNOM)を用いる．SNOMは，近接場光分布を誘起するための光を観測対象に照射しつつ，微小プローブの2次元走査によりその表面構造近傍に発生する近接場光分布の様子を取得する．

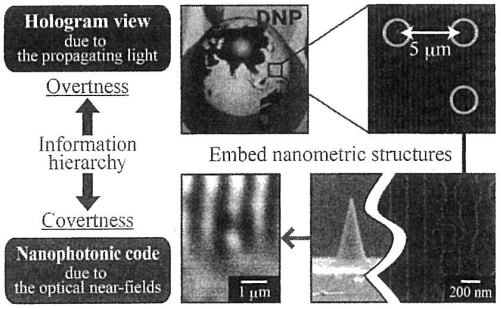

図7　階層型ホログラムの概要と大日本印刷（株）製の3次元計算機合成ホログラム・バーチャグラム®をベースに試作されたデバイスの外観

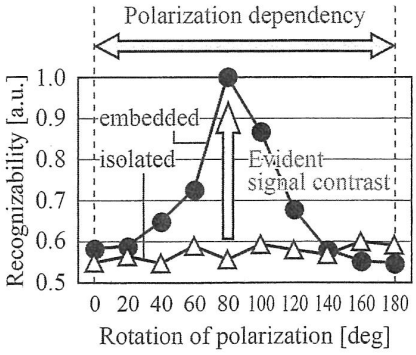

図8　照射光の偏光状態に依存する読み出されたナノフォトニックコードの特性

る．読み出された近接場光分布を，ホログラム本来の周期構造に由来する分布とのコントラストを元に独自に定義した信号顕在度(Recognizability)を用いて評価した結果を図8に示す．縦軸が信号顕在度，横軸が近接場光分布を誘起するために照射した光の偏光状態を表す．近接場光相互作用に基づいて定義されるナノフォトニックコードに特有の性質として，照射した光に対する明快な偏光依存性と顕在化効果とが確認された．これらの性質は，光照射に伴う表面電荷の局在と散逸がナノスケールの非周期構造とその周辺の周期構造において，それぞれ選択的に発生することによるものであり，今後近接場光分布の設計によりセキュリティ情報の符号化を進めていく上で重要な特徴である．

ナノフォトニックコードとしての近接場光分布は，階層型ホログラムに埋め込まれたナノ構造と微小プローブ先端との間に働く相互作用の結果として初めて読み出されることが重要であり，例えばバーコードで符号化された情報をバーコードリーダーで読み出すといった直接的な読み出しの方式とは本質的に異なる．昨今われわれはこのような特徴に基づくセキュリティシステムの概念を「相互作用型人工物メトリクス」と定義し，デバイスの設計から認証システム全体の構築までを体系的に進めている．そのセキュリティ性能は，ナノフォトニックコードで符号化されたセキュリティ情報からデバイス(ナノ構造)とリーダー(微小プローブ)の双方を正確に推定し複製すること

が逆問題的に困難であることによるデバイスおよびリーダーの個別性と耐クローン性から原理的に保証されるものであり，新しい情報物理セキュリティ技術としてのさらなる展開が期待される．

6．おわりに

本稿では，近接場光の概念を導入することで初めて体現される光学的な階層構造とそれに基づいて機能するナノ光情報システムの実態について，いくつかの実装例を挙げて解説した．本稿でとりあげたシステムは，いずれもマクロな環境下で活用されることを前提に提案・実証されたものであり，ナノフォトニクスの応用領域の拡張といった観点からも重要な施策の一つであるといえる．また，これらの特徴的な機能は，特殊な機能性材料等は一切用いずに実現されている．材料工学ではなく，寸法形状工学に基づいたナノ構造の設計と作製によりあたかも特殊な素材を用いているかのような効果や機能を得られることは，ナノフォトニクスにおける「質的変革」の新たな側面として今後もさまざまな分野において革新的な展開が期待される特質である．

謝　辞

本研究の一部は，新エネルギー・産業技術総合開発機構（NEDO）省エネルギー革新技術開発事業，文部科学省イノベーションシステム整備事業，および総務省戦略的情報通信研究開発推進制度（SCOPE）の委託研究の支援により行なわれました．また，日頃より有益なご議論とご協力をいただいております東京大学・大津研究グループの関係各位，横浜国立大学・松本勉教授，大日本印刷株式会社の関係各位に厚く御礼申し上げます．

参考文献

1）稲葉文男，一岡芳樹 編，「光コンピューティングの事典」，朝倉書店(1997)
2）M. Ohtsu, K. Kobayashi (eds.), *Optical Near-fields* (Springer-Verlag, 2003)
3）M. Ohtsu, K. Kobayashi, T. Kawazoe, T. Yatsui, M. Naruse, *Principles of Nanophotonics* (Taylor & Francis, 2008)
4）M. Naruse, T. Inoue, H. Hori, *Japanese J. Appl. Phys.* **46**, 6095 (2007)
5）M. Naruse, T. Yatsui, H. Hori, M. Yasui, M. Ohtsu, *J. Appl. Phys.* **103**, 113525 (2008)
6）M. Naruse, T. Yatsui, T. Kawazoe, N. Tate, H. Sugiyama, M. Ohtsu, *Appl. Phys. Exp.* **1**, 112101 (2008)
7）N. Tate, H. Sugiyama, M. Naruse, W. Nomura, T. Yatsui, T. Kawazoe, M. Ohtsu, *Opt. Exp.* **17**, 1 (2009)
8）M. Ohtsu, T. Kawazoe, T. Yatsui, M. Naruse, *IEEE J. Selected Topics in Quantum Electronics*, **14**, 1404-1417 (2008)
9）N. Tate, M. Naruse, W. Nomura, T. Kawazoe, T. Yatsui, M. Hoga, Y. Ohyagi, Y. Sekine, H. Fujita, M. Ohtsu, *Opt. Exp.* **19**, 18260 (2011)
10）W. Nomura, T. Yatsui, T. Kawazoe, M. Ohtsu, *J. Nanophotonics*, **1**, 011550 (2007)
11）谷口彰敏，「ホログラム最新技術 ~感光材料の開発から実製品への応用まで~」，情報機構(2006)
12）S.P. McGrew, *Proc. SPIE, Optical Security and Anticounterfeiting*, **66**, 1210 (1990)
13）N. Tate, W. Nomura, T. Yatsui, M. Naruse, M. Ohtsu, *Opt. Exp.* **16**, 607 (2008)
14）N. Tate, M. Naruse, T. Yatsui, T. Kawazoe, M. Hoga, Y. Ohyagi, T. Fukuyama, M. Kitamura, M. Ohtsu, *Opt. Exp.* **18**, 7497 (2010)

[Ⅳ] PUBLISHED BOOKS

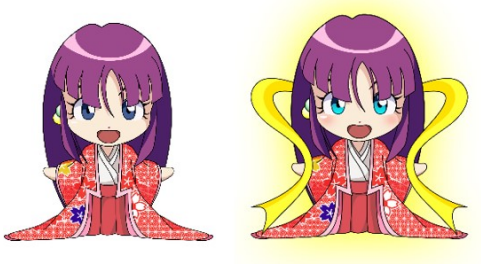

Motoichi Ohtsu
Editor

Handbook of Nano-Optics and Nanophotonics

With 732 Figures and 24 Tables

Springer Reference

Contents

Volume 1

Dressed Photon

ドレスト光子

光・物質融合工学の原理

大津 元一
［著］

朝倉書店

目　　次

Motoichi Ohtsu
Editor

Progress in Nanophotonics 2

Springer

Contents